ISSW 2025

20th International Ship Stability Workshop

Chania (Crete), Greece | 1 - 3 October 2025

Proceedings

Edited by:
K.J. Spyrou
D. Konovessis

ISSW 2025

20th International Ship Stability Workshop

Chania (Crete), Greece | 1 - 3 October 2025

Proceedings

Edited by:

Kostas J. Spyrou

Dimitris K. Konovessis

School of Naval Architecture and Marine Engineering
National Technical University of Athens

Hellenic Institute of Marine Technology

Proceedings of the 20th International Ship Stability Workshop (ISSW 2025)
Chania, Greece, 1-3 October 2025

Editors: Kostas J. Spyrou & Dimitris K. Konovessis

ABOUT THE INTERNATIONAL SHIP STABILITY WORKSHOP

The International Ship Stability Workshop (ISSW) is a part of a longstanding series of international technical meetings in the field of ship stability, dynamics and safety, consisting of the STAB conferences, which are held every third year, and the ISSW workshops, which are held in the years between the conferences. These conferences and workshops are initiated and supervised by an International Standing Committee (ISC) and arranged and hosted by a Local Organizing Committee, each time in different corners of the world. General information about ISSW, STAB, ISC, SRDC (Stability Research and Development Committee), proceedings from past events, and other information concerning ship stability, dynamics and safety, can be found at www.shipstab.org.

PREVIOUS INTERNATIONAL SHIP STABILITY WORKSHOPS

1995, Glasgow, UK
1996, Osaka, Japan
1997, Hersonissos, Crete, Greece
1998, St. John's, Newfoundland, Canada
2001, Trieste, Italy
2002, New York, USA
2004, Shanghai, China
2005, Istanbul, Turkey
2007, Hamburg, Germany
2008, Daejeon, Korea
2010, Wageningen, the Netherlands
2011, Washington, USA
2013, Brest, Brittany, France
2014, Kuala Lumpur, Malaysia
2016, Stockholm, Sweden
2017, Belgrade, Serbia
2019, Helsinki, Finland
2022, Gdansk, Poland
2023, Istanbul, Turkey

DISCLAIMER

CONTENTS

Session 4: Design and operational safety

Session 5: Probabilistic methods to ship stability and safety

Session 6: Application experience with the second generation intact stability criteria and possible regulatory updates

Session 7: Stability and safety of special vessels

Session 8: Emerging technologies and impact on stability and safety

Session 1
Studies on roll dynamics

Numerical investigation of avoiding parametric roll resonance through acceleration and deceleration

Hasan Islam Copuroglu, *Karadeniz Technical University,* hasancopuroglu@ktu.edu.tr
Emre Pesman, *Karadeniz Technical University,* pesman@ktu.edu.tr
Toru Katayama, *Osaka Metropolitan University,* katayama.marine@omu.ac.jp

ABSTRACT

This study examines the feasibility of avoiding resonance regions of parametric roll motion by adjusting a vessel's speed through acceleration or deceleration. It aims to address key operational questions, such as: "Should a vessel traverse the resonance region of parametric roll motion through acceleration or deceleration?" and "To what extent does the magnitude of acceleration or deceleration influence the reduction of roll amplitudes while passing through the resonance region?" Distinct from existing literature, this study is a numerical investigation, with the analysis conducted using a one-degree-of-freedom nonlinear roll motion equation. Considering that the study focuses on a single wave with a wavelength equal to the ship's length, velocity is identified as the primary tuning parameter in ship operation. The findings indicate that parametric roll motion can be mitigated by increasing the magnitude of acceleration or deceleration. However, the effectiveness of this approach is significantly influenced by the performance capabilities of the vessel's propulsion and braking systems. Comparisons with available experimental data are conducted to assess the representativeness of numerical study.

Keywords: Roll motion, Resonance region, Viscous effect, Parametric rolling

1. INTRODUCTION

The phenomenon of ship capsizing induced by parametric resonance, particularly in head and following wave conditions, has emerged as a critical safety concern, with incident frequency reportedly increasing in recent decades. Parametric roll represents a significant threat to maritime safety, jeopardizing not only vessel integrity but also the lives of crew members and the security of cargo. Documented cases involving container ships, fishing vessels, and Pure Car and Truck Carriers underscore the severity of this dynamic instability [1, 2]. Despite conformity with International Maritime Organization (IMO) regulations and compliance with the IS Code, vessels remain susceptible to parametric instabilities under adverse sea conditions. This vulnerability accentuates the pressing need for more precise modeling of ship motions in wave environments to enhance existing stability criteria [3].

Although parametric rolling has been the focus of substantial research, some complexities remain unresolved. A notable example includes the catastrophic loss of a C11-class container vessel during a 1998 storm event, which has served as a compelling impetus for continued investigation into the mechanisms and predictive models of such occurrences [4]. Recent advancements in numerical modeling and experimental methods have significantly improved the understanding of parametric resonance, facilitating the development of more robust and seaworthy ship designs.

Foundational work in this field is initiated by Watanabe [5] and Kempf [6], with subsequent contributions from Graff and Heckscher [7], Kerwin [8], Korvin-Kroukovsky [9], and Paulling and Rosenberg [10], who expanded the theoretical understanding of roll motion in a seaway. Paulling et al. [11] are credited with the first empirical identification of parametrically induced rolling in San Francisco Bay. While the phenomenon has long been acknowledged, its implications have garnered renewed attention due to its association with major maritime accidents. Experimental evidence has demonstrated that container ships, even when operated within IMO IS Code limitations, may experience substantial parametric rolling in irregular short-crested following seas and are at risk of capsizing in long-crested irregular conditions [12].

As a result, naval architects, regulatory bodies, and researchers have intensified efforts to investigate and mitigate this phenomenon. Scholars such as Neves and Rodríguez [2], Spyrou [13], and Bulian et al. [14] have explored the nonlinear dynamics of parametric roll, including the influence of tuning parameters on instability thresholds. Parallel studies by Belenky [15], Bulian et al. [16], Francescutto [17], and Hashimoto et al. [18] have addressed the stochastic nature of the roll response, emphasizing probabilistic modeling approaches.

Historically, parametric roll analyses have relied on potential flow theories, including strip method, free surface Green functions, and Rankine source methods. However, with the evolution of computational technologies, Computational Fluid Dynamics (CFD) has emerged as a powerful tool in this domain. For instance, Sadat-Hosseini et al. [19] applied CFD techniques to ONR Tumblehome hull forms, revealing strong couplings between pitch, heave, and roll motions. Tezdogan et al. [20] used CFD simulations on a KCS container ship to assess how increased added resistance impacts roll behavior during resonance events. Liu et al. [21] further expanded the analysis by incorporating internal liquid sloshing, identifying shifts in the roll natural period and changes in the unstable frequency bands.

Despite the high computational cost associated with CFD, these methods complement experimental findings and provide enhanced resolution of hydrodynamic interactions. Model-scale experiments remain the gold standard for capturing the intricate behaviors associated with parametric rolling. Zhou et al. [22] analyzed the roll behavior of an Offshore Research Vessel (ORV) with a low freeboard, observing that periodic deck immersion significantly compromised vessel stability. Likewise, Pesman et al. [23] investigated the effects of velocity changes on Ro-Ro vessels, concluding that deceleration phases tend to preserve large roll amplitudes during resonance. Schumacher et al. [24] characterized parametric rolling conditions across various wave spectra, while Yu et al. [25] tested early-warning algorithms through scaled model validations. Additional studies on fishing vessels and Floating Production Storage and Offloading (FPSO) units by Ghamari et al. [26] and Greco et al. [27] highlighted the destabilizing influence of water-on-deck phenomena.

Hybrid methodologies that integrate potential flow theory with CFD approaches have proven effective in unifying computational and experimental insights. Zhou et al. [28] utilized such a hybrid to predict roll damping coefficients, and Maki et al. [29] applied a stochastic-deterministic framework to evaluate complex motion responses. These studies align with Bu et al. [30], who developed a three-degree-of-freedom (3DOF) model revealing nonlinear relations between wave height and roll amplitude.

Numerical simulations have also seen substantial refinement. Liu and Papanikolaou [31] developed a three-dimensional nonlinear time-domain framework for container ship roll modeling, corroborated by simulation outcomes presented by Ma et al. [32]. Acanfora et al. [33] employed six-degree-of-freedom (6DOF) modeling in irregular wave conditions, demonstrating the sensitivity of resonance onset and roll amplitudes to wave pattern variability. Pesman [34] further examined the influence of ship acceleration and deceleration in longitudinal waves on roll amplitudes using numerical methods.

The progression from classical theoretical models to comprehensive numerical simulations and experimental validations underscores the complexity and practical significance of parametric roll phenomena. The integration of CFD techniques, hybrid modeling approaches, and scale experiments has contributed to a more robust predictive capability, guiding safer and more resilient vessel designs.

This study focuses on the dynamic behavior of ships experiencing velocity changes—specifically acceleration and deceleration—while transitioning through the parametric resonance region in regular head seas. In contrast to prior works [3, 23, 34], which primarily analyze parametric rolling under steady velocities or during already unstable conditions, this research uniquely explores how speed variations introduced prior to the onset of rolling may influence the development of parametric instabilities.

By employing numerical methods, this study aims to elucidate critical aspects of roll motion dynamics that occur during transitional speed states near resonance. The insights gained are expected to inform operational strategies, enabling ship

operators to proactively adjust speed profiles to mitigate rolling risks.

2. MATHEMATICAL MODEL

In the present study, a simplified form of the nonlinear one-degree-of-freedom (1DOF) parametric roll motion model, originally proposed by Bulian [35], is employed. Bulian analyzed this nonlinear equation using the first-order approximation of the Krylov–Bogolyubov (KB) method in the frequency domain and assessed the stability of the resulting solutions through the Routh–Hurwitz stability criterion. Subsequently, Peşman and Taylan [36] adopted a more simplified variant of Bulian's formulation to investigate the relation between bifurcation behavior and the restoring moment curves corresponding to wave crest and trough conditions. In their approach, the restoring moment term in the nonlinear roll equation is represented by a single sine function, derived from the polynomial approximations of the hydrostatically computed restoring moment curves. These curves, generated under both wave crest and trough conditions using a hydrostatic stability program, are fitted with seventh-degree polynomials to extract the amplitude and mean value parameters for the sine representation, as presented in Equation (1). The restoring moment curves corresponding to wave crest and wave trough conditions are obtained using a hydrostatic stability analysis program, and seventh-degree polynomial functions are fitted to these curves to determine the amplitude and mean value parameters of the equivalent sin(e) function.

$$\ddot{\varphi} + 2\mu\dot{\varphi} + \beta\dot{\varphi}|\dot{\varphi}| + \delta\dot{\varphi}^3 + \frac{{\omega_0}^2}{GM_0}\sum_{n=1}^{4}\begin{pmatrix} m_{2n-1} + \\ k_{2n-1}\,cos(\,\omega_e t)\end{pmatrix}\varphi^{2n-1} = 0 \quad (1)$$

In the equation above, 2μ denotes the linear damping coefficient, while β and δ represent the nonlinear damping coefficients. ω_0 refers to the natural frequency of the system, and ω_e is the encounter frequency. The terms m_{2n-1} and k_{2n-1} are defined in Equations (2) and (3), respectively. Both linear and nonlinear damping coefficients are evaluated using the method proposed by Ikeda (1979).

$$m_{2n-1} = \frac{c_{2n-1throu} + c_{2n-1crest}}{2} \quad (2)$$

$$k_{2n-1} = \frac{c_{2n-1throu} - c_{2n-1crest}}{2} \quad (3)$$

In Equations (2) and (3), the coefficients $c_{2n-1trough}$ and $c_{2n-1crestc}$ represent the polynomial coefficients fitted to the restoring moment lever curves corresponding to wave trough and crest conditions, respectively. These restoring moment levers are obtained through a hydrostatic solver. Equation (1) is analyzed in the frequency domain using the first-order approximation of the Krylov–Bogolyubov (KB) method to identify bifurcation behavior at the minimum and maximum resonant velocities. Additionally, numerical integration is performed using the Dormand–Prince (DP) method to simulate scenarios involving acceleration and deceleration. Further methodological details regarding the KB and DP methods are available in the study by Peşman and Taylan [36].

2.1. Mathematical background of the study

The roll motion behavior is represented through a mathematical formulation described as an initial value problem comprising ordinary differential equations. Due to the system's inherent nonlinearity, minor deviations in the initial conditions can significantly alter the resulting dynamics. To identify stable and unstable attractors across different excitation frequencies, one may apply approximate analytical methods within the frequency domain or adopt numerical integration techniques in the time domain. These approaches enable the visualization of attractor structures by plotting limit cycle amplitudes as functions of initial conditions. In this study, the Krylov–Bogolyubov (KB) method is employed for the frequency-domain analysis, while the Dormand–Prince (DP) method is utilized for the time-domain simulations. The resulting limit cycle amplitude distributions consistently indicate the existence of high-amplitude attractors. Notably, frequency-domain solutions offer superior practicality in detecting attractor configurations compared to their time-domain counterparts when initial conditions are varied.

In a broader dynamical context, the emergence of the jump phenomenon—attributable to nonlinear behaviors near unstable bifurcations—is characterized by the structure of the system's frequency response curve, as shown in Figure 1 [37]. This discontinuous transition in response amplitude can be triggered by variations in the excitation frequency. Notably, the occurrence of such jumps is evident even when the frequency is varied at an

extremely slow rate, approaching a quasi-static condition, as depicted in Figure 1.

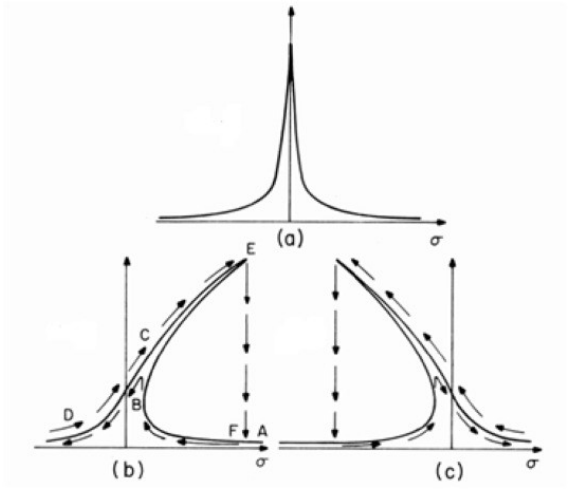

Figure 1. Explanation of jump phenomenon in frequency domain-a) a linear spring, b) a hardening spring, c) a softening spring (Nayfeh and Mook, [37]).

To achieve more accurate predictions, parametric roll motion in head waves should be modeled by incorporating nonlinear terms, as formulated in Equation (1). The nonlinear characteristics of this equation also give rise to the jump phenomenon, as illustrated in Figure 2 through the frequency domain solution.

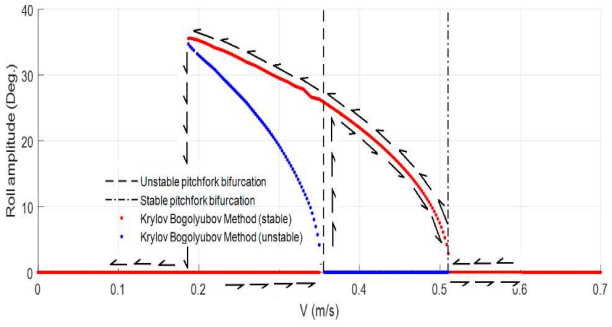

Figure 2. Jump phenomenon representation for parametric roll motion.

As previously mentioned, to replicate the response depicted in Figure 2, the variation in encounter frequency—represented in this study by ship velocity—must be sufficiently slow, effectively approaching zero. However, the rate of frequency variation, or in practical terms, the acceleration, significantly influences the system's dynamic response. The primary objective of this study is to investigate how varying magnitudes of acceleration affect parametric roll behavior. In the simulations, the model is accelerated from 0.3 m/s to 0.55 m/s and decelerated to 0 m/s under different acceleration rates. The initial roll angle and angular velocity for both acceleration and deceleration cases are set to (2°, 5°,10°) and 0, respectively.

Additionally, limit cycle amplitudes corresponding to different initial conditions are computed using a time-domain numerical solver and presented in Figure 3 for model velocities of 0.3 m/s, 0.4 m/s, and 0.55 m/s. As illustrated in Figure 3(a), two distinct attractors emerge at 0.3 m/s due to a bifurcation: a small-amplitude and a large-amplitude attractor. Figure 3(b) indicates that only a single large-amplitude attractor exists at the resonant velocity of 0.4 m/s. In contrast, Figure 3(c) reveals the presence of only a small-amplitude attractor at 0.55 m/s.

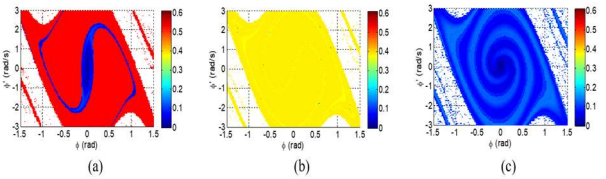

Figure 3. Limit cycle roll amplitudes with respect to initial values a) 0.3 m/s, b) 0.4 m/s, c) 0.55 m/s.

The attractors identified through time-domain numerical simulations, along with their correspondence to the stable solutions obtained from frequency-domain analysis, are illustrated in Figure 4 for model velocities of 0.3, 0.4, and 0.55 m/s. For constant forward speeds, limit cycle roll amplitudes can be reliably estimated using time-domain numerical solvers. The present study demonstrates that the influence of acceleration on roll motion can likewise be effectively evaluated through time-domain numerical simulations using a straightforward implementation. This approach has also been validated by experimental findings.

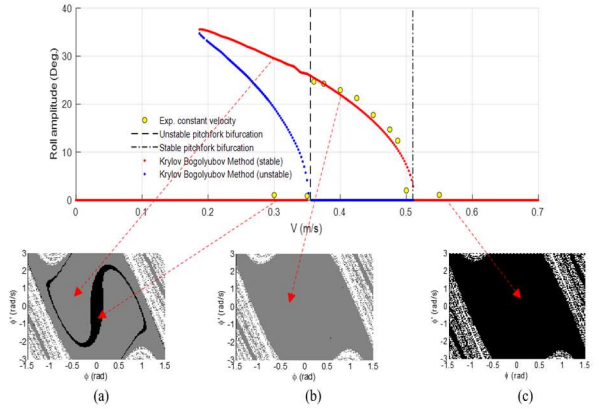

Figure 4: Attractors and relation with frequency domain results: grey color represents large angle attractor, black color represents small angle attractor; a) 0.3 m/s, b) 0.4 m/s, c) 0.55 m/s.

3. NUMERICAL SETUP

3.1. The Sample Ship

The sample ship analyzed in this study is a Ro-Ro type ship model, also a validation study with experimental tests conducted in the towing tank at Osaka Metropolitan University, Japan. The experiments account for 6 degrees of freedom (DOF). The ship model, designated as “Model 35”, is tested without bilge keels or appendages. Its primary characteristics are presented in Figure 5 and Table 1.

Table 1: Main characteristics of the sample ship model

Scale	1/50
Length [m]	1.12
Breadth [m]	0.246
Depth [m]	0.139
Draught [m]	0.059
Displacement[kg]	10.124
KG [m]	0.107
GM [m]	0.023
Roll Natural Frequency [rad/s]	5.236
Moment of Inertia [kgm^2]	0.12237

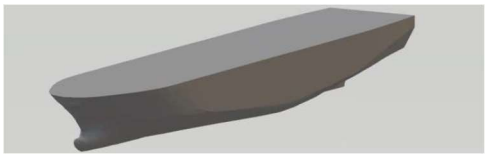

(a)

(b)

Figure 5: Model 35 (a) CAD view (b) profile view

The velocity range is categorized into three distinct zones, as shown in Figure 6: 'Before the unstable bifurcation (I),' 'Between the two bifurcations (II),' and 'After the stable bifurcation (III).' Zone II corresponds to the primary resonance region, and this study primarily concentrates on examining velocities within this critical zone. Hazardous velocities within the main resonance region can be identified using the Ince-Strutt diagram, which is derived by solving the Mathieu-Hill equation through Floquet theory [38]. As it can be seen yellow dots which are experimental results and the diagram (as the red line) has same regime.

By recognizing these hazardous velocities, operators can adjust the ship's speed to reduce potential risks. The scenarios, illustrated in Figure 6, are analyzed in this study. Roll amplitudes with respect to initial values are calculated and plotted for various model speed in Figure 7. Influence of acceleration on the phenomenon is also presented in Figure 7; acceleration cause the diagrams getting closer to each other and deceleration cause the diagrams moving away from each other.

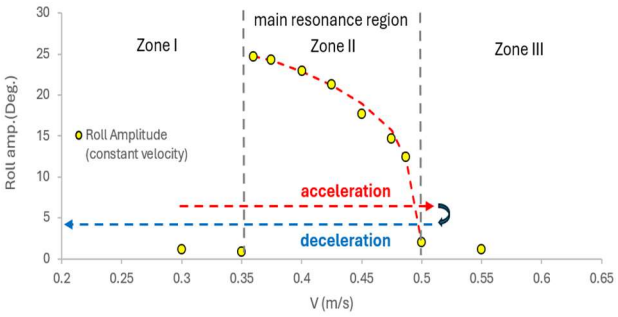

Figure 6. Main numerical conditions and comparison with experimental results shown by velocity and roll amplitude zones

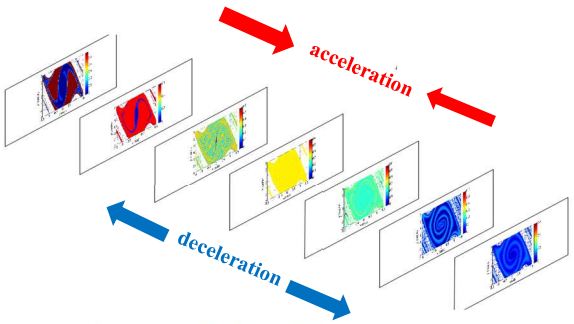

Figure 7. Main numerical conditions with shown in frequency domain

4. RESULTS

The results are divided into two main categories; phase 1 shows the results for acceleration cases and phase 2 shows the results for deceleration cases.

4.1. Phase 1 Results

The graph in Figure 8 presents the maximum roll angle values as a function of acceleration magnitude. In the figure, large negative acceleration values indicate deceleration, while positive values represent acceleration. Calculations are performed for three different initial conditions: 10°, 5°, and 2°, all with an initial angular velocity of zero. It can be observed from the figure that roll amplitudes decrease in regions where the magnitude of acceleration is high. Specifically, under acceleration,

roll amplitudes exhibit a parabolic form as the acceleration magnitude increases. For initial conditions of 2° and 5°, a noticeable jump in roll amplitude is observed within the acceleration range of approximately 0.14 to 0.2 × 10^{-3} g. As an example, Figure 9 illustrates a chaotic response between 0.14 × 10^{-3} g and 0.15 × 10^{-3} g for the 5° initial condition.

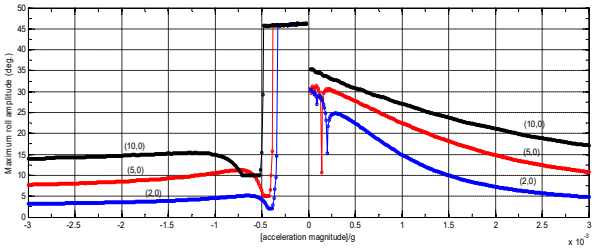

Figure 8. Maximum roll amplitudes with respect to magnitude of acceleration for initial values (10° and 0°/s)/s, (5° and 0°/s) and (2° and 0°/s)

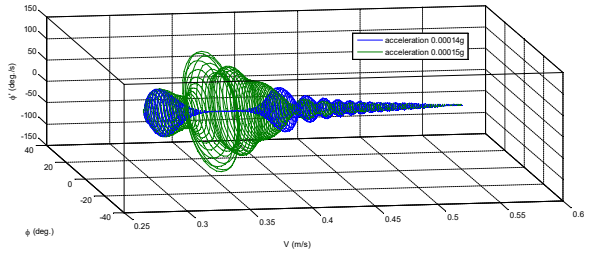

Figure 9. Phase diagram of parametric roll motion for acceleration values; 0.00014g and 0.00015g (initial value of 5° and 0°/s)

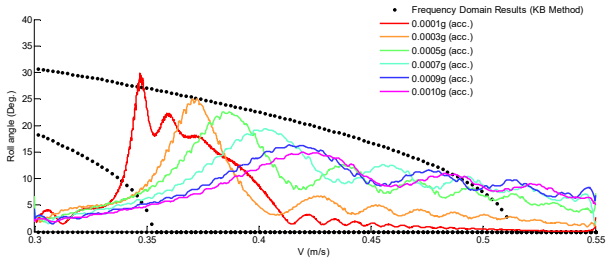

Figure 10. Roll angle envelope with respect to model velocity for acceleration at initial value [2° and 0°/s] (0.0001g-0.0010g)

The graph in Figure 10 presents roll amplitude values in the frequency domain as a function of ship speed, calculated using the Krylov–Bogoliubov (KB) method. The results exhibit bifurcation behavior. An **unstable bifurcation** is observed at a ship speed of approximately 0.35 m/s, while a **stable bifurcation** appears at around 0.51 m/s. As shown in Figure 10, at lower acceleration magnitudes, the maximum roll angles occur near the unstable bifurcation point. As the acceleration magnitude increases, the speed at which the maximum roll amplitude is observed shifts toward the stable bifurcation point. However, this increase in acceleration magnitude also leads to an increase in the amplitude of the roll motion.

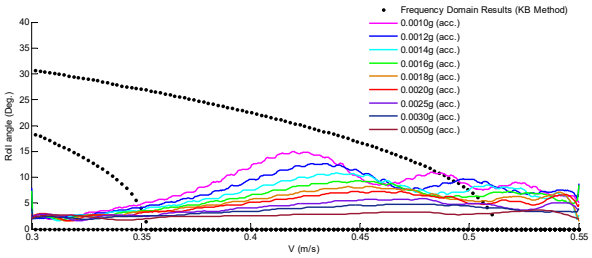

Figure 11. Roll angle envelope with respect to model velocity for acceleration at initial value [2°] (0.0010g-0.0050g)

As seen in Figure 11, a further increase in the acceleration magnitude leads to a decrease in both the oscillation amplitude and the roll angle values. This occurs because the peak point of the roll angle shifts toward higher velocity regions as the acceleration increases, reducing the overall oscillatory response.

4.2. Phase 2 Results

In high acceleration conditions, the maximum roll angles remain nearly constant up to certain threshold values—seen in Figure 8—depending on the initial conditions. Beyond these thresholds, as the deceleration magnitude decreases, a roll oscillation emerges at the corresponding initial condition. However, a sudden and significant increase in roll angles is observed as the acceleration further decreases, indicating a jump phenomenon. As an example, Figure 12 illustrates this behavior by comparing the acceleration values of 0.38× 10^{-3} g and 0.39× 10^{-3} g. The occurrence of such jump phenomena can be attributed to the behavior observed in Figure 7, where the phase diagrams generated for each speed converge under acceleration and diverge under deceleration. This implies that the roll amplitude is highly sensitive to initial conditions and varies accordingly.

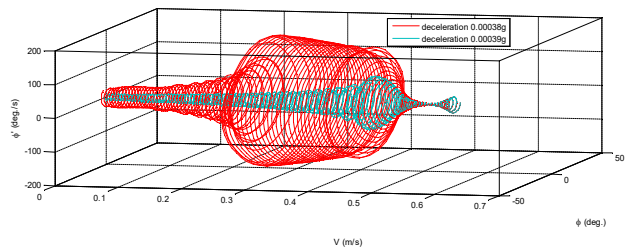

Figure 12. Phase diagram of parametric roll motion for deceleration values; 0.00038g and 0.00039g (initial value of 5° and 0°/s)

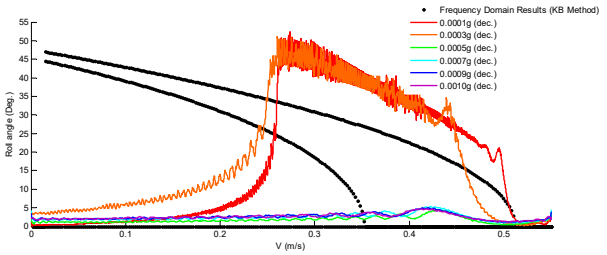

Figure 13. Roll angle envelope with respect to model velocity for deceleration at initial value [2° and 0°/s]

In Figure 13 it is observed that the jump phenomenon occurs as the threshold value increases within the range of 0.0001g to 0.0010g. As shown in Figure 13, roll amplitude values in the frequency domain are calculated using the Krylov–Bogoliubov (KB) method and plotted as a function of ship speed, revealing bifurcation characteristics. An **unstable bifurcation** is observed at a ship speed of approximately 0.35 m/s, while a **stable bifurcation** appears around 0.51 m/s. As can also be seen in Figure 13, when the deceleration magnitude is low, the maximum roll angles occur near the unstable bifurcation. As the deceleration magnitude increases, the speed at which the maximum roll angle is observed shifts toward the stable bifurcation region. However, this increase in deceleration magnitude also results in an increase in the amplitude of the roll oscillations.

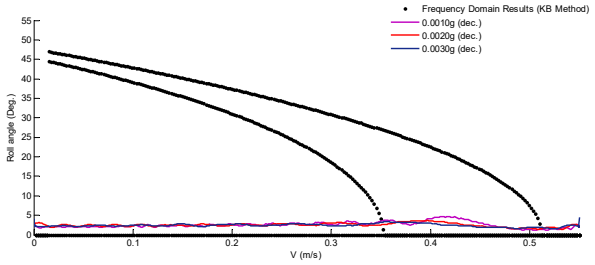

Figure 14. Roll angle envelope with respect to model velocity for deceleration at initial value [2° and 0°/s] (0.0010g-0.0030g)

5. DISCUSSION AND CONCLUSION

As the acceleration magnitude increases, roll amplitudes are observed to decrease for both acceleration and deceleration cases. This indicates that operators should pass through the parametric roll region using high-acceleration or high-deceleration maneuvers. However, deceleration appears to be significantly more critical than acceleration. For this model, it is predicted that sudden increases in roll amplitude may occur when the acceleration falls below approximately 0.5×10^{-3} g. Therefore, it is evident that deceleration should not be performed with low acceleration values under any circumstances.

Although the current simulation does not include a term for hydrodynamic forces related to forward acceleration, it is able to express the tendency of the relation between acceleration seen in the experiment and the amplitude of parametric roll, so in this paper, the simulation is used to investigate the details of relation between parametric rolling and acceleration. Although there is a quantitative difference, it is believed that the cause of this difference lies in the importance of properly considering the effects of forward acceleration on hydrodynamic forces, and its detailed investigation is planned in future research.

For future studies, the differences between the model scale and the full-scale ship can be investigated. The present study may also be extended using CFD techniques to explore additional scenarios. The effect of employing a bilge keel on roll behavior can be examined. Furthermore, the influence of maneuvering conditions, including acceleration and turning maneuvers, on parametric roll can be analyzed.

REFERENCES

[1] France W.N., Levadou M., Treakle T.W., et al., 2003, “An Investigation of Head-Sea Parametric Rolling and Its Influence on Container Lashing Systems”, *Marine Technology and SNAME News* 40, pp. 1–19. https://doi.org/10.5957/mt1.2003.40.1.1

[2] Neves M.A.S., Rodríguez C.A., 2007, “Influence of Non-linearities on the Limits of Stability of Ships Rolling in Head Seas”, *Ocean Engineering* 34, pp. 1618–1630. https://doi.org/10.1016/j.oceaneng.2006.11.010

[3] Copuroglu H.I., Pesman E., Taylan M., 2023, “Assessment of Second-Generation Intact Stability Criteria and Case

Study for a Ro-Ro Ship", *Proceedings of the 19th International Ship Stability Workshop (ISSW 23)*, Istanbul, pp. 1–10.

[4] Yoshida N., Pesman E., Copuroglu H.I., et al., 2024, "Effects of Bilge-keel Roll Damping on Parametric Rolling", *Proceedings of the 2nd International Conference on the Stability and Safety of Ships and Ocean Vehicles (STAB 2024)*, Wuxi, China, pp. 356–366.

[5] Watanabe Y., 1934, "On the Dynamic Properties of the Transverse Instability of a Ship Due to Pitching", *Journal of the Society of Naval Architects of Japan* 53, pp. 51–70.

[6] Kempf G., 1938, "Die Stabilität Beanspruchung der Schiffe Durch Wellen und Schwingungen", *Werft Reederei Hafen* 19, pp. 200–202.

[7] Graff W., Heckscher E., 1941, "Widerstand und Stabilität Versuche mit Drei Fischdampfer Modellen", *Werft Reederei Hafen* 22, pp. 115–120.

[8] Kerwin J.E., 1955, "Notes on Rolling in Longitudinal Waves", Unpublished report.

[9] Korvin-Kroukovsky B.V., 1955, "Investigation of Ship Motions in Regular Waves", *Proceedings of the Annual Meeting of the Society of Naval Architects and Marine Engineers (SNAME Transactions)*, Stevens Institute of Technology, Hoboken, USA, Paper No. 7.

[10] Paulling J.R., Rosenberg R.M., 1959, "On Unstable Ship Motions Resulting From Nonlinear Coupling", *Journal of Ship Research* 3, pp. 36–46. https://doi.org/10.5957/jsr.1959.3.2.36

[11] Paulling J.R., Kastner S., Schaffran S., 1972, "Experimental Studies of Capsizing of Intact Ships in Heavy Seas", Unpublished report.

[12] Umeda N., Hamamoto M., Takaishi Y., et al., 1995, "Model Experiments of Ship Capsize in Astern Seas", *Journal of the Society of Naval Architects of Japan* 177, pp. 207–217.

[13] Spyrou K.J., 2000, "Designing Against Parametric Instability in Following Seas", *Ocean Engineering* 27, pp. 625–653. https://doi.org/10.1016/S0029-8018(99)00019-0

[14] Bulian G., Francescutto A., Lugni C., 2004, "On the Nonlinear Modeling of Parametric Rolling in Regular and Irregular Waves", *Proceedings of the 8th International Conference on the Stability of Ships and Ocean Vehicles*, pp. 305–323.

[15] Belenky V.L., 2004, "On Risk Evaluation at Extreme Seas", *Proceedings of the 7th International Stability Workshop*, Shanghai, China, pp. 188–202.

[16] Bulian G., Francescutto A., Umeda N., Hashimoto H., 2008, "Qualitative and Quantitative Characteristics of Parametric Ship Rolling in Random Waves in the Light of Physical Model Experiments", *Ocean Engineering* 35, pp. 1661–1675. https://doi.org/10.1016/j.oceaneng.2008.09.002

[17] Francescutto A., 2007, "Intact Stability of Ships – Recent Developments and Trends", *Proceedings of the 10th International Symposium on Practical Design of Ships and Other Floating Structures*, Houston, USA, pp. 487–496.

[18] Hashimoto H., Umeda N., Matsuda A., 2006, "Experimental and Numerical Study on Parametric Roll of a Post-Panamax Container Ship in Irregular Waves", *Proceedings of STAB 2006 – 9th International Conference on Stability of Ships and Ocean Vehicles*, Rio de Janeiro, Brazil, pp. 181–190.

[19] Sadat-Hosseini H., Stern F., Olivieri A., et al., 2010, "Head-Wave Parametric Rolling of a Surface Combatant", *Ocean Engineering* 37, pp. 859–878. https://doi.org/10.1016/j.oceaneng.2010.02.010

[20] Tezdogan T., Demirel Y.K., Kellett P., et al., 2015, "Full-Scale Unsteady RANS CFD Simulations of Ship Behaviour and Performance in Head Seas Due to Slow Steaming", *Ocean Engineering* 97, pp. 186–206. https://doi.org/10.1016/j.oceaneng.2015.01.011

[21] Liu L., Feng D., Wang X., et al., 2022, "Numerical Study on the Effect of Sloshing on Ship Parametric Roll", *Ocean Engineering* 247, 110612. https://doi.org/10.1016/j.oceaneng.2022.110612

[22] Zhou Y., Sun Q., Shi X., 2022, "Experimental and Numerical Study on the Parametric Roll of an Offshore Research Vessel with Extended Low Weather Deck", *Ocean Engineering* 262, 111914. https://doi.org/10.1016/j.oceaneng.2022.111914

[23] Pesman E., Copuroglu H.I., Katayama T., 2024, "The Effect of a Ship's Acceleration and Deceleration on Parametric Roll Motion in Regular Head Waves at Resonance Conditions", *Ocean Engineering* 291, 116367. https://doi.org/10.1016/j.oceaneng.2023.116367

[24] Schumacher A., Ribeiro e Silva S., Guedes Soares C., 2016, "Experimental and Numerical Study of a Containership Under Parametric Rolling Conditions in Waves", *Ocean Engineering* 124, pp. 385–403. https://doi.org/10.1016/j.oceaneng.2016.07.034

[25] Yu L., Ma N., Wang S., 2019, "Parametric Roll Prediction of the KCS Containership in Head Waves with Emphasis on the Roll Damping and Nonlinear Restoring Moment", *Ocean Engineering* 188, 106298. https://doi.org/10.1016/j.oceaneng.2019.106298

[26] Ghamari I., Mahmoudi H.R., Hajivand A., Seif M.S., 2022, "Ship Roll Analysis Using CFD-Derived Roll Damping: Numerical and Experimental Study", *Journal of Marine Science and Application* 21, pp. 67–79. https://doi.org/10.1007/s11804-022-00254-1

[27] Greco M., Lugni C., Faltinsen O.M., 2014, "Can the Water on Deck Influence the Parametric Roll of a FPSO? A Numerical and Experimental Investigation", *European Journal of Mechanics – B/Fluids* 47, pp. 188–201. https://doi.org/10.1016/j.euromechflu.2014.01.009

[28] Zhou Y., Ma N., Lu J., Gu X., 2015, "A Study on Applicability of CFD Approach for Predicting Ship Parametric Rolling", *Proceedings of the 12th International Conference on the Stability of Ships and Ocean Vehicles*, Glasgow, UK.

[29] Maki A., Umeda N., Shiotani S., Kobayashi E., 2011, "Parametric Rolling Prediction in Irregular Seas Using Combination of Deterministic Ship Dynamics and Probabilistic Wave Theory", *Journal of Marine Science and Technology* 16, pp. 294–310. https://doi.org/10.1007/s00773-011-0133-2

[30] Bu S.-X., Gu M., Lu J., Abdel-Maksoud M., 2019, "Effects of Radiation and Diffraction Forces on the Prediction of Parametric Roll", *Ocean Engineering* 175, pp. 262–272. https://doi.org/10.1016/j.oceaneng.2019.02.006

[31] Liu S., Papanikolaou A., 2016, "Prediction of Parametric Rolling of Ships in Single Frequency Regular and Triple Frequency Group Waves", *Ocean Engineering* 120, pp. 274–280. https://doi.org/10.1016/j.oceaneng.2016.03.023

[32] Ma S., Ge W., Ertekin R.C., et al., 2018, "Experimental and Numerical Investigations of Ship Parametric Rolling in Regular Head Waves", *China Ocean Engineering* 32, pp. 431–442. https://doi.org/10.1007/s13344-018-0045-6

[33] Acanfora M., Balsamo F., Lauria D., Rizzuto E., 2020, "A New Identification Method for Non-linear Roll Resonance in Irregular Waves", *Ocean Engineering* 197, 106809. https://doi.org/10.1016/j.oceaneng.2019.106809

[34] Peşman E., 2016, "Influence of Variable Acceleration on Parametric Roll Motion of a Container Ship", *Journal of ETA Maritime Science* 4, pp. 205–214. https://doi.org/10.5505/jems.2016.74946

[35] Bulian G., 2004, "Estimation of Nonlinear Roll Decay Parameters Using an Analytical Approximate Solution of the Decay Time History", *International Shipbuilding Progress* 51, pp. 5–32.

[36] Peşman E., Taylan M., 2012, "Influence of Varying Restoring Moment Curve on Parametric Roll Motion of Ships in Regular Longitudinal Waves", *Journal of Marine Science and Technology* 17, pp. 511–522. https://doi.org/10.1007/s00773-012-0179-9

[37] Nayfeh A.H., Mook D.T., 2008, *Nonlinear Oscillations*, John Wiley & Sons, New York.

[38] Mathieu É., 1868, "Mémoire sur le Mouvement Vibratoire d'une Membrane de Forme Elliptique", *Journal de Mathématiques Pures et Appliquées* 13, pp. 137–203.

Experimental investigation of the effect of wave steepness on a damaged Ro-Pax ship model in regular waves

Mehmet Zeki SENER, *Department of Naval Architecture and Marine Engineering, Karadeniz Technical University,* senermehmetzeki@ktu.edu.tr

Hyeon Kyu YOON, *Department of Smart Ocean Mobility Engineering, Changwon National University,* hkyoon@changwon.ac.kr

Thi Thanh Diep NGUYEN, *Industrial Technology Research Center, Changwon National University,* nguyenthithanhdiep1994@gmail.com

Ercan KOSE *Department of Naval Architecture and Marine Engineering, Karadeniz Technical University,* ekose@ktu.edu.tr

ABSTRACT

Understanding the roll dynamics of ships under varying wave conditions is essential for improving maritime safety, especially for Ro-Pax vessels that are particularly sensitive to stability changes. This study experimentally investigates the effect of wave steepness on the roll motion of a Ro-Pax ship model in both intact and flooded conditions under regular waves. The experiments were conducted by keeping the wavelength constant and varying the wave height to produce three wave steepness ratios: 1/50, 1/75, and 1/100. Tests took place in a 20 m × 14 m × 1.8 m wave basin, where the ship model was assessed under both head and beam wave conditions. The roll response was measured in each case to evaluate how wave steepness influences the ship's dynamic behavior. The results show that increasing wave steepness leads to a significant amplification in roll motion, with observable differences between the intact and flooded states. These findings offer valuable insights for validating numerical models focused on roll dynamics and emphasize the importance of accounting for wave steepness in ship stability assessments. The study also supports the ongoing development of improved testing methodologies and more robust design guidelines for evaluating roll performance in waves.

Keywords: *Roll dynamics, wave steepness, flooded vessel, ship stability, model test, Ro-Pax ship.*

1. INTRODUCTION TITLE

Evaluating the stability of a damaged ship is inherently challenging, as it involves the coupled dynamics of ship motion and internal flooding. A ship experiencing hull breach must feature sufficient watertight subdivision to limit flooding spread, maintain residual buoyancy, and withstand environmental forces to prevent capsizing or sinking. Theoretical and experimental methodologies have jointly evolved as essential tools for investigating damaged ship dynamics. Building on prior developments, Umeda et al. (2004) carried out a comprehensive theoretical and experimental analysis of damaged ship stability in waves, emphasizing the importance of hydrodynamic modeling that incorporates sinkage and heel caused by internal flooding. Their findings indicate that benchmark testing methods, such as those used by the ITTC and in the Stockholm Agreement, may be insufficient for accurately predicting roll motions and survivability, particularly for ships with multiple decks like pure car carriers. In subsequent studies, theoretical models continued to be developed and validated under more complex conditions. Lee et al. (2007) conducted a theoretical and experimental study on the dynamic behavior of damaged ships in waves, focusing on the prediction of ship motion and accidental flooding. The experimental work, performed on a Ro-Ro ship subjected to various damage scenarios, recorded motions, drift forces, and water ingress levels. While the theoretical predictions generally aligned with the measurements, the work underscored the need for further improvements to address dynamic, three-dimensional flooding effects and obstacles' influence. These advancements are further

complemented by a historical perspective on how safety standards and regulatory thinking have evolved in response to maritime challenges. Francescutto and Papanikolaou (2011) presented a detailed examination of the historical progression of ship buoyancy, stability, and subdivision, tracing developments from Archimedes' principles to the implementation of probabilistic and performance-based standards under SOLAS 2009. Emphasis is placed on how major maritime disasters prompted shifts from empirical, deterministic models to risk-based approaches grounded in scientific reasoning and numerical simulation. The review highlights the increasing reliance on computational tools and probabilistic assessments to enhance the survivability of modern vessels, particularly in damage conditions, in response to growing ship sizes and heightened safety expectations.

Recent studies continue to address the flooding dynamics and motion behavior of damaged vessels under various sea conditions. Lee et al. (2015) performed an experimental analysis of six degree-of-freedom (6DOF) motions of intact and damaged ship models in regular beam waves, aiming to establish a dataset for CFD validations. As part of their findings, parametric roll was observed only in the intact condition at specific wave frequencies and amplitudes, but not in the damaged state due to asymmetrical restoring moments and the damping effect of internal flooding. The study also demonstrated that wave slope unexpectedly influenced roll responses and can be further assessed. Focusing on the damping characteristics introduced by flooding, Manderbacka et al. (2015) conducted roll decay and flooding experiments on a box-shaped barge. The results demonstrated that flooded water in subdivided compartments can substantially increase roll damping, whereas undivided compartments exhibit high damping only at lower flooding levels, approaching intact conditions as the volume of flooded water grows. These insights underscore the importance of compartment design and internal layout in predicting a vessel's dynamic behavior following damage. Ruponen et al. (2022a, 2022b) performed benchmark studies to evaluate the accuracy of time-domain simulation tools in modeling flooding and motion response in vessels, including a large cruise ship and Ro-Pax vessel in both calm and beam seas. While some aspects, such as maximum transient roll angles, were captured with reasonable accuracy, notable discrepancies emerged regarding flooding progression, particularly under severe conditions. Such outcomes emphasize the continued necessity for advancing time-domain simulation methodologies to ensure more reliable survivability assessments.

This study investigates the effect of wave steepness on the roll motion characteristics of a Ro-Pax ship model under regular wave conditions. Experiments were carried out in a controlled wave basin measuring 20 m × 14 m × 1.8 m. Three regular wave conditions were generated, each with a fixed wavelength and varying wave heights to produce three distinct wave steepness ratios. The tests were performed on the ship model in both intact and flooded states, subjected to head and beam wave directions. The experimental results provide insights into how increasing wave steepness influences the roll response and overall dynamic behavior of the vessel. The findings emphasize the importance of considering wave steepness when evaluating the roll performance of Ro-Pax ships under intact and flooding conditions in regular waves.

2. MATERIALS AND METHODS

The evaluation of ship stability can be conducted through model tests, enabling the investigation of various scenarios using multiple techniques. This section outlines the materials and methods adopted in the study and elaborates on their application.

Experimental Model

The design of Ro-Pax ships combines features from both Ro-Ro cargo ships and passenger vessels. This dual-purpose design, while practical, introduces specific challenges and risks. Among these are stability issues caused by the placement of heavy vehicles on the cargo deck and higher passenger accommodation, which can influence the ship's center of gravity. To mitigate these risks, assessing the ship's stability, both in intact and flooded conditions, is essential. Model ship testing plays a key role in this process, providing valuable insights that help improve design standards and guide safety regulations. The hull model examined in this study (Ruponen et al., 2022a) is based on a 162-meter-long Ro-Pax ship designed by Meyer Turku Shipyard (Meyer Turku Shipyard, 1737), adhering to SOLAS safety standards (IMO, 2020).

The main dimensions of the ship model are detailed in Table 1.

Table 1: Main dimensions of the ship model.

Overall length, L_{oa}	1.435 m
Length between perpendiculars, L_{bp}	1.310 m
Beam, B	0.250 m
Draft, T	0.054 m
Displacement volume, ∇	0.0115 m^3

To ensure the ship model accurately represents a real vessel, each production step was carefully planned and executed. According to ITTC (2017), the damaged area of a ship model should have a simple geometric shape, such as a rectangle or triangle. In this model, the damaged area is rectangular, located in compartments 2 and 3 of the hull, and measures 33 mm. It spans the full height of these compartments, allowing unrestricted water entry. The dimensions of the flooding compartments are provided in Table 2.

Table 2: Main dimensions of the flooded compartments.

Compartments	Length [m]	Width [m]	Depth [m]
Compartment 1	0.119	0.250	0.066
Compartment 2	0.119	0.250	0.066
Compartment 3	0.066	0.250	0.066

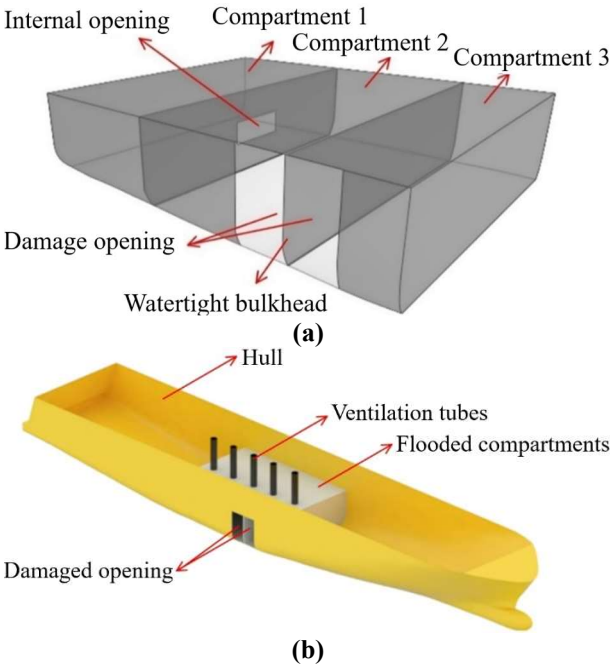

Figure 1: computer-aided illustrations of (a) compartment design, (b) model design.

To improve ventilation and prevent air from being trapped, 15 mm diameter tubes were added to allow airflow. Additionally, a mechanism was designed to open and close the flooded compartment. This mechanism uses a 0.8 mm thick sheet with magnetic and elastic properties, along with a 0.5 mm thick iron-reinforced paper applied around the damaged area. The computer-aided design (CAD) of the experimental model is illustrated in Figure 1 with necessary the descriptions.

The inclination experiment was carried out in an isolated tank to ensure a more controlled testing environment. A 0.500 kg weight was moved 0.080 m to both the starboard and port sides relative to the ship model's center of gravity. The purpose of this test was to establish an initial stability condition with GM set to 0.03125 m. Table 3 provides a comparison between the target initial stability values for the model ship and the experimental measurements obtained.

Table 3: Target and calculated initial stability values with measurements from the inclining test.

Target GM	Initial Incl.	Incl. to PS	Incl. to SB	Calculated GM
0.03125 m	0.01°	6.36°	−6.38°	0.03121 m

Swing tests are performed to determine the natural oscillation period and the corresponding moments of inertia. To calculate the moment of inertia about the vertical axis of the ship model a specialized device capable of capturing oscillatory motion was employed. The measurement setup used for this purpose is shown in Figure 2. Using the recorded oscillation period, the mass moment of inertia was determined to be 1.253 $kg{\cdot}m^2$.

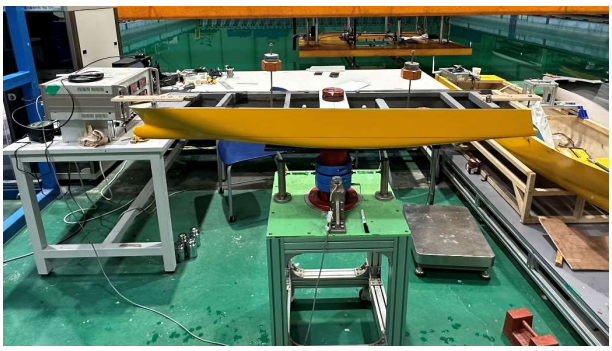

Figure 2: The measurement setup for swing test.

Measurements for the moments of inertia around the roll and pitch axes were obtained through free roll decay and pitch decay experiments (Figure 3 and Figure 4). However, as it was not feasible to measure sway motion via free decay, an alternative instrument was utilized for this measurement.

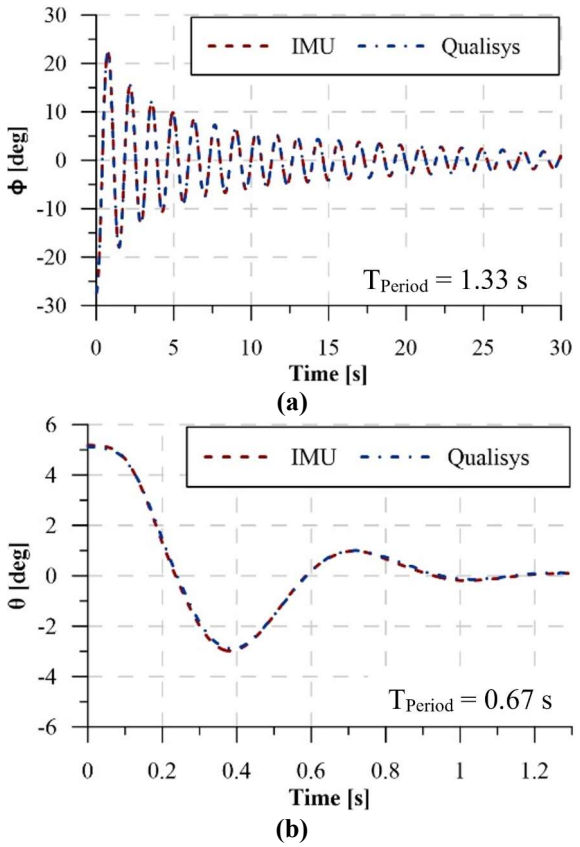

Figure 3: free decay tests for intact condition (a) roll-decay, (b) pitch-decay.

Experimental setup

In this study, experiments were conducted at the Ship Dynamics and Control Laboratory at Changwon National University as part of an international collaboration. The laboratory houses a wave basin with dimensions of 20 meters in length, 14 meters in width, and 1.8 meters in depth.

Calibration was performed to ensure the waves generated by the wave generator met the required characteristics at the model's location. The calculated wave heights were obtained using curve fitting with the Fast Fourier Transform (FFT) algorithm applied to the measured data. Table 4 presents the error rates between the observed and target wave heights. Analysis revealed that the error rates for generated waves (Figure 5) stayed within the acceptable threshold of 3%. To evaluate errors caused by random factors, ten repeated tests were performed for 1/50 wave steepness (Figure 6).

Table 4: Target and calculated wave heights.

Wave	λ [m]	H/ λ [s]	f [Hz]	H_{target} [cm]	H_{fitted} [cm]	Diff. [%]
1	2.62	1/50	0.772	5.24	5.20	-0.78
2	2.62	1/75	0.722	3.49	3.47	-0.67
3	2.62	1/100	0.772	2.62	2.58	-1.47

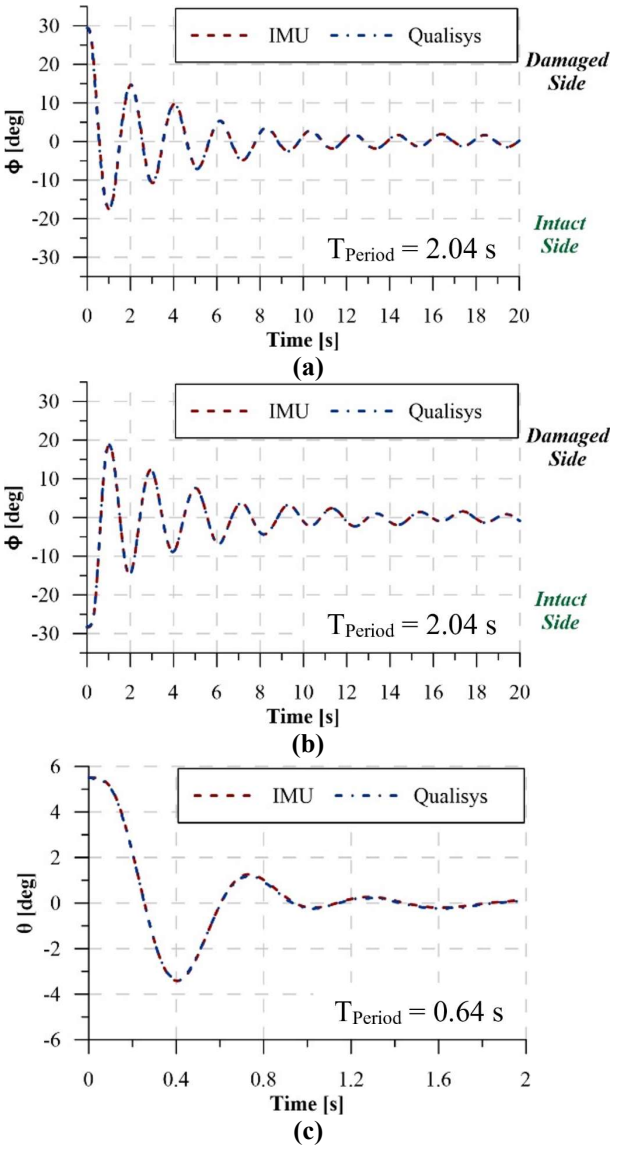

Figure 4: Free decay tests for flooded condition (a) roll-decay from the damaged side, (b) roll-decay from the intact side, (c) pitch-decay.

The experimental setup and equipment prepared for maritime tests are presented in detail in Figure 7. This setup includes various tools designed to ensure the successful execution of the experiments. Among these are GoPro cameras capable of capturing high-resolution recordings, a Qualisys motion tracking system for monitoring the three-dimensional movements of the model ship, mooring springs used to keep the ship fixed in a specific position during testing, tension gauges, an analog-to-digital (A/D) converter for transforming analog signals into digital data, an IMU sensor, a system for measuring wave heights, and the model ship itself. Each piece of equipment was carefully positioned to support a specific aspect of the experiment.

To assess the motion responses of the ship model under regular wave conditions, a soft mooring

system was employed to prevent unintended drift from its initial position. The motion responses were captured as time-series data during the seakeeping tests.

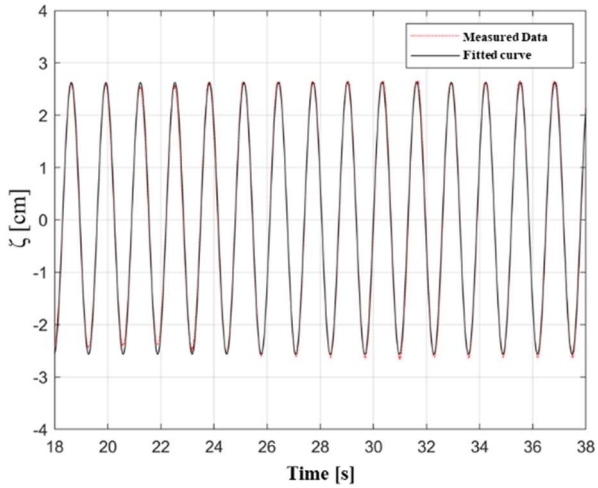

(a)

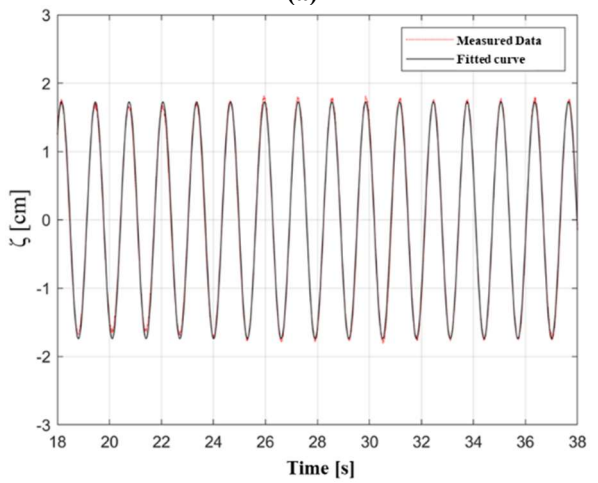

(b)

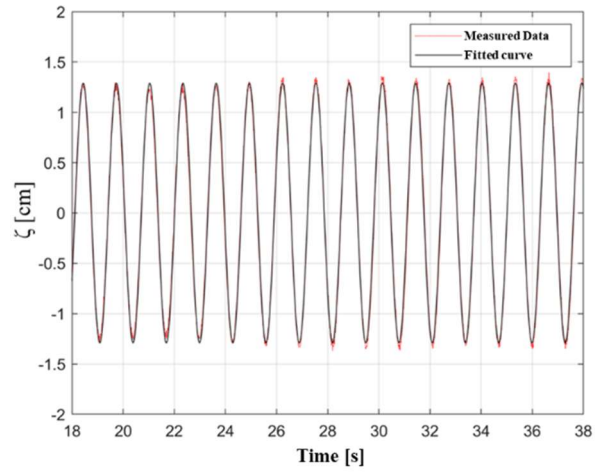

(c)

Figure 5: (a), (b), and (c) are the post-calibration measurements for waves 1 to 3, respectively.

After initiating flooding through the damaged opening, experiments were carried out only after a steady-state condition had been established within the affected compartments. This steady state was defined by a stabilized internal water level and the absence of any significant ongoing water inflow or outflow. Under these conditions, the dominant influences on the ship model's motion were the dynamic effects of sloshing and free surface movement. These phenomena introduced additional damping and altered the vessel's natural response characteristics, particularly in roll and pitch. Conducting tests at this equilibrium stage ensured that the measured behavior reflected the vessel's post-damage dynamic state, rather than the transient effects associated with active flooding. This approach enabled a more accurate and repeatable assessment of the impact of internal water dynamics on the model's stability and motion behavior under damaged conditions.

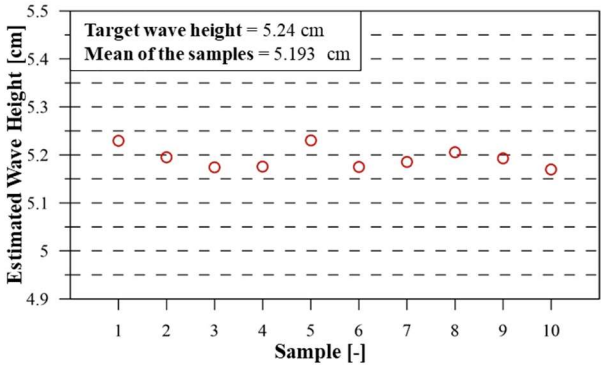

Figure 6: Repeated tests for the regular wave 1.

In the intact state, the damaged opening was fully sealed using the magnetic-elastic sheet, and the compartments were cleared of any residual water to ensure a completely watertight condition. This setup allowed for a baseline comparison under undamaged conditions, isolating the influence of flooding on the ship model's motion and stability by providing a controlled reference state for the experimental measurements.

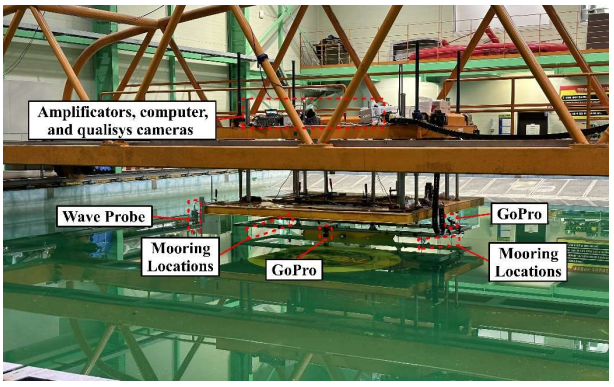

Figure 7: Experimental setup.

3. RESULTS AND DISCUSSION

The model ship, with its initial stability condition adjusted, was subjected to seakeeping tests to analyze its response in both intact and flooded states under head and beam sea conditions. The tests also aimed to evaluate the influence of wave steepness in regular wave environments (Figures 8 to 12).

The roll motions of the intact model (Figure 9) show a clear dependency on wave steepness. At the highest wave steepness (H/λ = 1/50), the roll response amplitude reaches approximately 12º, while for H/λ = 1/75 and H/λ = 1/100, the amplitudes decrease to around 10º and 9º, respectively. The roll oscillations stabilize after the initial transient phase and maintain a consistent frequency. The increase in wave steepness leads to higher energy transfer from the waves, resulting in larger roll amplitudes. The RAO values for roll motion increase with decreasing wave steepness, indicating that the ship is more responsive to smaller waves.

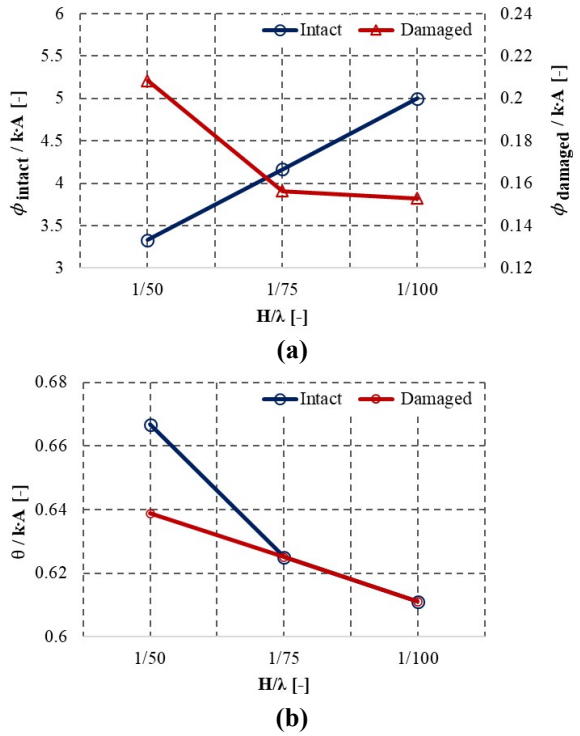

Figure 8: Response amplitude operators: (a) roll motion, (b) pitch motion.

In the flooded state (Figure 11), the roll amplitudes are significantly reduced due to the added damping effect caused by water ingress. The measured roll amplitudes are approximately 0.75° for H/λ = 1/50, 0.375° for H/λ = 1/75, and 0.28° for H/λ = 1/100. The oscillations appear irregular and heavily damped, particularly under the highest wave steepness condition.

This reduction in roll amplitude illustrates the impact of flooding on the ship model's roll dynamics. The presence of floodwater increases hydrodynamic damping and limits the model's responsiveness to wave-induced excitation. Correspondingly, the RAO values in the flooded state are significantly lower than those in the intact state, indicating a markedly reduced roll response.

For the intact model in head seas (Figure 10), the pitch response amplitudes increase with wave steepness. At H/λ = 1/50, the pitch amplitude reaches 2.4º. For H/λ = 1/75 and H/λ = 1/100, the amplitudes decrease to around 1.5º and 1.1º, respectively. The pitch motions exhibit periodic behavior after the initial transient phase, with consistent oscillation frequency. The RAO values indicate that the intact model is responsive to changes in wave steepness, with higher wave steepness producing larger pitch amplitudes due to greater wave energy input.

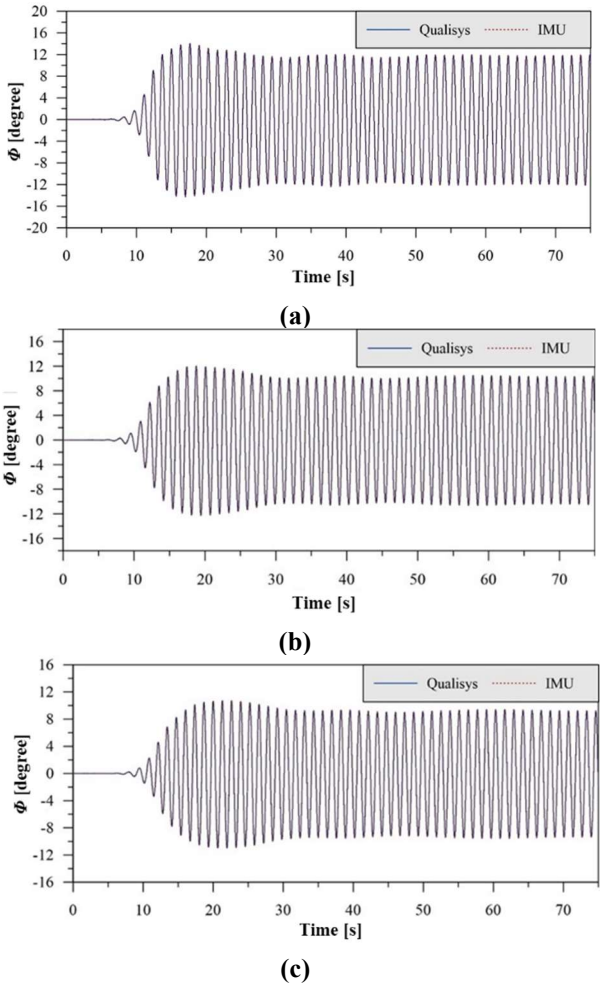

Figure 9: Roll motions of the intact model under regular waves approaching at 90° (λ = 2.620 m): (a) h/λ = 1/50, (b) h/λ = 1/75, and (c) h/ λ = 1/100.

In the flooded condition (Figure 12), the pitch amplitudes are approximately 2.3º for H/λ = 1/50, 1.5º for H/λ = 1/75, and 1.1º for H/λ = 1/100. The pitch motions remain relatively consistent and periodic despite the flooding, showing less reduction compared to roll motions. The RAO values for the flooded condition are slightly lower than those for the intact condition but still show that the ship retains its pitch response characteristics. This indicates that the impact of flooding on pitch motions is less severe than on roll motions, due to the ship's longitudinal stability.

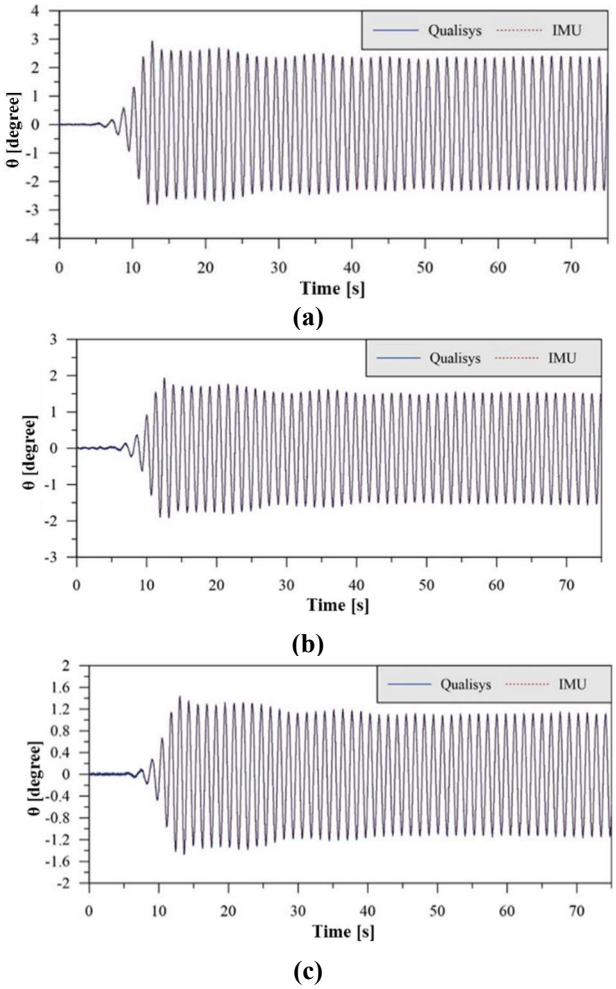

Figure 10: Pitch motions of the intact model under regular waves approaching at 180° (λ = 2.620 m): (a) h/λ = 1/50, (b) h/λ = 1/75, and (c) h/ λ = 1/100.

The comparison between intact and flooded conditions in beam seas reveals that flooding significantly reduces roll amplitudes. This reduction is primarily due to increased hydrodynamic damping caused by water inside the flooded compartments. As the ship rolls, this internal water moves relative to the hull, generating sloshing and free surface effects that dissipate kinetic energy and resist motion. While flooding also increases the vessel's inertia due to the added mass, this effect plays a secondary role compared to the energy dissipation caused by internal fluid movement. The intact model demonstrates large, consistent oscillations, whereas the flooded model exhibits smaller, more irregular responses. This behavior is primarily driven by the altered force components generated through the sloshing motion of water within the damaged compartments. As the ship undergoes roll and pitch motions, the internal water moves freely across these compartments, forming a dynamic free surface. This motion interacts with the ship's structure and induces additional hydrodynamic effects.

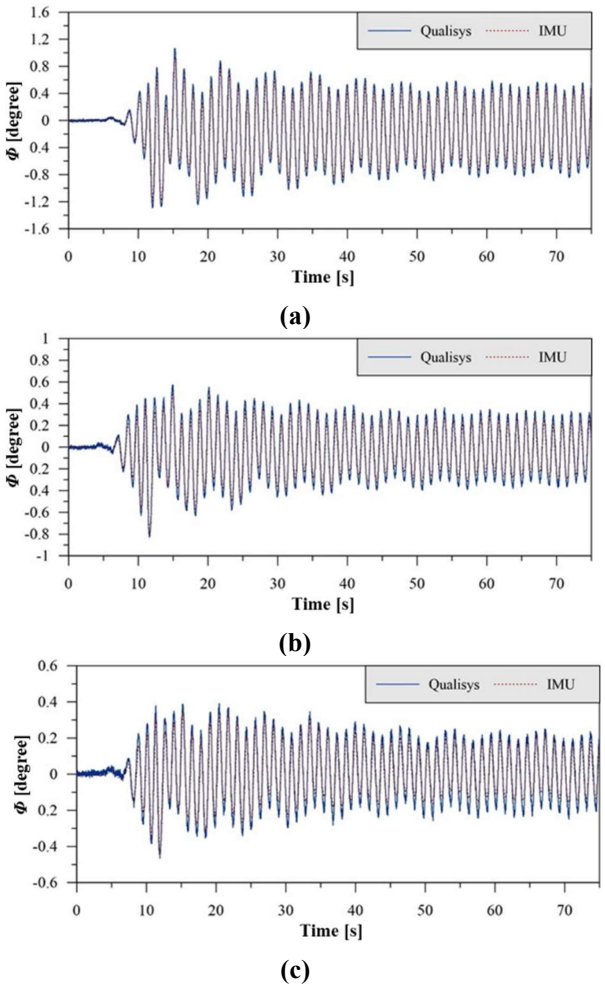

Figure 11: Roll motions of the flooded model under regular waves approaching at 90° (λ = 2.620 m): (a) h/λ = 1/50, (b) h/λ = 1/75, and (c) h/ λ = 1/100.

The irregular roll motion in the flooded condition is a direct result of the nonlinear and asymmetric nature of sloshing. Unlike the predictable roll patterns of the intact ship, the internal water in flooded compartments does not move in synchrony with the hull. Instead, it responds with delayed, uneven, and sometimes chaotic behavior, especially when stimulated near its natural

sloshing frequency. This leads to fluctuating hydrodynamic feedback forces that disrupt the regularity of the roll motion, producing irregular amplitudes, distorted cycles, and unstable oscillation patterns. As wave steepness increases, the difference between the two conditions becomes more pronounced, with the intact model responding dynamically and the flooded model exhibiting significant damping.

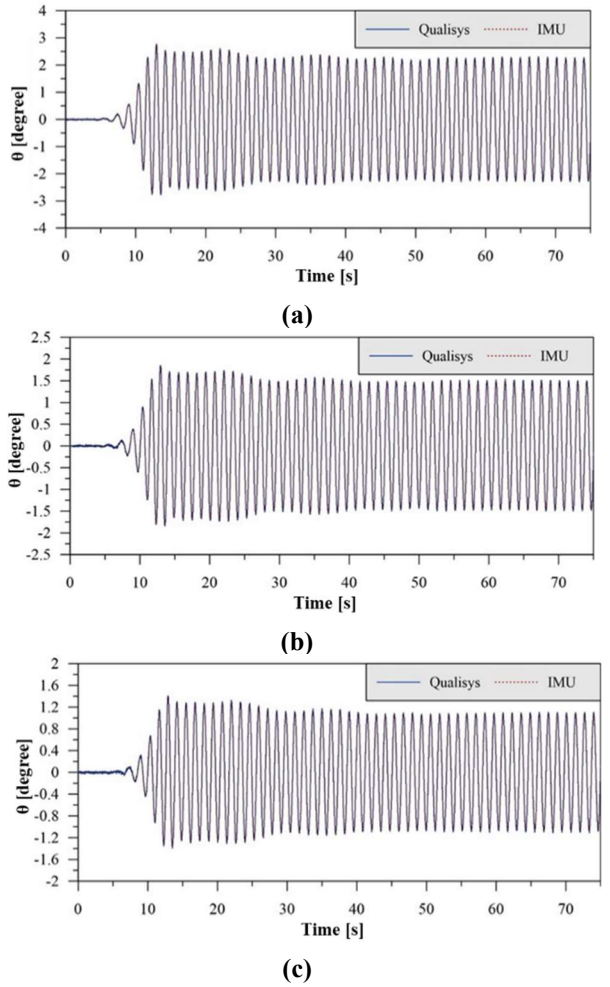

Figure 12: Pitch motions of the flooded model under regular waves approaching at 180° (λ = 2.620 m): (a) h/λ = 1/50, (b) h/λ = 1/75, and (c) h/ λ = 1/100.

In head seas, the difference between intact and flooded conditions is less pronounced compared to beam seas. The pitch amplitudes for the flooded model are only slightly reduced relative to the intact model. The consistent pitch response suggests that head seas pose a lower risk to the stability of a flooded vessel. The damping effect of water ingress is less impactful on pitch motions, making head seas a safer condition for flooded ships compared to beam seas in this flooded condition.

4. CONCLUSIONS

This study investigated the dynamic behavior of a Ro-Pax ship model in both intact and flooded states when subjected to regular waves with varying wave steepness under beam and head sea conditions. The results showed that higher wave steepness leads to increased roll and pitch amplitudes due to greater wave energy input. In beam seas, the intact model exhibited pronounced roll amplitudes, while the flooded model demonstrated significantly reduced and irregular roll responses as a result of increased hydrodynamic damping from internal flooding. In head seas, pitch motions were less influenced by the flooded condition, with both intact and flooded models displaying consistent and predictable behavior. Response Amplitude Operator (RAO) analysis confirmed that roll motion is highly sensitive to the flooding state, whereas pitch motion remains relatively stable. These findings underscore the importance of time-domain analyses for capturing transient and dynamic vessel responses, providing critical insights for evaluating roll dynamics under different loading and flooding scenarios.

Future research should extend the frequency range of analysis to capture frequency-dependent sloshing effects. Additionally, integrating real-time sensor data and machine learning could further enhance predictive capabilities, enabling faster and more informed emergency responses.

ACNOWLEDGEMENTS

The Scientific and Technological Research Council of Turkey (TUBITAK) for the 2214-A International Doctoral Research Fellowship Programme for the first author, the Ship Dynamics and Control Laboratory of Changwon National University, and Karadeniz Technical University are all acknowledged for their support to make this work possible. This work was supported by the National Research Foundation of Korea (NRF) grant funded by the Korea government (MSIT) (NRF-2022R1A2C1093055).

REFERENCES

Francescutto, A., and Papanikolaou, A. D., 2011, “Buoyancy, Stability, and Subdivision: From Archimedes to SOLAS 2009 and the Way Ahead,” Proceedings of the Institution of Mechanical Engineers, Part M: Journal of Engineering for the Maritime Environment, 225(1), pp. 17-32.

Umeda, N., Kamo, T., and Ikeda, Y., 2004, "Some Remarks on Theoretical Modeling of Damaged Stability," Marine Technology and Sname News, 41, pp. 45-49.

Lee, D., Hong, S., and Lee, G. J., 2007, "Theoretical and experimental study on dynamic behavior of a damaged ship in waves," Ocean Engineering, 34(1), pp. 21-31.

Lee, S., You, J. M., Lee, H. H., Lim, T., Park, S. T., Seo, J., and Rhee, K. P., 2015, "Experimental study on the six degree-of-freedom motions of a damaged ship floating in regular waves," IEEE Journal of Oceanic Engineering, 41(1), pp. 40-49.

Manderbacka, T., Ruponen, P., Kulovesi, J., and Matusiak, J., 2015, "Model experiments of the transient response to flooding of the box shaped barge," Journal of Fluids and Structures, 57, pp. 127–143.

Ruponen, P., Valanto, P., Acanfora, M., Dankowski, H., Lee, G. J., Mauro, F., . . . Veer, R. V., 2022a, "Results of an international benchmark study on numerical simulation of flooding and motions of a damaged ropax ship," Applied Ocean Research, 123.

Ruponen, P., van Basten Batenburg, R., Veer, R. V., Braidotti, L., Bu, S., Dankowski, H., & Tompuri, M., 2022b, International benchmark study on numerical simulation of flooding and motions of a damaged cruise ship," Applied Ocean Research, 129, 103403.

Meyer Turku Shipyard. (1737). Retrieved from https://www.meyerturku.fi/en/index.jsp.

International Maritime Organization, "International Convention for the Safety of Life at Sea (SOLAS)," Consolidated Edition 2020 (London: IMO, 2020.

ITTC, 2017, "Model Tests on Damage Stability in Waves, 7.5-02-07-04.2," ITTC Quality System Manual, Recommended Procedures and Guidelines.

Effects of forward speed on bilge-keel roll damping

Naofumi Yoshida, *Osaka Metropolitan University,* sa22743t@st.omu.ac.jp
Hasan Islam Copuroglu, *Karadeniz Technical University,* hasancopuroglu@ktu.edu.tr
Toru Katayama, *Osaka Metropolitan University,* katayama.marine@omu.ac.jp

ABSTRACT

To reduce the roll amplitude of ship in resonance condition, it is significant to increase its roll damping. The roll damping created by bilge-keels accounts for a large proportion of the total roll damping. The bilge-keel roll damping estimated by Ikeda's method is formulated based on the theoretical formulas with some empirical coefficients and the estimation method has been applied to various types of ships. However, there are some cases where the method can't estimate roll damping accurately, one of them is that ship has large breadth bilge-keels and it has forward speed. Ikeda and Katayama proposed the lift component of bilge-keel roll damping, which can well express the increase in the bilge-keel roll damping at medium forward speed ($0.1 < Fn \leq 0.18$). On the other hand, at low forward speed ($0 < Fn < 0.1$), the method can't express the tendency which is decrease of the bilge-keel roll damping according to increase in forward speed. To clarify the reason for the effects of forward speed, a forced roll test is carried out using commercial CFD (STAR-CCM+) and each component of the bilge-keel roll damping is investigated. And the way to take the effects into account is discussed.

Keywords: *Roll damping, Ikeda's method, Bilge-keel component.*

1. INTRODUCTION

The characteristics of roll motion are one of the important factors for ship safety. However, it is difficult to estimate roll motion accurately by only potential theory because of significant viscous effects on roll damping. Therefore, some empirical formulas are proposed to estimate the damping.

As one of estimation methods of the viscous effects on roll damping, Ikeda's method (Ikeda et al., 1978a, b) is well-known. Although it is widely used through ITTC Recommended Procedures and Guidelines, in some cases the estimated damping is not well as shown by Ikeda et al. (1994). The reason is the inaccuracy of the bilge-keel component.

To improve Ikeda's method, the forward speed effects are focused. In original Ikeda's method, the effects are neglected because the measured results on cargo vessels did not show such effects. However, the measured results by Ikeda (1973) show that while the normal force components and hull pressure components are changed with forward speeds, the total amount of bilge-keel roll damping is almost same. In addition, Ikeda et al. (1994) showed that the bilge-keel component of a frigate increases greatly in high-speed cases, which they attributed to the lift force acting on the bilge-keel, and the lift component of bilge-keel roll damping is proposed, and a new version of the estimation formula for the lift component is presented by Ikeda et al. (2024). At medium forward speed ($0.1 < Fn \leq 0.18$), the estimated result by new formula is better than the previous results, but at low forward speed ($0 < Fn < 0.1$), both formulas do not express the tendency according to increase in forward speed.

In this study, the effects of forward speed are investigated in more detail. To clarify the reason for the effects of forward speed, a forced roll test is carried out using commercial CFD (STAR-CCM+) and each component of the bilge-keel roll damping is investigated. And the way to take the effects into account is discussed.

2. BILGE-KEEL ROLL DAMPING

2.1 Original Ikeda's method

In original Ikeda's method, the bilge-keel component of roll damping coefficient B_{BK} is composed of two components,

$$B_{BK} = B_N + B_S \tag{1}$$

where B_N is normal force component due to normal force acting on bilge-keels and B_S is hull pressure component due to pressure on hull surface created by bilge-keels.

Equivalent linear sectional normal force component B'_N is

$$B'_N = \frac{8}{3\pi}\rho\, r^2 \omega\, \phi_a\, b_{BK} f^2 C_D\, l_1 \tag{2}$$

where ρ [kg/m^3] is density of fluid, r [m] is the distance from roll axis G to hull surface attached on bilge-keel, ω [rad/s] is roll angular frequency and ϕ_a [rad] is roll amplitude, b_{BK} [m] is breath of bilge-keel and l_1 [m] is the distance from roll axis G to the normal vector to bilge-keel which through the point where is on hull attached bilge-keel. C_D is the drag coefficient, and f is the correction factor to take account of increment of flow velocity caused by hull form at the point on hull surface where bilge-keel is attached, and they are determined by measured data as follows

$$C_D = \frac{22.5}{K_C \cdot f} + 2.4 \quad (4 < K_C < 20) \tag{3}$$

$$f = 1 + 0.3e^{\{-160(1-\sigma)\}} \tag{4}$$

where σ is area coefficient of cross-section and K_C is Keulegan-Carpenter number as follows

$$K_C = \frac{U_{\max} T}{D} = \frac{\pi r \phi_a}{b_{BK}} \tag{5}$$

where T [s] is period of the oscillation, $U_{\max}$ [m/s] is amplitude of characteristic velocity and D [m] is characteristic length. In the case of this study, T is roll period, $U_{\max}$ is the velocity caused by rolling at the point on hull surface where bilge-keel is attached and D is twice of breadth of bilge-keel.

Equivalent linear sectional hull pressure component B'_S is

$$B'_S = \frac{4}{3\pi}\rho\, r^2 \omega\, \phi_a f^2 \int_G C_P \cdot l\, dG \tag{6}$$

where G [m] is girth length along hull, l [m] is moment lever, C_P is hull pressure coefficient and its values for front and back face of bilge-keels are

$$C_P = \begin{cases} 1.2 & (\text{for } C_P^+) \\ 1.2 - C_D & (\text{for } C_P^-) \end{cases} \tag{7}$$

Fig. 1 shows two pressure distributions on hull measured by Ikeda et al. (1978b). To simplify the distribution as shown in Fig. 2, positive pressure coefficient C_P^+ is empirically taken as 1.2 at front of bilge-keels and 0 at water surface and keel. And negative pressure coefficient C_P^- is 1.2 - C_D from the relation of $C_D = C_P^+ + C_P^-$. Length of the negative-pressure S_0 [m] is obtained as

$$\frac{S_0}{b_{BK}} = 0.3\left(\frac{\pi f r \phi_a}{b_{BK}}\right) + 1.95 \tag{8}$$

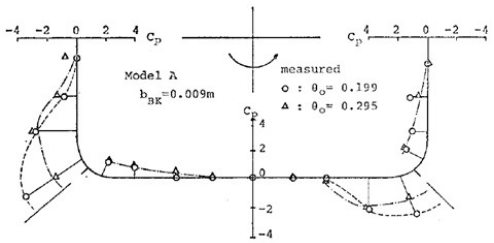

Figure 1: Pressure distributions on hull measured by Ikeda et al. (1978b).

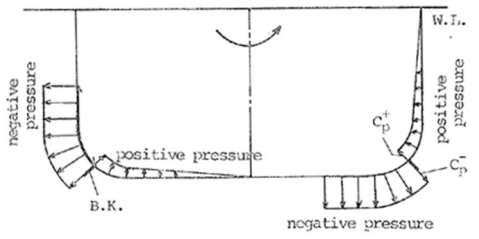

Figure 2: Assumed pressure distribution on hull created by bilge-keels by Ikeda et al. (1978b).

2.2 Lift component

Ikeda et al. (1994) formulated the effects as the lift component of bilge-keel roll damping using Jones's theory as shown in Equations (7) and (8) because the effects of forward speed of the bilge-keels for a frigate whose aspect ratio is larger than the conventional cargo vessels are significant.

$$B_{BKL} = \frac{2L\, l_1}{\phi_a \omega} \tag{7}$$

$$L = \frac{1}{2}\pi\, \rho\, \alpha\, V_r^{\,2}\, b_{BK}^{\,2} \tag{8}$$

where, L [N] is the lift force acting on the one side of the bilge-keel, l_1 [m] is the distance between the roll axis and the center of the bilge-keel. Using the forward speed of the ship U [m/s] and velocity of the bilge-keel due to the roll motion u_r [m/s], the attack angle α [rad] and the inflow velocity into the bilge-keel V_r [m/s] is obtained by Eq. (9) and (10).

$$\alpha = \mathrm{atan}(u_r / U) \tag{9}$$

$$V_r = \sqrt{u_r^{\,2} + U^2} \tag{10}$$

The new bilge-keel lift component is proposed by Ikeda and Katayama (2024). It is formulated by using the lift which is equivalently linearized in Eq. (11). This equation has the second term that is inversely proportional to the forward speed.

$$B_{BKL} = \pi\, \rho\, b_{BK}^2\, l_1^2 \left\{ U + \frac{3}{4} \frac{\left(l_1\, \phi_a\, \omega\right)^2}{U} \right\} \tag{11}$$

The non-dimensional bilge-keel lift component can be expressed in Eq.(12).

$$\hat{B}_{BKL} = \frac{B_{BKL}}{\rho \nabla B^2} \sqrt{\frac{B}{2g}} \tag{12}$$

3. FORCED ROLL TEST IN REAL TANK AND BILGE-KEEL LIFT CONPONENT

3.1 Subject model

Table 1 shows the principal particulars of the ship and Fig. 3 is a photo and 3D model of the subject ship.

Table 1:Principal particulars of the subject ship.

L_{PP} [m]	1.12
Breadth: B [m]	0.246
Depth: D [m]	0.139
Draught: d [m]	0.060
W [kgf]	9.742
KG [m]	0.107
GM [m]	0.023
Natural roll period: T_n [s]	1.42
Breadth of bilge-keel: b_{BK} [m]	0.011
Position of bilge-keel	ss 3.1 - ss 5.6

Figure 3: Photograph and 3D model of the subject ship.

3.2 Accuracy of the estimation formula for bilge-keel lift component

Yoshida et al. (2024) investigate the effects of forward speeds on bilge-keel roll damping. Fig.4 shows the measured results. The bilge-keel roll damping is affected by the forward speed. Especially, at Fn = 0.08 ~ 0.1, the damping becomes smaller than that of lower and higher speed conditions.

Comparing the measured results and the estimated results, the accuracy of the estimation formulas is confirmed. In Fig. 5, gray line and blue line represent the estimated results by the old formula (Eq.(7) and (12)) and the new formula (Eq.(11) and (12)), respectively. The results indicate that even the new formula for the bilge-keel lift component can't express the decrease in damping observed at Fn=0.08 ~ 0.1.

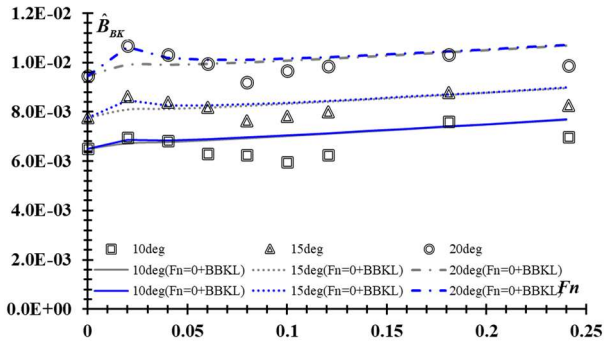

Figure 4: Non-dimensional bilge-keel roll damping coefficients for the same roll period (=T_n) at different forward speeds and the values obtained by adding the bilge-keel lift component obtained by old and new formula to the measured results at Fn=0.

4. FORCED ROLL TEST IN REAL TANK AND BILGE-KEEL LIFT CONPONENT

4.1 CFD setup

In this study, STAR-CCM+ is used for CFD calculation. Fig. 5 depicts the calculation domain and its boundary condition for the cases with and without forward speed.

To check the grid convergence, the calculation is done for three grids. Table 2 shows the calculation conditions and Fig. 6 shows the grid distribution for the three cases in this convergence study.

Calculated results are shown in Fig. 7. The results depict the difference in roll moment between the middle and fine cases is almost same.

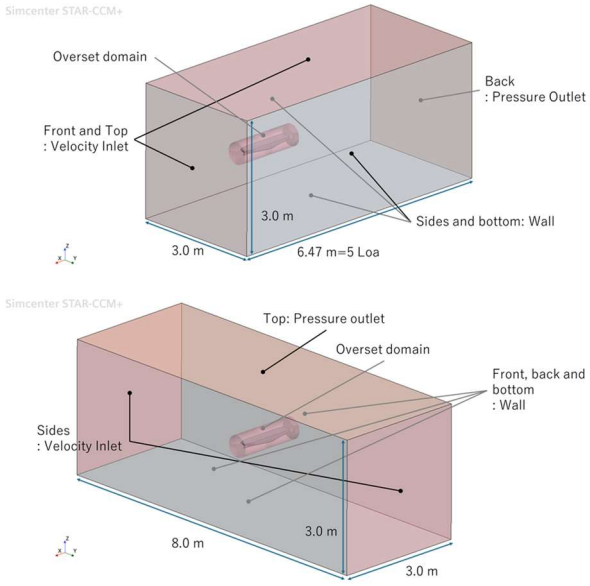

Figure 5: Calculation domains and boundary conditions (upper: with forward speed, lower without forward speed)

Table 2:Principal particulars of the subject ship.

Numerical solver	Implicit unsteady
Turbulence model	SST k-ω
Multiphase	VOF
Time step [s]	0.002
Temporal discretization	2nd-order accuracy
Wall function	All Y+
Number of layers	20
Layer expansion ratio	1.2
Physical time [s]	8.52
Velocity [m/s] (Fn)	0.8 (0.24)
Roll period [s]	1.42
Roll amplitude [deg]	15
Ship model	Hull and bilge-keel

Coarse

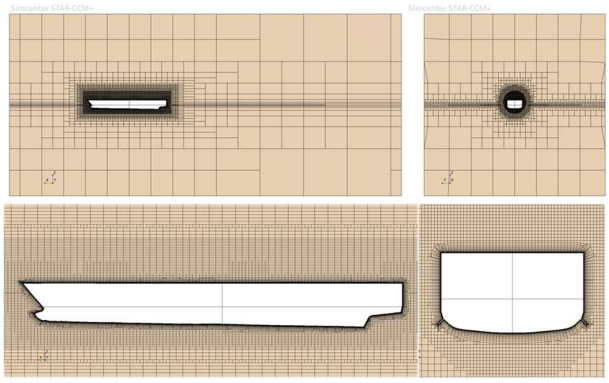

Medium

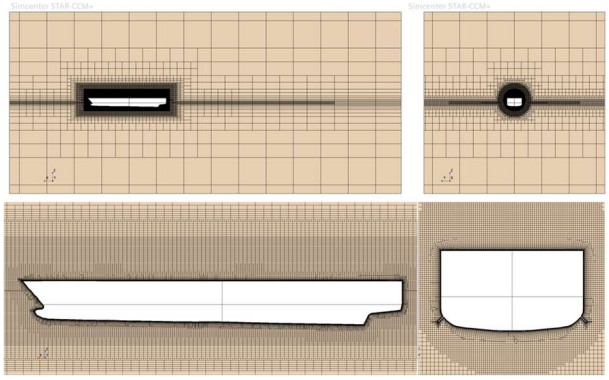

Fine

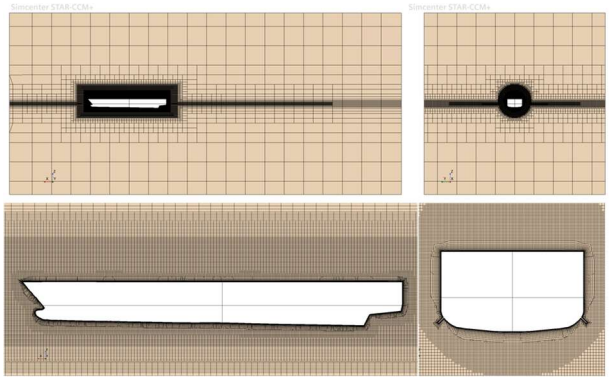

Figure 6: Grid distribution (Coarse, medium and fine).

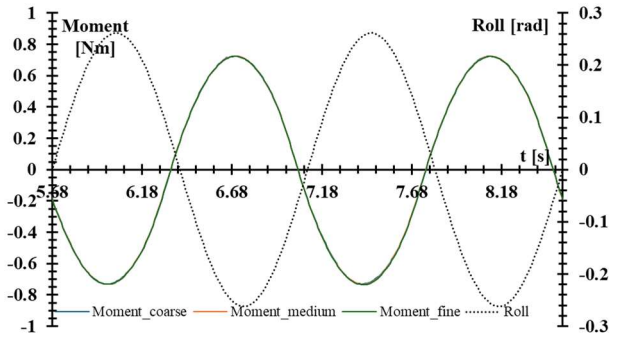

Figure 7: Roll moment at different grid cases.

The roll damping coefficient is obtained using roll moment as shown in Eq.(13) and its non-dimensionalized form is Eq.(14).

$$B_{44} = \frac{M_a \sin\varepsilon}{\phi_a \omega} \tag{13}$$

$$\hat{B}_{44} = \frac{B_{44}}{\rho \nabla B^2}\sqrt{\frac{B}{2g}} \tag{14}$$

where, M_a is the amplitude of the roll moment for the roll circular frequency component, ε is the phase shift between roll moment and roll angle, ϕ_a is the roll amplitude, ω is roll circular frequency.

Table 3 shows the non-dimensional roll damping coefficient. This result suggests that the middle case is dense enough to be adopted.

Table 3: Non dimensional roll damping coefficient at different mesh cases.

	Cell number	B_{44}hat	Ratio of each case to fine case
Coarse	1,317,503	2.66E-02	1.010
Medium	3,998,388	2.64E-02	1.001
Fine	9,451,460	2.63E-02	1

4.2 Calculated Bilge-keel roll damping by CFD

Using the conditions from the previous section, the forced roll test is performed for some speed cases. Table 4 shows the test conditions.

Fig. 7 shows the comparison of non-dimensional roll damping coefficient between CFD and the experiment. The calculation results are smaller than the measured results.

The non-dimensional bilge-keel component $\hat{B}_{BK}$ is obtained by subtracting $\hat{B}_{44}$ of the bare hull from that of the hull with bilge-keel as shown in Eq.(15). Fig. 8 shows the results. The calculated results do not show the reduction in bilge-keel roll damping from Fn = 0.02 to 0.08 as seen in the measured results.

$$\hat{B}_{BK} = \hat{B}_{44(\text{Hull with BK})} - \hat{B}_{44(\text{Bare hull})} \tag{15}$$

Table 4: Conditions of the forced roll test in CFD.

Velocity [m/s] (Fn)	0 (0), 0.066 (0.02), 0.265 (0.08), 0.331 (0.1) 0.8 (0.24)
Roll amplitude [deg]	15
Roll period [s]	1.42

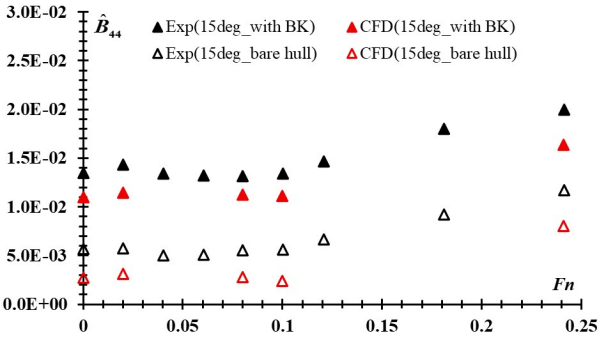

Figure 7: Non-dimensional bilge-keel component of roll damping coefficient at different forward speeds.

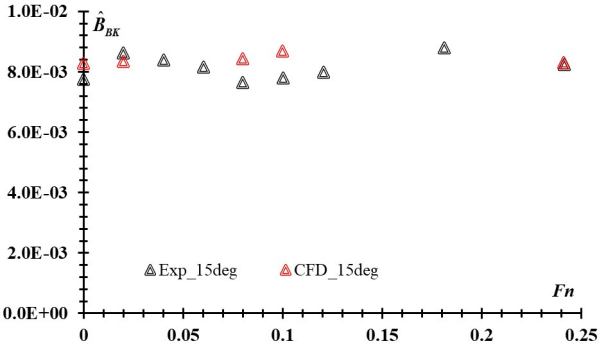

Figure 8: Non-dimensional bilge-keel component of roll damping coefficient at different forward speeds.

4.3 Forward speed effects on two components of bilge-keel roll damping

Each component of bilge-keel roll damping is also investigated. The normal force component is calculated by Eq. (16) and (17) using the roll moment acting on only the bilge-keel. However, this normal force component includes the bilge-keel lift component if there is forward speed.

$$B_N = \frac{M_{aBK} \sin \varepsilon_{BK}}{\phi_a \omega} \quad (16)$$

$$\hat{B}_N = \frac{B_N}{\rho \nabla B^2} \sqrt{\frac{B}{2g}} \quad (17)$$

where, M_{aBK} is the amplitude of the roll moment acting on the bilge-keel for the roll circular frequency component, ε_{BK} is the phase delay of the roll moment to roll angle.

The non-dimensional hull pressure component is calculated by Eq. (18)

$$\hat{B}_S = \hat{B}_{BK} - \hat{B}_N \quad (18)$$

Fig. 9 shows the effects of forward speed on each component of bilge-keel roll damping. The normal force component B_N is larger than the hull pressure component B_S, and B_N decrases at Fn=0.08-0.1 and then slitly increases. On the other hand, the hull pressure component B_S increases at Fn=0.1 and then decreases.

Fig. 10 shows the ratios of each component of forward speed cases to the zero speed case of each component. From this results, it can be said that the the forward speed effects of normal force component are not significant at Fn = 0 to 0.24, and the bilge-keel lift component is negligible small for typical size of bilge-keel. However, the forward speed effects on hull pressure component can't be neglected.

Using the calculation results, the reasons of the forward speed effects on the bilge-keel component are discussed. Fig. 11 shows the streamline from the starboard-side bilge-keel and the pressure acting on the bilge-keel at different forward speeds. When Fn = 0, the streamline makes vortices in transvers direction. When Fn = 0.1, the streamline which shows vortex in transvers direction caused by bilge-keel is flowed to backward by forward speed. When Fn = 0.24, the streamline line does not make vortices in transvers direction, but it is similar to that around slender wing. The pressure distribution on back-side of bilge-keel for roll velocity is almost same for longitudinal direction at Fn = 0, however, the pressure of the fore-area and aft-area on bilge-keel are decreased and increased at Fn = 0.24 by the longitudinal flow on back-side of bilge-keel respectively caused by forward speed.

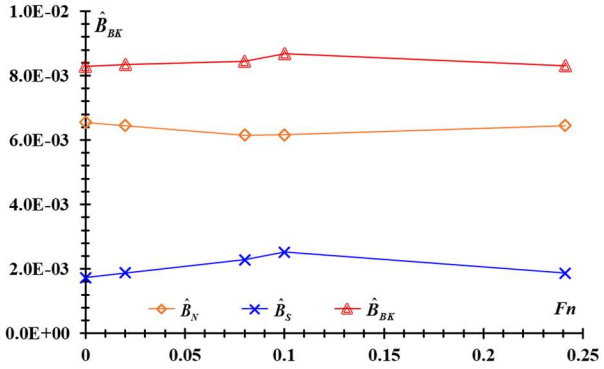

Figure 9: Non-dimensional bilge-keel normal force and hull pressure components at different forward speeds.

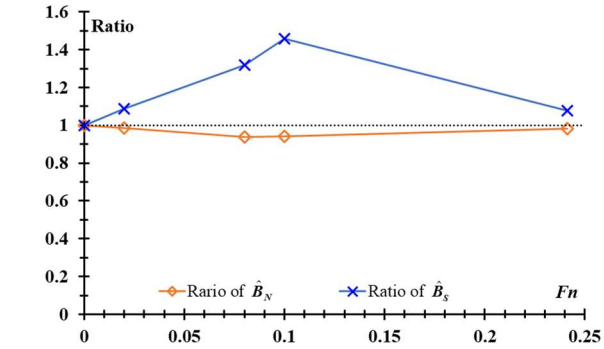

Figure 10: Ratios of the normal force and hull pressure components with different forward speeds to those of zero speed.

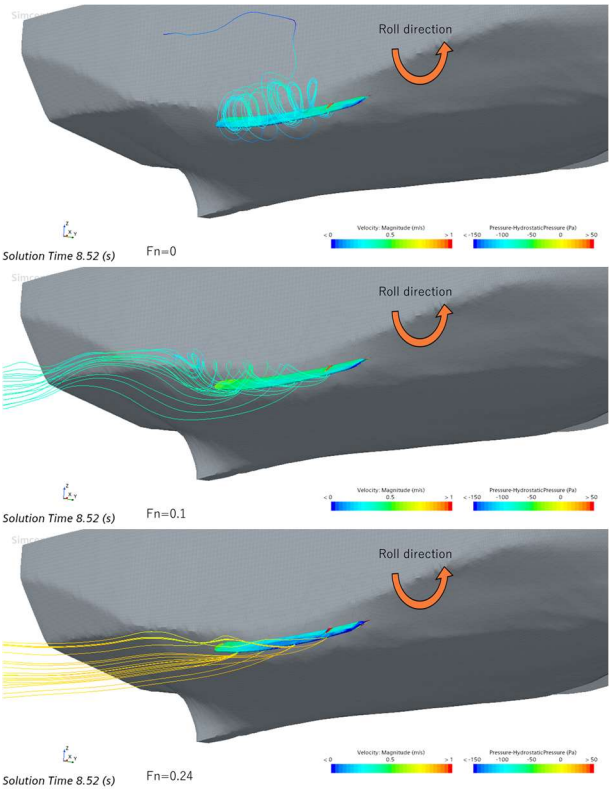

Figure 11: Streamlines around the starboard-side bilge-keel at different forward speeds by viewed from fore starboard-side.

5. CONCLUSIONS

In this study, the forced roll test at different forward speeds (Fn = 0 ~ 0.24) is carried out using CFD (STAR-CCM+) and the effects of forward speed on the bilge-keel roll damping is investigated. The following conclusions are drawn,

1) The non-dimensional roll damping coefficients for both the hull with bilge-keels and the bare hull, as obtained from calculations, were smaller than measured results. From these results the bilge-keel roll damping coefficient is obtained. It does not show the reduction from Fn = 0.02 to 0.08 as seen in the measured results.

2) The effects of forward speed on the normal force component and the hull pressure component of bilge-keel roll damping are also investigated. The normal force component, which includes the bilge-keel lift component if there is, is almost unaffected by forward speed across the range of Fn = 0 to 0.24. On the other hand, the hull pressure component is affected by the forward speed, and it increases from Fn = 0 to 0.1 and then decreases.

3) The streamlines around bilge-keel are confirmed. When Fn = 0, it makes vortices in transverse direction and at Fn = 0.1, it shows vortexes in transvers direction caused by bilge-keel are flowed to backward by forward speed. At Fn = 0.24, the streamline line does not make vortices in transvers direction but it is similar to that around slender wing.

4) The pressure distribution on back-side of bilge-keel for roll velocity is almost same for longitudinal direction at Fn = 0, however, the pressure of the fore-area and aft-area on bilge-keel are decreased and increased at Fn = 0.24 by the longitudinal flow on back-side of bilge-keel respectively caused by forward speed.

5) The lift component is composed of the lift acting on the bilge-keel. Since the roll damping obtained from the roll moment due to the force acting on the bilge-keel itself is not affected by the forward speed, it can be thought that for the size of bilge-keel used in this study, it is not necessary to consider the lift component when Fn = 0 to 0.24.

6) The forward speed effects on the hull pressure component are large. This component at Fn = 0.1 is approximately 1.4 times larger than when there is no forward speed. This highlights the importance of considering forward speed effects on the hull pressure component; however, further investigation is needed to fully clarify the underlying phenomena.

ACKNOWLEDGEMENT

Part of this study is supported by ClassNK, Fundamental Research Developing Association for Shipbuilding and Offshore (REDAS) and JST SPRING (Grant Number JPMJSP2139).

REFERENCES

Ikeda, Y., Himeno, Y., Tanaka, N., 1978a, “On roll damping force of ship -effects of friction of hull and normal force of bilge keels”, Report of Department of Naval Architecture, University of Osaka Prefecture, No.00401.

Ikeda, Y., Himeno, Y., Tanaka, N., 1978b, “A Prediction method for Ship Roll Damping, Report of Department of Naval Architecture”, University of Osaka Prefecture, No.00405.

Ikeda, Y., 1973, “Studies on Roll Damping of a Ship”, Doctor Thesis, University of Osaka Prefecture , in Japanese.

Ikeda, Y., Katayama, T., Hasegawa, Y., Segawa, M., 1994, “Roll damping of high speed slender vessels”, Journal of Kansai Society of Naval Architects, Japan, No.222, pp.73-81, in Japanese.

Ikeda, Y., Katayama, T., 2024, “Ikeda Method to Ikeda-Katayama Method -Bilge-keel component in Ship Roll Damping-”, Proceedings of the 2nd International Conference on the Stability and Safety of Ships and Ocean Vehicles, pp.49-57.

Yoshida, N., Pesman, E., Copuroglu, H., Taniguchi, T., Katayama, T., 2024, “Experimental and Numerical Investigation of Effects of Forward Speed on Bilge-keel Roll Damping of RORO Ship”, Proceedings of the 3rd International congress on ship and marine technology.

Stability in Waves Committee, 2011, ITTC Recommended Procedure Numerical Estimation Method of Roll Damping, International Towing Tank Conference, 26th ITTC, Report 7.5-02-07-04.5.

Tanaka, N., Himeno, Y., Ikeda, Y., Isomura, K., 1981, “Experimental study on bilge-keel effect for shallow-draft ship”, J. Kansai Soc. Nav. Archit. Japan. 180, pp.69–75. (in Japanese)

An investigation of viscous effects on roll damping of different scaled ships

Nguyen Thi Ha Phuong, *Osaka Metropolitan University (Osaka, Japan)*, *Vietnam Maritime University (Vietnam)* su22435l@st.omu.ac.jp; phuongnth.dt@vimaru.edu.vn

Tomoki Taniguchi, *Osaka Metropolitan University (Osaka, Japan)* taniguchi.marine@omu.ac.jp

Toru Katayama, *Osaka Metropolitan University (Osaka, Japan)* katayama.marine@omu.ac.jp

ABSTRACT

In this study, the viscous effects on roll damping components are analyzed for two vessels (Bettica and DTC) at various Reynolds and Froude numbers using numerical simulation. The numerical results of roll decay motion are validated with experimental data to ensure the reliability of CFD simulations. Using forced roll simulation, roll damping coefficient of different components are calculated and the flow field as well as velocity distribution are observed. The results show that besides the frictional damping component, bilge keel damping component is also affected by the viscous effects when the bilge keel breadth is too short compared to the unsteady boundary layer caused by roll motion (the breadth is much shorter than general size). A method to show the unsteady boundary layer created by roll motion is proposed and the cause of the scale effects on bilge keel damping component is explained.

Keywords: *Viscous Effect, Roll Damping Coefficient, Frictional Component, Bilge-keel Component, Boundary Layer Thickness.*

1. INTRODUCTION

As ship roll motion is significantly affected by viscous flow around the hull, it is important to investigate the viscous effects on roll damping in various conditions.

Some studies such as Grant (2008), Broglia et al. (2009) only focused on roll decay motion to investigate the scale effects, whereas their influence on different roll damping components are still unrevealed. In a previous study by Nguyen et al. (2024) on a light combatant vessel with a slender-shape hull and sufficiently long bilge keel breadth at model-scale and full-scale, the scale effects on roll motion were detected. Especially, the bilge keel damping component was found different between model-scale and full-scale when the bilge keel breadth was reduced to a half of designed breadth. Although scale effects on roll damping components were discovered, the underlying causes were not completely explained.

Therefore, this study aims at analysing the viscous effects on roll damping components and explain the cause of scale effects on bilge keel component. By simulating roll motions for two ships at various Reynolds and Froude numbers, roll damping coefficients are calculated and the flow field including velocity field, velocity vector and velocity distribution are observed. Based on viscous and inviscid simulation, a method to show the unsteady boundary layer created by roll motion is proposed and the unsteady boundary layer of two vessels in different conditions are determined. Finally, the cause of scale effects on bilge keel damping component related to the difference in the unsteady boundary layer between model-scale and full-scale is explained.

2. THEORETICAL BASIS

2.1 Motion equation of fluid

This study uses a computational tool STAR-CCM+, which solves the Reynolds-Averaged Navier-Stokes (RANS) equations for viscous fluid and the Euler equations for inviscid fluid. The general form of RANS equations for viscous incompressible flow are represented as follows:

$$\frac{\partial \rho}{\partial t} + \frac{\partial (\rho u_i)}{\partial x_i} = 0 \tag{1}$$

$$\frac{\partial(\rho u_i)}{\partial t}+\frac{\partial}{\partial x_j}(\rho u_i u_j) = -\frac{\partial p}{\partial x_j}+\frac{\partial}{\partial x_j}\mu(\frac{\partial u_i}{\partial x_j}-\rho\overline{u_i' u_j'})+S_j \quad (2)$$

where, ρ is fluid density, u_i and u_j are the time-averaged values of the velocity component, p is the pressure, μ is dynamic viscosity and S_j is the source term. For inviscid flow ($\mu = 0$), RANS equation is degraded to Euler equation and represented as:

$$\frac{\partial(\rho u_i)}{\partial t}+\frac{\partial}{\partial x_j}(\rho u_i u_j) = -\frac{\partial p}{\partial x_i}+S_j \quad (3)$$

2.2 Roll damping coefficients calculation

There are five components of roll damping proposed by Ikeda et al. (1978), which are: frictional, wave making, eddy making, lift and bilge keel damping components. The roll damping coefficients can be calculated from forced roll simulation results (see detailed description in Yildiz and Katayama, 2017). From the time history of roll moments (M_E), the equation of roll damping moment can be expressed as:

$$M_E = M_0 sin(\omega t+\varepsilon) \quad (4)$$

where, M_0 – amplitude of roll moment, ω - roll angular frequency, ε – phase angle between roll amplitude and roll moment. The equivalent roll damping coefficient (b_{44}) and dimensionless damping coefficient (B_{44}) are defined as:

$$b_{44}=\frac{M_0 sin(\varepsilon)}{\phi_0 \omega}; B_{44}=\frac{b_{44}}{\nabla\rho B^2}\sqrt{\frac{B}{2g}} \quad (5)$$

where, ϕ_a - roll amplitude, ∇ - displacement volume of the ship, g - gravitational acceleration, ρ - water density and B – breadth. From the time history of frictional moment, dimensionless frictional damping coefficient (B_{44F}) are defined as:

$$B_{44F}=\frac{b_{44F}}{\nabla\rho B^2}\sqrt{\frac{B}{2g}} \quad (6)$$

For the vessel with a slender shape hull like Bettica, as the hull pressure component of the bilge keel damping component is not large, dimensionless bilge keel damping coefficient (B_{44BK}) is defined as:

$$B_{44BK}=\frac{b_{44BK}}{\nabla\rho B^2}\sqrt{\frac{B}{2g}} \quad (7)$$

For the vessel with a round shape hull like DTC, as the hull pressure component of the bilge keel damping component is large, dimensionless bilge keel damping coefficient is defined as:

$$B_{44BK} = B_{44\text{ with BK}} - B_{44\text{ without BK}} \quad (8)$$

Total roll damping coefficient of other components such as wave making (B_{44W}), eddy making (B_{44E}), lift damping (B_{44L}) is defined as:

$$B_{44W}+B_{44E}+B_{44L} = B_{44}-B_{44F}-B_{44BK} \quad (9)$$

3. STUDIED VESSELS

Two vessels with different scales are selected as research objects, one is a combatant vessel named Bettica and the other is a container vessel named DTC. The detailed information of Bettica and DTC vessels can be seen in Grant (2008) and Moctar et al. (2012), respectively. Figure 1 illustrates the three dimensional geometry and Table 1 summarises the main particulars of both vessels.

a) Bettica (full appendages)

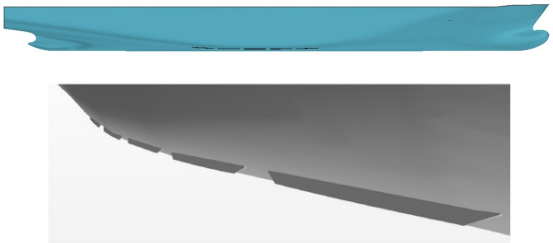

b) DTC (hull with BK)

Figure 1: 3D geometry of Bettica and DTC.

Table 1: Main particulars of Bettica and DTC.

Parameters	Symbol	Unit	Bettica		DTC	
			Ship	Model	Ship	Model
Scale factor	λ	-	1	20	1	59.4
Length between perpendiculars	L_{pp}	m	80	4.0	355	5.976
Breadth	B	m	12.2	0.61	51	0.858
Draught	d	m	3.2	0.16	12	0.2
Block coefficient	C_B	-	0.455	0.455	0.629	0.629
Mass	W	t	1399	0.174	140,033.0	0.650
Metacentric height	GM	m	1.107	0.055	4.57	0.077
Roll radius of gyration in X direction	k_{xx}	kg.m^2	4.27	0.213	19.39	0.326
Pitch and yaw radius of gyration in Y, Z direction	k_{yy}, k_{zz}	kg.m^2	20.0	1.0	95.86	1.614
Natural roll period	T_r	s	9.65	2.3	20.3	2.6
Bilge keel breadth	b_{BK}	m	0.45	0.0225	0.4	0.007

4. NUMERICAL SETTING

4.1 General setting parameters

This section briefly presents the general parameters set for simulation in viscous and inviscid flow conditions. The setting parameters are chosen so that the accuracy of simulation results is ensured based on the recommendations of ITTC (2011) and the experience obtained from previous studies (Gokce and Kinaci, 2018; Liu et al., 2021; Ghamari et al., 2022). Summary of main setting parameters applied for both vessels in viscous and inviscid simulation condition are given in Table 2. Figure 2 and Figure 3 show the dimension of computational domains and boundary conditions set for Bettica and DTC, respectively. All simulation parameters and boundary conditions are applied the same for viscous flow and inviscid flow, only the fluid property is changed from viscosity to inviscid. In addition, there is no need to use turbulence model, wall function and prism layer meshing model for inviscid flow because boundary layers and viscous effects are not solved in the Euler equations.

In previous study (Nguyen et al., 2024), grid sensitivity study was carried out for Bettica and the medium mesh was determined. In present study, this kind of mesh type is also used for both vessels to save the calculation time. Meshes are refined in essential areas where the flows are concerned. Figure 4 and Figure 5 are examples of medium mesh created for viscous and inviscid flow of Bettica and DTC, respectively. The information of mesh base size and number of mesh cells in various conditions is given in Table 3.

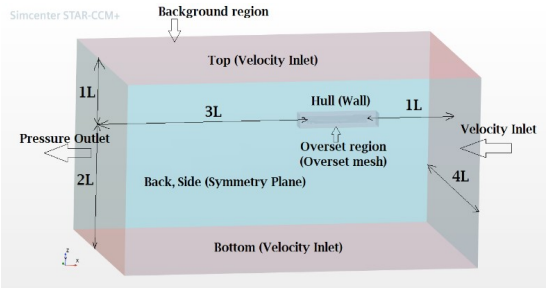

Figure 2: Dimensions of computational domains and boundary conditions (Bettica ship).

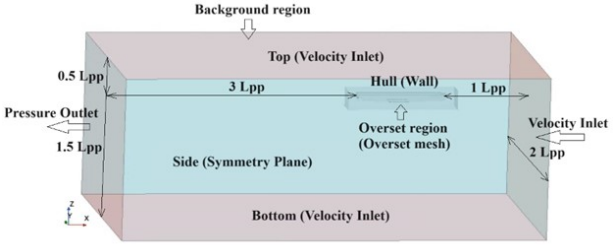

Figure 3: Dimensions of computational domains and boundary conditions (DTC ship).

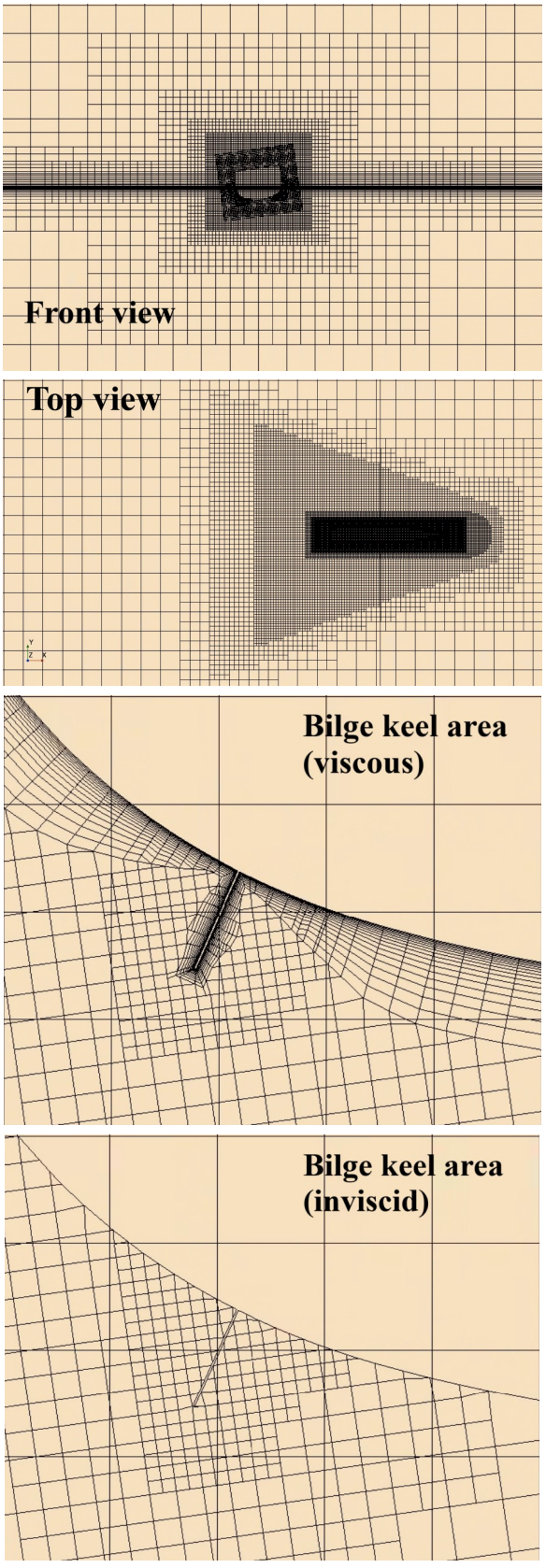

Figure 4: The mesh generated for viscous and inviscid flow (Bettica, at full-scale).

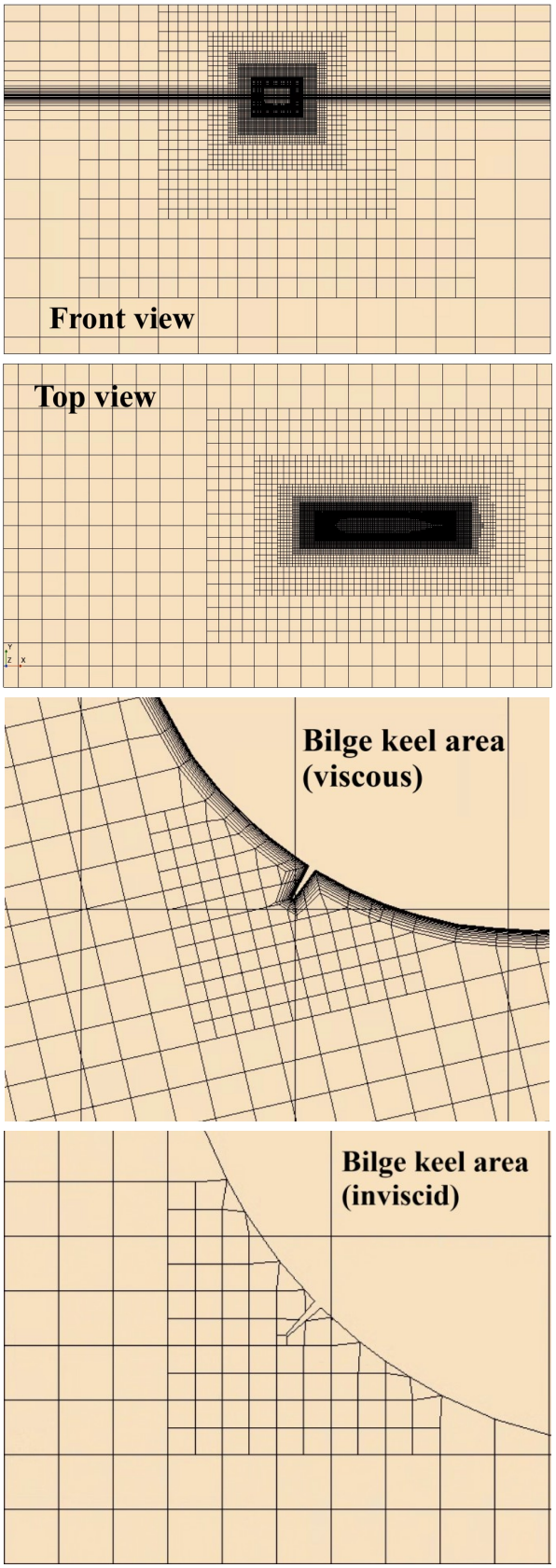

Figure 5: The mesh generated for viscous and inviscid flow (DTC, at full-scale).

4.2 Selecting wall y+ for viscous flow simulation

For viscous flow simulation, the boundary layer is modeled using wall function. Therefore, it is essential to select related parameters so that the wall y+ value of model and ship lies in a appropriate range. Based on the experiences gained from previous studies (Song et al., 2019; Song et al., 2021; Terziev et al., 2022), wall y+ value is set from 1.0 to 2.5 for model-scale and from 30 to 300 for full-scale and these settings are applied for both vessels. Figure 6 and Figure 7 shows the wall y+ values on the hull surface of Bettica and DTC at different scales and Froude numbers, respectively.

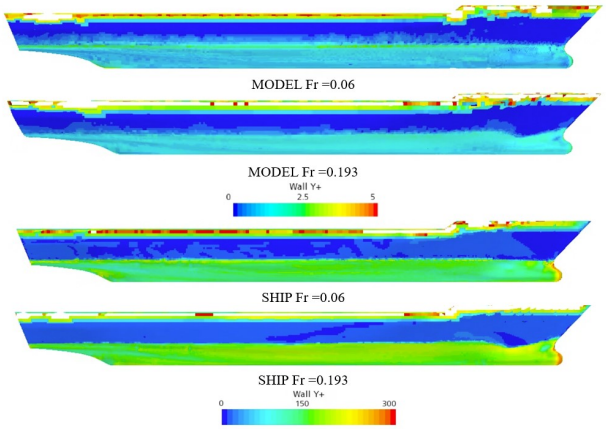

Figure 6: Wall y+ values on the hull surface of Bettica ship (naked hull).

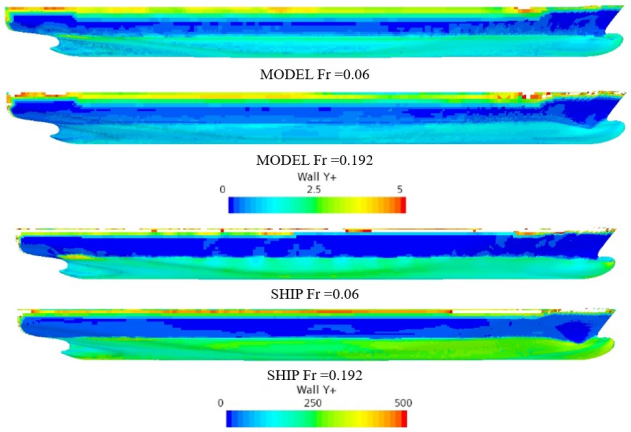

Figure 7: Wall y+ values on the hull surface of DTC ship (naked hull).

Table 2: General setting parameters of Bettica and DTC.

Parameters	Viscous flow	Inviscid flow
Solvers	Segregated flow	Segregated flow
Time model	Implicit unsteady	Implicit unsteady
Multiphase	Eulerian multiphase: water and air	Eulerian multiphase: water and air
Multiphase model	VOF waves (Volume of Fluid)	VOF waves
Viscous model	Viscous turbulent	Inviscid
Turbulence model	Shear Stress Transport k-ω	Not applied
Wall function	All y+ wall treatment	Not applied
Mesh technique	Overset mesh	Overset mesh
Meshing models	Surface remesher Automatic surface repair Trimmed cell mesher Prism layer mesher	Surface remesher Automatic surface repair Trimmed cell mesher

Table 3: Mesh for naked hull (Bettica and DTC).

Bettica	Viscous flow		Inviscid flow	
	Model-scale	Full-scale	Model-scale	Full-scale
Base size (m)	0.12	1.8	0.12	1.8
Mesh cells (million cells)	1.38	2.6	0.96	1.92
DTC	**Viscous flow**		**Inviscid flow**	
	Model-scale	Model-scale	Model-scale	Full-scale
Base size (m)	0.16	8.0	0.16	8.0
Mesh cells (million cells)	2.11	3.2	1.63	2.6

4.3 Choosing the time step

In simulation of viscous flow, the time step is chosen based on Courant number (C) (should be less than 1.0) and wall y+ value to ensure the accuracy of the numerical results. In some cases when $C > 1.0$, instead of reducing the time step, it is better to adjust the parameters related to wall y+ such as prism layer thickness, number of prism layers, total prism layer thickness to achieve $C < 1.0$. Therefore, the time step can be selected the same for various speeds and hull conditions. Time steps set for both vessels in viscous flow simulation are given in Table 4.

On the other hand, in inviscid flow simulation, wall y+ is not applied and time step is selected only based on Courant number. If $C > 1.0$, it is needed to reduce the time step to achieve $C < 1.0$, which increases the calculation time. Time steps set for both vessels in inviscid flow simulation are given in Table 5. From the Table 5, it is seen that the time step in the case of high speed is smaller, hence it takes much more time to calculate than the case of low speed. At the same speed, the time step in the case of hull with bilge keels (BK) is smaller than that in the case of naked hull. Because forced roll motion of Bettica and DTC with two hull conditions (naked hull, hull with BK) at various forward speeds are studied in this paper, time step is set the same for both hull conditions so that the obtained results do not depend on the bilge keels.

Table 4: Time step set for viscous simulation of Bettica and DTC.

Time step (s)					
Hull condition	**Froude number**	**Bettica Full-scale**	**Bettica Model-scale**	**DTC Full-scale**	**DTC Model-scale**
Naked hull	$Fr = 0.06$	0.04	0.014	0.07	0.01
	$Fr = 0.192$ (DTC); $Fr = 0.193$ (Bettica)	0.04	0.014	0.07	0.01
Hull with BK	$Fr = 0.06$	0.04	0.014	0.07	0.01
	$Fr = 0.192$ (DTC); $Fr = 0.193$ (Bettica)	0.04	0.014	0.07	0.01

Table 5: Time step set for inviscid simulation of Bettica and DTC.

Time step (s)					
Hull condition	**Froude number**	**Bettica Full-scale**	**Bettica Model-scale**	**DTC Full-scale**	**DTC Model-scale**
Naked hull	$Fr = 0.06$	0.024	0.01	0.05	0.005
	$Fr = 0.192$ (DTC); $Fr = 0.193$ (Bettica)	0.01	0.003	0.01	0.003
Hull with BK	$Fr = 0.06$	0.024	0.01	0.05	0.005
	$Fr = 0.192$ (DTC); $Fr = 0.193$ (Bettica)	0.01	0.003	0.01	0.003

5. RESULTS AND DISSCUSIONS

5.1 Validation

In this section, the validation of numerical simulation strategy is carried out by comparing the CFD results to experimental data (EFD). The experimental data of roll decay test of Bettica ship can be found in Grant (2008) and Broglia et al. (2009). The experimental results of roll decay test of DTC ship can be found in Moctar et al. (2012). All cases are simulated with the medium mesh and defined time step as shown in section 4. Simulated conditions defined based on the experimental results are given in Table 6. Figure 8 and Figure 9 show the comparison between CFD and EFD results for different cases of two vessels. The results show that model-scale and full-scale roll decay motion simulation results of both vessels have a good agreement with measurements. Therefore, numerical strategy applied for roll motion simulation in this study is reasonable and it can be used for next study cases.

Table 6: Simulated conditions for free roll decay test.

	Case 1	Case 2	Case 3	Case 4
Vessel name	Bettica	Bettica	DTC	DTC
Hull condition	Full appendages	Full appendages	Hull with rudder and bilge keels	Hull with rudder and bilge keels
Scale	Model-scale	Full-scale	Model-scale	Model-scale
Draft (m)	0.1685	3.2	0.202	0.202
Initial roll angle (deg.)	10.0	8.0	15.2	13.0
Froude number	0.227	0.193	0.0	0.105

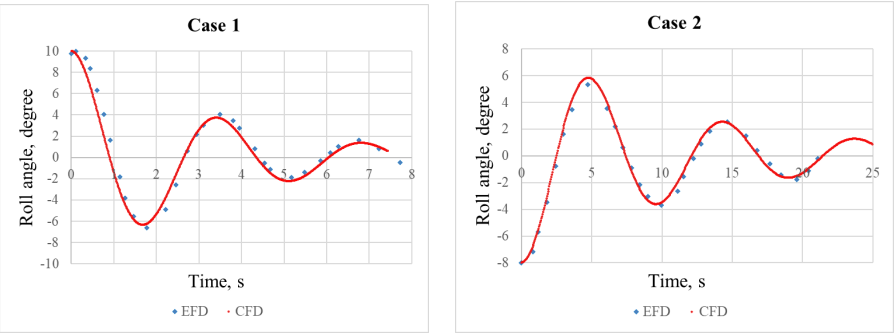

Figure 8: The validation results (Bettica ship).

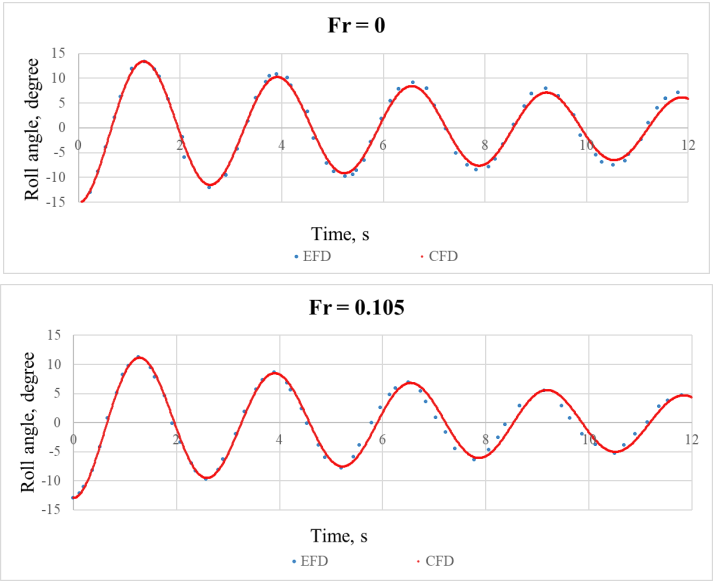

Figure 9: The validation results (DTC ship).

5.2 Viscous effects on roll damping components

To investigate the viscous effects on roll damping components, forced roll motion of two vessels are simulated in different conditions of Froude number and Reynolds number (see Table 7). Roll damping coefficients of some damping components are obtained and the flow fields around the hull are observed. The time steps set for different conditions are the same as mentioned in Table 4 with a total of 16 cases. The results of roll damping components and their contributions (%) are shown in Figure 10. Figure 11 shows the non-dimensional velocity field (in X direction) around the hull with bilge keel of two vessels at the mid-hull section ($0.5L_{pp}$) under without rolling.

Table 7: Simulated conditions for forced roll test.

Vessel name	Bettica		DTC	
Scale	Model scale	Full-scale	Model scale	Full-scale
Hull condition	Naked hull; Hull with bilge keels	Naked hull; Hull with bilge keels	Naked hull; Hull with bilge keels	Naked hull; Hull with bilge keels
Roll amplitude (deg.)	8.0	8.0	13.0	13.0
Roll period (s)	2.3	9.65	2.6	20.3
Froude number	0.06; 0.193	0.06; 0.193	0.06; 0.192	0.06; 0.192

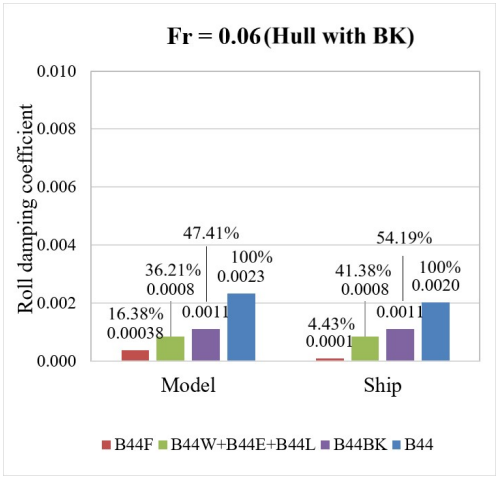

Bettica
(8 deg; T_r =2.3 s at model scale; T_r = 9.65 s at full-scale)

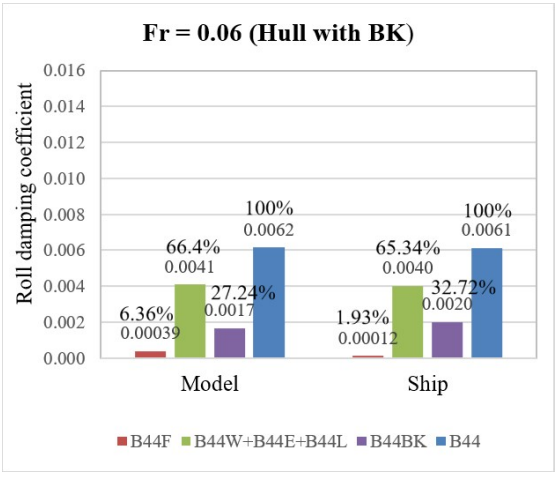

DTC
(13 deg; T_r =2.6 s at model scale; T_r = 20.3 s at full-scale)

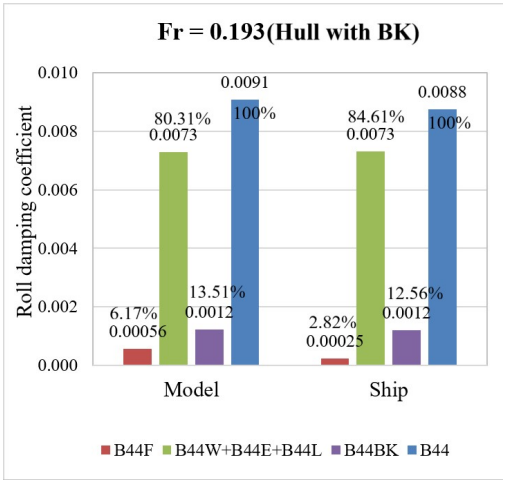

Bettica
(8 deg; T_r =2.3 s at model scale; T_r = 9.65 s at full-scale)

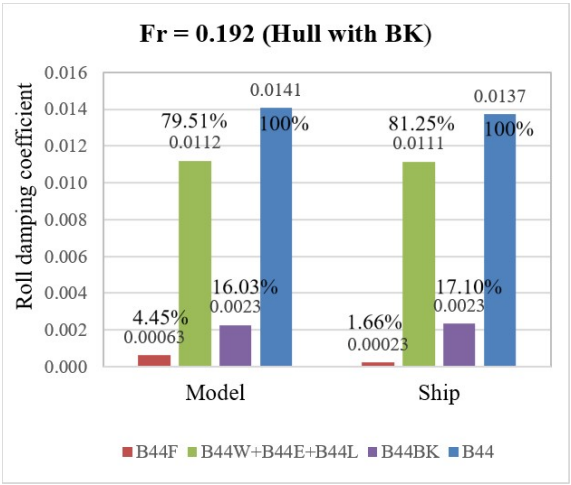

DTC
(13 deg; T_r =2.6 s at model scale; T_r = 20.3 s at full-scale)

Figure 10: Roll damping coefficients obtained by forced roll test and their contributions of Bettica and DTC.

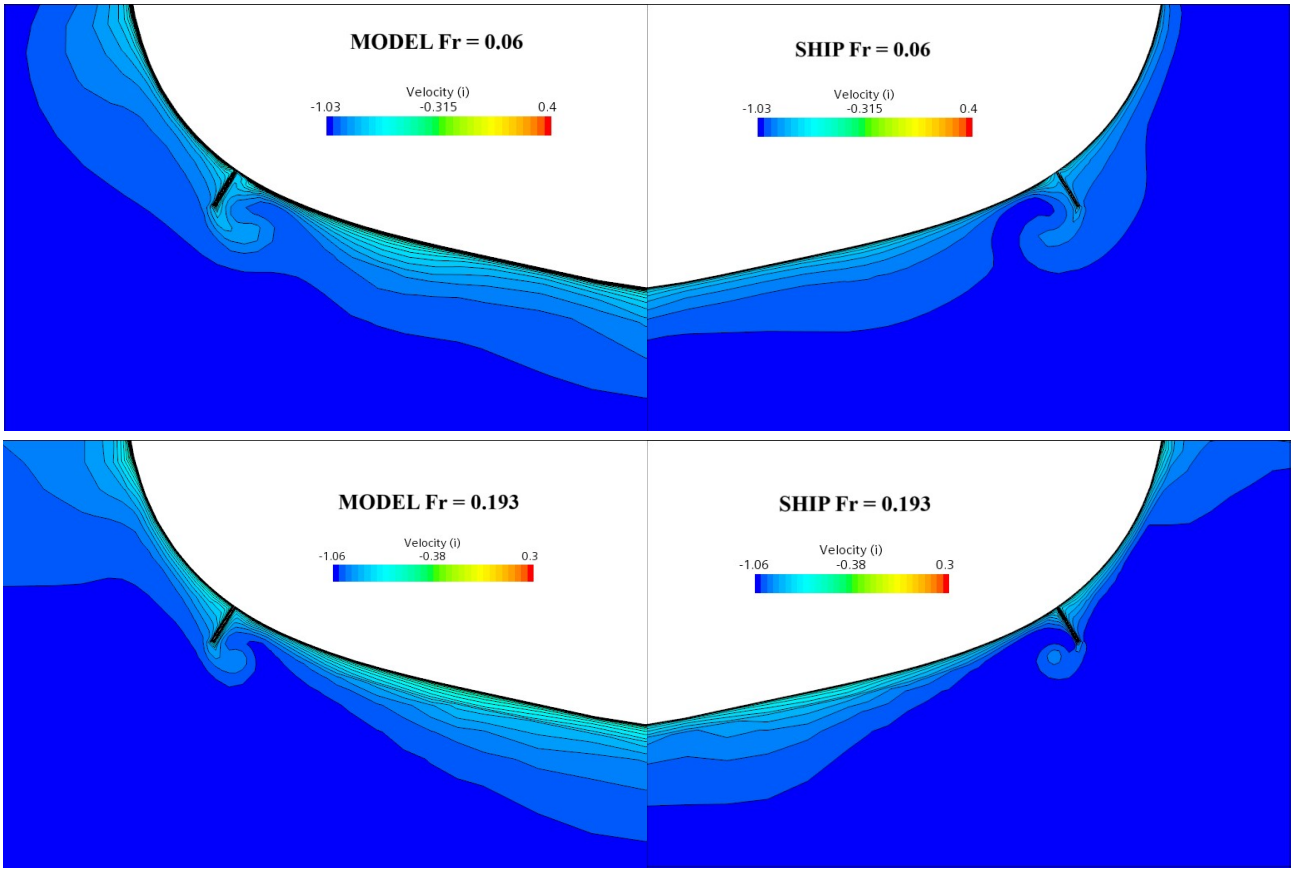

a) Bettica

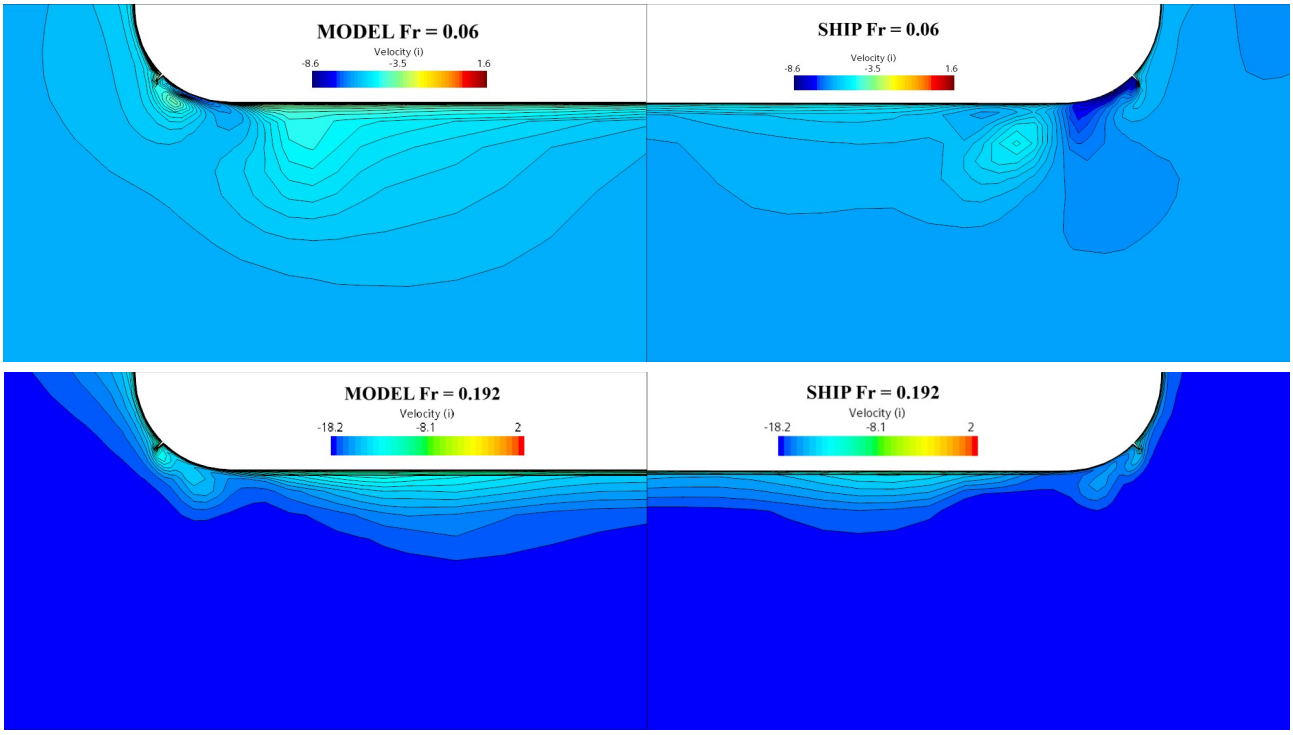

b) DTC

Figure 11: Non-dimensional velocity field in X direction of Bettica and DTC (Hull with BK) without rolling.

From Figure 10, it is noted that for both Bettica and DTC, frictional damping coefficient of model-scale (model) is larger than that of full-scale (ship) and its percentage is lager in the case of low forward speed. When the speed increases, although the frictional damping coefficient in the case of high speed is larger than that in the case of low forward speed, its contribution drops to only 4-6% in the model-scale and 1-3% in the full-scale. In respect of bilge keel damping component, there is no difference in B_{44BK} between model-scale and full-scale of Bettica ship, whereas for DTC, B_{44BK} of model-scale is slightly smaller than that of full-scale in the case of low forward speed. This indicates that viscous effects not only affect the frictional damping component, but also may affect the bilge keel damping component in certain cases.

Observing the non-dimensional velocity field in X direction around the hull of two vessels (Figure 11), it is noted that the boundary layer in X direction of the model-scale is thicker than that of the full-scale, and the boundary layer in X direction at low forward speed is thicker than that at high forward speed. As mentioned in previous studies (Nguyen et al., 2023; Nguyen et al., 2024), it is believed that the difference in the boundary layer thickness in X direction between model-scale and full-scale as observed in Figure 11 might result in the smaller B_{44BK} of model-scale at low forward speed. However, this boundary layer is created by only forward speed and it seems difficult that flow velocity in X direction significantly affects bilge keel damping component. Therefore, to explain the cause of the scale effects on bilge keel damping component, unsteady boundary layer in YZ direction (shown in Figure 12) created by roll motion and forward speed is clarified in the next section.

5.3 Estimation of the unsteady boundary layer created by roll motion

Generally, the boundary layer around hull with roll motion and forward speed is a combination of steady boundary layer created by forward speed and unsteady boundary layer created by roll motion. In this study, the term “unsteady boundary layer” is used with the meaning of unsteady boundary layer created by roll motion with or without forward speed (FS).

The estimation of the boundary layer is based on the idea that the boundary layer appears due to the viscosity of the fluid. If the fluid is non viscous, there will be no friction and no boundary layer. Therefore, comparing the velocity distribution of a ship in viscous and inviscid fluid conditions can be a good solution for determining the boundary layer created by only viscous effects. Numerical strategy applied for viscous and inviscid simulations was given in details in section 4.

From forced roll simulation results of two vessels, the flow fields of naked hull (on earth fixed coordinate system) in various conditions are observed and analysed. Simulation conditions are the same as mentioned in Table 4 and Table 5. The survey location is at the mid-hull (0.5Lpp) and around where bilge keel is attached, and the survey time is the moment when hull is upright under forced roll motion. To investigate the boundary layer created by roll motion and forward speed, the velocity field is observed in X and YZ directions, in which X direction parallels to the longitudinal axis of the ship, and YZ direction perpendiculars to bilge keel surface on the midship cross section. Figure 12 illustrates the X and YZ directions in the coordinate system, in which red arrow presents the vector of roll angular velocity. To compare model-scale with full-scale, the velocity in X and YZ directions is described in non-dimensional form as defined in formulae from (10) to (12).

$$\hat{V}_X = \frac{V_X}{V} \tag{10}$$

$$V_{YZ} = V_Y \cos\theta + V_Z \sin\theta \tag{11}$$

$$\hat{V}_{YZ} = \frac{V_{YZ}}{V_m} \tag{12}$$

where, V_X - velocity in X direction; V - forward speed; V_{YZ} - velocity in YZ direction, V_Y - velocity in transverse direction; V_Z - velocity in vertical direction; $V_m = r\omega\theta_0$ - roll angular velocity; r - rolling arm; b - distance from the survey point to the hull surface; θ_0 - roll amplitude.

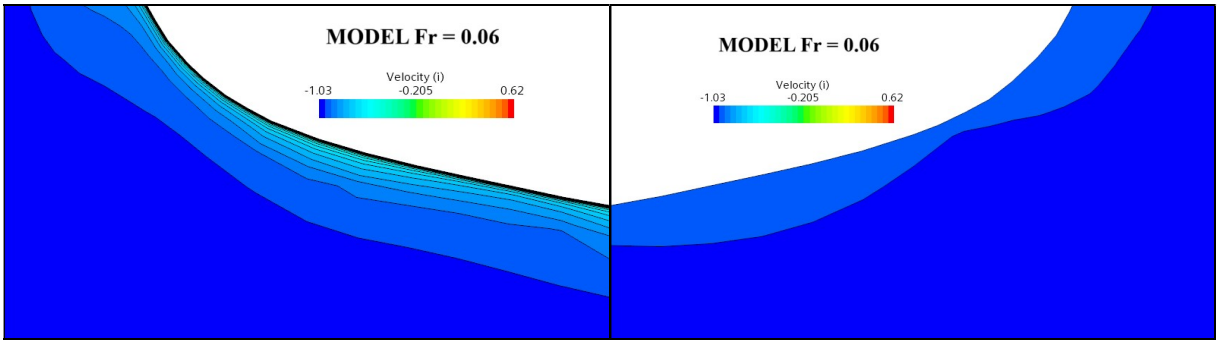

Viscous **Inviscid**

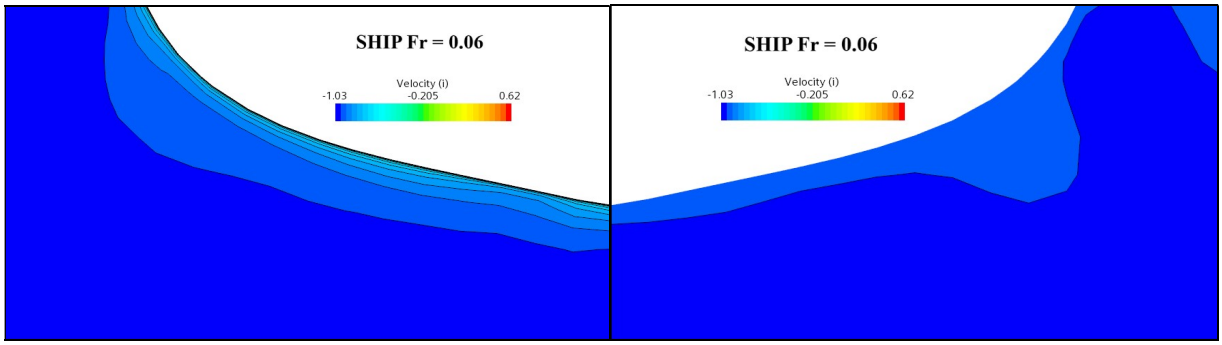

Viscous **Inviscid**

Figure 13: Non-dimensional velocity fields in X direction at different scales compared between viscous and inviscid flow (Bettica, naked hull; Fr = 0.06, with rolling).

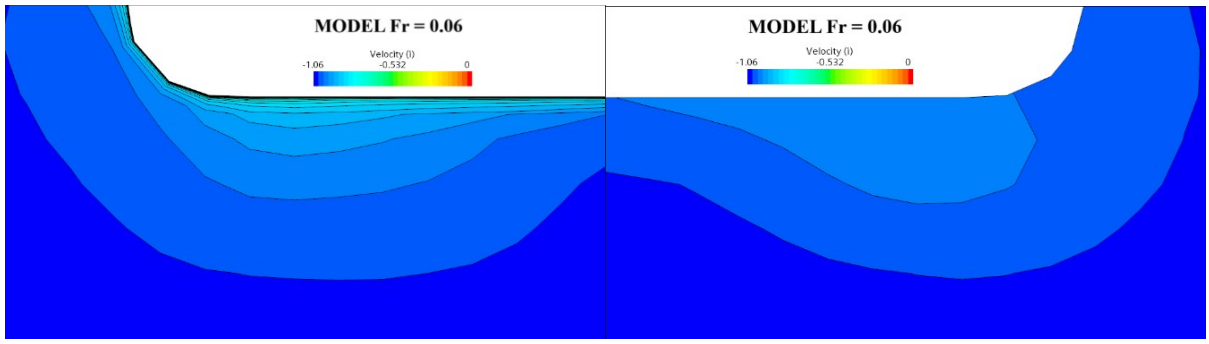

Viscous **Inviscid**

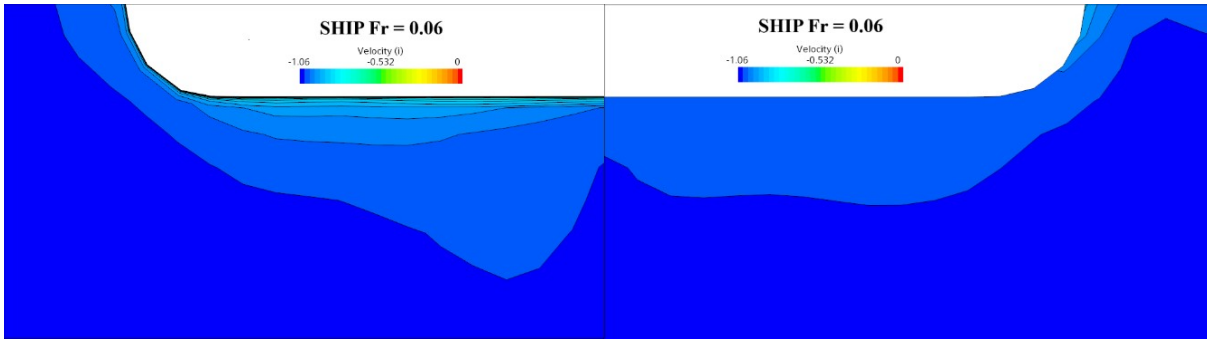

Viscous **Inviscid**

Figure 14: Non-dimensional velocity fields in X direction at different scales in comparison between viscous and inviscid flow (DTC, naked hull; Fr = 0.06, with rolling).

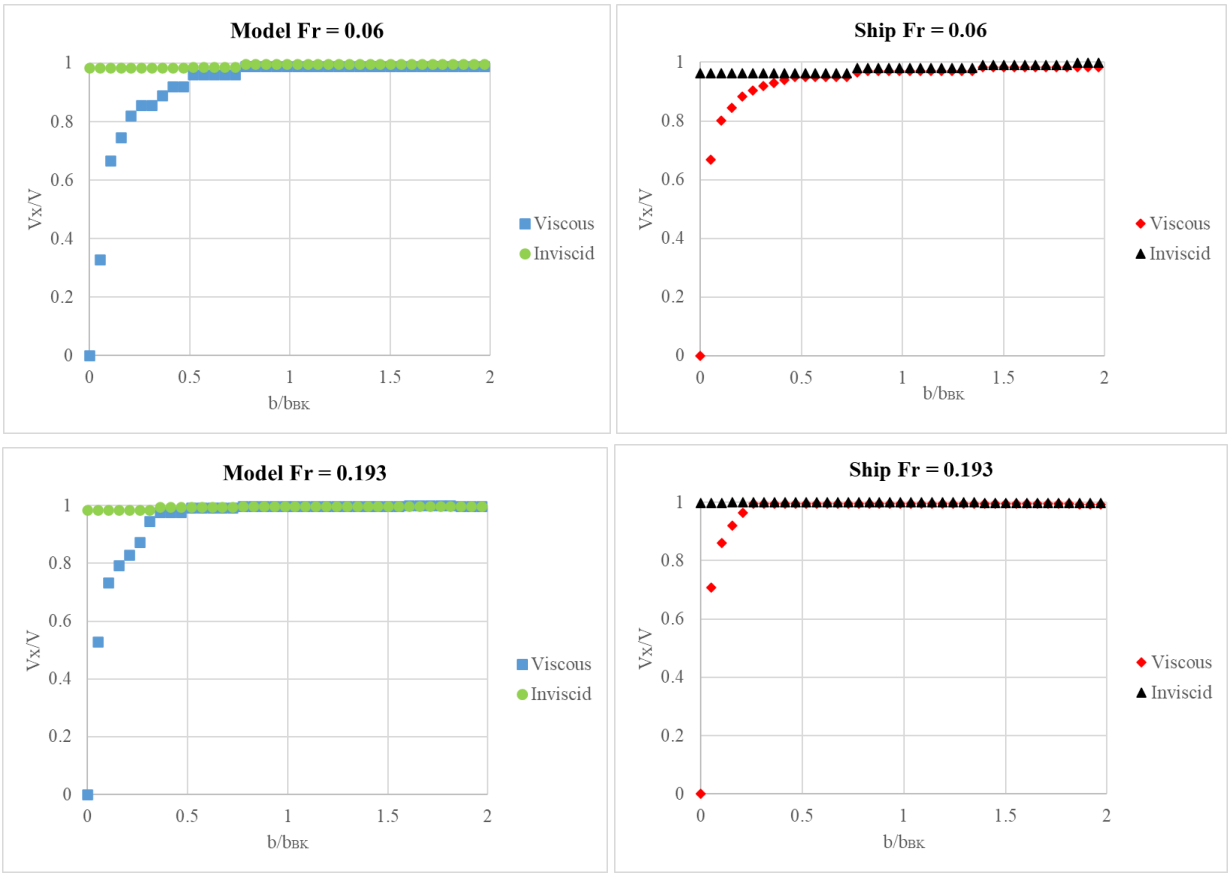

Figure 15: Viscous-inviscid non-dimensional velocity distribution in X direction at different forward speeds and scales (Bettica vessel, naked hull; roll with FS).

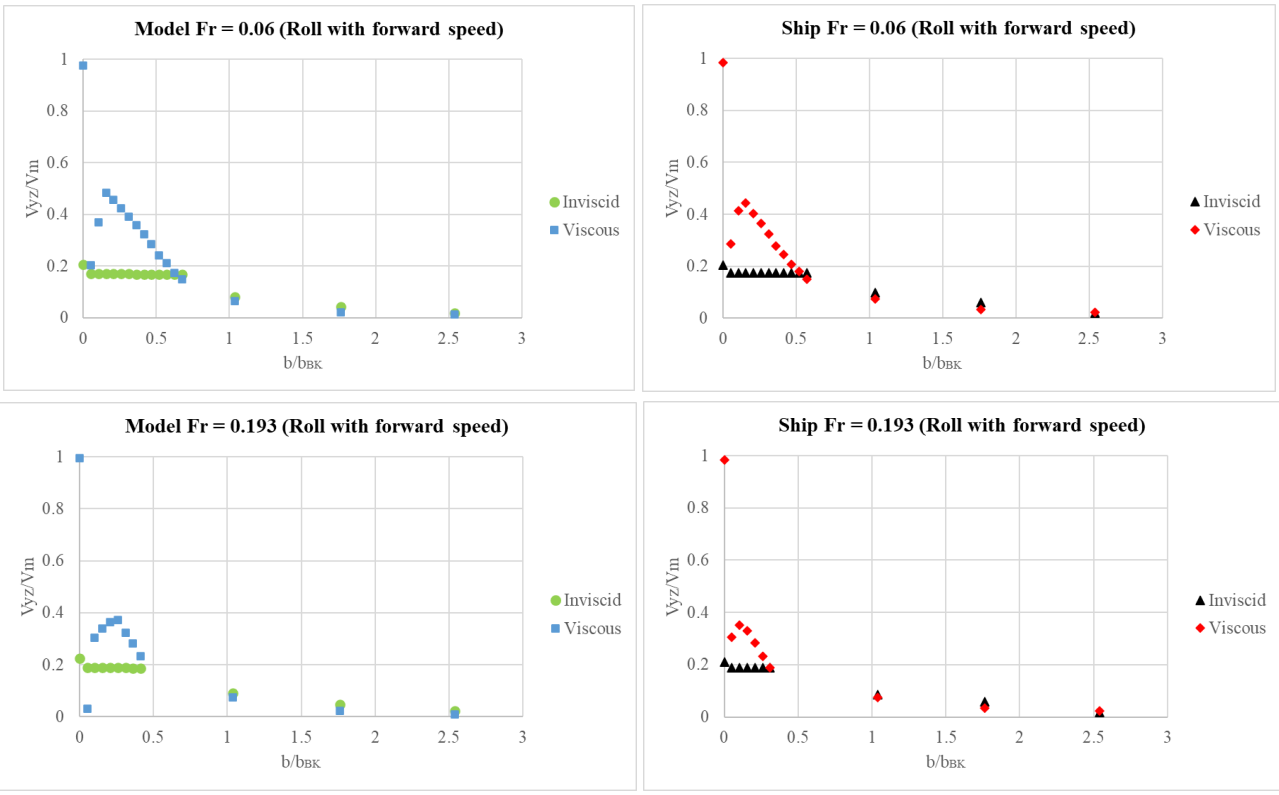

Figure 16: Viscous-inviscid non-dimensional velocity distribution in YZ direction at different forward speeds and scales (Bettica vessel, naked hull; roll with FS).

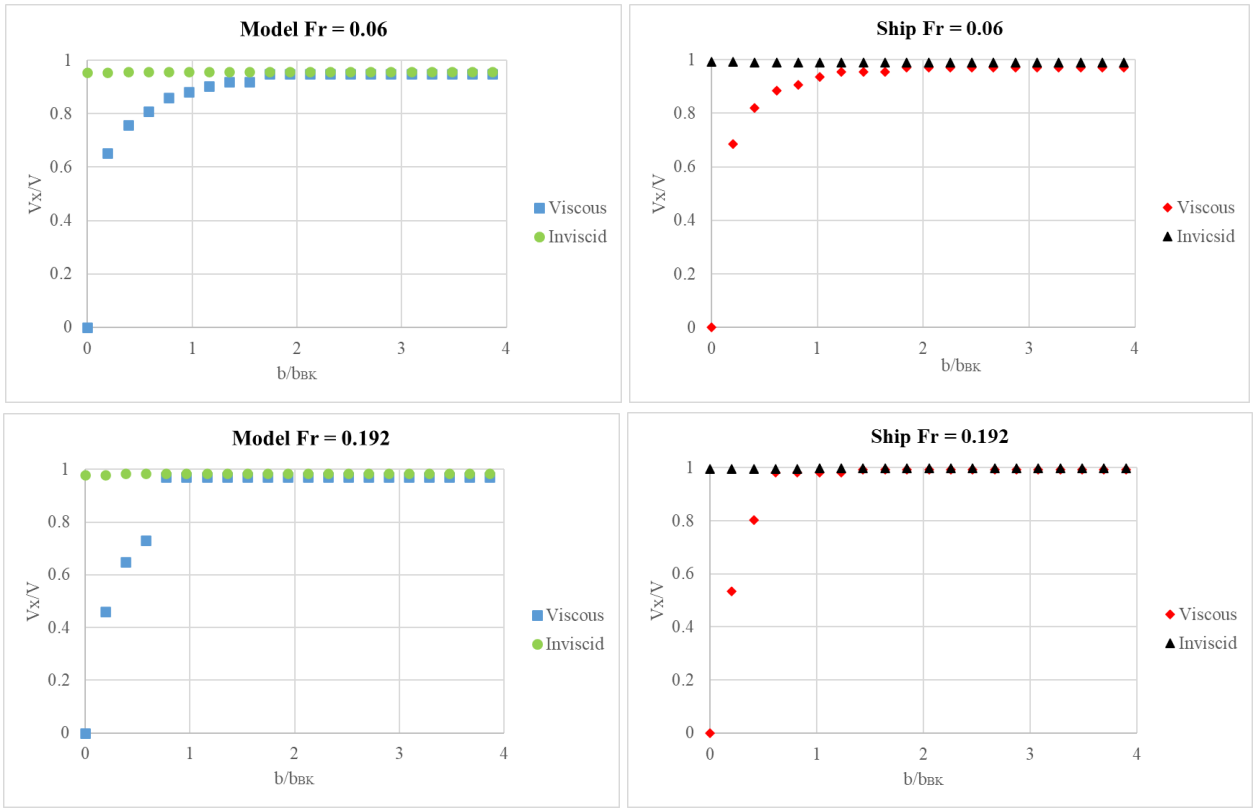

Figure 17: Viscous-inviscid non-dimensional velocity distribution in X direction at different forward speeds and scales (DTC vessel, naked hull; roll with FS).

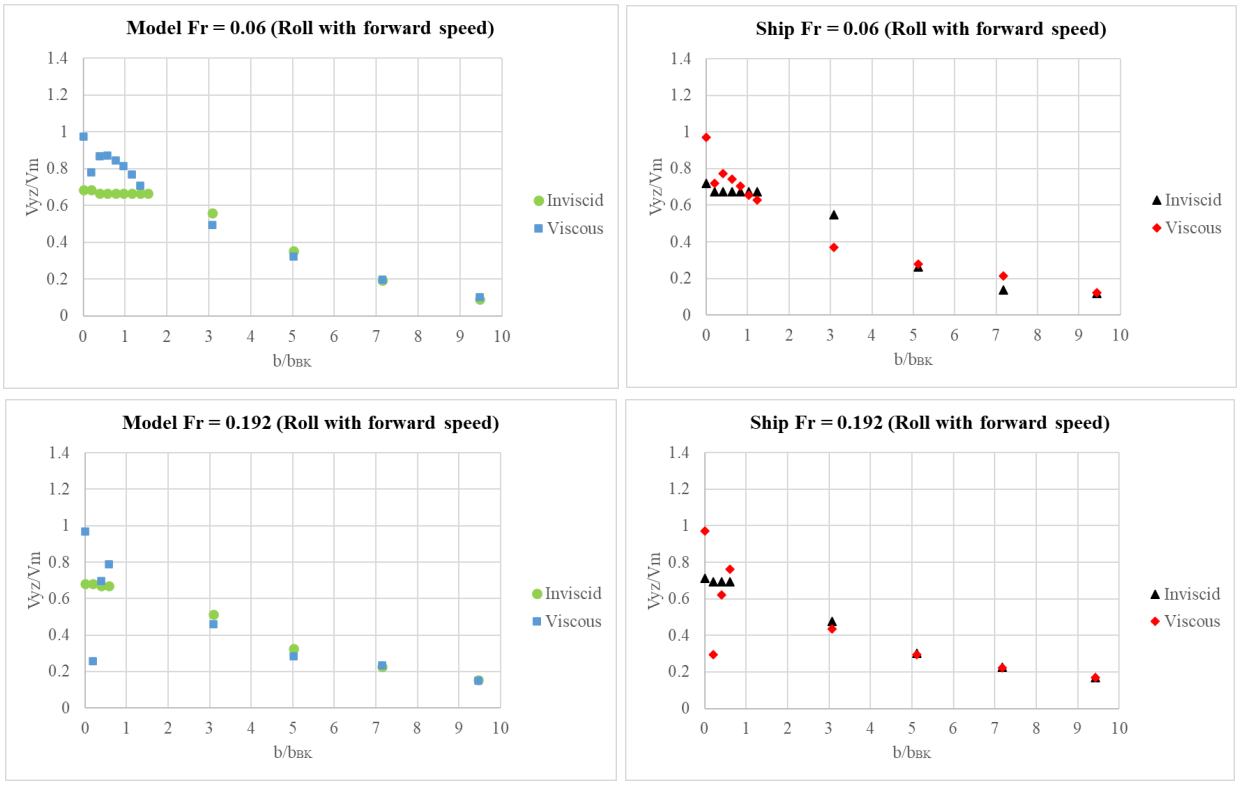

Figure 18: Viscous-inviscid non-dimensional velocity distribution in YZ direction at different forward speeds and scales (DTC vessel, naked hull; roll with FS).

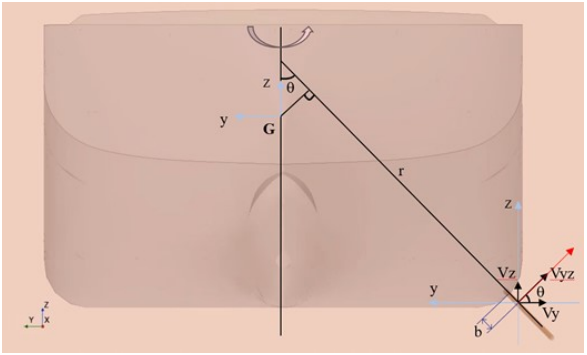

Figure 12: X direction and YZ direction in the coordinate system.

Figure 13 and Figure 14 show the non-dimensional velocity fields in X direction at different scales in comparison between viscous flow and inviscid flow at F_r = 0.06 observed for Bettica and DTC, respectively.

Figure 15 and Figure 17 show the comparison between viscous and inviscid flow of non-dimensional velocity distribution in X direction at different speeds and scales observed for Bettica and DTC, respectively. Figure 16 and Figure 18 show the comparison between viscous and inviscid flow of non-dimensional velocity distribution in YZ direction at different speeds and scales observed for Bettica and DTC, respectively. Note that the condition of roll motion in these Figures is rolling with forward speed. These figures show the velocity value at points along the position of bilge keel from the hull surface towards the far field as depicted in Fig. 12. Here, the horizontal axis is expressed as a ratio b/b_{BK} for conveniently comparing with the bilge keel breadth (b_{BK}), in which the position b/b_{BK} = 1.0 represents the bilge keel tip.

In Figure 13 and Figure 14, there is a difference in the non-dimensional velocity field between viscous flow and inviscid flow, that is there is naturally no boundary layer in the case of inviscid flow. From Figure 15 and Figure 17, it is seen that V_X/V is almost 1.0 in inviscid flow and increases gradually from zero before reaching the results of inviscid flow in viscous flow.

In Figure 16 and Figure 18, V_{YZ}/V_m decreases gradually to zero from the hull surface towards the far field, but there is a difference in velocity distribution between viscous and inviscid flows.

Based on these differences in Figure 15 and Figure 17, the boundary layer thickness (δ) in X direction can be determined as the distance from the hull surface to the position where velocities in viscous and inviscid flows are the same. The results show that the boundary layer in X direction of the model-scale is larger than that of the full-scale (in the correlation of scale factor) and the boundary layer in X direction at low speed is larger than that at high speed. This is also suitable with the velocity field images observed in Figure 11.

5.4 An explanation of the cause of the scale effects on bilge keel damping component

This section focus on explaining the cause of the scale effects on bilge keel damping component through observing and comparing the flow field (on earth fixed coordinate system) around the bilge keel position of naked hulls of Bettica and DTC vessels.

The non-dimensional velocity vector in YZ direction is given in Figure 19 and Figure 20. For Bettica vessel, Figure 21 shows the non-dimensional velocity distribution in YZ direction created by only forward speed (FS) and Figure 22 shows non-dimensional the velocity distribution in YZ direction created by only roll motion (by subtracting the non-dimensional velocities in Figure 16 with ones in Figure 21). For DTC vessel, Figure 23 shows the non-dimensional velocity distribution in YZ direction created by only forward speed and Figure 24 shows non-dimensional the velocity distribution in YZ direction created by only roll motion (by subtracting the non-dimensional velocities in Figure 18 with ones in Figure 23). These figures compare model-scale to full-scale data of both vessels in viscous flows at different Froude numbers.

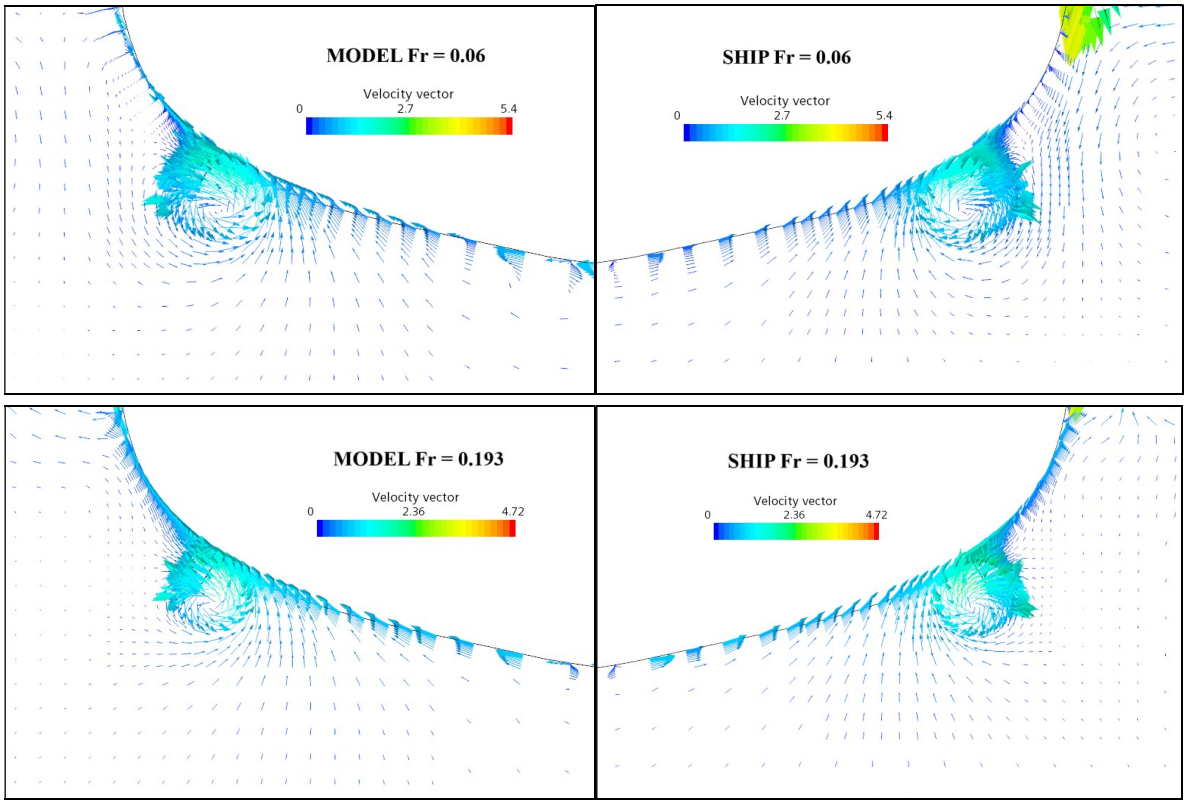

Figure 19: Non-dimensional velocity vector in YZ direction of model-scale and full-scale (Bettica ship, hull with BK, roll with FS).

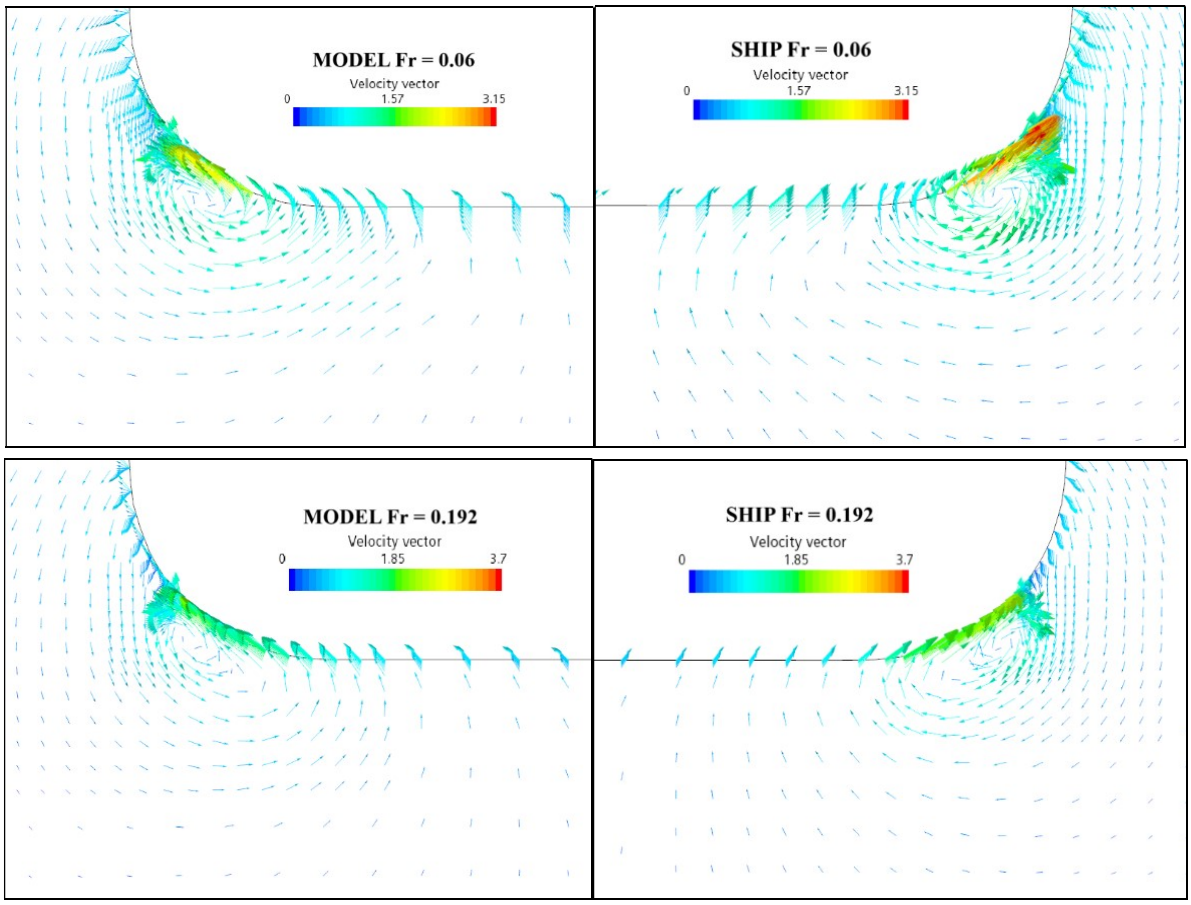

Figure 20: Non-dimensional velocity vector in YZ direction of model-scale and full-scale (DTC, hull with BK, roll with FS).

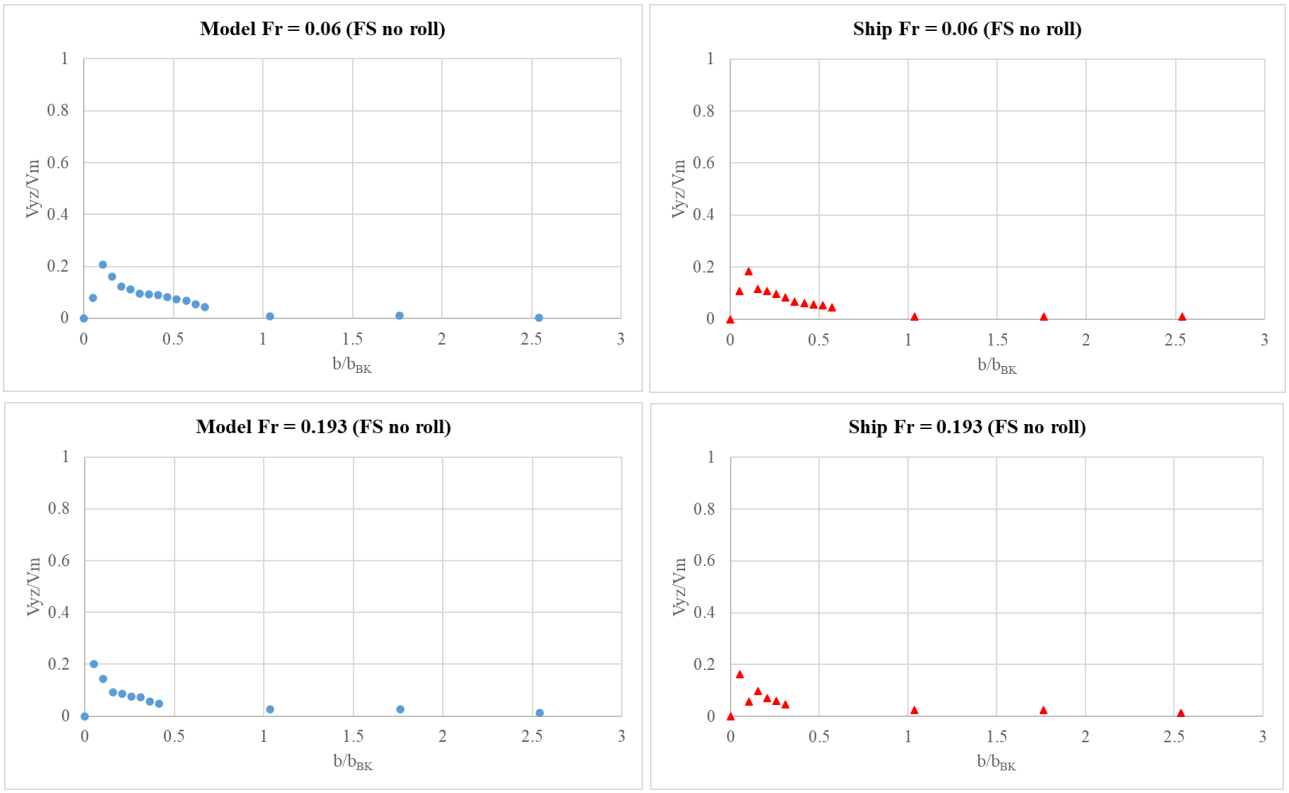

Figure 21: Non-dimensional velocity distribution in YZ direction created by only forward speed without roll motion (Bettica, naked hull).

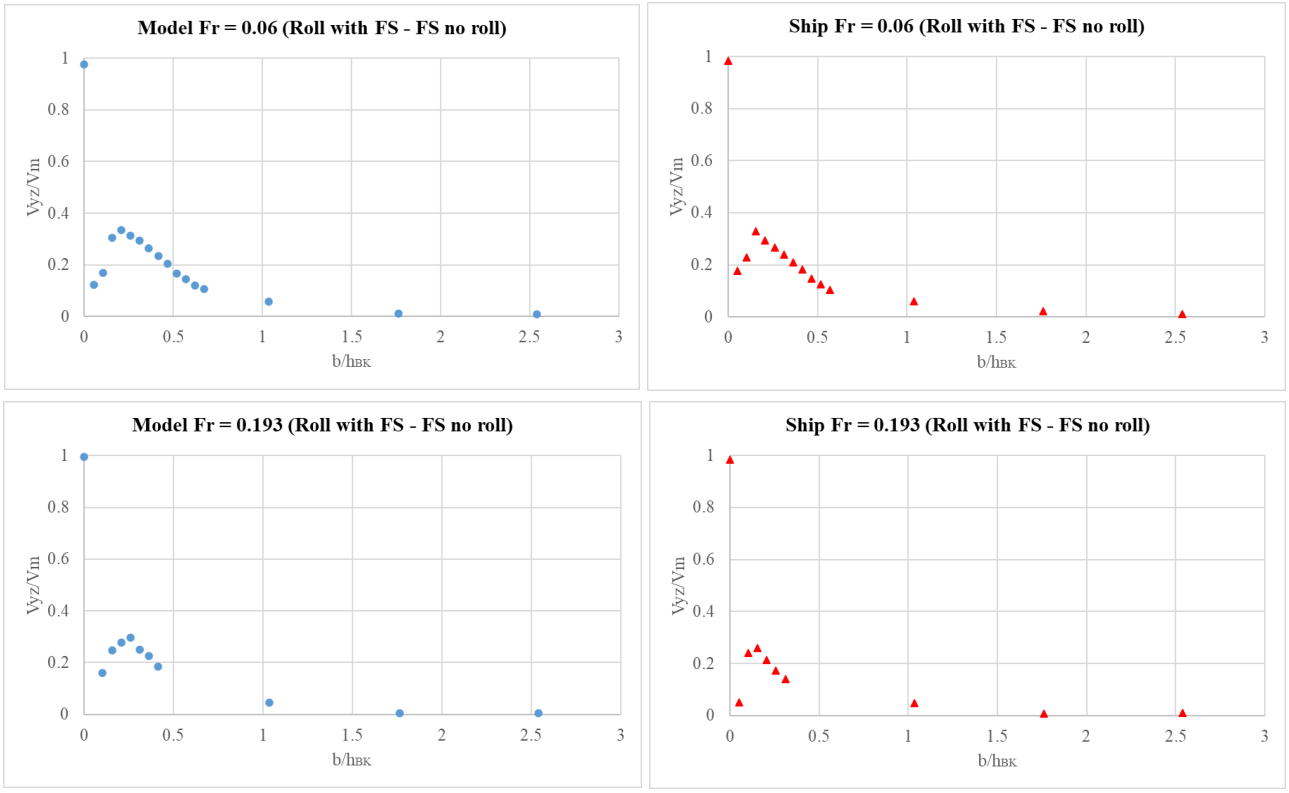

Figure 22: Non-dimensional velocity distribution in YZ direction created by only roll motion (Bettica, naked hull).

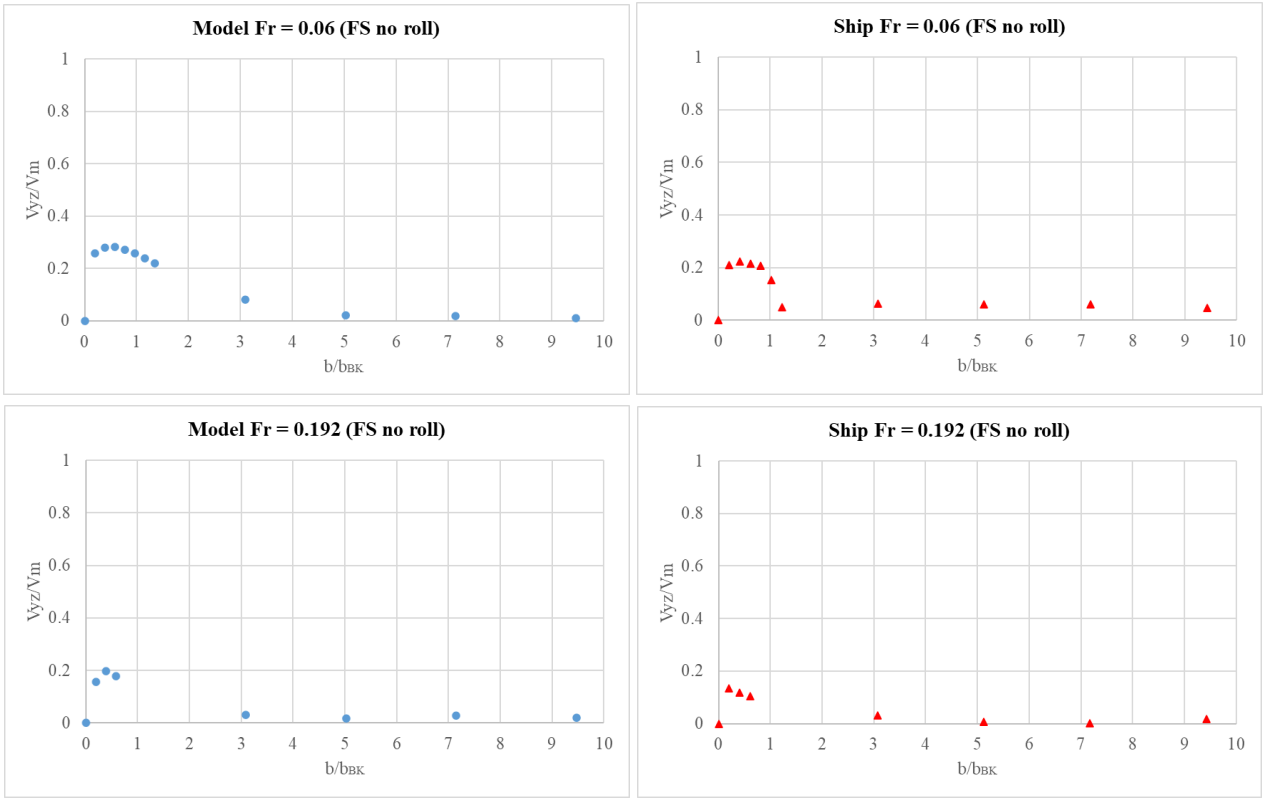

Figure 23: Non-dimensional velocity distribution in YZ direction created by only forward speed without roll motion (DTC, naked hull).

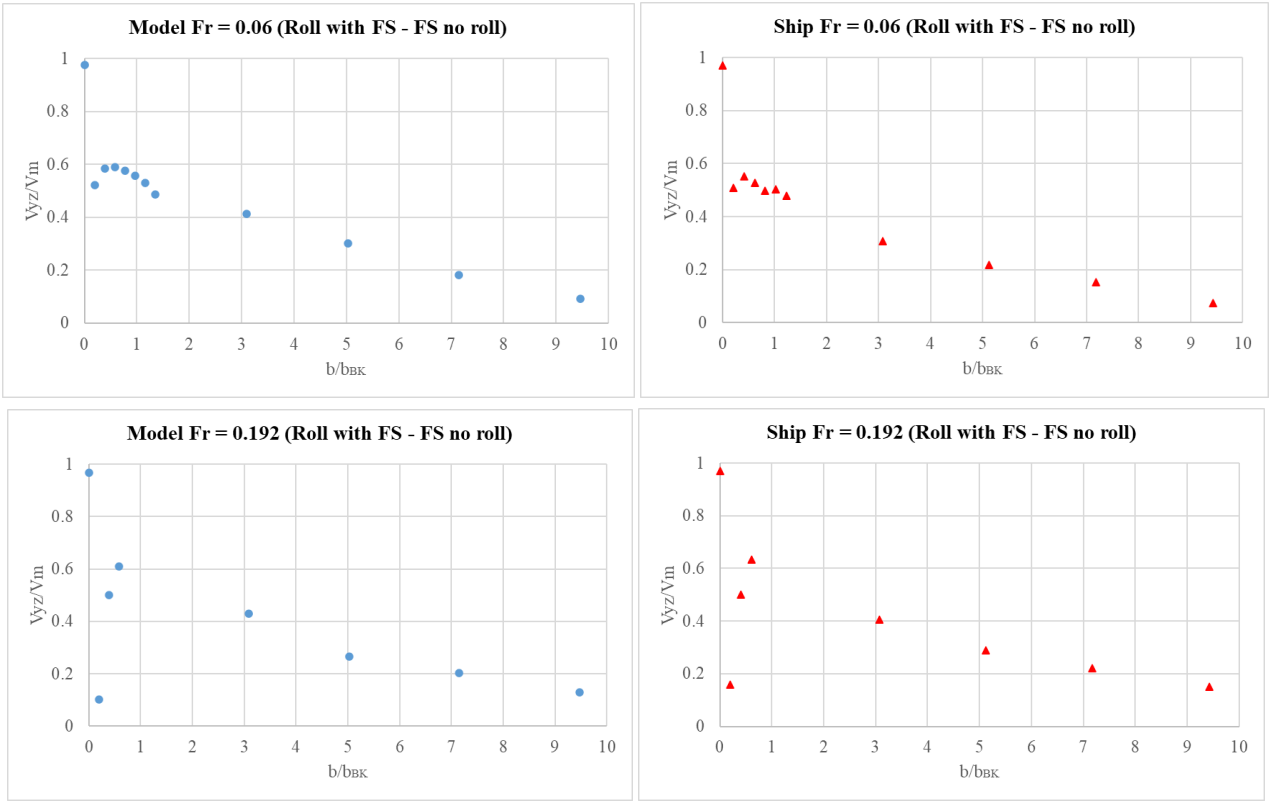

Figure 24: Non-dimensional velocity distribution in YZ direction created by only roll motion (DTC, naked hull).

For the ship Bettica (Figure 19), which the bilge keel damping is not affected by scale effects, it is observed that the size of vortex of the full-scale is similar as that of the model-scale at various Froude numbers. On the other hand, the scale effects on bilge keel damping can be clearly seen in Figure 20, in which the size of vortex created near the bilge keel of the full-scale is larger than that of the model-scale at low Froude number, whereas it is similar at high Froude number. In addition, observing the non-dimensional velocity distributions in various cases of DTC vessel (Figure 24), the difference is noticed in the low forward speed case, in which the non-dimensional velocity at b/b_{BK} = 1.0 of full-scale is smaller than that of model-scale. This means the relative velocity of fluid particle to the bilge keel tip of the model-scale is smaller than that of the full-scale. This results in the smaller vortex size and B_{44BK} at model-scale as seen in Figure 20 and Figure 10, respectively. In the case of Bettica, the relative velocity of fluid particle to the bilge keel tip of the model-scale is similar between model-scale and full-scale (Figure 22). This leads to the similarity in vorticity size and B_{44BK} of full-scale and model-scale as seen in Figure 19 and Figure 10, respectively.

6. CONCLUSIONS

Using numerical method, full-scale and model-scale roll motions are simulated for DTC and Bettica ships to investigate the scale effects on roll damping components. The followings are important conclusions:

- In section 5.2, the scale effects on the frictional damping component are found for both vessels. In addition, the scale effects on the bilge keel damping component appear in the case of DTC vessel at low forward speed.

- In section 5.3, a method is proposed to show the boundary layer created by only roll motion based on viscous and inviscid simulation.

- In section 5.4, based on analysing the velocity distribution and velocity vector observed for both vessels, the cause of scale effects on bilge keel damping component is explained detailly. In general, when the relative velocity of fluid particle to the bilge keel tip is significant to vortex size and its differences between model-scale and full-scale are proved to be the cause for the difference in the B_{44BK} at different scales.

7. ACKNOWLEDMENTS

This work was supported by JST SPRING, Grant Number JPMJSP2139.

8. REFERENCES

Broglia, R., Bouscasse, B., Di Mascio, A., Lugni, C., Atsavapranee, P., 2009, “Experimental and numerical analysis of the roll decay motion for a patrol boat”, The Nineteenth International Offshore and Polar Engineering Conference, OnePetro.

Ghamari, I., Mahmoudi, H.R., Hajivand, A., Seif, M.S., 2022, “Ship Roll Analysis Using CFD-Derived Roll Damping: Numerical and Experimental Study”, Journal of Mar. Sci. and Appl. 21, 67–79.

Gokce, M.K., Kinaci, O.K., 2018, “Numerical simulations of free roll decay of DTMB 5415”, Ocean Eng., 159, 539-551.

Grant, D. J., 2008, “Full Scale Investigation of Bilge Keel Effectiveness at Forward Speed”, Virginia Tech.

Ikeda, Y., Himeno, Y., Tanaka, N., 1978, “Components of roll damping of ship at forward speed”, Journal of the society of Naval Architects of Japan, Vol. 143, pp. 113-125.

ITTC Recommended Procedures and Guidelines, 2011, “Practical guidelines for ship CFD applications”, ITTC 7.5–03-02–03.

Liu, L., Chen, M., Wang, X., Zhang, Z., Yu, J., Feng, D., 2021, “CFD prediction of full-scale ship parametric roll in head wave”, Ocean Eng., 233, 109-180.

Moctar, O., Shigunov, V., Zorn, T., 2012, “Duisburg Test Case: Post-Panamax Container Ship for Benchmarking”, Ship Technology Research, 59(3), 50-64.

Nguyen, T.H.P., Taniguchi, T., Katayama, T., 2023, “Numerical Simulation Strategy of Full-scale Ship Roll Decay Motion”, Conference Proceedings, The Japan Society of Naval Architects and Ocean Engineers. Nagasaki, Japan.

Nguyen, T.H.P., Yoshida, N., Taniguchi, T., Katayama, T., 2024, “Investigation of the scale effects on roll motion for the ship Bettica using numerical simulation”, Polish Marit. Res. 31, 4-12.

Song, S., Demirel, Y. K., Atlar, M., 2019, “An investigation into the effect of biofouling on the ship hydrodynamic characteristics using CFD”, Ocean Engineering, Vol. 175, pp. 122-137.

Song, K., Guo, C., Sun, C., Wang, C., Gong, J., Li, P., Wang, L.,

2021, “Simulation strategy of the full-scale ship resistance and propulsion performance”, Engineering Applications of Computational Fluid Mechanics, Vol. 15(1), pp.1321-1342.

Terziev, M., Tezdogan, T., Incecik, A., 2022, “Scale effects and full-scale ship hydrodynamics: A review”, Ocean Engineering, vol. 245.

Yildiz B., Katayama T., 2017, “Bilge keel–free surface interaction and vortex shedding effect on roll damping”, Journal of marine science and technology, Vol. 22, pp. 432-446.

Session 2
Damage stability

Alternative crashworthy ship designs for enhancing safety and environmental performance

Dracos Vassalos, *University of Strathclyde, UK,* d.vassalos@strath.ac.uk
Francesco Mauro, *University of Trieste, Italy,* fmauro@units.it
Jeom Kee Paik, *University College of London, UK,* j.paik@ucl.ac.uk

ABSTRACT

This paper proposes a dual-strategy framework for enhancing damage stability in passenger ships, integrating crashworthy structural design (passive safety) with flood prevention measures (proactive safety). While traditional approaches—rooted in Rahola's early work and codified in SOLAS regulations—have focused primarily on survivability through subdivision, the maritime industry has seen diminishing returns from this singular emphasis. To address this, the present study repositions risk prevention as a core design objective alongside survivability, with the aim of developing safer and more environmentally efficient passenger vessels. Using a medium-sized cruise ship as a case study, the paper investigates six alternative hull configurations incorporating crashworthy structures and variations in main dimensions. Each design is assessed through Level 1 flooding risk analysis and preliminary speed-power predictions using modified Holtrop & Mennen methods. The results show that combining increased hull length with reduced breadth—while integrating crashworthy structures in high-risk zones—can yield significant reductions in both power consumption and flooding risk, thus achieving a balanced improvement in safety and energy efficiency. The study also highlights the potential for greater benefits when crashworthiness is combined with other risk control options, such as foam or deployable barriers. Overall, the findings advocate for a paradigm shift toward prevention-oriented ship design, offering practical guidance for the future development of safer and more sustainable cruise ships.

Keywords: *Damage stability; crashworthiness; flooding prevention; passenger ships; proactive safety design*

1. INTRODUCTION

Safety is one of the key performance indicators in the design of passenger ships, particularly cruise ships (Vanem et al., 2007; Vassalos and Guarin, 2009; Papanikolaou et al., 2013). It encompasses various engineering disciplines and operational tasks across a vessel's lifecycle (Hetherington et al., 2006). Over the past few decades, both industry and academia have primarily focused on improving safety in terms of survivability following a flooding incident. This focus has led to the development of a risk-based framework that replaces static assumptions with probabilistic approaches to damage stability. As a result, several major European research and joint industry projects have been undertaken to advance regulatory frameworks and promote innovative design solutions for enhanced safety, including HARDER (1999–2003), NEREUS (1999–2002), ROROPROB (1999–2002), SAFEDOR (2005–2009), and FLARE (2019–2022) (Luhmann et al., 2018).

Within this context, the FLARE project (2019–2022), the most recent European initiative focused on flooding risk safety, emphasized risk reduction through the implementation of both passive (design-based) and active (operational) risk control options (RCOs) (Vassalos et al., 2022). The project explored a range of alternative and complementary solutions aimed at enhancing vessel safety following a flooding event. Among the various strategies investigated, the incorporation of crashworthy structures in high-risk areas of the ship emerged as a promising option for reducing flooding risk (Cardinale et al., 2022). Leveraging the extensive application of super-element codes for crash analysis (Conti and Hirdaris, 2020; Mauro et al., 2023), the project enabled direct evaluation of how crashworthy structures influence the damage distribution scenarios considered in both statutory and advanced damage stability assessments. This approach has proven applicable across a wide spectrum of flooding hazards, including collisions, side groundings, and bottom groundings (Conti et al., 2022).

However, within the FLARE project, the application of crashworthiness was primarily directed at enhancing existing vessel designs, with

the objective of assessing risk reduction on operational ships (Vassalos et al., 2022a). While valuable, this reactive approach focused on post-design interventions. In contrast, the present study proposes a dual-strategy framework for damage stability, integrating crashworthy design (passive safety) and flood prevention (proactive safety) at the concept design stage. This approach reframes safety not merely as compliance with regulatory requirements but as a core design attribute that defines the overall quality and resilience of a new vessel.

In this framework, crashworthy structures are introduced as passive safety elements to limit structural deformation and reduce the extent of initial damage during collisions or groundings. The crashworthy structure intends to prevent the breaching of the hull instead of limiting structural deformations. Simultaneously, flood prevention strategies are incorporated to contain or delay the progression of floodwater into adjacent compartments, thereby improving survivability. This dual focus ensures both mitigation of damage consequences and reduction of the likelihood of progressive flooding.

To demonstrate the practical implications of this approach, this paper examines how the inclusion of crashworthy structures can influence the main dimensions of a vessel, while also targeting improved propulsive efficiency. In particular, increasing the length-to-breadth (*L/B*) ratio is explored as a means to enhance hydrodynamic performance and environmental sustainability. Six alternative design configurations, derived from an existing cruise ship, are developed—each varying in length and breadth while maintaining a constant displacement and draught. The main engine room, identified as a high-risk zone for flooding based on the original vessel's risk profile, is reinforced with crashworthy structural elements in all variants.

Each design alternative is assessed using Level 1 risk analysis in accordance with the FLARE framework, quantifying flooding risk and survivability. Simultaneously, propulsive performance is estimated using an in-house empirical-statistical model to evaluate trade-offs between safety and efficiency.

2. CRASHWORTHYNESS CONCEPT

Crashworthiness has been recognized as an effective risk mitigation measure for damage stability since the early 1990s (Egge and Bockenhauger, 1991; Pedersen, 1994; Naar et al., 2002; Paik, 2020; Bai and Paik, 2024). However, its routine application in the early stages of passenger ship design has been limited, primarily due to the absence of suitable analysis tools and the additional complexity introduced by the Alternative Design and Arrangements process outlined in MSC.1/Circ.1212, which can be tedious and time-consuming.

Despite these challenges, crashworthiness refers to the structural capacity to withstand impact and minimize the extent of damage resulting from collisions or groundings. Consequently, the design of crashworthy structures in passenger ships requires a comprehensive reevaluation of the layout of main longitudinal and transverse structural elements, with an emphasis on optimizing energy absorption and damage localization.

Within the FLARE project, a focused study was conducted to establish crashworthiness as a viable risk control option for mitigating flooding risk. The objective was to develop a generalized scaling methodology that adapts conventional damage dimension distributions—traditionally used for damage stability assessments—to new distributions that account for structural reinforcement effects (Mauro and Vassalos, 2022; Cardinale et al., 2022).

According to the FLARE risk analysis framework, the types of damage considered for damage stability assessment include collisions, side groundings, and bottom groundings. Each damage type is characterized by specific marginal distributions for the associated variables defining damage dimensions and locations.

The true effectiveness of a crashworthy structure in limiting damage extent can only be validated through the occurrence of a real collision or grounding. In the absence of such data, numerical simulations serve as a viable alternative for performance evaluation. To this end, simulations have been carried out using super-element-based codes—SHARP (Le Sourne et al., 2012) and FLAGS (Pineau et al., 2022)—to model structural responses under collision, side grounding, and bottom grounding scenarios. The simulations were

performed on a reference cruise ship, modeling impacts with a representative sample of other vessels in the case of collisions, and predefined rigid obstacles in the case of side and bottom groundings. These scenarios aim to evaluate how crashworthy reinforcements influence damage propagation and energy absorption characteristics.

3. FRAMEWORK FOR ENERGY EFFICIENCY AND ENVIRONMENTAL IMPACT

In parallel with safety, energy efficiency and environmental impact are of paramount importance in the design of modern and future passenger ships. Addressing only one of these aspects in isolation may inadvertently compromise the other. Therefore, safety and energy efficiency should be addressed concurrently within an integrated design framework, aiming to achieve an optimal balance between these two critical attributes.

The implementation of risk control options (RCOs)—such as static foam installation in void spaces and crashworthy structural enhancements—has the potential to significantly influence both the safety and environmental performance of future ship designs. For instance, the integration of deployable barriers or foam systems requires sufficient internal space, potentially prompting a reconfiguration of the vessel's internal layout. Similarly, the adoption of crashworthy structures may necessitate the repositioning of transverse bulkheads away from the conventional B/5 spacing mandated by current regulations.

Recent studies (Vassalos et al., 2024) have demonstrated up to a 40% reduction in flooding risk when applying selected RCOs to limited sections of an existing vessel. This suggests that a comprehensive rethinking of passenger ship design, incorporating such measures from the early design stage, may yield even greater risk reductions than traditional design approaches.

A lower overall risk profile achieved through such RCOs may also affect key design parameters, including the vessel's main dimensions. Over the past two decades, cruise ship designs have exhibited a trend toward decreasing length-to-breadth (*L/B*) ratios, as shown in Figure 1, which plots *L/B* values for cruise ships built between 2000 and 2023. This trend is largely driven by the need to increase breadth (*B*) to improve initial stability and ensure compliance with damage stability regulations.

However, a vessel designed with risk-prevention strategies, such as crashworthy structures and passive flooding mitigation systems, may no longer require increased breadth solely to meet damage stability criteria. This opens up the possibility of reducing breadth, thereby increasing the *L/B* ratio—a change that is generally favorable for reducing hydrodynamic resistance and improving fuel efficiency.

Nonetheless, this approach must be carefully balanced, as increasing the *L/B* ratio—by reducing breadth—negatively affects transverse stability. Specifically, a decrease in breadth reduces the initial metacentric height (KM), due to a lower moment of inertia of the waterplane area. Assuming a constant vertical center of gravity (KG), this results in a lower GM, and thus diminished overall stability. This reduction in GM may challenge compliance with statutory intact and damage stability criteria.

In this context, the application of RCOs such as crashworthiness can be leveraged to offset the stability penalty by lowering the vessel's flooding risk profile, providing greater flexibility in hull form design. In essence, enhanced structural protection may allow for more slender, energy-efficient designs while still maintaining—or even improving—compliance with safety regulations.

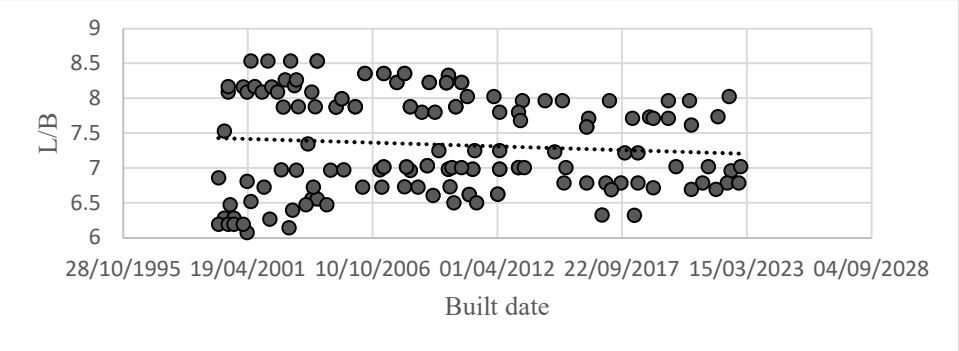

Figure 1: . *L/B* trend for cruise vessels in the last 20 years.

Considering the above, achieving an optimal balance between safety and energy efficiency in modern passenger ship design requires a structured and iterative framework, comprising the following key steps:

- Preparation of the initial geometry and general arrangement
- Flooding risk analysis of the baseline design
- Powering performance assessment of the baseline design
- Identification of vulnerable zones based on flooding risk analysis
- Implementation of crashworthy structural solutions in high-risk areas
- Re-evaluation of flooding risk with the added structural enhancements
- Modification of the ship's main dimensions and internal layout to accommodate crashworthy structures
- Reassessment of both flooding risk and powering performance based on the updated geometry
- Verification of performance improvements and compliance with statutory regulations

With the exception of the initial baseline design development, these steps should be performed recursively, allowing continuous refinement until the design meets the targeted energy efficiency goals while maintaining a low flooding risk profile and ensuring regulatory compliance.

This optimization framework relies on the execution of flooding risk assessments and powering performance predictions. For the risk assessment, the methodology follows the flooding risk calculation framework developed in FLARE, applying either Level 1 or Level 2 analysis depending on the detail and fidelity required by the designer.

One of the most straightforward approaches is to compare the power curves of different design iterations. By evaluating absorbed power at equivalent speeds, the designer can directly quantify improvements in energy efficiency introduced by design changes, including those driven by crashworthy structure integration and layout optimisation.

$$\Delta P_B = 100\left(1 - \frac{P_{B_{new}}}{P_{B_{old}}}\right) \quad (1)$$

An alternative to evaluating the whole speed-power curve of the vessel is adopting a statutory index of efficiency. This is the case of the Energy Efficiency Design Index (EEDI) (IMO, 2024).

As for a cruise ship, it is not achievable to reduce the installed power between two concurrent designs due to the electrical loads absorbed by the hotel and supposing to have projects with the same DWT to preserve the final payload, the only variable that changes is the Vref. Therefore, the change in EEDI is proportional to the ratio between the attained velocities of the two designs.

Given this, to evaluate the safety and environmental efficiency of two concurrent designs, the *PLL* and EEDI (or *ΔPB*) can be employed, aiming at reducing both variables (in the case of *ΔPB* this should be increased).

4. CRASHWORTHY DESIGNS

To investigate the benefit of implementing a crashworthy structure onboard a cruise ship it is worth considering a specific example on a reference ship. The ship is an example of a large cruise ship, firstly assessed in its original configuration calculating the *PLL* at Level 1, as previously defined. The execution of preliminary risk analysis allows for determining the most critical areas along the ship, thus identifying the regions for implementing Risk Control Options. Fig. 2 shows the 'static risk profile' of the vessel, presenting the non-dimensional penetration and location of the critical damages identified by the static damage stability calculations, which means the damages where the p(1-s) value is above 1E-4.

The figure supports the identification of high-risk flooding zones, specifically highlighting two critical areas: one located on the fore shoulder and the other on the aft shoulder of the ship. Among these, the aft shoulder is identified as the most vulnerable, exhibiting damage scenarios with greater penetration depths. This region houses the engine rooms, which are characterised by large compartments interspersed with a relatively high number of void spaces—features that contribute to a higher flooding risk.

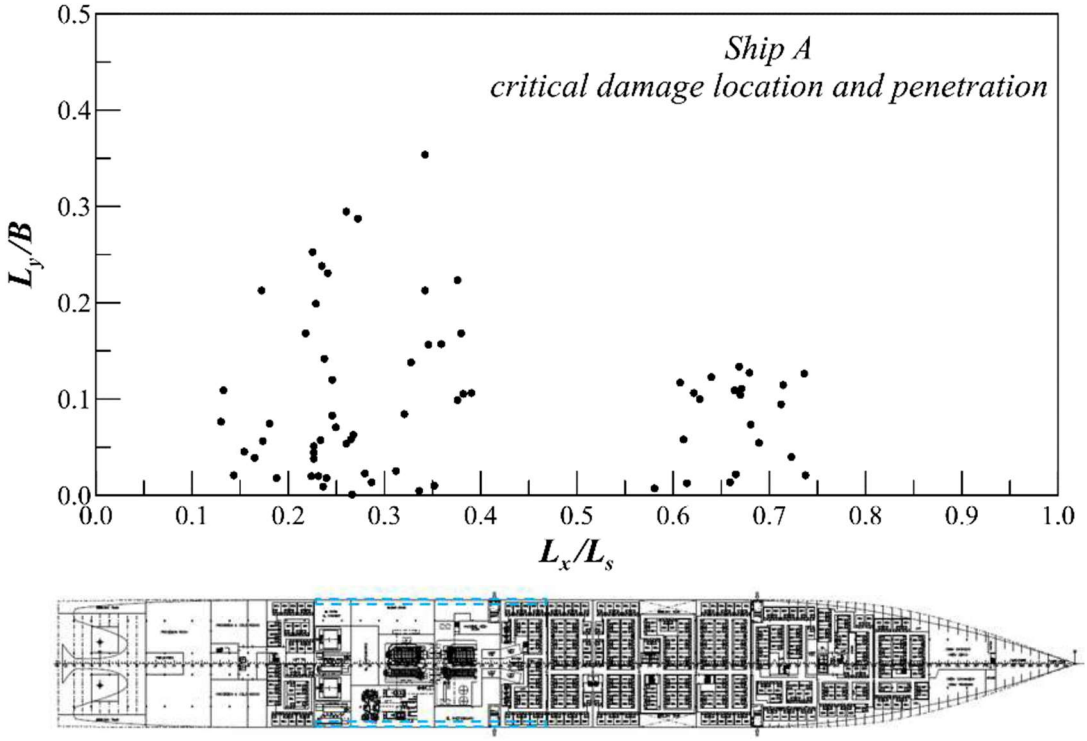

Figure 2: . Critical damage locations and penetrations for the reference ship and locations of the crashworthy structure.

Enhancing structural protection in this area can significantly reduce the overall flooding vulnerability of the vessel. Figure 2 also illustrates the general arrangement of the vessel with the integration of a proposed crashworthy structure in the aft shoulder, identified as the most critical zone. The identified area for the installation of the double hull does not exactly extend over the whole area of critical damages, but has been selected, following designers' indications, to fit an area where it was possible to install the structure. As such, the area extends a bit forward to the critical zone but covers the region where most critical damages are identified.

The proposed crashworthy solution involves the installation of a watertight double hull positioned at B/20, reinforced locally with 12 mm plating. This configuration corresponds to one of the design options described in the previous section. Based on this structural enhancement, it was possible to evaluate the Potential Loss of Life (*PLL*) by applying the damage model correction methodology outlined earlier.

Table 1 presents the *PLL* results for both the original and crashworthy configurations, assessed under Level 1 risk analysis. The results indicate a 14.62% reduction in *PLL* for the crashworthy configuration compared to the original design. This demonstrates that the proposed structural reinforcement is highly effective in mitigating flooding risk associated with impact scenarios.

These findings open the possibility of further exploring alternative configurations of the ship's main dimensions, taking into account not only safety enhancements but also energy efficiency, thereby supporting a multi-criteria project evaluation and ranking approach for future vessel designs.

Table 1: *PLL* Level 1 values for the reference ship.

Damage type	Original configuration	Crashworthy design
Collision	0.3549	0.2716
Side grounding	0.5349	0.4721
Bottom grounding	0.1990	0.1859
Total	1.0880	0.9296 (-14.62%)

5. CRASHWORTHY AND ENVIRONMENTALLY EFFICIENT DESIGNS

In the previous section, it has been demonstrated that a crashworthy structure is beneficial for reducing the risk of flooding for a passenger ship. According to the damage stability framework, a reduction in risk at Level 1 is associated with an increase in the statutory A-index. This, in turn, reflects a change in the limiting GM of the vessel,

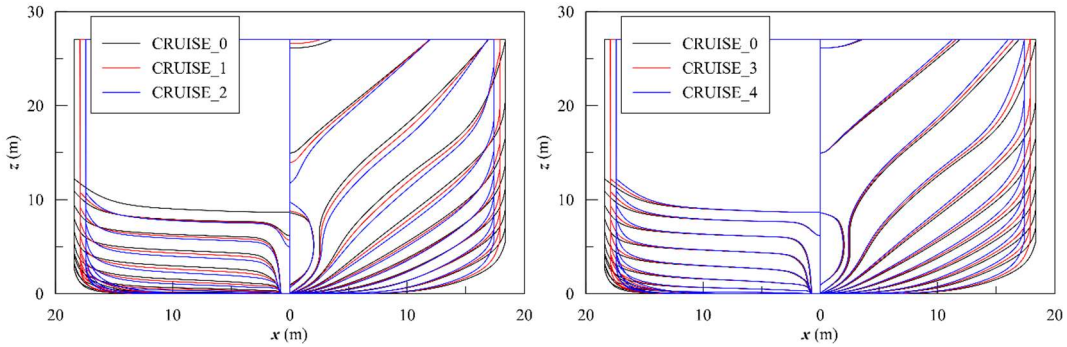

Figure 3: . Transversal section comparison of the sample cruise ships.

requiring the achievement of a lower GM compared to the original configuration. Such a consideration opens the possibility of studying design configurations having lower initial GM, whilst achieving a reasonable level of risk for the vessel.

With this aim, it could be possible to increase the L/B ratio of the vessel, reducing the hull's breadth to achieve higher propulsive performance. However, B reduction is not beneficial for the vessel's initial KM, as a reduced *B* corresponds to a lower inertia of the waterplane with a consequent reduction of the metacentric height. As a matter of fact, considering comparable internal layouts for the ship, the solutions with higher *L/B* will have higher levels of *PLL*. However, adopting a crashworthy structure could lead to risk levels comparable to the original design. To investigate the potential benefit of an increase in the *L/B* ratio, six different design solutions have been studied:

- CRUISE_0: is the original hull form of the ship. The vessel is not equipped with a crashworthy structure.
- CRUISE_0c: is the original hull form of the ship equipped with a crashworthy double hull at B/20 (see Fig. 3).
- CRUISE_1: the breadth has been decreased by 1 meter while increasing the length by 1 meter. The draught is constant. Such a solution decreases the initial KM by 1 meter compared to CRUISE_0. The vessel is equipped with a crashworthy double hull at *B*/20 (see Fig. 3).
- CRUISE_2: breadth has been decreased by 2 metres while increasing the length by 2 metres. The draught is constant. Such a solution decreases the initial KM by 2 metres compared to CRUISE_0. The vessel is equipped with a crashworthy double hull at B/20 (see Fig. 3).
- CRUISE_3: the breadth is decreased by 1 meter while the length is increased by 8.5 metres. The draught remains constant. Such a solution decreases the initial KM by 0.865 m. The vessel is equipped with a crashworthy double hull at B/20 (see Fig. 3).
- CRUISE_4: the breadth is decreased by 2 metres while the length is increased by 17.5 metres. The draught remains constant. Such a solution decreases the initial KM by 1.715 m. The vessel is equipped with a crashworthy double hull at *B*/20 (see Fig. 3).

Fig. 3 compares the hull forms obtained by the above-mentioned iso-displacement transformations. It can be observed that the first two hulls (CRUISE_1 and CRUISE_2) have a less slender waterline compared to CRUISE_0, as the necessity to keep the volume constant while reducing the breadth results in increasing the area of the fore and aft sections. Such a form is not beneficial for wave resistance. However, it should be noted that both hulls have a lower wetted surface compared to CRUISE_0, leading to a lower frictional resistance. Therefore, the remaining two hulls have been modelled in such a way as to compensate for the volume losses due to reduced breadth with an increased length. Follwing this strategy, the sections in the aft ship remain the same as for CRUISE_0, while the fore section is slightly slender compared to the mother ship. Also in this case, both CRUISE_3 and CRUISE_4 have a reduced wetted surface compared to CRUISE_0.

To perform risk analysis and propulsive performance predictions on the 5 different design solutions, the following assumptions have been considered:

- The internal layout of the vessel has been considered similar among the different solutions. The main internal spaces have been scaled according to the changes in *L* and *B*.

- The total amount of installed power has been kept constant among the design solutions.
- The displacement, and consequently the payload, is constant between the solutions.
- The vertical centre of gravity is constant between the solutions.
- The risk assessment has been performed at Level 1.
- Powering prediction has been performed with empirical-statistical methods.
- The evaluation of environmental performances has been assessed in terms of *ΔPB* at the reference speed of 20 knots.

The following sections present the calculation methods and the results obtained for the 5 different design options concerning risk analysis and propulsive performances.

Risk analysis

Simplified prediction methods have been applied to estimate the risk profile of the six design solutions as well as propulsive performance. For Level 1 risk analysis, the code PROTEUS III (Jasionowski, 2001) has been employed, evaluating the p and s factors of 30,000 damages (including collisions, side and bottom groundings) and then evaluating the associated risk.

To generate the three damage types for the analysis of the six different configurations, a method based on Quasi-Monte Carlo sampling (Mauro and Vassalos, 2022) has been used. Such a strategy allows estimation of the same damage distributions between the vessels, namely all the damage cases generated by the same Sobol sequence of quasi-random numbers. Table 2 presents the PLL values at Level 1 for the six designs, showing the attained value for each damage type and the final level. As already mentioned above, CRUISE_0c has a *PLL* reduction of 14.62% compared to CRUISE_0, with a significant contribution given by the reduction of collisions and side grounding risks. Analysing the results of alternative vessels with higher *L/B* ratio, CRUISE_1 shows a PLL decrease of 0.84 % compared to CRUISE_0, which means that the crashworthy structure compensates for the GM reduction. CRUISE_2 has a flooding risk increase of 18.82% compared to CRUISE_0; therefore, for this design solution, the crashworthy structure is not capable of compensating for the GM reduction. CRUISE_3 has a risk reduction of about 5% compared to CRUISE_0, showing promising results while increasing also the ship length. Finally, CRUISE_4 has a *PLL* increase of 4.82% compared to the original design solution, highlighting how the length increase, and the crashworthy structure do not balance the reduction of the GM.

From this initial preliminary risk analysis, some configurations present benefits compared to the original design, while others increase the flooding risk level. Therefore, it is worth to analyse also the propulsive performances of the different design solutions to better understand the benefits and disadvantages of the proposed solutions.

Propulsive analysis

To explore the potential benefits of hull breadth reduction on energy efficiency, preliminary powering calculations were carried out for five alternative hull forms. These calculations employed the Holtrop & Mennen power prediction method over a speed range of 0 to 24 knots. An in-house powering tool was used, incorporating a modified version of the classical Holtrop and Mennen approach (Holtrop and Mennen, 1988), which includes a speed-dependent form factor to improve accuracy across the operational range.

Hull-propulsor matching was assessed using B-series propellers (Kuiper, 1992), ensuring realistic performance estimations. Due to the unavailability of complete generator data for the original ship, the *ΔPB* (change in brake power) was used as an alternative metric to evaluate environmental performance, in place of the Energy Efficiency Design Index (EEDI).

Table 2: *PLL* Level 1 values for the reference ship

Damage type	CRUISE_0	CRUISE_0c	CRUISE_1	CRUISE_2	CRUISE_3	CRUISE_4
Collision	0.3549	0.2716	0.3904	0.4436	0.3584	0.4081
Side grounding	0.5349	0.4721	0.4883	0.6312	0.4814	0.5255
Bottom grounding	0.1990	0.1859	0.2010	0.2189	0.1930	0.2050
Total	1.0880	0.9296 (-14.62%)	1.0796 (-0.84%)	1.2937 (+18.82%)	1.0329 (-5.14%)	1.1386 (+4.58%)

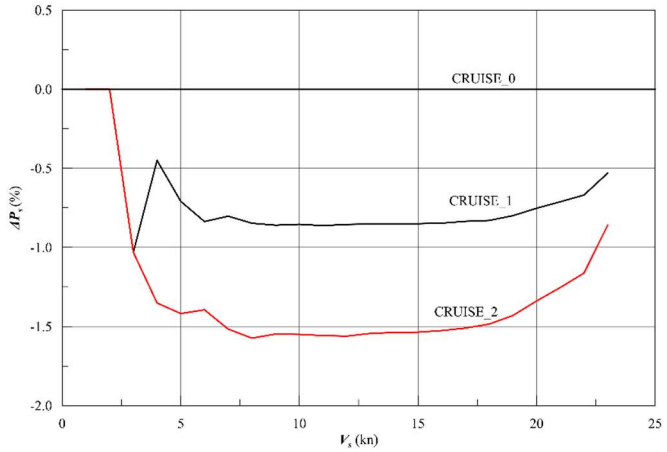

Figure 4: . Comparison between shaft power of CRUISE_0 with CRUISE_1 and CRUISE_2

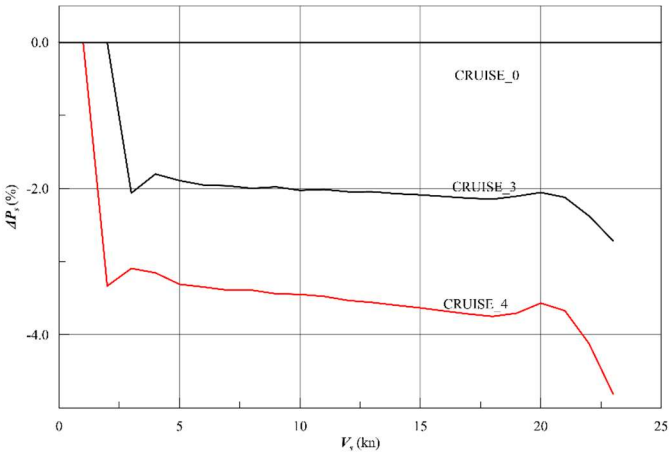

Figure 5: . Comparison between shaft power of CRUISE_0 with CRUISE_3 and CRUISE_4

Figure 4 presents the shaft power predictions for CRUISE_1 and CRUISE_2, expressed as a percentage relative to the baseline shaft power of the original configuration (CRUISE_0). The results indicate a modest improvement in power consumption across the full speed range for both designs. CRUISE_1 achieved a reduction of less than 1%, while CRUISE_2 attained a slightly higher improvement of approximately 1.5%.

In contrast, the results for CRUISE_3 and CRUISE_4 demonstrate more substantial improvements. Figure 5 illustrates the speed-power curves for these two hulls, showing clear benefits from increased slenderness. CRUISE_3 exhibited a consistent power reduction of around 2% across the speed range, while CRUISE_4 achieved the most significant improvement, with reductions ranging from 3.5% to 4%.

These findings suggest that reducing hull breadth—while maintaining structural safety through crashworthy design—can contribute to measurable gains in propulsive efficiency and environmental performance, particularly in more slender configurations such as CRUISE_4.

6. DISCUSSION

The previous section presented the outcomes of both the flooding risk analysis and the speed-power performance predictions for the six alternative design configurations investigated in this preliminary study. The results reveal varying trends across the different hull forms, with each design offering distinct trade-offs between risk reduction and propulsive efficiency. Consequently, a combined analysis of these two performance indicators is essential for drawing meaningful conclusions.

To facilitate this comparison, the two key performance metrics—Potential Loss of Life reduction (ΔPLL) and brake power reduction at 20 knots (*ΔPB*)—are plotted together in a single diagram. Figure 6 displays the percentage values of *ΔPB* (y-axis) versus *ΔPLL* (x-axis) for each of the six design configurations. This visual representation allows for a more intuitive understanding of the

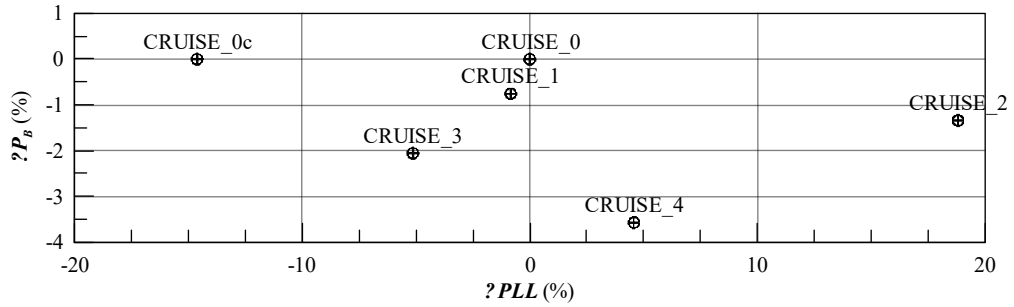

Figure 5: . Comparison of the six design solutions in terms of ΔPLL and ΔP_B.

balance achieved between safety and energy efficiency in each case.

From the diagram, it is immediately apparent that the original designs (CRUISE_0 and CRUISE_0c) are the least favorable in terms of propulsive performance, as both share the same hull form and therefore yield no reduction in power consumption. However, CRUISE_0c, which incorporates crashworthy features, exhibits the greatest reduction in *PLL*, highlighting its value as a safety-enhanced baseline. Among the modified designs:

- CRUISE_1 achieves marginal improvements in both risk and power reduction, offering a slight but balanced gain across both objectives.
- CRUISE_2 shows a modest improvement in power consumption, but performs poorly in terms of flooding risk, resulting in a configuration that is considered unsafe.
- CRUISE_3 demonstrates a moderate reduction in PLL along with a notable decrease in power, presenting a well-balanced compromise between safety and efficiency.
- CRUISE_4, while showing a slightly increased risk, achieves the most significant reduction in power, making it the most efficient design from an environmental standpoint, albeit with a trade-off in safety performance.

These results underscore the importance of an integrated design approach that considers both safety and environmental performance simultaneously. While no single design dominates in both criteria, the analysis illustrates how crashworthy structures and main dimension adjustments can be strategically combined to yield optimized solutions tailored to specific design priorities.

Based on this preliminary study, several key insights can be drawn regarding the conceptual design of safer and more environmentally efficient passenger ships:

- Simple breadth reduction, along with the associated adjustment of hull form coefficients to maintain constant displacement, is not favorable from a flooding risk perspective. This is exemplified by CRUISE_1 and CRUISE_2, which exhibit only modest improvements in power reduction but fail to offer comparable benefits in risk reduction—particularly in the case of CRUISE_2, where a significant increase in flooding risk is observed. These findings suggest that a basic crashworthy structure alone cannot adequately offset the reduction in metacentric height (GM) resulting from decreased breadth.
- A more promising approach involves the combined reduction of breadth and increase in length, as seen in CRUISE_3 and CRUISE_4. These configurations demonstrate notable improvements in propulsive efficiency while maintaining acceptable safety levels. CRUISE_3 achieves a slight reduction in flooding risk, whereas CRUISE_4 sees a minor increase, though both remain compliant with statutory safety requirements. This indicates that lengthening the hull can compensate for the negative stability impact of reduced breadth when combined with crashworthy features.
- Further reductions in Potential Loss of Life (*PLL*) may be achieved through a combined application of crashworthy structures and additional Risk Control Options (RCOs)—both passive (e.g., foam installation, double hulls) and active (e.g., deployable barriers). However, to better quantify the effectiveness of these measures, it is recommended to perform Level 2 risk analysis, using direct numerical flooding simulations in critical damage scenarios.

It must be emphasized that this study is preliminary in nature, intended to explore design trends and trade-offs for future cruise ship development. Several simplifications were employed in the assessment of design attributes, which will be refined in future research. Nevertheless, the methods used align with current state-of-the-art practices in the maritime design community and are consistent with tools adopted by classification societies.

Additionally, assumptions regarding the internal compartmentation of the vessel were made to simplify the comparison—specifically, by applying a direct stretch to the original subdivision of CRUISE_0c. In real-world applications, future ships may require revised internal layouts to better integrate crashworthy structures and accommodate changes in main dimensions.

Despite these simplifications, this study offers a solid foundation for the conceptual design of next-generation passenger vessels that aim to balance safety and environmental performance. Importantly, it reinforces the idea that a truly environmentally responsible cruise ship must also prioritize risk prevention, thereby supporting higher safety standards alongside sustainability goals.

7. CONCLUSIONS

This study presents a novel design approach focused on the integration of crashworthy structures as a means to reduce flooding risk in cruise ships. The implementation of this concept on a reference vessel has demonstrated promising results, achieving a reduction in Potential Loss of Life (*PLL*) exceeding 18%. Building upon this outcome, the study explored whether such safety-enhancing strategies could be combined with geometric modifications—specifically, a reduction in the length-to-breadth ratio (*L/B*)—to also improve the vessel's environmental performance, particularly through power consumption reduction.

To investigate this, six alternative hull form configurations were developed and evaluated using Level 1 risk assessments and preliminary speed-power predictions. This enabled a comparative analysis of both safety and propulsive efficiency across a spectrum of design variants. The combined results reveal that a strategic combination of increased hull length, reduced breadth, and the application of a crashworthy structure can yield a balanced improvement in both safety and energy efficiency.

Importantly, this configuration appears to compensate for the reduction in initial metacentric height (GM) associated with decreased breadth, thereby maintaining a favorable risk profile without compromising compliance with intact and damage stability requirements. Among the six configurations studied, two demonstrated particularly strong performance in terms of both risk reduction and power savings—pointing to a viable design direction for future passenger vessels.

The results also suggest that even greater safety benefits may be realized by combining crashworthy structures with additional Risk Control Options (RCOs) such as static foam installations or deployable barriers. However, such multi-layered configurations would require more advanced assessment techniques, such as Level 2 risk analysis or first-principles flooding simulations, to accurately capture the interaction between structural enhancements and flooding progression in complex damage scenarios.

Despite the simplifications inherent in this preliminary study—including assumptions regarding internal compartmentation, uniform displacement, and idealized structural reinforcements—the methodology aligns with current state-of-the-art practices used in early-stage ship design. The findings offer a strong foundation for future development and refinement of integrated design strategies that aim to align safety enhancement with environmental sustainability.

Ultimately, this work highlights the need to reframe passenger ship design around the concept of risk prevention, rather than solely survivability. By proactively incorporating crashworthy and energy-efficient features at the concept design stage, future vessels can better meet evolving safety and environmental standards—delivering not only regulatory compliance but also improved resilience, operational performance, and societal value.

REFERENCES

Bai Y, Paik JK. 2024. Risk assessment and management for ships and Offshore Structures. Elsevier, The Netherlands.

Bulian G, Cardinale M, Dafermos G, Eliopoulou E, Francescutto A, Hamann R, Lindroth D, Luhmann H, Ruponen P, Zaraphonitis G. 2019. Considering collision, bottom

grounding and side grounding/contract in a common non-zonal framework. In Proceedings of the 17th International Ship Stability Workshop, Helsinki, Finland: 245-257.

Cardinale M, Sarkka J, Bertin R, Wurst S, Murphy A, Hamann R, Paterson D, Conti F. 2022. D7.2 – Analysis of Risk Control Options. WP7 EU Project FLARE.

Conti F, Hirdaris S. 2020. D-3.3 Damage Accident Modelling beyond Current Statistics. WP3 report Project FLARE.

Conti F, Le Sourne H, Vassalos D, Kujala P, Linderoth D, Kim S, Hirdaris S. 2022. A comparative method for scaling SOLAS collision damage distributions based on a ship crashworthiness application to probabilistic damage analysis of a passenger ship. *Ships and Offshore Structures*. 17(7): 1498-1514.

Egge ED, Bockenhauer M. 1991. Calculation of the collision resistance of ships and its assessment for classification purposes. *Marine Structures*. 4(1): 35-56.

FLARE. 2019-2022. EU H2020 – MG2.2. Flooding Accident Response.

HARDER. 1999-2003. Harmonization of Rules and Design Rational. Project Funded by the European Commission. DG XII BRITE.

Harvald SA. 1983. Resistance and propulsion of ships. Wiley.

Hetherington C, Flin R, Mearns K. 2006. Safety in shipping: The human element. *Journal of Safety Research*. 37(4): 401-411.

Holtrop J, Mennen GG. 1978. A Statistical Power Prediction Method. *International Shipbuilding Progress*. 25(290): 253-262.

Holtrop J. Mennen GG. 1988. A statistical Resistance Prediction method with a speed-dependent form factor. In Scientific and Methodological Seminar on Ship Hydrodynamics, Varna, Bulgaria.

IMO. 2020. International Convention for the Safety of Life at Sea (SOLAS). Consolidated Edition as of 2020. International Maritime Organisation.

IMO. 2024. Regulation 24 – Required EEDI. International Maritime Organisation.

Jasionowski A. 2001. An Integrated Approach to Damage Ship Survivability Assessment. PhD dissertation. University of Strathclyde.

Kuiper G. 1992. The Wageningen propeller series. Maritime Research Institute of the Netherlands.

Le Sourne H, Besnard N; Cheylan C, Buannic, N. 2012. A Ship Collision Analysis Program Based on Upper Bound Solutions and Coupled with a Large Rotational Ship Movement Analysis Tool. *Journal of Applied Mathematics*. SI09: 1-27.

Luhmann H, Bulian G, Vassalos D, Olufsen O, Seglem I, Pottgen J. 2018. eSAFE-D4.3.2 – executive summary. Joint industry project eSAFE – enhanced damage stability after a flooding event. In: A joint industry project on Damage Stability for Cruise Ships, rev. 3.

Mauro F, Vassalos D. 2022. The influence of damage breach sampling process on the direct assessment of ship survivability. *Ocean Engineering*, 250: 111008.

Mauro F, Conti F, Vassalos D. 2023. Damage surrogate models for real-time flooding risk assessment of passenger ships. *Ocean Engineering*. 285: 115493.

Mauro F, Vassalos D, Paterson D, Boulougouris E. 2023a. Evolution of ship damage stability assessment – Transitioning designers to direct numerical simulations. *Ocean Engineering*. 268: 113387.

Naar H, Kujala P, Simonsen BC, Ludolphy H. Comparison of the crashworthiness of various bottom and side structures. *Marine Structures*. 15(4-5): 443-460.

NEREUS. 1999-2002. First-Principles Design for Damage Resistance against Capsize. EC Project. CONTRACT No. G3RD-CT 1999-00029.

Paik JK. 2020. Advanced structural safety studies with Extreme Conditions and Accidents. Springer, Singapore.

Papanikolaou A, Hamman R, Lee B, Mains C, Olufsen O, Vassalos D, Zaraphonittis G. 2013. GOALDS: Goal based damage ship stability and safety standards. *Accid. Anal. Prev*. 60: 353-365.

Pedersen PT. 1994. Ship grounding and hull-girder strength. *Marine Structures.* 7(1): 1-29.

Pineau JP, Conti F, Le Sourne H, Looten T. 2022. A fast simulation tool for ship grounding damage analysis. *Ocean Engineering*. 262: 112248.

ROROPROB. 1999-2002. Probabilistic Rules-Based Optimal Design for Ro-Ro Passenger Ships. EU FP5 RTD Project. G3RD-CT-2000-00030.

SAFEDOR. 2005-2009. Design, Operation and Regulation for Safety. EU Project. FP6-516278.

Tompuri M, Ruponen P, Linderoth D. 2020. D6.3 Risk Control Options. WP6 deliverable, project FLARE.

Vanem E, Rusas S, Skjong R, Olufsen O. 2007. Collision damage stability of passenger ships: Holistic and risk-based approach. *International Shipbuilding Progress*. 54(4): 323-337.

Vassalos D, Guarin L. 2009. Designing for Damage Stability and Survivability – Contemporary Developments and

Implementation. *Ship Science & Technology*. 3(5): 59-72.

Vassalos D, Mujeeb-Ahmed M. 2021. Conception and evolution of the probabilistic methods for ship damage stability and flooding risk assessment. *Journal of Marine Science and Engineering*. 9(6): 667.

Vassalos D, Paterson D, Mauro F, Atzampos G, Assinder P, Janicek A. 2022. High-Expansion Foam: A Risk Control Option to Increase Passenger Ship Safety during Flooding. *Applied Sciences*. 12: 4949.

Vassalos D, Paterson D, Mauro F, Mujeev-Ahmed M, Boulougouris E. 2022a. Process, methods and tools for ship damage stability and flooding risk assessment. *Ocean Engineering*. 281: 114847.

Vassalos D, Mauro F, Paterson D, Salem A. 2024. The importance of first-principles tools for safety enhancement in the design of passenger ships in the case of flooding events. In Proceedings of the 15th International Marine Design Conference IMDC, Amsterdam, the Netherlands.

A rational framework for life-cycle damage stability and flooding risk management of passenger ships

Dracos Vassalos, *University of Strathclyde,* d.vassalos@strath.ac.uk
Francesco Mauro, *University of Trieste,* fmauro@units.it

ABSTRACT

Maritime accidents of passenger ships have shaped the approach adopted by the maritime industry towards designs with sufficient resilience to ensure a fail-safe mode post-flooding accident. As a result, the focus has always been towards mitigating measures to contain and control flooding emergencies. This is further hindered primarily by a rules-based approach, applicable principally to new buildings and reflecting a bygone era which has not evolved significantly, despite impressive technological innovation and advancement. As a result, most existing ships operate at lower safety standards, with limited armory at hand even to maintain such standards whilst in operation. Moreover, focus on accident prevention has taken second place with minor advances that fail to capture contemporary developments in this direction, thus depriving the maritime industry from cost-effective solutions to maintain or significantly advance the safety level in ships. There is clearly a need for a cultural shift from protection post-accidents to prevention of such accidents in the first place, such approach offering unfathomable potential to target a zero tolerance to human life loss in the maritime industry. More importantly, to aim at and achieve significant advances in designing and operating safer ships. This paper describes such an approach and delineates all the requisite elements to aim at and achieve such transformation.

Keywords: *Flooding Risk, Damage Stability, Passenger Ship, Vessel Lifecycle, Risk Management Framework.*

1. INTRODUCTION

Damage stability failure represents 90% of the risk to human lives in maritime accidents, affecting over 2 billion people who travel on passenger ships each year and around 100,000 commercial vessels, operated by 1.5 million crew. Inadequate damage stability has been the cause of 53% of all vessel losses over the past decade and was the primary cause of 65% of losses in 2018 (Figure 1). In particular, for passenger ships, the maximum number of passengers carried by the largest cruise ships each year has risen dramatically, almost doubling to 6,800 in 2019 compared to 1999 (Figure 2). This means that there is now a far greater risk of passenger fatality from any given single accident. Similarly, there is about 1,000 damage stability-linked fatalities per year in the general shipping industry for ships over 550 GT and an astonishing 55,000 fatalities per year, considering just two groups of smaller ship sizes (fishing vessels, 25,000 per year; domestic ferries 30,000 per year).

Analysis of 230,000 marine insurance industry claims with a value of almost $10bn between July 2013 and July 2018 (Clarkson, 2019) shows that ship sinking/collision incidents are the most expensive cause of loss for insurers, accounting for 16% of the value of all claims – equivalent to more than $1.5bn over this period (Vassalos and Mujeeb-Ahmed 2021). Most importantly, solving the damage stability problem for ships is the holy-grail in naval architecture with a huge transformational impact on the design and operation of every type and size of ship and the whole maritime industry.

The present paper deleniates the historical development of damage stability and associated flooding risk in more than 30 years of research int he field. Starting from analysisng the historical pittfalls in understanding the implication of risk prevention, the paper focuses on defining the way forward for the proper consideration of risk prevention measures in a modern flooding risk management framework.

One of the most important elements is related to the concept of prevention in the whole ship life-cycle

of the ship. To stress this the paper is articulated in two main sections: the first on the key elements and pitfalls of the exisiting framework for damage stability, and the second on the way forward need to be pursued, aiming to improve the current state-of-the-art.

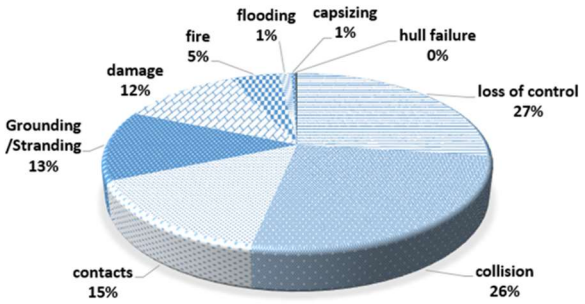

Figure 1: Casualty events for ships in the period 2011-2019.

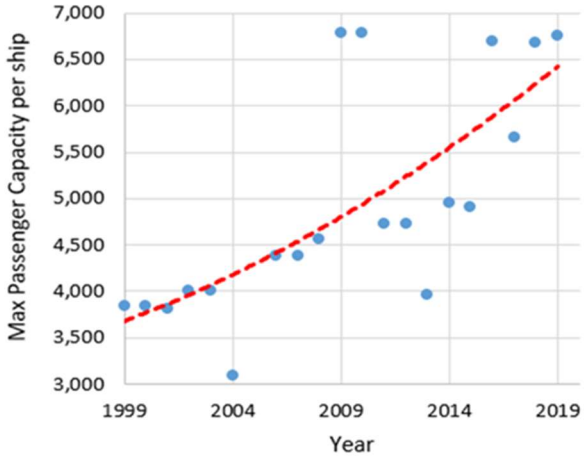

Figure 2: Trend on Capacities of largest passenger ships by year.

2. KEY ELEMENTS AND PITFALLS OF THE CURRENT FRAMEWORK

Overcoming the Titanic Syndrome: "If it is made of steel, it can sink", (Figure 3). Therefore, total emphasis on resilience in ship design to ensure that should an accident happened, the ship will fail safe, but what happened to "an ounce of prevention is a pound of mitigation? Given this, why not ensuring that an accident will not happen in the first place?

Paving our way through an archaic regulatory framework

Presently, damage stability assessment is based on key performance indicators with unclear risk content (A and R-Indices). More specifically indices focussing and reflecting one aspect of ship design, namely subdivision below the bulkhead deck.

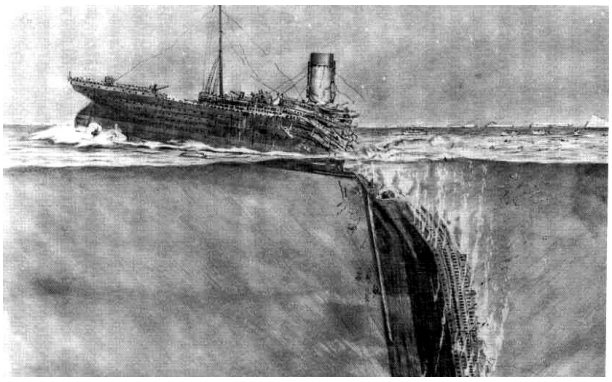

Figure 3: The sinking of Titanic.

The area of operation, reflected through the s-factor is generalistic, i.e., 4m of significant wave height H_s, not representing the specific area of operation and based, more latterly, on RoPax model tests (SOLAS, 2009), with only one cruise ship bring involved in its derivation (Figure 4). Moreover, the p-factor is based on accident accidents involving cargo ships and tankers of a bygone era. Interestingly, based on numerous applications, static assessment of survivability has been shown to be too conservative for passenger ships, as depicted in Figure 5.

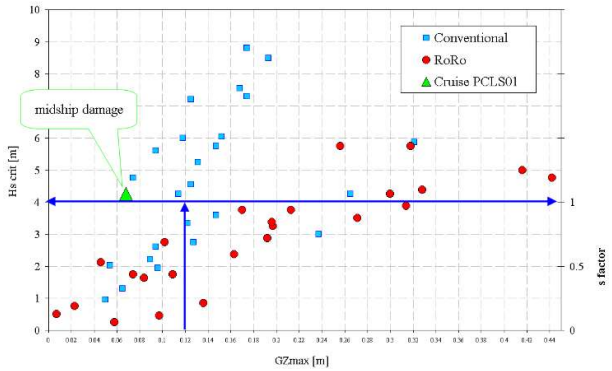

Figure 4: Derivation of the s-factor for passenger ships

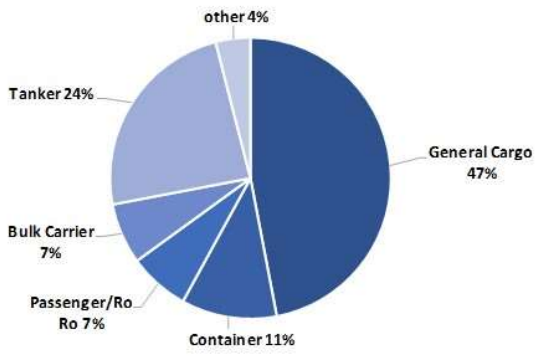

Figure 5: The p-factor is based on accident accidents involving cargo ships and tankers of a bygone era.

Sustained Research and Development But Limited Focus leads to Limited Progresses

Sustained research for over 25 years by experts from Industry, Government and Academia helped develop the subject of damage stability to standards comparable with any other transport industry. Despite this, limited focus (internal subdivision) leads to limited progress, thus depriving the shipping industry from cost-effective solutions to meet the ever-increasing demands for higher safety of passenger ships. Some of the key projects, paving the way and leading to Project FLARE, including the ones listed in Table 1.

Table 1: Sustained Research and Development in Damage Stability and Flooding Risk.

Project	Achievement Highlights
HARDER (1999-2002)	Harmonisation of damage stability regulations for cargo and passenger ships – probabilistic concept.
SAFEDOR (2005-2009)	Risk-Based Design; update of accident data; detailed risk models for collision and grounding.
GOALDS (2009-2013)	Improved probabilistic models for collision and grounding; proposals to IMO for revision of the required subdivision index.
EMSA III (2013-2016)	New required index R for passenger ships (SOLAS 2020) for collision, results from grounding used to support political decisions.
eSAFE (2018-2019)	Combination of collision, bottom and side grounding hazards; safety metric for combined analysis of collision and grounding events.
FLARE (2019-2023)	Life cycle (design, operation and emergencies) flooding risk assessment and management to enhance passenger ship damage stability cost effectively.

A number of these projects addressed flooding risk directly, accounting for all flooding hazards, including methodologies for risk estimation and management being submitted to IMO. Hence, Political compromises led to continuing focus on indices and to adopting significantly lower safety levels than those demonstrated in the aforementioned research projects (Figure 6). More importantly, reliance on a framework offering only subdivision as a key risk control option for flooding risk, led to saturation of such measures thus depriving the wider profession from cost-effective solutions to reduce, mitigate and control flooding risk, (Figures 7).

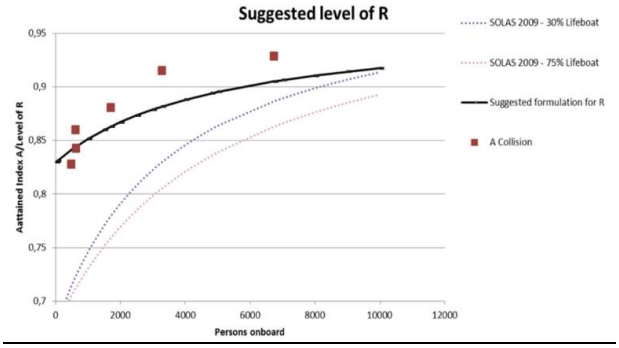

Figure 6: Proposed to IMO (red squares) and adopted (black line) safety levels for damage stability (Index R)

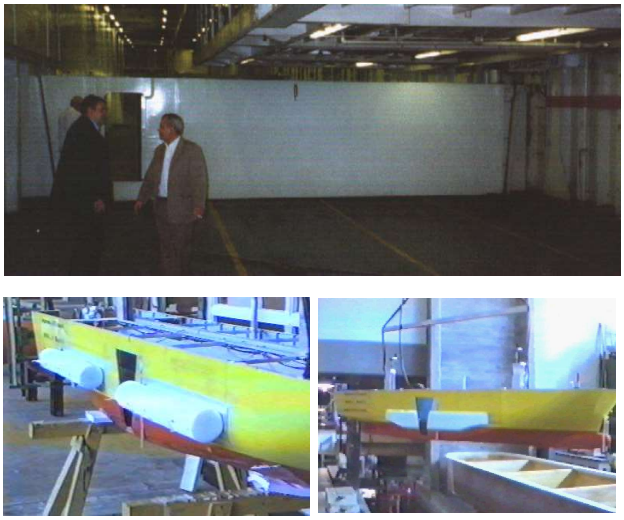

Figure 7: More subdivision, more volume, more complexity

Evolution of Passenger Ship Hazards

Most importantly, with SOLAS focussing on collision only and with attention by ship designers on protection by this hazard, the risk from unattended hazards such as bottom and side groundings has now become dominant for both RoPax and cruise ships (Bulian et al. 2019). Recent damage statistics as portrayed in this slide indicate that the frequency of grounding hazards for both cruise ships and RoPax account for 80% for both categories of ships whist the flooding risk attributed to groundings has grown to 75% for RoPax and an astounding 95% for cruise ships (Figure 8).

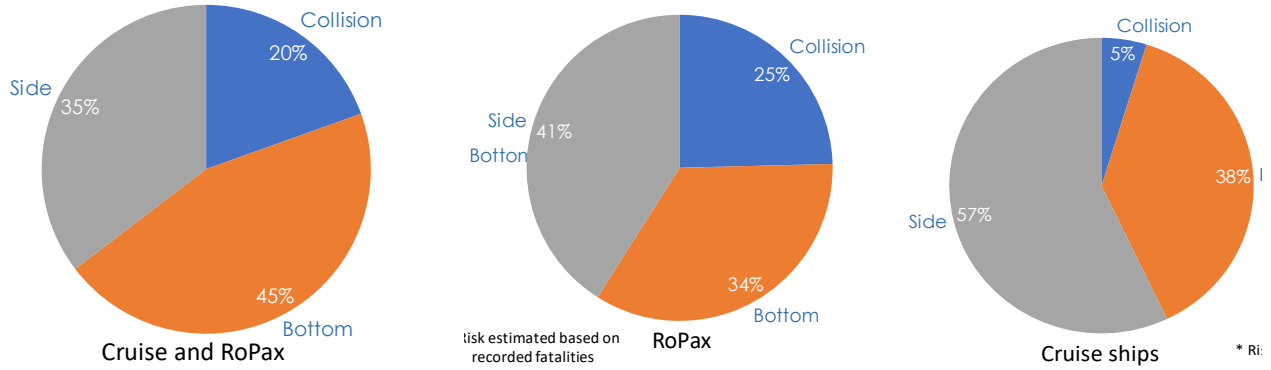

Figure 8: Unattended flooding hazards

Old Ships vs New Ships

The shipping industry is very old and, consequentially, very traditional. Damage protection in the form of watertight bulkheads was the first risk control option proposed in 1854, but it has taken many more accidents and significant loss of life, including the Titanic, for it to be internationally adopted as SOLAS 1929. It is more than likely that the delay was primarily due to the fact that the industry was keenly aware that serving safety will compromise functionality and earnings, ultimately viability of business and this contrast and conflict continues to this day. This is clearly obvious in that new regulations for damage stability apply only to newbuildings (Grandfathers Clause). Hence, assuming a 5% constant growth of the industry over the years, this leaves the majority of ships (existing ships) with an inferior damage stability standard and damage protection, a gap that widens progressively to the extent that SOLAS becomes less and less relevant. The only way that this "landslide" will be arrested is if cost-effective active damage control measures were made available, thus incentivising the industry to adopt these for life-cycle risk management of damage stability.

Passive Vs Active Protection

In the quest for damage stability improvement, design (passive) protection have traditionally been the only means to achieve this in a measurable/auditable way (SOLAS 2009, Ch. II-1). However, it is undeniable that the consequences from inadequate damage stability can also be reduced by operational (active) measures, which may be very effective in reducing loss of life (the residual risk). As a matter of fact, active and passive measures for damage control have co-existed almost from the outset. One could imagine that in the absence of decks, old seamen would have had to use buckets, later on pumps and other means to empty floodwater from ship hulls, plug holes with any matter of means, adjust sails and so on. More latterly, safety equipment, LSA, drill teams, Safety Centres, Safety Masters, all active damage protection measures have been progressively introduced, most in the wake of accidents. So, why this myopic and uncompromising focus only on passive protection? There are two reasons for this. The first relates to the traditional understanding that operational measures safeguard against erosion of the design safety envelop (increase of residual risk over time). The second derives from lack of measurement and verification of the risk reduction potential by any active measures. Notwithstanding this, the exact contribution of active measures to safety has never been considered, even as a discussion topic, irrespective of how effective these might be as damage protection control options. The dogma that "if it cannot be measured, it cannot be improved" has gone a step further in the maritime industry to become "if it cannot be measured, it cannot be regulated". Hence, all these options, however cost-effective and safety-effective might be, they are not being considered as a means of damage protection, in the same way that passive measures are. For example, for passive protection we have indices of subdivision, indices for damages, indices for survival, indices for everything. There is some refreshing new ground on passenger evacuation metrics but this is still highly general (some say arbitrary) and incomplete. Novel Technology Qualification (risk assessing and de-

risking the novelty), offers a portal for introducing active means of damage protection and modern tools offer enhanced capability to estimate flooding risk over the life cycle, even live-risk on-board ships. This is the requisite platform to facilitate change and Project FLARE facilitated a systematic and structured way to account for such developments. This, in turn, will change the maritime safety agenda and its evolution. In simple terms, what is needed is the means to account for risk reduction by operational (interventional) means as well as measures that may be taken during emergencies. Such risk reduction may then be considered alongside risk reduction deriving from design measures. Therefore, new measures for risk reduction (operational and in emergencies) should be considered in addition to design measures. What needs to be demonstrated and justified is the level of risk reduction and a way to account for it, the latter by adopting a formal process and taking requisite steps to institutionalise it.

Prevention Vs Mitigation

"One ounce of prevention is worth a pound of cure". This is almost a dogma in most fields of science and engineering. There are, however, two aspects worth considering from a different perspective. The first is residual risk, which for large passenger ships is so excessive that reducing this must be priority. For example, consider the largest ship built to date, which is a 10,500 People On Board (POB) ship. In the IMO FSA for cruise ships, it has been proposed that Risk Control Options for ship safety enhancement will be costed against the propensity of society to spend towards saving one life, which for the western world is $8M. With the A-Index of this ship being approximately 0.9, according to IMO SOLAS 2009 and assuming that collision has taken place, the residual risk is worth €8.4B, a few times over the worth of the ship. The second relates to the feasibility of preventive Vs mitigating measures. For effective preventive measures, we should be searching far into the left of the fault tree, where the emphasis lies on sociotechnical, organisational and safety culture matters, which will require long term investment and effort to identify and bring to fruition effective RCOs. Mitigation measures, on the other hand, are linked strongly to technological innovation, where the strength currently lies. Hence, solutions are likely to be of shorter term and, more than likely, cost-effective. Therefore, mitigation still remains a key target. In this respect, the prevailing situation can be drastically improved through understanding of the underlying mechanisms leading to vessel loss and to identification of governing design and operational parameters to target flooding risk reduction cost-effectively. This, in turn, necessitates the development and institutionalisation of appropriate methods, tools and techniques capable of meaningfully addressing the physical phenomena involved, one key target of the EU Project FLARE (Mauro et al, 2022).

Considering that 80% of flooding scenarios in passenger ships (90% considering older ships) refer to transient flooding, current measures of flooding protection fail catastrophically. Hence, prevention is the only credible way forward.

A risk-based approach opens new routes for passive and active flooding protection. Emphasis to date has been placed on improving damage survivability, namely increasing factor-s and hence mitigating measures. Little attention has been focused on the p-factor and hence on damage prevention measures. A summary of such measures for both prevention and protection are shown in Table 2 (notable that prevention is evolving but still in embryonic state).

Table 1: Protection/Prevention Measures for Damage Stability and Flooding Risk

s-factor (Passive/active Protection)	p-factor (Prevention)
– Protection of critical openings – Protection of critical spaces (WT/semi-WT doors, Deployable Foam barriers) – Seals (Stairwells) – Sponsons (external modifications) – Flooding control, counter ballasting – Permanent ballast – Additional WT protection (mainly WT bulkheads) – Static (passive) foam – Connection between starboard and port compartments	– Safe navigation (capability today to target zero tolerance in maritime accidents) – Structural Crashworthiness – Static (passive) foam

3. THE WAY FORWARD

The first Key Word is "Lifecycle"

The realisation that risk is inextricably linked to operation and a derivative of exposure has driven the

industry to life-cycle considerations for effective flooding risk management. Key to life-cycle flooding risk management is the understanding that both the operational phase (monitoring and management of residual risk) as well as emergencies (emergency response) depend crucially on having identified during the design phase pertinent design vulnerabilities, which lead to critical accident scenarios in pre-specified loading and environmental conditions and, on the basis of this, having taken appropriate measures to ensure damage protection and control to satisfy adopted tolerable levels. We normally refer to these measures as recovery control measures or mitigating and controlling measures (barriers is another term, Figure 9), which as indicated and explained in the foregoing, traditionally have focussed on passive measures of damage protection after the flooding incident accident has occurred.

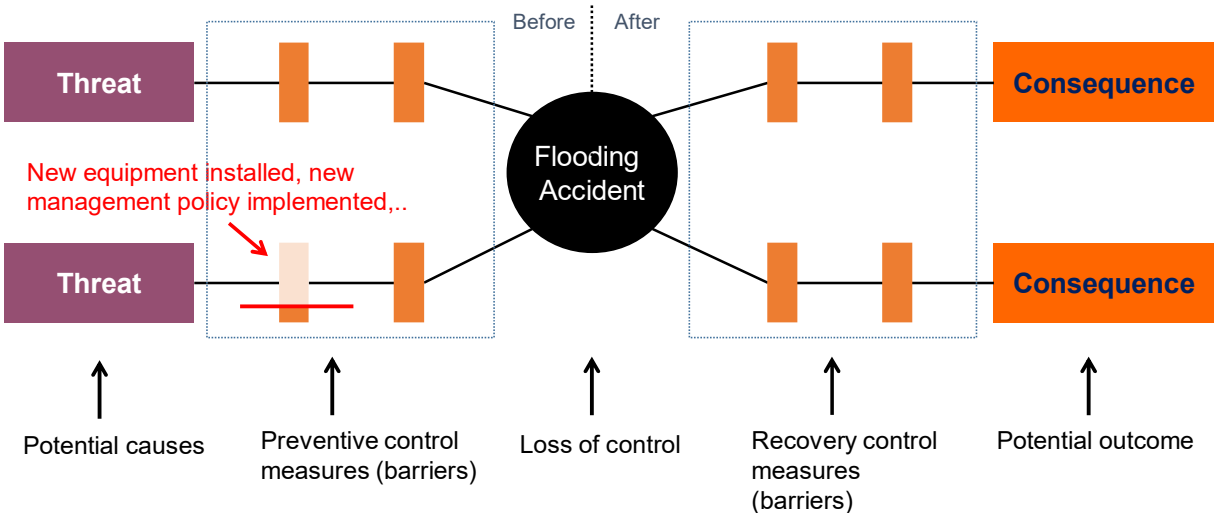

Figure 9: Life-Cycle Flooding Risk Management .

However, safety affects everything on the lifecycle of a ship and is, in turn, affected by everything, so why focussing singularly on design (passive protection) and ignoring any interventional (active) measures during normal operation and in emergencies?

Utilising the IMO probabilistic damage stability framework, the provisions for AD&A and Goal-Based Standards and Safety-Level Approach, a Life-Cycle Flooding Risk-Based Regulatory Framework will enable and support a continuous evolution of regulations, ensuring the risk level is ALARP (As Low As Reasonably Practicable) whilst providing a sound platform for benchmarking alternative/novel ship and system designs and operating procedures for new and existing ships. To this end, a fundamental requisite is that pertinent risks need to be quantified, in many cases almost in real time throughout the life cycle of the ship, from design and daily operation to crisis situations. Consequentially, there is a clear need for a wider consideration of measures of flooding risk mitigation and control, namely active as well as passive measures of flooding protection, in a way that every measure is assigned a risk metric and is accounted for in such risk assessment.

The second Key Word is "Holistic"

The gap in the aforementioned framework at the end of Project FLARE will still be that emphasis on prevention will have been only cursory with strong emphasis once again on damage limitation, post-accident (Vassalos et al. 2023, Mauro et al. 2024). Therefore, the scope need not only be "life-cycle", addressing active and passive means of damage mitigation and control, but also "holistic", addressing both prevention and mitigation/control measures through a "Holistic, Risk-Based Regulatory Framework for Damage Stability". A typical formulation of the flooding risk will be in the form:

$$R_f = P_f \cdot P_{b/f} \cdot P_{sc/b} \cdot P_{loss/sc} \qquad (1)$$

Namely: Flooding Risk = Probability that a flooding event has occurred times Probability of hull

breach, conditional on the flooding event times Probability of sinking/capsize, conditional on hull breach times Probability of human life loss, conditional on ship sinking/capsizing.

.

Table 3: FLARE innovation and Impact.

FLARE Research	Current State and SOLAS Practice	FLARE Innovation and Impact
Ship Geometry	Geometry definition lacks granularity	New guidelines for modelling ship geometry and internal arrangements.
Operational data	Old cargo ship data	Permeability, drafts, traffic data for passenger ships and area of operation.
Accident data, frequencies and breach distributions	Old cargo ships, ship structure unaccounted	New accident database, flooding risk model, frequencies and non-zonal breach distributions for collisions and groundings. Influence for crashworthiness accounted.
Benchmarking of numerical tools	Static stability analysis for collision, benchmarking by academia, RoPax.	Model experiments for ship survivability in calm water and in waves (0,2,4 and 7 metres Hs),(1:40 models, cruise ship and RoPax), two model basins (MARIN and HSVA); transient and progressive flooding scenarios. Benchmark studies for quasi-static and dynamic flooding simulation tools, FLARE partners and worldwide.
Situational awareness	Simplistic methods based on statics.	First-principles approach and inference, using AIS data, response-surfaces based on crash analysis, survivability and evacuation assessment and flooding severity assessment.
Ship stability and survivability analysis	Static stability and vulnerability screening for collision only	Physics based survivability analysis and forensics for specific sips, operational environment and conditions, new methods for vulnerability assessment and flooding severity assessment.
Flooding risk assessment (design, normal operation and emergencies)	A & R indices offering no explicit risk content and limited choice RCOs	Direct estimation of flooding risk (Potential Loss of Life (PLL)), with a multi-level approach. Application by shipyards in FLARE to 7 cruise ships and 2 RoPax (one existing ship) showed practicability and potential for use in normal design practice. Demonstrator developed for flooding risk estimation before and during emergencies.)
IMO proposals	Collisions,indices. Bottom grounding, partly by deterministic requirements.	Shortcomings identified, proposals made to address these. Introduction of non-zonal approach for damage breach sampling, grounding hazards (bottom and side groundings); new holistic evaluation framework for passenger ship damage stability. Guidance for the assessment of novel RCOs for damage stability enhancement.

The current framework addresses only part of the 2nd term (namely, probability of hull breach, conditional on a collision event, p-factor) and part of the 3rd term (namely, the compliment of the probability of capsize/sinking as a result of collision only). Therefore, flooding events as a result of side and bottom groundings are not considered and neither is the probability of having a flooding event. Adopting such a framework will bring together every aspect of risk prevention, mitigation and control, targeting a balance of all credible RCOs and leading to the most cost-effective means of flooding risk management.

The "Towards Zero Maritime Accidents" initiative, coupled with the efforts made in FLARE will provide the maritime industry with a "Holistic, Risk-Based, Life-Cycle Regulatory Framework for Flooding Risk Prevention, Mitigation and Control", offering the requisite flexibility to address flooding risk ontologically and methodologically, thus catalysing a transformative improvement in maritime safety.

The contribution to all the above from project FLARE is summarised in Table 3.

4. CONCLUSIONS

The present paper describes the current framework for flooding risk management, highlighting the pitfalls and the assumptions on the base of its development. Starting from a digression on the different research studies that lead to the definition of the framework in force by SOLAS, the paper describes the enhancements provided by the recent developments in project FLARE, where for

the first time the effective focus was on the applicability of first-principle tools for the flooding risk estimation on passenger ship through the whole ship lifecycle.

Bearing in mind the above, the paper proposes a way forward for further developments in the field of flooding risk management, with the focus of attention on risk prevention primarily, with protection measures reinforcing rather than preceding or unitarily being addressed. In fact, the enhancements introduced by project FLARE together with the more advanced technologies that can be employed onboard to ensure safe navigation, allows for effectively considering prevention as a primary measure to reduce risk. Such an approach should be studied carefully, with a dedicated focus on the applicability of novel technologies and knowledge acquired by research. This will lead to reshaping the classic methodologies of design currently in use by shipyards in developing new projects, with safety being addressed cost-effectively, particularly concerning flooding risk over the life cycle of passenger ships.

REFERENCES

Bulian G., Cardinale M., Dafermos G., Eliopoulou E., Francescutto A., Hamann R., Linderoth D., Luhmann H., Ruponen P., Zaraphonitis G. 2019, "Considering collision, bottom grounding and side grounding/contact in a common non-zonal framework", Proceedings of the 17th Ship Stability International Workshop.

Clarckson 2019, "Ship Databased", accessed in December 2019.

EMSA 2013-2016, "EMSA III Project", Joint Industry Project.

eSAFE 2018-2019, "Damage Stability of Cruise Ships"; Joint Industry Project; Cruise Ship Safety Forum (CSSF).

FLARE 2019-2023, "Flooding Accident Response", EU Horizon 2020 project.

GOALDS 2009-2013. "Goal-Based Damage Stability"; Project funded by the European 13th Commission, FP7-DG Research, Grant Agreement 233876.

HARDER 1999-2002, "Harmonisation of Rules and Design Rationale"; EC Contact No. GDRB-CT-1998-00028.

IMO 2009, "SOLAS-International Convention for the Safety of Life at Sea"; IMO: London, UK.

IMO 2020, "SOLAS-International Convention for the Safety of Life at Sea"; IMO: London, UK.

Mauro F., Vassalos D., Paterson D., Boulougouris E. 2022, "Evolution of ship damage stability assessment—Transitioning designers to direct numerical simulations", *Ocean Engineering* 268, 113387.

Mauro F., Paterson D., Vassalos D. 2024, "Real-time estimation of the Potential Loss of Life in case of ship-to-ship collisions", *Ocean Engineering* 298, 117238.

SAFEDOR 2005-2009, Design, Operation and Regulation for Safety, Integrated Project, FP6_2 Contract TIP4-CT-2005-516278.

Vassalos D., Paterson D., Mauro M. 2023, "Real-time flooding risk evaluation for ship-to-ship collisions based on first principles", *Ocean Engineering* 281, 114847.

Vassalos D., Mujeeb-Ahmed M.P. 2021,"Conception and evolution of the probabilistic methods for damage stability and flooding risk assessment", *Journal of Marine Science and Engineering* 9, 667.

Bottom damage stability issues of hopper dredgers

Arie de Jager, *Project manager and naval architect at the Maritime Research Institute Netherlands (MARIN),* a.d.jager@marin.nl

ABSTRACT

In 2001, special guidelines regarding the (damage) stability of trailing suction hopper dredgers (TSHD) came into force in the five European countries of the world leading dredging companies. The calculation approaches presented in these guidelines, named DR-67, are different from those for general cargo ships, for reasons, but were not adopted by IMO. IMO only sent Circular Letter No. 2285, informing all members about the existence of these guidelines. Per delegation these guidelines were discussed in non-European countries (having a dredger fleet) with US Coastguard, CCS and IRS for the purpose of acceptance. In these guidelines reference to SOLAS was made with regard to the required index for damage stability. Later in 2008, requirements regarding stability in case of bottom damage came into force. This was not foreseen in DR-67. For this reason DR-67 was modified into DR-68 by adding the sentence "to comply with Chapter II-1 of SOLAS 1974 as amended". From that time, hopper dredger were required to comply with SOLAS regarding bottom damage stability according to the calculation approach for general cargo ships. This was a step backwards and additional measures must be taken to get the TSHD compliant. These measures, affecting the CAPEX of the TSHD, appear to be not necessary for safety but for compliance only. When applying the calculation approach typically for hopper dredgers and as put forward in DR-68 for damage stability, the TSHD complies without additional measures.

A brief description of the stability of the TSHD and of the development of the special guidelines will be provided. Then, the detrimental effect of imposing general rules on special vessels will be discussed.

Keywords: *Hopper Dredger, Bottom Damage Stability, Regulations.*

1. HOPPER DREDGER DESCRIPTION

To enable a suitable calculation approach for the stability of hopper dredgers, one must understand the principal of operation these vessels. Although the hopper dredger is considered a cargo ship by international regulations regarding stability, there are a number of typical characteristics which clearly distinguish it from general cargo ships and which mean that the application of those regulations does not lead to the correct insight into its stability and safety. The hopper dredger has the following distinctive features:

- The hold, called "hopper", has an open top.
- In fact, the hopper has an open bottom as well, because it is provided of one or two rows of non-watertight bottom doors.
- The nature of the cargo is wet and can be fully liquid or almost solid, or something in between.
- By means of hydraulic actuated bottom doors, she is able to dump her cargo in short time.
- She is not operating in deep sea and oceans, but in harbors, estuaries and near shore, so that her sailing distances between the dredging and disposal area is short.
- She has two loading conditions, fully loaded and empty. Empty means that her hopper communicates with the sea.
- She has a reduced freeboard.

The reduced freeboard of these vessels is in fact based on making these vessels economically viable. The hopper dredger has a heavy dredging installation on board and also has a large amount of lost displacement due to the dredging system. Increasing her draught by reducing the freeboard was allowed on the condition that the vessel complies with stability requirements at that deeper draught and that she is able to dump her cargo in case of emergency in a few minutes, reducing her draught form the deep

dredging draught to the summer draught. To ascertain this draught reduction, the actuating system of the bottom dump doors must be of the positive type, that means that the cargo pressure must be able to open these doors without making use of power.

Trailing suction hopper dredgers are able to load themselves by means of pumps connected to suction tubes alongside the vessel. A mixture of seawater and solid particles goes through the suction tube, dredge pump and delivery pipe line into the hopper. The process water flows off through an adjustable overflows, see Fig. 1, or through spill-ways.

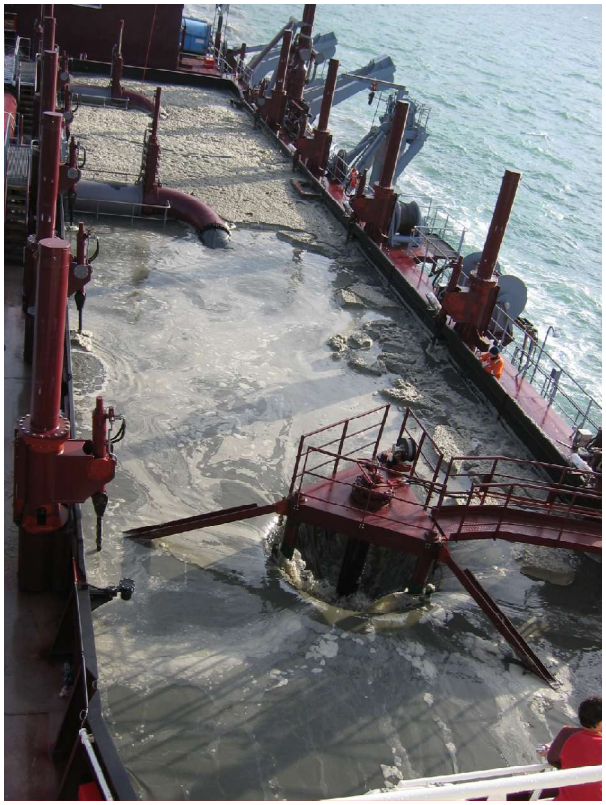

Figure 1: Loading process with adjustable overflow.

There is preferably no variety in cargo mass, the hopper is designed such that for a wide variety of densities the vessel can be loaded to her deep dredging draught. This means that the hopper dredger does normally not sail on an intermediate draught. Only in case of light material like spoil or seawater, it can be that the deep dredging draught cannot fully be achieved. In most cases, however, the loading consists of sand or clay, a mixture of sand and gravel or a mixture of sand and clay, having a density sufficient to get the vessel on her deep dredging draught. Due to loading by pumps and taking it form the seabed, all loadings are mixed with seawater.

Most of the hopper dredgers are meant for a wide variety of loadings. This means that the hopper must be of sufficient volume to get the vessel on her deep dredging draught when loaded with cargo of a low density. For the higher cargo densities, the hopper will be partly filled then. Gravel hopper dredgers, however, have a hopper with a relatively small volume that is designed for high density cargo only. Discharge by bottom dump doors is not intended, the purpose is gravel extraction and thus the cargo is to be discharged in drained condition by unloading equipment like a bucket wheel or a grab.

From the above description it can be concluded that this vessel is different from a general cargo vessel, and given the special layout of the vessel and the special cargo, it should therefore be treated differently with regard to stability.

2. HOPPER DREDGER STABILITY

The stability of the hopper dredger depends for a major part on the nature of the cargo and the fact that the hopper is open at the top. Regarding the cargo, if this has a liquid nature, a huge free surface moment affects the stability. However, because the hopper is open at the top, at a certain angle of heel, the cargo will spill out over the upper edge of the hopper. This effect can be seen in Fig. 2 where the increase of GZ indicates the point when spill-out starts.

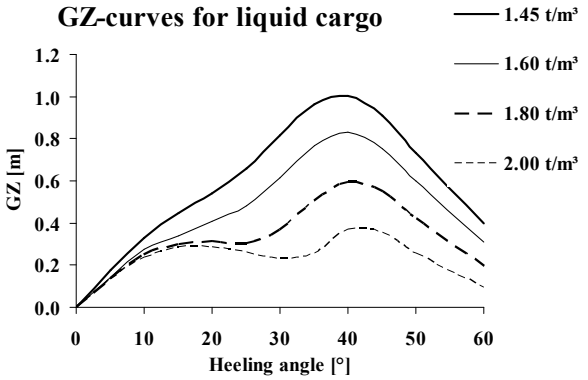

Figure 2: GZ-curves for liquid cargo.

In Fig. 2 it can be clearly seen that cargo of the highest density, and thus resulting in the lowest cargo level and related lowest KG, has worst stability.

As soon as the cargo spills out, the stability of the vessel improves. If the density of the cargo is high, the level of the cargo is low. In that case it can happen that water ingress from the sea, see Fig. 3, over the upper edge of the hopper takes place prior

to cargo spill-out. This effect will worsen the stability. It must be noted that sea water ingress can take place through the overflow as well.

Figure 3: Sea water ingress

The latter is valid for cargo with a solid nature, having a high density normally, as well. Cargo is called to be "solid" if after dredging the process water has flown off and the remainder is packed sand, see Fig. 4.

Figure 4: Solid cargo in the hopper.

This type of cargo will never spill-out and although there is no cargo free surface moment affecting the stability, substantial increase of draught due to water ingress (which has a free surface moment) results in a worse the stability then. This can be seen in Fig. 5 where the sudden decrease of GZ indicates the point when sea water ingress starts.

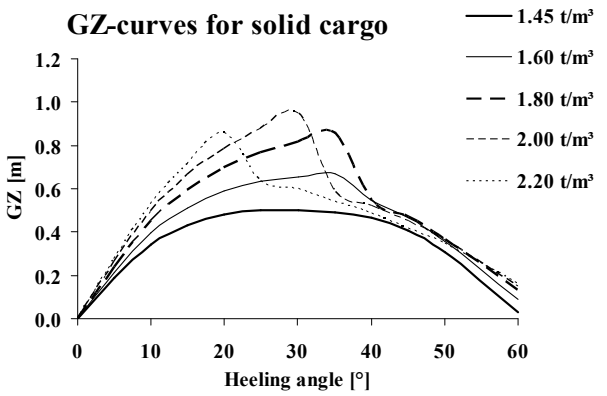

Figure 5: GZ-curves for solid cargo.

Another point of concern in hopper dredger stability is that asymmetric dumping can take place when having two rows of bottom dump doors. In case of emergency, the hydraulic pressure which keep the doors closed will be released by means of accumulators. How the dumping process will take place is unsure then. It can happen that at one side the dumping will go faster than at the other side. For this unsafe condition a requirement is justified.

From the description above the following can be understood:

- Hopper dredgers experience phenomena affecting their stability in normal operation, which general cargo ships do not.
- All over the stability range to be calculated, the displacement of a hopper dredger will not be constant due to water ingress or cargo spill-out.
- The highest KG is not per definition the worst case. The effect of the free surface moment of cargo of a high density (low level, thus low KG) and of water ingress (or a combination of these two), can result in a worse stability. A traditional KG-max curve indicating compliance cannot be made for this vessel type.

To ascertain the safety of this type of vessels, a calculation approach which captures the experienced phenomena was required.

3. REGULATIONS FOR HOPPER DREDGER STABILITY

That hopper dredgers should be treated differently regarding stability was recognized from the beginning by national authorities. France (Bureau Veritas), The Netherlands, United Kingdom and the United States of America developed their own regulations for these vessels. Unfortunately, these regulations were different and IMO did never adopt special stability requirements for hopper dredgers. This situation caused different hopper dredger designs, depending on the port of registry, and many discussions with countries having a dredger fleet but which were not familiar with dedicated regulations of other countries. For these countries, hopper dredgers must comply with the IMO stability regulations, and the result of this was a rather artificial approach, not capturing the real effects as described above.

To harmonize regulations for dredger's stability, a working group was established in 1998, in which authorities and dredging companies of France, Belgium, United Kingdom, Germany and The Netherlands (chair) participated. This working group discussed about the safety of hopper dredgers and developed guidelines which assure the safety without harming the vessel's exploitation. Both intact and damage stability was considered. The intact stability was classified as a "fail safe" case. This resulted in the assumption that the cargo must be seen as of a liquid nature up to and including a density of 2.0 t/m^3. This is rather extreme and this assumption clearly led to wider ships. More about this can be found in the second reference.

In order to not essentially deviate from IMO, criteria for supply vessels are to comply with. The reason for selecting these criteria is that due to the effect of spill-out of the cargo or sea water ingress, the maximum GZ cannot be beyond 25° heel in all cases, although the stability is amply sufficient. Furthermore, the heeling moment due to wind is to be considered as well, as for other ships, referring to IMO Code on Intact Stability A.749(18) Chapter 3.2. Finally, criteria were added for asymmetric dumping of the cargo.

For damage stability, some relaxation was accepted in order to not pile up emergencies on extremes. The cargo with a density up to and including 1.4 t/m^3 is seen as of a liquid nature, from 2.0 t/m^3 and above as of a solid nature and in between it is seen as sliding with an angle linearly depending on the density. In order to not essentially deviate from SOLAS 1974, reference is made to Part B-1, Chapter II-1 and as amended by MSC.47(66) and as further amended by the three sections of the guidelines which describe the calculation method and the contribution of the loaded and unloaded condition to the total attained index. Whereas for cargo ships in loaded condition the attained index A was to be at least 0.5R at that time, for dredgers it was to be at least 0.7R instead, to ascertain safety at the reduced freeboard. On top of that, no partial draught is to be taken into account. The reason for this is, that a hopper dredger has usually no partial draught within its operational profile. Hopper dredgers are not depending on available freight, they are loading themselves. An hypothetical partial draught, at which the vessel amply complies, leads to a high attained index $A = 0.4A_s + 0.4A_p + 0.2A_l$, whereas the loaded condition, which contributes to 50% in the operational profile, plays a minor role in this formula, thus indicating a safety level that is not true in reality. Last but not least, the permeability of the hopper below the cargo level is seen as being zero due to the wet cargo, and above the cargo as 1.0.

In 2001 the final developed Guidelines, named Dr-67, came into force after approval by the European Commission and communication with the IMO, see the first reference. The new Guidelines, DR-67, was discussed with the authorities of other countries, like the USA, India and China. The USA and India accepted the use of these guidelines for their dredgers. CCS of China implemented these guidelines in their rules, but with small changes.

4. BOTTOM DAMAGE

In 2008, bottom damage stability requirements came into force. However, DR-67 only referred to SOLAS 1974, Part B-1, Chapter II-1 and as amended by MSC.47(66), and thus bottom damage stability requirements were not covered by these guidelines for hopper dredgers.

From that time, troubles begun for the designer of hopper dredgers. On the one hand because a hopper dredger has necessary recesses in the double bottom and on the other hand because different authorities had different opinions.

Regarding the necessary recesses in the double bottom, a dredge pump must be as low as possible in

the ship to be able to start up in empty condition. The pump must be submerged. Furthermore, to be able to completely unload the hopper by the dredge pump, suction pipelines must be positioned as low as possible in the ship. All such dredging equipment protrudes the tank top and thus bottom damage stability have to be considered. On top of that, the cargo hold, the hopper, has no double bottom at all.

Regarding the authorities, all were convinced that the requirement of s = 1 for each individual bottom damage case is too stringent for the dredger at reduced freeboard, that is at her deep dredging draught (for general damage stability s may be lower than one under that condition that the attained index is equal to or higher than the required index). The factor s indicates the residual stability in case of damage, GZmax and range, related to what is supposed to be safe. If s = 0 it is supposed that there is no probability survival. From s = 1 to s = 0 the probability of survival decreases. For dredgers however, there is another probability of survival: their capability of dumping their cargo. For damage stability before 2008, this capability was disregarded in DR-67. The dredger must comply on her deep dredging draught, and s < 1 or even 0 is allowed for individual damage cases as long as the attained index is equal to or higher than the required index.

Consequently, some authorities went back to the damage stability approach of the past, allowing the dredger to have the hopper in communication with the sea, see Fig. 6, in damage cases.

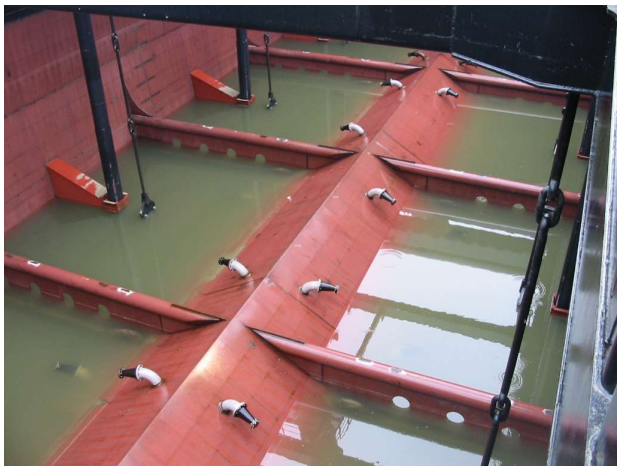

Figure 6: Hopper open to sea.

This would mean that the dredger has completely discharged the cargo by means of the bottom dump doors shortly after being damaged. Others stuck to what is stated in SOLAS and required the dredger to be on the summer draught in case of bottom damage. This would mean that the dredger has partly discharged the cargo.

It can be justified to require the hopper dredger on summer draught, fulfilling bottom damage stability criteria, because the time needed to release the cargo completely is a safety factor. An example of the dumping of a hopper dredger with only four bottom dump doors is given in Fig. 7.

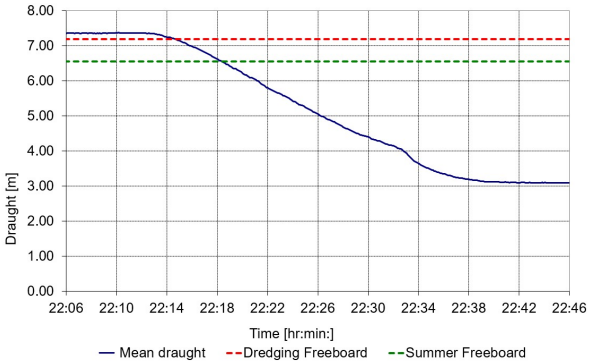

Figure 7: Draught recording during dumping the cargo.

In this figure it can be seen that within 6 minutes the dredger went from the dredging freeboard to the summer freeboard, but approx. half an hour was needed to get the hopper completely empty. For hopper dredgers with a different bottom door arrangement, time can be shorter. However, a criterion for the time needed to release the cargo completely would be justified then. Another difference in opinion of authorities is about the hopper having no double bottom. In the determination of the bottom damage cases, for some the hopper must be seen as a compartment without double bottom. In fact the hopper is a space open to sea, as can be seen in Fig. 6. The practice is that during unloading when the bottom doors are open or when the dredge pump sucks the hopper empty trough an inlet chest, it communicates with the sea. Only shortly before dredging light material, like spoil, all the water is pumped out of the hopper because no settlement of the spoil and no overflow of process water takes place then. However, the bottom dump doors are not of an approved watertight quality and never act such.

All these things, explaining the operational reality of this ship type, requires a special consideration with regard to safety and appropriate regulations.

5. IMPERFECT MODIFICATION OF DR-67

Having no reference in DR-67 to part B2 of SOLAS regarding bottom damage, DR-67 was changed, resulting in DR-68 in 2010. Whereas DR-67 referred to "Part B-1 of Chapter II-1 of SOLAS 1974 as amended by MSC.47(66)" only, DR-68 refers to "Chapter II-1 of SOLAS 1974 as amended, relevant to damage stability and as further amended and modified by 6.2.1, 6.2.2 and 6.2.3 of these Guidelines". Section 6.2.1, 6.2.2 and 6.2.3 in DR-68 indicate the calculation approach for dredgers. Section 6.2.2 indicates the loading conditions and there the "dredger load line" is mentioned, which is the deep dredging draught at reduced freeboard according to section 2 of DR-68.

So, from 2010, even more troubles existed. Authorities not requiring dredgers to comply with criteria regarding bottom damage stability on the deep dredging draught, required the vessel to be compliant according the SOLAS approach for general cargo ship. Other authorities, like the Dutch Flag, required the dredgers to be compliant on summer draught according to the DR-68 calculation approach and to be compliant according to the SOLAS approach for general cargo ships. This led to the strange situation that dredgers did comply according to the DR-68 approach, but did not according to the SOLAS approach. Finally, measures must be taken to get the dredger compliant, leading to more expensive ships. This is a non-preferred situation due to an imperfectness of the modification of the guidelines DR-67.

6. CONSEQUENCE OF THE SOLAS APPROACH FOR DREDGERS

Making use of the SOLAS approach for cargo ships when calculating bottom damage stability of hopper dredgers, several things are going wrong. SOLAS Chapter II-1, Part B-1, Regulation 5-1, 4 indicates that ships have to fulfil stability requirements in case of minimum GM or maximum permissible KG for the three draughts. In Regulation 7-3, 2, a permeability for Cargo liquids is 0.7 at the deepest subdivision load line and 0.95 at the light service draught. As explained in Chapter 2 of this paper, for a dredger the highest KG does not necessarily say that the stability is worst. Stability depends on the density and nature of the cargo and thus a range of densities and the nature of the cargo must be considered to provide an idea of the safety of the dredger. Furthermore, as explained in Chapter 3 of this paper, an intermediate draught according to the SOLAS definition is hypothetical for a dredger and does not give a reliable indication of the safety of the vessel. Finally, by law the cargo of a dredger is wet because it must be transported by pumps. The porosity of this wet cargo is nil and thus the permeability is nil below the cargo surface. Above the cargo surface the permeability is 1.

The consequence of calculating the bottom damage stability of a hopper dredger (under construction now) is clearly demonstrated in Fig. 8. A typical bottom damage case was selected in which the hopper is involved according to the opinion of some authorities (because it has no double bottom), a double bottom dry tank and the compartment in front of the hopper above the tank top.

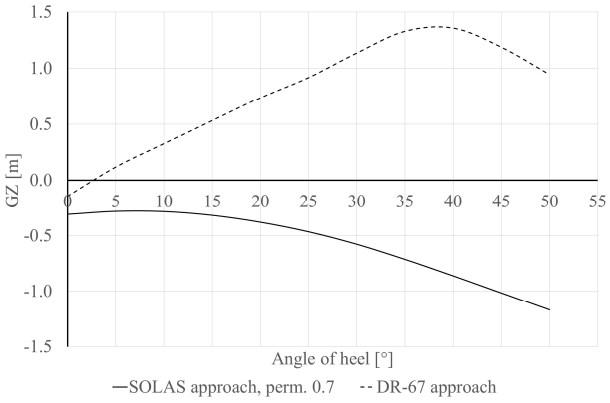

Figure 8: GZ-curves according to different approaches

The GZ-curves in this Fig. 8 are both valid for the same draught, displacement and KG. The hopper is filled with wet cargo up to the upper edge, having a density is above 1.4 t/m3. In case of the SOLAS approach, the spill-out of the cargo and the ingress of sea water are ignored, and the permeability of the hopper is 0.7. According to the DR-67 approach, shifting of the cargo, eventual spill-out and sea water ingress are considered, and the permeability of the hopper below the cargo surface is 0 and above the cargo surface 1.

To get this vessel compliant according to the SOLAS approach would require to reduce the summer draught by 1 m, apart from additional watertight hatches and doors. This was not accepted by the ship owner. To solve this problem, it was suggested to make use of Regulation 7-3, 3 of SOLAS Chapter II-1, Part B-1, where it is stated that "other figures for permeability may be used if substantiated by calculations". For the typical cargo

of a dredger it is not needed to substantiate the permeability by calculations because all pores, if any, are filled with seawater. It was suggested the hopper to have a permeability of 0 below the cargo surface. Above the cargo surface the permeability should be 1, however, one should notice that at the highest possible KG, as SOLAS requires, the hopper is filled to the upper edge, and therefore, no space is left above the cargo surface. Fig. 9 demonstrates the effect of the permeability of the hopper. Now, the GZ-curves are rather close together. Differences can be attributed to spill-out of the cargo up to approx. 38° of heel and ingress of sea water beyond that point.

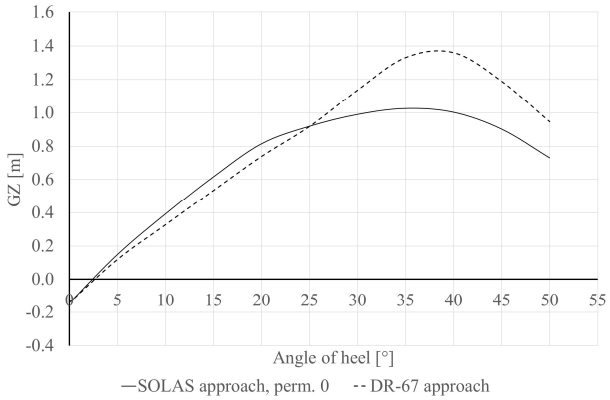

Figure 9: GZ-curves for cargo density of 1.4 t/m^3

The GZ-curves in Fig. 9 are valid for a cargo density of approx. 1.4 t/m^3, as a result of the cargo deadweight required to get the vessel on her summer draught and of having the hopper filled to the upper edge.. Immediately the question came up what this would mean for higher cargo densities, when the cargo level in the hopper is lower. Cargo spill-out will be delayed then and for the highest density sea water ingress will take place prior to cargo spill-out, expected to worsen stability. Indeed, a good question, but just these situations and their effect on the stability were the main reasons for developing DR-67. In Fig. 10 the GZ-curves are given for a cargo density of 2.0 t/m^3, which density results in a rather low cargo level.

Due to the bottom damage, resulting in an increase of draught and in a trim, ingress of sea water into the hopper almost immediately takes place then, increasing the draught even more and worsening the stability. It can be seen that the GZ-curve according to the calculation approach of DR-67 is significantly lower than that according to the calculation approach of SOLAS. This is due to the fact that the SOLAS approach do not consider sea water ingress. Although this vessel has sufficient stability, for other dredger designs it can be different. This is to say more critical, and therefore these effects should be considered.

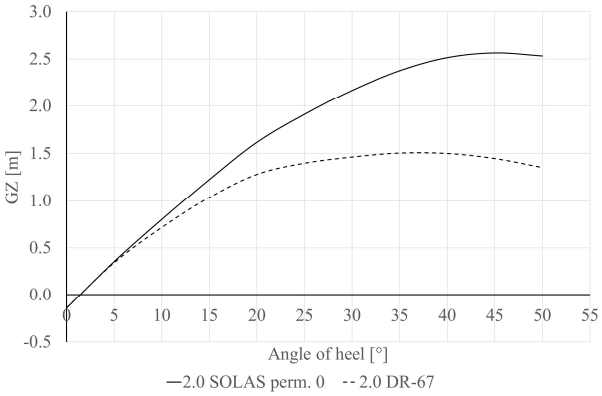

Figure 10: GZ-curves for cargo density 2.0 t/m^3

7. CONCLUSIONS & RECOMMENDATION

From the above description the following can be concluded:

- DR-67 is especially developed for hopper dredger to assure their safety with regard to stability, considering all practical effects which play a role in the stability.
- Regarding stability, the SOLAS approach for cargo ships is not sufficient for hopper dredgers to assure their safety.
- The modification of DR-67 into DR-68 was imperfect because bottom damage stability was not considered well; no indication is given that the summer draught may be used as the deepest subdivision load line.
- Requiring the vessel to comply according to both approaches, results in unnecessary additional calculation work with different outcome, leading to confusion.

It is recommended to correct DR-68, such that it is clear that the summer draught may be taken as the deepest subdivision load line for bottom damage stability calculation. The amendments mentioned in the introduction of section 6.2 of DR-68 regarding damage stability, stipulate the use of the typical calculation approach for dredgers.

Furthermore, because of the growing need for having SPS (Special Purpose Ship) notation on these vessels, it would be wise to cover this as well in DR-68, avoiding the need for a new round of corrections in the near future.

REFERENCES

IMO Circular letter No. 2285, 17 January 2001, "Communication from the Government of The Netherlands, regarding Guidelines for the construction and operation of dredgers assigned reduced freeboard in accordance with Article 6(3) of the International Convention on Load Lines, 1966."

Jager, A. de, 2005, "New stability requirements for hopper dredgers and their effect on the design", Proceedings of the International Conference on Marine Research and Technology, (ICMRT), Ischia, Italy.

IMO LL.3-Circ.205, 27 October 2011, "Exemptions for dredgers under article 6, Communication by the Government of the Netherlands".

Jager, A. de, 2013, "Special rules intended for special vessels", Proceedings of the International Symposium on Practical Design of Ships and Other Floating Structures (PRADS), Changwon, South Korea.

IMO Circular letter No. 3573, 21 August 2015, "Alternative methodology accepted under regulation II-1/4.2 of the 1974 SOLAS Convention, Communication from the Government of The Netherlands".

Application of SOLAS regulation II-1/9 to dredgers, website https://puc.overheid.nl/nsi/doc/PUC_1349_14/ of the Dutch Government.

Stochastic dynamic analysis of a damaged vessel capsizing in random beam seas by path integration method

Jianwen Duan, State Key Laboratory of Ocean Engineering, School of Naval Architecture, Ocean and Civil Engineering, Shanghai Jiao Tong University, Shanghai, China, sjtudjw@sjtu.edu.cn

Ning Ma, State Key Laboratory of Ocean Engineering, School of Naval Architecture, Ocean and Civil Engineering, Shanghai Jiao Tong University, Shanghai, China, ningma@sjtu.edu.cn

Qiqi Shi, State Key Laboratory of Ocean Engineering, School of Naval Architecture, Ocean and Civil Engineering, Shanghai Jiao Tong University, Shanghai, China, graceshqq@sjtu.edu.cn

Jinya Zhang, State Key Laboratory of Ocean Engineering, School of Naval Architecture, Ocean and Civil Engineering, Shanghai Jiao Tong University, Shanghai, China, zjy0628@sjtu.edu.cn

ABSTRACT

Extreme roll motion response in realistic seas is a significant threat to ship stability, particularly for damaged vessels with weak maneuverability, as it increases the probability of capsizing. In this paper, a stochastic framework coupling nonlinear roll dynamics with flooding mechanics is established, providing new analytical pathways for quantifying capsize probabilities in damaged vessel scenarios. A four-dimensional (4D) stochastic differential equation (SDE) which integrates a single degree of freedom (SDOF) roll motion equation with a linear filter model is constructed to study the nonlinear roll motion and the probability of a damaged vessel capsizing during progressive flooding state and steady state in random beam seas. A damage-flooding probability model is formulated through dynamic probabilistic coupling with the 4D SDE. The target vessel in this paper is DTMB 5415 which has symmetrical compartments. The numerical stability of the 4D path integration (PI) method is assessed by comparing its results with those obtained from Monte Carlo simulations (MCS). The conclusion is that the results obtained from the PI method are in good agreement with those from MCS and PI method provides smoother low-probability results in both progressive flooding and steady states.

Keywords: *Stochastic dynamic analysis, Damaged vessel, Stochastic differential equation, Markov system, Path integration method.*

1. INTRODUCTION

The survivability of damaged vessels in realistic seas is always focused on by designers and researchers. The stochastic nature of breach characteristics and realistic wave conditions necessitates probabilistic characterization of the flooding process, motion response, and their consequences (potential loss of lives) of damaged vessels through defined statistical distributions.

The current criteria SOLAS (IMO, 2020a) based on static assessment considers ship stability residual parameters and the Attained Survivability Index (A-index) is used to reflect the survivability of damaged vessels. Although static simulation is widely favored by designers because of its high efficiency, it is limited by low fidelity computational models and is difficult to consider the impact of random waves on the capsizing probability of damaged vessels in realistic seas, which has led researchers to develop higher fidelity models with acceptable calculation efficiency (Mauro et al., 2023).

A series of research projects such as HARDER project (HARDER, 2000-2003), GOALDS project (GOALDS, 2009-2012) and eSAFE project (eSAFE, 2016-2018) have introduced the critical sea state H_S^* based on different methods for calculating s-factor (probability to survive after flooding of each damage case) in SOLAS. But H_S^* does not always affect the value of s-factor and instead, the s-factor is often only affected by the stability residual parameters.

4 DOF and 6 DOF time domain dynamic models are effective tools for simulating the flooding process and motion characteristics of damaged vessels in irregular waves in which water ingress/egress is modelled with modified Bernoulli's equation and floodwater motions are coupled with

ship dynamics (Acanfora and Cirillo, 2017; Manderbacka and Ruponen, 2016). Based on these models, the probability of capsizing or stability failure is calculated by fitting some specific distributions such as a Poisson process (direct counting method) (IMO, 2020b) with a small number of calculations in the given sea state and is represented as the marginal probability for time to capsize (TTC) or stability failure (Bu et al., 2023). But for the calculation of the probability of capsizing or stability failure under all damage conditions, the calculation time of these models is often unacceptable. Another way is to apply these models to calculate the survivability of critical damage conditions (Mauro et al., 2023).

A single degree of freedom (SDOF) roll motion dynamic model has higher efficiency because of the neglect of coupling effects in different degrees of freedom motion. Based on the SDOF model, the probability of capsizing or stability failure is calculated by direct Monte Carlo simulations (MCS) with a large number of calculations (Zhan et al., 2024) or direct counting method with a small number of calculations (Duan et al., 2023). But Monte Carlo simulation is only a brute force method, and its accuracy and associated computational efficiency for prediction of the extreme responses would be a main drawback. Therefore, the calculation of capsizing probability related to extreme responses is often not accurate enough based on Monte Carlo simulation.

For such nonlinear dynamic models of damaged vessels, assessing the statistics of extreme roll response and the corresponding low probability levels is a difficult task. Based on the theory of stochastic process, the stochastic differential equation (SDE) is introduced to study the dead ship condition in random beam seas and parametric roll in random head seas (Chai et al, 2016; Liu et al, 2023; Maki et al, 2023). And Markov diffusion theory, which is only valid for a system driven by Gaussian white noise or filtered white noise processes, is popular for stochastic dynamic analysis of nonlinear systems because probabilistic properties of this system are governed by the Fokker-Planck (FP) equation. FP equation can be solved by many numerical methods such as finite elements (FE) (Kumar et al, 2014), finite difference (FD) (Kumar and Narayanan, 2006) and path integration (PI) (Chai et al, 2016). However, the so-called ”curse of dimension” problem will appear when the high-dimensional FP equation is solved based on FE method or FD method. It will cause an increase in computer storage needed and a decrease in accuracy. Instead, PI method is a great alternative method because the FP equation is not solved directly and the probability density function (PDF) of response is calculated step by step. This means the probability density function (PDF) at a given time depends only on the PDF at a slightly earlier time and the conditional PDF—a term describing the probability of transitioning between system states (e.g., roll angle, flooding water mass) over that time interval.

For the stochastic nonlinear system of damaged vessels, the stochastic characteristics of the flooding process should be given special consideration. Based on the PI method, the PDF of responses is calculated step by step and the PI mehod enables the derivation of the flooding process PDF through the responses PDF at each calculation step.

In this paper, a stochastic framework coupling nonlinear roll dynamics with flooding mechanics is established, providing new analytical pathways for quantifying capsize probabilities in damaged vessel scenarios. Firstly, a four-dimensional (4D) stochastic differential equation (SDE) is constructed to study the nonlinear roll motion and the probability of a damaged vessel capsizing during progressive flooding state and steady state in random beam seas. The 4D SDE employs a single degree of freedom (SDOF) roll motion equation (rather than higher-dimensional 4DOF/6DOF models) coupled with a linear filter, as the SDOF framework sufficiently captures the dominant nonlinear roll dynamics critical to capsizing analysis while balancing computational tractability by intentionally reducing the system's complexity. A damage-flooding probability model is formulated through dynamic probabilistic coupling with the 4D SDE. The PDF of flooding water mass at any given time is determined by the PDF of the roll angle (derived from the 4D SDE) at this time and the PDF of flooding water mass at a slightly earlier time. The model reflects how water ingress/egress is influenced by the instantaneous motion of damaged vessels and cumulative flooding history. The flooding water mass directly affects the 4D SDE by altering the roll restoring moment and inertia of damaged vessels, while also influencing hydrostatic and hydrodynamic forces through changes in the

submerged hull shape. These alterations impact restoring moment coefficients and wave excitation, which are crucial for accurate predictions of capsizing. PI method is used to solve the 4D SDE and meanwhile the flooding process PDF is calculated at each calculation step. The target vessel in this paper is DTMB 5415 which has symmetrical compartments. The numerical stability of the 4D PI method is assessed.

2. MATHEMATICAL MODEL OF DAMAGED VESSELS

Pre-calculation considering incremental flooding water accumulation

Neglecting the dynamic effects of jet flow during breach formation, the equilibrium attitude parameters (including sinkage $\tilde{\xi}$, heel angle $\tilde{\phi}$, trim angle $\tilde{\theta}$ and the center of gravity $\widetilde{x_g}$ $\widetilde{y_g}$ $\widetilde{z_g}$) of damaged vessels transitioning from the progressive flooding stage to the steady flooding stage can be expressed as a function of the flooding water mass.

$$\begin{aligned} &\tilde{\xi} = \tilde{\xi}(m)\ \ \tilde{\phi} = \tilde{\phi}(m)\ \ \tilde{\theta} = \tilde{\theta}(m) \\ &\widetilde{x_g} = \widetilde{x_g}(m)\ \ \widetilde{y_g} = \widetilde{y_g}(m)\ \ \widetilde{z_g} = \widetilde{z_g}(m) \end{aligned} \tag{1}$$

Where the superscript ~ represents the parameters in the equilibrium state. m is the flooding water mass.

On the premise of establishing three-dimensional Non-Uniform Rational B-Spline (NURBS) surfaces for the damaged vessels, the pre-calculation of these parameters is based on the instantaneous wetted surface integration method and follows the steps outlined in Figure 1.

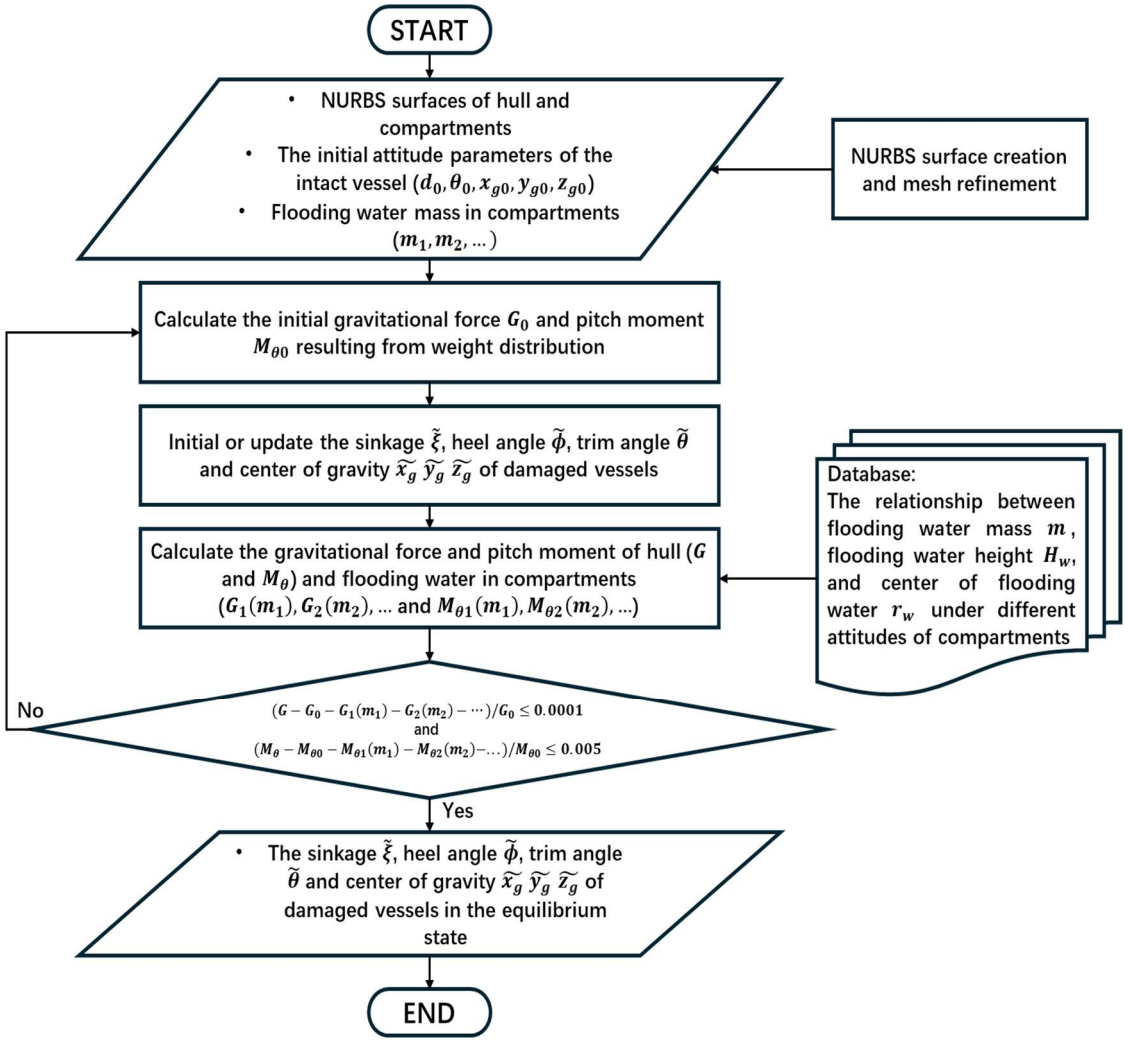

Figure 1: Flowchart for pre-calculation of sinkage, heel angle, trim angle and the center of gravity in the equilibrium state.

The flowchart in Figure 1 is used to evaluating the equilibrium state of damaged vessels during progressive flooding state and steady state. The process begins with inputs including NURBS surface models of the hull and compartments, initial intact vessel parameters (draft, trim angle and center of gravity), and flooding conditions (flooding water mass in compartments). Initial gravitational force and pitch moment of hull are calculated based on the weight distribution or initial attitude. The effects of flooding water are incorporated by computing gravitational forces and pitch moments for each damaged compartment based on a pre-calculated database which links flooding water mass to flooding water height and center across varying attitudes. The model iteratively updates the damaged vessel's sinkage, heel, trim, and center of gravity to achieve force and moment equilibrium. Convergence criteria are applied to ensure that residuals remain below 0.01% for forces and 0.5% for moments. The output defines the equilibrium state of the damaged vessels, including sinkage, heel angle, trim angle, and the center of gravity in that state.

Equation of roll motion

Assuming that the pitch and heave motions are quasi-static whose equilibrium position can be simulated under different flooding water mass through hydrostatic simulation, the nonlinear roll motion of damaged vessels in random beam seas is described by a SDOF roll motion equation based on added weight method:

$$\begin{aligned}(I_{44} + I_{w44}(m) + J_{44}(m))\ddot{\phi}(t) \\ + B\left(\dot{\phi}(t)\right) + (\Delta g \\ + mg)GZ(\phi(t), m) \\ = M_{wave}(t, m)\end{aligned} \tag{2}$$

Where $\ddot{\phi}(t)$, $\dot{\phi}(t)$ and $\phi(t)$ are roll acceleration, roll velocity and roll angle, respectively. I_{44} is the moment of inertia, $J_{44}(m)$ is the added moment of inertia and $I_{w44}(m)$ is the increased moment of inertia caused by flooding water. $B\left(\dot{\phi}(t)\right)$ is the roll damping moment. $(\Delta g + mg)GZ(\phi(t), m)$ is the roll restoring moment and Δ is the displacement of intact vessels. $M_{wave}(t, m)$ is the random wave excitation moment. g is the gravitational acceleration.

The roll damping moment has strong nonlinearity and is divided into wave, friction, eddy and bilge keel components at zero forward speed of intact vessels based on Ikeda's method (Ikeda and Katayama, 2024). But the interaction between these components and flooding water will affect the accuracy of the simulation for damaged vessels. In this paper, the linear-plus-quadratic damping (LPQD) model is used and the damping coefficients are from free roll decay experiments of damaged vessels:

$$\begin{aligned}B\left(\dot{\phi}(t)\right) = B_{44l}\dot{\phi}(t) \\ + B_{44q}\dot{\phi}(t)\left|\dot{\phi}(t)\right|\end{aligned} \tag{3}$$

Where B_{44l} and B_{44q} are linear and quadratic damping coefficients, respectively.

It is worth mentioning that the roll damping $B\left(\dot{\phi}(t)\right)$ should be the function of flooding water mass m for damaged vessels. But the accurate roll damping $B(\dot{\phi}(t), m)$ needs to be based on a large number of experiments or CFD simulations which will take a lot of time and resources. Therefore, the effect of flooding water mass on roll damping moment has been neglected in this paper.

The roll restoring moment $(\Delta g + mg)GZ(\phi(t), m)$ is function of roll angle of damaged vessels $\phi(t)$ and flooding water mass m. The roll restoring arms $GZ(\phi(t), m)$ can be calculated by the instantaneous wetted surface integration method at different equilibrium attitudes which are pre-calculated considering incremental flooding water accumulation. It should be noted that for intact vessels and symmetrically damaged vessels, the roll restoring arm (GZ) curve is typically modeled using odd functions to reflect the symmetric restoring characteristics of roll motion (Chai et al, 2016; Liu et al, 2023). However, for asymmetrically damaged ships, flooding introduces asymmetric contributions to the restoring moment. This study adopts a polynomial function to represent the GZ curve for both symmetrically and asymmetrically damaged vessels. This approach can effectively capture both the asymmetric and symmetric restoring behavior within the single degree of freedom (SDOF) framework, enabling rapid computation of nonlinear restoring forces while maintaining accuracy at large roll angle. The

effect of m is implicitly included in the coefficients of polynomial function:

$$GZ(\phi(t),m) = \sum_{i=1}^{n} C_{2i-2}(m)\phi^{2i-2}(t) + \sum_{j=1}^{n} C_{2j-1}(m)\phi^{2j-1}(t) \quad (4)$$

Where $C_{2i-2}(m)$ and $C_{2j-1}(m)$ are coefficients of the roll restoring arm and $C_{2i-2}(m) = 0$ when flooding condition is symmetrical flooding. The $C_{2i-2}(m)$ and $C_{2j-1}(m)$ are fitted with different $GZ(\phi(t),m)$ curves considering incremental flooding water accumulation.

Random wave excitation moment $M_{wave}(t,m)$ can be achieved through the wave excitation moment spectrum $S_{MM}(\omega,m)$. The wave excitation spectrum $S_{MM}(\omega,m)$ can be obtained through the wave density spectrum $S_{\zeta\zeta}(\omega)$ and Response Amplitude Operator (RAO) $|F_{roll}(\omega,m)|$:

$$S_{MM}(\omega,m) = |F_{roll}(\omega,m)|^2 S_{\zeta\zeta}(\omega) \quad (5)$$

The Response Amplitude Operators (RAOs) $|F_{roll}(\omega,m)|$ considering incremental flooding water accumulation are calculated based on the strip theory at different frequencies ω. When the flooding water mass is different, the geometry of two-dimensional cross-sections below the waterline is different due to changes in the equilibrium attitudes of the hull. The added moments of inertia $J_{44}(m)$ considering incremental flooding water accumulation are also calculated by the strip theory at infinite frequency.

In order to express Eq. (2) more clearly in the form of a stochastic differential equation (SDE), divide both sides of Eq. (2) by $(I_{44} + I_{w44}(m) + J_{44}(m))$ and the final differential equation is given as:

$$\ddot{\phi}(t) + b_{44l}(m)\dot{\phi}(t) + b_{44q}(m)\dot{\phi}(t)|\dot{\phi}(t)| + \sum_{i=1}^{n} c_{2i-2}(m)\phi^{2i-2}(t) + \sum_{j=1}^{n} c_{2j-1}(m)\phi^{2j-1}(t) = m_{wave}(t,m) \quad (6)$$

Where $b_{44l}(m)$, $b_{44q}(m)$, $c_{2i-2}(m)$, $c_{2j-1}(m)$ and $m_{wave}(t,m)$ can be expressed as dividing B_{44l}, B_{44q}, $C_{2i-2}(m)$, $C_{2j-1}(m)$ and $M_{wave}(t,m)$ by $(I_{44} + I_{w44}(m) + J_{44}(m))$, respectively.

The relative wave excitation moment $m_{wave}(t,m)$ can be achieved through the relative wave excitation moment spectrum $S_{mm}(\omega,m)$:

$$S_{mm}(\omega,m) = |F_{roll}(\omega,m)|^2 S_{\zeta\zeta}(\omega) / (I_{44} + I_{w44}(m) + J_{44}(m))^2 \quad (7)$$

The SDOF roll equation as Eq. (6) can be transformed to a state-space equation including two stochastic differential equations (SDEs):

$$\begin{cases} dx_1 = x_2 dt \\ dx_2 = (-b_{44l}(m)x_2 - b_{44q}(m)x_2|x_2| - \sum_{i=1}^{n} c_{2i-2}(m)x_1^{2i-2} - \sum_{j=1}^{n} c_{2j-1}(m)x_1^{2j-1} - x_3)dt \end{cases} \quad (8)$$

Where x_1 represents roll angle $\phi(t)$. x_2 represents roll velocity $\dot{\phi}(t)$. x_3 represents relative wave excitation moment $m_{wave}(t,m)$.

In realistic seas, wave elevation and relative wave excitation moment obey the distribution of the spectrum. The random characteristics of wave elevation and relative wave excitation moment can be simulated using the filter technique due to its simplicity and practicality.

Shaping filter technique

Assuming that relative wave excitation moment is a stationary stochastic process, the relative wave excitation spectrum $S_{mm}(\omega,m)$ under varying flooding mass can be approximated using linear fitting techniques. In this paper, a second-order filter technique is applied (Dostal and Kreuzer, 2011):

$$\begin{cases} dx_3 = (x_4 - \beta x_3)dt + \gamma dW \\ dx_4 = -\alpha x_3 dt \end{cases} \quad (9)$$

Where x_3 represents relative wave excitation moment $m_{wave}(t,m)$ and x_4 is intermediate state variables. $dW = W(t+\Delta t) - W(t)$ represents a vector of increments of independent standard Wiener processes and $W(t)$ is a Wiener process. α, β and γ are fitting parameters and can be obtained by approximating the fitted spectrum in Eq. (10) to the target spectrum $S_{mm}(\omega, m)$ based on the least square method (Dostal and Kreuzer, 2011; Dostal et al, 2012).

$$S_{2nd}(\omega) = \frac{1}{2\pi}\frac{(\gamma\omega)^2}{(\alpha - \omega^2)^2 + (\beta\omega)^2} \quad (10)$$

The relative wave excitation spectrum $S_{mm}(\omega, m)$ at any flooding water mass is narrow-band spectrum and single-sided. But the fitted spectrum in Eq. (10) is double-sided. Therefore, the restrictions $\omega > 0$ should be added in application.

Finally, the 4D SDE of damaged vessels motion in random beam seas is constructed by combining the state-space equation of a SDOF roll model in Eq. (8) and the second-order filter model in Eq. (9).

$$\begin{cases} dx_1 = x_2 dt \\ dx_2 = (-b_{44l}(m)x_2 - b_{44q}(m)x_2|x_2| \\ -\sum_{i=1}^{n} c_{2i-2}(m)x_1^{2i-2} - \sum_{j=1}^{n} c_{2j-1}(m)x_1^{2j-1} - x_3)dt \\ dx_3 = (x_4 - \beta x_3)dt + \gamma dW \\ dx_4 = -\alpha x_3 dt \end{cases} \quad (11)$$

Damage-flooding probability model

One result of solving Eq. (11) is the probability density function (PDF) of the state variables x_1, x_2, x_3, x_4. Where x_1 is roll angle $\phi(t)$. The damage-flooding probability model is constructed based on the PDF of roll angle.

The initial probability distribution of flooding water mass m is set as a Dirac delta function with infinite value at $m = 0$.

$$\delta(m) = \begin{cases} \infty, & m = 0 \\ 0, & m \neq 0 \end{cases} \quad (12)$$

The probability distribution of equilibrium sinkage $f(\tilde{\xi})$ and trim angle $f(\tilde{\theta})$ can be calculated based on the pre-calculation in Figure 1. The process is as follows: Once the initial probability distribution of the flooding water mass is established, random samples of the flooding water mass are generated using the Monte Carlo sampling method. Subsequently, the random samples of sinkage and trim angle are calculated through the deterministic relationships illustrated in Figure 1, and their probability distributions are estimated statistically.

The probability distribution of instantaneous roll angle $f(\phi)$ can be obtained from the solution of Eq. (11) at any given time based on path integration (PI) method (Karlsen, 2006; Chai, 2016). Once the stochastic excitation is defined within the 4D SDE framework, the probability distribution of roll angle is calculated by the deterministic dynamics and stochastic excitation.

Modified Bernoulli equation is used to calculated the probability distribution of flooding rate of mass as shown in Figure 2 and Eq. (13).

$$\begin{aligned} f(\dot{m}_{ij}) &= f(\rho v_{ij}) \\ &= \rho K \int_{s_A}^{s_C} b_{ij} sign(f(\Delta p)) \sqrt{\frac{2f(\Delta p)}{\rho}} ds \\ f(\Delta p) &= \rho g h(s, f(\tilde{\xi}), f(\tilde{\theta}), f(\phi), \zeta_{i,j}) \end{aligned} \quad (13)$$

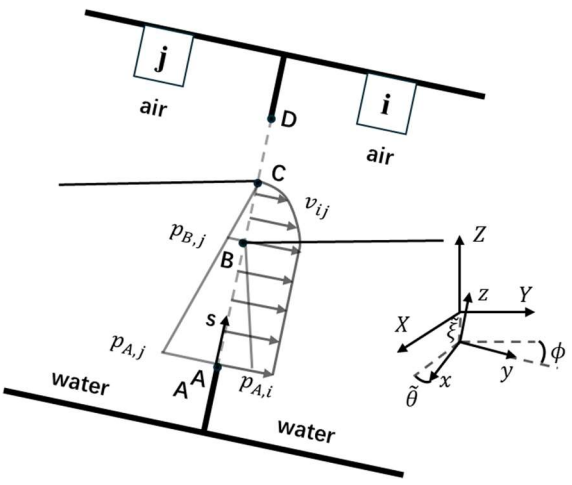

Figure 2: Flooding rate of mass calculation.

Where $f(\dot{m}_{ij})$ is the probability distribution of flooding rate of mass and $\dot{m}_{ij}$ is the flooding rate of mass between the rooms i and j. v_{ij} is the flooding rate of volume between the rooms i and j. ρ is the

flooding water density. K is the discharge coefficient which is generally determined by experiment. b_{ij} is the breadth of the breach between the rooms i and j. $f(\Delta p(s))$ is the probability distribution of pressure difference at s, which is the function of $f(\tilde{\xi})$, $f(\tilde{\theta})$, $f(\phi)$ and $\zeta_{i,j}$. $\zeta_{i,j}$ is the free surface height in the rooms i and j. s is the position variable along the height of the breach. s_A and s_C are the positions of the bottom and top points at which $\Delta p \neq 0$, respectively.

The probability distribution of flooding water mass is expressed as the integral of the probability distribution of flooding rate of mass:

$$f(m_{ij}) = \int_0^{t_i} f(\dot{m}_{ij})dt \tag{14}$$

Where $f(m_{ij})$ is the probability distribution of flooding water mass. t_i is the instant given time.

3. PATH INTEGRATION METHOD

The path integration (PI) method (Karlsen, 2006; Chai, 2016) is a robust numerical technique for analyzing the probabilistic evolution of high-dimensional stochastic dynamic systems governed by Markov processes. By leveraging the Markov property and discretizing the temporal domain, this method efficiently computes global response statistics through iterative integration of local transition probabilities. In this paper, the PI method is used to solve the 4D SDE as shown in Eq. (11).

Time discretization of the SDE

Consider the four-dimensional (4D) Markov process described by the stochastic differential equation (SDE) as Eq. (11), the $Itô$ SDE (Itô, 1944) can be represented as:

$$d\boldsymbol{x} = \boldsymbol{a}(\boldsymbol{x}, t)dt + \boldsymbol{b}(t)d\boldsymbol{W}(t) \tag{15}$$

Where $\boldsymbol{x}(t)$ is the vector of state variables $(x_1(t), x_2(t), x_3(t), x_4(t))^T$. $\boldsymbol{a}(\boldsymbol{x}, t)$ is drift term and $\boldsymbol{b}(t)$ is diffusive term.

In this paper, a fourth-order Runge-Kutta-Maruyama (RKM) (Chai, 2016) scheme is used for time discretization:

$$\begin{aligned}
&\boldsymbol{x} = \boldsymbol{x}' + \boldsymbol{r}(\boldsymbol{x}', t', \Delta t) + \boldsymbol{b}(t')\boldsymbol{\Delta W}(t') \\
&\boldsymbol{k_1} = \boldsymbol{a}(\boldsymbol{x}', t') \\
&\boldsymbol{k_2} = \boldsymbol{a}\left(\boldsymbol{x}' + \frac{\Delta t}{2}\boldsymbol{k_1}, t' + \frac{\Delta t}{2}\right) \\
&\boldsymbol{k_3} = \boldsymbol{a}\left(\boldsymbol{x}' + \frac{\Delta t}{2}\boldsymbol{k_2}, t' + \frac{\Delta t}{2}\right) \\
&\boldsymbol{k_4} = \boldsymbol{a}(\boldsymbol{x}' + \Delta t\boldsymbol{k_3}, t' + \Delta t) \\
&\boldsymbol{r}(\boldsymbol{x}', t', \Delta t) = \frac{1}{6}(\boldsymbol{k_1} + 2\boldsymbol{k_2} + 2\boldsymbol{k_3} \\
&\qquad + \boldsymbol{k_4})\Delta t
\end{aligned} \tag{16}$$

Where $\boldsymbol{x} = \boldsymbol{x}(t)$ and $\boldsymbol{x}' = \boldsymbol{x}(t')$. $\Delta t = t - t' > 0$ is the time step. $\boldsymbol{r}(\boldsymbol{x}', t', \Delta t)$ is the explicit fourth-order Runge-Kutta (RK4) approximation. $\boldsymbol{\Delta W}(t') = \boldsymbol{W}(t) - \boldsymbol{W}(t')$ is a Gaussian variable for every t'.

Principle of the PI method

The temporal evolution of the $Itô$ SDE's conditional probability density function which is also called as transition probability density $p(\boldsymbol{x}, t|\boldsymbol{x}', t')$ is governed by the Fokker-Planck (FP) equation (Risken, 1989):

$$\begin{aligned}
&\frac{\partial}{\partial t}p(\boldsymbol{x}, t|\boldsymbol{x}', t') \\
&= -\sum_{i=1}^{4}\frac{\partial}{\partial x_i}a_i(\boldsymbol{x}, t)p(\boldsymbol{x}, t|\boldsymbol{x}', t') \\
&+ \frac{1}{2}\sum_{i=1}^{4}\sum_{j=1}^{4}\frac{\partial^2}{\partial x_i \partial x_j}(b(t)b^T(t))_{ij}p(\boldsymbol{x}, t|\boldsymbol{x}', t')
\end{aligned} \tag{17}$$

For high-dimensional SDE, directly solving the FP equation becomes computationally intractable. The PI method circumvents this 'curse of dimension' through a recursive integration strategy.

The one time-step transition probability density can be approximated by the following degenerate Gaussian distribution with the accuracy to the order of $O(\Delta t2)$ (Risken, 1989):

$$\begin{aligned}
&p(\boldsymbol{x}, t|\boldsymbol{x}', t') \\
&= \delta(x_1 - x_1' - \boldsymbol{r_1}(\boldsymbol{x}', t', \Delta t))\delta(x_2 - x_2' \\
&- \boldsymbol{r_2}(\boldsymbol{x}', t', \Delta t))\tilde{p}(x_3, t|x_3', t')\delta(x_4 - x_4' \\
&- \boldsymbol{r_4}(\boldsymbol{x}', t', \Delta t))
\end{aligned} \tag{18}$$

Where $\tilde{p}(x_3, t|x_3', t')$ is given as:

$$\tilde{p}(x_3, t|x_3', t') = \frac{1}{\sqrt{2\pi\gamma^2\Delta t}} \exp\left\{-\frac{(x_1 - x_1' - \boldsymbol{r_1}(\boldsymbol{x}', t', \Delta t))^2}{2\gamma^2\Delta t}\right\} \quad (19)$$

The probability density function of $\boldsymbol{x}$ based on PI method can be calculated by:

$$p(\boldsymbol{x}, t) = \int_{R^4} p(\boldsymbol{x}, t|\boldsymbol{x}', t')p(\boldsymbol{x}', t')d\boldsymbol{x}' \quad (20)$$

Where $d\boldsymbol{x}' = \prod_{i=1}^{4} dx_i'$. R^4 is four-dimensional integration domain of x_1, x_2, x_3, x_4.

Starting from an initial PDF $p(\boldsymbol{x}, t_0)$, the global PDF evolution is computed iteratively:

$$p(\boldsymbol{x}, t) = \int_{R^4} \dots \int_{R^4} \prod_{k=1}^{n} p(\boldsymbol{x}^k, t_k|\boldsymbol{x}^{k-1}, t_{k-1})p(\boldsymbol{x}, t_0)d\boldsymbol{x}^0 .. d\boldsymbol{x}^{n-1} \quad (21)$$

Where $\boldsymbol{x}^k = \boldsymbol{x}(t_k)$ and $t_k = t_0 + k\Delta t$.

In practice, a computational grid is defined over the state space. At each step, interpolation techniques (e.g., B-splines) represent the current PDF, and numerical integration updates the PDF for the next time step.

4. CALCULATION METHOD FOR CAPSIZING PROBABILITY

The mean upcrossing rate, $\nu^+(\zeta)$, serves as a critical metric for quantifying extreme response statistics and evaluating reliability in marine engineering applications (Naess and Moan, 2012). For the roll angle process, this rate is derived from the joint probability density function (PDF) of the roll angle $\phi(t)$ and roll velocity $\dot{\phi}(t)$, which can be directly computed via the 4D path integration (PI) method. Utilizing the Rice formula (Rice, 1945), the mean upcrossing rate is expressed as:

$$\nu^+(\zeta) = \lim_{t\to\infty} \nu^+(\zeta; t)$$
$$\nu^+(\zeta; t) = \int_0^\infty \dot{\phi} f_{\phi\dot{\phi}}(\zeta, \dot{\phi}; t)d\dot{\phi} \quad (22)$$

Where $\nu^+(\zeta; t)$ is the expected number of upcrossing for the ζ-level per unit time at time t by the roll angle process $\phi(t)$. $f_{\phi\dot{\phi}}(\zeta, \dot{\phi}; t)$ is the joint PDF of $\phi(t)$ and $\dot{\phi}(t)$ for the ζ-level at time t. The joint PDF $f_{\phi\dot{\phi}}(\phi, \dot{\phi}; t)$ is obtained by integrating through the entire range of the third and fourth state variables x_3, x_4 in Eq. (11).

The mean upcrossing rate, $\nu^+(\zeta)$ represents the probability of damaged vessels capsizing as time approaches infinity. In practical applications, the probability of capsizing should be expressed as a marginal probability for time $\nu_T^+(\zeta)$, which can enable designers and researchers to have a clear estimate of time to capsize (TTC):

$$\nu_T^+(\zeta) = \lim_{t\to T} \nu^+(\zeta; t) \quad (23)$$

5. NUMERICAL RESULTS

Research object and hydrodynamic calculation

The frigate vessel DTMB 5415 is selected as the research object and calculation condition is in random beam seas at zero speed.

The main particulars of the intact DTMB 5415 vessel (full scale) can be seen in Table 1.

Table 1: Main particulars of DTMB 5415 (full scale).

Items	Values
Length, Lpp/m	142.200
Breadth, B/m	19.082
Depth, D/m	12.470
Mean draught, T/m	6.150
Displacement, Δ/ton	8635
Metacentric height, GM/m	1.938
Height of COG, Z_G/m	7.555
Roll radius of inertia in water, kxx/m	6.932
Pitch radius of inertia in air, kyy/m	36.802
Yaw radius of inertia in air, kzz/m	36.802

The vessel subdivision is presented in Figure 3. The definition of damaged compartments and distribution in the direction of ship length (positive direction: from stern to bow) are presented in Table 2.

Table 2: The damaged compartments definitions of DTMB 5415 (full scale).

Name	After end(m)	Forward end(m)
com1	-	30.86
com2	30.86	65.66
com3	65.66	76.15
com4	76.15	90.02
com5	90.02	108.63
com6	108.63	130.56
com7	130.56	-

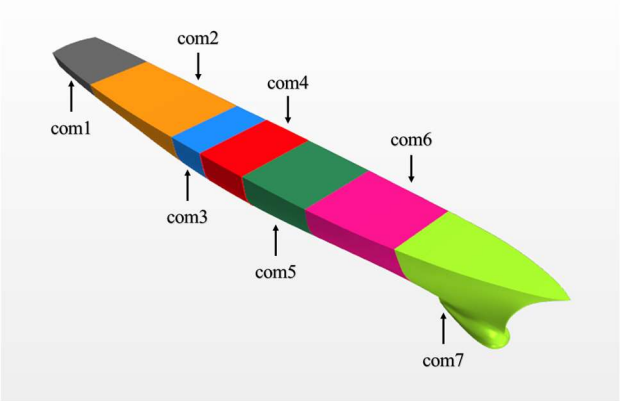

Figure 3: The subdivision of DTMB 5415.

In this paper, the compartments named com3 and com4 are damaged. The stochastic roll response during progressive flooding state and steady state are studied.

The roll restoring arm affected by the flooding water mass of two compartments m_1, m_2. On the one hand, flooding water can affect the floating attitude of damaged vessels, and on the other hand, flooding water itself can cause additional loss of roll restoring moment. Therefore, the influence of flooding water mass on the roll restoring moment of damaged vessels has been considered. The results of the roll restoring arm $GZ(\phi(t), m)$ in Eq. (2) and its fitting curve based on Eq. (4) under different combinations of m_1 and m_2 are shown in Figure 4.

The random stationary sea state is represented by the JONSWAP spectrum, which is widely used for simulate random sea states. The wave energy spectrum is given as:

$$S_{\zeta\zeta}(\omega) = \frac{\alpha_\zeta g^2}{\omega^5}\exp\left(-\frac{5}{4}\left(\frac{\omega_p}{\omega}\right)^4\right)\gamma_\zeta^{\exp\left(\frac{(\omega-\omega_p)^2}{2\sigma^2\omega_p^2}\right)} \qquad (24)$$

$$\alpha_\zeta = \left(\frac{H_s\omega_p^2}{4g}\right)^2 \frac{1}{0.065\gamma_\zeta^{0.803} + 0.135}$$

Where α_ζ is the energy scale measure. ω_p is spectral peak frequency, $\omega_p = 2\pi/T_p$. T_p is spectral peak period. H_s is the significant wave height. γ_ζ is the peak factor, and in this paper $\gamma_\zeta = 3.3$. σ is the shape parameter. When the wave frequency $\omega < \omega_p$, $\sigma = 0.07$, else when $\omega > \omega_p$, $\sigma = 0.09$. In this paper, $H_s = 4.0m$ and $T_p = 11.0s$.

The JONSWAP spectrum is not the function of flooding water mass. But the Response Amplitude Operators (RAOs) $|F_{roll}(\omega, m)|$ is the function of flooding water mass and frequency. This is because of the changes of the geometry of two-dimensional cross-sections below the waterline. Therefore, the wave excitation spectrum $S_{MM}(\omega, m)$ and the relative wave excitation spectrum $S_{mm}(\omega, m)$ is the function of flooding water mass based on Eq. (5). The results of relative wave excitation spectrum $S_{mm}(\omega, m)$ and its fitting spectrum based on Eq. (10) under different combinations of m_1 and m_2 are shown in Figure 5.

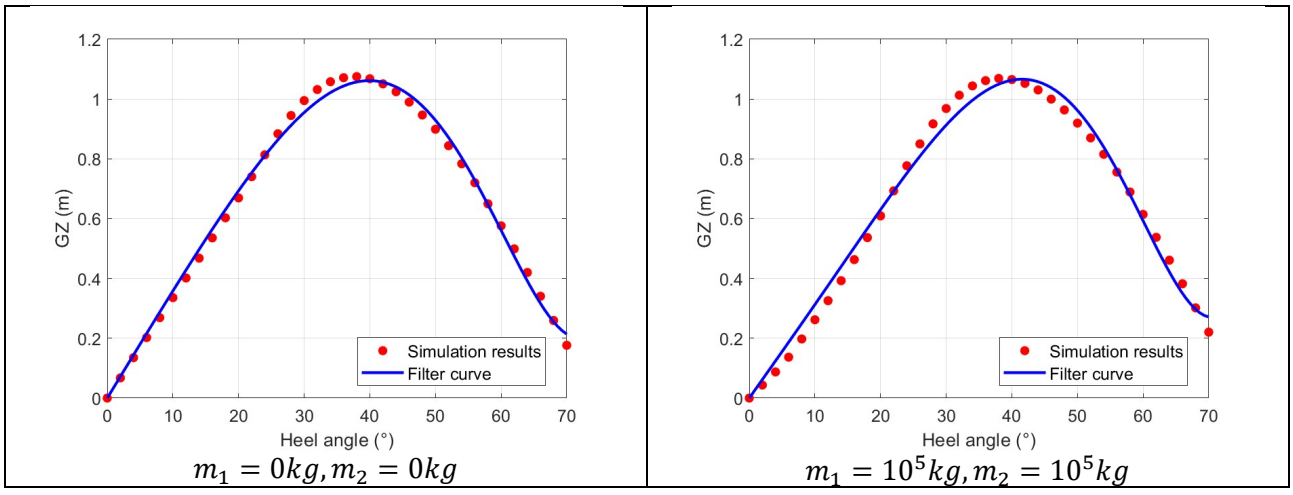

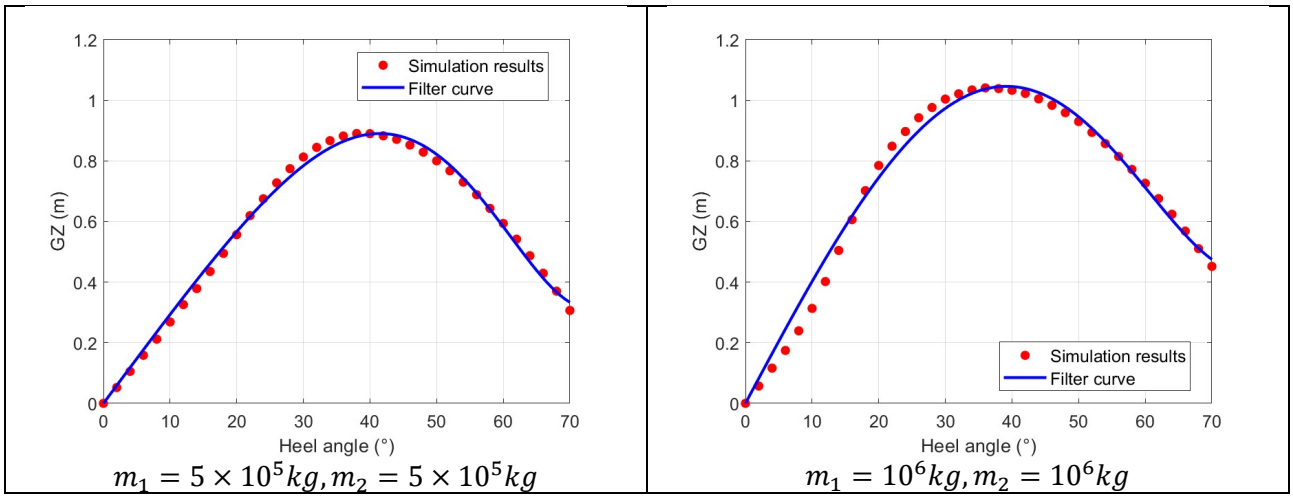

Figure 4: The GZ curve and its fitting curve considering incremental flooding water accumulation.

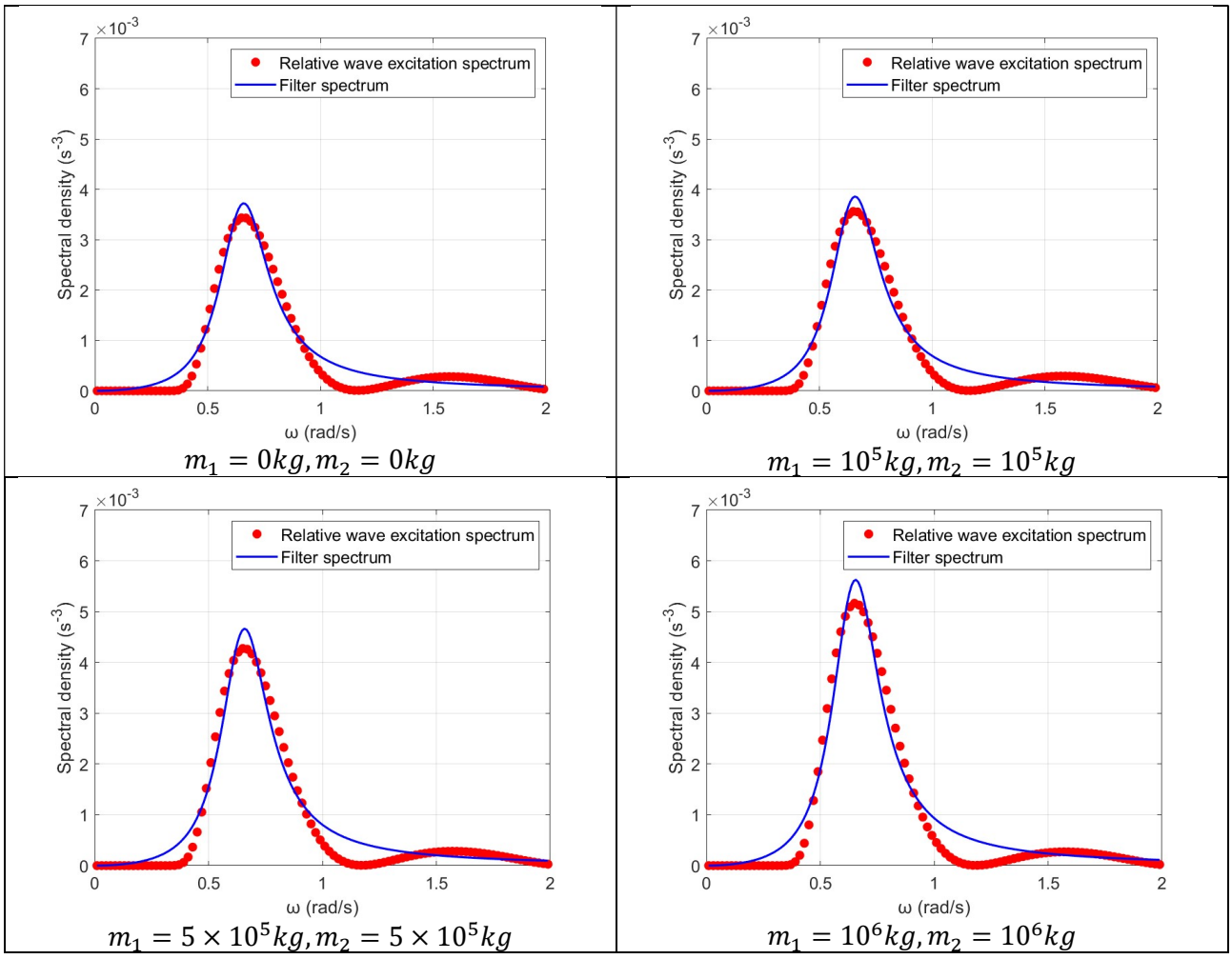

Figure 5: The relative wave excitation spectrum and its fitting spectrum considering incremental flooding water accumulation.

In Figure 4, the roll restoring arm (also called GZ) curve has high fitting accuracy within heel angle of 70 degrees considering incremental flooding water accumulation. This ensures that the 4D SDE has high accuracy in simulating the probability distribution of extreme roll motion for damaged vessels. When the flooding water mass increases, the maximum value of the GZ curve initially rises and then falls, while the corresponding heel angle of the maximum GZ value gradually decreases. The reason for the rise of

the GZ curve is as follows: When the DTMB 5415 is on an even keel, the freeboard of the vessel at the stem is greater than that at the stern. When a substantial volume of water floods the vessel, it results in a significant trim angle at the stem. During a large heel inclination, the contribution of the stern's restoring force increases, while the contribution of the stem's restoring force does not significantly decrease. This pattern is associated with the relative magnitudes of roll restoring moment and flooding water mass:

$$GZ = \frac{M_{roll}^{res}}{(\Delta g + \sum_{i=1}^{N_{com}} m_i\, g)} \tag{25}$$

Where M_{roll}^{res} is roll restoring moment calculated by the instantaneous wetted surface integration method. N_{com} is number of damaged compartments. m_i is the flooding water mass in ith damaged compartment.

In Figure 5, the fitted spectrum has a slight overestimation relative to the relative wave excitation spectrum, especially near the peak frequency, which makes the 4D SDE calculation results relatively conservative. When the flooding water mass increases, the relative wave excitation increases. This is because the two-dimensional cross-sectional area of the hull below the waterline increases.

Stochastic roll response and capsizing probability

The joint probability density function of the stochastic process $\boldsymbol{x}(t)$ can be derived using the 4D PI technique or MCS. The joint PDF $f_{\phi\dot{\phi}}(\phi, \dot{\phi}; t)$ characterizing the roll angle $\phi(t)$ and roll velocity $\dot{\phi}(t)$ processes are obtained by integrating across the complete domain of the third and fourth dimensions which are shown in Figure 6 at given time $t = 10s, 20s, 100s, 200s$. The PDF of roll angle $\phi(t)$ and flooding water mass $m_1(t)$, $m_2(t)$ at different given time are shown in Figure 7. For MCS, the calculation sample size is 100000.

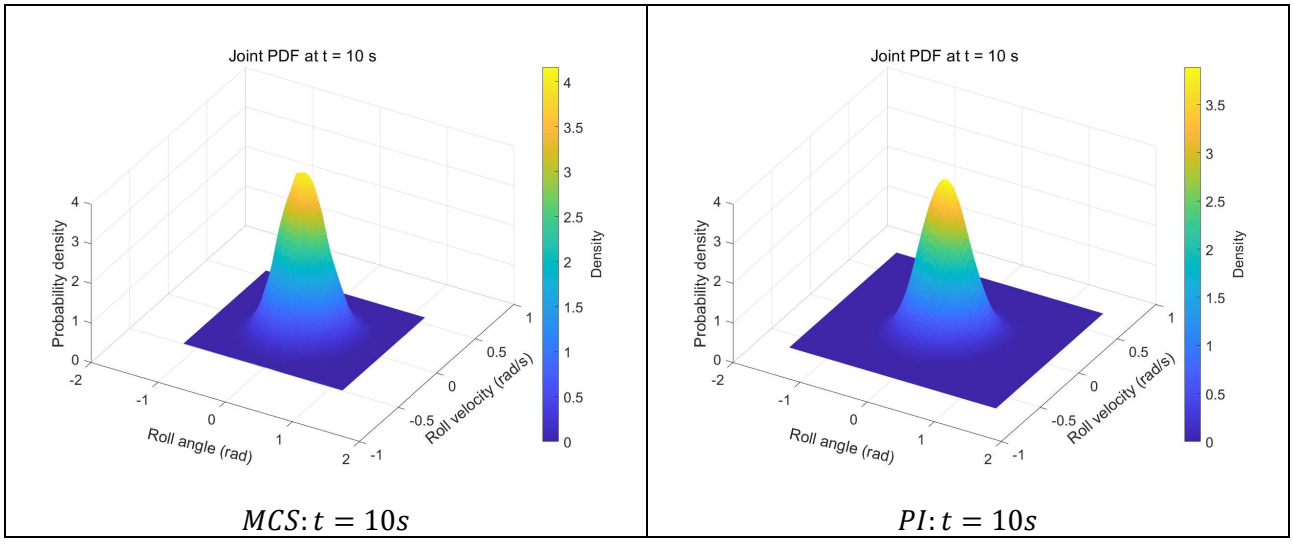

$MCS: t = 10s$ $PI: t = 10s$

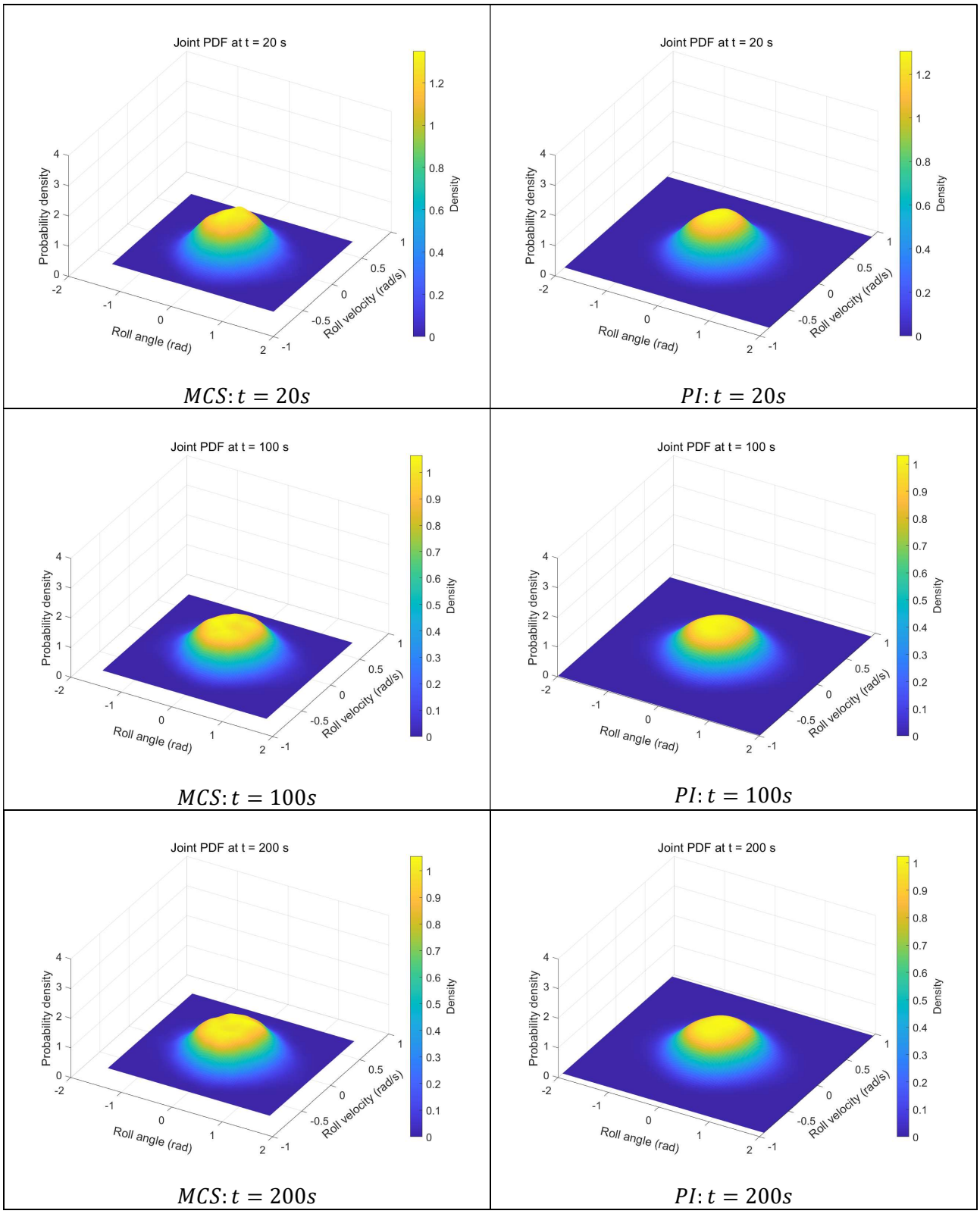

Figure 6: The joint PDF of roll angle and roll velocity at different given time (10s, 20s, 100s, 200s) based on MCS and PI method.

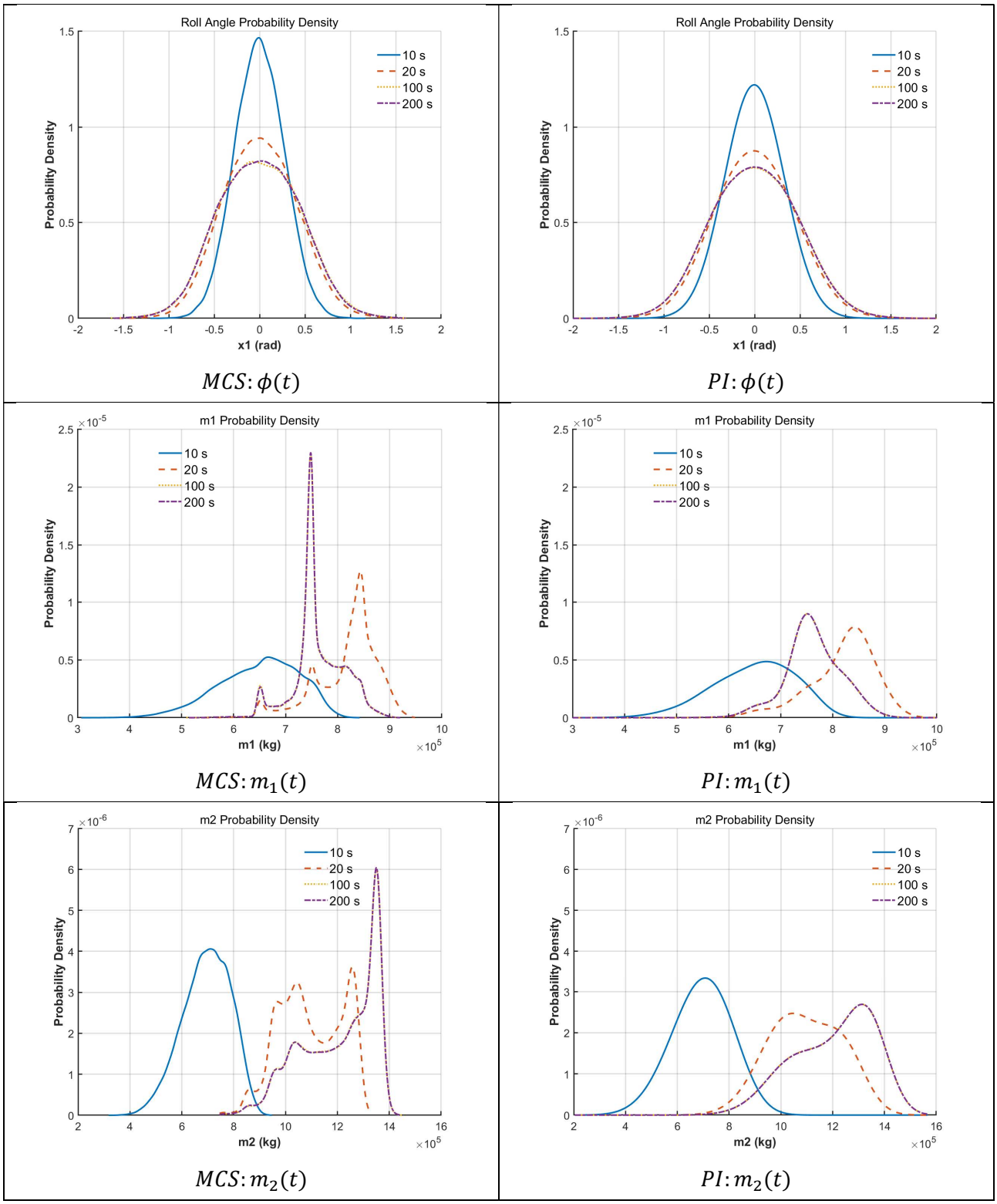

Figure 7: The PDF of roll angle and flooding water mass based on MCS and PI method.

In Figure 6 and Figure 7, the simulation results based on PI method are in good agreement with the calculation results based on MCS, and the PI method produces smoother results at low probability levels. During progressive flooding state ($t < 20s$), the joint PDF of roll angle and roll velocity, as well as the PDF of roll angle and flooding water mass are rapidly evolving. And in steady flooding state ($20s < t < 200s$), the joint PDF and PDF tend to stabilize.

Based on the joint PDF of roll angle and roll velocity, the capsizing probability (mean upcrossing

rate) at time t ($0s < t < 200s$) is calculated based on PI method and MCS, as shown in Figure 8. The critical roll angle is set as 40 degrees.

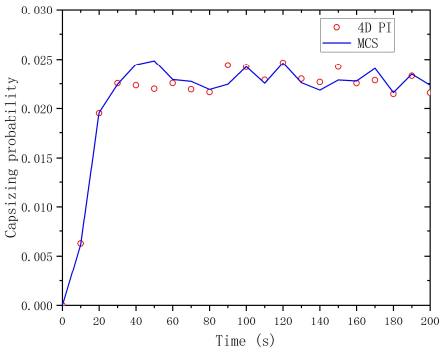

Figure 8: The capsizing probability at different given time based on MCS and PI method.

In Figure 8, the capsizing probability calculated by PI method have a good agreement with the capsizing probability calculated by MCS. The results based on both two methods show that the capsizing probability increases rapidly in progressive flooding state ($t < 20s$) and experiences stable oscillations in steady flooding state ($20s < t < 200s$). It can be qualitatively validated through Zhan's research (Zhan et al., 2024) results that the capsizing probability is less than 0.1 if $H_s \leq 7.0m$ and $T_z = 3.86(H_s)^{1/2}s$ in random beam seas. Quantitative validation based on higher fidelity models or experiments should be studied in the future.

6. CONCLUSIONS

In this paper, a stochastic framework coupling nonlinear roll dynamics with flooding mechanics is established. This stochastic framework is used for simulation of DTMB 5415 damaged vessel during progressive and steady flooding stages. The results show that:

The simulation results based on PI method are in good agreement with the calculation results based on MCS, and the PI method produces smoother results at low probability levels.

In progressive flooding state, roll angle and flooding water mass of damaged vessels have significant changes, and the capsizing probability increases rapidly based on whether MCS or PI method. In steady flooding state, roll angle and flooding water mass tend to stabilize, and the capsizing probability experiences stable oscillations.

In future research, the dynamic impact of flooding water on damaged vessels should be considered in the stochastic model.

ACKNOWLEDGEMENTS

This study is financially supported by "the Fundamental Research Funds for the Central Universities", "the Open Research Fund Project for State Key Laboratory of Maritime Technology and Safety (QZ2022-Y020)".

REFERENCES

Acanfora, M., Cirillo, A., 2017, "A simulation model for ship response in flooding scenario", *Proc. Inst. Mech. Eng*, Part M: J. Eng. Marit. Environ, 231,

Bu, S., Gu, M., Yang, C., Zhang, P., 2023, "Investigation on the capsizing probability of damaged ship in irregular seaway", Proceedings of the 19th International Ship Stability Workshop, (ISSW2023), Istanbul, Turkey, pp. 87-94.

Chai, W., 2016, "Stochastic dynamic analysis and reliability evaluation of the roll motion for ships in random seas", Norwegian University of Science and Technology, PhD Thesis, 2016:224.

Chai, W., Naess, A., Leira, b., 2016, "Stochastic roll response for a vessel with nonlinear damping models and steady heeling angles in random beam seas", *Ocean Eng*, 120, pp. 202–211.

Dostal, L., Kreuzer, E., 2011, "Probabilistic approach to large amplitude ship rolling in random seas", *Proc. Inst. Mech. Eng*, Part. C: J. Mech. Eng. Sci, 225, pp. 2464-2476.

Dostal, L., Kreuzer, E., Sri Namachchivaya, N., 2012, "Non-standard stochastic averaging of large-amplitude ship rolling in random seas", *Proceedings of the Royal Society A: Mathematical, Physical and Engineering Sciences*, 468(2148), pp. 4146-4173.

Duan, J., Ma, N., Shi, Q., Gu, X., Li, X., 2023, "An improved method for dynamic assessment of survivability of damaged ships in waves", Proceedings of the 19th International Ship Stability Workshop, (ISSW2023), Istanbul, Turkey, pp. 77-86.

eSAFE, 2016-2018, "Enhanced stability after a flooding event", A Joint industry project on damage stability for Cruise Ships.

GOALDS, 2009-2012, "GOAL based damage stability", EU-funded FP7 project.

HARDER, 2000-2003, "Harmonization of rules and design rational", EU Funded Research Project, FP5, DG XII-BRITE.

Ikeda, Y., Katayama, T., 2024, "Ikeda Method to Ikeda-

Katayama Method-Bilge-keel component in Ship Roll Damping", Proceedings of the 2nd International Conference on the Stability and Safety of Ships and Ocean Vehicles, (STAB2024), Wuxi, China, pp. 49-57.

IMO, 2020a, "International convention for the safety of life at sea (SOLAS)", Technical Report, IMO, Consolidated edition as of 2020.

IMO, 2020b, "MSC.1/Circ. 1627 - Interim Guidelines on the Second Generation Intact Stability Criteria", International Maritime Organization, London, UK.

Itô, K., 1944, "109. stochastic integral", *Proceedings of the Imperial Academy*, 20(8), pp. 519-524.

Karlsen, H., 2006, "Statistics of wave induced nonlinear loads and responses", Norwegian University of Science and Technology, PhD Thesis, 2006:180.

Kumar, P., Narayanan, S., 2006, "Solution of Fokker–Planck equation by finite element and finite difference methods for nonlinear system", *Sadhana* 31 (4), pp. 455–473.

Kumar, P., Narayanan, S., Gupta, S., 2014, "Finite element solution of Fokkern Planck equation of nonlinear oscillators subjected to colored non-Gaussian noise", *Probabilistic Eng. Mech*, 38, pp. 143–155.

Liu, Y., Liu, L., Maki, A., Lu, J., Dostal L., 2023, "The improvement of stochastic averaging method to solve the ship rolling response excited by narrow-band waves", *Ocean Eng*, 281, 114737.

Maki, A., Maruyama, Y., Sakai, M., Dostal, L., 2023, "Recent results on wind and wave generation, stability of parametric rolling, method of moment equation and maneuvering stability for ship dynamics in irregular seas", Proceedings of the 19th International Ship Stability Workshop, (ISSW2023), Istanbul, Turkey, pp. 133-139.

Manderbacka, T., Ruponen, P., 2016, "The impact of the inflow momentum on the transient roll response of a damaged ship", *Ocean Eng*, 120, pp. 346–352.

Mauro, D., Vassalos, D., Paterson, D., Boulougouris, E., 2023, "Evolution of ship damage stability assessment—Transitioning designers to direct numerical simulations", *Ocean Eng*, 268, 113387.

Naess, A., Moan, T., 2012, "Stochastic dynamics of marine structures", Cambridge University Press.

Rice, S., 1945, "Mathematical analysis of random noise", *The Bell System Technical Journal*, *24*(1), pp. 46-156.

Risken, H., 1989, "Fokker-Planck Equation", Springer.

Zhan, X., Mao, X., Lai, G., Yu, X., 2024, "Model Test and Prediction for Roll Motion and Capsizing Probability of Damaged Ship in Random Waves and Wind", Proceedings of the 2nd International Conference on the Stability and Safety of Ships and Ocean Vehicles, (STAB2024), Wuxi, China, pp. 609-618.

Session 3
Mathematical modeling and dynamics

Assessment and mitigation of motion instabilities of a towed barge: Phase I

Mohammed Islam[1*], Trevor Harris[1], Dong Seo[1], Kent Brett[1], Thomas Hall[1], Kevin L Krasulak[2]

[1]Ocean Coastal and River Engineering Research Centre, National Research Council of Canada, 1 Arctic Avenue, St. John's, NL, A1B3T5

[2]Florida Crystals Corporation, 1 North Clematis Street, Suite 400, Palm Beach, FL 33401, USA

[*]Mohammed.Islam@nrc-cnrc.gc.ca

ABSTRACT

This research investigates the motion (sway and yaw) instabilities and mitigation solutions of a towed barge operating in ocean environments. To complete the investigations, a systematic multi-phased design optimization and procedure based on computational fluid dynamics (CFD) and physical modelling techniques was developed and practiced.

During the first phase, the research team developed CFD models that predicted the full-scale motion instabilities of a towed barge and compared them with the full-scale observations. Physical model tests of the towed barge operations were also conducted to reproduce the field observations. Commercially available and slightly modified or optimized solutions were modelled using CFD and physical modelling techniques to evaluate their performance in mitigating the unsafe motions of the barge during towing operations. The CFD modelling techniques were thoroughly validated using physical model testing measurements, both techniques confirming that the motion minimization achieved by the commercial solution and its variations were unacceptable.

In the second phase of the research, several in-house developed solutions were designed and investigated using the CFD model, and recommendations were provided to confirm performance through a second set of physical model testing in a flume basin. The most promising mitigation strategies were identified based on physical test results, aligning with full-scale CFD predictions. Following these findings, in the third and final phase of the research, the optimal solutions were implemented on the full-scale barge, leading to significant improvements in motion stability, as confirmed by full-scale trials. This study presents a rigorous and integrated approach combining high-fidelity CFD and physical model testing to investigate the hydrodynamics and motion instabilities of a towed barge. The findings yield critical insights that inform practical design strategies to improve towing stability, safety, and operational performance.

This paper summarizes the background, methodologies and procedures developed and utilized for the research and outcomes of the investigations undertaken during the first phase of the research.

Keywords: *Barge Towing, Motion Instabilities, Physical Model Tests, Computational Fluid Dynamics (CFD) Modelling.*

1. INTRODUCTION

Towed barges are essential for transporting goods in inland and coastal waters. Yet, they often experience significant directional and motion instabilities. These arise primarily from their bluff hull forms, shallow drafts, and lack of self-propulsion, making them particularly sensitive to hydrodynamic forces in varying environmental conditions. Instabilities can manifest as excessive yaw, sway, and roll, posing risks to navigation safety and operational efficiency.

Initial studies, such as those conducted by Moss and Townsend (1967), examined the influence of hull geometry on the course stability of towed barges. Barges with finer bows and fuller sterns displayed more stable towing performance, whereas blunt-bow designs were prone to vortex shedding and yaw-inducing unsteady hydrodynamic forces. The addition of passive appendages such as skegs

has been a prevalent strategy to mitigate such instabilities. Investigations into skeg configurations, including work by Im et al. (2015), have demonstrated that deeper and elongated skegs improve course-keeping by enhancing lateral resistance and yaw damping, although this often comes at the expense of increased drag. In computational fluid dynamics (CFD) intensive research, the authors analyzed the skeg-induced characteristics of course stability in different types of barges by scrutinizing the effects of nonlinearity, such as skeg-induced generation of three-dimensional vortices. The research demonstrated that the position and number of skegs contribute to improving course stability by influencing the shape of the vortex generated in the stern section.

Refinements, such as Hydralift skegs introduced by Nautican (2015), and multiple-skeg designs have been proposed to optimize the trade-off between stability and resistance. These configurations have been validated both through empirical towing tank tests and CFD simulations. CFD studies, which have corroborated experimental findings showing that optimized skeg placements significantly alter the pressure distribution and wake structure, thereby enhancing stability.

The impact of the stern shape of towed barges on directional behaviour has also been widely studied. Allan (2022) conducted a comprehensive assessment of stern configurations, revealing that flared and overhanging sterns minimize flow separation and reduce yaw excitations. These observations have been supported by CFD analyses, confirming the role of aft-body design in influencing hydrodynamic behaviour.

Towline configuration plays a pivotal role in overall barge dynamics. Ushakov and Yatsuk (2024) conducted experimental research, demonstrating that V-shaped or dual-point towing arrangements result in better directional control than single-point towing. These results were confirmed by CFD models presented in Fitriadhy et al. (2019), which incorporated barge-tug coupling to analyze the course stability of the towed ship associated with a symmetrical bridle towline configuration with varied towline length and towing velocity. The results revealed that increasing towline length and velocity degrade the course stability of the towed ship.

Environmental forces, including wind, waves, and currents, can further complicate the stability of a towed barge by inducing coupled motions of pitch, roll, and yaw. Physical model tests, as documented by Baso (2021), have revealed that increasing the towline length can buffer dynamic interactions, thereby mitigating certain instabilities. Simulations under irregular wave conditions have shown that environmental inputs have a significant impact on wake dynamics, lateral forces, and resulting motion responses.

Although passive measures currently dominate practice, there is growing interest in integrating active stabilization techniques to enhance the motion stability of towed barges. Concepts involving dynamic foils or control surfaces, although not yet widely adopted for barge applications, have shown promise in preliminary studies. BAR Technologies (2025) has explored assisted foiling solutions that generate hydrodynamic lift to counteract rolling and yawing motions, albeit with challenges in real-world implementation.

The above studies confirm that the synergy of physical and numerical methods has significantly enhanced the understanding of towed barge behaviour. RANS-based CFD solvers have emerged as powerful tools for simulating realistic barge responses under complex environmental loading, especially when validated against experimental data. With the growing sizes of barges and more complex bow and stern shapes and skeg configurations, further advancements in physical and CFD modelling techniques are needed to capture complex transitional flows and appendage-induced vortices accurately.

Initial voyages of a newly constructed, state-of-the-art 450-foot ocean-going dry cargo barge revealed significant motion instability during fully loaded towing, manifesting as large-amplitude sway and yaw as shown in Figure 1. These instabilities diminished markedly when the barge was towed empty. The barge is equipped with twin push skegs intended for directional stability. However, observations indicate that the skegs are hydrodynamically inefficient and less effective than expected. A large notch at the stern and a sharp rise in its profile appear to further disrupt inflow conditions, possibly contributing to the instability.

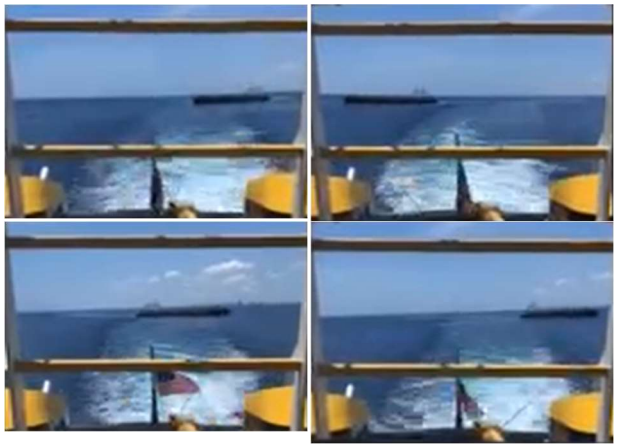

Figure 1: The real full-scale barge showing extreme sway and yaw motions during the field trials after launching.

To address these challenges, an R&D project was initiated at the National Research Council of Canada, adopting a systematic approach based on high-fidelity CFD modelling and physical model tests to assess the motion characteristics and towing resistance of the barge under various load, trim, towline, and skeg configurations. Next, the team developed and assessed different skeg and foil configurations to mitigate the motion instabilities across different barge loading and towing speeds. Finally, the optimized solution was implemented in the real barge, and significantly improved motion stability was recorded during the post-retrofit field trials.

This paper presents the systematic scientific investigations and methodologies developed to conduct the research; however, it only presents the outcomes and insights from the first stage of the research. The following section provides a detailed account of the methodologies employed in conducting the research, followed by an analysis of the outcomes and discussions of the findings from Phase 1 of the research.

2. METHODOLOGY

The flowchart in Figure 2 outlines the structured, three-phase investigation framework, which was designed to address and mitigate motion instabilities of the towed barge through a systematic combination of numerical and physical modelling, evaluation, and implementation. A brief description of the R&D activities at each research phase is provided below.

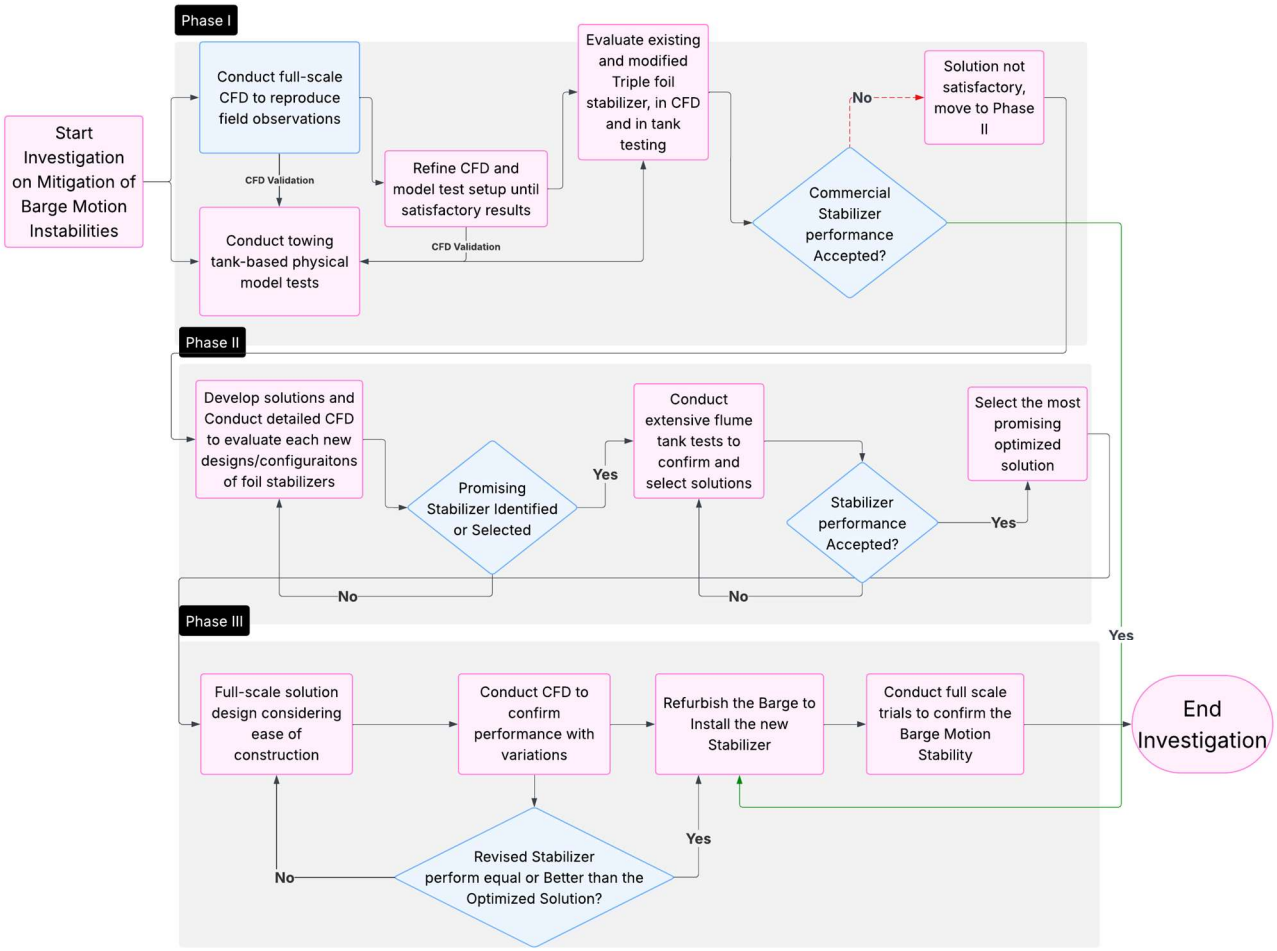

Figure 2: Flowcharts illustrating the workflows at various phases of motion instability mitigation research.

Phase I - Baseline Assessment and Validation: The investigation begins with reproducing the field-observed motion instabilities of the subject barge using full-scale Computational Fluid Dynamics (CFD) simulations. These simulations are validated against real-world data. Parallel to the numerical efforts, towing tank-based physical model tests are conducted to further understand the instability mechanisms and validate the numerical approach.

Once a reliable baseline is established for both CFD and physical models, two commercially available variations of the triple foil stabilizer design are evaluated, first through CFD and then through model testing, to assess their performance in mitigating motion stability issues. According to the flow chart, if the commercial stabilizer demonstrates acceptable performance, the investigation is concluded. If not, the study proceeds to Phase II.

Phase II – In-house Stabilizer Development and Optimization: In this phase, in-house stabilizer designs are developed and analyzed through detailed CFD simulations. The goal is to explore a range of new configurations, primarily based on foil stabilizers, to identify promising candidates for further development.

Based on the CFD predictions, multiple promising stabilizers are identified, and extensive flume tank tests are conducted to verify and refine the solution. Based on the CFD and flume tank assessments, if satisfactory, the most effective stabilizer design is selected for implementation on the full-scale barge. Otherwise, further refinement or new concepts are pursued iteratively.

Phase III - Implementation and Final Validation: The full-scale design of the selected stabilizer is conducted, accounting for construction feasibility. CFD simulations are conducted to assess the performance of the as-designed and design-for-build stabilizer. If the design-for-build stabilizer shows equal or better performance than the optimized solution, it is chosen for final implementation.

Subsequently, the barge is refurbished to incorporate the selected stabilizer, followed by full-scale sea trials to validate its effectiveness in mitigating motion instabilities. Upon successful validation, the investigation concludes.

This flowchart illustrates a robust, evidence-driven approach that integrates CFD modelling, physical testing, and full-scale validation to systematically identify and implement effective solutions for reducing barge motion instabilities. Further details of the process, including data and validation, are provided below, demonstrating that any implemented solution is technically sound, practical, and validated across all relevant conditions.

The remainder of this section provides brief descriptions of the technical aspects of physical and CFD modelling techniques.

Model Test Facilities

Physical model tests were conducted to reproduce motion instabilities and assess and optimize mitigation solutions for the towed barge in two distinct phases, utilizing two separate hydrodynamic testing facilities in St. John's, Newfoundland and Labrador, Canada. Phase I testing was performed in the Clear Water Tank (CWT), a 200-meter-long towing and wave basin operated by the National Research Council (NRC), see Figure 3. This facility, with a width of 12 meters and a maximum still water depth of 7 meters, offers a usable towing length of approximately 120 meters and a maximum carriage speed of 10 m/s. These characteristics make it well-suited for testing configurations involving large sway and yaw motions, as were anticipated for the barge when fitted with its original skegs and towed with a long line.

Figure 3: The Clear Water Tank (CWT) facility at NRC.

Phase II testing was conducted at the flume tank facility housed within the Marine Institute of Memorial University. The flume tank is the largest of its kind globally, measuring 22 meters in length (with an 18-meter usable test section), 8 meters in width, and 4 meters in depth (see Figure 4). The basin is capable of generating continuous flow speeds up to 1 m/s, equivalent to 10.2 knots at full

scale, making it ideal for simulating steady-state hydrodynamic conditions. It is particularly advantageous for tests involving reduced motions, as expected for the barge fitted with the optimized skegs. Additionally, the flume is equipped with underwater viewing windows, which facilitate detailed observation of fluid-structure interaction and skeg behaviour during towing. All tests were conducted in calm water conditions.

Figure 4: The Flume tank facility at MUN-MI

Physical Barge Modelling

The design and fabrication of the barge were developed for physical model testing at a scale ratio of 27.5. This scale was chosen to minimize scaling uncertainty, particularly the effects associated with Reynolds number differences; the barge was designed to be large enough to achieve a Reynolds number exceeding 4.2 million. This decision aimed to ensure that the model's performance could be reliably extrapolated to full scale.

The Construction followed established procedures using CNC-milled foam sections and plywood laminations. Renshape™ was used in areas needing additional strength, particularly near appendages (Murdey, D.C., 1999). The hull surface was glassed, gel-coated, sanded, and faired to final shape. Skegs were made replaceable to allow for different configurations to be tested. The model was painted with yellow Imron™, marked with waterlines and 11 vertical stations, and included incremental draft markings at key locations to help visualize wave run-up during tests. To ensure similarity in flow conditions between the model and the full-scale, turbulence stimulators were installed on the model, following ITTC and NRC practices, which further minimized scale effects and improved the accuracy of the test data. The finished hull met standard tolerances, ±1 mm for dimensions under 2000 mm, ±0.05% for longer dimensions, and less than 2 mm template gaps below the waterline. The completed barge model is shown in Figure 5.

Figure 5: The Barge model showing the stern, notch and original skegs

The towing setup included both a bridle and main tow line, which was selected based on the most common configuration used for the subject full-scale barge towing. The bridle was made from flexible chains, designed to match the chain lengths and pivot locations of the full-scale arrangement, see Figure 6. The tow line was modelled with a light, non-elastic line to avoid hydrodynamic drag. Two tow line lengths were tested, corresponding to 875 feet and 1375 feet in full scale. The original skegs were constructed using the same techniques as the hull. The design allowed for the skegs to be removed and swapped with alternative configurations as needed.

Figure 6: The Barge model showing the bow, tow bridle, and turbulence stimulator.

Skegs Designs and Modelling

In Phase 1 of the research, a commercial supplier developed two multi-foil-based configurations of skegs to replace the original skegs of the barge, addressing the issue of excessive barge motions. The first configuration, (N1), consists of three identical vertical foils on each side of the barge, arranged in a uniform pattern. The second configuration (N2) follows a similar layout but introduces larger foil sizes for the middle and inboard positions, placed in a staggered manner. This staggered layout was

designed to maximize the foil surface area within the spatial constraints at the stern of the barge.

All three skeg configurations, the original, N1, and N2, were modelled at the same scale and tested under controlled conditions, with motion response data collected to assess their relative effectiveness (see Figure 1). A novel 3D printing technique was employed to construct both commercial skegs using a water-resistant material. Minor surface finishing was carried out post-printing to achieve the required hydrodynamic smoothness of the foil surfaces.

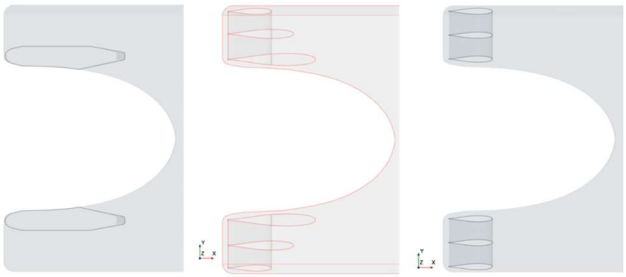

Figure 1: A CAD of the Barge stern showing the original, N2 and N1 skegs.

During Phase 2 work, in addition to the N1 and N2 skegs, multiple foiled skegs were designed and assessed using CFD, and selected designs were manufactured and tested in the flume basin. Each skeg configuration was modelled in Computer-Aided Design (CAD) and then constructed using the same techniques as the commercial Skegs. The construction process ensured that the skegs could be removed and replaced with other skegs.

Measurement Instrumentation

Instrumentation used in both phases of the physical experiments was carefully selected and rigorously validated to ensure accurate and repeatable measurements. Before testing commenced, all sensors were calibrated using the data acquisition systems available in the respective facilities. Data were recorded at a sampling rate of 50 Hz, and a 10 Hz low-pass filter was applied to all signals to remove high-frequency noise and ensure clarity in the acquired data.

A consistent set of instrumentation was employed across both phases. Model speed was measured using a carriage-mounted tachometer (towing tank) or using a flow meter (flume tank). The tow force was captured using strain-gauge type load cells installed between the towing post and the model. The angle of the tow line, a key parameter in assessing lateral forces and yaw tendencies, was measured using a rotational potentiometer. The barge's six-degree-of-freedom (6-DOF) motions were captured using the Qualisys™ optical tracking system, which provided precise positional data for X, Y, and Z translations, as well as roll, pitch, and yaw angles. The Qualisys™ system operates with four infrared cameras that track the movement of up to eight reflective marker targets mounted on the model. The positions of the markers are triangulated to resolve the model's full motion state, with translations and yaw referenced to tank coordinates and roll and pitch referenced to the model's body coordinates. To ensure measurement fidelity, all passive markers were placed farthest apart from each other and the primary marker as close as possible to the barge's center of gravity.

Video recordings were collected to support the quantitative data. Only above-water videos were captured during the towing tests, whereas both above and underwater recordings were collected during the flume tank tests. Additionally, handheld digital cameras were used to collect still images of relevant test configurations and activities. The majority of the flume tank footage focused on the overhead view to maintain consistency with Phase I recordings and facilitate visual comparison of motion responses.

The same instrumentation suite, calibration protocols, and data processing procedures were applied during both testing phases. This continuity ensured that data from both facilities could be compared reliably, supporting consistent analysis of the barge's dynamic behaviour across different skeg configurations and hydrodynamic conditions. The experimental setup was thus robust, allowing for high-quality motion characterization essential for evaluating motion stability and skeg performance during the towing operations.

Model Testing Procedure

The model testing setup and subsequent data analysis followed the NRC's standard right-hand coordinate system, with the origin at the barge's center of gravity, aligned along the hull's centerline and baseline. Positive X, Y, and Z directions corresponded to forward, starboard, and downward, respectively. Rotations followed the same convention: pitch (bow up), roll (starboard down), and yaw (bow to starboard). Motions were described in the body-fixed frame as surge, sway, and heave. All procedures adhered to ITTC guidelines unless

otherwise noted. The method for carrying out the towing stability experiments was based on that described by Burcher and Zhang (1995).

The test matrix utilized for the towing tank and flume tank facilities included three loading conditions, corresponding to full-scale drafts of 24 ft (3 ft stern trim and level trim), 13.9 ft (3 ft stern trim), and 5 ft (level trim), two towline configurations, three towing speeds and multiple skeg arrangements for both testing phases see Table 1 and Table 2, respectively. For both cases, the barge model was ballasted to target draft and verified using trim hooks with an accuracy of ±1 mm. While exact mass properties are critical for seakeeping tests, they were not essential in this case. However, approximate values for pitch and roll inertias were used (the target radii of gyration for roll being ~0.45B and pitch being ~0.25L), and these were validated through CAD modelling and static tests (inclining experiments).

Table 1: The Phase 1 Towing Tank Test Matrix

Skeg Config.	Barge Loading	Barge Trim	Towline Length	Towing Speed (Knots)
Original	Full, Light	3' Stern, Level	1375', 875'	7,8,9
N1	Full	3' Stern	1375'	7,8,9
N2	Full	3' Stern	1375'	7,8,9

Table 2: The Phase 2 Flume Tank Test Matrix

Skeg Config.	Barge Loading	Barge Trim	Towline Length	Towing Speed (Knots)
N1	Full, Light	3' Stern, Level	1375', 875'	7,8,9
N2	Full	3' Stern	1375'	7,8,9
Foil Skegs (SF10)	Full	3' Stern, Level	1375'	7,8,9
Original + F10	Full, Light	3' Stern, Level	1375'	7,8,9
Original + F15	Full, Light, Empty	3' & 1' Stern, Level	1375'	7,8,9
Original + F20	Full, Light, Empty	3' & 1' Stern, Level	1375'	7,8,9

In towing tank tests, directional stability was assessed by offsetting the model transversely (up to two beam widths) and sometimes with initial yaw. The model was towed at constant speed after a gradual acceleration and decelerated near the tank end. Time histories were recorded for motion and force responses.

In the flume tank, a similar procedure was followed, with the model released from a transverse offset and subjected to a steady current. The tow line remained fixed to simulate ocean towing. Each test ran for 30 to 45 minutes (model scale), and video was recorded for both above-water and underwater views. Test procedures across both phases ensured consistent, reliable data under controlled conditions.

Data Analysis and Reduction

During both phases of testing, real-time data monitoring ensured that all instruments responded correctly and that signals were free from anomalies. Time histories of all sensor channels were reviewed, and key segments were selected for analysis based on steady-state conditions. Basic statistics, e.g. mean, maximum, minimum, and standard deviation, were calculated for all signals of interest.

Model-scale data were converted to full-scale using standard Froude scaling laws, with relevant scaling factors applied to quantities such as length, force, acceleration, and speed. Motion measurements were translated to the model's center of gravity using rigid body motion (RBM) theory. Each test run was divided into segments, with an initial "tare" segment recorded before motion began. This baseline was used to correct for any sensor offsets by subtracting the mean of the tare segment from the main data.

Towing force and motion statistics were compiled from the steady-speed segment of each test. While the towing basin's length limited the number of oscillation cycles observed, comparative assessments of sway and yaw motions across configurations were conducted. Zero-crossing analysis (ZCA) methods were applied to estimate motion period and amplitude, and trends in decay or growth were evaluated by fitting slopes to peak amplitudes. However, classical damping analysis was not possible due to the insufficient number of cycles in the recorded motion signals collected during the tow tank tests (only 1 to 2 cycles of motion were recorded due to the limited basin length). The flume tank data were analyzed for oscillation period, amplitude, and damping characteristics using standard ZCA methods.

CFD Modelling and Analysis

A comprehensive full-scale CFD study was undertaken across Phase I and Phase II to simulate and reproduce the field observations of the barge motions and then analyze the dynamic behaviour of the full-scale barge under various operating and skeg configurations. Both phases employed the commercial RANS-based CFD software SIEMENS STAR-CCM+ (version 2206), a tool extensively

validated and used at NRC for marine resistance, propulsion, and maneuvering simulations. This software solves the Reynolds-Averaged Navier-Stokes (RANS) equations using a finite volume method. The general simulation procedures followed the International Towing Tank Conference (ITTC) guidelines. However, numerical setups not prescribed by ITTC, such as mesh density and time-stepping strategies, were based on NRC's in-house best practices.

The following numerical models and schemes were selected for their proven robustness and computational efficiency:

Turbulence Model: Shear Stress Transport (SST) k-ω, selected for its accuracy in capturing flow separation and adverse pressure gradients.

Free Surface Modelling: Volume of Fluid (VOF) method with a modified High-Resolution Interface Capturing (HRIC) scheme, utilizing a Courant number tuning approach to preserve interface sharpness.

Body Motion: The Dynamic Fluid-Body Interaction (DFBI) module was used to simulate barge motions with three degrees of freedom (surge, sway, and yaw).

Boundary Damping Control: Far-field boundaries included wave-damping/forcing zones of at least one ship length to mitigate wave reflection artifacts.

Time-Stepping: For steady simulations, the ITTC-recommended time-step size of 0.005 × L/U was adopted; smaller steps were used for dynamic cases.

Water properties were based on ITTC 2011 recommendations, assuming seawater at 15°c.

The barge geometry was prepared in SolidWorks™ and converted to a STEP file. Surface corrections (e.g., sealing small gaps, resolving overlapped surfaces) were performed to ensure grid compatibility. In addition to the barge model, the towing system, including the bridle and main towing line, was also modelled. The towing arrangement included:

Towline: The elastic coefficient and damping coefficient for the main line were selected to be 2.0 × 10^7 N/m and 1.0 × 10^4 N · s/m for all simulations.

Bridle Lines: The ropes in the bridle arrangement have mechanical properties of 1.0e7 N/m and 0.5e4 N · s/m, corresponding to elastic and damping coefficients.

Mass Effects: The own weight of the tow cable was excluded, simulating a dry, high-tension setup, more conservative compared to field conditions where hydrodynamic damping by submerged cables may reduce motion amplitudes.

Simplified Towing: A simplified single-line towing configuration was also tested and showed negligible difference in barge motion compared to the dual-bridle case.

The computational domain dimensions adhered to ITTC (1999, 2008, 2011) guidelines, with extended boundaries and damping zones to minimize reflection effects. The domain utilized a ship-fixed coordinate system (OXYZ), with the origin located at the intersection of the fore perpendicular, still waterline, and centerline plane. The OX axis pointed forward, OY to port, and OZ upward.

The barge was free to move in surge, sway, and yaw during dynamic simulations via the DFBI module. The inlet, outlet, and side boundaries were positioned at 1.8, 2.6, and 2.2 times the barge length (L_pp), respectively. The vertical domain limits extended 1.5 L_pp below and 0.7 L_pp above the free surface. Temporal and spatial terms were discretized using first- and second-order schemes, respectively, with a typical time step of 0.2 s.

Mesh generation was performed using STAR-CCM+'s trimmed cell mesher with hexahedral core elements. Gradual refinement transitions were achieved using slow growth settings, as shown in Figure 2. The maximum far-field cell size was 5 m, while finer grids were used near the barge and in regions of high gradients, particularly around the bow, stern, and skegs (Figures 8–14). Around the vessel, grid aspect ratios were controlled to 4:1.

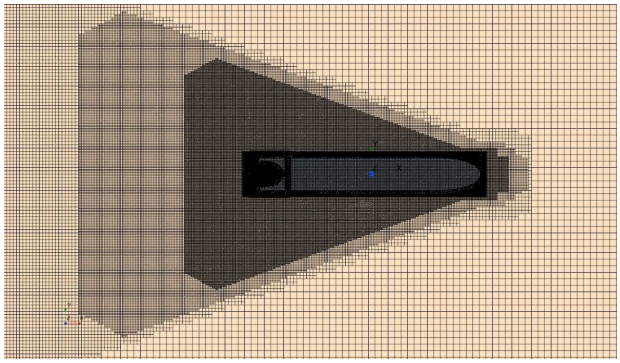

Figure 2: Grid refinement steps around free surface area for the dynamic towing simulation, mean water plane view.

To resolve boundary layers, 15 prismatic layers were applied to the hull with a growth ratio of 1.2. The first layer thickness was selected to maintain average y^+ values near 150, balancing resolution with computational cost. Surface and volume meshes were customized for each skeg configuration, original, N1, N2, SF10, F10-F20, with local refinements focused on the stern notch and skeg flow interaction zones.

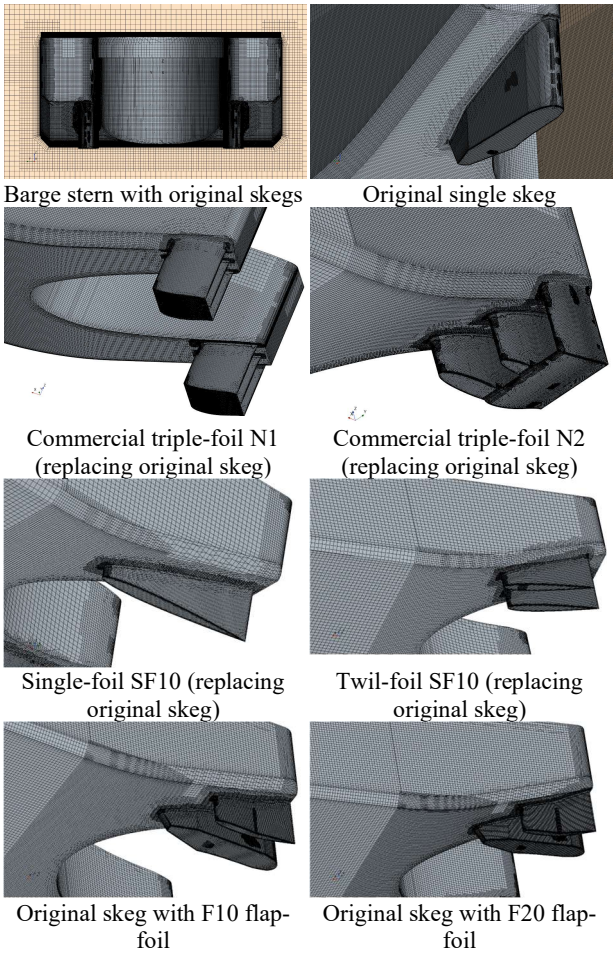

Figure 3: Close-up view of the Extra grid refinement around different stern skegs.

This mesh strategy ensured accurate resolution of flow separation, vortex shedding, and interface capturing, enabling high-fidelity simulation of barge dynamics under towing conditions.

CFD Mesh Convergence Study

A mesh convergence study was conducted to evaluate the numerical sensitivity of CFD predictions to grid resolution and to establish an optimal meshing strategy for the remaining simulations. The barge configuration with the original skeg was selected as the reference case, as only minor local modifications were introduced in the alternative skeg designs. Therefore, similar convergence behaviour was assumed for all configurations.

The study followed the ITTC (2011) recommended procedure for estimating numerical uncertainty. A total of five meshes were generated using a constant refinement ratio of $\sqrt{2}$ (i.e., 1.414), with base cell sizes ranging from 0.5 m to 2.0 m. A slow growth rate was applied to minimize abrupt transitions between refinement zones and reduce interpolation errors. The y^+ values were maintained around 199 across all meshes to ensure consistent treatment of the near-wall region.

The test case simulated a fully loaded barge with a 3′ trim by the stern, towed at 8 knots using a 1,375 ′ towline. Although this setup differed slightly from the model basin and field trial conditions, the mesh dependency results were not significantly affected.

Time-domain signals for sway and yaw motions were extracted from each simulation, and Fast Fourier Transform (FFT) analyses were performed to determine the maximum amplitudes and dominant oscillation periods. A comparison of motion responses across all grids (Figure 4) indicated that the Grid-C mesh (base cell size of 1.0 m) produced stable and converged results. Further grid refinement yielded only marginal differences in predicted responses. This final setup generated approximately 10–11 million cells per case while maintaining target y^+ values.

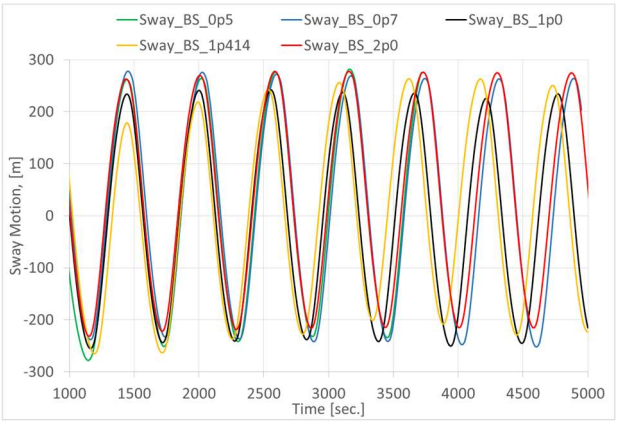

Figure 4: Comparison of predicted sway motions for all grids used in the mesh sensitivity study.

For the remaining simulations, the same barge, towline and meshing parameters were used across all cases. All simulations were performed at full scale, with durations ranging from 2000 to 5000 seconds. Due to the high computational cost, typically 5–10 days per simulation, depending on processor allocation, consideration was given to running

model-scale simulations in a smaller domain. However, to avoid potential scaling-related inaccuracies, full-scale simulations were retained throughout the study.

3. RESULTS AND DISCUSSIONS

Reproducibility of Full-Scale Observations

This section compares full-scale extrapolated basin measurements of the 1:27.5 scale barge model with the full-scale CFD predictions for barge configurations using its original skegs. Despite differences in towline lengths and limited measurement data for certain conditions, the CFD results generally align well with measured sway and yaw motions, validating its capability to capture key dynamic behaviours. In these conditions, flow visualization from CFD revealed large-scale separation zones along the original skeg surface and tip, which were consistent with unstable force trends observed in the experimental data (see Figure 9).

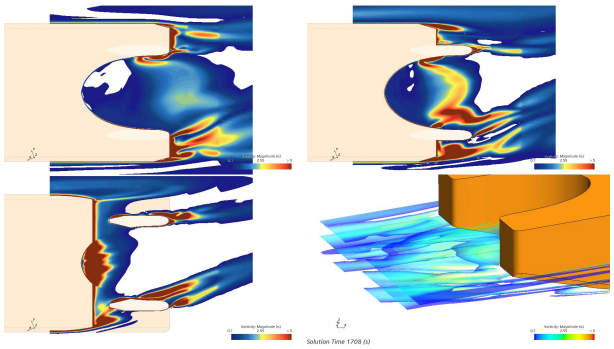

Figure 5: The predicted velocity distribution around the skegs at different horizontal sections for the barge with original skegs with 3' trim towed at 9 knots.

Both model-scale measurements and CFD predictions revealed significant sway and yaw motions, generally consistent with full-scale field observations. In several cases, the model barge contacted the basin walls due to the extent of motion, suggesting that even greater amplitudes could occur in an unrestricted environment (see Figure 8). However, the limited basin length constrained the number of oscillation cycles captured, preventing standard damping analyses. Typically, only one to two oscillations were observed before tests were terminated, see Figure 6 and Figure 7.

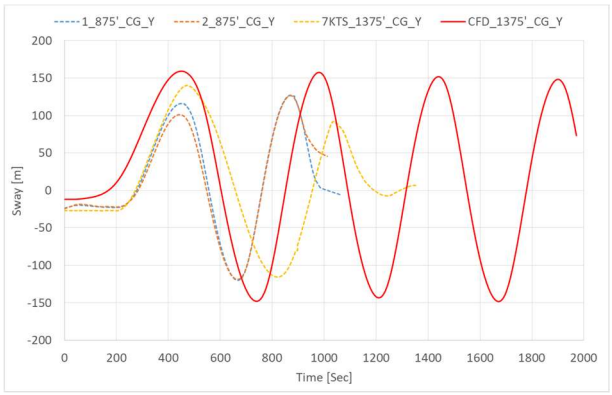

Figure 6: Comparison of sway motions of the barge between the measurements (875' tow line) and the predictions (1375' tow line): fully loaded barge, 3' trim, 9 knots towing speed.

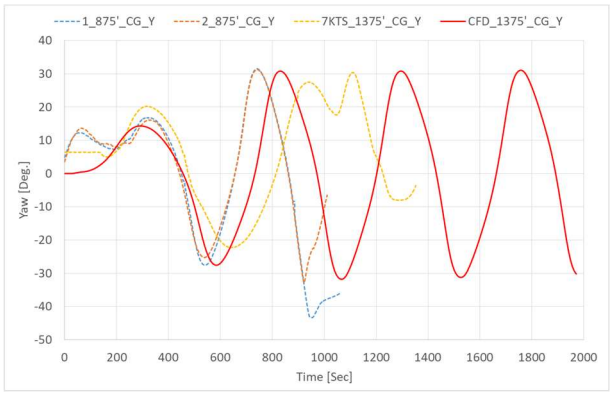

Figure 7: Comparison of yaw motions of the barge with original skegs between the measurements (875' tow line) and the predictions (1375' towing line): fully loaded barge, 3' trim, 9 knots towing speed.

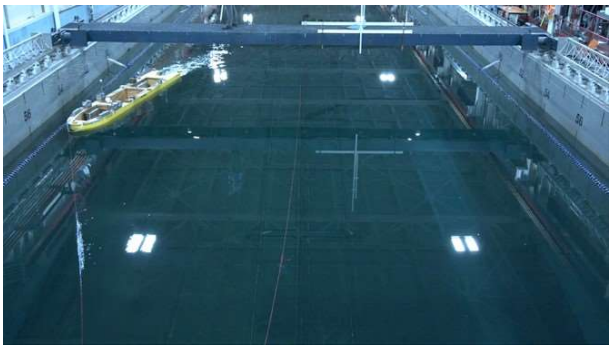

Figure 8: Video image (upper view) showing the movements of the barge fitted with the original skegs when towed at 7 knots (1375' tow line).

This comparison study also sheds some light on the effects of towing speed, towline length, and barge trim on motion characteristics. While a clear trend in motion behaviour with increasing speed was not discernible, higher speeds did result in increased towing forces. Comparisons between trim conditions suggested slightly larger motions in the level trim configuration. An increase in towline length appeared to amplify the sway and yaw motions,

although these trends were based on limited data and require further validation.

CFD Validations and Predictions of Commercial Skeg Solutions

Both CFD and physical tests revealed a more linear and symmetric hydrodynamic response, indicating enhanced damping and control of the towed barge's motions when fitted with both N1 and N2 skegs. CFD predictions were validated by the physical test data with a high degree of confidence, particularly in capturing the relative trends in yaw and sway motions between skeg configurations, see Figure 9, and Figure 10. The overall agreement supported the use of CFD as a reliable tool for assessing skeg performance and informing design optimization.

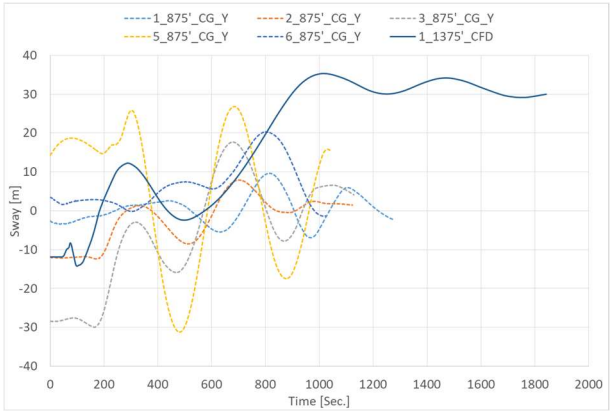

Figure 9: Comparison of sway motions of the barge with N1 skegs between the measurements (875' tow line) and the predictions (1375' tow line): fully loaded barge, 3' trim, 9 knots towing speed.

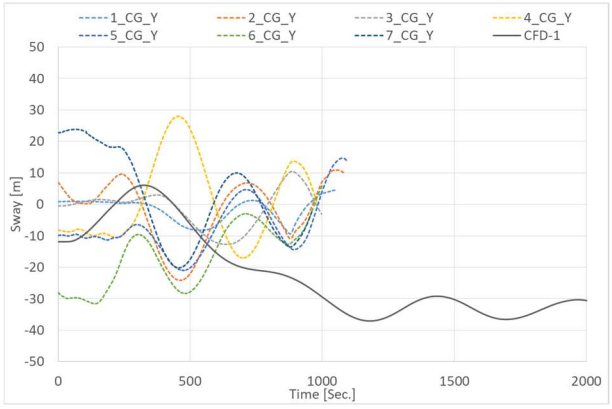

Figure 10: Comparison of sway motions of the barge with N2 skegs between the measurements (1375' tow line) and the predictions (1375' towing line): fully loaded barge, 3' trim, 9 knots towing speed.

Both designs were originally intended to mitigate motion instability and reduce sway motions to ±0.5B, especially under a 3' trim by stern condition. The systematic evaluation of the barge fitted with both N1 and N2 skeg configurations through model-scale towing tests revealed that, while significant motion reductions were achieved compared to the barge fitted with the original skegs, neither design provided a consistent or desired level of reduction in barge yaw and sway motions under the full range of tested conditions (see Figure 15).

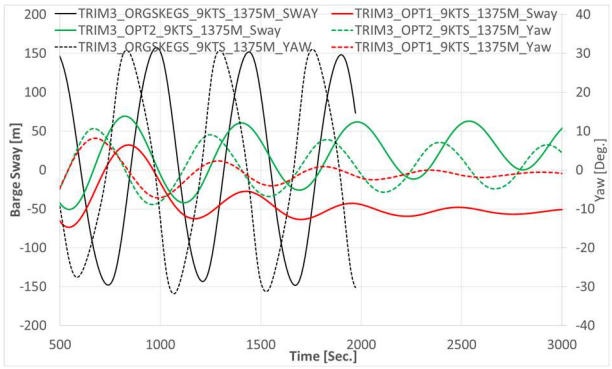

Figure 11: N1 versus N2 performance compared to the original skegs in mitigating sway and yaw motions of the barge at 9 knots, 3' trim.

Despite minor differences, the barge motion characteristics with N1 largely mirrored those seen in the N2 tests: limited reduction in oscillation amplitudes, a high dependency on initial conditions, and inconsistent trends across trim and towing speeds. Moreover, due to the limited physical space in the towing basin, many tests had to be terminated before the natural damping response of the system could be fully observed. This constraint made it challenging to extract definitive insights about long-term dynamic stability or to estimate reliable damping coefficients for the barge from the towing tank tests.

While both N1 and N2 designs showed some promise under very specific conditions, typically at 3' trim with longer tow lines, the overall performance across the required operational envelope fell short of expectations. Notably, some of the largest motion amplitudes and least favourable decay behaviours were recorded at level trim, which raises concerns about the robustness of these skeg geometries to varying draft conditions.

CFD-predicted flow fields also confirmed persistent flow attachment over both N1 and N2 skeg surfaces, minimal tip vortex shedding, and higher-pressure recovery along the span, substantiating the better performance of N1 and N2 designs compared

to the bridge fitted with the original skegs (see Figure 12 and Figure 13). However, in some CFD predictions, there was evidence of consistent oscillatory motions and, in some cases, growing oscillations in either sway or yaw, suggesting potential design-induced resonance or insufficient damping.

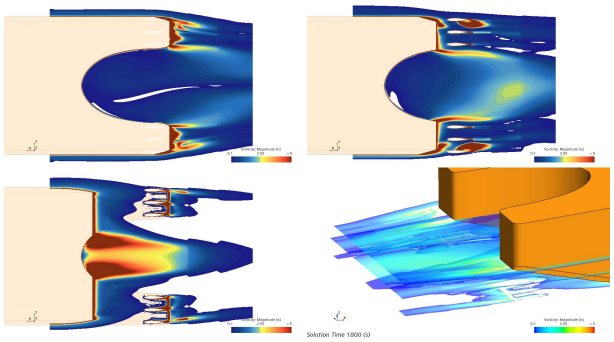

Figure 12: The predicted velocity distribution around the skegs at different horizontal sections for the barge with N1 skegs with 3' Trim during Towing at 9 knots.

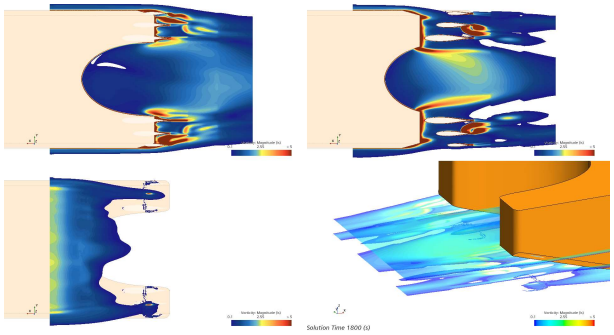

Figure 13: The predicted velocity distribution around the skegs at different horizontal sections for the barge with N2 skegs with level trim during towing at 9 knots.

Motivations for Phase II Research

The Phase 1 model testing, conducted in NRC's large towing tank, provided valuable insights into the yaw and sway response of the subject barge with the original, N1 and N2 skeg configurations. However, due to the limited length of the facility and the long-period oscillations of the barge, the tests did not allow for capturing sufficiently long time series to assess the damping behaviour of these motions. To resolve this limitation, further physical model testing was recommended in a flume basin, where the flow can be maintained indefinitely, allowing extended observations of motion decay under consistent inflow conditions across a matrix of loading states, trims, and towing speeds.

In parallel, CFD-based investigations required extending to refine the skeg geometries and explore alternative skeg/foil arrangements. The exploration could include rotating the skegs outboard by 5–15 degrees to redirect flow more effectively and enhance directional stability, coupled with partial or complete filling of the stern notch to promote smoother inflow to the aft body and skegs. CFD offers an excellent means to screen these variants, evaluate their practicality and verify promising candidates through flume testing.

4. CONCLUSION

The combined application of CFD simulations and physical model testing provided a robust foundation for evaluating and mitigating the motion instabilities of the full-scale towed barge under various operating conditions and skeg configurations. Based on the outcomes of Phase 1 of the research, the following remarks can be made:

- The towing tank testing program successfully captured the barge's dynamic response to lateral instabilities, particularly sway and yaw motions, allowing for direct comparisons among design iterations, including the original, optimized, and practical skeg solutions.
- The full-scale CFD predictions closely matched model-scale measurements extrapolated to full scale, confirming its effectiveness in capturing the key dynamic behaviours of towed barge motions, including sway and yaw responses and flow separation characteristics.
- Although both commercially designed triple foil skegs, N1 and N2, showed improved performance over the original design, neither achieved consistent motion reduction across all tested conditions. Significant sway and yaw persisted, particularly at level trim, highlighting the need for further design refinement.
- The limited length of the towing tank restricted the observation of full damping cycles, making it difficult to evaluate long-term motion stability and accurately estimate damping characteristics.
- Phase 2 of the research was motivated by the need for flume tank testing and refined CFD studies to optimize skeg geometry, test alternate arrangements and enhance motion control under a broader range of operational conditions.

REFERENCES

Dunwoody A.B., 1989, "Roll of a Ship in Astern Seas – Response to GM Fluctuations", *Journal of Ship Research*

33(4), pp. 284-290.

IMO 2006, "MSC.1/Circ.1200 - Interim Guidelines for Alternative Assessment of the Weather Criterion", 24 May.

Kawahara, Y., Maekawa, K., Ikeda, Y., 2009, "A Simple Prediction Formula of Roll Damping of Conventional Cargo Ships on the Basis of Ikeda's Method and Its Limitation", Proceedings of the 10th International Conference on Stability of Ships and Ocean Vehicles, (STAB2009), St. Petersburg, Russia, pp. 387-398.

Moss, J. L.; Townsend, Corning III, 1967, Design Considerations and the Resistance of Large, Towed, Seagoing Barges, Technical Report, Naval Architecture and Marine EngineeringUniversity of Michigan, https://deepblue.lib.umich.edu/handle/2027.42/96608

Im, N.K., Lee, S.M., Lee C.K., 2015, The influence of skegs on course stability of a barge with a different configuration, Ocean Engineering, Volume 97, 2015, Pages 165-174, ISSN 0029-8018, https://doi.org/10.1016/j.oceaneng.2015.01.017.

Nautican. (2015). Hydralift Skegs. https://nautican.com/wp-content/uploads/2015/06/Nautican-product-sheet-hydralift-skegs.pdf

Murdey, D.C., (1999), "Construction of Models of Ships, Offshore Structures and Propellers (42-8595-S/GM-1)", Ocean, Coastal and River Engineering Standard Test Methods, Version 9, 19 pages.

Butt, S., (2004), "Model Test Co-ordinate System & Units of Measure GM-5", Ocean, Coastal and River Engineering Standard Test Methods, Version 6, 7 pages.

Islam, M.F., and Seo, D.C., 2022. "CFD Modelling to Investigate the Motion Instabilities and Mitigation Measures of a Towed Barge ," NRC/OCRE-RC Technical Report NRC-OCRE-2022-TR-058, NRC/OCRE-RC, St. John's, NL, Canada.

Islam, M.F., Harris, T., 2023. "Physical Modelling to Investigate the Motion Instabilities and Mitigation Measures of a Towed Barge," NRC/OCRE-RC Technical Report NRC-OCRE-2022-TR-057, NRC/OCRE-RC, St. John's, NL, Canada.

Islam, M.F., Harris, T., 2023b. "Developing and Evaluating Techniques for Mitigating Motion Instabilities of a Towed Barge using CFD Modelling and Flume Tank Testing," NRC/OCRE-RC Technical Report NRC-OCRE-2023-TR-022, NRC/OCRE-RC, St. John's, NL, Canada.

R. K. Burcher and H. Zhang, 'Determination of Maneuverability Characteristics by Tow-line Tests', RINA, Spring Meetings, London, England, 1995.

Murdey, D.C., (2004A), "Resistance in Open Water (42-8595-S/TM-1)", Ocean, Coastal and River Engineering Standard Test Methods, Version 6, 24 pages.

Fitriadhy, A., Aldin, N. A., Aqilah Mansor, N., A., (2019). CFD Analysis on Course Stability of a Towed Ship Incorporated with Symmetrical Bridle Towline, CFD Letters 11, Issue 12 (2019) 88-98, https://www.akademiabaru.com/doc/CFDLV11_N12_P88_98.pdf

Allan, R. (2022). The Effects of Various Stern Configurations on the Directional Stability of Towed Barges. Technical report for Transportation Development Centre, Transport Canada, https://ral.ca/technical_paper/the-effects-of-various-stern-configurations-on-the-directional-stability-of-towed-barges

Ushakov, K. M., Yatsuk, Yu.V. , 2024, Experimental study on the course stability of a towed barge model, Herald of the Admiral S.O. Makarov State University of Sea and River Fleet, volume 15, issue 6, pages 1066-1075, 10.21821/2309-5180-2023-15-6-1066-1075

Baso, Suandar & Fitriadhy, Ahmad & Anggriani, Andi & Ardianti, Andi & Rosmani, & Arifuddin, Andi. (2021). Investigating the motions' characteristics of a towed barge in extreme heading wave. IOP Conference Series: Earth and Environmental Science. 799. 012002. 10.1088/1755-1315/799/1/012002.

BAR Technologies. (2022). Assisted Foiling for Stability. https://www.bartechnologies.uk/leisure-boats/assisted-foiling/.

Eliciting the bifurcation structure of cumulative broaching

Vicky D. Margari, *National Technical University of Athens*, vickymargari@mail.ntua.gr
Kostas J. Spyrou, *National Technical University of Athens,* k.spyrou@central.ntua.gr

ABSTRACT

The phenomenon of cumulative broaching is studied by applying numerical continuation techniques to the dynamical system describing the horizontal-plane motions of a ferry in regular stern quartering waves. The branch of subharmonic yaw motions, generated via a period doubling bifurcation, is traced as the nominal Froude number is gradually raised. On this branch, rapid increase of yaw amplitude leads to a limit-point-of-cycles (branch folding backwards) wherefrom a jump is inevitable. The paper discusses the potential outcomes of the jump and the conditions under which it may lead to broaching. The branch continues with unstable states and eventually merges with the branch of ordinary yaw motions, which had persisted after the period-doubling bifurcation but had since become unstable. This merger is basically another period doubling (realized however in reverse order), which generates stable ordinary yaw motions in the nonlinear surging regime. Further bifurcation phenomena are observed on this branch. Continuation analysis with two control parameters provides the system's stability boundaries in parameters' space. The robustness of the phenomena is evaluated regarding the intensity of excitation and the control method, while inspiring interactions with surf-riding are also discussed.

Keywords: *Ship motions, Stability, Cumulative broaching, bifurcations*

1. INTRODUCTION

Cumulative (or direct) broaching can be identified as the horizontal plane instability which is not triggered by surf-riding. Although the scientific literature relating to it is scarce and mostly of empirical nature, the possibility of a ship exhibiting this type of instability has been long recognized (see for example Renilson, 1981). It is believed to occur at speeds that are not necessarily very high, however its occurrence seems to require steeper waves, compared to the classical broaching through surf-riding. Additionally, its dependence on the rudder's control method has been investigated (Margari & Spyrou, 2022).

Earlier results have indicated that cumulative broaching is a result of parametric instability in yaw, which causes rapid increase of the exhibited yaw motion amplitude, due to a *period doubling* (*flip) bifurcation* (Spyrou, 1996). Moreover, based on a limited number of simulations, the ensuing rapid turn of broaching has been attributed to a fold bifurcation, triggering a jump to a distant attractor, from a limit-point-of-cycles. The sudden and non-continuous nature of this jump phenomenon matches the dynamic behavior associated with broaching (Spyrou, 1996; Tigkas & Spyrou, 2012).

Despite these insights, several uncertainties about the mechanism of cumulative broaching remain unresolved and warrant further investigation. Even more so, as this phenomenon is likely to gain prominence in the era of highly autonomous vessels. These remarks motivated the present study, whose main objective is to elucidate the full bifurcation structure of cumulative broaching in regular waves, relying mainly on the numerical continuation technique and on selected simulations. As the focus is on the fundamental dynamics, a standard 3DoF mathematical model describing horizontal ship motions is adopted, taking into account Froude-Krylov and diffraction excitations, while the rudder's movement is modeled by a simple PD control.

Numerical continuation is an advanced and efficient numerical tool used in the study of nonlinear dynamical systems. Through application of a correction-prediction scheme, this method calculates branches of steady states, both stable and unstable, in an automated manner, showing their evolution as a control parameter varies. Additionally, the loci and type of bifurcation that

cause the system's changes are also identified using test functions, rendering this method perfectly suited for the task at hand. Bifurcation loci, i.e. evolution of bifurcations as two parameters vary, can also be traced. These are extremely useful, since they define regions of different stability on a parameters' plane. A thorough presentation of continuation can be found in Seydel (2010) and in Dhooge et al. (2003). In the latter, the continuation software MatCont, which was employed in this study, is presented.

2. MATHEMATICAL MODEL

A nonlinear 3DoF model of horizontal ship motions is considered in this study, written for an axes system placed amidships:

$$m(\dot{u} - rv - x_G r^2) = X_H + X_P + X_R + X_W \quad (1)$$

$$m(\dot{v} + ru + x_G \dot{r}) = Y_H + Y_R + Y_W \quad (2)$$

$$I_z \dot{r} + m x_G (\dot{v} + ru) = N_H + N_R + N_W \quad (3)$$

The standard notations are used for the system's variables (u and v being the surge and sway velocity, r the yaw rate and $U = \sqrt{u^2 + v^2}$ is the ship's speed on xy-plane) and the ship's characteristics (m is the ship's mass, I_z its yaw moment of inertia and x_G is the longitudinal distance of ship's centre of gravity from the moving axes' origin, O). The forces presented on the right-hand side of the equations are based on a modular MMG-type model and they include: the hydrodynamic hull reaction (*H*) and rudder (*R*) forces, that are expressed as in (Mikelis, 1985); the propeller (*P*) forces, given by a simple polynomial form (see Spyrou, 2006); and the wave (*W*) excitation forces. The wave forces are expressed as functions of the ship's longitudinal position x on the wave, measured from a trough. They include both Froude-Krylov and diffraction excitations according to Hamamoto, (1991) and Salvesen et. al. (1970), Lewandowski (2004) respectively. The rudder angle δ is assumed to follow a simple control law with no consideration of delay effects (Lewis, 1989):

$$\delta = -k_1(\psi - \psi_r) - k_2 r \quad (4)$$

where, k_1 and k_2 are the proportional and differential gain of the rudder respectively and ψ_r is the desired heading.

For applying numerical continuation, it is needed to transform the system of motion equations into a state-space representation complying with certain conditions. Initially, the system is brought into the form:

$$\dot{\mathbf{z}} = \mathbf{f}(\mathbf{z}; \mathbf{a}) \quad (5)$$

where $\mathbf{z}$ is the vector of the state variables $\mathbf{z} = (u, v, r, x, \psi)$; and $\mathbf{a} = (k_1, k_2, Fn, \frac{\lambda}{L}, \frac{H}{\lambda}, \psi_r)$ is the vector of system's parameters (Fn is the nominal Froude number, λ and H are respectively the wave length and wave height). However, as state variables needed to be bounded when oscillatory phenomena are studied with continuation, and also time should not appear explicitly, the x variable appearing in the wave forces models as $\sin kx$ and $\cos kx$ needed to be replaced by the state variables a and b respectively, satisfying the following equations (see Doedel et. al, 1997; Tigkas & Spyrou, 2012):

$$\dot{a} = a + k\dot{x}b - a(a^2 + b^2) \quad (6)$$

$$\dot{b} = b - k\dot{x}a - a(a^2 + b^2) \quad (7)$$

A thorough and complete presentation of the used system and the assumptions involved can be found in (Margari & Spyrou, 2024; 2025).

3. RESULTS AND DISCUSSION

A passenger ship (L=172 m, B=25 m, T=6.2 m and C_B =0.585), whose geometry is presented in Margari & Spyrou (2025), has been used as a case study.

Numerical continuation calculations as one selected parameter (nominal Froude number) varied, produced the results shown in Figure 1, for a ship sailing in regular waves of length equal to ship length, wave steepness 1/20, proportional and differential control gains 1 and 3 respectively and desired heading set at 10 degrees (0.17 rad). The identified bifurcations are marked on the graph with asterisks and their type is indicated by their initials (PD: period doubling/flip; LPC: limit-point-of-cycles/fold). Period-doubling is the transition from a response at the period-of-encounter to another one of double period. A limit-point-of-cycles occurs when two cycles of different stability collide and

annihilate each other. The graph shows both stable and unstable branches of the system's solutions, with the later ones represented by a dotted line and indicated with a "u". Time simulations of surge velocity and yaw angle corresponding to key points of this diagram are provided in Figure 2 to Figure 4.

The maximum yaw angle reached is monitored in Figure 1, as the nominal Froude number is varied. The stable periodic yaw of relatively small amplitude corresponding to solutions on branch (a), changes to one of doubled period [point on branch (b)]. The ordinary yaw motion that was dominating earlier has turned unstable. This is confirmed from the time simulation results provided in Figure 2. This flip bifurcation is inherent to the yaw dynamics. It is not fundamentally affected by the surge dynamics and the possibility of surf-riding, due to occurring prior to the nonlinear surging regime.

Following the steady states on branch (b), the amplitude of this period-doubled oscillation increases rapidly, as the Froude number acquires larger values, up to a point, and then, in a slower manner until the LPC1 occurs. Just before LPC1 the vessel is already performing large amplitude yaw motion. As the Froude number is raised, the characteristic asymmetry associated with nonlinear surging becomes prevalent, implying that we are not far from surf-riding (see plot 0.293(b) in Figure 3). Upon further increase of the Froude number, the LPC1's location is exceeded and the system needs to settle on another branch of steady states; a transition inevitably coming about with a jump phenomenon. If another branch of stable steady states is found at lower ψ_{max} values, like branch (c) in Figure 1, then the transition could eventually end there. An example of the kind of behavior that the ship exhibits after the jump at LPC1 can be seen in Figure 4 (see Fn=0.298). In this case, the ship presents strongly nonlinear behavior, and as the surge velocity and the yaw angle increase, it turns facing almost beam seas, leaving momentarily the surf-riding territory, until the yaw angle to the waves' direction becomes small enough, leading to sailing again in following/quartering seas.

Branch (c) corresponds to system's solutions of lower amplitude, like these of branch (a), and they have also comparable periods, in most parts (see Fn =0.293(c) in Figure 3), and same as before, increment of amplitude is followed by that of the oscillation's period. Notably, it coexists, for a range of nominal Froude numbers, with branch (b), providing two possible steady states for the system to settle depending on the initial conditions (see Figure 3). Two period doubling bifurcations occur on this branch, before reaching to a fold bifurcation. The branches emerging between PD3 and PD4 remain in the close vicinity of the (c) branch, producing oscillations of low amplitude, or, in some cases, instabilities, leading the system to settle on branch (b), for some parameter values. The branch concludes to a fold bifurcation (LPC2), leading the system to jump to the only available stable branch close by, branch (b), as seen in Figure 4 (for Fn=0.296). The dynamics associated with the states of this branch are strongly nonlinear, with multiple occurring bifurcations, and is greatly influenced by these states' placement close to the surf-riding territory. These rich, but complex phenomena, exceed the scope of this paper, focusing on cumulative broaching, and will be discussed separately in future work.

At this point, it is worth noting that the general geometry of the branches presented in Figure 1, including the rate that the amplitude increases and the maximum value that reaches, but also the relative position of the fold bifurcations located on the branches (b) and (c), determine the progression of this phenomenon, and are both parameter and ship dependent.

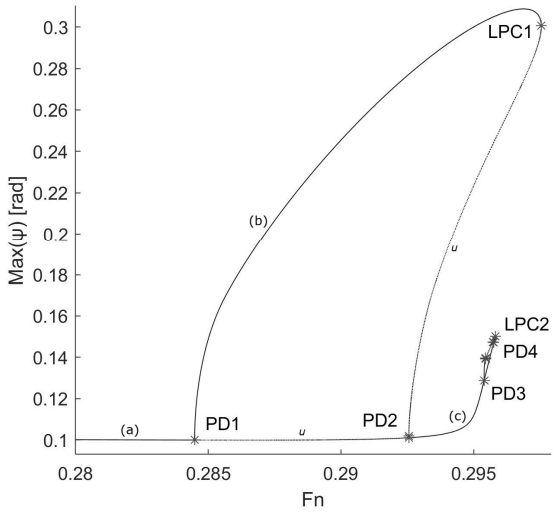

Figure 1: Key result of continuation analysis - Maximum steady-state yaw angle, as the nominal Froude number varies [λ=L, H/λ=0.05, (k_1, k_2)=(1, 3), ψ_r=0.17 rad].

The effect of wave steepness is shown in Figure 5. Although the same branches and the main bifurcations appear, indicating the robustness of this

phenomenon's structure (PD1 and LPC1), the relative position of them changes. The structure appears at lower nominal Froude numbers as the wave steepness increases, placing it far from the surf-riding territory. The most notable difference, however, is the relation between the two coexisting branches; (b) and (c). At lower wave steepness, branch (c) spreads to higher parameter values, providing a safe small amplitude oscillation for the system to settle after the jump at LPC1 (see Figure 6, for H/λ =0.03), that prevents the motion of increased amplitude, that was triggered at PD1, to lead to broaching, which corresponds well with the theory of cumulative broaching appearing for steeper waves. Broaching, in this case, can occur after PD3 (see Figure 7). In this case, the location of PD3 seems to be very close to the surf riding region, as opposed to PD3 appearing in Figure 1, for wave steepness 0.05. As can be seen in Figure 8, after the bifurcation, the system follows a branch of steady solutions that emerges there.

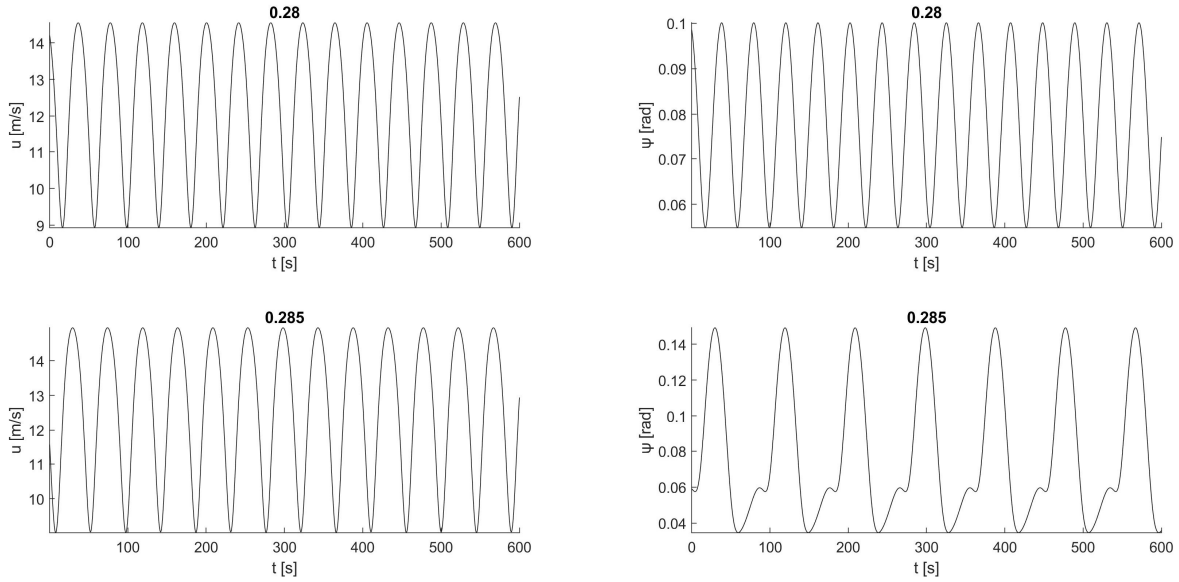

Figure 2: Confirmation of occurrence of first period-doubling (PD1) in yaw motion, through simulations, for points just before the PD1 [Fn=0.28 on branch (a)] and after that [Fn =0.285 on branch (b)]. [λ=L, H/λ=0.05, (k_1, k_2)=(1, 3), ψ_r=0.17 rad.]

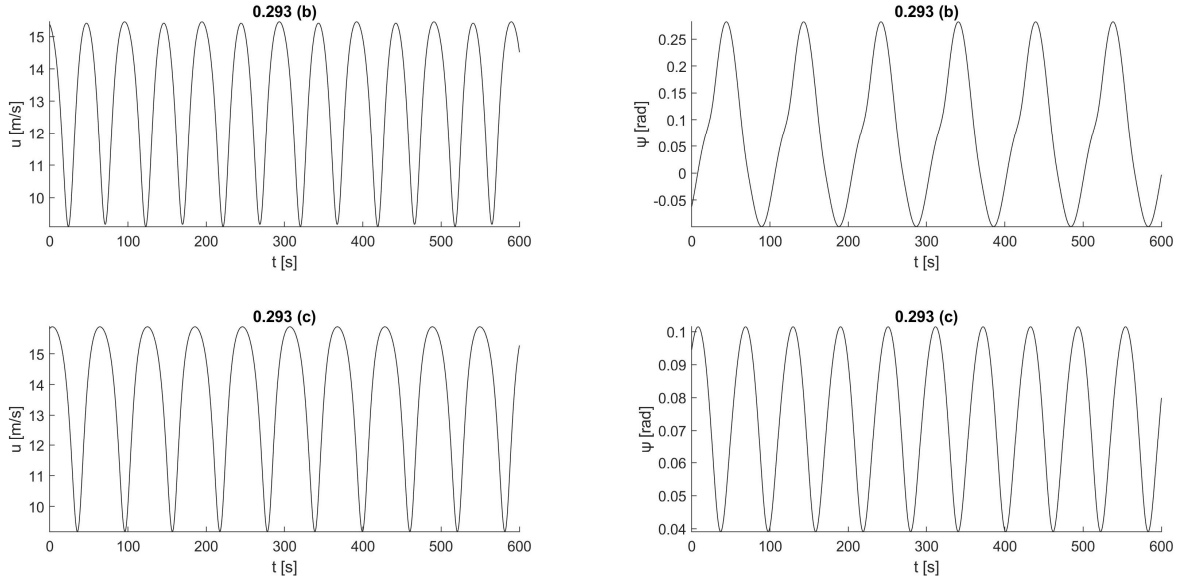

Figure 3: Coexisting stable steady-states for Fn=0.293, referring to points located at the upper part of branch (b) and on branch (c) [λ=L, H/λ=0.05, (k_1, k_2)=(1, 3), ψ_r=0.17 rad].

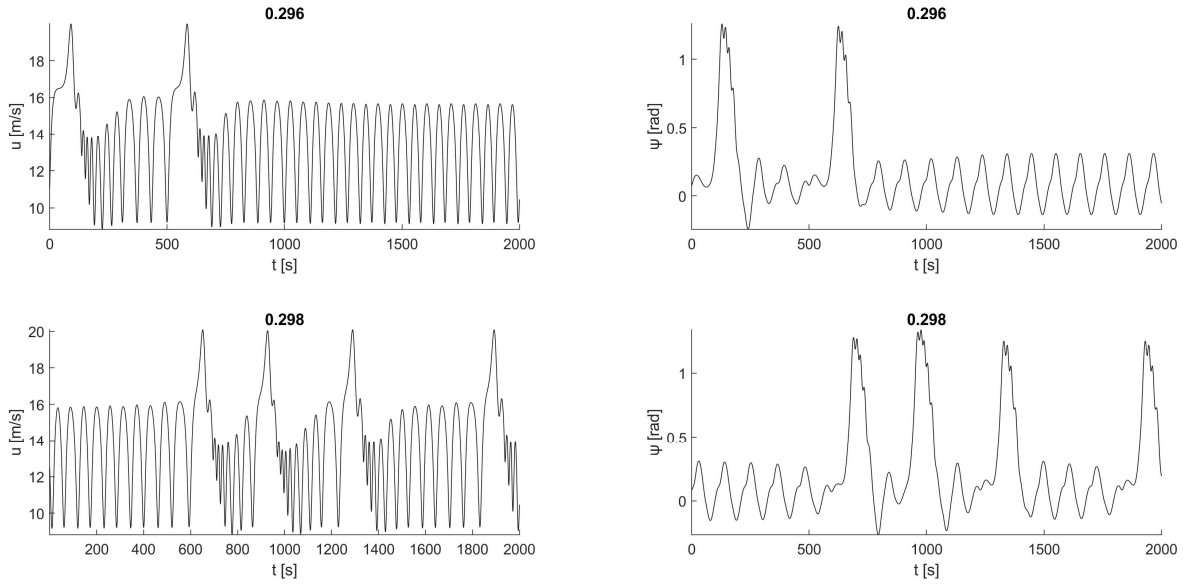

Figure 4: Upper diagrams: Jump from the lower branch (c) towards the upper (subharmonic) branch (b) [Fn=0.296, just after LPC2]. Broaching realized in transient, with yaw motion later becoming confined according to the corresponding state of the upper broach. Lower diagrams: Jump from the upper branch (b) [Fn=0.298, just after LPC1] that leads to broaching [λ=L, H/λ=0.05, (k_1, k_2)=(1, 3), ψ_r=0.17 rad].

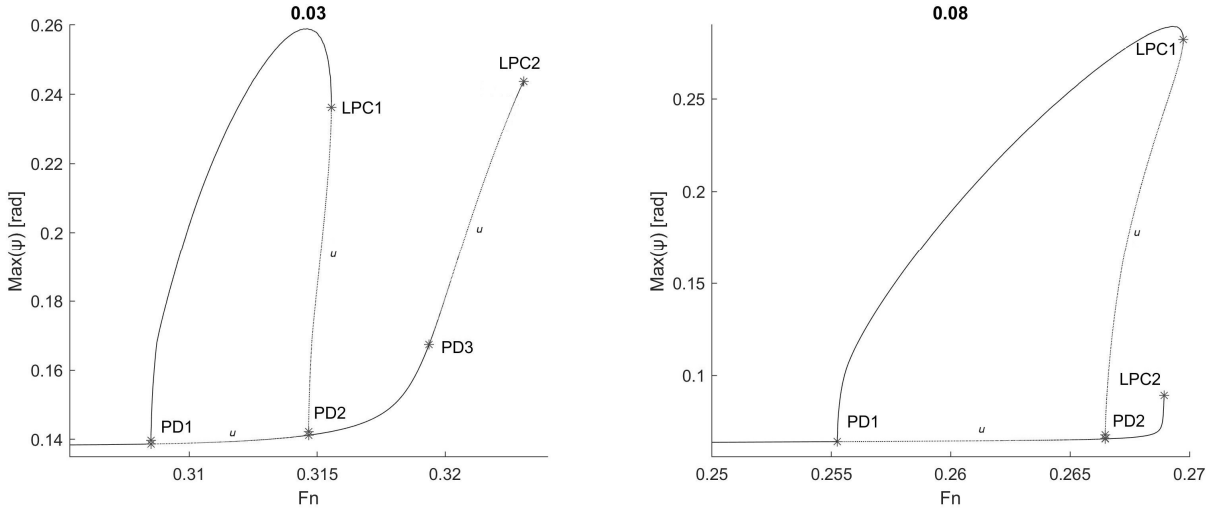

Figure 5: Effect of wave steepness (H/λ) on the branches of steady-states for ranging Fn [λ=L, (k_1, k_2)=(1, 3), ψ_r=0.17 rad].

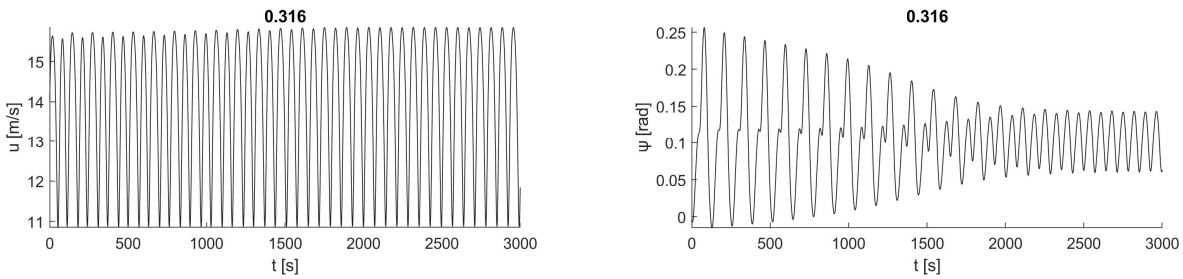

Figure 6: Response at Fn=0.316 (located between LPC1 and LPC2), using as initial condition a point of the upper branch, slightly before LPC1 (reference to Figure 5) [λ=L, H/λ=0.03, (k_1, k_2)=(1, 3), ψ_r=0.17 rad].

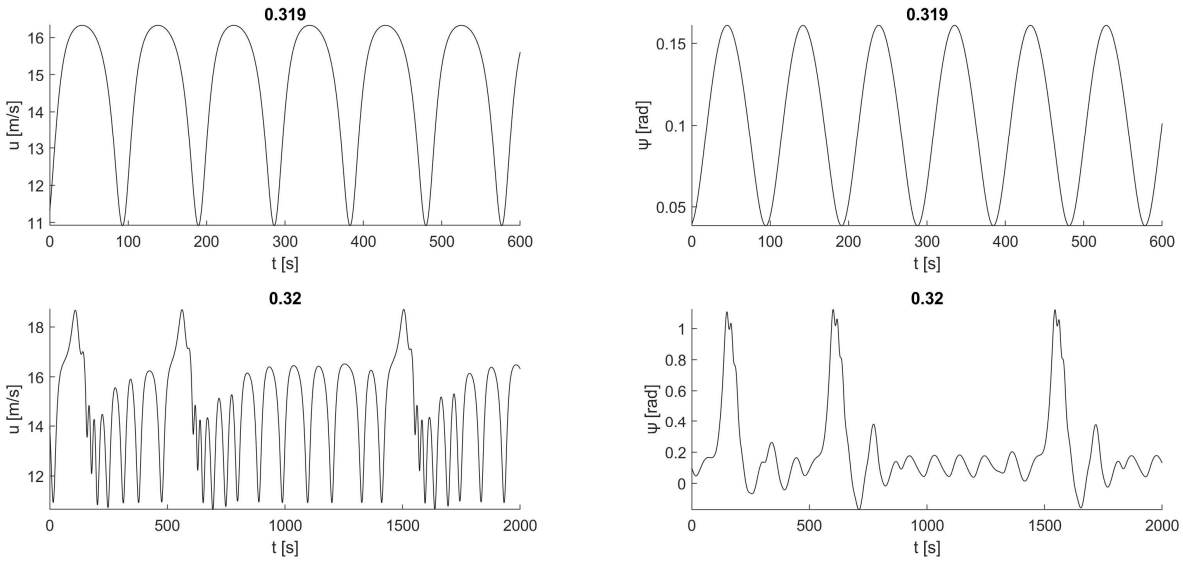

Figure 7: Very large yawing (broaching), with time intervals of surf-riding, occurring very soon after the PD3 point is exceeded (reference to Figure 5). Upper diagram: Fn=0.319 (just before PD3); lower diagram: Fn=0.321 (just after PD3) [λ=L, H/λ=0.03, (k_1, k_2)=(1, 3), ψ_r=0.17 rad].

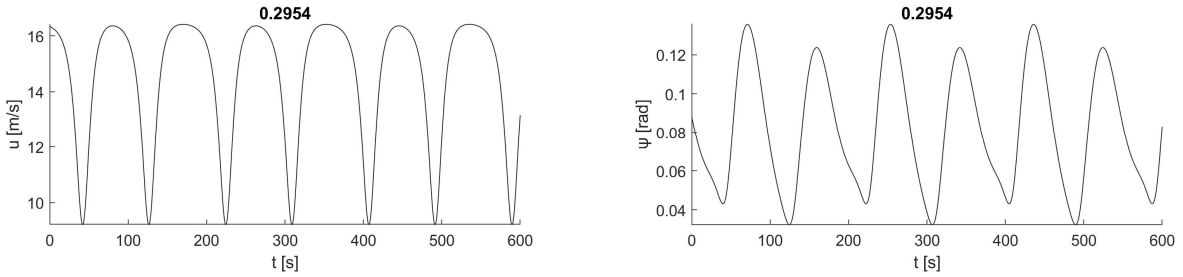

Figure 8: Behavior after the (PD3) on the lower branch (c), with the ship exhibiting nonlinear surging (reference to Figure 1) [Fn=0.2954, λ=L, H/λ=0.05, (k_1, k_2)=(1, 3), ψ_r=0.17 rad].

Some indications of the effect of controller gains appear in Figure 9. These parameters affect both the relative position of LPC1 and LPC2, but also how close the PD1 and PD2 are located, which affects the geometry of branch (b), containing LPC1. Larger values of controller gains also bring the fold bifurcations closer, with k_2 having the greater effect as it increases, while higher values of k_1 seem to pull PD1 and PD2 further apart.

A more useful for applications presentation of these results would be the loci of these bifurcations in parameters' space. These bifurcation curves, calculated via numerical continuation as two parameters simultaneously vary, define the stability boundaries of the system, as can be seen in Figure 10. The bifurcation curves are given for combinations of nominal Froude number and wave steepness, and drawn over simulation results, marking with white motions of small yaw angle and with grey those higher than five times the set initial yaw angle (in these case ψo=0.075 rad, so the limit was 0.375 rad).

A secondary result from Figure 10 is the robustness of these sequence of phenomena that define the bifurcation structure of cumulative broaching, i.e. period doubling followed by fold bifurcation, as regards wave excitation, represented by the wave steepness, and controller gains. The bifurcation curves of PD1 and LPC1 cover a vast range of wave steepness values without changing relative position to one another. This remains also true for the tested combinations of controller gains. The previously referenced scenario of the higher parameter value of the branch (c) exceeding that of branch (b), which translates to LPC1 appearing before LPC2, is also present in these plots, for lower values of wave steepness. Additionally, it is revealed that PD1 and PD2 belong on the same curve (in this parameter space), with PD1 being the first encountered bifurcation as either parameter

increases. Also, the LPC1 curve moves closer to it as the wave steepness decreases, ending at its minimum, where the period doubled motion disappears, which is expected considering the structure presented in Figure 1.

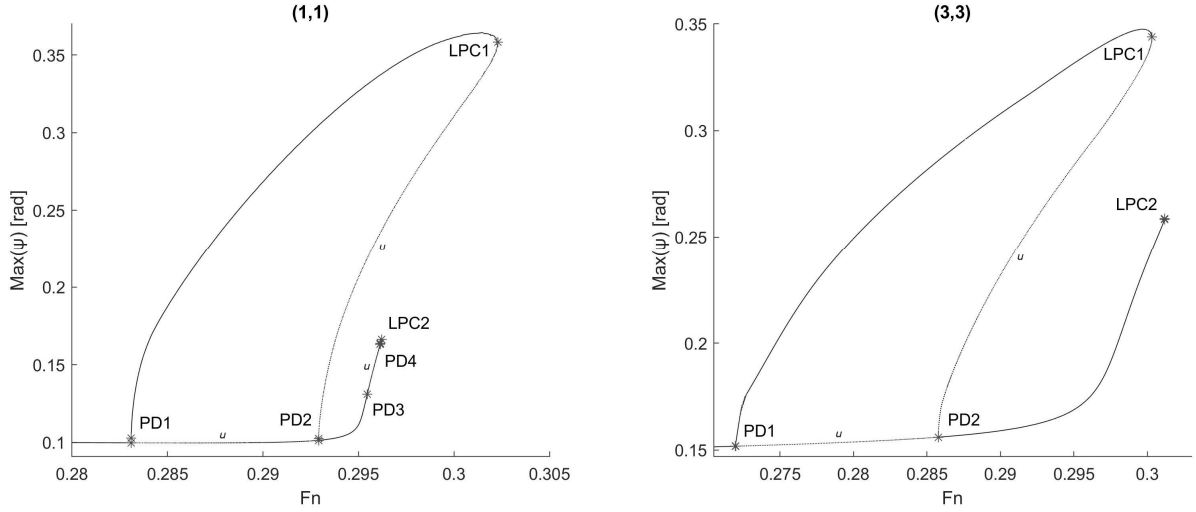

Figure 9: Effect of controller gains (k_1, k_2) on the result of continuation analysis for ranging Fn [λ=L, H/λ=0.05, ψ_r=0.17 rad]

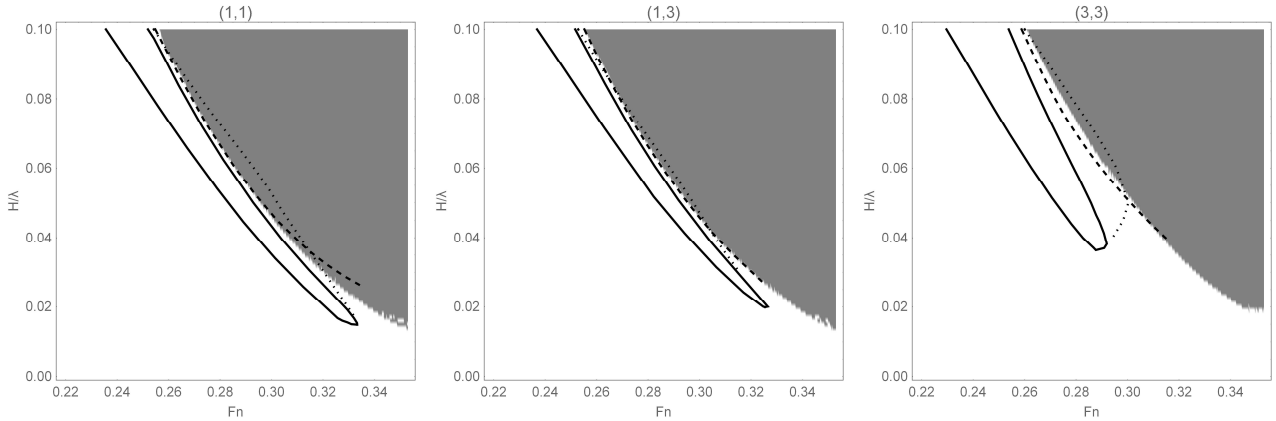

Figure 10: Dynamic stability diagram with bifurcation curves for different control gain values (k_1, k_2) [λ=L, ψ_r=0.17 rad] [Curves: continuation results for two parameters ranging simultaneously (PD1 and 2: continuous line, LPC1: dotted line, LPC2: dashed line); Points (white/stable and grey/unstable): simulations]

4. CONCLUDING REMARKS

The current study offers insights into the full dynamic structure involved in cumulative broaching, using a passenger ship. Simulations and numerical continuation methods were employed, in order to identify dynamically different types of behavior, and subsequently locate and characterize types of bifurcations triggering them. Bifurcation curves were also acquired from continuation calculations, as two parameters varied, and were drawn over simulation results, producing dynamic stability diagrams. These being the loci of bifurcations on a parameter plane, mark the dynamic stability boundaries on it.

Cumulative broaching has been described as a loss of stability after the amplitude's increase of the ship's oscillation in yaw, due to yaw parametric instability. Continuation calculations as a selected parameter varied (nominal Froude number, marked as Fn, identified a period-doubling bifurcation, occurring at a Froude number before the influence of the oncoming surf-riding phenomenon. After this bifurcation the oscillation's amplitude is shown to increase rapidly as the Fn increases. This branch of stable subharmonic yaw steady states ends with a fold bifurcation which, as well-known, it is

associated with a jump phenomenon; i.e. the system needs to settle on another (distant) steady state, in a non-continuous manner, as the control parameter varies. These cases are potentially dangerous, depending on the available steady-states that the system could settle following the jump. In several of the examined scenarios, no states of low yaw amplitude were available, and broaching occurred. This bifurcation structure appears to be robust as regards to both wave excitation and controller gains, making this phenomenon relevant in a range of operating conditions.

Additional branches of steady states were also found in the process, and have been partially analyzed, but were not the focus of this study, due to being affected by the surf-riding phenomenon. The bifurcation structure of these states will be part of future research.

5. ACKNOWLEDGEMENTS

This work was supported by the Office of Naval Research (ONR) under Dr. Woei-Min Lin and by ONR Global under Dr. Richard Meyer, Grant No N629092512001.

REFERENCES

Dhooge, A., Govaerts, W., Kuznetsov, Yu. A., 2003, "MATCONT: A MATLAB Package for Numerical Bifurcation Analysis of ODEs", AMC Transactions on Mathematical Software, ISSN: 0098-3500.

Doedel, E. J., Champneys, A. R., Fairgrieve, T. F., Kuznetsov, Yu. A., Sandstede, B., Wang X.J., 1997, "AUTO97-00: Continuation and Bifurcation Software for Ordinary Differential Equations (with HomCont)", User's Guide, Concordia University, Montreal, Canada.

Hamamoto, M., 1991, "Study on Ship Motions and Capsizing in Following Seas", *Journal of The Society of Naval Architects of Japan*, Vol. 170, pp. 173-182.

Lewandowski, E. M., 2004, "The Dynamics of Marine Craft, Advances Series on Ocean Engineering", BMT Designers and Planners, USA.

Lewis, E. V. (ed.), 1989, "Principles of Naval Architecture, Vol. III, Motions in Waves and Controllability", SNAME.

Margari, V. & Spyrou K. J., 2022, "A Vulnerability Criterion of Dynamic Instability for Ship Course-Keeping in Following Waves", Journal of Ship Research. Vol. 67, No 3, pp. 1-12, doi: https://doi.org/10.5957/JOSR.03220010.

Margari, V. D. & Spyrou, K. J., 2024, "Dynamics of Cumulative Broaching-to in Heavy Astern Seas", 2nd International Conference on the Stability and Safety of Ships and Ocean Vehicles, (STAB 2024), Wuxi, China.

Margari, V. D. & Spyrou, K. J., 2025, "Robustness to Hydrodynamic Model Assumptions of Cumulative Broaching Predictions", 20th International Congress of the International Maritime Association of the Mediterranean, (IMAM 2025), Crete, Greece.

Mikelis, N. E., 1985, "A Procedure for the Prediction of Ship Maneuvering Response for Initial Design", Proceedings of International Conference on Computer Applications in the Automation of Shipyard Operation and Ship Design Proceedings, ICAAS, Elsevier Publishers B. V., North Holand, pp. 437-446.

Renilson, M.R., 1981, "The broaching of ships in following seas", PhD Thesis, University of Glasgow.

Salvesen, N., Tuck, E., and Faltinsen, O., 1970, "Ship Motions and Sea Loads", Trans. SNAME Vol. 78, No. 8, pp. 250–287.

Seydel, R., 2010, "Practical Bifurcation and Stability Analysis", Third Edition, Springer, eBook ISBN: 978-1-4419-1740-9.

Spyrou, K. J., 2006, "Asymmetric surging of ships in following seas and its repercussions for safety", Nonlinear Dynamics, Vol. 43, pp. 149-272.

Spyrou, K., 1996, Dynamic instability in quartering seas: the behavior of a ship during broaching Journal of Ship Research, Vol. 40, No 1, pp. 46-59.

Tigkas I. & Spyrou K.J. 2012, "Continuation Analysis of Surf-Riding and Periodic Responses of a Ship in Steep Quartering Seas", 11th International Conference on the Stability of Ships and Ocean Vehicles, (STAB 2012), Athens, Greece.

On the usefulness of surf-riding experiments conducted at a towing tank with limited capacity

Michał Struk, *Gdańsk University of Technology* michal.struk@pg.edu.pl

Przemysław Krata, *Gdańsk University of Technology* przemyslaw.krata@pg.edu.pl

ABSTRACT

As the surf-riding phenomenon can result in dangerous broaching-to, it should be avoided to keep the ship operation safe. Numerous studies aimed at addressing this issue leading to a good understanding of the mechanism behind surf-riding in regular waves. However, the same cannot be said for irregular waves conditions, for which mainly statistical approach has been applied to date. Therefore, the idea of applying the simplest possible irregular wave consisting of two harmonic ones, i.e. bi-chromatic, was created in recent theoretical works. This seeks experimental investigation in order to confirm or deny the predictions made with the use of theoretical models. The experimental research conducted at Gdańsk University of Technology explores the surf-riding phenomenon and compares results obtained in two different scales using a small and a mid-size towing tank. The initial experiment was made in a 40 m towing tank using the ITTC A2 purse-seiner in 1/64 scale. This confirmed the feasibility of reproducing surf-riding in bi-chromatic waves. Then the corresponding experiment followed, where the towing tank facilities were significantly larger reaching the tank's length 270 m and the same design A2 purse-seiner built in 1/14 scale. The comparison between those two experiments generally confirmed the qualitative agreement of results obtained in both experiments, while the quantitative aspects revealed a more complex behavior depending on the distance to the ship velocity threshold demarcating the transit between the earlier identified response patterns.

Keywords: *bi-chromatic wave, following seas, surf-ridings, surging*

1. INTRODUCTION

The basics behind the surf-riding phenomenon are generally known as well as the potentially dangerous aftermaths. Especially broaching-to that is the sudden turn preceded by the ship surf-riding and triggered by the directional instability, may result in a large angle of heel, possibly even capsizing (Szozda and Krata, 2022). When a ship broaches, recovery may be hardly feasible thus frightening to seamen, which behavior was known since the sail era (Spyrou, 2010). Therefore, a number of scientific works can be found in the literature. Given the inherent vulnerability of fast, small to mid-size ships to surf-riding, the potential loss of directional stability in waves represents a significant concern. As this phenomenon occurs when a ship is captured by the following wave and accelerated to the wave celerity, naturally the regular wave system has been the first and most investigated surf-riding condition.

The key principle underlying surf-riding in regular waves is that the wave surging force combined with the propulsion force speeds up the ship to the velocity exceeding its command calm water speed (IMO, 2022). Depending on the steepness of the considered following wave, the wave force may be sufficient to accelerate the ship to wave celerity, thereby establishing a dynamic equilibrium at the front slope of the wave, thus the surf-riding phenomenon. This dynamic equilibrium for regular waves is defined as a state where the combined propulsion and wave force match the ship's resistance at wave celerity. The ship is

attracted to this equilibrium, and it can be seen to be "captured" by the wave. As the directional instability may develop, the conditions enabling a surf-riding failure need to be strictly avoided. Therefore, the ability to identify the conditions leading to the ship surf-riding remain crucial in order to ensure safe navigation of small and fast vessels.

In recent years, in order to deepen the knowledge on the surf-riding phenomenon, a number of free-running model experiments were conducted not only for regular, but also for irregular following seas (Matsubara et al., 2023; Umeda et al., 2016). They mainly focused on a vast important issue which is an estimation of the surf-riding probability in irregular waves. That approach employs a deterministic surf riding threshold and the joint probability of local wave heights and wave periods, as proposed by Umeda (1990). The purpose of this research undertaken at Gdańsk University of Technology is to further expand the knowledge about the surf-riding phenomenon in irregular waves, specifically for the simplest possible irregular wave system composed of two harmonic waves.

The consideration of the bi-chromatic wave is directly justified by the results of the theoretical studies (Spyrou et al., 2016, 2018; Tigkas I and Spyrou K, 2021; Tigkas and Spyrou, 2023). Numerous interesting predictions of the response of a ship subjected to the bi-chromatic wave action were presented there like for instance the ship velocity oscillations typical for surging while the ship surf-rides with the velocity of the other wave component.

First, two preliminary studies were conducted, i.e. one focusing on the ship response patterns identification based on 1 DoF time-domain simulations (Warnke-Olewniczak and Krata, 2024), while the second was experimental aiming at the feasibility assessment of the reproduction of the theoretically predicted patterns in a towing tank (Struk and Krata, 2024). Once the positive preliminary results were obtained, the significantly wider experimental campaign has been launched. The extensive set of the ship model runs were executed in bi-chromatic wave conditions, first using the small towing tank at Gdańsk University of Technology followed by the over one-month lasting campaign utilizing the 270 m long towing tank at the Maritime Advanced Research Centre in Gdańsk. A part of the experimental research was determination whether there are meaningful qualitative differences between the ship response recorded in the small and mid-size towing tank for the ship models built in 1/64 and 1/14 scale, respectively. Furthermore, the first attempt to the assessment of the quantitative variances of results has been undertaken. Those two research questions constitute the main plot of the research reported here.

The remainder of this paper is organized as follows: Section 2 describes the experimental setup utilized in the research and some details of the examined sample ship, as well as the considered scenarios of sailing; Section 3 presents the obtained results and their comparison; Section 4 discusses those results, while Section 5 concludes.

2. EXPERIMENTAL SETUP AND APPLIED METHODOLOGY

This study contains results of two very similar experimental setups utilization. The general idea is to measure the position of a free-running ship model in coordinate system fixed to towing tank carriage. The global velocity of the vessel is calculated as the sum of the speed of the towing tank carriage and the velocity of the ship model relative to the carriage. Both experiments included a scale model of the ITTC A2 purse-seiner as seen on Figure 1 (e.g. Umeda et al., 1995)

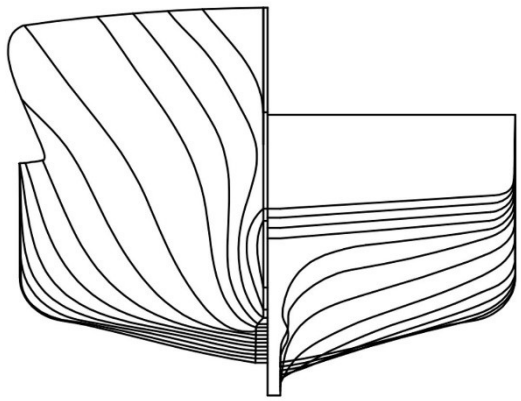

Figure 1. Lines plan of the ship model i.e. the ITTC A2 purse-seiner

One of the experiments was carried out at Gdańsk University of Technology towing tank: 40 m long, 4 m wide and 3 m deep. This towing tank is equipped with an electric panel wave generator and QualiSys motion capture cameras mounted on towing tank carriage as shown in Figure 2. The speed of towing tank carriage was set as constant during each experimental run. The ship model used at this facility was 1/64 scale ITTC A2 as shown in Figure 3, which is called the 'small model' here. The principal dimensions of the small model are as follows: L_{bp}=0.54m, L_{oa}=0.64m, B=0.12m, d=0.04m and the model mass was 1.58 kg.

Figure 2. Towing tank carriage with QualiSys motion capture system cameras

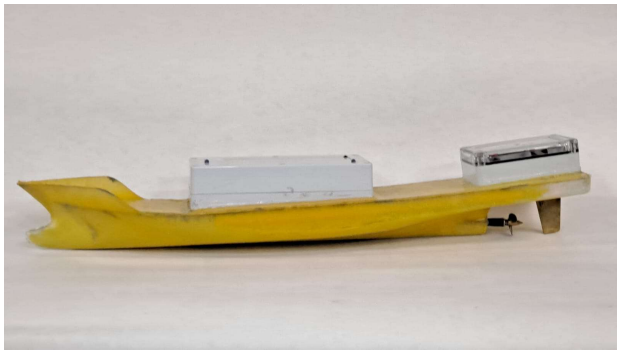

Figure 3. The in-house manufactured 1/64 scale model of the ITTC A2 purse-seiner (the 'small model')

The other experiment was conducted at Maritime Advanced Research Centre (CTO S.A.) located at Gdańsk, Poland. The towing tank located there is 270 m long, 12 m wide and 6 m deep, equipped with a hydraulic flap-type wave generator and QualiSys motion capture system, same type as the one available at the universities' short towing tank. The speed of the towing tank carriage was controlled by an operator and recorded in synchronisation with QualiSys logs. The ship model used at this facility was 1/14 scale ITTC A2 as shown in Figure 4, which is called the 'large model' here. The principal dimensions of the large model are as follows: L_{bp}=2.51m, L_{oa}=2.93m, B=0.55m, d=0.18m and the model mass was 151.2 kg.

Figure 4. The in-house manufactured 1/14 scale model of the ITTC A2 purse-seiner (the 'large model')

Both ship models were free-running and had the well-tested ability to maintain a constant known commanded speed. The models were radio controlled by operator who had the control over rudder as well as the preset propulsion RPM. The test runs results were obtained using QualiSys system by tracking position of infrared diodes (in case of the small model) or reflective markers (in case of the large model). The proper recording of data stream was ensured further processing.

The arrangement overview of the experimental setup is shown in Figure 5.

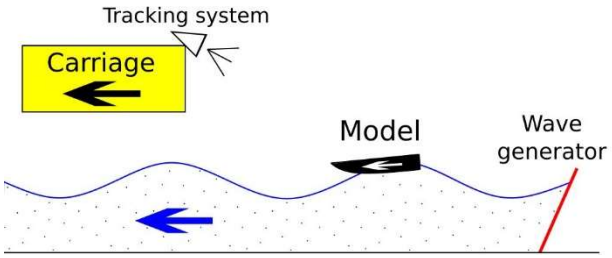

Figure 5. Sketch of the experimental setup, arrows indicate direction of the carriage, ship and wave movement

As this study compares results of two similar experiments carried out in two different scales, two corresponding sets of parameters were examined. The parameters used for 1/14 scale experiment are presented in Table 1 while the second experiment was carried out using the parameters rescaled to scale of 1/64 as shown in Table 2.

Table 1. Parameters of test cases applied for experimental exploration of surf-riding in bi-chromatic following waves, at 1/14 scale.

Case No	f_1[Hz]	f_2[Hz]	A_1[cm]	A_2[cm]	v_c[m/s]
1	0.625	0.438	2.59	1.91	2.18
2	0.641	0.445	2.95	1.46	2.18
3	0.742	0.711	0.60	4.56	1.84
4	0.742	0.711	0.88	4.41	1.84
5	0.742	0.711	0.94	4.50	1.84
6	0.727	0.688	0.94	4.45	1.98
7	0.727	0.688	0.61	4.98	1.98
8	0.727	0.688	0.94	4.92	1.98
9	0.727	0.688	0.61	4.99	1.92
10	0.727	0.688	0.90	4.88	1.92
11	0.727	0.688	0.58	5.04	1.84
12	0.727	0.688	0.85	5.08	1.84
13	0.727	0.688	0.69	5.10	1.73
14	0.727	0.688	0.84	5.04	1.73

Table 2. Rescaled parameters of cases used in the experiment carried out in 1/64 scale.

Case No	f_1[Hz]	f_2[Hz]	A_1[cm]	A_2[cm]	v_c[m/s]
1	1.336	0.936	0.57	0.42	1.02
2	1.370	0.951	0.65	0.32	1.02
3	1.586	1.520	0.13	1.00	0.86
4	1.586	1.520	0.19	0.96	0.86
5	1.586	1.520	0.21	0.98	0.86
6	1.554	1.471	0.21	0.97	0.93
7	1.554	1.471	0.13	1.09	0.93
8	1.554	1.471	0.21	1.08	0.93
9	1.554	1.471	0.13	1.09	0.90
10	1.554	1.471	0.20	1.07	0.90
11	1.554	1.471	0.13	1.10	0.86
12	1.554	1.471	0.19	1.11	0.86
13	1.554	1.471	0.15	1.12	0.81
14	1.554	1.471	0.18	1.10	0.81

The wave celerity and lengths are evaluated based on linear wave theory. A linear scale was applied to all the dimensions, while a quadratic scale was applied to time and speed.

3. COMPARISON OF EXPERIMENTS: 1/64 vs. 1/14 SCALE.

The obtained results of both experiments are presented in common plots for the sake of clarity. The corresponding cases are compared, therefore the small model scale is used as a basic one while the results from the large model scale are recalculated accordingly. Figures 6 to 19 show the forward velocity of both models, i.e. the small and the large one. The bold blue curve denotes the small model velocity and the thin black line presents the large model velocity, rescaled for the sake of making it comparable. The additional velocities are the wave celerity (c_1 and c_2 denote the celerities of first and second component of the bi-chromatic wave) and the commanded speed of the vessel (v_c). They are shown as horizontal dashed and dotted lines at relevant values.

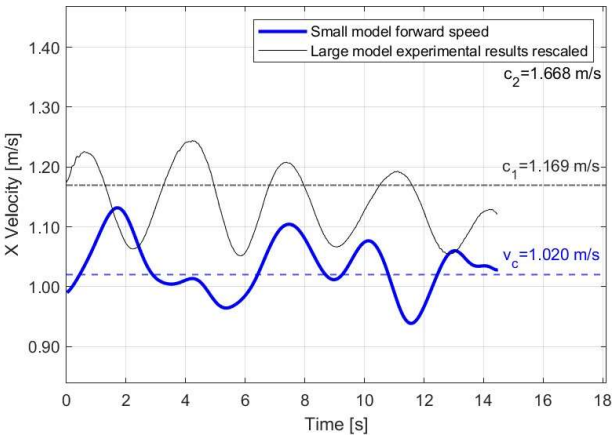

Figure 6. Case No 1: λ_1=0.875 m=LBP*1.591; A_1=0.567cm; λ_2=1.781m; A_2=0.418cm; v_c=1.02m/s

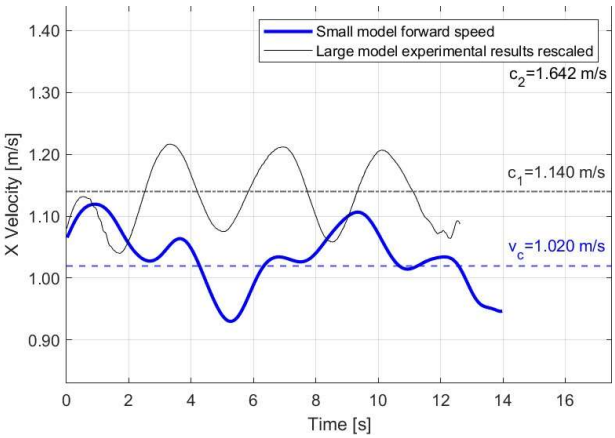

Figure 7. Case No 2: λ_1=0.832 m=LBP*1.512; A_1=0.645cm; λ_2=1.726m; A_2=0.319cm; v_c=1.02m/s

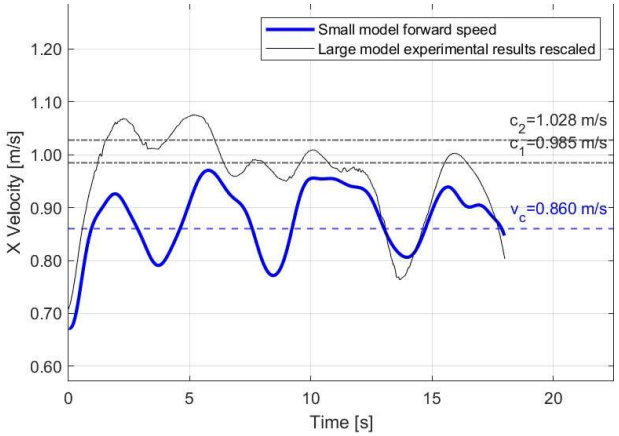

Figure 8. Case No 3: λ_1=0.621 m=LBP*1.129; A_1=0.131cm; λ_2=0.676m; A_2=0.997cm; v_c=0.86m/s

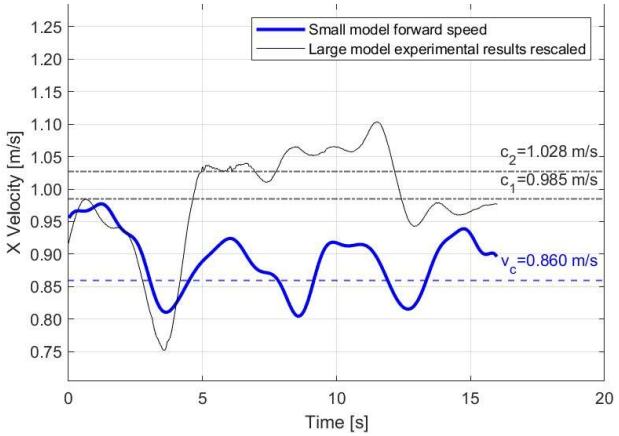

Figure 9. Case No 4: λ_1=0.621 m=LBP*1.129; A_1=0.193cm; λ_2=0.676m; A_2=0.965cm; v_c=0.86m/s

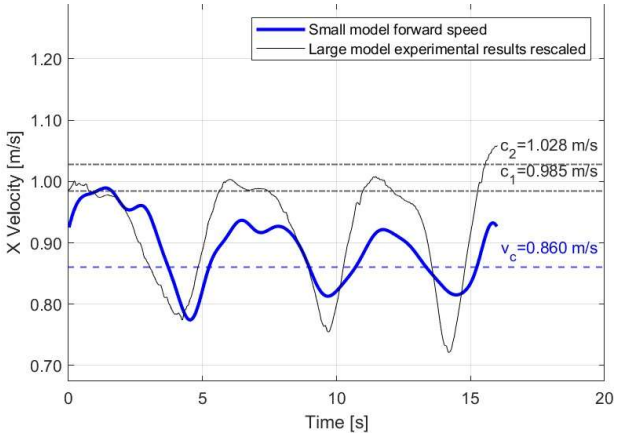

Figure 10. Case No 5: λ_1=0.621 m=LBP*1.129; A_1=0.206cm; λ_2=0.676m; A_2=0.984cm; v_c=0.86m/s

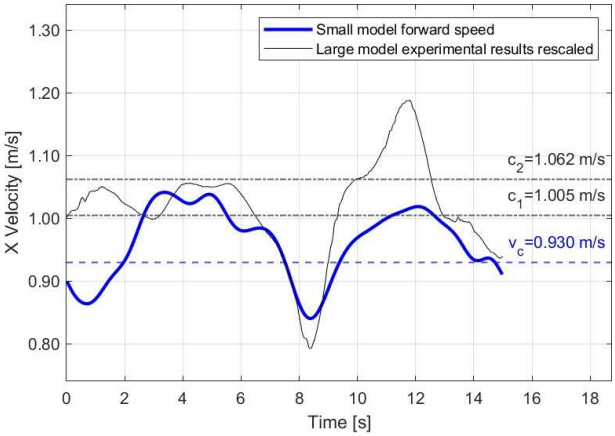

Figure 11. Case No 6: λ_1=0.647 m=LBP*1.176; A_1=0.206cm; λ_2=0.722m; A_2=0.973cm; v_c=0.93m/s

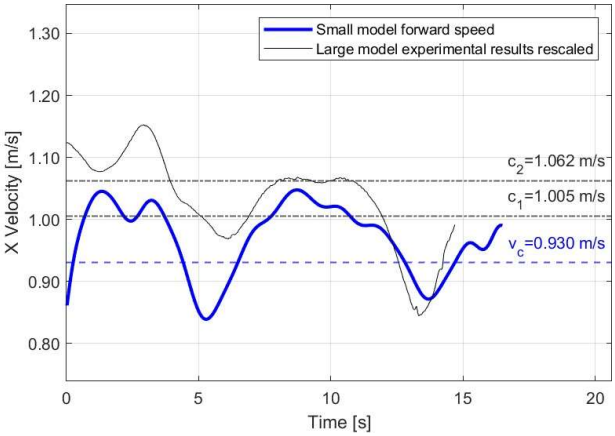

Figure 12. Case No: 7 λ_1=0.647 m=LBP*1.176; A_1=0.133cm; λ_2=0.722m; A_2=1.089cm; v_c=0.93m/s

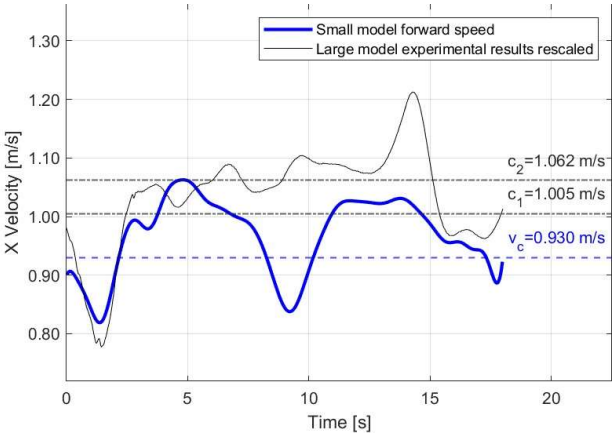

Figure 13. Case No: 8 λ_1=0.647 m=LBP*1.176; A_1=0.206cm; λ_2=0.722m; A_2=1.076cm; v_c=0.93m/s

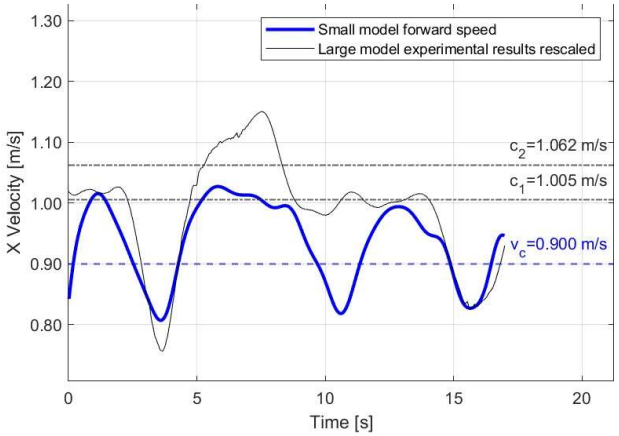

Figure 14. Case No: 9 λ_1=0.647 m=LBP*1.176; A_1=0.133cm; λ_2=0.722m; A_2=1.092cm; v_c=0.9m/s

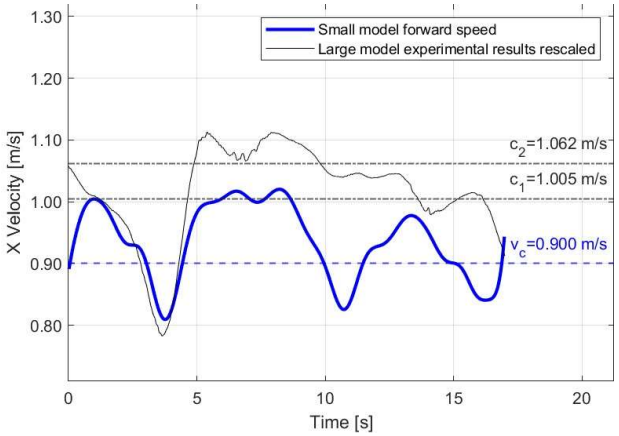

Figure 15. Case No: 10 λ_1=0.647 m=LBP*1.176; A_1=0.197cm; λ_2=0.722m; A_2=1.068cm; v_c=0.9m/s

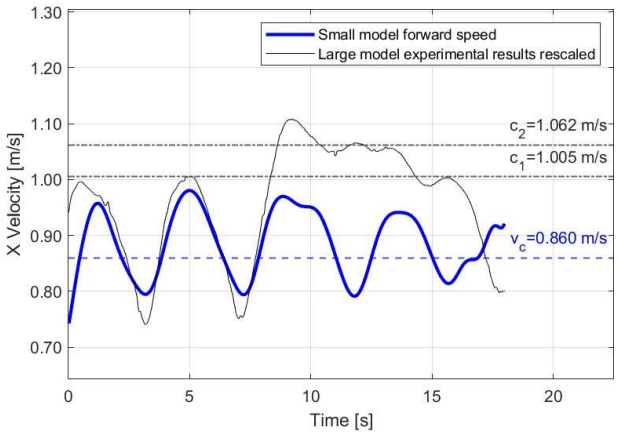

Figure 16. Case No: 11 λ_1=0.647 m=LBP*1.176; A_1=0.127cm; λ_2=0.722m; A_2=1.103cm; v_c=0.86m/s

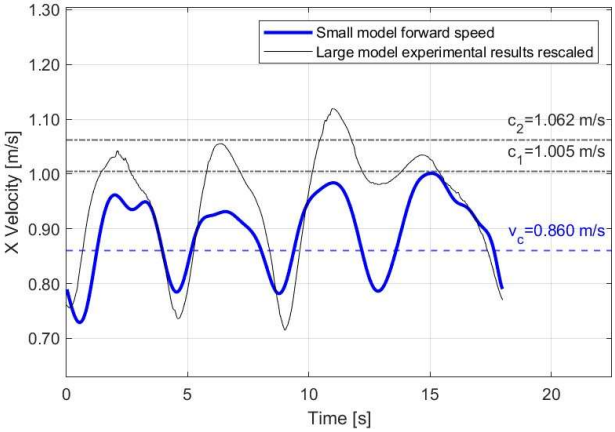

Figure 17. Case No: 12 λ_1=0.647 m=LBP*1.176; A_1=0.186cm; λ_2=0.722m; A_2=1.111cm; v_c=0.86m/s

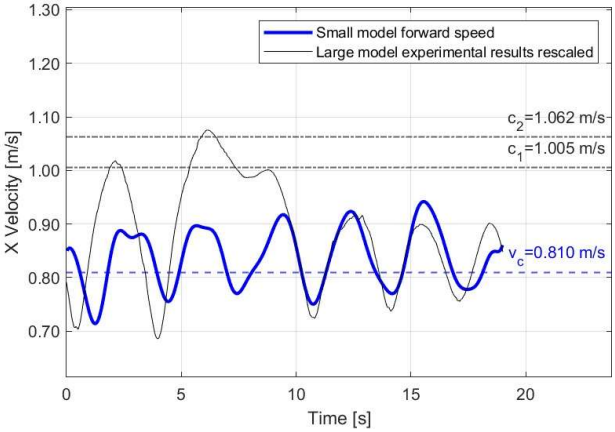

Figure 18. Case No: 13 λ_1=0.647 m=LBP*1.176; A_1=0.151cm; λ_2=0.722m; A_2=1.116cm; v_c=0.81m/s

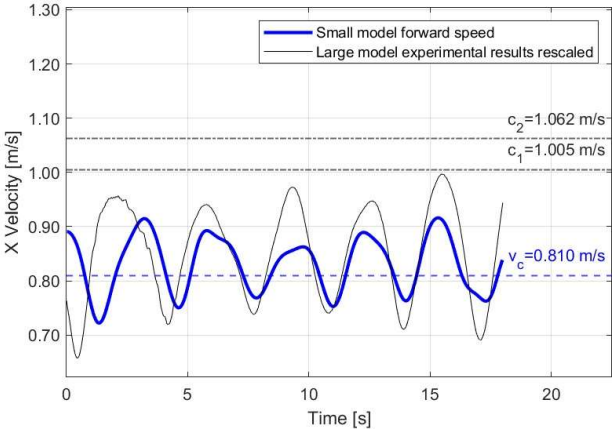

Figure 19. Case No: 14 λ_1=0.647 m=LBP*1.176; A_1=0.184cm; λ_2=0.722m; A_2=1.103cm; v_c=0.81m/s

4. DISCUSSION

The observations made in both experiments include the following phenomena described in (Warnke-Olewniczak and Krata, 2024):

- Beating oscillations in surge;
- High runs on primary wave;
- Surf-riding on primary wave;
- High runs on secondary wave;
- Surf-riding on secondary wave.

Additionally, one more type of response is observed which can be classified as *Catch and release with transition between celerities*. Such a response of the ship was not identified in the recalled theoretical work (Warnke-Olewniczak and Krata, 2024).

The classification of all considered cases is presented in Table 3. These results show that only 4 of 14 cases are matched qualitatively with a good accuracy. However, the difference is similar to that, which would occur if the steepness of the waves or the commanded speed were too low in the small model experiment. This suggests that simply rescaling the dimensions and time is insufficient for accurately reproducing experiments at different scales, since some response types are highly sensitive to slight changes in conditions.

Quantitative differences can be analyzed by comparing experiments 6, 7 and 14, since the response is qualitatively very similar in these three cases.

In case No 6, presented in Figure 11, the velocity amplitude at the first high run is 24% higher in the large model experiment. In case No 7, presented in Figure 12, the amplitude of the velocity at the second high run is 3% higher in the large model experiment. In case No 14, presented in Figure 19, the highest velocity amplitude is 58% higher in the large model experiment. However, this comparison is not fully reliable as the run time for each case is very limited in the short towing tank.

Table 3 Classification of results by the type of the surf-riding phenomena

Case No	Response type	
	small model	large model
1	Beating oscillations in surge	Surf-riding on primary wave
2	Beating oscillations in surge	Surf-riding on primary wave
3	High runs on primary wave	Catch and release with transition between celerities
4	Beating oscillations in surge	Catch and release with transition between celerities
5	Beating oscillations in surge	Catch and release with transition between celerities
6	High runs on secondary wave	High runs on secondary wave
7	High runs on secondary wave	High runs on secondary wave
8	High runs on secondary wave	Surf-riding on secondary wave
9	High runs on primary wave	Catch and release with transition between celerities
10	High runs on primary wave	Catch and release with transition between celerities
11	Beating oscillations in surge	Catch and release with transition between celerities
12	Beating oscillations in surge	High runs on secondary wave
13	Beating oscillations in surge	Beating oscillations in surge
14	Beating oscillations in surge	Beating oscillations in surge

The inherent limitation in the small model experiment was the very confined length of the towing tank (40m), which caused the short run time. Another limitation was lack of autopilot, as control actions by the operator were arbitrary. However, manual course corrections do not appear to have much influence on the final results. An additional limitation was the absence of phase shift measurement for the two wave components. While this does not prevent the analysis of results, it restricts the exact comparison in the same conditions. The ‘same conditions’ here refer to the exact wave realization, since the bi-chromatic wave components

were well controlled thus the phase-shift remained the only parameter random to a certain degree.

Due to the limitations in the manufacturing process, the models' propellers and rudders were only roughly suited to the required scale. It should be noted that even though the models mass was precisely scaled, the moments of inertia were not rescaled so well, since the most crucial phenomena refer to the x-axis direction. It is of note that the geometry of the hulls was only slightly altered at sharp edges due to the manufacturing limitations, but this change is minimal. Therefore, the hulls can be considered precisely reproduced.

The differences in response between two considered scale experiments could be caused by:

- Water on the deck. In the case of a small model, even a small amount of water, like 0.5mm, could cause a significant difference in mass.
- Change in the proportion of the surge added mass of water to the mass of the model.
- Some possible differences in thrust characteristics.
- Different type of wave generator available at the towing tank.
- More significant wave degradation observed in the large towing tank.

5. CONCLUSION

The purpose of this research was determination whether there are meaningful qualitative differences between the ship response recorded in the small (40 m long) and mid-size (270 m long) towing tank for the ship models built in 1/64 and 1/14 scale, respectively. Furthermore, the first attempt to the assessment of the quantitative variances of results has been undertaken.

All the runs presented in this work demonstrate the complexity and sensitivity of the surf-riding phenomenon. While the majority of cases can be easily classified, this process remains dependent on a certain degree of experience in observing the phenomenon. Conducting quantitative comparisons necessitates a significantly greater investment of time and effort, both by the authors of this paper and by the broader scientific community. Conducting experiments at other towing tanks using different models and methods would allow to determine with greater certainty the impact of varying scales on experimental outcomes.

The obtained results suggest that, with an improved method of scaling the experiment, it is possible to qualitatively study the surf-riding phenomenon in a short towing tanks using small models. This approach empowers researchers to investigate a greater number of cases with a reduced research budget. These efforts are intended to further expand the knowledge of the phenomena occurring in the bi-chromatic following seas.

The authors of this paper wish to encourage discussion on the development of shared methods for conducting experiments in small towing tanks, with a view to ensuring reliable and accurate results.

ACKNOWLEDGEMENT

The study was performed as a part of the "Experimental exploration of the ship surf-riding in bi-chromatic following seas with the view to expand the understanding of this phenomenon in irregular wave conditions" research project (number N62909-23-1-2083), funded by the US Office of Naval Research and US Office of Naval Research Global under supervision of Dr. Martina Siwek, Dr.Woei-Min Lin and Dr. Robert Brizzolara.

We would also like to thank the members of the Students Science Club KSTO KORAB for their exceptional passion and engagement in helping to conduct experimental work.

REFERENCES

IMO, 2022. Explanatory notes to the Interim Guidelines on second generation intact stability criteria. MSC.1-Circ.1652.

Matsubara, K., Umeda, N., Matsuda, A., 2023. Probabilistic estimation of the large heel due to broaching associated with surf-riding for a ship in short-crested irregular waves and its experimental validation. Ocean Engineering 269, 113540. https://doi.org/10.1016/j.oceaneng.2022.113540

Spyrou, K., 2010. Historical trails of ship broaching-to. The International Journal of Maritime Engineering.

Spyrou, K., Kontolefas, I., Themelis, N., 2016. Dynamics of the Surf-Riding Behaviour of A Ship in A Multi-Chromatic Sea Environment, in: 31st Symposium on Naval Hydrodynamics Monterey.

Spyrou, K.J., Themelis, N., Kontolefas, I., 2018. Nonlinear surge motions of a ship in bi-chromatic following waves. Commun Nonlinear Sci Numer Simul 56, 296–313. https://doi.org/10.1016/j.cnsns.2017.08.013

Struk, M., Krata, P., 2024. Preliminary Results of Experimental Exploration of Surf-riding in Bi-chromatic Following Waves, in: Proceedings of the 2nd International Conference on the Stability and Safety of Ships and Ocean Vehicles. Wuxi.

Szozda, Z., Krata, P., 2022. Towards evaluation of the second generation intact stability criteria - Examination of a fishing vessel vulnerability to surf-riding, based on historical capsizing. Ocean Engineering 248, 110796. https://doi.org/10.1016/j.oceaneng.2022.110796

Tigkas I, Spyrou K, 2021. Continuation Analysis of Ship Motions in Bi-chromatic Following/Quartering Seas, in: 1st International Conference on the Stability and Safety of Ships and Ocean Vehicles (STABS 2021).

Tigkas, I.G., Spyrou, K.J., 2023. Hybrid surging and surf-riding motions of a ship in steep Bi-chromatic following seas. Ocean Engineering 269, 113522. https://doi.org/10.1016/j.oceaneng.2022.113522

Umeda, N., 1990. Probabilistic study on surf-riding of a ship in irregular following seas, in: Proceedings of the 4th International Conference on Stability of Ships and Ocean Vehicles. University Federico II of Naples.

Umeda, N., Hamamoto, M., Takaishi, Y., Chiba, Y., Matsuda, A., Sera, W., Suzuki, S., Spyrou, K., Watanabe, K., 1995. Model Experiments of Ship Capsize in Astern Seas. Journal of the Society of Naval Architects of Japan 1995, 207–217. https://doi.org/10.2534/jjasnaoe1968.1995.207

Umeda, N., Usada, S., Mizumoto, K., Matsuda, A., 2016. Broaching probability for a ship in irregular stern-quartering waves: theoretical prediction and experimental validation. J Mar Sci Technol 21, 23–37. https://doi.org/10.1007/s00773-015-0364-8

Warnke-Olewniczak, K., Krata, P., 2024. Numerical simulation of surging and surf-riding in bi-chromatic following waves in support of the model test., in: Proceedings of the 2nd International Conference on the Stability and Safety of Ships and Ocean Vehicles. Wuxi.

Revisiting the basic model of broaching-to

Vadim Belenky, *David Taylor Model Basin (NSWCCD),* vadim.belenky.civ@us.navy.mil
Kostas J. Spyrou, *National Technical University of Athens* k.spyrou@central.ntua.gr

ABSTRACT

The paper describes a simple model of broaching in regular waves that may be considered "basic" using only equations for sway and yaw. Hull forces are linearized to match a given steady state diameter of the turn, while a linear approximation is used for wave forces. An autopilot is included with proportional and differential gains. Two variants of the model are considered: one model is completely linear, while the other model has a limit for the rudder. A numerical study reveals three distinct types of instability: unbounded growth (corresponding to broaching preceded by surf-riding), parametric resonance in yaw, and yaw oscillation with increasing amplitudes and mean.

Keywords: *Broaching, Directional Instability, Maneuvering in Waves*

1. INTRODUCTION

Broaching-to (or just broaching) is an uncontrollable violent turn that occurs despite maximum steering effort to maintain course (ITTC definition – see IMO SDC 8/INF.2). The phenomenon has been known since the Age of Sail (Spyrou 2011), and has been the subject of research since the middle of the twentieth century: see Davidson (1948), Du Cane & Goodrich (1962), and Wahab & Swaan (1964).

Broaching is usually preceded by surf-riding, when a ship is "caught" by a steep wave i.e. accelerated to wave celerity. As many ships will broach while surf-riding, the latter is recognized as a mode of stability failure by IMO in the second generation intact stability criteria (SGISC) described in MSC.1/Circ. 1627 and MSC.1/Circ. 1652.

Developments in the field of nonlinear dynamics in the 1980s provided powerful concepts and tools for understanding both surf-riding and broaching, see Spyrou (1996, 1996a, 1997) and Umeda (1999). Furthermore, while studying the nonlinear properties of equations of horizontal-plane-motions in waves, Spyrou (1997) observed a yaw instability not related to surf-riding and occurring at lower speeds, manifesting itself as oscillations with increasing amplitude. The use of an autopilot seemed to contribute to the occurrence of this type of yaw instability.

While such a type of broaching (identified as "cumulative broaching") has been discussed in the past based on the experience of mariners, it did not receive much attention until recently, possibly because the use of an autopilot is prohibited in heavy weather when broaching is relevant. However, autopilots will be required for autonomous vessels and must be able to handle all weather conditions.

Spyrou (2000, 2011a) remarked on the macroscopic similarity between roll and yaw dynamics, drawing an analogy between broaching, preceded by surf-riding with pure loss of stability while cumulative broaching was compared to parametric roll. Spyrou (1997) and Margari & Spyrou (2022) demonstrated that parametric resonance in yaw is the triggering mechanism behind the cumulative broaching. The study was carried out for linear sway and yaw equations in Nomoto form (Nomoto et al 1957; Spyrou, 1997, 2008) and resulted in an approximate analytical solution for the instability boundary. Margari and Spyrou (2023) introduced the surge equation into the study, in a step towards a more engineering-level model. The most recent development included addressing robustness of the model in Margari & Spyrou (2025) and, more importantly, a bifurcation study, to be presented at this workshop (Margari & Spyrou 2025a), closing the loop started in 1997.

While the studies of Margari and Spyrou (2023, 2025, 2025a) are directed towards a more realistic mathematical model, the objective of this paper is to formulate the simplest possible qualitative model for broaching. This model will be akin to Mathieu's equation for parametric roll.

2. BASIC MODEL OF BROACHING

2.1 Equations of Motion

Following Margari & Spyrou (2022), consider a system of linear sway and yaw in following waves.

$$\begin{cases} (M - Y_{\dot{v}})\dot{v} - Y_{\dot{r}}\dot{r} + MUr + Y_v v + Y_r r \\ \quad +Y_\delta\big((k_1(\psi - \psi_c) + k_2 r)| < \delta_{lim}\big) \\ \quad = Y_w \psi \cos(\omega_e t - \varphi_1) \\ (I_z - N_{\dot{r}})\dot{r} - N_{\dot{v}}\dot{v} + N_v v + N_r r \\ \quad +N_\delta\big((k_1(\psi - \psi_c) + k_2 r)| < \delta_{lim}\big) \\ \quad = N_w \psi \cos(\omega_e t - \varphi_2) \end{cases} \quad (1)$$

where ψ_c is the commanded heading, U is forward speed (approach speed), v, r, ψ are sway velocity, yaw rate and angle, respectively, and $\dot{v}, \dot{r}$ are the sway and yaw acceleration, M and I_z are mass and horizontal mass moment of inertia, $Y_{\dot{v}}, Y_{\dot{r}}, N_{\dot{r}}, N_{\dot{v}}$ are coefficients for hydrodynamic forces, proportional to accelerations, Y_v, Y_r, N_v, N_r are coefficients for hydrodynamic forces proportional to velocities (maneuvering hull forces), Y_δ, N_δ are coefficients for rudder force and moment, ω_e is encounter frequency.

The autopilot is modeled with proportional and differential gains k_1 and k_2. A rudder angle limit $\delta_{lim} = 35^o$ is introduced to identify the maximum steering effort (even though it formally violates the linearity of the dynamical system).

Linear formulae for amplitudes of the Froude-Krylov force and moment Y_w, N_w are taken from Margari and Spyrou (2022):

$$\begin{aligned} Y_w &= 2\pi\rho g d \frac{h_w}{\lambda_W} \int_{-0.5L}^{0.5L} b(x)\cos(k_w x)dx \\ &= \frac{h_w}{\lambda_W} Y_{cw}(k_w) \\ N_w &= 2\pi\rho g d \frac{h_w}{\lambda_W} \int_{-0.5L}^{0.5L} b(x) x \sin(k_w x)dx \\ &= \frac{h_w}{\lambda_W} N_{cw}(k_w) \end{aligned} \quad (2)$$

where d is draft, ρ is water density, h_w is wave height, λ_W is wavelength, k_w is wave number, L is ship length, $b(x)$ half-breadth at the waterline at the distance x from the midship section. Y_{cw} and N_{cw} are "kernels" of amplitudes and depend only on wavelength. Phases are taken as $\varphi_1 = -0.5\pi, \varphi_2 = 0$.

2.2 Maneuvering Coefficients

Linear models are normally used to determine the inception of instability. However, they may be significantly inaccurate when considering a large yaw angle. However, a set of reasonable linear approximations for maneuvering coefficients is available from Clarke et al (1982).

As the objective in this work is a qualitative study, the linear system in equation (1) can be calibrated to reproduce "reasonable" calm-water turning characteristics. The equation of motion (1) is complemented with a surge equation:

$$(M - X_{\dot{u}})\dot{u} - R(u) + T(u,n) = 0 \quad (3)$$

where $X_{\dot{u}} = -0.1M$ is added mass in surge, written in the maneuvering notation, u is the instantaneous forward speed, $R(u)$ is calm water resistance and $T(u,n)$ is the thrust, while n is the number of revolutions.

The resistance $R(u)$ is modeled by a linear interpolation of a calm water resistance curve, computed with regression formulae of Holtrop (1984); Holtrop & Mennen (1982).

Thrust is simulated in a similar way:

$$T(u,n) = \tau_0 n^2 + \tau_1 n u + \tau_2 u^2 \quad (4)$$

where τ_0, τ_1, τ_2 are approximated from a thrust curve that can be computed from any thrust coefficient approximation. In this work, formulae by Oosterveld & van Oossanen (1975) were used.

When setting the wave height to zero and the rudder angle to a non-zero value, a joint solution of the equations (1) and (3) produces a turning circle. Calibration is performed by multiplying the values of Y_r and N_r by a single coefficient C:

$$Y_\delta^* = C \cdot Y_\delta; \quad N_\delta^* = C \cdot N_\delta \quad (5)$$

The value of C is adjusted to provide the desired steady state diameter and other turning characteristics. Figure 1 shows a turning circle simulated for a notional configuration (lines are included in an inset), principal dimensions and other relevant parameters are given in Table 1 and 2.

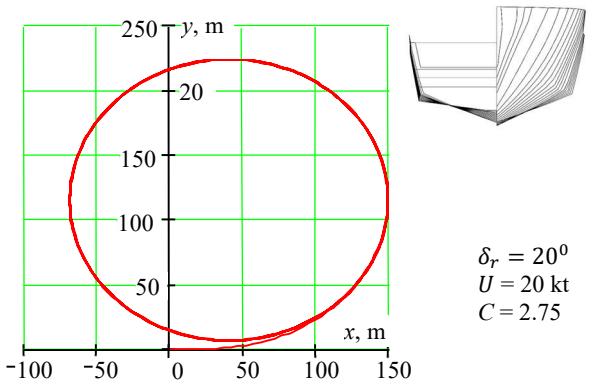

Figure 1: Turning circle simulated with model (1, 3)

Table 1: Parameters of a sample ship

Parameter	Value	Parameter	Value
Length, m	30	Appendage area, m^2	0
Breadth, m	7.05	Draft at FP, m	-0.14
Draft, m	2.0	Draft at AP, m	2.0
Block coeff. (CB)	0.467	Number of props	2
Waterplane coeff. (CW)	0.785	Prop. diameter, m	1.4
Midship coeff. (CM)	0.649	Pitch ratio	1.5
Prismatic coeff. (CP)	0.720	Developed area ratio (DAR)	0.9
Longitudinal Center of Buoyancy (LCB), m	-0.845	Numb. of blades	5
Bulb area, m^2	0	Numb. of rudders	2
Transom area, m^2	0	Rudder area, m^2	1.02
Half angle of entrance, i_E, deg	20	Coefficient of stern shape	0

Table 2: Thrust approximation

Thrust approximation	τ_0	τ_1	τ_2
Coefficient values	5.28	-1.534	-0.291

Turning chracteristics are summarized in Table 3. Calibration was perfomed for a midrange rudder deflection. Results are included in Figure 1.

Table 3: Parameters of turning circle shown in Figure 1

Parameter	Target	Model
Tactical diameter (lengths)	7.3	7.4
Steady-state diameter (length)	7.3	7.3
Advance (lengths)	4.4	4.9
Transfer (lengths)	3.0	3.3

The model (1) is similar to the model used by Margari and Spyrou (2022), but is written as a system of two second-order differential equations rather than in Nomoto form. The only substantial difference is the rudder limit.

3. NUMERICAL ANALYSIS

3.1 Boundary of Directional Stability

Following Margari and Spyrou (2022), a search for the boundary of directional instability is performed. The search is performed numerically, using $|\psi|-\psi_c > 40^0$ as a criterion. The parameters studied were speed, wave height, proportional gain and wavelength. While not explicitly related to "maximum steering effort", exceedance of this criterion was almost always associated with the rudder achieving the limit of 35^0. The differential gain of the rudder was k_2=0.5, while commanded heading was ψ_c=5^0. Numerical solution of the system (1) was computed for 240 seconds.

The boundary is plotted in the speed-wave height coordinates. Results are shown in Figures 2 through 4 for wavelengths of 30 m (L), 45 m (1.5L) and 60 m (2L), respectively. "Kernel" values for wave force amplitudes are shown in Table 4.

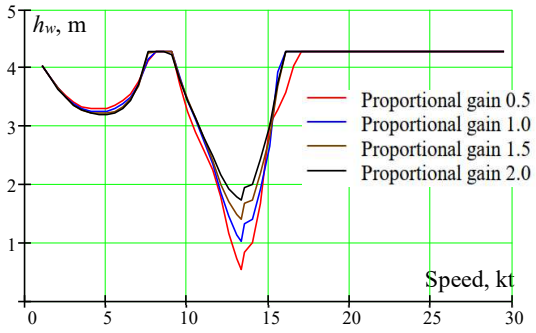

Figure 2: Boundary of directional stability λ_w=L=30 m

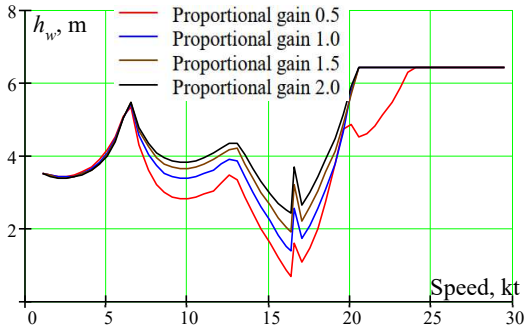

Figure 3: Boundary of directional stability λ_w=1.5L=45 m

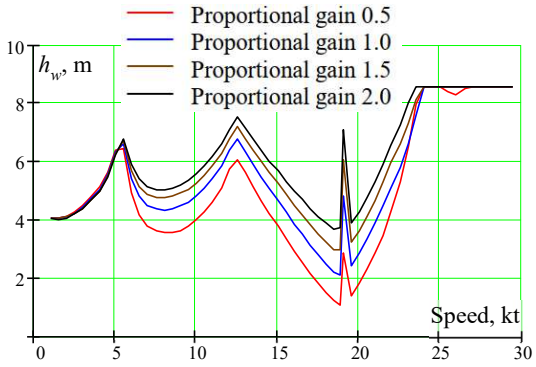

Figure 4: Boundary of directional stability λ_w=2L=60 m

Table 3: "Kernels" of Wave Force Amplitude

Wavelength, m	30	45	60
Wave celerity, kt	13.3	16.3	18.8
Sway force, kN 10^3	2.519	10.54	14.59
Yaw moment, kNm 10^5	1.002	1.206	1.086

The case where the wavelength is equal to ship length, shown in Figure 2, has two obvious instability zones that correspond to cumulative broaching at low speeds and "traditional broaching" (i.e. near wave celerity). There is also some kind of a "shelf" near wave celerity.

Figures 3 and 4 show three instability zones, while a "shelf" near wave celerity turns into a gap. Influence of proportional gain is not surprising as it plays a role in the stiffness of the system. However, it has surprisingly low influence in the first instability zone.

3.2 Observed Responses

To study the yaw response, the wavelength $\lambda_w=1.5L=45$m was selected as it shows three instability zones. The summary of the observed response is depicted in Figure 5. Solid lines are boundaries for directional stability, taken directly from Figure 3. Dashed lines separated different types of observed responses.

In the case of slow speed and large wave height, the calculation shows oscillations in yaw with an increase of the amplitude (Figure 1a). The result is typical for parametric resonance and is consistent with the results of Margari and Spyrou (2022).

Decreasing the wave height leads to a normal periodic response (Figure 1b) and further to a slow-decay response (Figure 1c), which is also consistent with parametric resonance. A response to small waves shows some course-keeping error which is dependent on the values of autopilot gains (Figure 1d).

An increase in speed leads to the appearance of an interesting type of instability—oscillation with increasing amplitudes and mean (Figure 1e).

A further increase in forward speed brings the ship closer to the wave celerity, leading to monotonic growth (Figure 1f). This mechanism of instability is the same as for broaching preceded by surf-riding; the only difference being that the speed near wave celerity is prescribed, rather than being caused by surf-riding.

The gap near wave celerity is not a numerical error, its nature will be considered in the next subsection.

On the boundary of high-speed instability, an asymmetric periodic response is observed (Figure 1g). The ship seems to be knocked off course by the wave, but was able to recover.

Finally for the high speed and small wave height, a normal course-keeping response is observed (Figure 1h).

Figure 5 shows surprisingly rich dynamics for a system (1), which is essentially linear. If one removes rudder limit, the response will not qualitatively change, only it will take a bit longer for the instability to develop (see Figure 6), as the rudder is unrealistically efficient.

Neglecting rudder limits allows for defining the problem as completely linear and opens up the application of many analytical tools.

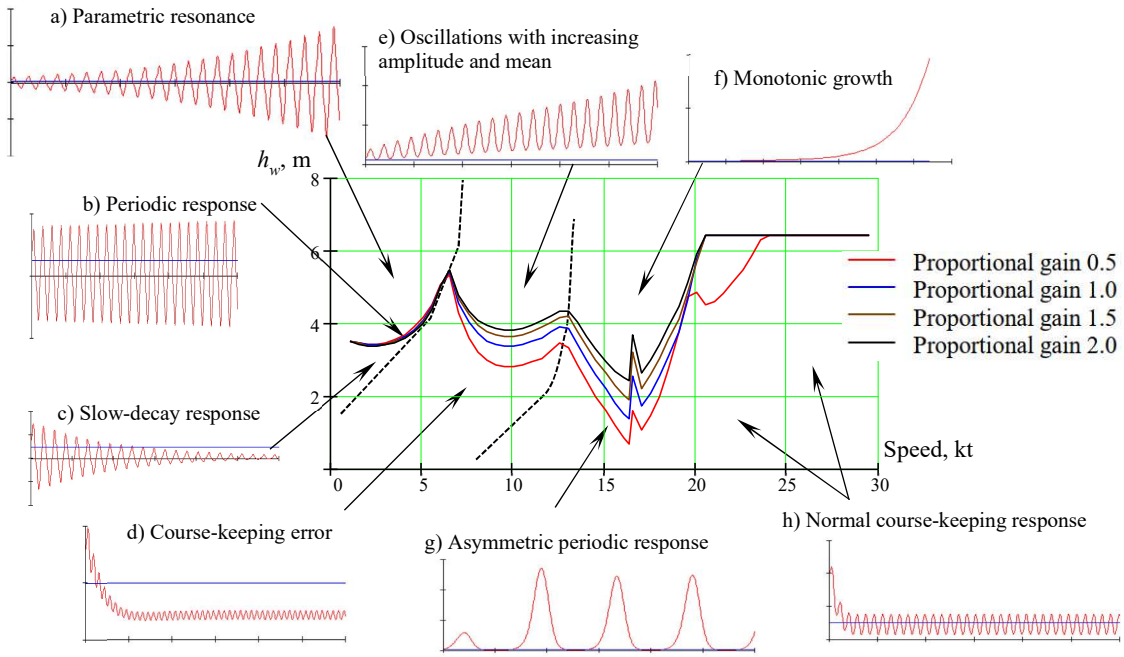

Figure 5: Summary of yaw response for $\lambda_w=1.5L=45$m. (Arrow (b) points on the boundary, other arrows identify typical responses for an area)

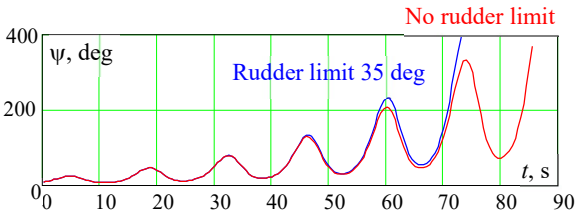

Figure 6: Yaw response at λ_w=1.5*L*=45 m, wave height h_w=4.0 m, speed 10 kt

3.3 "Gap" Response

The appearance of the "gap" just above the wave celerity at the boundary of directional stability may seem counter-intuitive at first glance. However, as is explained below, this is essentially an artifact of the simulation campaign's setup, since the required time of simulation for making the instability noticeable increases exponentially as the zero frequency of encounter is approached.

As recalled, broaching, preceded by surf-riding, is associated with forward speed, equal to wave celerity. To understand the appearance of the "gap", consider a yaw response for a wave height at the boundary of directional instability, while the forward speed equals the wave celerity. For comparison, add one more case with the slightly larger wave height, while the forward speed is just above the wave celerity, see Figure 7. The study is done for the wavelength equal to 1.5*L*.

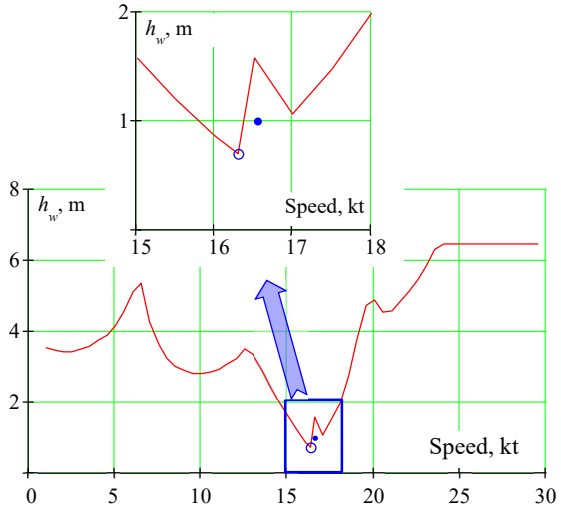

Figure 7: Cases for "Gap" study; λ_w=1.5*L*=45 m, speeds: U_1=c_w=16.292 kt, h_{w1}=0.685 m, U_2=16.542 kt, h_{w1}=1.0 m

Figure 8 shows time history of the yaw response. The numerical solution of the equations of motion (1) was carried out for longer interval of time: 400 s compare to 240 s, while computing the boundary of directional instability.

The "gap" mystery clears itself immediately. Directional instability for the speed right above the celerity does exist, but it takes longer. So if the boundary of directional instability would be computed with longer simulation time, the "gap" would be narrower. At speed exactly equal to wave celerity, the instability is displayed only if the vessel is initially placed in the vicinity of a wave trough. If placed close to a wave crest (and since during the simulated run it will remain there forever) there will be no possibility to enter the instability region of the wave. This singular case is of course theoretically interesting but has no real practical significance.

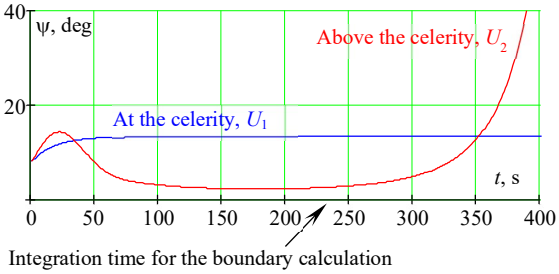

Figure 8: Yaw responses time history of "gap" study

CONCLUSIONS AND FUTURE WORK

The main motivation for this study was to look for a basic mathematical model that represents broaching dynamics. The formulation of this model includes sway and yaw equations with linear maneuvering and Froude-Krylov terms. While the autopilot model remained linear, a limit for the rudder was introduced to implement the broaching definition. However, this limit seems to not be necessary as it does not affect the qualitative outcome.

The basic mathematical model for broaching can be completely linear. As expected, the dynamics of this linear system includes parametric resonance (for cumulative broaching) and monotonic growth (for "classic" broaching near wave celerity). In addition to these phenomena, an interesting behavior was observed near the wave celerity, influenced by the very small encounter frequency.

Another interesting observation was made when the wave was longer than a ship: yaw oscillations with increasing amplitude and mean. This mode of directional instability was encountered for speeds between the parametric resonance and unlimited growth and looks like a combination of both of them. Understanding the nature of this instability remains for the future work.

ACKNOWLEDGMENTS

The work has been supported by the US Office of Naval Research (ONR) and ONR Global under Drs. Woei-Min Lin, Bob Brizzolara and Rich Meyer.

REFERENCES

Clarke, D., Gedling, P. and Hine, G., 1982, "The Application of Maneuvering Criteria in Hull Design Using Linear Theory", *Trans. RINA*.

Davidson, K. S. M., 1948, ″A note on the steering of ships in following seas.″ *Proc. of 7th Int. Congress Applied Mech.*, London.

Du Cane, P. and Goodrich, G. J., 1962, ″The following sea, broaching and surging.″ *Trans. RINA,* Vol. 104, pp. 109–140.

IMO MSC.1/Circ.1627 Interim Guidelines on the Second Generation Intact Stability Criteria. London, December, 2020.

IMO MSC.1/Circ.1652 Explanatory notes to the interim guidelines on the second generation intact stability criteria. London, April, 2023.

IMO SDC 8/INF.2 Physical Background and Mathematical Models for Stability Failures of the Second Generation Intact Stability Criteria. Submitted by ITTC, London 2021.

Holtrop, J. (1984) "A Statistical Re-Analysis of Resistance and Propulsion Data", *Int. Shipbuilding Progress*, Vol 31, No 363, pp. 272-276.

Holtrop, J. and G. G. J. Mennen (1982) "An Approximate Power Prediction Method", *Int. Shipbuilding Progress,* Vol. 29, No. 335, pp. 166-170

Margari, V. and Spyrou, K. J., 2022, "A Vulnerability Criterion of Dynamic Instability for Ship Course-Keeping in Following Waves." *Journal of Ship Research* doi: https://doi.org/10.5957/JOSR.03220010.

Margari, V., and Spyrou, K. J., 2023, "Evaluation of Practical Criterion of Ship Dynamics Course Stability for Regular Following Waves", in *Sustainable Development and Innovation in Marine Technologies*, *Proc. of the 19th Intl. Congress of the Intl. Maritime Assoc. of the Mediterranean* (*IMAM 2022*), Ergin, S. and Guedes Soares, K., eds. Taylor and Francis, ISBN 978-1-032-41618-2, pp. 17-24.

Margari, V. and Spyrou, K. J., 2025, "Robustness to Hydrodynamic Model Assumptions of Cumulative Broaching Predictions" *Proc. of the 20th Intl. Congress of the Intl. Maritime Assoc. of the Mediterranean* (*IMAM 2025*), Springer (to appear).

Margari, V. and Spyrou, K. J., 2025a, "Eliciting the bifurcation structure of cumulative broaching", Proc. of 20th Intl. Ship Stability Workshop, Chania, Greece (to appear)

Nomoto, K., Taguchi, T., Honda, K. and Hirano, S. (1957) On the steering qualities of ships, *International Shipbuilding Progress*, Vol. 4.

Oosterveld, M. W. C. and P van Oossanen (1975) Further Computer-analyzed Data of the Wageningen B-screw Series' " *Int. Shipbuilding Progress,* Vol. 22, No. 251, pp. 251 – 262. DOI: 10.3233/ISP-1975-2225102

Spyrou, K., 1996, "Dynamic Instability in Quartering seas: the Behavior of a Ship during Broaching", *Journal of Ship Research*, Vol. 40, No 1, pp. 46-59.

Spyrou, K., 1996a, "Dynamic Instabilities in Quartering seas – Part II: Analysis of Ship Roll and Capsize for Broaching", *Journal of Ship Research*, Vol. 40, No 4, pp. 326-336.

Spyrou, K., 1997, "Dynamic instabilities in quartering seas – part III: nonlinear effects on periodic motions", *Journal of Ship Research*, Vol. 41, No 3, pp. 210-223.

Spyrou, K.J. 2000, "Similarities in the yaw and roll dynamics of ships in extreme astern seas", in *IUTAM Symposium on Recent Developments in Non-linear Oscillations of Mechanical Systems,* Nguyen Van Dao and E.J. Kreuzer eds., Kluwer Academic Publishers, Dodrecht/Boston/London, ISBN 0-793-6470-8, pp. 279-290.

Spyrou, K. J., 2008, "A note on a simplified model of ship yawing in steep following seas" in *Maritime Industry, Ocean Engineering and Coastal Resources*, Guedes Soars, C. and Kolev, P., eds., Taylor & Francis Group, London, ISBN 978-0-415-45523-7, pp. 85-93.

Spyrou, K. J., 2011, "Perceptions of Broaching-To: Discovering the Past", Chapter 22 of "*Contemporary Ideas on Ship Stability*", Neves, M.A.S., Belenky, V., de Kat, J. O., Spyrou, K. and N. Umeda, eds., Springer, ISBN 978-94-007-1481-6, pp. 399-414.

Spyrou, K. J., 2011a, "Parallels of Yaw and Roll Dynamics of Ships in Astern Seas and the Effect of Nonlinear Surging", Chapter 20 of "*Contemporary Ideas on Ship Stability*", Neves, M.A.S., Belenky, V., de Kat, J. O., Spyrou, K. and N. Umeda, eds., Springer, ISBN 978-94-007-1481-6, pp. 363-378.

Umeda, N., 1999, ″Nonlinear Dynamics on Ship Capsize due to Broaching in Following and Quartering Seas″ *J. Marine Science and Technology*, Vol. 4, pp. 16–26.

Wahab, R. and W. A. Swaan (1964) ″Coursekeeping and broaching of ships in following seas.″ *J. Ship Research*, Vol. 7, No. 4, pp. 1–15.

Session 4
Design and operational safety

Estimation of the natural roll period of a large containership from ship motion observed during voyages

Yuhei Higo, *Graduate School of Engineering, Osaka Metropolitan University*
sh23154c@st.omu.ac.jp
Ryo Chikamori, *Graduate School of Engineering, Osaka Metropolitan University*
sh24455i@st.omu.ac.jp
Hirotada Hashimoto, *Graduate School of Engineering, Osaka Metropolitan University*
hashimoto.marine@omu.ac.jp
Yusuke Yamamoto, *The Japan Fisheries Research and Education Agency*
yamamoto_yusuke94@fra.go.jp
Yoriyuki Masutani, *The Japan Fisheries Research and Education Agency*
masutani_yoriyuki29@fra.go.jp
Akihiko Matsuda, *The Japan Fisheries Research and Education Agency*
matsuda_akihiko34@fra.go.jp

ABSTRACT

To properly evaluate a ship's vulnerability to parametric rolling, it is desirable to know its natural roll period during voyages. In this study, a practical method is proposed to estimate the natural roll period from ship motion data observed during voyages. The aim is to better understand the actual characteristics of the natural roll period of modern large containerships during operations. First, roll and pitch motions were measured during a voyage of a small research vessel capable of directly measuring the natural roll period. From the measurements, the basic idea to estimate the natural roll period from measured ship motions was derived. Second, a free-running model test simulating a large containership was conducted, and a practical method was proposed to estimate the natural roll period from measured roll and pitch motions in long-crested and short-crested irregular waves. Finally, the proposed method was applied to motion data of a large containership observed during actual voyages, and the distribution of natural roll period was estimated. As a result, the actual characteristics of the natural roll period in a recent large containership during voyages were clarified.

Keywords: *Natural Roll Period, Large Containership, Parametric Roll.*

1. INTRODUCTION

In the assessment of parametric rolling, the estimation accuracy of the natural roll period has a significant impact. The IMO's Interim Guidelines (MSC.1/Circ.1627) on Second Generation Intact Stability Criteria (SGISc) allow the use of the weather criterion formula from the 2008 IS Code when reliable data are unavailable. However, it has been pointed out that this formula is not accurate for large containerships. The explanatory notes to the SGISc (MSC.1-Circ.1652) include an estimation formula for the natural roll period that accounts for the loading conditions of containerships. However, the number of reports on the actual value of natural roll period of modern large containerships is limited, e.g. [Grin, 2024], it is difficult to evaluate the merits and drawbacks of each estimation formula.

To properly assess a ship's vulnerability to parametric rolling, it is essential to know the natural roll period during voyages. For containerships, whose natural roll period varies significantly depending on loading conditions, it is particularly important to establish a method that allows easy and accurate estimation while at sea. Recently, a methodology based on the Fast Fourier Transform (FFT) was proposed for the real-time estimation of the natural roll period, and it was validated in a real environment using a trawler [Santiago Caamaño et al., 2022]. The FFT has been used to estimate the natural roll period of ships so far, its accuracy significantly depends on the roll motion data to

which the FFT is applied. In this study, conditions for extracting data of measrued roll motions suitable for FFT analysis were derived, and then the natural roll period of a large containership was estimated from observed ship motions during actual voyages.

2. ESTIMATION OF NATURAL ROLL PERIOD FROM SHIP MOTION OF A SMALL RESEARCH VESSEL

On October 10 and 11, 2024, ship motions were measured onboard using a smartphone app developed by the authors [Higo et al., 2024], during a wave measurement experiment by Yokohama National University outside Tateyama Bay, Chiba, Japan. The experiment was carried out using the Takamaru, a fisheries research vessel (Length 29.5m) operated by the Japan Fisheries Research and Education Agency.

On October 10, an octagonal sailing was performed at a speed of 4 knots, consisting of eight 6-minute runs in directions spaced at 45-degree intervals following the previous research [Terada et al., 2018]. Additionally, a square sailing was conducted at a speed of 8 knots, consisting of four 6-minute runs in directions spaced at 90-degree intervals. The octagonal sailing was repeated on October 11.

The measured roll motion was analyzed using a 6-minute segmented data with drift components removed. The FFT was applied to the data, and the peak frequency/period of the resulting power spectrum, referred to as dominant frequency/period hereafter, was used as the estimated natural roll period. The information of waves encountered was provided by Yokohama National University, and the reference natural roll period was supplied by the National Maritime Research Institute. The definition of wave encounter angle is shown in figure 1.

The analysis results of the octagonal and square sailings conducted on October 10, as well as the octagonal sailing on October 11, are summarized in Table 1. Among the 16 data points from eight directions, 13 were estimated with less than 10% error, and the remaining 3 had errors exceeding 10%. Additionally, among the four data points collected from 4 directions, 3 were estimated with less than 10% error, and the remaining 1 had an error exceeding 10%. The error of 10% was set as an acceptable error because the accuracy of the estimation formulae for the natural roll period proposed by classification societies was somewhat more than 10% maximum for the subject vessel [Higo et al., 2024]. Since these estimation formulae require a metacentric height (GM) value, they are difficult to apply to the estimation of natural roll period during voyages.

Focusing on the four results with poor estimation accuracy, no consistent trend was observed indicating reduced accuracy at specific wave encounter angles. A possible cause of the large errors is that roll motion occurred at or near the wave encounter period. To investigate this, the difference between the dominant period of roll and pitch motions was analyzed. For the four data points with large errors, the differences between the dominant period of roll and pitch motions were 0.38, 0.40, 1.14, and 0.00 seconds, indicating that the dominant periods of roll and pitch were close in these cases.

The value of GM of ships is typically unknown and can vary significantly depending on the loading condition. Therefore, a practical method focusing on the dominant periods of roll and pitch, both of which can be measured using a smartphone app, will be considered. When data points with a difference between the dominant period of roll and pitch motions of less than or equal to 1.14 seconds were excluded, 10 out of the 20 total data points were removed. Among those removed, the 4 data points with poor estimation accuracy were included. The average of the remaining 10 data points yielded a natural roll period of 5.60 seconds, with an estimation accuracy of 0.93%.

In addition, to examine the effect of measurement time, an octagonal sailing for 12 minutes in each direction was performed on October 12, and the analysis results are shown in Table 2. The waves encountered were not measured on the day. As the measurement time increased, the number of data points that can be used to estimate the natural roll period increased. This indicates the possibility that the longer the measurement time, the more appropriate the data can be collected in estimating the natural roll period from the roll and pitch motions.

From the above, it was confirmed that by excluding roll data occurring near the wave encounter period, the natural roll period can be estimated only using the FFT with sufficient accuracy for practical applications.

Table 1: Estimated natural roll period of the Takamaru (6-minitute sailing in each direction).

2024/10/10 Octagonal sailing

H1/3 [m]	T02 [sec]	Peak direction [deg]	Natural roll period [sec]	
1.07	4.24	307.5	5.65	
Wave encounter angle [deg]	Dominant period of roll motion [sec]	Estimation errpr of the natural roll period [%]	Dominant period of pitch motion [sec]	Difference between the dominant period of roll and pitch motions [sec]
7.5	5.605	-0.8	5.77	-0.16
52.5	5.845	3.5	6.705	-0.86
97.5	5.625	-0.4	5.855	-0.23
142.5	4.57	-19.1	4.195	0.38
187.5	3.98	-29.6	3.575	0.40
232.5	5.29	-6.4	3.495	1.80
277.5	5.49	-2.8	3.56	1.93
322.5	5.56	-1.6	4.22	1.34

2024/10/10 Square sailing

H1/3 [m]	T02 [sec]	Peak direction [deg]	Natural roll period [sec]	
0.89	3.72	40.7	5.65	
Wave encounter angle [deg]	Dominant period of roll motion [sec]	Estimation errpr of the natural roll period [%]	Dominant period of pitch motion [sec]	Difference between the dominant period of roll and pitch motions [sec]
49.3	4.855	-14.1	3.72	1.14
139.3	5.215	-7.7	3.02	2.20
229.3	5.49	-2.8	5.46	0.03
319.3	5.845	3.5	9.21	-3.37

2024/10/11 Octagonal sailing

H1/3 [m]	T02 [sec]	Peak direction [deg]	Natural roll period [sec]	
1.1	5.034	196.5	5.65	
Wave encounter angle [deg]	Dominant period of roll motion [sec]	Estimation errpr of the natural roll period [%]	Dominant period of pitch motion [sec]	Difference between the dominant period of roll and pitch motions [sec]
28.5	5.875	4.0	5.48	0.40
73.5	5.625	-0.4	5.175	0.45
118.5	5.695	0.8	4.14	1.56
163.5	5.555	-1.7	3.995	1.56
208.5	5.77	2.1	4.625	1.15
253.5	6.16	9.0	4.22	1.94
298.5	5.395	-4.5	8.23	-2.84
343.5	7.925	40.3	7.925	0.00

Table 2: Estimated natural roll period of the Takamaru (12-minitute sailing in each direction).

2024/10/12 Octagonal sailing

H1/3 [m]	T02 [sec]	Peak direction [deg]	Natural roll period [sec]	
N/A	N/A	N/A	5.65	
Wave encounter angle [deg]	Dominant period of roll motion [sec]	Estimation errpr of the natural roll period [%]	Dominant period of pitch motion [sec]	Difference between the dominant period of roll and pitch motions [sec]
N/A	5.385	-4.7	3.675	1.71
N/A	5.375	-4.9	3.3	2.08
N/A	5.47	-3.2	2.945	2.53
N/A	5.455	-3.5	4.645	0.81
N/A	5.455	-3.5	3.205	2.25
N/A	5.47	-3.2	3.31	2.16
N/A	5.455	-3.5	3.11	2.35
N/A	3.99	-29.4	3.975	0.02

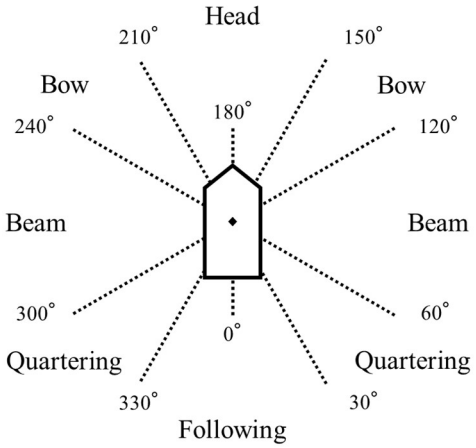

Figure 1: The definition of wave encounter angle/direction.

3. ESTIMATION OF NATURAL ROLL PERIOD OF SCALED MODEL OF A LARGE CONTAINERSHIP

It is essential to verify that the natural roll period can be estimated for modern containerships, which are known to be vulnerable to parametric rolling and exhibit a wide range of natural roll periods. To this end, a free-running model test simulating a containership over 350 meters in length was conducted at the Marine Dynamics Basin of the Japan Fisheries Research and Education Agency.

The most frequent values of significant wave height and wave period were obtained from the IACS Rec. No.34 (Rev.1) [IACS, 2000] used in the Interim Guidelines on SGISc and were adopted as the wave conditions for both long-crested irregular waves and short-crested irregular waves. Regarding ship speed, the propeller rotation rate was determined to coincide with the median value of speed over gournd of containerships over 300 meters during actual navigation, which is corredponding to the Froude number of 0.163, as identified in the authors' previous analysis of satellite AIS data [Hashimoto and Furusho, 2022]. Since the natural roll period during voyages is unknown, the value of the subject ship is presumed by the regression formula proposed by Morita [IMO, 2024], which does not include the ship length as a variable, and the value scaled down to the ship model is used. The wave encounter angles were set from head seas to bow seas and from following seas to quartering seas, due to the limited width of the basin.

Table 3: Estimated natural roll period of scaled model of a large containership.

Free-running model test Long-crested irregular waves

H1/3 [m]	T01 [sec]	Natural roll period [sec]		
0.015	1.04	2.44		
Wave encounter angle [deg]	Dominant period of roll motion [sec]	Estimation error of the natural roll period [%]	Dominant period of pitch motion [sec]	Dominant period ratio (roll / pitch) [%]
180	2.33	-4.5	0.98	237.8
157.5	1.97	-19.3	1.07	184.1
135	2.56	4.9	0.91	281.3
5	2.13	-12.7	1.16	183.6
22.5	1.6	-34.4	1.97	81.2
45	1.6	-34.4	1.71	93.6

Free-running model test Short-crested irregular waves

H1/3 [m]	T01 [sec]	Natural roll period [sec]		
0.015	1.04	2.44		
Wave encounter angle [deg]	Dominant period of roll motion [sec]	Estimation error of the natural roll period [%]	Dominant period of pitch motion [sec]	Dominant period ratio (roll / pitch) [%]
180	2.33	-4.5	1.11	209.9
157.5	2.23	-8.6	1.02	218.6
135	2.33	-4.5	1.07	217.8
5	1.71	-29.9	1.65	103.6
22.5	2.13	-12.7	1.97	108.1
45	1.83	-25.0	1.22	150.0

Table 3 presents the results of estimating the natural roll period from roll and pitch motion data measured in the free-running model tests in both long-crested and short-crested irregular waves. In the case of long-crested irregular waves, 2 out of 6 data points had errors less than 10% in estimating the natural roll period, while the remaining 4 showed errors exceeding 10%. In the case of short-crested irregular waves, 3 out of 6 data points had errors less than 10%, and the remaining 3 showed errors exceeding 10%.

For the data with large errors, the absolute differences between the dominant periods of roll and pitch were relatively small, with values of 0.90, 0.97, 0.37, 0.11, 0.06, 0.16, and 0.61 seconds. In order to avoid judging the data to be excluded by using the dimensional value of the difference, the exclusion judgment was performed on the condition that the dominant period of roll was more than 2 times the dominant period of pitch, which was determined by the experimental results. Finally, the average of natural roll periods was 2.39 seconds, with a estimation accuracy of 2.0% error, which is sufficient for practical applications.

4. ESTIMATION OF NATURAL ROLL PERIOD OF A LARGE CONTAINERSHIP FROM SHIP MOTIONS OBSERVED DURING VOYAGES

The estimation of natural roll period of a large containership was attempted using the same method derived from the results of free-running model test in the previous section. The method relies on roll and pitch motion data measured onboard during navigation. For this study, approximately eight months of voyage data of a containership over 350 meters in length were used. Only data collected when the onboard wave radar was activated were used for the estimation. As it provides updates at 10-minute intervals, consequently, 10-minute motion data segments were subjected to FFT analysis to determine dominant periods of roll and pitch. The time series data used for the analysis were recorded at a sampling frequency of 10 Hz. In the FFT, the linear trend was removed and the Hanning function was used as the window function. The peak frequency in the range of 0.02 Hz to 5.0 Hz was extracted from the obtained spectrum. To ensure meaningful results, only data with significant wave height of 1.5 meters or greater were considered to exclude negligibly small roll motions. In accordance with the findings of the preceding section, datasets in which the dominant period of roll was at least twice that of the pitch were extracted, and the average of these values was considered as the natural roll period of the subject containership.

Figure 2 shows the estimated results of natural roll periods for each wave direction in a box-and-whisker plots (whisker length in the range of 5~95%). The definition of wave direction can be found in figure 1. For reference, the frequency distributions of dominant period of roll and pitch, and log speed for each wave direction are shown in figure 3, 4 and 5.

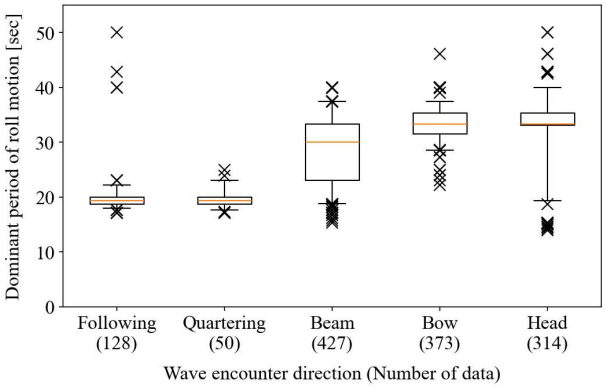

Figure 2: Estimated natural roll period of a large containership using extracted data whose dominant period of roll is longer than two times that of pitch.

In figure 2, the results in following and quartering seas exhibited a different trend compared to other wave encounter directions. Although the natural roll period can widely change depending on the loading condition, the distribution of it should not vary a lot with the wave encounter direction. To investigate this discrepancy, the correlation between the wave encounter period, observed from the wave radar, and the peak period of the pitch power spectrum, derived using the FFT, was examined. As shown in figure 6, a significant mismatch between the two periods was observed under following and quartering sea conditions.

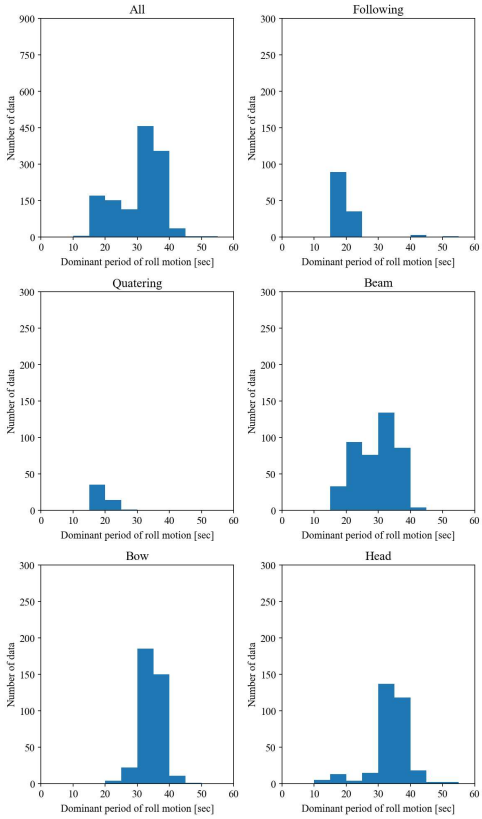

Figure 3: Histogram of dominant period of roll of a large containership (after extraction).

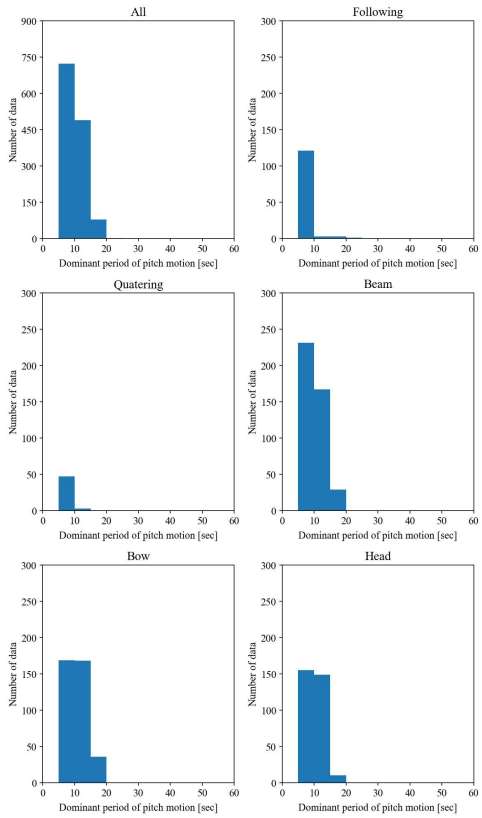

Figure 4: Histogram of dominant period of pitch of a large containership (after extraction).

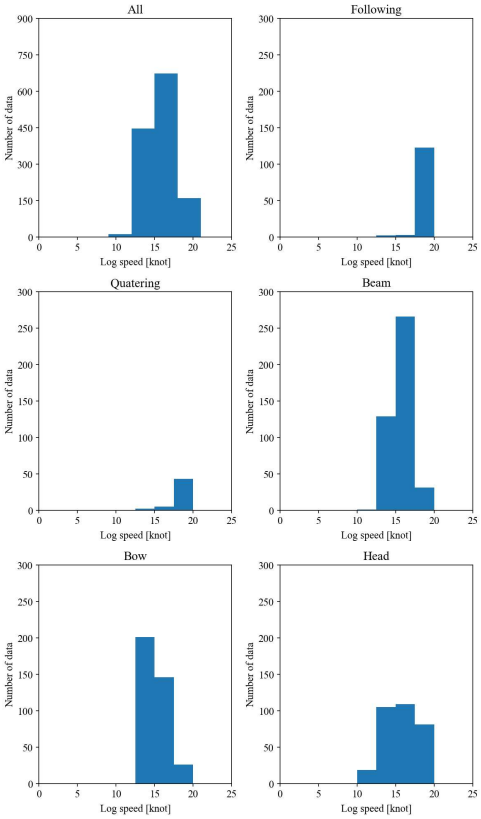

Figure 5: Histogram of log-speed of a large containership (after extraction).

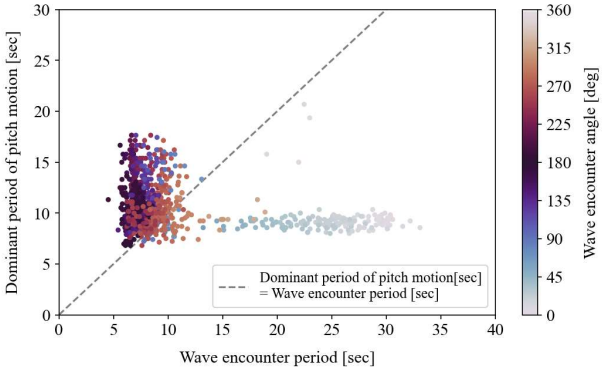

Figure 6: Correlation between the wave encounter period and the dominant period of pitch.

Figure 7 shows an example of the time series of roll and pitch in following seas, and FFT analysis results. The wave encounter period by the wave radar was 29.68 seconds, while the dominant period of roll was 8.82 seconds, which is a large discrepancy. Although a second highest peak can be confirmed near the wave encounter period, the natural pitch period of the subject ship is assumed to be around 9 seconds, and it is inferred that the first highest peak appears near the natural pitch period. Noted that the tendency that the estimation accuracy of the natural roll period is poor in the following and

quartering seas is consistent with the results of the free-running model tests shown in Tables 3-4.

By excluding data associated with two directions, following and quartering seas, the estimated natural roll period was determined to be 32.7 seconds on average.

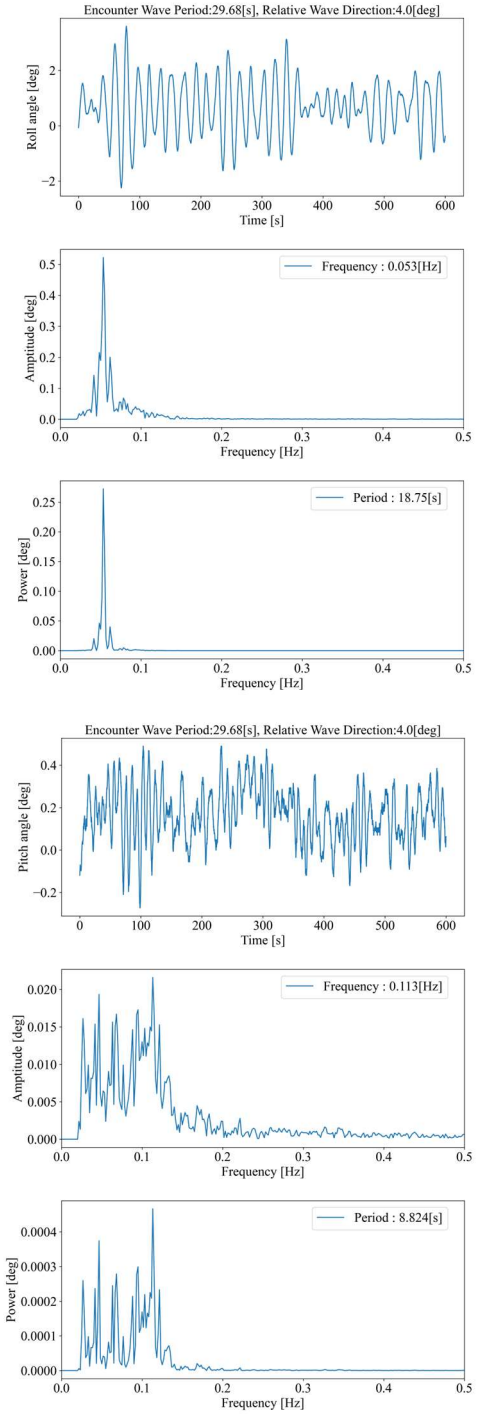

Figure 7: An example where the wave encounter period does not coincide with the dominant period of pitch (wave encounter angle of 4°).

For reference, figures 8-10 show the histograms of dominant periods of roll and pitch, and encounter wave period by the wave radar in the data before extraction, i.e., all data with a significant wave height of 1.5 m or more. From the comparison of figure 8 and 10, it can be confirmed that the roll motion of the subject large containership occurs not only near the wave encounter period but also in a wide range of periods. From the comparison of figure 9 and 10, it can be confirmed that, except for the following sea, the dominant period of roll roughly agrees with the frequency distribution of the wave encounter period.

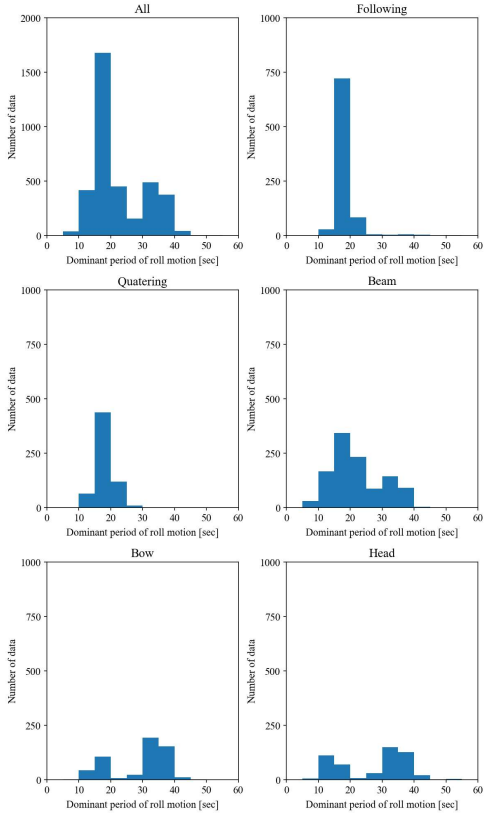

Figure 8: Histogram of dominant period of roll of a large containership (before extraction).

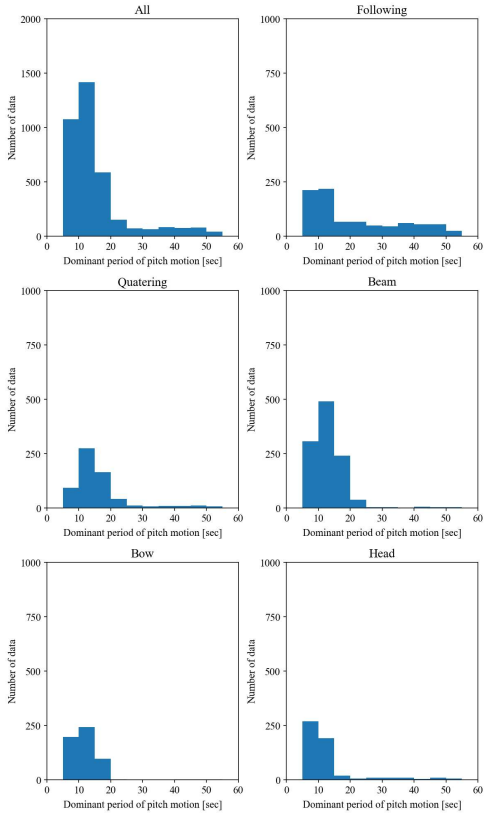

Figure 9: Histogram of dominant period of pitch of a large containership (before extraction).

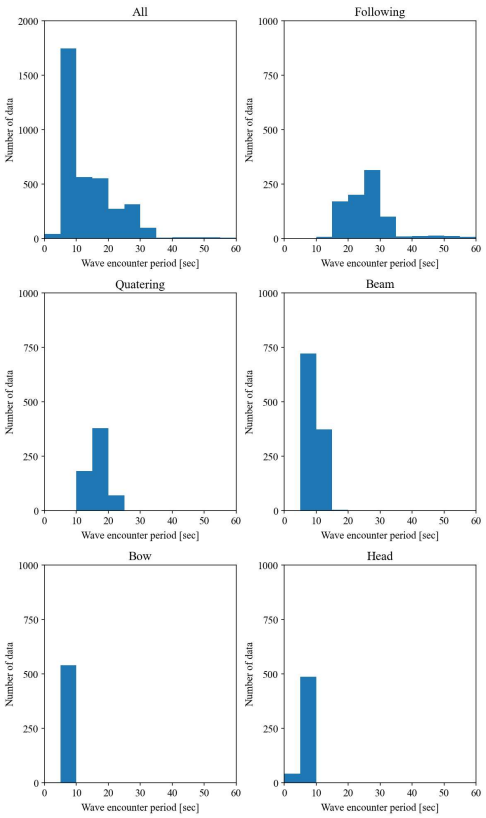

Figure 10: Histogram of wave encounter period of a large containership (before extraction).

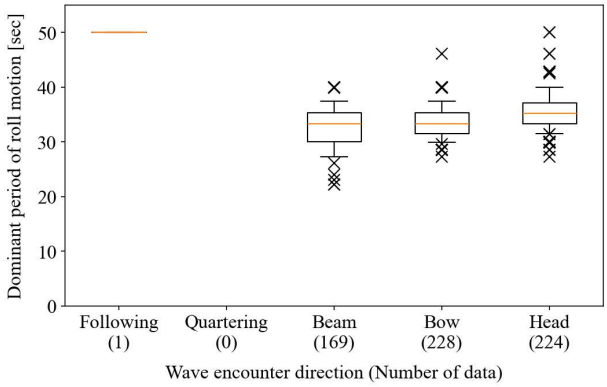

Figure 11: Estimated natural roll period of a large containership using extracted data whose dominant period of roll is longer than three times that of pitch.

Since the measurement data of wave radar was included in the voyage data, it was possible to omit the data in which the dominant period of pitch and the wave encounter period did not coincide. However, in general, the data of wave radar is not available. Therefore, the data extraction condition was changed to be more conservative as a trial. Figure 11 shows the estimated results of natural roll period using extracted data in which the dominant period of roll is longer than 3 times the dominant period of pitch. This extraction condition is intended to extract data in which the dominant period of roll is surely differ from the wave encounter period. In addition, it can eliminate data at low-frequency encounter waves that are difficult to distinguish from the roll at around natural roll period. As a result, the number of extracted data for following and quartering seas became one, and the natural roll period was estimated to be 34.0 seconds on average.

5. CONCLUSIONS

It was confirmed that the natural roll period can be estimated from the motion data of the small research vessel when there is a sufficient difference between the dominant periods of roll and pitch. Subsequently, free-running model tests were conducted simulating a large containership, and it was confirmed that the natural roll period can be estimated under conditions where the dominant period of roll is at least twice the dominant period of pitch, both in long-crested and short-crested irregular waves. Finally, the same method and extraction condition used in the model experiments was applied to the motion data of the large

containership observed during its voyage. If excluding following and quartering seas, where the correlation between the wave encounter period and the dominant period of pitch is poor, the estimated natural roll period during approximately eight months of the voyage was 32.7 seconds on average. In addition, the estimation result when the more conservative extraction condition of the data was applied was also presented.

ACKNOWLEDGEMENT

This research was carried out as a research activity of the Goal-based Stability Criteria Project of the Japan Ship Technology Research Association in the fiscal year of 2024, funded by the Nippon Foundation. The authors would like to express sincere gratitude to NYK Line who provided the voyage data of a large containership, the crews of Takamaru cooperated for the onboard measurement, Prof. Yoshiaki Hirakawa who provided the wave measurement results, and Dr. Takako Kuroda who provided the free-roll test result of the Takamaru, and Prof. Emeritus Naoya Umeda for his thoughtful discussions.

REFERENCES

Grin, R., 2024, On empirical methods to predict the rolling period of ships, in Proceedings of 15th International Marine Design Conference (IMDC-2024), Amsterdam.

Hashimoto, H., Furusho, K., 2022, Influence of sea areas and season in navigation on the ship vulnerability to the parametric rolling failure mode, Ocean Engineering, 266(1), 112714.

Higo, Y., Hashimoto, H., Matsuda, A., Yoshioka, H., 2024, Using Smartphones to Estimate Natural Roll Period of Ships in Actual Navigation, in Proceedings of the 2nd International Conference on the Stability and Safety of Ships and Ocean Vehicles, Wuxi.

IACS, 2000, IACS Recommendation No.34 (Rev.1), Standard Wave Data.

IMO, 2024, Alternative Roll Period Formula to Be Used for the Second Generation Intact Stability Criteria, submitted by Japan, MSC 108/INF.7.

Santiago Caamaño, L., Míguez González, M., Allegue García, S., 2022, Evaluation of Onboard Stability Assessment Techniques Under Real Operational Conditions, Ocean Engineering, Vol. 258, pp. 111841.

Terada D, Hashimoto H, Matsuda A, Umeda N., 2018, Direct estimation of natural roll frequency using onboard data based on a Bayesian modelling procedure. in Proceedings of the 13th international conference on the stability of ships and ocean vehicles, Kobe.

Application of a stability monitoring system to naval vessels

Lucía Santiago Caamaño, *Grupo Integrado de Ingeniería, CITENI, Campus Industrial de Ferrol, Universidade da Coruña,* lucia.santiago.caamano@udc.es

Ismael Díaz González, *Centro Mixto de Investigación UDC-Navantia,* ismael.diaz1@udc.es

Marcos Míguez González, *Grupo Integrado de Ingeniería, CITENI, Campus Industrial de Ferrol, Universidade da Coruña,* marcos.miguez@udc.es

ABSTRACT

This paper presents the adaptation and application of a real-time stability monitoring system to a naval vessel. Originally developed for fishing vessels, the system has been enhanced to meet the requirements of military operations, where mission constraints and extended vessel lifespans pose significant challenges to weight management and stability. Using roll motion data and spectral analysis, the system provides continuous estimates of natural roll frequency and metacentric height, enabling onboard assessment of the ship's stability level without requiring interaction with the crew. The system was deployed and tested on a naval vessel over a four-day navigation in Galician waters. Results show that the system successfully tracks variations in natural roll frequency with reasonable accuracy, and the use of averaged estimates significantly reduces output dispersion, offering a reliable basis for real-time stability awareness and safety alerts in naval environments.

Keywords: *Stability monitoring, Real-time, Naval vessel, Navigation.*

1. INTRODUCTION

Stability guidance systems have emerged as alternative to deal with the problematic in the fishing sector: the high fatal accident rate. Accidents have multiple natures, however, the main cause of fatalities are the stability-related issues (Transportation Safety Board of Canada, 2012).

Several guidance systems have been developed and implemented through the past years to try to sort of the problem. Some well-known approaches are the Womack matrix and the Norwegian stability poster (Deakin, 2005). Nevertheless, there are also some computer based systems such as SEMPEO or the one proposed by Terada et al. (D. Terada, Hashimoto, et al., 2018; D. Terada, Tamashima, et al., 2018; Daisuke Terada et al., 2016; Varela et al., 2010).

In previous workshops and STAB Conferences (ISSW 2017, STAB 2018, ISSW 2019 and ISSW 2022), some of the authors have proposed different alternatives for developing a real-time stability assessment system aimed at being used onboard fishing vessels, which could operate with no need of crew interaction.

Under the framework of Centro Mixto de Investigación UDC-Navantia in which the authors collaborate, one of the areas in the research line of digital twins is the development of a stability monitoring system for naval vessels. Despite of any operation of navy involves a certain level of risk, the situation is quite different from fishing vessels or any other comercial vessel. On the one hand, navy is not governed by IMO regulations and a naval vessel cannot modify or cancel a mission due to harsh weather conditions (Peters, 2019; Reed, 2011).

On the other hand, the source of stability related problems comes from the control of weights on board. Naval vessels are designed with a life expectancy of 25-35 years. During their service life, it is expected that weapon systems will be replaced several times and a variation on the demand of carrying payloads of unknown weight. But at the same time, it is expected to cope during the entire life span with the initial requirements and design standards. For this reason, naval vessels are desined for a certain displacement and vertical center of gravity (KG) including acceptable margins for future growth over the life expectancy (Fleisher & Catton, 2024; Gale, 1975; Kern, 1982; Pedatzur, 2016; Perrault et al., 2010).

Monitoring the displacement and KG become crucial to not reach the future growth margin in a few years and verify that the vessel still comply with the safety requirements. Usually an increase in weight leads to a

reduction in the stability level. The non-compliance of the standards could imply restrictions on the vessel's operability or the need of a ship life extension program, which is very expensive (Fleisher & Catton, 2024; Gale, 1975; Kern, 1982; Pedatzur, 2016; Perrault et al., 2010).

As regulations do not force to perform an inclining test each time an upgrade is done, it is very difficult to carry out an appropiate control of weight and KG. In consequence, the stability margins are unknown.

Considering all these facts, stability monitoring systems are becoming very attractive in the sector as they provide stability information and some guidance.

In this paper, the stability monitoring system developed by the authors has been adapted and applied to a naval vessel. The purpose is to provide information to the crew about the stability level in real-time. In case the stability could be compromise an alarm will be triggered. The system has been tested in a real ship during a 4-days navigation in Galician waters.

The paper is structured as follows. Sections 2 and 3 contains the methodology and navigation descriptions meanwhile sections 4 and 5 provide the results and conclusions.

2. METHODOLOGY

The real-time stability monitoring system is built on the methodology developed in (Míguez González et al., 2017, 2018). The methodology is based on the assumption that roll spectrum has a peak around its natural frequency. Then, if roll spectrum can be calculated the natural roll frequency can be obtained and, in consequence, the metacentric height. Therefore, the methodology can be considered vessel model independent, as the only data required are the roll motion and the beam of the ship.

The architecture of the system is shown in Figure 1.

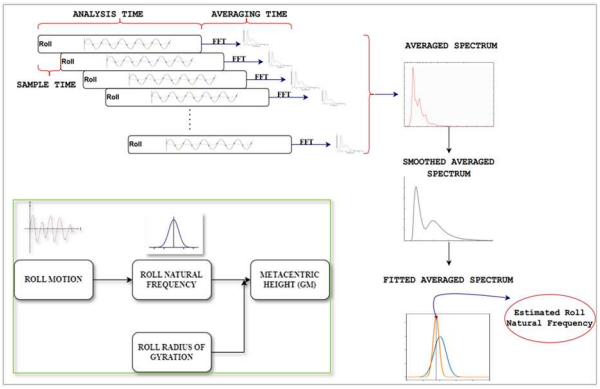

Figure 1: System architecture.

First, roll motion is measured during three minutes and the spectrum is computed using the Fast Fourier Transform (FFT). As stated in previous papers, three minutes have been considered, on the one hand, to have a sufficiently long time series to compute the FFT with a certain quality, and on the other hand, to have an output in the system in a very short time to be able to take action if needed before the vessel capsizes. A fishing vessel may sink in 8 minutes.

In order to have an output in the system in less than three minutes, overlap has been considered. In consequence, new roll measurements will contain 10 new seconds plus 170 seconds of the previous chunk.

After obtaining 12 roll spectra, the average spectrum is computed. The purpose is to avoid possible variations of the roll spectrum with time due to external factors.

Then, the averaged spectrum is smoothed with a Savitzky-Golay filter and fitted with a Gaussian function. After this process, the main peak of the spectrum is assumed to be the natural roll frequency.

Furthermore, in order to try to reduce the number of outliers in the estimated natural roll frequency, the average of the past 12 estimations is computed.

The results will be analyzed comparing the median and the percentiles 95th and 5th.

Finally, for each obtained value of natural roll frequency the metacentric height can be approximated as:

$$GM = \frac{{k_{xx}}^2 {\omega_0}^2}{g} \quad (1)$$

Being k_{xx} the roll gyradius taken as a 40% of the beam, ω_0 the natural roll frequency and g the gravity acceleration.

3. NAVIGATION

The system was installed on board a naval vessel whose main characteristics are shown in Table 1.

Table 1: Test vessel main characteristics.

Dimension	Test Vessel
Displacement (Δ)	1051.67 t
Overall length (L_{oa})	68.66 m
Beam (B)	11.10 m
Depth (D)	7.00 m
Draft (T)	3.36 m

In order to calculate the loading condition details, data from the vessel has been provided by the

crew. At the departure from port, drafts have been registered and during navigation, every 8 hours, the consumptions have been monitored. Also, the lightweight has been provided. With these data, the displacement, the coordinates of the center of gravity and the GM of the ship during the entire navigation have been calculated. No inclining experiment has been performed due to the high cost.

It is important to mention that the loading condition did not change significantly during the navigation as the only variation onboard were the consumptions that did not have a big impact. In consequence, for the entire navigation the calculated value of the natural roll frequency is 0.63 rad/s.

Figure 2: System installed on board.

To monitor roll motion in real-time, a laptop and an Inertial Measurement Unit (IMU) have been installed on board (Figure 2). The IMU is the MRU 6000 Marine from Norwegian Subsea and the sampling frequency was 10 Hz. After a brief training, the crew operated the software with the implemented methodology with no incidences.

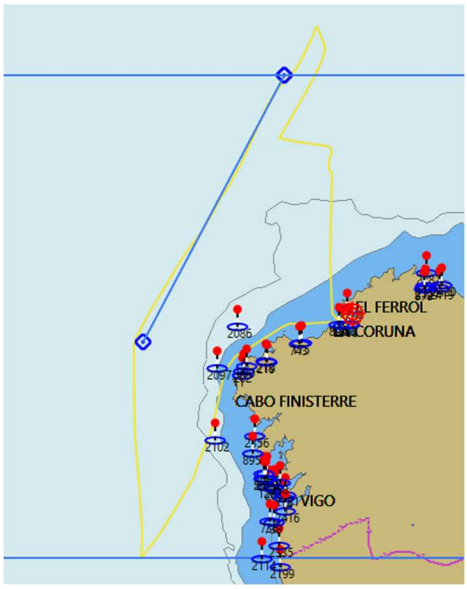

Figure 3: Approximated navigation route.

The navigation took place in October 2024 and last 4 days. The departure and arrival port was Ferrol and the route was in Galician waters. The approximated route is marked in Figure 3. The results provided correspond to the section of the route that is marked with a straight blue line.

The average speed on the navigational route was 8.7 knots, with a minimum speed of 4.9 knots and a maximum of 14.9 knots. Except on the departure from or arrival to the estuary where the port is located in which the speed is limited due to the characteristics of the area.

Regarding the sea state during the navigation, wave conditions have been provided by Puertos del Estado (Puertos del Estado, 2021) via the closest wave rider buoy and can be seen in Table 2.

Table 2: Wave parameters.

Day	Time	T_p (s)	H_s (m)	Peak Direction (deg)
1	16:00	7.23	1.88	262
2	00:00	9.18	2.70	208
2	08:00	13.28	4.22	242
2	16:00	11.72	3.16	245
3	00:00	10.55	2.23	256
3	08:00	10.55	1.41	225
3	16:00	7.23	1.17	267
4	00:00	9.96	0.94	329
4	08:00	7.62	0.94	290

4. RESULTS

In this section, the results of the output of the system are presented. In total 27 hours of navigation have been analyzed.

Figure 6 shows, on the top, the roll motion during the first 15 minutes and, on the bottom, the output of the system. The green dots represent the estimated natural roll frequency, the red line the average of the past 12 estimates and the black dashed line the target natural roll frequency (0.63 rad/s). As it can be seen, roll amplitude is small not reaching 5 degrees. Regarding the performance of the system, it can be appreciated that during the first 5 minutes there is no output. The reason is that the first measurement takes 3 minutes and the other 2 minutes correspond to the time to average the spectrum. In any case, as in that moment the vessel is leaving the port it would not suppose any risk for the crew.

To have a more detailed picture of what is happening inside the system, Figures 4 and 5 plot the computation of the spectra and the main peak. The blue line represents the roll spectrum obtained from FFT, the orange line represents the roll spectrum after the smoothing and the green dashed line the roll spectrum after the Gaussian fitting. Finally, the red

dot represents the estimated natural roll frequency, i.e., the peak of the roll spectrum after the Gaussian fitting.

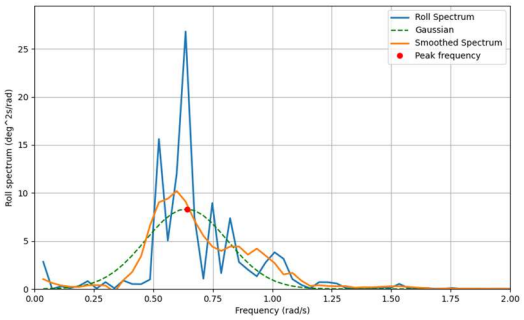

Figure 4: Roll spectrum computed with the FFT, after smoothing and after the Gauss fitting for the time trace 8.82 minutes.

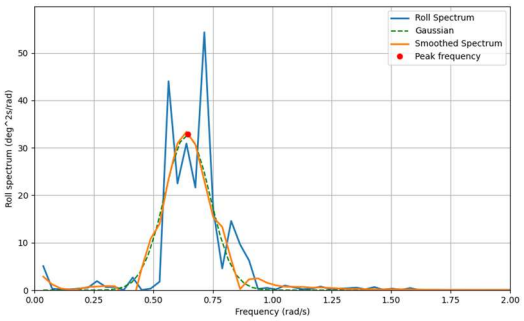

Figure 5: Roll spectrum computed with the FFT, after smoothing and after the Gauss fitting for the time trace 12.15 minutes.

Figure 4 corresponds to the time trace 8.82 minutes. As expected the roll spectrum calculated with the FFT is very spiky. Nevertheless, the main peak is very close to the target value. The smoothed spectrum reduces the spikes; however, in this case the main peak is slightly deviated. This deviation disappears after the Gaussian fitting and the main peak almost matches the target natural roll frequency (0.64 rad/s).

Figure 5 corresponds to a different time trace, 12.15 minutes. As it can be seen, the obtained spectrum with the FFT contains 2 main peaks and none of them correspond to the natural roll frequency. This situation can happen sometimes due to the FFT itself but it is more common that it is related to the wave encounter frequency as it is also contained in the roll spectrum. After the smoothing and fitting process the multi peaks disappear and, in this occasion, the main peak corresponds to the natural roll frequency. Nonetheless, it is not always possible to still extract the natural roll frequency as it is masked by the wave encounter frequency. This situation can be observed in the dispersion of the estimates in Figures 6, 7 and 8.

Figures 6, 7 and 8 presents the results for the total 27 h, divided in time series of 9 hours. On the top of the figures, roll motion displayed. As it can be seen, the amplitude is not so large. During the first 9 hours the amplitude reach as much 7 degrees, meanwhile during the rest of the navigation was less than 5 degrees. This behavior was expected as the wave encounter frequency was not close to the natural roll frequency of the vessel and wave height was small.

On the bottom of the figures, the output of the system is presented. In general, the estimated natural roll frequency values are very close to the target value, oscillating around it. This dispersion is clearly reduced calculating the average of the past 12 estimated values.

It has to be mentioned that there are some outliers which show a poor performance of the methodology in those time traces. This behavior is obtained when the roll motion time series presents some drift and it usually happens when the roll amplitude is quite small. Also, it can happen when the roll motion time series is too irregular. Nonetheless, it is not the common behavior of the system and it is limited to specific cases.

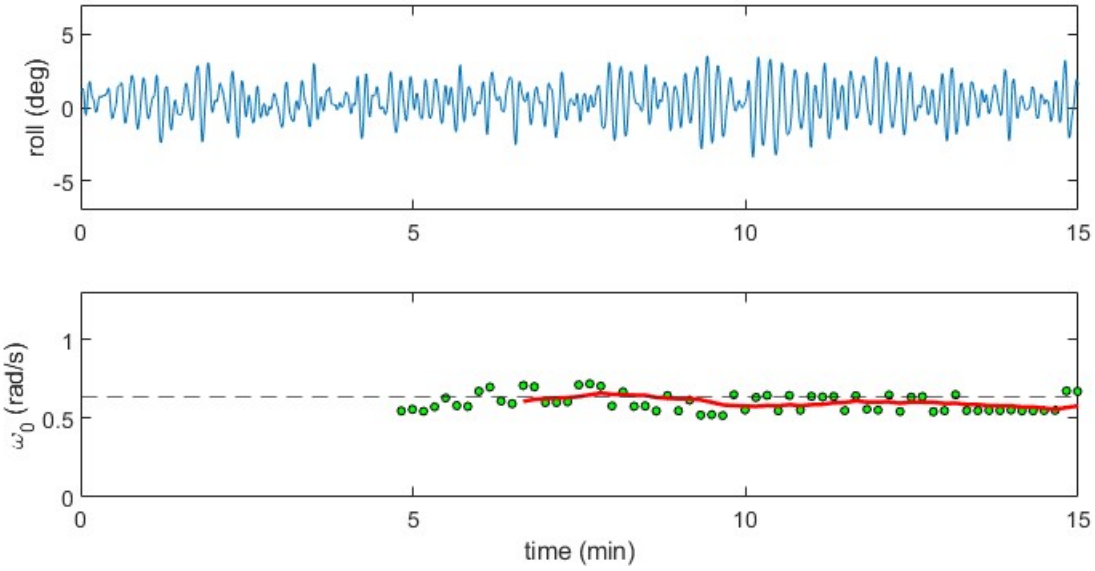

Figure 6: Output of the stability monitoring system during the first 15 minutes.

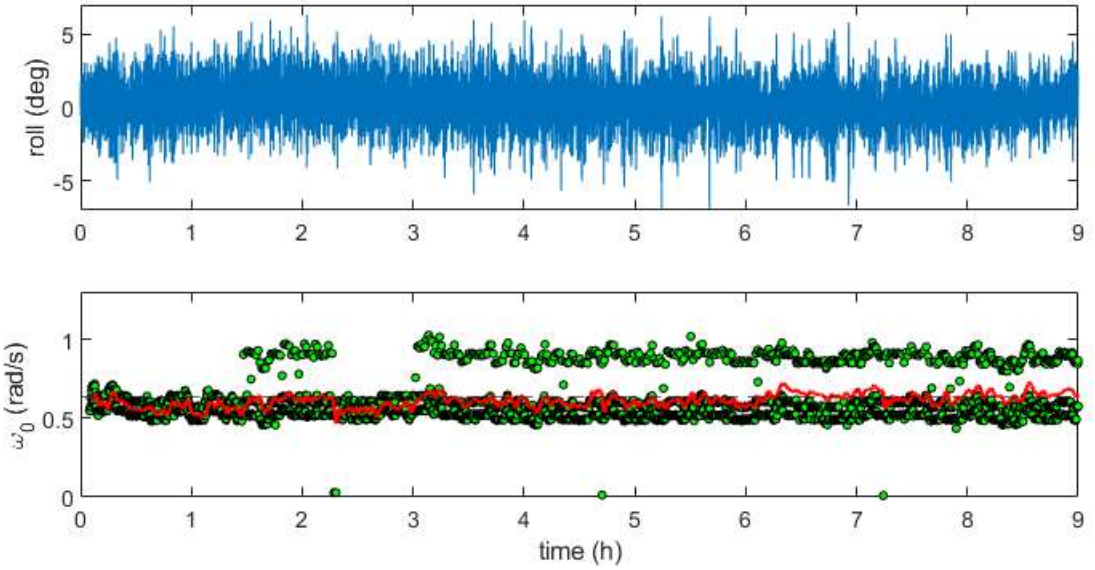

Figure 7: Output of the stability monitoring system part I.

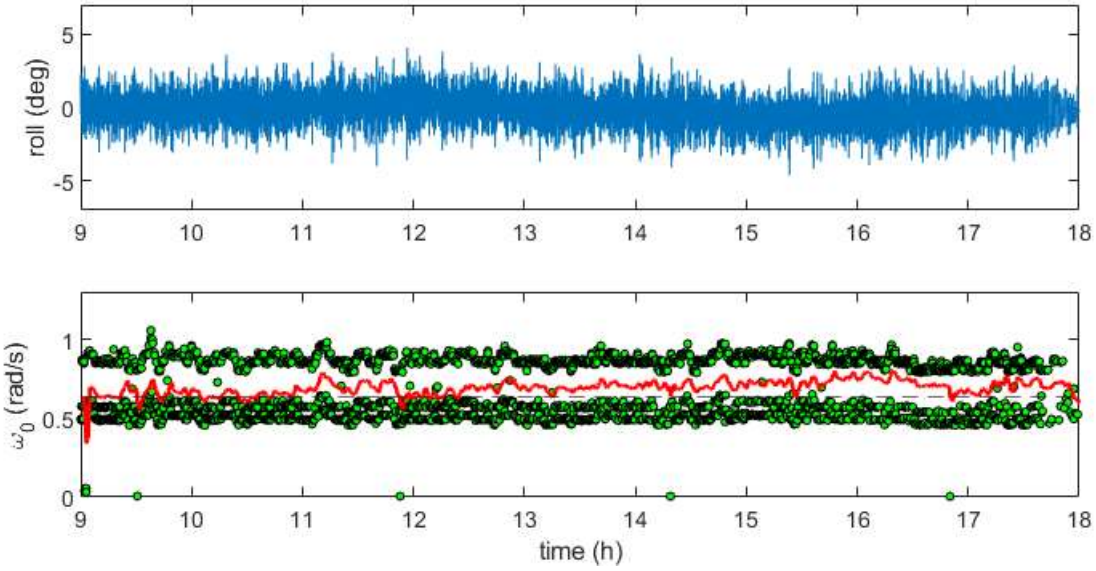

Figure 8: Output of the stability monitoring system part II.

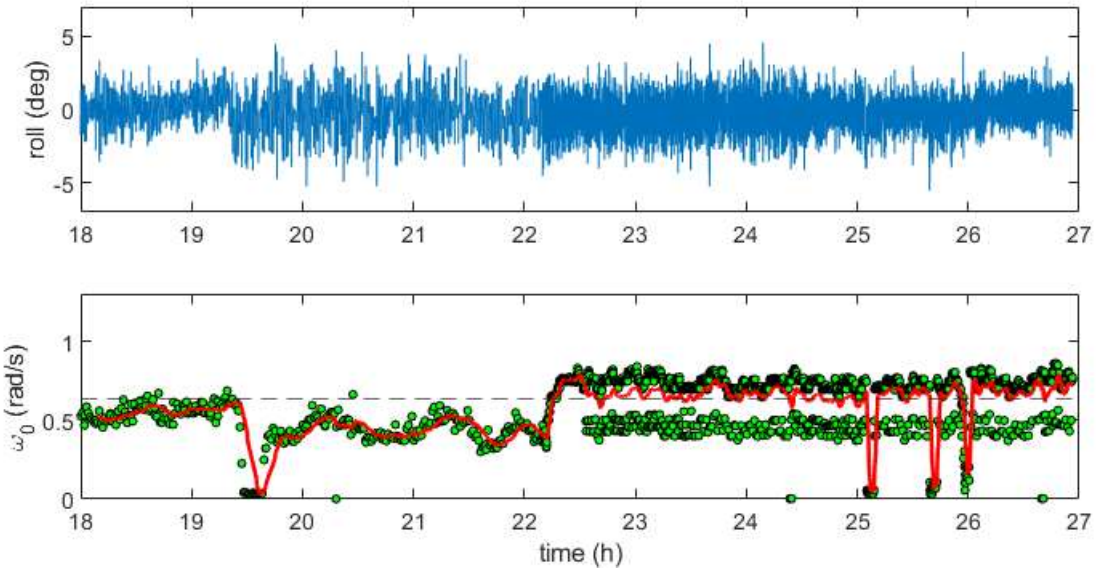

Figure 9: Output of the stability monitoring system part III.

In order to have a better understanding of the impact of applying the mean of the past 12 estimates, the boxplot of the results of the natural roll frequency estimates and the boxplot of the results of the average of the past 12 estimates are shown in Figure 10.

As it can be appreciated, the output of the system has some dispersion, being the median 0.60 rad/s and the percentiles 95th and 5th 0.90 and 0.45 rad/s respectively. If these values are expressed in terms of percentage of deviation from the target value, the median has a deviation of 5%. In spite of this, the performance is quite good.

For the results after computing the average the median is 0.65 rad/s and the percentiles 95th and 5th 0.75 and 0.53 rad/s respectively, being the deviation of the median 3%. In comparison with no computing the mean of the previous 12 estimates, there is no big difference in the value of the median. Nevertheless, the percentiles improve significantly which means a reduction in the dispersion and in consequence the performance of the system is more stable and reliable.

Finally, Figure 11 shows in blue color the natural roll frequency estimates for the 27 hours of navigation versus its percentage of occurrence and in orange color the natural roll frequency estimates after computing the average of the past 12

estimates. As it can be observed, for the first case the percentage of occurrence concentrates around 2 values 0.5-0.55 and 0.85-0.9 rad/s. However, when the average is calculated the largest percentage of occurrence is around 0.65-0.7 rad/s, that is very close to the target value. In conclusion, it is advisable to compute the average of the past 12 estimates to reduce the dispersion in the output of the system.

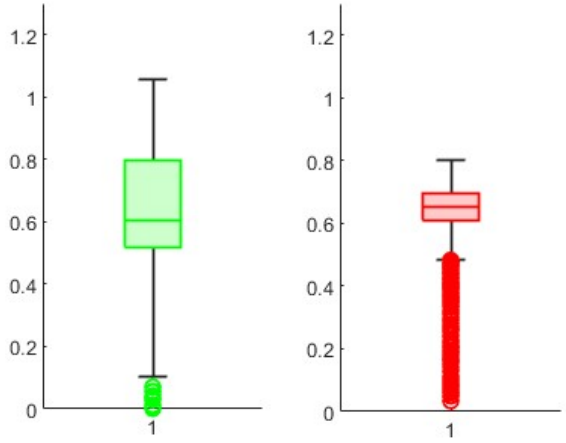

Figure 10: Boxplot of the obtained natural roll frequency estimates (left) and boxplot of the average of the past 12 estimations (right).

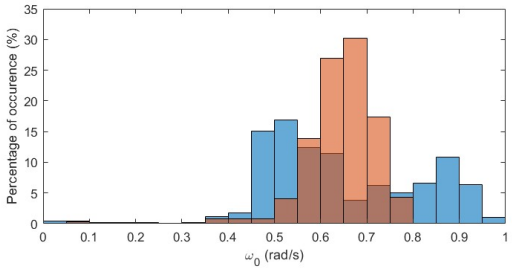

Figure 11: Percentage of occurrence of the natural roll frequency during the 27 h of navigation.

5. CONCLUSIONS

The stability monitoring system presented in this work has shown its applicability and potential benefits when installed on a naval vessel. The system effectively estimates the natural roll frequency in real time using only roll motion data and vessel beam.

Field testing on a naval vessel revealed that the system's estimations closely match expected values and remain stable even in varying sea conditions. Although some outliers were observed, the use of the average of the last 12 estimates significantly enhanced performance by reducing output dispersion. This contributes to more stable and reliable real-time stability assessments.

Given the challenges of maintaining accurate weight and stability records throughout a naval vessel's lifespan—especially in the absence of frequent inclining tests—this system offers a valuable tool for maintaining safety margins, detecting early signs of compromised stability, and ultimately supporting decision-making for vessel operability and upgrades.

ACKNOWLEDGEMENTS

This work has been supported by the Xunta de Galicia (Government of Galicia) through the Axencia Galega de Innovación (GAIN) under grant IN853C 2022/01, UDC-NAVANTIA Joint Research Centre "O estaleiro do futuro", which will be valid until the end of September 2025. The support was inherited from both the start-up and consolidation stages of the same project throughout 2015-2018 and 2018-2021, respectively. This stage is also co-financed with EU ERDF funds under the ERDF Galicia 2021-2027 program.

The authors would like to thank Puertos del Estado for providing the wave data used in this work (Puertos del Estado, Ministerio de Fomento, Gobierno de España, www.puertos.es).

REFERENCES

Deakin, B. (2005). Development of simplified stability and loading information for fishermen. *RINA, Royal Institution of Naval Architects International Conference - Fishing Vessels, Fishing Technology and Fisheries*, 37–46.

Fleisher, S., & Catton, L. (2024). Margins – their use as Metrics and Key Performance Indicators when Designing and Building Warships. *17th International Naval Engineering Conference & Exhibition*. https://doi.org/https://doi.org/10.24868/11168

Gale, P. A. (1975). Margins in Naval Surface Ship Design. *Naval Engineers Journal*, *87*(2), 174–188. https://doi.org/10.1111/j.1559-3584.1975.tb03728.x

Kern, P. H. (1982). A statistical examination of weight and KG margin values for U.S. Navy surface ships. *19th Annual Technical Symposium*.

Míguez González, M., Bulian, G., Santiago Caamaño, L., & Díaz Casás, V. (2017). Towards real-time identification of initial stability from ship roll motion analysis. *Proceedings of the 16th International Ship Stability Workshop*.

Míguez González, M., Santiago Caamaño, L., & Díaz Casás, V. (2018). On the applicability of real time stability

monitoring for increasing the safety of fishing vessels. *Proceedings of the 13th International Conference on the Stability of Ships and Ocean Vehicles*.

Pedatzur, O. (2016). Weight Design Margins in Naval Ships Design – A Rational Approach. *Naval Engineers Journal*, *128–2*, 57–64.

Perrault, D. E., Hughes, T., & Marshall, S. (2010). Naval Ship Stability Guidelines: Developing a Shared Vision for Naval Stability Assessment. *Transactions of the Royal Institution of Naval Architects Part A: International Journal of Maritime Engineering*, *152*(A3), A99–A118. https://doi.org/10.5750/ijme.v152iA3.832

Peters, A. J. (2019). Tolerable capsize risk of a naval vessel. In *Fluid Mechanics and its Applications* (Vol. 119). Springer International Publishing. https://doi.org/10.1007/978-3-030-00516-0_54

Puertos del Estado. (2021). *PORTUS (Puertos del Estado)*. https://portus.puertos.es/index.html#/

Reed, A. M. (2011). A naval perspective on ship stability. In *Fluid Mechanics and its Applications* (Vol. 97). https://doi.org/10.1007/978-94-007-1482-3_45

Terada, D., Hashimoto, H., Matsuda, A., & Umeda, N. (2018). Direct estimation of natural roll frequency using onboard data based on a Bayesian modeling procedure. *Proceedings of the 13th International Conference on the Stability of Ships and Ocean Vehicles*.

Terada, D., Tamashima, M., Nakao, I., & Matsuda, A. (2018). Estimation of metacentric height using onboard monitoring roll data based on time series analysis. *Journal of Marine Science and Technology*. https://doi.org/10.1007/s00773-018-0552-4

Terada, Daisuke, Tamashima, M., Nakao, I., & Matsuda, A. (2016). Estimation of the metacentric height by using onboard monitoring roll data based on time series analysis. *Proceedings of the 15th International Ship Stability Workshop*.

Transportation Safety Board of Canada. (2012). *Marine investigation report. Safety issues investigation into fishing safety in Canada. Report Number M09Z0001*.

Varela, S. M., Guedes Soares, C., & Santos, T. (2010). Monitoring system for safety of fishing vessels subjected to waves. *The Portuguese Maritime Sector*, 1–10.

PAPER NOT PRESENTED DURING THE WORKSHOP

Naval architecture emergency response for UK naval ships – lessons learned

Morgan Griffiths*, Olgun Hizir,
Ministry of Defence, UK
**Corresponding author; e-mail: morgan.griffiths1987@gmail.com*

ABSTRACT

The UK Ministry of Defence (MOD) has a requirement to provide specialist technical support, from ashore, to the surface ships of the Royal Navy in an Emergency Response (ER) incident or accident in times of peace and war. This requirement is fulfilled by Naval Architects working within the Ship Project Teams. The provision of ER support in the MOD has evolved over several years and several incidents have highlighted the need for an in-house capability. The MOD Naval Authority oversees the training and development of Naval Architect's ER skills through formal training and regular exercises. ER Exercises involve multiple teams of Naval Architects working through a scenario over the course of two days. The scenario starts from the initial incident and progresses through to the recovery of the damaged vessel. Teams must manage information flow, make time critical decisions based on sometimes inconsistent or incoherent data, and communicate effectively with all stakeholders. This paper discusses in detail the lessons learned from Emergency Response Exercises with a specific focus on stability and structural integrity of Naval Ships

Keywords: *Emergency Response, Damage Stability, Naval Ships, Training and Competence*

1. INTRODUCTION

The UK MOD Shipping Regulations for Safety and Environmental Protection sets the requirement for an emergency preparedness system that is equivalent to that required for merchant shipping, i.e. to be able to provide technical assistance from ashore to a stricken vessel. The response will provide technical support to the onboard damage control activity to allow the platform to maintain and/or recover its defence capability.

Most commercial shipping companies will enrol their vessels into a service provided by Class Societies, such as Lloyd's Register Ship Emergency Response Service (SERS) and DNV Emergency Response Service (ERS). ER Services provided by Class Societies have a wide range of services from oil spill migrating with environment to real time stability and strength assessment of vessels. However, due to the difference in operating philosophy and security classification of warships the MOD maintains an inhouse capability staffed by Naval Architects already working within the Platform Teams of their respective ship class.

Recently, the importance of the emergency response exercises on naval ships has been demonstrated in the collision of HNoMS Helge Ingstad with Oil Tanker Sola TS in Norway. The Accident Investigation Board Norway (AIBN) and Defence Accident Investigation Board Norway (DAIBN) performed an investigation on the incident. The Norwegian Safety Investigation Authority (NSIA) (2021) revealed the frigate could have been prevented from sinking had she been shut down before she was evacuated. The NSIA also advised with adequate instruction and training of the crew and better decision support tools than those that were available the vessel would have been saved. This highlights the importance of ER exercising.

In the last decade with the advancement in the computational resources more research has been performed to integrate simulation techniques into maritime training programmes. Valera et. Al (2014) worked on on-board decision support system for ship

flooding emergency response focusing on real time flooding simulations to estimate progressive flooding of ship compartments, flooding time and stability parameters. Perkovic et. Al (2016) identified that offering a realistic environment for training simulators can contribute to effective emergency response strategies.

Most of the papers related to ER research, focussed on specific damage responses, i.e. flooding time and dynamic stability assessment, evacuation, life-saving appliances and fire assessment. The present paper provides a high-level view into how to manage ER competence through exercises and provides lessons learned so far.

2. INCIDENT PHASES

All incidents consist of three phases which are irrespective of the severity of damage, this is graphically displayed in Figure 1:

- Initial
- Intermediate
- Recovery and Remediation

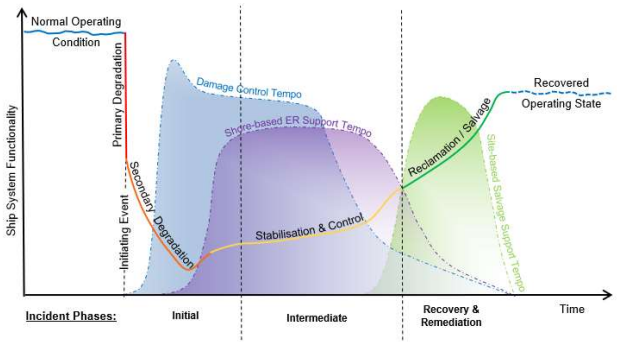

Figure 1: Status of ship system functionality over the period of an incident and tempo of ER activities.

The Initial Phase

This phase is the period immediately following the damage event, resulting in an immediate and steep decline in ship system functionality. The shipboard response will initiate and will begin with a period of information gathering and survey for the ship's Command to build a picture of the severity of the damage and capability degradation. The response will build in tempo as the Damage Control Teams consolidate and stabilise the situation. The shoreside ER support is also initiated but will take time to achieve situational awareness and will be "always behind the curve" in this phase.

The Intermediate Phase

This phase will commence once the shoreside ER team has developed their first response situational awareness based upon reports from the damage control parties onboard. At the same time the shipboard tempo will level off as the Damage Control Teams prevent additional degradation and address specific symptoms as directed to achieve the Command Aim of the ship's Command team. The shoreside support will generate the first diagnosis and prognosis and will prescribe treatment options to the Command. This cycle will repeat as new data is provided and will continue until the casualty enters a state of recovery.

The Recovery and Remediation Phase

This phase initiates as the shoreside ER teams develop detailed repair and recovery plans for the platform and prepare for handover to the MOD Salvage and Marine Operations (SALMO) Team. The aim of the phase is to return the casualty vessel to a steady state operating condition where the risk to the platform, crew, environment, and mission, is to an accepted level. However, this may be abandonment by the crew and full handover to the Salvage Team.

3. EMERGENCY RESPONSE PROCEDURE

The MOD Naval Architects within the shoreside ER team will be required to build a picture of the damaged platform's stability and structural capability. The basic procedure follows an iterative loop of activities, as shown in Figure 2, from consultation to diagnosis, and from prognosis to treatment, and then into the monitoring phase. Repetition of this process at every transfer of new data from the shipboard damage control team allows the Naval Architect to assess, manage, or reduce uncertainty.

Figure 2: ER Exercise Procedure

Consultation

The ER team needs to gather and assimilate ship specific, voyage/mission specific, and incident specific information and data. This will come from several different sources such as readouts from the onboard stability computer, logbooks, and situation reports. All of which will enable the Naval Architect to build a pre-incident condition of the vessel and allow inconsistencies and uncertainty to be identified within the post-incident assessment. The consultation phase is the key element of the ER response where inaccurate data acquisition and/or inaccurate data evaluation will affect subsequent phases.

Diagnosis

The diagnosis activity mirrors that of an emergency medical doctor, where ambiguous symptoms, and changing severity over time inform a hypothesis on the cause. The Naval Architect will be required to test assumptions until data from the casualty vessel narrows the problem space. In addition, they will be required to manage the fidelity of data and work within the limitations and assumptions of static analysis tools.

Prognosis

To generate a prognosis the stability and structural performance of the casualty is modelled to determine capacity and margins for both stability and structural. This activity will require iteration as the fidelity of information improves, or if new issues are diagnosed. The aim of this activity is to provide the command team with the best possible picture of the risk, now and in the future, to support decision making and risk assessment.

Treatment

From the analysis in previous stages the Naval Architect will present remediation activities that reduce the stability and structural risks back to an acceptable level to allow the platform to return to operations or to be recovered safely.

Monitoring

The final activity is monitoring, which is to ensure that the prescribed treatments are achieving their aims. The Naval Architects will continue to investigate the consequence of any failure in the treatment activities to generate mitigation strategies. This strategy will be required to support any salvage operation.

4. INFORMATION CHALLENGES

An effective response to an emergency incident relies on all parties, onboard and ashore, having a knowledge and understanding of what is happening around them, i.e. situational awareness. The complicated nature of naval ships coupled with the complex consequences of an incident, and subsequent obscuration of evidence, challenges the Command Team and Naval Architect to build situational awareness that is consistent, complete, and free from uncertainty. Therefore, a significant part of the Naval Architects role is to decipher and interpret the information provided using their own professional judgment and expertise. Fidelity of information is prioritised over accuracy.

To assist with the transfer of information, the Naval Authority developed the Maritime Incident Report Form (MIRF) that is included within the Survivability & Stability Book (SSB) mandated to be carried by all RN Ships. The MIRF is used by the onboard Damage Control team to record details of the incident and an approximate readout of the pre-incident condition of the ship. The form was developed in response to the acknowledged differences in culture between the Operator (Royal Navy) and the shore-based teams, therefore the MIRF aims to standardise the format of the initial information and ensure commonality to shoreside computer models.

Other information sources available include the onboard operator guidance, this in the form of the SSB and may also include onboard stability computers. The SSB for Naval Ship's is a "navalised" Stability Information Book used by commercial ships. The SBB contains all the relevant stability, and some structural, information required by the ship crew to operate the vessel safely. Some guidance is provided on ultimate stability in a selection of damage scenarios, this allows the crew to quickly and effectively assess the impact of damage without the need for detailed modelling and analysis. Additional supporting information, such as system schematics and ship drawings are contained within the ship's salvage pack which is held onshore by the Project Team and is available for quick access in an emergency incident.

5. MODELLING METHODOLOGY & CHALLENGES

Naval Authority approved Stability Software has been developed to be used to support stability and structural analysis for the safety certification of RN Surface Ships since the early 2000s. In 2015 the Naval Authority tasked an independent Naval Architecture & Salvage Consultancy to review the software that would be required to support an Emergency Response incident. This led to the enhancement of the software with specific Emergency Response (ER) functionality which has now matured to support the following analysis:

- Estimate hole area and location for flooding assessment
- Multiple point grounding analysis
- Seabed representation
- Influence of tide
- Hull girder response
- Emergency Response time simulation

Most of the listed objects are used specifically for ER and are independent of the analysis conducted by Naval Architects to support the safety certification of their class of warship. This increases the challenges for effective ER as the skills and experience in using these modelling objects are not regularly used outside of ER training exercises. This is reflected in the methodology for grounding which is reliant on soundings from the ship to initiate the analysis. From the soundings the software can generate a seabed surface that, with additional details on the seabed properties and freeboard measurements, can be used to determine the ship's grounded attitude, load distribution on the keel, and hull girder response. All of which can be used alongside tide data to determine float off, or the forces necessary to pull the damaged ship off the seabed if the ship's structure remains capable.

Similarly with the stability modelling, the intact vessel's structural definition is already included in the base model. Naval Architects can add additional structural deformation, for example holes in bulkheads or cracking, and compare the load distribution in structural analysis to determine the hulls structural response in longitudinal bending when damaged. Additional structural analysis methodologies such as bulkhead collapse analysis and fracture propagation have also been developed for application in an ER incident.

The Bulkhead collapse methodology was initially used as part of the onboard stability software to advise the Damage Control party on the shoring requirement for a flooded compartment. The methodology was further adapted and included into the approved stability software to determine whether progressive flooding will lead to structural failure of watertight bulkheads between ship compartments.

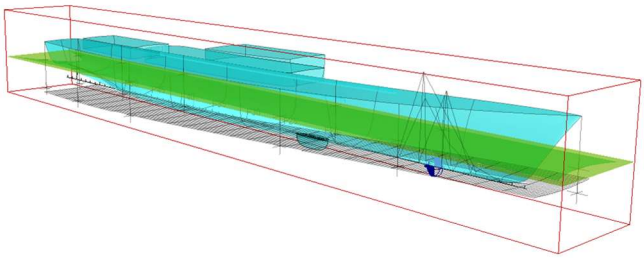

Figure 3: Modelling of grounded ship

Data from the MIRF is inputted into the ship's stability model, but this relies on the model being maintained accurately prior to any incident. Configuration issues such as incorrect modelling of watertight subdivision, differences in compartment naming conventions, tank modelling, and methods in modelling appendages, will affect the Naval Architects situational understanding and the accuracy of any prognosis. In addition, the Naval Architects ability to understand and operate the Stability Model has significant importance. The Naval Authority have published several guidance documents to ensure modelling commonality and alignment with the MIRF. Additionally, each stability model is audited by the Naval Authority as part of the ship's safety certification process.

6. NAVAL ARCHITECT EMERGENCY RESPONSE COMPETENCE

An emergency incident is a low probability but high consequence event that requires skills that are not routinely exercised in the day-to-day activities of MOD Naval Architects. The challenge to the MOD is to maintain a high level of corporate subject matter expertise that is ready to deploy in the event of an incident. To achieve this the Naval Authority developed a functional competence assessment that is used to assess the skills of Naval Architects in ER, these competencies cover:

- General Skills: Data assimilation, record keeping, managing inconsistencies, reporting, and handover
- Understanding of reserve of stability & buoyancy: pre and post incident condition, response to the Command Aim
- Understanding of reserve of strength: pre and post incident condition, response to the Command Aim

These competencies are assessed through testing and taught through bespoke training courses, a published handbook, and through group training exercises. The handbook has been produced by the Naval Authority and is structured to guide Naval Architects through the phases of an ER incident, is an aide memoir on the analysis methodologies. The handbook also provides guidance on best practice for reporting and information management. The handbook is expected to be used alongside the experience built in the training exercises and to reinforce learning from training courses.

7. TRAINING EXERCISE

The Naval Authority organises an annual training exercise for MOD Naval Architects. This is one element of the system to develop and maintain Emergency Response skills. The exercise takes place over two days with four teams of Naval Architects.

Goals

The goal of the exercise is to provide a realistic training environment for an enduring incident where naval architects can use and develop their skills. Each exercise will have an overall training goal chosen by the Naval Authority following an assessment of internal capabilities and experience, for example an exercise will focus on a damage scenario with a residual structural capacity issue if there is a need to improve experience in this area. The learning outcomes of the exercise will also reflect the competency framework with the technical challenges for each session specially designed and selected to ensure differential learning for each candidate's level of experience.

Each team will be comprised of naval architects with different levels of experience and seniority. The goal is to take into consideration differential learning between individuals where candidates may have certain skill development needs. This allows candidates with lesser experience to be exposed and influenced by an expert. This will then be built upon in future exercises ensuring an upward trend in experience and skill development in candidates.

The four sessions, or 'quadrants', will also contain additional learning goals that will reflect the related phase of the incident as described in section 2. Some quadrants are more difficult than others requiring deeper skill sets and stronger leadership, for example earlier quadrants may focus on data gathering and preparation of models, while others will be more focused on the salvage and remediation activities. Difficulty is introduced by purposefully withholding information or presenting several courses of action to be investigated and prioritised with a compressed time frame. The sessions are also designed to overlap allowing teams to practice a handover to each other, which reflects the process in a real incident.

Preparation

The Naval Authority selects one Naval Architect each year to design and build the scenario for the training exercise. The selected candidate is usually in a junior role with little existing ER experience but is required to have a basic working knowledge of stability and structures analyses

The designer models both the ship and the crew's response to an incident. Modelling both the stability and structural response of the vessel through various stages of the scenario. From the modelling the designer will generate all the information provided to the teams within the exercise. Part of this requires the designer to purposefully create inconsistency and confusion, along with anticipating every avenue of the team's response.

8. EXAMPLE EXERCISE

The following sections provide an example of the annual Naval Authority training exercise. The exercise is attended by 16 Naval Architects split into teams of four. Each group participates in a four hour 'quadrant' which includes a one-hour handover period between teams. The exercise takes place over two eight-hour days with the exercise timeline paused between days.

Background

A Ship is transiting through narrow straits and is involved in a collision with a fishing vessel. The

damage causes the vessel to lose propulsion after flooding in the Engine Room and Auxiliary Machinery Room, an explosion also occurs in the Control Room compromising power distribution. The Ship is drifting towards a small island and shallow water. A support vessel is in the vicinity of the incident but will not arrive for several hours to assist.

Team One

The first team is initially provided with a MIRF and a signal from the ship outlining the damage and the pre incident condition. The team should assign roles and discuss their plan to provide a response to Command on the status of the Ship's stability and structural performance now, and in the future. A copy of the ship's incident board is provided, and the Team should begin to mark up the damage that has been reported. The team can provide a quick prognosis by using the information in the Survivability & Stability Book (SSB) which contains a summary of the ultimate ship capabilities in damage and will be able to identify, with assumptions, that the ship remains stable in the short term, allowing time for a more detailed analysis and prognosis to be formulated within the modelling software.

Team Two

The ship will be unable to get propulsion back online and during the handover between the teams the ship will run aground on the rocks close to the small island. A series of signals and reports will follow that will allow the team to build a better picture of damage and the grounded attitude of the Ship. The team should manage this flow of information filtering out inconsistencies and inaccuracies until they can generate a prognosis.

Halfway through the session a Senior Naval Officer requests a briefing from the team on the stability & structural performance and whether the ship will be able to float off at high tide. This will require the team to identify a spokesperson to lead the brief and to ensure they have some guidance on the status of the Ship to be presented. The stability software will be used to model the grounded condition and to predict if, or when, float off will occur.

Team Three

The previous Team should have identified that float off will occur during Team Three's session and briefed this during the handover. However, without making additional changes to the ship's condition, the window will be small and there is risk of grounding again. Team three will need to continue the grounding assessment within the modelling software to prepare the Command for float off and advise on any necessary weight shifts to improve the float off window. Propulsion will not be returned to the vessel by the crew so the team will need to decide on the correct course of action. This is to either, continue with float off, or remain grounded until a support vessel arrives.

Team Four

This session will contain a team of the most experienced ER Naval Architects, and the scenario will try and reflect this by ramping up the difficulty. Irrespective of the previous team's solution, the Ship will be able to float free and will drift. This will be simulated as the Ship crew not receiving communication from ashore and proceeding on their own initiative. Once floating free the Ship will immediately ground again on a sand bar and several signals and reports will be passed to the team for review and sentencing within a short period of time. The compressed timescale and near saturation of information will aim to test the experience of the team. Additionally, the team is expected to enter the recovery phase and prepare for the response to be handed over to the salvage teams by preparing the ship to be pulled off the sand bar.

9. DISCUSSION

Lessons learned from ER Exercises are the most valuable output to develop the ER skills of Naval Architects. The outcome of each exercise allows the Organisation to reflect on the overall state of Naval Architect's ER competence and the overall health of the training available. While ER exercises returned with many minor & major points of feedback, the most prominent fall under the following themes:

Competence

Teams are purposefully comprised of naval architects of varying levels of competence, not just in their understanding of naval architecture but in the additional general skills required by ER. This is achieved by a mix of seniority and work experience,

however in general most candidates will have had some experience working with naval ships. The introduction of time pressures on decision making within the scenario test time management, decision making, and problem-solving skills. The ability of the team to assign roles based on the strengths and weakness of each member is essential, the exercise provides an excellent opportunity for those with less experience to observe those with more. The regular drumbeat of exercises also allows candidate to self-reflect and develop their capability in time for the next exercise.

The key competencies of leadership and communication are exercised by every team throughout the scenario. Each team should allocate roles, one of which will be to act as team leader. The leader must maintain a wide strategic situational awareness of the scenario and should not get drawn into detailed analysis. Senior Naval Officers visit each team to simulate the real incident requirement to brief shore-based Command. The visit tests the team's ability to convey key briefing points in an accurate and confident manner. In some cases, the team will not have the answer to a specific query at that time, therefore the ability to identify this short falling and provide a course of action, and timescale, to rectify is important.

Information

To mimic a real emergency response environment, data is provided to the teams with intentional inconsistencies and errors. This reflects the real emergency environment which accounts for human factors i.e. busy and stressed crew, severity of the damage, and environmental conditions impacting onboard data collection and information recording. Keeping detailed records that allows new data to be compared against previous iterations helps to highlight inaccuracies and identify trends. Using the previous example of freeboard readings, an experienced naval architect would be able to uses the recorded values to identify that the ship's draught is increasing over time and would draw the conclusion that there may be unreported slow flooding somewhere on the vessel.

Handover reporting is one of the most important phases of the ER exercise as real-life incidents may require support for several days with the participation of different naval architects. The handover is subject to the stress within the team and prioritisation of information presented. An improperly prepared handover report might mislead subsequent teams, and the situation might be out of control until experienced Naval Architects take over the task. It has been revealed that the clarity of the handover report is more important than the accuracy. This is due to the dynamic condition of the incident where regardless of accuracy it may not reflect the reality of the stability and structural status seen by the ship which might deteriorate or recover.

Tools

Modelling the incident within software tools takes up a large amount of time and effort within an exercise. Teams have candidates with different levels of experience with each aspect of the software, ranging from awareness to expert users. While one goal of the exercise is to test competence with the software, this is then stretched by applying time pressures, and inconsistencies, when working on a solution. Teams can split the workload by allocating different members to focus on discrete aspects of the modelling, which is usually split between stability and structural analysis. However, care must be taken to ensure configuration control and consistency of the data between the models.

10. CONCLUSIONS

Emergency Response is a low probability, but high impact situation that requires specialist skills and training. Although there have been several papers published focussing on specific damage responses i.e. flooding and evacuation assessments, the present paper provides a high-level view into how to manage ER competence. It has been identified that competency, information, and tools are the three key elements to an effective response to an incident, see figure 4. The effectiveness of these three elements is tested as part of the annual Naval Authority training exercise. The three key elements can be further explained as:

- Competence – the ability to understand and process ER specific issues and apply effective assessment criteria.
- Information – the ability to access and manage data to support situational awareness and decision making throughout the response.

- Computational Tools – effective modelling and analysis tools that contain specific ER functionality

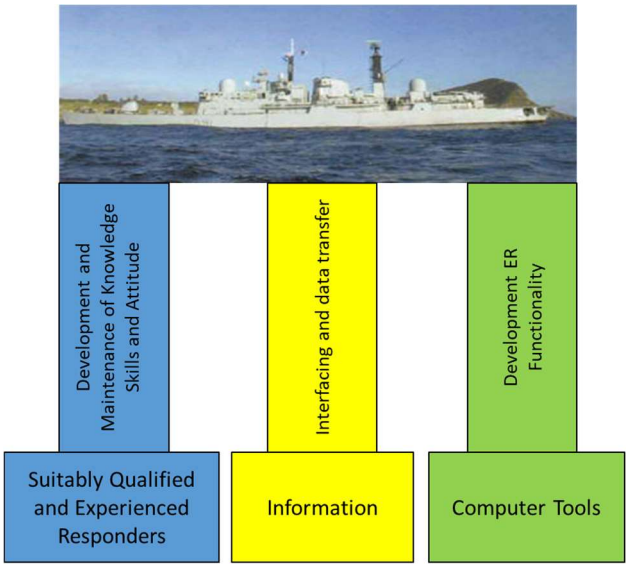

Figure 4: Key elements supporting effective ER

Competency developed from formal training and published guidance is tested and stretched by the exercise. A naval architect's competence in stability and structural integrity of vessels can have a significant influence on the outcome of the ER. Competency of the responders are assessed during the exercise by putting into practice formal training and ensuring knowledge transfer from more experienced members. Additionally, the regular drumbeat of exercises ensures responders' development in accordance with the established competency framework.

The exercise exposes the efficiency of existing information management and data processing, and tests how information is used to build situational awareness. The MIRF was developed following feedback from a real-life incident, and it is expected that regular use in the exercise environment will not only build familiarity, but also identify future development opportunities. Additionally, the exercise has had a positive impact on how project teams maintain the Salvage Pack for their class of ship.

Effective software tools and well-maintained ship models have paramount importance and are used extensively within exercises to support decision making. The current tools used by naval architects have been developed and enhanced following feedback gathered within exercises.

Overall, elements interact with each other, for example competent naval architects require situational awareness and accurate information to feed computational tools with the appropriate functionality, all three elements contribute to a valid prognosis. The exercise therefore is an appropriate enabler to ensure that each element is healthy and contributes to an effective Emergency Response.

REFERENCES

Norwegian Safety Investigation Authority, Part Two Report on the Collision Between Frigate HNOMS Helge Ingstad and the Oil Tanker Sola TS, April 2021.

Varela, J.M., Rodrigues, J., Soares, C.G., 2014. On-board decision support system for ship flooding emergency response. Procedia Computer Science 29, 1688–1700.

Perkovic, M.; Ristea, M.; Lazuga, K. Simulation based emergency response training. *Sci. Bull. Nav. Acad*., 2016, *19*, 85-90.

UK Ministry of Defence, Maritime Acquisition Publication, 01-035, Naval Emergency Response Handbook – The Naval Architects Guide, Issue 01, November 2019

Session 5
Probabilistic methods to ship stability and safety

Prediction of parametric roll of containership in regular and irregular waves using machine learning technique

Jaehak Lee, *Seoul National University, Republic of Korea*, jhlee1022@snu.ac.kr
Yonghwan Kim, *Seoul National University, Republic of Korea*, yhwankim@snu.ac.kr

ABSTRACT

This study addresses the prediction of parametric roll motions in a modern containership operating in various sea conditions. A series of time-domain hydrodynamic simulations based on the nonlinear impulse response function (IRF) method were carried out to generate motion responses under head-sea regular and short-crested irregular waves. Based on the simulation data, a data-driven model was constructed to predict wave-induced roll motions and investigate their dynamic behavior. The predicted responses exhibit key nonlinear features of parametric roll, including resonance amplification and non-ergodic variability across realizations. The results suggest that the proposed approach can serve as a promising framework for the deterministic prediction and physical interpretation of parametric roll phenomena.

Keywords: *Parametric roll, impulse response function (IRF), machine learning (ML), convolutional neural network (CNN), long short-term memory (LSTM)*

1. INTRODUCTION

Parametric roll, induced by periodic variations in transverse stability, is recognized as a critical threat to ships and crew safety (Peter and Belenky, 2022). This phenomenon is particularly pronounced in containerships due to their large vertical variation in wetted surface area. Accordingly, the Second Generation Intact Stability Criteria (SGISC) have been provisionally introduced as interim guidelines (MSC.1/Circ.1627) to improve the safety of modern vessels, with particular emphasis on identifying and preventing parametric roll. Nevertheless, the real-time deterministic prediction of parametric roll during operation remains a challenging task, primarily due to its highly nonlinear and non-ergodic characteristics. Thus, achieving accurate real-time predictions of parametric roll can significantly enhance the safety and operability of modern containerships.

Numerous studies have extensively examined the theoretical characteristics of parametric roll. Mathieu-type second-order differential equations and Ince-Strutt diagrams have been widely employed to identify parametric resonance under longitudinal regular wave conditions (Kerwin, 1955; Paulling, 1961). Inspired by the efforts to describe parametric resonance based on Mathieu-type dynamics, many researchers have devoted their efforts to investigating parametric roll by further enhancing the mathematical models based on differential equations, particularly focusing on the improved modelling of parametric excitation (Francescutto, 2001; Bulian et al., 2004; Lee and Kim, 2016).

Direct time-domain numerical simulations have emerged as alternative strategies for investigating parametric roll motions over the past few decades, owing to their advantages in accounting for the fully nonlinear characteristics of ship motions. Beyond traditional methods such as the potential theory-based impulse response function (IRF) and the three-dimensional Rankine panel method, computational fluid dynamics (CFD) approaches are currently used for the direct assessment of parametric roll motions, owing to the improved capabilities of computational hardware (Shin et al., 2004; Sadat-Hosseini et al., 2010; Park et al., 2013; Kapsenberg et al., 2020). Systematic investigations aimed at clarifying the dynamic properties of parametric roll motions using various numerical approaches have widely recognized that parametric roll motions exhibit a non-ergodic nature, which is attributed to their highly nonlinear dynamics, making their description difficult based on probabilistic and stochastic perspectives (Belenky et al., 2003).

Despite the rapid development of numerical technologies for analyzing nonlinear dynamic systems of ship motions, direct time-domain simulation methods continue to face challenges in achieving real-time prediction of parametric roll motions. Recent advancements in investigating parametric resonance focus on the real-time identification of its occurrence based on its dynamic properties (Galeazzi et al., 2013; Yu et al., 2016; Luthy et al., 2023). All of these advancements have contributed to the development of real-time identification of the occurrence of parametric resonance, but real-time direct simulation of parametric roll motions in the time domain is still under development. Data-driven machine learning approaches, which have recently emerged as alternative strategies for predicting wave-induced ship motions, have demonstrated their capabilities in the literature (Silva and Maki, 2022; Lee et al., 2023), but systematic studies on their application to investigating parametric roll motions are still insufficient.

In this study, the dynamic behavior of parametric roll motions in a modern containership is investigated through data-driven prediction and subsequent physical analysis. Time-domain simulations based on the nonlinear IRF method were conducted under both regular and irregular wave conditions to generate representative motion data. These results were used to train a predictive model that captures the deterministic features of parametric roll. The predicted responses were then analyzed to explore their resonance behavior, temporal amplification, and statistical variability. The study aims to demonstrate a practical approach for identifying the onset and characteristics of parametric resonance in operationally relevant conditions.

2. THEORETICAL BACKGROUND

Weakly nonlinear method based on impulse response function method

For investigating the physics of parametric resonance and constructing the training datasets, this study employs a time-domain simulation approach based on the nonlinear impulse response function (IRF) method (Cummins, 1962). In this framework, wave-induced ship motions are calculated using the convolution integral of the retardation function, which accounts for memory effects in fluid-structure interactions. The IRF coefficients, including added mass and damping, are derived from precomputed frequency-domain hydrodynamic results.

$$\zeta(x,y,t)=\sum_{l=1}^{N_l}A_l\cos\begin{bmatrix}k_l(x+Ut)\cos\chi_l\\+k_l y\sin\chi_l-\omega_l t+\varepsilon_l\end{bmatrix} \tag{1}$$

$$\begin{aligned}&\left(M_{jk}+M_{jk}^{\infty}\right)\ddot{\xi}_k(t)+\int_{-\infty}^{t}R_{jk}(t-\tau)\dot{\xi}_k(\tau)d\tau\\&+C_{jk}^{R}\xi_k(t)=F_{diff,j}(t)+F_{FK,j}(t)\\&+F_{rest,j}(t)+F_{damp,j}(t)\end{aligned} \tag{2}$$

$$R_{jk}(t)=\frac{2}{\pi}\int_0^{\infty}B_{jk}(\omega)\cos\omega t d\omega \tag{3}$$

$$M_{jk}^{\infty}-\frac{C_{jk}^{R}}{\omega^2}=A_{jk}(\omega)+\frac{1}{\omega}\int_0^{\infty}R_{jk}(\tau)\sin\omega\tau d\tau \tag{4}$$

Here, A_l, k_l, χ_l, ω_l, and ε_l represent the amplitude, wave number, wave heading, frequency, and phase of each wave component, respectively. In the equations of ship motions, M_{jk}, M_{jk}^{∞}, and C_{jk}^{R} denote the inertia, infinite-frequency added mass, and radiation-restoring matrices, respectively. R_{jk} represents the retardation function, A_{jk} and B_{jk} are pre-calculated coefficients of added mass and damping, derived from the efficient two-dimensional strip theory (Salvesen et al., 1970). $F_{diff,j}$, $F_{FK,j}$, $F_{rest,j}$, and $F_{damp,j}$ represent the diffraction, Froude-Krylov, restoring, and (viscous) damping forces, respectively. In this study, the weakly nonlinear simulation considers the instantaneous variation of the ship's wetted surface when calculating the Froude-Krylov and restoring forces.

Machine learning model

In this study, the data-driven machine learning framework proposed by Lee et al. (2023) is introduced to predict the parametric roll motions in containerships. The integrated machine learning model is designed to predict wave-induced ship motions a few minutes into the future ($\xi^{(pr)}_k(t)$), based on training using the input of anticipated future wave fields ($\zeta^{(pr)}(x,y,t)$) and past motion records ($\xi^{(re)}_k(\tau)$):

$$\begin{aligned}&\xi_k^{(pr)}(t)=L^{(w)}\left\{C^{(w)}\left\{\zeta^{(pr)}(x,y,t)\right\};L^{(m)}\left\{\xi_k^{(re)}(\tau)\right\}\right\}\\&\text{where } \tau\in\left[t_0-T_{re},t_0\right) \text{ and } t\in\left[t_0,t_0+T_{pr}\right)\end{aligned} \tag{5}$$

Here, $C^{(w)}$ represents multiple convolutional layers, while $L^{(w)}$ and $L^{(m)}$ denote distinct LSTM layers for processing compressed wave vector time series and motion records, respectively. As illustrated in Figure 1, multiple convolutional layers consecutively compress the surrounding wave fields at each time step, capturing the spatial information of encounter waves. Then, the LSTM layer processes the compressed vector sequence to generate future motion responses. In addition, to account for memory effects, the LSTM encoder layer learns the dynamic properties of ship responses from past motion records.

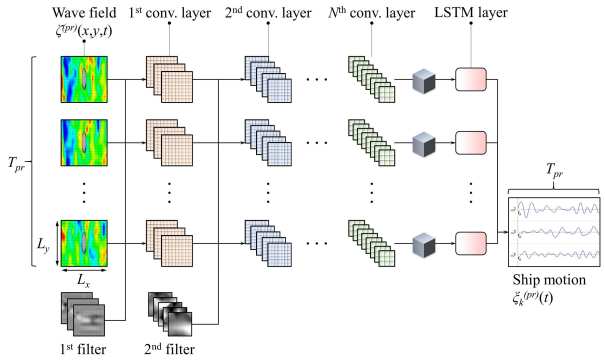

Figure 1: Configuration of machine learning framework.

3. RESULTS AND DISCUSSION

Hydrodynamic simulation results

The subject ship model for investigating the parametric roll is the Korea Research Institute of Ships and Ocean Engineering (KRISO) container ship (KCS) with a metacentric height of 1.27m. The KCS exhibits a substantial flare distribution near the bow and stern regions, indicating susceptibility to parametric resonance. The principle dimensions of the subject ship model are summarized in Table 1.

To construct the training databases, systematic weakly nonlinear IRF simulations were conducted. As listed in Table 2, the target cases for database generation encompassed various ship operations and sea state conditions, with five different realizations for each case. Accordingly, a total of 1,125 hours of ship motion and wave field time series were constructed and used for offline training of the machine learning model. Notably, the operational conditions addressed in this study were selected to be particularly vulnerable to the occurrence of parametric resonance, to ensure the inclusion of sufficient parametric roll time series within the training databases.

Table 1: Principal dimensions of KCS.

Specifications	Value
Length between perpendicular, L_{BP} (m)	230.0
Draft, T_{ship} (m)	10.8
Block coefficient, C_B	0.650
Transverse metacentric height, GM (m)	1.27
Roll natural period, $T_{n,44}$ (s)	21.6

Table 2: Ship operation and sea state parameters for IRF-based hydrodynamic simulations.

Parameters	Value				
Ship speed, U (knots)	5.0 ~ 15.0				
Main heading, χ_{main} (deg)	120 ~ 240				
Sig. wave height, H_S (m)	3.0	4.0	5.5	7.0	9.0
Mean wave period, T_2 (s)	6.7	7.7	9.1	10.2	11.6

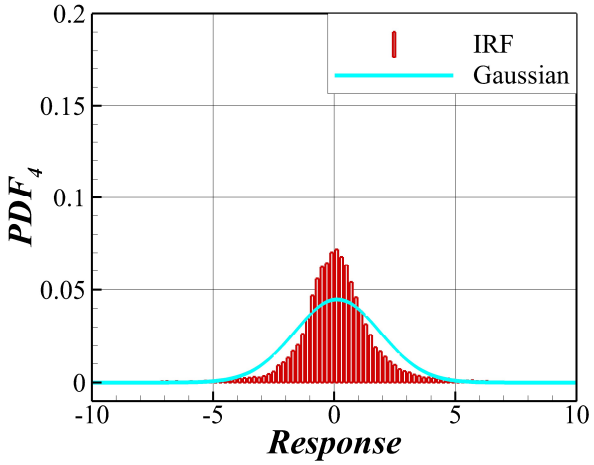

Figure 2: Probabilistic distributions of roll responses established from nonlinear IRF simulations.

Prior to training the machine learning model, the dynamic characteristics of parametric roll motions were analyzed based on the nonlinear IRF simulations. Figures 2 and 3 illustrate the probability distributions and statistical metrics of the roll responses observed under parametric resonance conditions. The probability distribution of the simulated roll motion time series reveals pronounced nonlinear characteristics, showing substantial deviation from a Gaussian distribution.

Moreover, due to the inherent nonlinearity, the roll response variances across different realizations

failed to converge, which indicates strong non-ergodic behavior. These results confirm that the constructed time series database sufficiently captures the complex dynamic features of highly nonlinear parametric roll motions.

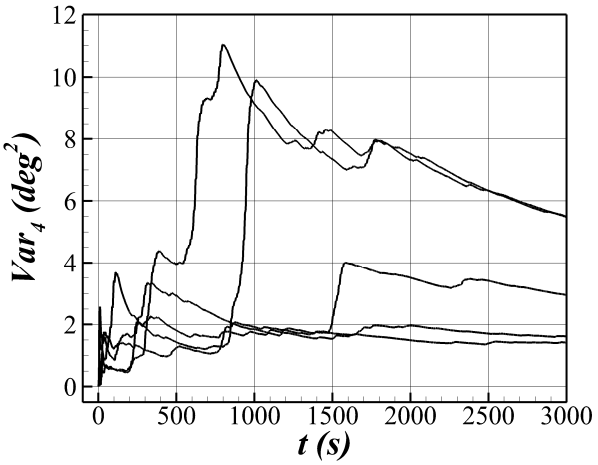

Figure 3: Temporal evolutions of variances of roll motions for different realizations.

Parametric roll in regular waves

The offline-trained machine learning model was first applied to investigate the parametric roll under regular head sea conditions. To impose the roll disturbance required for initiating parametric resonance, a small-amplitude regular wave component was superimposed in the bow-quartering propagation directions, allowing the machine learning model to recognize the transverse disturbances from the input wave fields.

Figure 4 presents the time-series roll responses and their corresponding FFT analysis results under varying wave heights and wavelengths. The ship roll motions rapidly increased, exceeding 20~30 degrees of quasi-steady amplitude, particularly when the parametric excitation frequency (encounter frequency; ω_e) became approximately twice the natural roll frequency ($\omega_{n,44}$). It is well established that such conditions correspond to the fundamental principle of Mathieu-type instability (kerwin, 1955). Despite slight discrepancies in the timing of resonance onset, the proposed machine learning model effectively predicted the occurrence and deterministic characteristics of parametric resonance in regular head seas.

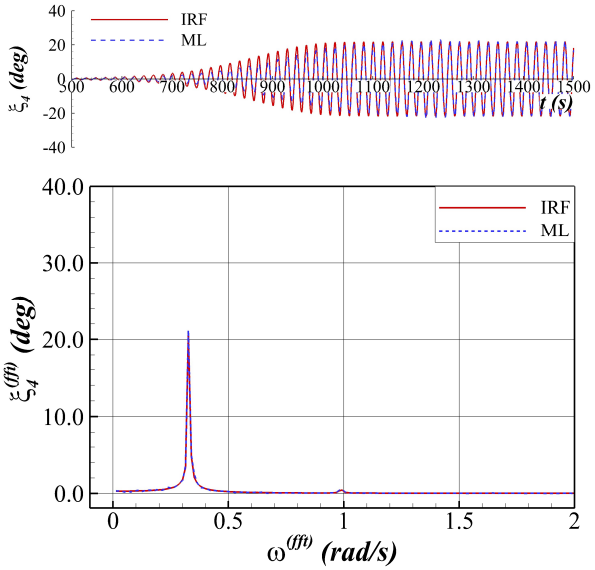

Figure 4: Parametric roll simulation in regular head sea condition ($\omega_e/\omega_{n,44}$=2.26).

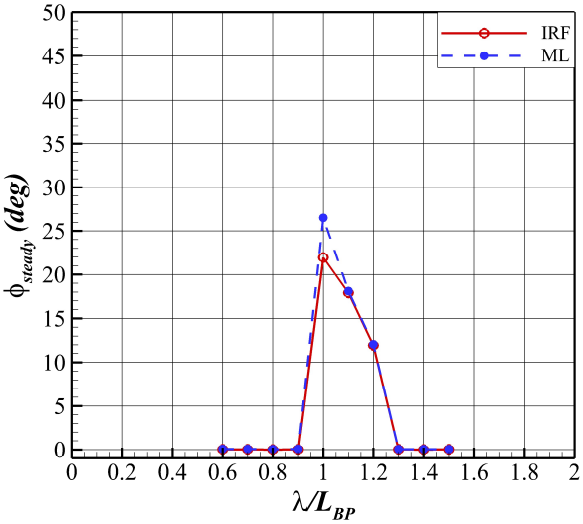

Figure 5: Steady-state amplitude of parametric roll motions (H/L_{BP}=0.014).

Figure 5 shows a comparison of the steady-state amplitudes of parametric roll motions for various wavelengths. The machine learning model tended to slightly underestimate the steady-state amplitudes, particularly in cases of relatively steep waves, as also illustrated in Figure 6. Nevertheless, the model successfully predicted the occurrence of parametric resonance across varying wave steepness and wavelengths, demonstrating its capability to identify the general characteristics of parametric excitation. Notably, despite being trained on time-series data in irregular waves encompassing a wide range of environmental conditions, the machine learning

model accurately reconstructed severe parametric resonance events.

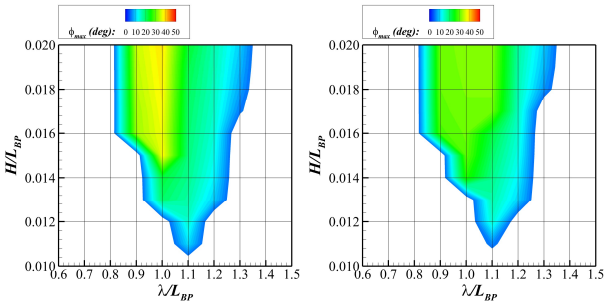

Figure 6: Comparison of steady-state amplitude of roll motions under parametric resonance across diverse regular wave conditions.

Parametric roll in short-crested irregular waves

Parametric roll in irregular waves exhibits complex dynamic properties, primarily due to its highly nonlinear characteristics. As shown in the time-series example of Figure 7, inconsistent amplification and attenuation of responses were observed, making robust prediction challenging. However, machine learning techniques effectively addressed these challenges, accurately predicting significant roll responses in the time domain.

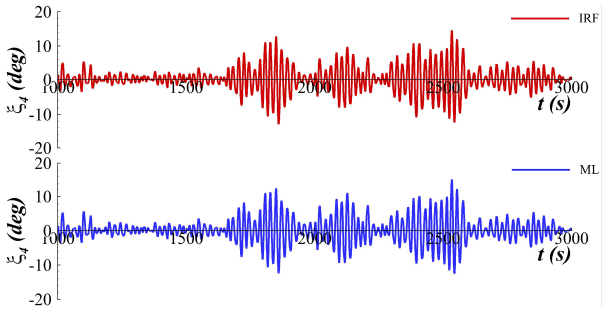

Figure 7: Time series comparison of roll responses in short-crested irregular waves.

Figures 8 and 9 present the statistical properties (variances) and exceedance probabilities of roll responses in cases where parametric resonance occurred. Time-domain simulations were carried out for 50 different realizations (wave seeds), each lasting one hour. The statistical properties of each realizations and the average probabilistic characteristics across all realizations were investigated. For the selected cases, the statistical properties of roll responses revealed a strong non-ergodic nature, which is due to their susceptibility to parametric resonance.

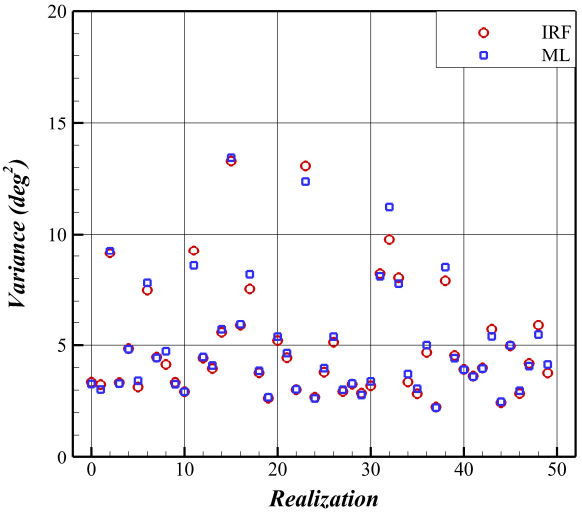

Figure 8: Variances of roll motions across different realizations under the occurrence of parametric resonance.

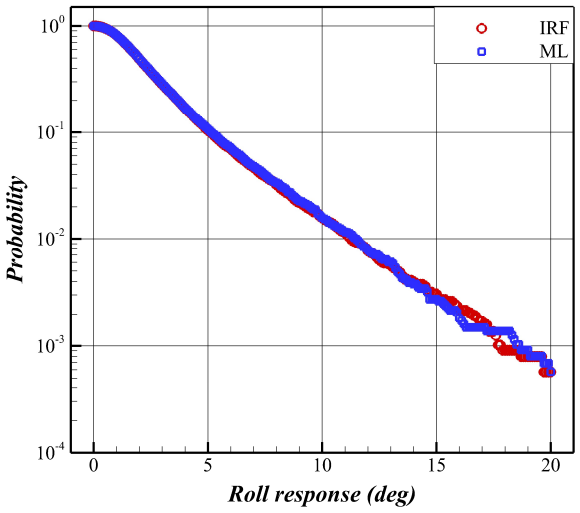

Figure 9: Comparison results of exceedance probability of roll responses in short-crested irregular waves.

The machine learning model accurately estimated the statistical properties of roll motions under parametric resonance across different realizations, capturing the non-ergodic characteristics of the phenomenon. Moreover, the proposed neural network system demonstrated its capability to capture the probabilistic characteristics of roll motions under severe parametric resonance.

4. CONCLUSIONS

In this study, an integrated machine learning technique was employed to predict the parametric roll motions of a containership under regular head seas and short-crested irregular seaways. Based on a systematic investigation of the model's predictability and the dynamic characteristics of the predicted ship responses, the following conclusions were drawn:

- The machine learning approach effectively predicted the parametric roll motions in regular head sea conditions. Although a slight underestimation of the steady-state amplitude was observed, the proposed model successfully captured the occurrence of resonance.
- It was demonstrated that the proposed machine learning model enabled the prediction of complex amplification and attenuation of roll responses under parametric resonance in an irregular seaway. Notably, the statistical non-ergodicity and probabilistic characteristics of the parametric roll responses were well reproduced by the proposed model.

ACKNOWLEDGEMENT

This study was supported by the Shipbuilding & Marine Industry Technology Development Program (20024292, Development of Digital Twin System for Health Management of Hull based on Marine Environment and Hull Response Measurement Data) funded by the Ministry of Trade, Industry & Energy (MOTIE, Republic of Korea). Also, it was partly supported by the Lloyd's Register Foundation Research Center in SNU (LRFC), the grant number GCY-100002. Furthermore, the Research Institute of Marine System Engineering (RIMSE) and the Institute of Engineering Research (IOER) of Seoul National University (SNU) are credited for their administrative support.

REFERENCES

Belenky, V.L., 2003, "Probabilistic analysis of roll parametric resonance in head seas", *Proceedings of the 8th International Conference on Stability of Ships and Ocean Vehicles*, Madrid, Spain.

Bulian, G., Francescutto, A., Lugni, C., 2004, "On the nonlinear modeling of parametric rolling in regular and irregular waves", *International Shipbuilding Progress* 51(2-3), pp. 173-203.

Cummins, W.E., 1962, "The impulse response function and ship motion", *Schiffstechnik* 47(9), pp. 101-109.

Francescutto, A., 2001, "An experimental investigation of parametric rolling in head waves", *Journal of Offshore Mechanics and Arctic Engineering* 123(2), pp. 65-69.

Galeazzi, R., Blanke, M., Poulsen, N.K., 2012, "Early detection of parametric roll resonance on container ships", *IEEE Transactions on Control Systems Technology* 21(2), pp. 489-503.

IMO, 2020, "2020 Interim guidelines on the second generation intact stability criteria", *International Maritime Organization*, MSC.1/Circ.1627.

Kapsenberg, G., Wandji, C., Duz, B., Kim, S., 2020, "A comparison of numerical simulations and model experiments on parametric roll in irregular seas", *Journal of Marine Science and Engineering* 8(7), pp. 474.

Kerwin, J.E., 1955, "Notes on rolling in longitudinal waves", *International Shipbuilding Progress* 2(16), pp. 597-614.

Lee, J.H., Kim, Y., 2016, "Development of a semi-analytical method for the efficient prediction of parametric roll", Ocean Engineering 112, pp. 1-15.

Lee, J.H., Lee, J., Kim, Y., Ahn, Y., 2023, "Prediction of wave-induced ship motions based on integrated neural network system and spatiotemporal wave-field data", *Physics of Fluids* 35, pp. 097127.

Luthy, V., Grinnaert, F., Billard, J.Y., Rapp, J., 2023, "Real-time identification of parametric roll", *Journal of Ship Research* 67(3), pp. 174-183.

Park, D.M., Kim, Y., Song, K.H., 2013, "Sensitivity in numerical analysis of parametric roll", *Ocean Engineering* 67, pp. 1-12.

Paulling, J.R., 1961, "The transverse stability of a ship in a longitudinal seaway", *Journal of Ship Research* 4(4), pp. 37-49.

Peter, W.S., Belenky, V.L., 2022, "Second generation intact stability criteria: An overview", *SNAME Maritime Convention, Houston*, Texas, USA, SNAME-SMC-2022-049.

Sadat-Hosseini, H., Stern, F., Olivieri, A., Campana, E.F., Hashimoto, H., Umeda, N., Bulian, G., Francescutto, A., 2010, "Head-wave parametric rolling of a surface combatant", *Ocean Engineering* 37(10), pp. 859-878.

Salvesen, N., Tuck, E.O., Faltinsen, O.M., 1970, "Ship motions and sea loads", *Society of Naval Architects and Marine Engineers*, New York, USA.

Shin, Y.S., Belenky, V.L., Paulling, J.R., Weems, K.M., Lin, W.M., 2004, "Criteria for parametric roll of large containerships in longitudinal seas", *ABS Technical Papers*, pp. 117-147.

Silva, K.M., Maki, K.J., 2022, "Data-driven system identification of 6-DoF ship motion in waves with neural networks", *Applied Ocean Research* 125, pp. 103222.

Yu, L., Ma, N., Gu, X., 2016, "Early detection of parametric roll by application of the incremental real-time Hilbert-Huang transform", *Ocean Engineering* 113, pp. 224-236.

Statistics of parametric roll in irregular waves

Reint P. Dallinga, retired MARIN Sr. Project Manager, r.p.dallinga@gmail.com
Rob Grin, MARIN Sr.Project Manager, r.grin@marin.nl

ABSTRACT

The account for parametric roll in ship design and operation obviously requires a particular resolution of the adopted assessment method. Assuming a time-domain simulation for this purpose, this resolution relates, amongst others, to the particular statistical character of the parametric response. The present contribution to the ISSW Workshop investigates this aspect of deriving practical design values from these simulations.

Starting point for the work is the notion that the parametric excitation in roll as induced by the time-varying wetted geometry of the hull in waves is largely proportional to the instantaneous heel and the amplitude of the incident wave. Combining this approach with the use of a 1DOF representation of the roll response yields a very efficient way to generate extremely long non-repeating realisations of the response. A first step in the analysis of these results was to check the merits of different ways to characterize the magnitude of the parametric roll component and the number of parametric roll events. It is concluded that the characteristics of the envelope of the roll motion offer the best prediction of extreme value statistics. A second step established the reliability of the derived extreme value predictions with increasing simulation duration. These results show that the self-reenforcing character of parametric roll makes it hard to obtain converged results.

Keywords: *Seakeeping, Parametric Roll, Extreme Value Statistics.*

1. REQUIREMENTS FOR ASSESSING RISK

Its non-linear character implies that a 'brute force' time-domain simulation offers the most practical way to quantify parametric roll. However, a simulation of the exposure of the ship in a given condition does not offer immediate insight into the risk of exceeding a particular extreme response in an exposure of a given duration. Assuming the use of 'Order-Statistics' for this purpose, this insight requires a generalization of the simulation results in terms of the expected number of independent 'events' and the probability density function of their magnitude.

2. ADOPTED SIMULATION TECHNIQUE

In linear seakeeping theories, the wave induced excitation and the motion induced reaction forces are dealt with as independent problems. The former is proportional to the amplitude of the incident wave, the latter are proportional to the motion amplitude. A non-linear 'parametric' excitation can be understood as the contribution of the change in the roll excitation induced by the roll response itself. Its name refers to the fact that, if this change is proportional to the instantaneous inclination of the hull, it can be expressed in a change in the restoring parameter in the equation of motion.

Following the above line of thought, the present analysis of the statistical aspects of parametric roll builds on a simple 1-DOF simulation of this behavior which solves the following equation:

$$a.\ddot{\varphi} + b_L.\dot{\varphi} + b_Q.\dot{\varphi}.|\dot{\varphi}| + (c + \delta c).\varphi = M_x^M \qquad (1)$$

The frequency independent coefficients a and c describe the sum of the structural inertia in roll and the added mass and the roll restoring term in calm water. The equation accounts for a linear and a quadratic damping component with frequency independent coefficients b_L and b_Q. The response is driven by a time dependent first-order wave induced roll modal excitation M_x^M and its change with the instantaneous roll inclination of the hull. Because the latter is assumed to be proportional to the roll angle it is expressed as a time dependent change in the restoring term δc.

Because both the first-order excitation and its change with the instantaneous inclination are assumed to be proportional to the amplitude of the incident wave they can be expressed in linear transfer functions which can be calculated by means of a linear potential flow code.

The direct results of a linear calculation method comprise the wave induced forces experienced by the restrained hull in waves, the motion induced reaction forces in calm water and the resulting motion response. The modal excitation M_x^M was obtained by correcting the captive excitation for the additional roll excitation induced by the sway and yaw motions. Repeating the calculations for modest inclinations (2 and 5deg) of the hull and subtracting the excitation on even keel yielded, after dividing by the adopted inclination, an estimate of the parametric excitation. Dividing the result by the displacement weight $\Delta.g$ yields an equivalent variation δGM.

Both the first-order and the parametric excitation are a function of the ship speed v_s and the heading μ. Calculations for several values of the height of the CoG (and related transverse metacentric height GM), several heel angles and several speeds suggest that the heel-derivative of the modal excitation is only weakly dependent on these parameters. The strongest non-linearity of the modal roll excitation with the heel seem to occur at reduced speed in waves from the aft sector.

Fig. 1 indicates the effect of heading and wave frequency on the RAO of the GM variations parametric excitation as obtained with the MARIN Rankine source code SEACAL. The highest variation occurs in waves from 165 (almost from ahead) and 75 deg (just aft of beam waves). In agreement with the common notion that the pitch response plays a role in the parametric excitation, the location of these peaks corresponds with the location of the highest pitch response.

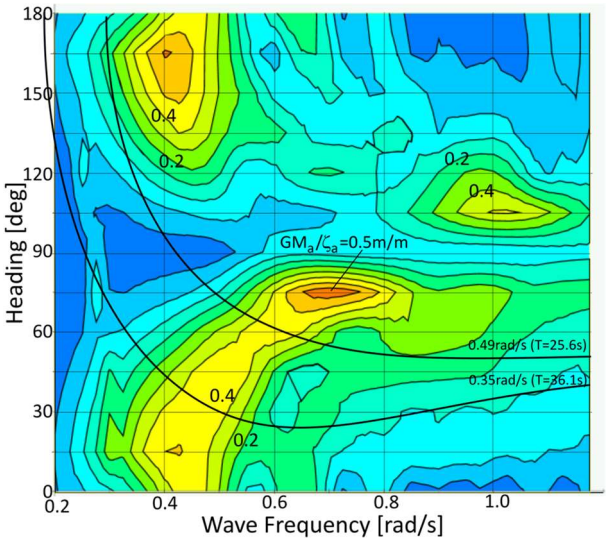

Figure 1: Adopted RAO of the GM Variations, 15kTEU container vessel, 15knots.

By assuming constant speed, time histories of the first-order and parametric excitation were obtained with an inverse FFT technique. The energy associated with each of the encounter frequency components was derived from the spectral density of the incident wave, the square of the transfer function of both excitation components and a correction for the rate of change in the encounter frequency per unit wave frequency. The problem that in waves from the aft sector multiple wave frequencies may contribute to the energy at a single encounter frequency was addressed by assuming that, being the sum of three components with a random mutual phasing, the largest determines the total value.

Adopting 2^{18} FFT frequencies in the range between 0 and 4.π rad/s, non-repeating 36.4hr time histories of the excitation were generated.

3. CONSIDERED CASES

The present work uses the hull form of the 352m L_{pp} 15kTEU container vessel used in the MARIN TOPTIER Joint Industry Project [P., 2024]. The 1:50 7m self-steering model was fitted with the equivalent of 40cm bilge keels.

Two loading conditions were considered. One with a fairly high initial GM (3.0m) and one with a low GM (1.5m). The latter case yields a rather long natural period of roll of 36s. See Table 1.

4. ROLL DAMPING

In the adopted roll damping the effects of the wind forces and the helm response of the ship on the roll-induced yaw were neglected. In addition, the contribution of 'false' (non-roll related) cross-flow velocities in the bilge area in the energy dissipated by the quadratic roll damping component was ignored as well. Leaving the damping of the hull in calm water as the main component, the results of forced roll experiments with the above model were adopted.

The linear damping component, due to wave making and lift effects, increases with speed. At higher speed it decreases with the natural frequency of roll. The quadratic component increases roughly with the square root of the natural frequency of roll.

The results of the forced roll experiments, which cover roll angles up to 15-20deg, are represented well by the sum of a linear and a quadratic damping component. Their values are summarized in Table 1. Fig. 2 shows that, at 15knots, the quadratic component dominates the total roll damping at roll amplitudes beyond 10deg.

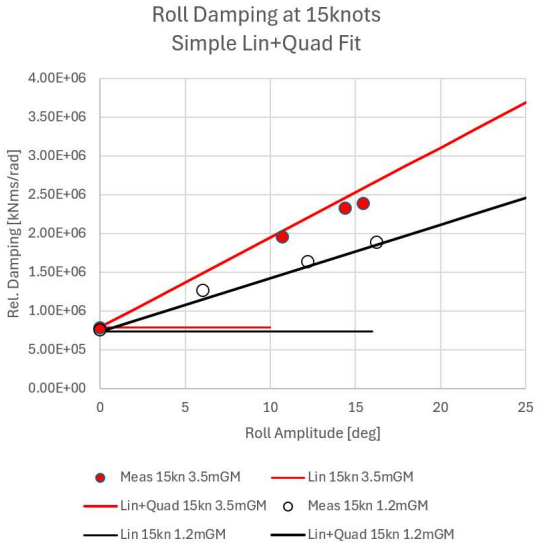

Figure 2: Adopted Roll Damping.

Table 1: Adopted Loading Conditions.

GM	ω_φ	T_φ	b_L	b_Q
[m]	[rad/s]	[s]	[kNms/rad]	[kNms^2/rad^2]
1.5	0.174	36.1	9.7E5	2.5E7
3.0	0.245	25.7	10.4E5	3.0E7

5. CHARACTERIZING PARAMETRIC ROLL

The response of a ship subject to first-order and parametric excitation shows a distinct dual character. This can be understood by considering the modal excitation of a ship, sailing in a regular wave while being simultaneously subject to a forced roll motion. In this case the parametric excitation equals the product of the change in excitation per unit heel and the instantaneous forced roll inclination. An evaluation of the power associated with the work of the parametric excitation in roll yields a non-zero mean in the case where the encounter frequency ω_e is twice the frequency ω_φ of roll motion. With φ_a for the roll amplitude its magnitude (the sign of which depends on the phase angles ε_φ and ε_{GM}) equals:

$$\overline{P_{M_x^P}} = GM_a.\Delta.g.\omega_\varphi \frac{\varphi_a^2}{4}.\sin(2.\varepsilon_\varphi - \varepsilon_{\delta GM}) \qquad (2)$$

The above can be compared with the power dissipated by a linear roll damping b_L given by:

$$\overline{P_{b_L}} = \frac{1}{2}.b_L.\omega_\varphi^2.\varphi_a^2 \qquad (3)$$

From eq. 1 and 2 it follows that the power added to or extracted from the roll mode by the parametric excitation can be expressed as a change in the effective roll damping. This change becomes:

$$\delta b_{\varphi\varphi} = \frac{GM_a.\Delta.g}{2.\omega_\varphi}.\sin(2.\epsilon_\varphi - \varepsilon_{\delta GM}) \qquad (4)$$

In irregular waves the above change in effective roll damping becomes a time-varying quantity. The parametric response occurs in (and for some time after) 'windows' where the sum of the roll damping of the hull and the reduction induced by the parametric excitation becomes negative. The resulting self-reenforcing response is determined by the persistence of a window, the evolution of the parametric excitation along that window as well as the roll response at the start of the event. The latter is governed by the first-order response as well as decaying remnants from earlier parametric roll events. Note that in waves from ahead and athwartships the persistence of the above windows is strongly affected by the bandwidth of the incident waves (with a role for the JONSWAP Peak Enhancement Factor γ). Of course, ship speed and heading play a significant role as well, in particular in waves from the aft sector.

In conditions where parametric roll events occur infrequently, using an over-all characteristic of the combined first-order and parametric response, such as the RMS of the signal or the mean amplitude, appears to be an inadequate measure for assessing the magnitude of the parametric component. Therefore, contrary to the approaches described by Bulian [B., 2006], Belenky and Weem [B, 2011] and Polo and Neves [P., 2018], the present work is based on methods which isolate the parametric component from the total response.

Quick fixes to isolate the parametric component, like introducing a minimum threshold for the roll amplitude, have the disadvantage that the adopted threshold value affects the results of the analysis. This makes it impossible to compare results obtained with different thresholds.

To characterize the parametric component of the roll response two alternative methods were developed.

The first follows the traditional analysis of first-order responses by considering all individual

amplitudes in the time history; it simply counts the number of amplitudes exceeding a given threshold. Varying the threshold yields a cumulative distribution of the number of exceedances as a function of the roll amplitude. Extrapolating the "higher" amplitudes down to zero yields an estimate of the number of amplitudes associated with the parametric response. This way of isolating the parametric component makes use of the fact that the cumulative distribution of their magnitude largely follows a Negative Exponential distribution. As long as the first order response is low, the slope of the least-squares fit through the higher part of the distribution offers a fairly robust estimate of the mean amplitude μ_{φ_a} of the parametric component. The estimated number of individual amplitudes associated with parametric roll includes a fairly large number of 'virtual' amplitudes which 'drown' in the low first order response.

With n_0 for the intercept (the estimated number of amplitudes associated with the parametric response) and μ_{φ_a} for the mean roll amplitude the fitted formulation for the cumulative density function CDF is:

$$n(\varphi_a) = n_0 . e^{-\varphi_a/\mu_{\varphi a}} \quad (5)$$

With D for the duration of the underlying time history and $ER = n_0/D$ for the related event rate ER the 3-hr most probable extreme (see Fig. 9) becomes:

$$MPE_{3hr} = \mu_{\varphi_a} . \ln(3.ER) \quad (6)$$

When applying Order Statistics in the prediction of extreme values, the typical high correlation between individual amplitudes in the roll response may become a problem. The second method is an effort to circumvent this problem by analyzing the envelope of the response. This method, which resembles the Envelope over Threshold approach described by Belenky and Weem [B, 2011], simply counts the number of windows in between an up-crossing and a subsequent down-crossing in which the signal exceeds a given threshold. Varying the threshold yields the required distribution, extrapolation of the results obtained for the 'higher' thresholds to zero yields an estimate of the number of events. This analysis makes use of the fact that the cumulative distribution generally resembles a two-parameter Weibull distribution. Like in the case of the individual amplitudes, the extrapolation to zero yields a number of virtual peak values which are not visible in the signal because they drown in the noise.

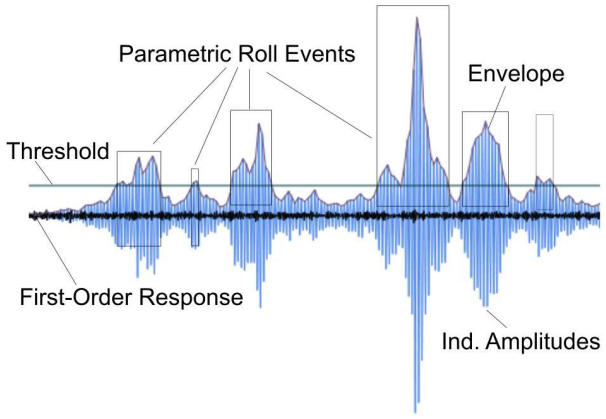

Fig. 4: Identification Parametric Roll Events.

With A for the scale factor and B for the shape factor the Weibull CDF of the envelope peak values is given by:

$$n(\varphi_a) = n_0 . e^{-(\varphi_a/A)^B} \quad (7)$$

The associated mean of the fitted CDF equals:

$$\mu_{\varphi_a} = A.\Gamma(1 + 1/B) \quad (8)$$

The most probable 3hr maximum MPM becomes:

$$MPM_{3hr} = A.[\ln(3.ER)]^{1/B} \quad (9)$$

6. PREPARATIONS

In 1989 Dunwoody [D., 1989] published estimates for the expected decrease in the roll damping induced by the parametric excitation in irregular waves. In the case of broad-band variations of the GM, the spectral density of these variations at a single encounter-frequency (at twice the natural frequency of roll) drives the result.

The encountered spectral density follows from the spectral density of the incident wave, the transfer function of the GM variations and a correction for forward speed and heading.

Both the wave spectrum and the transfer function of the GM variations (Fig. 1) are available as a function of the (zero-speed) wave frequency ω. The product of the spectral density and the square of the transfer function of the GM variations yields a spectrum of the latter as a function of the wave frequency ω. The spectral density as encountered follows from the deep-water dispersion relation given in Eq. 10. The derivative of the encounter frequency describes a frequency dispersion (in waves from forward direction) or concentration (in waves from the aft sector). The encountered spectral density in Eq. 11 (as a function of ω_e) follows from

the 'zero-speed' spectrum (as a function of ω) with a correction $\partial\omega_e/\partial\omega$ for this effect.

$$\omega_e = \omega - \frac{\omega^2}{g}.U.\cos(\mu) \quad (10)$$

$$S_{GMe}(\omega_e) = \frac{S_{GM}(\omega)}{\partial\omega_e/\partial\omega(\omega)} \quad (11)$$

With $\omega_{\omega\varphi}$ for the wave frequency that is encountered at twice the natural frequency of roll ω_φ, $k_{\varphi\varphi}$ for the effective radius of inertia in the roll mode and $\partial\omega_e/\partial\omega(\omega_{\omega\varphi})$ for the rate of change of the encounter frequency with the wave frequency at the aforementioned wave frequency, the adopted interpretation of the broad-band (BB) Dunwoody estimate of the decrease in roll damping becomes:

$$\Delta b^{BB} = \frac{b_{CR}.\pi.g^2}{4.\omega_\varphi^3.k_{\varphi\varphi}^4}.\frac{\left[\frac{GM_a}{\zeta_a}(\omega_{\omega\varphi})\right]^2 S_{\zeta\zeta}(\omega_{\omega\varphi})}{2.\frac{d\omega_e}{d\omega}(\omega_{\omega\varphi})} \quad (12)$$

In the above b_{CR} denotes the critical damping $2.\sqrt{c.a}$ and GM_a/ζ_a denotes the transfer function of the GM variations (see Fig.1).

The above expression takes half of the spectral density as commonly defined in a seakeeping analysis as input. When integrating up to half the Nyquist Frequency, it yields an area that corresponds with the variance of the signal.

Equating the above reduction with the available roll damping requires a linearization of the quadratic damping component. If the individual amplitudes of the parametric roll component follow a negative exponential distribution the equivalent linearized damping becomes:

$$b_{EQ} = 8/\pi.b_Q.\mu_{\varphi a}.\omega_\varphi \quad (13)$$

The total damping amounts to:

$$b_T = b_L + 8/\pi.b_Q.\mu_{\varphi a}.\omega_\varphi \quad (14)$$

Combining equations 12 and 14, the resulting 'analytical estimate' of the mean and RMS (which are the same for the assumed negative exponential distribution) amplitude $\mu_{\varphi a}$ becomes:

$$\mu_{\varphi a} = \frac{b_{CR}.\frac{\pi.g^2}{4.\omega_\varphi^3.k_{\varphi\varphi}^4}.\frac{S_{GM}(\omega_{\omega\varphi})}{2.\frac{d\omega_e}{d\omega}(\omega_{\omega\varphi})} - b_L}{\frac{8}{\pi}.b_Q.\omega_\varphi} \quad (15)$$

The above expression (see also Figs. 7 and 12) illustrates different roles of the linear and quadratic component. Because the parametric excitation increases with the square of the incident wave height, the first, b_L, determines a threshold below which parametric roll will not occur. The second, the quadratic term b_Q, determines the growth above the threshold with increasing wave height.

Figs. 7 and 12 also show the results of Roberts' [R., 1980] estimate on the rms of the over-all roll response. This method makes no a-priori assumption on the distribution of the resulting roll amplitudes.

Visualizing the response

The main operational factors affecting the estimated mean response are the ship speed and heading as well as, for a given wave height, the spectral peak period and shape (JONSWAP γ) of the incident wave. A common way to visualize the response assumes, by assuming a typical spectral peak period, that the ship heading and speed are 'free' parameters. Typical polar plots are shown by Polo and Grin [P., 2024]. It would be useful to complete them with an indication of practical speed limits like those imposed by the installed power as well as issues like green water and bow flare impacts. In following seas, slamming below a flat transom stern offers similar reasons to avoid speeds below, say, 13 knots.

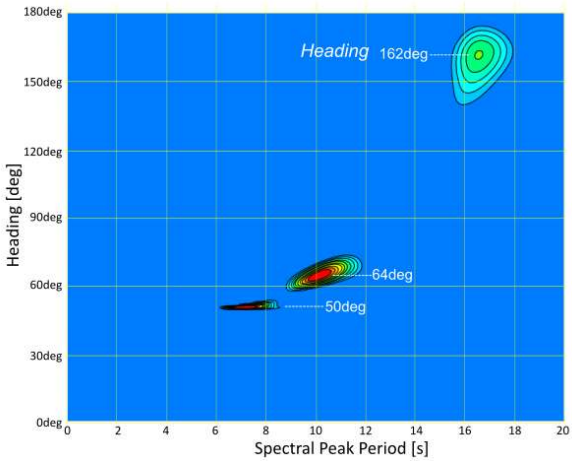

Fig. 5: Character of the Analytical Estimate of the Mean Roll Amplitude, 3.0mGM, T_φ=25.6s, 15knots, γ=3.3, 8m Hs.

In the present work the response is plotted for a fixed speed and a given wave height as a function of the heading and the spectral peak period. Of course, a visualization like that (Fig. 5) requires an interpretation of the peak period in terms of the (maximum) wave height that might occur at a given spectral peak period.

7. TYPICAL RESULTS

Broad-Band Excitation: 3m GM, 15kn, 162deg

Fig. 5 shows an analytical estimate of the response in 8m waves; it indicates three potentially critical areas, one in waves from almost straight ahead and two in waves from the stern-quarter.

The spectra of the parametric excitation in the waves from forward directions show the highest bandwidth. The case around 50deg heading, which occurs at the point where the frequency of wave encounter becomes almost independent of the wave frequency, shows the lowest bandwidth with, at the single frequency where the factor $\partial\omega_e/\partial\omega$ tends to zero, a value tending towards infinity.

The time histories of the simulated roll response in Fig. 6 illustrate the instationary character of the response; quiet periods with a low first-order response are interrupted by events with a much higher, erratic, self-reenforced response. In lower waves the latter occur as isolated events, in higher waves the response is more continuous.

In the subject case the analytical estimate, which suggests a threshold wave height of 6m (Fig. 7), underestimates the mean amplitude of the parametric component at 162deg heading. Roberts' approach over-estimates the response.

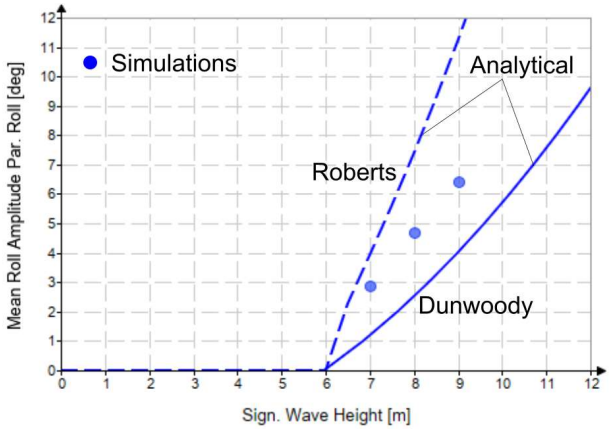

Figure 7: Analytical and Simulation Results, Critical Peak Period, 15knots, γ=3.3, 162deg Heading, 3.0mGM.

Derived distributions

The cumulative frequency of exceedance of the individual amplitudes and the envelope peak values in Fig. 8 are compared with the fitted cumulative probability density functions (CDF).

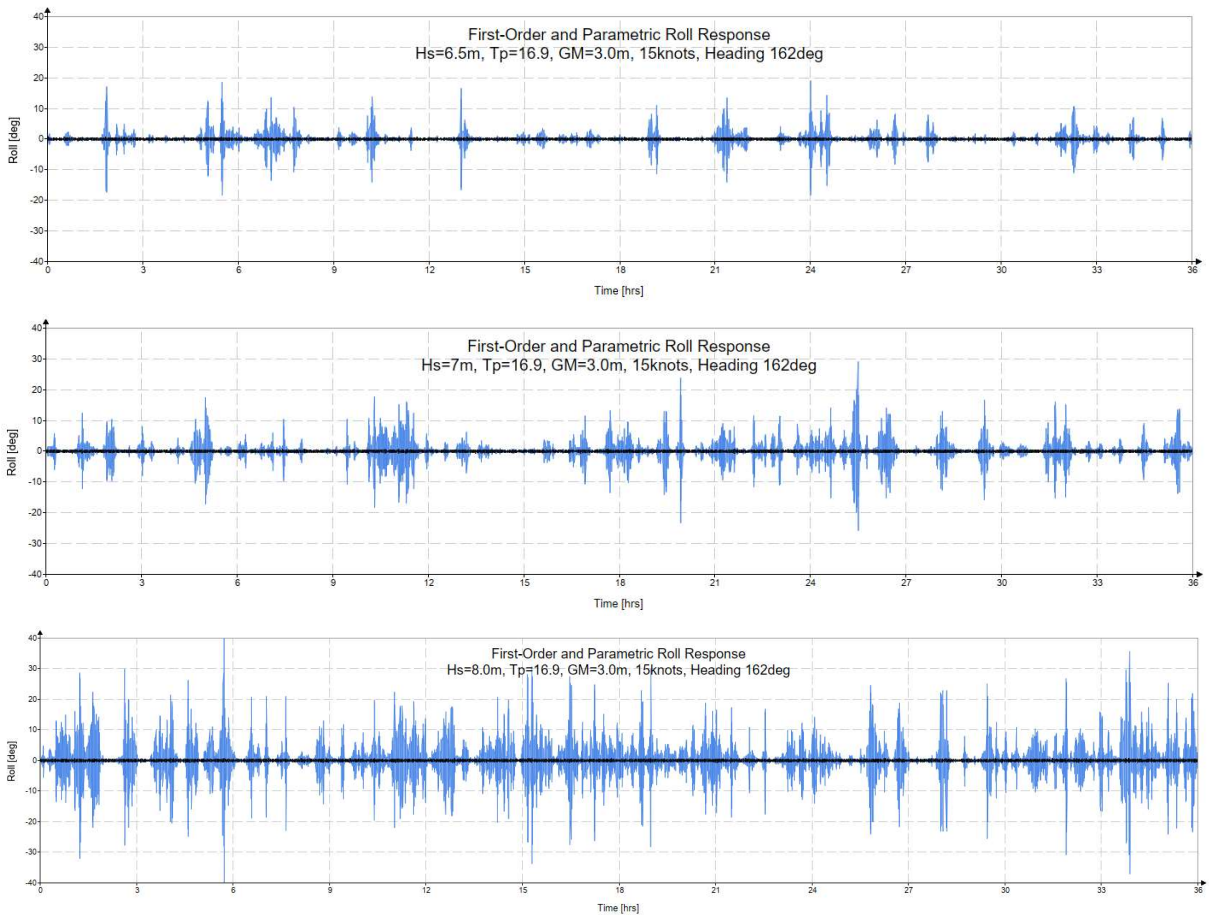

Fig. 6: 36hr Time Histories Roll Response, 3.0mGM, 15knots, 162deg Heading.

These results were obtained for a run duration of extreme duration, 7x36.4hrs. It shows that the individual amplitudes closely follow a negative exponential distribution. This justifies the adopted equivalent linearization of the quadratic damping component in the analytical estimate.

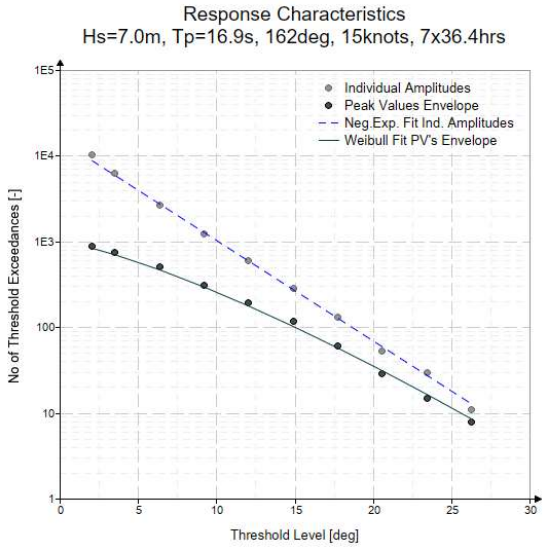

Fig. 8: Distributions of the No of Threshold Exceedances and fitted CDFs.

Experience with the Weibull fit on the envelope peak values in other cases shows a variation of the shape factor B with the wave height (or, more precisely, with the number of parametric roll events). From values around 1, typical for rather instationary time histories, it tends to around 2 in cases with a more stationary response. This suggests a certain degree of saturation of the highest response, which may be explained by the quadratic damping component.

Predicting Extreme Values

The extreme simulation duration that underlies the fitted CDFs was adopted in an effort to obtain converged results. The probability of exceeding a particular extreme value in a shorter exposure can be derived from this fitted CDFs by considering the statistics of the 'ordered' values (Order Statistics, Ochi, 1990). A key assumption in this procedure is that the individual entries which are used to derive the underlying cumulative PDF are uncorrelated from a statistical point of view.

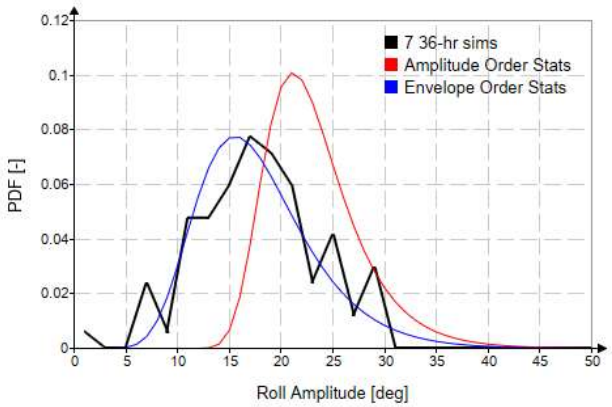

Figure 9: Distribution of 3hr Extremes, 15knots, 7mHs, γ=3.3, 162deg Heading, 3.0mGM.

A way to check on this potential problem is to split the original extremely long time history in subsequent shorter windows and to compare the frequency distribution of window-maxima with the prediction from Order Statistics. This was achieved by splitting the total 7x36.4hr record into 3-hr 'windows'. Fig. 9 compares the distribution of the maximum values in these 3-hr windows with the Order-Statistics prediction, using the number of events and the shape of the fitted CDFs. The comparison in 7m waves suggests that, if a reliable estimate of the underlying distributions is available (from a simulation of a rather extreme duration), the results obtained for the peak values in the envelope offer the best assessment of extreme value statistics. Again, this agreement suggests that the described fitting procedure characterizes the parametric response fairly well.

Comparisons for other cases show that in lower waves, with a more instationary response, the agreement deteriorates. The same is true for shorter target windows, presumably because the events show an increasing interdependency.

Narrow-Band Excitation: 1.5m GM, 15kn, 38deg

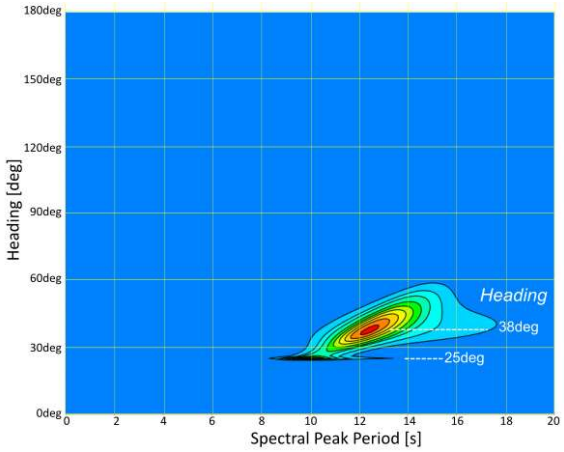

Fig. 10: Character of the Analytical Estimate of the Mean Roll Amplitude, 1.5mGM, T_φ=36s, 15knots, γ=3.3, 8mHs.

For a narrow-band excitation a case with 1.5m GM was adopted. Fig. 2 shows that the quadratic roll

damping component is lower than that in the previous (3.0mGM) case.

Fig. 10 shows the analytical estimate of the mean roll amplitude in 8m waves. It shows that the most important peak around occurs around 38deg heading. The response in waves from forward directions is, in line with the low excitation in the resonant range (Fig. 1) very small.

Fig. 11 shows a fair agreement between the mean value of the individual amplitudes (of the parametric component of the roll response) from the simulations with the analytical estimates. It raises the question why they are not more commonly used to establish the critical combinations of heading and the spectral peak period of the incident wave.

The response in waves from the aft sector is considerably higher than in the previous case. See also Table 2. One reason for this relates to the lower quadratic damping component. A second reason resides in the magnitude of the parametric excitation in the area where the frequency of wave encounter is twice the natural frequency of roll, see Fig.1. It increases from just below 0.2m/m to over 0.4m/m in the present case. A third reason concerns the rate of

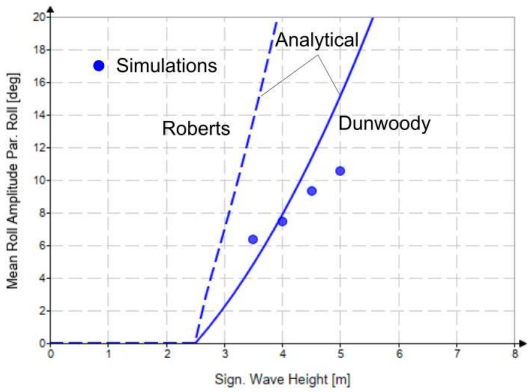

Fig. 11: Analytical and Simulation Results, Critical Peak Period, 15knots, γ=3.3, 38deg Heading, 1.5mGM.

change of the encounter frequency with the wave frequency, which decreases from 1.4 (3.0mGM, 162deg), to 0.4 (1.5mGM, 38deg). The lower value in waves from the stern quarter concentrates the excitation in an increasingly narrower frequency band.

Increasing the GM in the analytical estimate shows that the observed critical condition at 38deg heading and 12.2 spectral peak period migrates towards more beam-on wave directions. The predicted severity of this range of cases raises the question why these are not commonly reported from

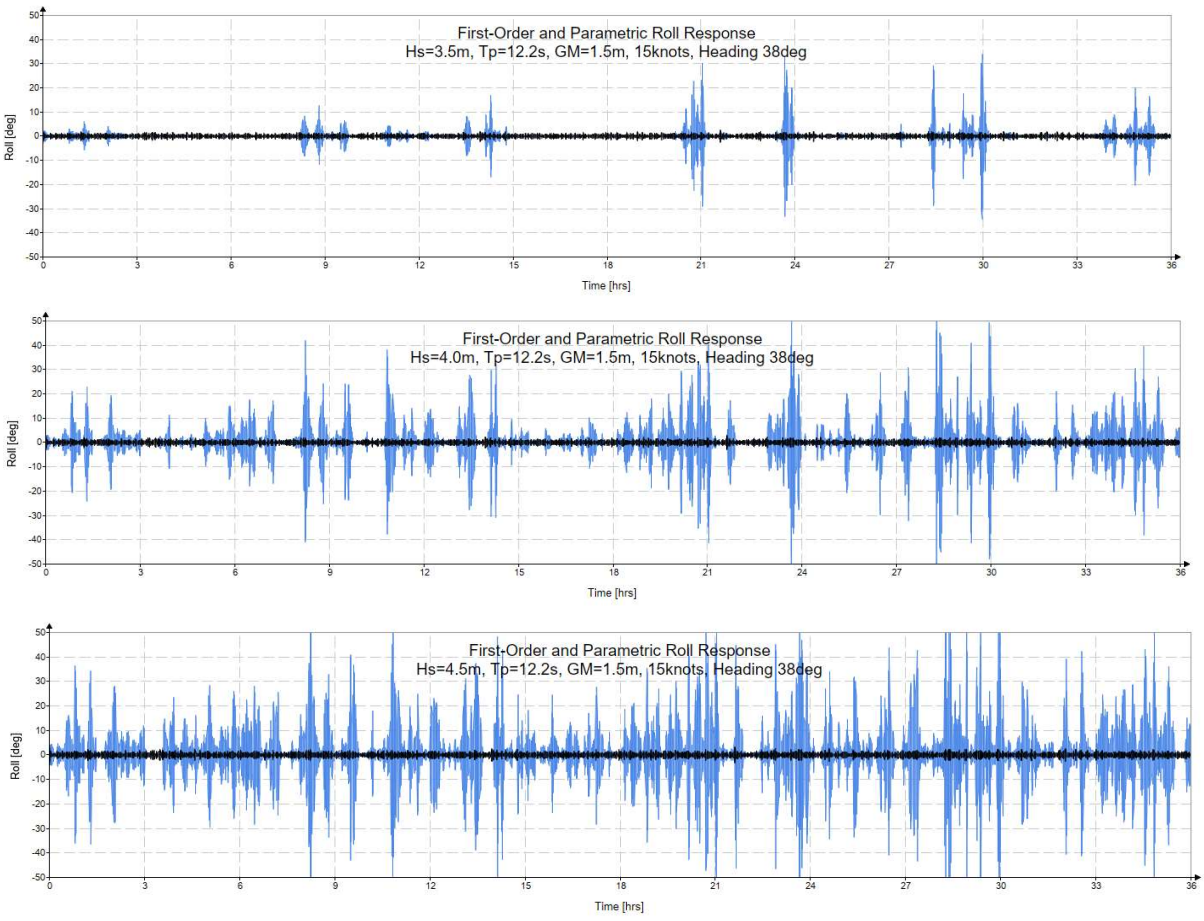

Fig. 12: 36hr Time Histories Roll Response, 1.5mGM, 15knots, 38deg Heading.

practice. A possible explanation is that the critical wave conditions are rather steep; apart from physically limiting the wave height due to wave breaking, simply its sheer occurrence may motivate the master to change course.

Compared to the 3mGM case the time histories (see Fig. 12) of the response suggest a more discontinuous character.

Derived Distributions

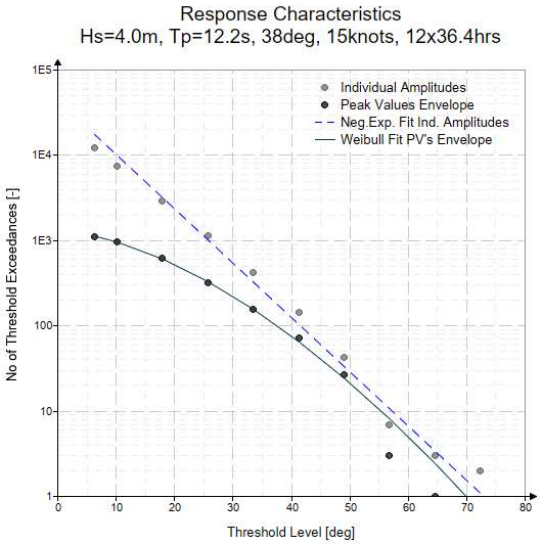

Fig. 13: Distributions of the No of Threshold Exceedances and fitted CDFs.

Like in the previous case, the fitting procedure seems to yield a very good representation of the observed frequency of exceedance of the individual amplitudes and the envelope peak values. See Fig. 13. However, despite the greater length of the underlying time history (12 instead of 7 36.4hr runs), the predicted distribution of the 3hr extremes is not that good. See Fig. 14. The fact that it improves with a larger window length (12 instead of 3hrs, see Fig. 15) suggests that the interdependency of the peak values is larger in waves from the stern quarter. Apparently, as already suggested in the literature [B, 2016, B., 2011, P., 2024], in these conditions even procedures based on an analysis of the envelope do not guarantee a reliable prediction of practical extreme values.

8. RELIABILITY

A simulation of a relatively long duration can be used to test if the response (for instance the 3hr MPM) in the simulated condition remains below a critical design level.

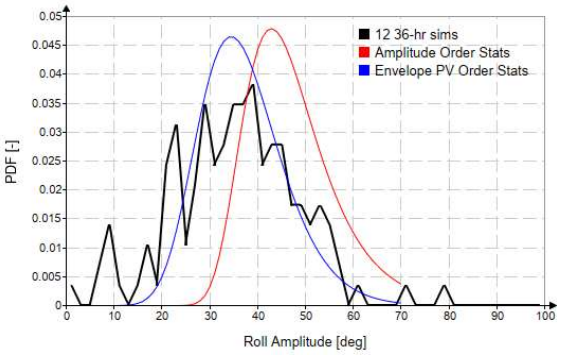

Figure 14: Distribution of 3hr Extremes, 15knots, 4mHs, γ=3.3, 38deg Heading, 1.5mGM.

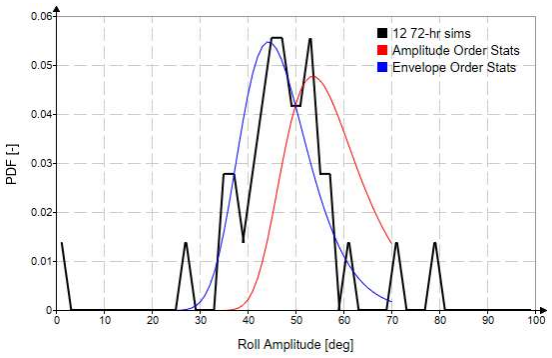

Fig. 15: Distribution of 12hr Extremes, 15knots, 4mHs, γ=3.3, 38deg Heading, 1.5mGM.

Table 2: Key Parameter, 15knots

GM	μ	H_s		ER	A	B
[m]	[deg]	[m]		[1/hr]	[deg]	[-]
1.5	38	4.0	All	67.3	7.70	1.00
			Envelope	2.80	21.60	1.80
3.0	162	7.0	All	62.4	3.66	1.00
			Envelope	3.36	7.93	1.30

In the foregoing it was shown that a fitting procedure yields a reliable way to characterize and quantify the parametric component of the roll response if simulation runs of extreme duration are available. The reliability of results from shorter simulations was checked by repeating the fitting analysis for each of the individual 36.4hr records and sub-sets of increasingly shorter duration. The spread of these results, the ratio of the RMS and mean values of the 3hr-MPM's, is a measure for the reliability of a prediction.

Fig. 16 shows the spread for 6.5 and 8.0m waves from 162deg (3mGM) and 4m waves from 38deg (1.5mGM). The spread derived for 36.4, 18.2 and 9.1hr simulation duration increases from around 8 to around 22%. The trend largely follows that of the reciprocal of the square root of the number of peak values expected for the adopted simulation duration.

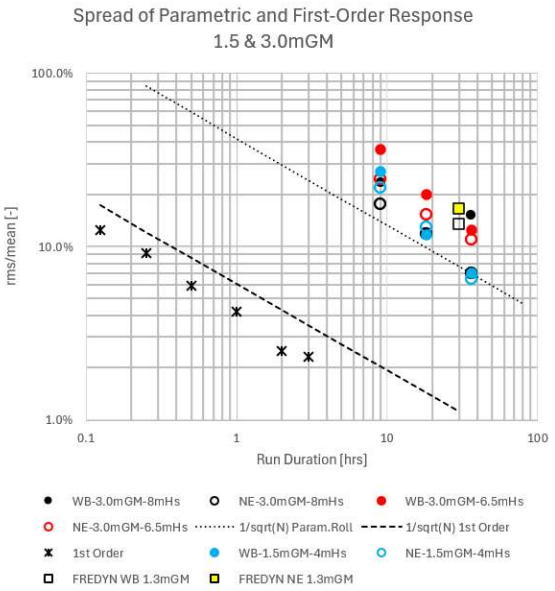

Fig. 16: Spread of the 3-hr MPM vs Simulation Run Duration, WB=Weibull Fit, NE=Negative Exponential Fit.

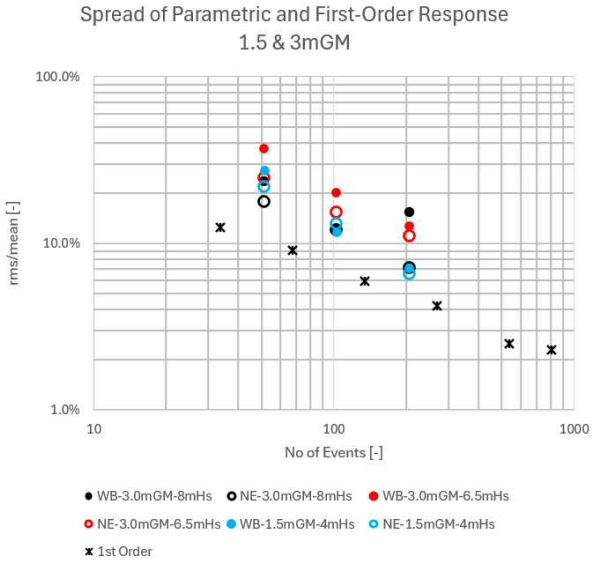

Fig. 17: Spread of the 3-hr MPM vs Simulation the Number of Individual Amplitudes and Envelope Peak Values.

As a reference, Fig. 16 also shows the spread of a first-order quantity; in this case that of the computed GM variations. The comparison shows that the spread in the parametric roll response is about 10 times higher than the spread observed in a typical first-order response. Achieving the reliability of a 'normal' seakeeping assessment the simulation requires a 100-fold longer simulation duration.

A simulation result can be used to test if the response in the simulated condition remains a critical design level. The probability of a false positive result depends on the difference between the simulation result and the design value, the RMS of the predicted response and the PDF of the simulation results. Assuming a Gaussian distribution for the latter, a difference of 1.65 times the RMS yields a probability of a false positive result of 5%. Assuming that a 1hr simulation predicts a first-order MPM with a spread of 4%RMS (see Fig. 16), this means that any condition with a simulation result below (roughly) 93% of the design level passes the test. Similarly, assuming that a 32hr simulation predicts the parametric MPM with a spread of 10%RMS, a condition with a simulation result below (roughly) 86% of the design level passes the test.

Plotting the spread as a function of the expected number of events (Fig. 17) shows a closer agreement for both types of response. This means that the difference in the expected number of events (the number of peak values in the envelope vs the number of individual amplitudes observed in a first-order response) largely causes the much higher uncertainty of the predicted the parametric response. The noise in the fitting procedures that are used to isolate the parametric component from the total response cause the remaining increase.

It should be kept in mind that the above results are related to cases with a more or less stationary response in which the fitting functions reproduced the distributions fairly well. In lower waves and/or off-resonant conditions the fitting becomes more problematic, also because in many individual windows no parametric roll occurs at all; a result already observed by Polo and Neves [P., 2018]. As a consequence the risk of occurrence of parametric roll in moderate or more or less off-resonant conditions, is much harder to predict.

Perhaps inherent to the effort to isolate the parametric component of the roll response is the observation that the spread in the parameters that govern the foregoing result (the Weibull scale and shape factors and the identified event rate) is considerably larger than the spread in the 3hr MPR.

9. FREDYN SIMULATIONS

Because of the unconventional nature of the assumptions and techniques that are used to establish the relation between run duration and the statistical reliability of derived predictions, additional simulations were performed the MARIN simulation code FREDYN [P., 2024].

The "FREDYN" markers in Figs. 16 were obtained for a total of 100 3-hr runs. The observed

spread is very similar to the one derived from the present 1DOF simulations.

10. CONCLUSIONS

In a first step the present work investigates ways to characterize the incidence and magnitude of parametric roll and the extent to which they are a measure for extreme value statistics. It was found that, given a time history of adequate length and a more or less stationary parametric roll response, a Weibull fit on the envelope peak values yields an adequate prediction for 3-6hr time windows. In lower waves and off-resonant conditions the adopted fitting procedure becomes problematic.

In a second step the effect of simulation duration on the spread of the predicted 3-hr MPM's was quantified. The results in more or less stationary conditions showed a spread which is roughly 10-fold the value found for a first-order result. The main reason for this is the low rate of independent parametric roll events. Reducing the spread to a few percent, levels where reliable conclusions and comparisons can be made requires simulations of very extreme duration.

A by-product of the present work was the realization that, although the magnitude of the response is not predicted very accurately, the analytical estimates of the parametric response offers clear insight in the potentially problematic combinations of ship heading and spectral peak period.

11. CONCLUDING REMARKS

The statistical character as described is not the only problem in assessing parametric roll; also modelling the physics of parametric roll accurately is 'challenging' and because this requires detailed knowledge from quite different areas. Of course, one needs the roll natural period and the transverse radius of inertia of the ship, which may be hard enough in practice [G., 2016]. And one needs an estimate of the parametric excitation. Also, the response depends strongly on the magnitude of the linear and quadratic roll damping component of a ship at sea. Because this damping is very small, it seems rather unlikely that the damping of the hull in calm water offers a reliable estimate of the damping experienced by a ship at sea. Last but certainly not least, the success of the proposed analytical formulation seems to indicate that the response depends critically on spectral details of the incident wave. The fact that common storm conditions often show quite variable, often bi-modal character with a different spectral shape [T, 2004], directional spread and direction of propagation per component makes it hard to define a typical case.

In summary, a set of time domain simulations to distinguish improved hull designs, safe loading conditions and reliable operational guidance at sea must always be accompanied with a proper convergence analysis to ensure its validity.

REFERENCES

Belenky, V. and Weems, K.M., 2011, "On the Distribution of Parametric Roll", 12th Int. Ship Stability Workshop

Bulian, G., Francescutto, A. and Lugni, C., 2006, "Theoretical, numerical and experimental study on the problem of ergodicity and 'practical ergodicity' with an application to parametric roll in longitudinal long crested irregular sea", Ocean Eng. 33 (2006) 1007-1043

Dunwoody A.B., 1989, "Roll of a Ship in Astern Seas – Response to GM Fluctuations", *Journal of Ship Research* 33(4), pp. 284-290.

Grin, R., Ruano, S.F., Bradbeer, N, Koelman, H., 2016, On the prediction of weight distribution and its effect on seakeeping, PRADS 2016, Copenhagen, Denmark

Ochi, M.K., 1990, "Applied probability and stochastic processes in engineering and physical sciences", Wiley, ISBN 0-471-85742-4

Polo, J. and Neves, M., 2018, "Study of the Properties of the Parametric Roll Stochastic Process of a Containership", 13nd Int. Conf. on the Stability of Ships and Ocean Vehicles, 16-21 September 2018, Kobe, Japan

Polo, J. and Grin, R., 2024, "Operational Guidance from Perspective of SGISC", 2nd Int. Conf. on the Stability and Safety of Ships and Ocean Vehicles, 14-18 October 2024, Wuxi, China

Roberts, J.B., 1980, The Effect of Parametric Excitation on Ship Rolling Motion in Random Waves, NMI Rept.,UK, R100

Torsethaugen, K. Haver, S., 2004, Simplified double peak spectral model for ocean waves, Paper No. 2004-JSC-193, ISOPE 2004 Toulon, France

Comparison of the critical wave groups method with different extrapolation approaches for direct stability assessment in waves

Kevin M. Silva, *Naval Surface Warfare Center, Carderock Division,* kevin.m.silva14.civ@us.navy.mil
Kevin J. Maki, *University of Michigan*, kjmaki@umich.edu

ABSTRACT

Statistical extrapolation methods are vital for predicting ship dynamic stability with time-domain numerical simulation. Several of these extrapolation methods are included in the guidelines of the International Maritime Organization (IMO) and recommended procedures of the International Towing Tank Conference (ITTC). Previous research compared different recommended extrapolation methods utilizing the same case study with the ITTC A-1 Containership. However, the Critical Wave Groups (CWG) method is not currently considered at IMO or ITTC and has a lack of statistical validation in stern-quartering seas. This paper addresses this gap by solving the 1-to-3 mapping problem required for the CWG method in stern-quartering seas and applies the method to a case study utilized to validate other extrapolation methods. Leveraging a *natural initial condition* approach, the CWG method's roll exceedance rate predictions correlate well with the established methods. These results provide confidence in the CWG method for ship stability assessment, supporting their practical application within IMO and ITTC procedures.

Keywords: *Extreme Events, Critical Wave Groups, Extrapolation, Ship Motions*

1. INTRODUCTION

All problems involving ships on the surface of the ocean (the free surface) involve waves (a.k.a. surface gravity waves), Several statistical extrapolation methods for dynamic stability of a ship in waves have been developed over the course of decades and are gaining adoption in practical everyday use. These extrapolation methods enable the statistical characterization of motion extremes (dynamic stability failures) without the required exposure time needed to develop probabilistic predictions through direct observations. The Explanatory Notes to the Second Generation Intact Stability Criteria (SGISC) in MSC.1/Circ. 1652, published by IMO in 2023, contains description of five extrapolation methods:

- Extrapolation over Wave Height (EWH)
- Envelope Peaks-over-Threshold Method (EPOT)
- Split-time / Motion Perturbation Method (MPM)
- Critical Wave Method
- Linear Superposition Method

In addition to the Explanatory Notes to the SGISC, the EWH, EPOT, and MPM methods are also described in detail in the International Towing Tank Conference (ITTC) Recommended Procedure 7.5-02-07-04.6 “Extrapolation for Direct Stability Assessment in Waves” (ITTC, 2024a). In Belenky et al. (2024), the EWH, EPOT, and MPM methods were all applied to the same set of ship motion data resulting in a favorable comparison of the approaches outlined in the ITTC procedure. Figure 1 shows the result of the comparison from Belenky et al. (2024), where the quantity of interest was the rate of roll exceeding 40 deg. Not only are the predictions for all the extrapolation methods similar, but they also compare favorably with the *true answer* from direct observations of a large volume dataset. The findings shown in Figure 1 were an important step forward in the validation of these methodologies to provide confidence in them as they gain a wider adoption.

The observation (*true answer*) in Figure 1 is provided for three different direct counting approaches, utilizing either exponential, probability, or binomial distributions. These different approaches are described in the Explanatory Notes to the SGISC as well as in ITTC Recommended Procedure 7.5-02-02-10 “Frequency of Random Events” (ITTC, 2024b). As a consequence of the three different methods of direct counting, there are

also three different methods of EWH that are included in Figure 1 from Belenky et al. (2024)

One method that was not included in Belenky et al. (2024) and is not currently a part of the Explanatory Notes in SGISC or ITTC Recommended Procedures is the Critical Wave Groups (CWG) method. The CWG method was first proposed for regular waves in Themelis and Spyrou (2007) and then later extended to irregular waves in Anastopoulos and Spyrou, (2016, 2017, 2019) and implemented for higher fidelity hydrodynamic simulations in Silva and Maki (2021, 2023, 2024a, 2024b), Silva et al. (2021, 2022), and Silva (2023). Comparisons with Monte Carlo simulations have been performed with the CWG method (see Malara et al. (2014) and Shigunov et al. (2019) but the scope of those studies were limited and more comparisons are required for proper validation of the CWG method.

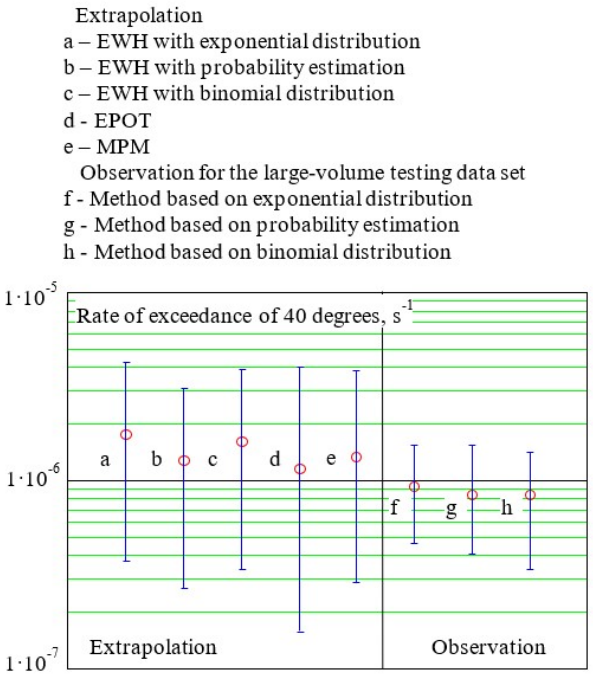

Figure 1. Comparison of different extrapolation methods for the same ship motion dataset (Belenky et al., 2024).

Similar to the other methods compared in Belenky et al. (2024), the CWG method can produce probability estimates of a particular response exceeding a threshold. The CWG method differs from other methods in that deterministic wave groups with known probabilities are constructed and combined with different encounter conditions (sometimes referred to as initial conditions) of the ship's motion state. At a given response threshold, a series of *critical* wave groups are identified that lead to a near exceedance of the threshold and their probabilities are combined to identify the total probability of exceedance. One distinct advantage the CWG method has is that the evaluations can be performed in either simulation or in physical experiments as was performed in Bassler et al. (2009, 2019) and has the potential for a significant reduction in computational cost to evaluate extreme events compared to other methods.

The initial implementations of the CWG method focused on ordinary differential equation (ODE) models of roll motion in beam seas and did not have to consider the effects of forward speed, heading, and the corresponding encountering of the wave group in physical space. Silva et al. (2022) and Silva (2023) introduced the concept of a *natural initial condition* which enabled a completely free-running implementation of the CWG method. The CCS framework from Silva (2023) combines the **C**WG method with **C**omputational Fluid Dynamics (CFD) and **S**urrogate modeling to predict extreme events with high fidelity numerical simulations. Since the CCS framework was originally intended for use with CFD, statistical validation in previous research of the CWG portion of the methodology was impractical due to computational cost. Limited validation was performed using the Large Amplitude Motion Program (LAMP) (Shin et al., 2003), a medium-fidelity potential flow simulation tool, in Silva and Maki (2024b). However, the case studies with LAMP were typically performed in beam seas to achieve large roll angles while avoiding the well-known 1-to-3 mapping problem in stern-quartering seas of converting waves from the encounter to the absolute frame. A solution to this mapping problem was mentioned in Silva (2023) and Silva and Maki (2024b) based on the work in Nielsen (2017) but was not formally described and validated for reconstructing a wave field in the absolute frame from time-histories following the ship in the encounter frame.

The objective of the present paper is to continue building upon the previous research with the free-running implementation of the CWG method and describe a solution to the 1-to-3 mapping problem that is required for stern-quartering seas evaluations within the current framework. Then, the same case study from Belenky et al. (2024) for the ITTC A-1 Containership (Umeda et al., 2000) is exercised with

the CWG method and added to the comparison of methods shown in Figure 1.

2. CRITICAL WAVE GROUPS METHOD

The free-running implementation of the CWG method follows the probabilistic approach proposed in Anastopoulos and Spyrou (2019) and described in further detail in Silva (2023). Wave groups are constructed with Markov chains where a wave group is solely defined by the height (H_c) and period (T_c) of the largest wave in the group and the number of waves in the group (j). The wave groups are then combined with encounter conditions (ship state when encountering the wave group) to identify responses that cross the threshold of interest.

Equation (1) shows the probability of exceedance calculation for a response ϕ exceeding the threshold ϕ_{crit}. In this paper, wave groups are classified in terms of their run length j and wave period groupings in m. The parametrization utilizing j and m results in wave groups that contain the same number of waves and each wave in the group is within a similar range of period. $wg_{m,j}^{(k)}$ are all the wave groups leading to a response threshold exceedance with j waves, wave periods in the m^{th} wave period range, and the k^{th} encounter condition. The probability of exceedance is broken into two separate components: the probability of the k^{th} encounter condition $p[ec_k]$ and the probability of wave group exceedance $p[wg_{m,j}^{(k)}]$, for the m^{th} wave period range, j waves in the group, and the k^{th}encounter condition.

$$p[\phi > \phi_{crit}] = \sum_k \sum_m \left(1 - \prod_j \left(1 - p[wg_{m,j}^{(k)}]\right)\right) \times p[ec_k] \quad (1)$$

Equation (1) is focused on calculating the probability of exceedance. However, to compare against the exceedance rate in Belenky et al. (2024), Equation (2) converts Equation (1) from a probability to an exceedance rate through the introduction of the exceedance rate of the largest wave in the critical wave group $\lambda_{H_{c_{m,j}}^{(k)}}$.

$$\lambda[\phi > \phi_{crit}] = \sum_k \sum_m \left(1 - \prod_j \left(1 - \lambda_{H_{c_{m,j}}^{(k)}} p[wg_{m,j}^{(k)}]\right)\right) \times p[ec_k] \quad (2)$$

3. NATURAL INITIAL CONDITION

Previous applications of the CWG method, as presented in Themelis and Spyrou (2007), Anastopoulos et al. (2016), and Anastopoulos and Spyrou (2016, 2017, 2019), typically employed single degree-of-freedom ordinary differential equation (ODE) models for roll. These models allowed for a straightforward definition of the dynamic state when encountering the wave group through initial conditions. However, real-world scenarios and higher fidelity hydrodynamic simulations demand a more nuanced approach, as the complete dynamic state of the vessel and surrounding fluid cannot be instantaneously prescribed. To address this limitation, Silva and Maki (2021, 2024) and Silva et al. (2021) introduced the *natural initial condition* for implementing the CWG method with CFD, initially for extreme roll of a two-dimensional midship section and later extended to free-running vessels in Silva et al. (2022) and Silva (2023).

The core concept of the natural initial condition is to achieve the desired encounter conditions organically, rather than through forced initial state prescriptions. This is accomplished by embedding deterministic wave groups into a series of pre-existing irregular seaways, creating a composite wave train (see Silva (2023) for the detailed formulation). A similar approach of embedding the wave group in a wave train was considered in Bassler et al. (2009) where waves were generated experimentally with pneumatic wavemakers. As the ship navigates these seaways, it naturally encounters a variety of conditions, eventually reaching the wave group of interest. This approach avoids the problems associated with artificially setting initial conditions, allowing the fluid flow and ship responses to evolve realistically. Furthermore, it preserves the integrity of the CWG methodology, which was originally developed for ODEs, while extending its applicability to higher fidelity numerical hydrodynamic simulation tools and physical experiments.

The natural initial condition method allows for the enforcement of the encounter conditions of interest and generation of the wave group in a natural manner without intrusive and nonphysical measures or mechanisms (physical or virtual). All of the necessary information needed for the observation is contained within the composite wave train. Figure 2 reflects an ensemble of composite waves that possess the same wave group with different irregular preludes. The time-histories in Figure 2 have been

shifted such that the peak of the largest wave in the group occurs at the same time for the composite wave trains to illustrate the methodology. All of the irregular preludes must account for the ramping up of the wave generation and the vessel reaching its target speed. This logic ensures that the vessel will reproduce the previously observed results that led to the encounter condition of interest.

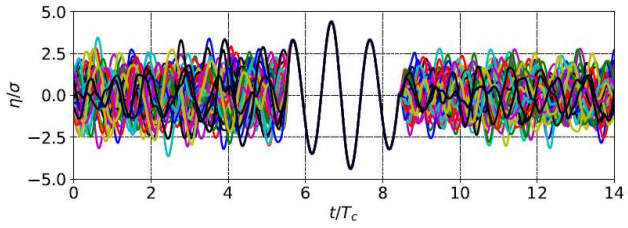

Figure 2. Ensemble of various waves with corresponding different irregular preludes for the same wave group that is shifted in time such that the largest wave in the group's peak occurs at the same time.

Solution to 1-to-3 Mapping Problem

The relationship between the absolute wave frequency (ω_0) and encounter frequency (ω_e) is governed by Equations (3) and (4) in deep water, where U is the ship's forward speed, g is the acceleration due to gravity, and β is the relative wave heading with 180 and 0 deg corresponding to head and following seas, respectively.

$$\omega_e = \omega_0 - \omega_0^2 \psi \tag{3}$$

$$\psi = \frac{U}{g}\cos(\beta) \tag{4}$$

From beam to head seas (90-180 deg), the transformation from encounter to absolute frame is straightforward and there is only a 1-to-1 mapping. In following and stern-quartering seas, 1-to-3 mapping problem arises where a single encounter frequency corresponds to three different absolute frequencies. This is also known as the *Doppler Shift* that is relevant whenever an observer is moving relative to traveling waves. This 1-to-3 mapping problem is highlighted in Figure 3 from Neilsen (2017), where depending on the value of ω_e and ψ, the 1-to-3 mapping occurs.

The 1-to-3 mapping problem is particularly relevant for shipboard sea state estimation, where methods are typically attempting to estimate sea state parameters such as significant wave height, wave period, and spectral shape. Nielsen (2017) provided a solution to the 1-to-3 mapping problem where the objective was to recover the underlying wave spectrum. In the context of the CWG method, the 1-to-3 mapping problem is important in that the composite wave trains are constructed in the encounter frame and it is necessary to extract Fourier components that describe the wave train in the absolute frame for input into hydrodynamic simulations. Nielsen (2017) was not concerned with reconstructing a spatio-temporal description of the wave field. Therefore, the approach was not applied for the relevant use case required of the CWG method.

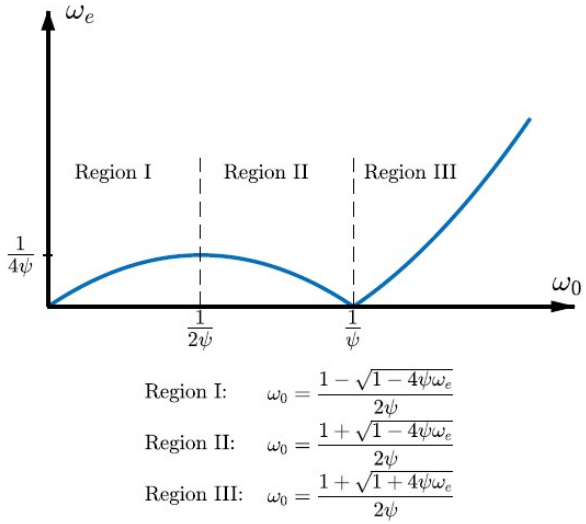

Figure 3. Relationship between encounter and absolute frequencies (Nielsen, 2017).

The approach taken in this paper utilizes the algorithm based on spectral ratios (Algorithm 1 from Nielsen (2017)). For situations where an encounter frequency corresponds to 3 different absolute frequencies (see Figure 3), the spectral ratios approach multiplies the spectral ordinate of the encounter frequency by a scaling ratio to spread the energy across the mapped absolute frequencies. The scaling ratios for a single encounter frequency are shown in Equations (5) through (7) where a_1, a_2, and a_3, correspond to the ratios in Regions 1, 2, and 3, respectively in Figure 3.

$$a_1 = \frac{S_{p01}}{S_{p01} + S_{p02} + S_{p03}} \tag{5}$$

$$a_2 = \frac{S_{p02}}{S_{p01} + S_{p02} + S_{p03}} \tag{6}$$

$$a_3 = \frac{S_{p03}}{S_{p01} + S_{p02} + S_{p03}} \tag{7}$$

S_{p01}, S_{p02}, and S_{p03} represent parametrized spectral ordinates at a given encounter frequency. The parameterized spectral ordinates come from integrated wave parameters from the wave elevation in the encounter frame. In the case of composite

wave train, the wave elevation time-history is used to define a H_s and $T_{z,e}$ from Equations (8) through (10). The values of H_s and $T_{z,e}$ are then input into a nominal spectrum (e.g. JONSWAP, Bretschneider) that is close to the expected shape of the wave spectrum to calculate the parameterized spectral ordinates S_{p01}, S_{p02}, and S_{p0} .

$$m_n = \int_0^\infty \omega_e^n S_e(\omega_e) d\omega_e \quad (8)$$

$$H_s = 4\sqrt{m_0} \quad (9)$$

$$T_{z,e} = 2\pi\sqrt{\frac{m_0}{m_2}} \quad (10)$$

After calculating the scaling ratios at each encounter frequency, the absolute spectral ordinate ($\hat{S}_0$) can be calculated based on encounter spectral ordinate ($\hat{S}_e$) and the corresponding ratios. Equations (11) through (16) show the calculation of the absolute spectral ordinate.

$$\hat{s}_{01} = a_1 \hat{s}_e \frac{d\omega_e}{d\omega_0}|_{\omega_{01}} \quad (11)$$

$$\hat{s}_{02} = -a_2 \hat{s}_e \frac{d\omega_e}{d\omega_0}|_{\omega_{02}} \quad (12)$$

$$\hat{s}_{03} = -a_3 \hat{s}_e \frac{d\omega_e}{d\omega_0}|_{\omega_{03}} \quad (13)$$

$$\frac{d\omega_e}{d\omega_0}|_{\omega_{01}} = 1 - 2\hat{\omega}_{01}\psi \quad (14)$$

$$\frac{d\omega_e}{d\omega_0}|_{\omega_{02}} = 1 - 2\hat{\omega}_{02}\psi \quad (15)$$

$$\frac{d\omega_e}{d\omega_0}|_{\omega_{03}} = 1 - 2\hat{\omega}_{03}\psi \quad (16)$$

From the calculation of the absolute spectral ordinates, the corresponding amplitude of the frequency components can be calculated with Equation (17), where an example is shown for Region 1.

$$\hat{a}_{01} = \sqrt{2\,\hat{s}_{01} d\omega} \quad (17)$$

The implementation of the spectral ratios method from Nielsen (2017) presented in this paper for time-history reconstruction assumes that when the encounter frequency is mapped to the different absolute frequencies and the amplitudes are scaled, the corresponding phases at each frequency stay the same. Figure 4 shows an example of a wave time-history at a moving ship's center of gravity (CG) being reconstructed with the described solution to the 1-to-3 mapping problem. *Original Wave* corresponds to the measured wave time-history at the ship's CG traveling at 10 knots in stern-quartering seas in the ship's encounter frame. A fast Fourier transform (FFT) is performed on the encounter wave time-history to extract encounter frequency, amplitude, and phase components. Those Fourier components were then run through the described algorithm based on spectral ratios to calculate a new set of Fourier components in the absolute frame. The dispersion relation was applied to the Fourier components with the same constant speed and heading as the *Original Wave*, which resulted in the *Reconstruction* result in Figure 4, which is the reconstructed wave time-history in the encounter frame at the ship's CG traveling at 10 knots in stern-quartering seas.

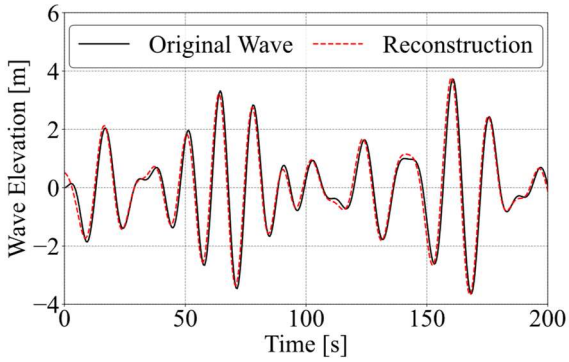

Figure 4. Example wave reconstruction in the encounter frame at the ship's CG for a constant forward speed of 10 knots in stern quartering seas (45 deg).

4. CASE STUDY

Numerical Simulation Tool

The case study utilized the computationally efficient, multi-fidelity time-domain simulation tool SimpleCode (Weems & Wundrow, 2013; Weems & Belenky, 2023). SimpleCode employs a volume-based body-nonlinear formulation, specifically for hydrostatic and Froude-Krylov forces, contributing to its computational efficiency. This efficiency enables validation of extrapolation methods where the *true value* requires long exposure times that could consist of thousands of hours.

Originally designed for the statistical validation of extrapolation methods, SimpleCode prioritizes computational speed while accurately modelling the key nonlinearity of ship motions: the inseparability of nonlinear hydrostatic restoring and incident wave (Froude-Krylov) forcing (Weems & Wundrow, 2013). Accurate modelling of these forces is vital for correctly representing the probabilistic properties of stability variation in irregular waves. While initially considered a qualitative tool due to a simplified representation of diffraction and radiation, recent advancements (Kim et al., 2023) now allow SimpleCode to approximate these effects using data

from potential flow simulation tools like LAMP (Shin et al., 2003). More details of the simulation setup in SimpleCode for this case study are described in Belenky et al. (2024).

Calculations and Comparison

The case study performed in this study mimics the calculations performed in Belenky et al. (2024) for the ITTC A-1 Containership utilizing simulations with SimpleCode. Figure 5 shows the lines of ship considered in the study and Table 1 summarizes the relevant particulars

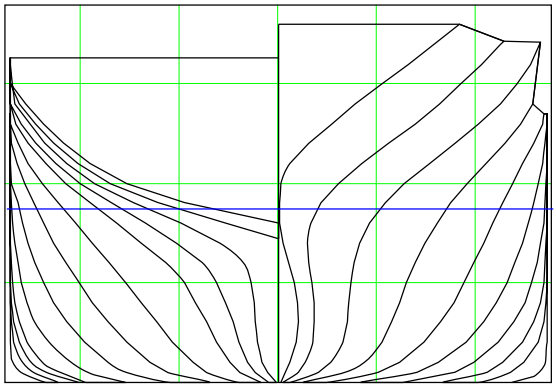

Figure 5. Lines of the ITCC A-1 Containership utilized in SimpleCode.

Table 1. Particulars of the ITTC A-1 Containership.

Parameter	Units	Value
Length Between Perpendiculars (LBP)	m	150
Beam	m	27.2
Draft	m	8.5
Vertical Center of Gravity (KG)	m	10.24
Transverse Metacentric Height (GM)	m	1.38
Block Coefficient	-	0.667
Midship Coefficient	-	0.959
Waterplane Coefficient	-	0.786

Table 2 summarizes the run conditions for the case study. The SimpleCode simulations are performed with a forward speed of 10 knots in stern-quartering seas with a significant wave height of 6 m and modal period of 14 s. The simulations are performed with only three degrees of freedom (heave, roll, and pitch). Therefore, speed and heading are held constant.

Table 2. Run conditions for ITTC A-1 Containership case study.

Parameter	Units	Value
Forward Speed	kt	10
Relative Wave Heading	deg	45 (Stern-Quartering)
Significant Wave Height	m	6
Modal Period	s	14
Spectrum	-	Bretschneider
Total Duration for *True Value*	hours	3,330

The procedure of the CWG method in this paper follows a similar procedure to what was outlined in Silva (2023). First, 10,000 hours of random waves were generated to develop the successive wave probabilistic relations required for the wave group construction and probabilities. For this case study, wave groups were constructed for $j \leq 3$, T_c ranging from 12 to 16 s in 1 s increments, and H_c ranging from 6 to 15 m in 1 m increments. Then, one hour of the ship in random waves was simulated with SimpleCode for the run condition in Table 2 to calculate the probability of encounter conditions (roll and roll velocity) in Figure 6 and the irregular wave preludes that correspond to the encounter conditions of interest. The black circles in Figure 6 correspond to the selected encounter conditons for this case study.

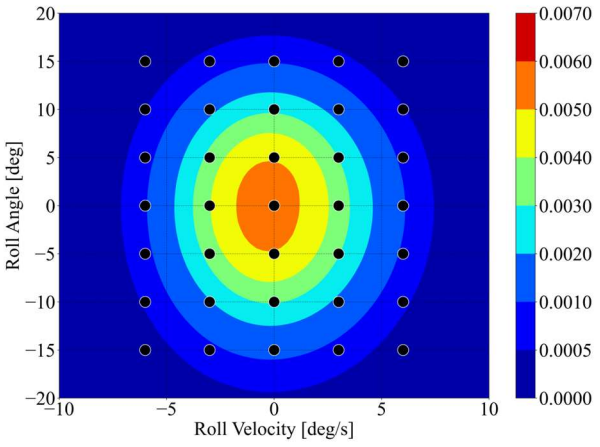

Figure 6. Probability distribution of the encounter conditions.

The deterministic wave groups are then combined with the irregular wave preludes to construct composite wave trains. The composite wave trains are then simulated in SimpleCode and

the maximum response due to the encounter condition and the wave group is recorded. For each wave group shape and encounter condition, the maximum response is interpolated with respect to the largest wave in the group H_c to calculate the critical wave group that leads to a response crossing the threshold of interest. The probability of exceeding the individual critical wave groups are then combined with Equation (2) to calculate the exceedance rate.

Figure 7 shows an adapted version of Figure 1, where the results of the CWG method are compared to EWH, EPOT, and MPM, as well as *true values* from direct counting. Overall, the CWG method agrees well with the other methodologies and the direct counting values.

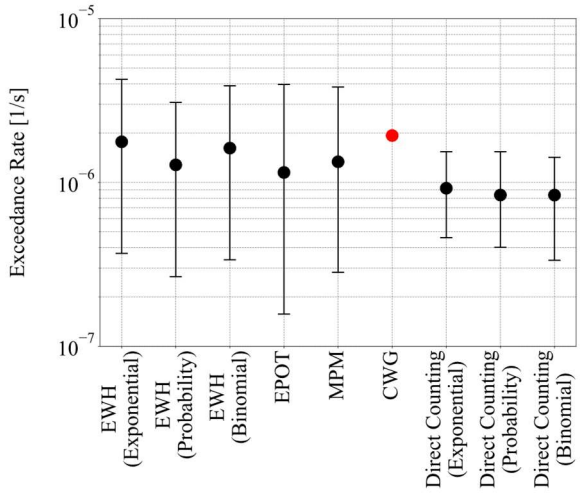

Figure 7. Addition of CWG method to the comparison of different extrapolation methods from Belenky et al. (2024).

The estimated rate falls within the confidence intervals of all the extrapolation methods and slightly above the confidence interval from direct counting. There is currently not a methodology for estimating a confidence interval for the CWG method but from what is shown from other extrapolation methods, the lower confidence interval is expected to overlap with the upper confidence interval of the direct counting estimates.

The comparison of the CWG method in Figure 7 to the other methodologies is a significant step forward in the adoption of the CWG method by the larger community and possible addition to an ITTC recommended procedure. The CWG method, especially when combined with surrogate modeling (Silva, 2023), provides a possibility of significant computational cost savings compared to other methodologies as well as the ability to apply the methodology to physical experiments with targeted short duration events.

5. CONCLUSION AND FUTURE WORK

This work successfully compares the Critical Wave Groups (CWG) method to a set of three other statistical extrapolation techniques for assessing ship dynamic stability in waves. By addressing the 1-to-3 mapping problem inherent in stern-quartering seas, a significant hurdle to the method's practical application, the feasibility and accuracy of a free-running implementation of CWG has been demonstrated. The results obtained when applying CWG to a benchmark dataset, are consistent with established methods like EWH, EPOT, and MPM, underscore the potential of CWG as a valuable tool for naval architects and regulatory bodies. This work contributes to the growing body of evidence supporting the use of statistical extrapolation methods for predicting extreme stability events, fostering safer ship design and operational practices aligned with IMO guidelines and ITTC recommendations. Further research with the CWG method will focus on:

- Developing a method for constructing confidence interval
- Exploring sensitivity to the various parameters (e.g. number of wave group shapes, initial conditions, etc.) of the CWG method to reduce the overall computational cost
- Expanding the application to a wider range of ship types as well as operational and environmental conditions
- Explore alternative methods to blend the deterministic wave group in the encounter frame that maintain the shape of the wave group with forward speed

ACKNOWLEDGEMENTS

This work was supported by the Department of Defense (DoD) Science, Mathematics, and Research for Transformation (SMART) scholarship, the Naval Surface Warfare Center Carderock Division (NSWCCD) Extended Term Training (ETT), and the NSWCCD Naval Innovative Science and Engineering (NISE) programs.

The authors would also like to acknowledge Prof. Kostas Spyrou, Mr. Panayiotis Anastopoulos, and

Prof. Nikolaos Themelis from National Technical University of Athens (NTUA). The idea of the CWG method originated at NTUA with them developing the probabilistic foundation of the methodology. This work relies heavily on their previous efforts.

REFERENCES

Anastopoulos, P.A., Spyrou, K.J., 2016, "Ship dynamic stability assessment based on realistic wave group excitations", Ocean Engineering Vol. 120, pp. 256–263.

Anastopoulos, P.A., Spyrou, K.J., 2017. "Evaluation of the critical wave groups method for calculating the probability of extreme ship responses in beam seas", In: Proceedings of the 16th International Ship Stability Workshop, Belgrade, Serbia. pp. 131–138.

Anastopoulos, P.A., Spyrou, K.J., 2019, "Evaluation of the critical wave groups method in calculating the probability of ship capsize in beam seas", Ocean Engineering Vol. 187, pp. 106213.

Bassler, C.C., Dipper, M.J. & G.E. Lang (2009) "Formation of Large-Amplitude Wave Groups in an Experimental Basin" in *Proc. 10th Int. Conf. on Stability of Ships and Ocean Vehicles (STAB 2010)*, 673-686, St. Petersburg, Russia.

Bassler, C.C., Dipper, M.J & M. Melendez (2019) "Experimental Ship Dynamic Stability Assessment Using Wave Groups" *Chapter 30 of Contemporary Ideas on Ship Stability. Risk of Capsizing*, Belenky, V., Spyrou, K., van Walree F., Neves, M.A.S., and N. Umeda, eds., Springer, ISBN 978-3-030-00514-6, pp. 507-520.

Belenky, V., Weems, K., Pipiras, V., 2024, "Comparison of Extrapolation Methods," Proceedings of the 2nd International Conference on the Stability and Safety of Ships and Ocean Vehicles (STAB&S 2024).

IMO MSC. 1/Circ.1652, Explanatory notes for interim guidelines on the second-generation intact stability criteria, London, April 2023.

ITTC, 2024a, Recommended Procedure 7.5-02-07-04.6 "Extrapolation for Direct Stability Assessment in Waves", Rev. 1.

ITTC, 2024b, Recommended Procedure 7.5-02-01-10 "Frequency of Random Events", Rev. 0.

Kim, M., Pipiras, V., Reed, A. M. and Weems K., 2023, "Calibration of low-fidelity ship motion codes through regressions of high-fidelity forces," Ocean Eng., Vol. 290, 116321.

Malara, G., Spanos, P.D. & F. Arena 2014. Maximum roll angle estimation of a ship in confused sea waves via a quasi-deterministic approach. *Probabilistic Eng. Mech.* Vol. 35, pp. 75-81.Nielsen, U.D., 2017, "Transformation of a wave energy spectrum from encounter to absolute domain when observing from an advancing ship" Applied Ocean Research, Vol. 69, pp. 160-172.

Shigunov, V., Themelis, N. & K. Spyrou (2019) "Critical wave groups vs. direct Monte-Carlo Simulations for Typical Stability Failure Modes of a Container Ship" Chapter 24 of Contemporary Ideas on Ship Stability. Risk of Capsizing, Belenky, V., Spyrou, K., van Walree F., Neves, M.A.S., and N. Umeda, eds., Springer, ISBN 978-3-030-00514-6, pp. 407-421.

Shin, Y. S, Belenky, V. L., Lin, W. M., Weems, K. M. and Engle, A. H. 2003, "Nonlinear time domain simulation technology for seakeeping and wave-load analysis for modern ship design," SNAME Trans., Vol. 111, pp. 557-578.

Silva, K.M., 2023, "A Computational Fluid Dynamics Driven Machine-Learning Framework for Observation and Quantification of Extreme Ship Responses", Ph.D. Thesis, The University of Michigan, Ann Arbor, MI.

Silva, K.M., Maki, K.J., 2021, "Towards a Computational Fluid Dynamics implementation of the critical wave groups method", Ocean Engineering, Vol. 235, pp. 109451.

Silva, K.M., Maki, K.J., 2023, "Considerations for a Free-Running Implementation of the Critical Wave Groups Method", Proceedings of the 19th International Ship Stability Workshop.

Silva, K.M., Maki, K.J., 2024a, "Implementation of the critical wave groups method with computational fluid dynamics and neural networks", Ocean Engineering Vol. 292, pp. 116468.

Silva, K.M., Maki, K.J., 2024b, "Towards a Statistical Validation of the Critical Wave Groups Method for Free-Running Vessels in Beam Seas," Proceedings of the 2nd International Conference on the Stability and Safety of Ships and Ocean Vehicles (STAB&S 2024).

Silva, K.M., Knight, B.G., Maki, K.J., 2022, "Numerical Prediction of Extreme Roll of a Free-Running Ship with Computational Fluid Dynamics and Neural Networks", Proceedings of the 34rd Symposium on Naval Hydrodynamics.

Silva, K.M., Xu, W., Maki, K.J., 2021, "Critical Wave Group Implementation with Computational Fluid Dynamics and Neural Networks," Proceedings of the 1st International Conference on the Stability and Safety of Ships and Ocean Vehicles (STAB&S 2021), Virtual.

Themelis, N., Spyrou, K.J., 2007, "Probabilistic assessment of ship stability", SNAME Transactions, Vol. 115, pp. 181–206.

Umeda, N., A. Munif and Hashimoto, H., 2000, "Numerical

Prediction of Extreme Motions and Capsizing for Intact Ships in Following/ Quartering Seas," Proc. of the 4th Osaka Colloquium on Seakeeping Performance of Ships, Osaka, Japan, pp. 368-373.

Weems, K., and Wundrow, D., 2013, "Hybrid Models for Fast Time-Domain Simulation of Stability Failures in Irregular Waves with Volume-Based Calculations for Froude-Krylov and Hydrostatic Force," Proc. of 13th Intl. Ship Stability Workshop, Brest, France, pp. 130-137.

Weems, K., and Belenky V., 2023, "Reduced-order model for ship motions incorporating a volume-based calculation of body-nonlinear hydrostatic and Froude-Krylov forces," Ocean Eng., Vol. 289, 116214.

Session 6
Application experience with the second generation intact stability criteria and possible regulatory updates

Possible influence of the IACS Rec. No. 34 Rev. 2 on the second generation intact stability criteria

Takako Kuroda, *National Maritime Research Institute,* tkuroda@m.mpat.go.jp
Masahiro Sakai, The University of Osaka, sakai@naoe.eng.osaka-u.ac.jp

ABSTRACT

The interim guidelines for the second-generation intact stability criteria approved by the International Maritime Organization (IMO) in 2020 indicate that environmental data refer to standard wave data published by the International Association of Classification Societies (IACS) Recommendation No. 34 (Corr. Nov. 2001). The IACS revised this recommendation in 2022 and published it as IACS Rec. No. 34 (Rev. 2, Dec. 2022).

This paper examines the influence of the updated IACS Rec. No.34 on the vulnerability criteria for parametric rolling and excessive acceleration failure modes, among the five failure modes addressed in the interim guidelines. The results of the vulnerability assessment using wave scatter diagrams from IACS Rec. No. 34 (Corr. 1) and IACS Rec. No. 34 (Rev. 2) for container ships, including accidental ships in each failure mode, are presented. These results show that the assessed outcomes and pass/fail judgements differed if the wave scatter diagram was changed.

Keywords: *IACS Rec. No. 34, Second generation intact stability criteria, Parametric roll, Excessive acceleration.*

1. INTRODUCTION

The interim guidelines for second-generation intact stability criteria approved by the International Maritime Organization (IMO) (MSC. 1/ Circ. 1627) (IMO, 2020) refer to the International Association of Classification Societies (IACS) Rec. No.34 (Corr. Nov.2001) as the standard wave data for the North Atlantic with the wave spectrum and wave scatter table provided in Section 2.7.2.1. On the other hand, the IACS revised it as IACS Rec. No.34 (Rev. 2 Dec. 2022). The revision extends not only to the wave scatter diagram but also to the wave spectrum. The recommended wave spectrum type changes from Bretschneider to JONSWAP, and the wave period from the average zero up-crossing wave period T_z to the mean energy wave period T_{0m1}. The standard values for each failure mode in the vulnerability criteria of the second generation intact stability criteria were set such that the judgement results for Levels 1 and 2 were consistent, and the accident vessel that caused failure mode was assessed as vulnerable. If the environmental data used in the vulnerability criteria are changed, the standard values of the vulnerability criteria should be reconsidered.

In this study, the vulnerability criteria of the second generation intact stability criteria for parametric rolling and excessive acceleration failure modes were assessed for sample container ships using both standard wave data from IACS Rec. No. 34 (Corr. Nov. 2001) and IACS Rec. No. 34 (Rev. 2, Dec. 2022). The results were compared to investigate the influence of the updated standard wave data on the vulnerability criteria.

2. STANDARD WAVE DATA

The wave scatter diagram of IACS Rec. No. 34 (Corr. Nov. 2001), hereinafter referred to as Corr. 1, is organized according to the significant wave height H_s and the average zero up-crossing wave period T_z. The wave scatter diagram for Corr. 1 is shown in Table 1. The spectral density of sea wave elevation, $S_{Corr.1}(\omega)$, is provided by the Bretschneider wave energy spectrum using the average zero up-crossing wave period T_z as a function of the wave frequency, ω, as follows:

$$S_{Corr.1}(\omega) = \frac{{H_s}^2}{4\pi}\left(\frac{2\pi}{T_z}\right)^4 \omega^{-5} exp\left[-\frac{1}{\pi}\left(\frac{2\pi}{T_z}\right)^4 \omega^{-4}\right] \quad (1)$$

On the other hand, the wave scatter diagram of IACS Rec. No. 34 (Rev. 2 Dec. 2022), hereinafter referred to as Rev. 2, consists of the significant wave height H_s and the mean wave period T_{0m1}. The wave scatter diagram for Rev. 2 is presented in Table 2. Rev. 2 uses the JONSWAP wave spectrum with $\gamma = 1.5$ described by the following expression:

$$S_{Rev.2}(\omega) = \alpha S_{PM}(\omega)\gamma^{exp\left[-\frac{(\omega/\omega_p-1)^2}{2\sigma^2}\right]} \quad (2)$$

where $S_{PM}(\omega)$ is the Bretschneider spectrum using the wave peak period T_p expressed as follows:

$$S_{PM}(\omega) = \frac{5}{16}H_s^2\left(\frac{2\pi}{T_p}\right)^4\omega^{-5}exp\left[-\frac{5}{4}\left(\frac{2\pi}{T_p}\right)^4\omega^{-4}\right] \quad (3)$$

γ, ω_p T_p, α, and σ are as follows:

γ : the non-dimensional peak shape parameter, taken as 1.5

T_p: the peak wave period

$$\alpha = \frac{1}{5}\left(\frac{1}{0.1160 + 0.0594\sqrt{\gamma} + 0.0246\gamma}\right)$$

$$\sigma = \begin{cases} 0.07\ for\ \dfrac{\omega}{\omega_p} \le 1 \\ 0.09\ for\ \dfrac{\omega}{\omega_p} > 1 \end{cases}$$

ω_p: the peak angular frequency [rad/s] (4)

$S_{PM}(\omega)$ shown in Eq. 3, and $S_{Rev.2}(\omega)$ expressed as the JONSWAP wave spectrum with $\gamma = 1.5$ were compared in Fig. 1. The JONSWAP spectrum exhibited a more pronounced peak. The relationship between the mean wave period T_{0m1} in the scatter diagram and the peak wave period T_p is evaluated using the following equation:

$$T_{0m1} = 2\pi\frac{m_{-1}}{m_0} = \left(0.7757 + 0.0965\sqrt{\gamma} - 0.0144\gamma\right)T_p \quad (5)$$

when $\gamma = 1.5$, T_{0m1} is expressed as $0.872T_p$. Using the integral value of the spectrum $\left(\frac{T_p}{\bar{T}_z}\right)^2 = \frac{\tilde{m}_2}{\tilde{m}_0}$=1.869 given by Yamaguchi (1984), the relationship between T_{0m1} and T_z is as follows,

$$T_z = \sqrt{\frac{\tilde{m}_0}{\tilde{m}_2}}\frac{\tilde{m}_0}{\tilde{m}_{-1}}0.838T_{0m1} \quad (6)$$

The probability densities of significant wave heights for Corr. 1 and Rev. 2 are shown Fig. 2. The probability density of significant wave heights of 1.5 m and 2.5 m in Rev. 2 was larger than that in Corr. 1, but lower for larger significant wave height. Rev. 2 is defined using state-of-the-art wave data sources combined with a ship position dataset. It is assumed that the less severe sea conditions such as the low probability of large wave height in the revised IACS Rec. No. 34 are an effect of the widespread use of weather routing and the avoidance of severe weather (Austefjord, et al. 2023). The probability densities of the wave periods for Corr. 1 and Rev. 2 are shown in Fig. 3, with T_{0m1}in Rev. 2 converted to T_z using Eq. (6). The probability density of short-wave periods in Rev. 2 was higher than that in Corr. 1. The mean wave period of T_z in Corr. 1 is 8.9 seconds, and that of T_{0m1} in Rev. 2, when converted to T_z as 7.2 seconds.

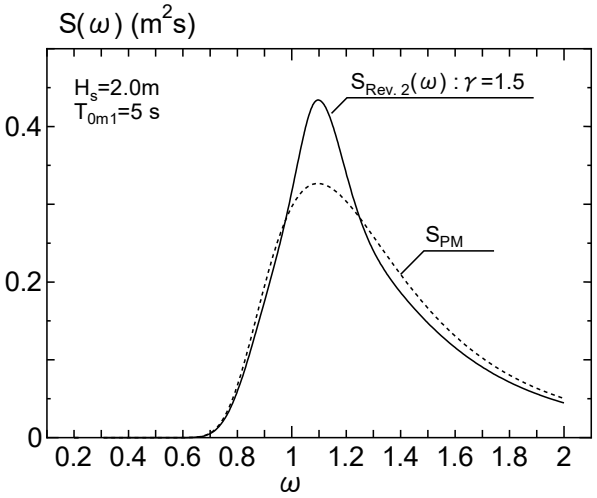

Figure 1: Comparison of wave spectra of Corr. 1 and Rev. 2

Table 1: Wave scatter table for IACS Rec. No. 34 Corr.1 Nov. 2001

Hs (m) \ Tz (s)	3.5	4.5	5.5	6.5	7.5	8.5	9.5	10.5	11.5	12.5	13.5	14.5	15.5	16.5	17.5	18.5	Sum
0.5	1.3	133.7	865.6	1186.0	634.2	186.3	36.9	5.6	0.7	0.1							3050.4
1.5		29.3	986.0	4976.0	7738.0	5569.7	2375.7	703.5	160.7	30.5	5.1	0.8	0.1				22575.4
2.5		2.2	197.5	2158.8	6230.0	7449.5	4860.4	2066.0	644.5	160.2	33.7	6.3	1.1	0.2			23810.4
3.5		0.2	34.9	695.5	3226.5	5675.0	5099.1	2838.0	1114.1	337.7	84.3	18.2	3.5	0.6	0.1		19127.7
4.5			6.0	196.1	1354.3	3288.5	3857.5	2685.5	1275.2	455.1	130.9	31.9	6.9	1.3	0.2		13289.4
5.5			1.0	51.0	498.4	1602.9	2372.7	2008.3	1126.0	463.6	150.9	41.0	9.7	2.1	0.4	0.1	8328.1
6.5			0.2	12.6	167.0	690.3	1257.9	1268.6	825.9	386.8	140.8	42.2	10.9	2.5	0.5	0.1	4806.3
7.5				3.0	52.1	270.1	594.4	703.2	524.9	276.7	111.7	36.7	10.2	2.5	0.6	0.1	2586.2
8.5				0.7	15.4	97.9	255.9	350.6	296.9	174.6	77.6	27.7	8.4	2.2	0.5	0.1	1308.5
9.5				0.2	4.3	33.2	101.9	159.9	152.2	99.2	48.3	18.7	6.1	1.7	0.4	0.1	626.2
10.5					1.2	10.7	37.9	67.5	71.7	51.5	27.3	11.4	4.0	1.2	0.3	0.1	284.8
11.5					0.3	3.3	13.3	26.6	31.4	24.7	14.2	6.4	2.4	0.7	0.2	0.1	123.6
12.5					0.1	1.0	4.4	9.9	12.8	11.0	6.8	3.3	1.3	0.4	0.1		51.1
13.5						0.3	1.4	3.5	5.0	4.6	3.1	1.6	0.7	0.2	0.1		20.5
14.5						0.1	0.4	1.2	1.8	1.8	1.3	0.7	0.3	0.1			7.7
15.5							0.1	0.4	0.6	0.7	0.5	0.3	0.1	0.1			2.8
16.5								0.1	0.2	0.2	0.2	0.1	0.1				0.9
Sum	1.3	165.4	2091.2	9279.9	19921.8	24878.8	20869.9	12898.4	6244.6	2479.0	836.7	247.3	65.8	15.8	3.4	0.7	100000

Significant wave height, Hs (m)

Table 2: Wave scatter table for IACS Rec. No. 34 Rev. 2 Dec. 2022

Hs (m) \ T_{0m1} (s)	4.5	5.5	6.5	7.5	8.5	9.5	10.5	11.5	12.5	13.5	14.5	15.5	16.5	17.5	18.5	19.5	Sum
0.5	6.82	202	333.61	187.76	45.59	4.74	0.21										780.73
1.5	0.33	2028.35	12750.8	11693.4	7215.76	3006.8	846.07	160.77	20.63	1.79	0.1						37724.81
2.5		3.38	2805.81	8517.74	7835.85	5885.37	3608.3	1805.81	737.71	246	66.96	14.88	2.7	0.4	0.05		31530.96
3.5			23.06	2742.51	4666.81	4100.83	2936.41	1713.38	814.68	315.65	99.66	25.64	5.38	0.92	0.13	0.01	17445.07
4.5				82.06	1759.81	2069.19	1715.42	1151.29	625.51	275.12	97.96	28.24	6.59	1.24	0.19	0.02	7812.64
5.5				0.08	149.74	811.81	791.81	609.66	375.67	185.26	73.12	23.09	5.84	1.18	0.19	0.02	3027.47
6.5					1.02	147.59	305.37	271.71	190.23	104.79	45.42	15.49	4.16	0.88	0.15	0.02	1086.83
7.5						4.77	88.62	107.2	86.26	53.35	25.36	9.27	2.6	0.56	0.09	0.01	378.09
8.5						0.02	9.4	38.7	36.8	25.95	13.63	5.33	1.55	0.34	0.05	0.01	131.78
9.5							0.2	9.34	15.15	12.51	7.39	3.12	0.94	0.2	0.03		48.88
10.5								0.81	5.73	5.96	4.08	1.9	0.6	0.13	0.02		19.23
11.5								0.02	1.29	2.68	2.23	1.18	0.4	0.08	0.01		7.89
12.5									0.11	1.01	1.14	0.72	0.27	0.06	0.01		3.32
13.5										0.22	0.51	0.42	0.18	0.04			1.37
14.5										0.02	0.19	0.21	0.12	0.03			0.57
15.5											0.04	0.09	0.07	0.02			0.22
16.5												0.03	0.04	0.01			0.08
17.5												0.01	0.02	0.01			0.04
18.5													0.01	0.01			0.02
Sum	7.15	2233.73	15913.3	23223.54	21674.58	16031.12	10301.81	5868.69	2909.77	1230.31	437.79	129.62	31.47	6.11	0.92	0.09	100000

Significant wave height, Hs (m)

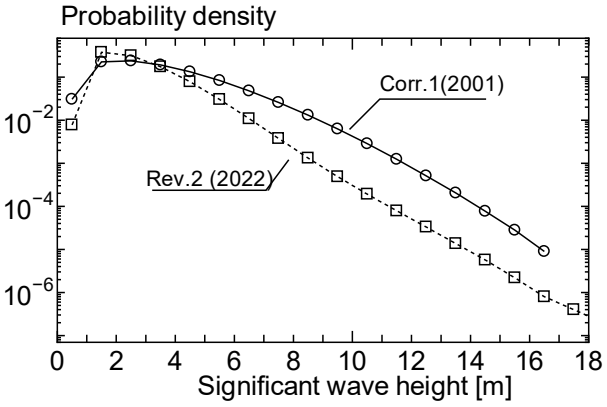

Figure 2: Probability density of significant wave heights of Corr. 1 and Rev. 2

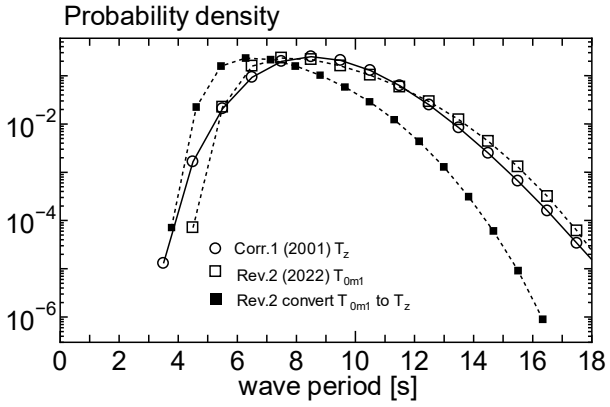

Figure 3: Probability density of wave periods of Corr. 1 and Rev. 2

3. PARAMETRIC ROLLING FAILURE MODE

3.1 Vulnerability criteria for parametric rolling

Level 1 and the first check of Level 2 criteria for parametric rolling assess vulnerability based on the stability of the upright condition. The second check of Level 2 criterion assesses vulnerability based on the parametric rolling amplitude in waves.

In Level 1 and the first check of Level 2 criteria, the occurrence of parametric rolling in regular waves is used to assess vulnerability. The wave conditions, namely the wave length λ_i, the wave height H_i, and the occurence probability of the wave W_i, are derived from the wave scatter diagram. Same as in IACS Rec. No. 34 Corr. 1, when $T_{z,i}$ $(i = 1, \dots, N)$, $H_{1/3,j}$ $(j = 1, \dots, M)$, and the probability of sea-states $p_{i,j}$ is given by:

$$T_{ref,i} \triangleq T_{01,i} = 1.0864 T_{z,i} \tag{7}$$

$$\lambda_i = \frac{g}{2\pi} {T_{ref,i}}^2 \tag{8}$$

$$\left.\begin{aligned} H_{1/3,ref,i} &\triangleq E\{H_{1/3,j} \mid T_{z,i}\} \\ &= \frac{1}{W_i} \sum_{j=1}^{M} p_{ij} H_{1/3,j} \end{aligned}\right\} \tag{9}$$

$$\left.\begin{aligned} H_i &= k_{PR} H_{1/3,ref,i} \\ &with\, k_{PR} = 0.70 \end{aligned}\right\} \tag{10}$$

$$S_{w,i} = \frac{H_i}{\lambda_i} \tag{11}$$

$$W_i = \sum_{j=1}^{M} p_{ij} \tag{12}$$

Here, $E\{\}$ denotes the expected value. The wave scatter diagram of IACS Rec. No. 34 Rev. 2 is provided with $T_{0\mathrm{m1}}$ and H_{S}, although that of IACS Rec. No. 34 Corr. 1 is provided with T_{z} and H_{s}. Here, T_{0m1} is defined in Eq. 5. m_n in the equation is as follows:

$$m_n \triangleq E\{\omega^n\} = \int_0^\infty \omega^n S(\omega) d\omega \tag{13}$$

$$T_{01,i} = 0.9075 T_{0m1,i} \tag{14}$$

Here, m_n is the n-th order spectral moment, and $S(\omega)$ is the wave spectrum. In this study, the mean wave period $T_{0\mathrm{m1}}$ provided in IACS Rec. No. 34 Rev. 2 was converted into T_{01} by the above equation. In Level 1 criterion, a wave whose length was the same as the L_{BP} and whose wave steepness was the same as the steepest wave among the N wave cases was used.

In the second check of Level 2 criterion, the parametric rolling amplitude in regular waves is used to assess vulnerability. The wave conditions involved waves with the same length as the ship length L_{BP}. The wave steepness $\Theta_{\mathrm{eff}}(H_{1/3}, T_{\mathrm{z}})$ is calculated based on Grim's effective wave theory as:

$$\Theta_{eff} = \frac{4.0043\sqrt{m_{0,eff}}}{L_{BP}} \tag{15}$$

$$m_{0,eff} = \int_0^\infty \left[\frac{\frac{\omega^2 L_{BP}}{g} sin\left(\frac{\omega^2 L_{BP}}{2g}\right)}{\pi^2 - \left(\frac{\omega^2 L_{BP}}{2g}\right)^2} \right]^2 S(\omega) d\omega \tag{16}$$

Here, g is the gravitational acceleration. Since $S(\omega)$ is the wave spectrum and differs depending on the wave scatter diagram, the wave steepness to be considered in the second check of Level 2 criterion depends on the employed $S(\omega)$.

3.2 Sample ships for the vulnerability criteria of parametric rolling

Two container ships were assessed by both the wave scatter diagram of the North Atlantic Ocean: IACS Rec. No. 34 Corr. 1 and the revised version, IACS Rec. No. 34 Rev. 2, used in Levels 1 and 2 of the vulnerability criteria for parametric rolling.

The first was a C11-class Post-Panamax containership (C11) with a ship length of 262.0 m (MSC. 1/Circ. 1652) (IMO, 2023). The assessment conditions for the C11-class containership are the same as those in the example of the Level 2-based operational limitations assessment related to the

maximum wave height shown in Table 2.7.1, Section 2.7.1 of Appendix 5 of the explanatory notes (MSC. 1/Circ. 1652). Table 3 shows the principal particulars and assessment conditions.

Another is ITTC A1 containership (A1), and Table 4 shows the principal particulars and assessment conditions.

Table 3 The principal particulars and assessment condition of C11 Class containership for Parametric Rolling

Item	Value
Length [m]	262.0
Breadth [m]	40.0
Draft at midship [m]	11.5
Trim [m]	0.0
Block coefficient	0.56
Metacentric height without free-surface correction [m]	1.965
Natural roll period T_ϕ [s]	25.1
Bilge keel length ratio l_{BK}/L_{pp}	0.292
Bilge keel height ratio h_{BK}/B	0.010
Bilge keel area [m^2]	30.6

Table 4 The principal particulars and assessment condition of ITTC A1 Containership for Parametric Rolling

Item	Value
Length [m]	150.0
Breadth [m]	27.2
Draft at midship [m]	8.5
Trim [m]	0.0
Block coefficient	0.667
Metacentric height without free-surface correction [m]	1.0
Natural roll period T_ϕ [s]	20.1
Bilge keel length ratio l_{BK}/L_{pp}	0.25
Bilge keel height ratio h_{BK}/B	0.0201
Bilge keel area [m^2]	20.5

3.3 Assessment results for Parametric rolling

The authors performed sample calculations based on the vulnerability criteria for parametric rolling. The results are presented in Tables 5–7. The C11 containership failed at Level 1 and the first check of Level 2 vulnerability criteria with both IACS Rec. No. 34 Corr. 1 and Rev. 2. In the second check of Level 2 criterion, C_2 values for both the C11 containership and the A1 containership decreased in Rev. 2. Moreover, C11 containership failed with Corr. 1, but passed with Rev. 2, using the criterion of $C_2 \leq R_{\mathrm{PR,L2C2}} = 0.025$.

Table 5 Level 1 vulnerability criterion for parametric rolling in the case of C11

C11	$\frac{GM_{\mathrm{amp}}}{GM_{\mathrm{mean}}}$	$R_{\mathrm{PR,L1}}$	Judge
Corr. 1	1.05326	0.41343	Fail
Rev. 2	1.47664	0.41343	Fail

Table 6 First check of the Level 2 vulnerability criterion for parametric rolling in the case of C11

C11	C_1	$R_{\mathrm{PR,L2C1}}$	Judge
Corr. 1	0.4364	0.06	Fail
Rev. 2	0.1061	0.06	Fail

Table 7 C_2 values used in the second check of the Level 2 vulnerability criterion for parametric rolling in the case of C11 and ITTC A1

C_2	C11	A1
Corr. 1	0.02592	0.001563
Rev. 2	0.009511	0.0001924

3.4 Discussion on the effects of the wave scatter diagrams on the vulnerability criteria for Parametric rolling

Wave steepnesses $S_{w,i}$ were calculated from the wave conditions of IACS Rec. No. 34 Corr. 1 and Rev. 2, as listed in Tables 8 and 9, respectively. As these tables, along with Tables 1 and 2, show, the probability of steeper and longer waves was lower in Corr. 1 than in Rev. 2. Therefore, within the framework of Level 2 vulnerability criteria for parametric rolling, the assessment with Rev.2 is less stringently than Corr.1, as shown in Tables 6 and 7. For the first and second checks of Level 2, considering the characteristics of the wave scatter diagram and the sizes of ships that induce parametric rolling, if changing from Corr. 1 to Rev. 2, it is necessary to appropriately reset the value of R_{PR}, at least for the second check of Level 2, because the C11 passes the vulnerability criteria with $R_{\mathrm{PR,L2C2}} = 0.025$, even though this value was intended to prevent C11 from satisfying the criteria.

In constant, Corr. 1 assesses within the framework of Level 1 the assessment with Corr. 1 is more conservative. This is because Rev. 2 uses a steeper wave, which is based on a short wave with $\lambda_i = 38.896$ [m]. Such short waves are unlikely to induce parametric rolling in ocean-going merchant ships. The explanatory notes (MSC. 1/Circ. 1652) may be unduly strict. When using a wave scatter diagram other than IACS Rec. 34 Corr. 1, reasonable modifications, such as selecting the wave steepness for Level 1 from waves with λ_i comparable to the length of the target ship, should be considered.

Table 8 The wave steepness of IACS Rec. No. 34 Corr. 1

No.	T_{02} [s]	T_{01} [s]	λ_i [m]	W_i	$H_{1/3,\mathrm{ref},i}$ [m]	H_i [m]	$S_{\mathrm{w},i}$
1	3.5	3.802	22.574	0.000013	0.500	0.350	0.0155
2	4.5	4.889	37.316	0.001654	0.707	0.495	0.0133
3	5.5	5.975	55.743	0.020912	1.225	0.857	0.0154
4	6.5	7.062	77.857	0.092799	1.850	1.295	0.0166
5	7.5	8.148	103.655	0.199218	2.474	1.732	0.0167
6	8.5	9.234	133.139	0.248788	3.150	2.205	0.0166
7	9.5	10.321	166.309	0.208699	3.852	2.697	0.0162
8	10.5	11.407	203.164	0.128984	4.537	3.176	0.0156
9	11.5	12.494	243.705	0.062446	5.179	3.625	0.0149
10	12.5	13.580	287.931	0.024790	5.771	4.040	0.0140
11	13.5	14.666	335.843	0.008367	6.315	4.421	0.0132
12	14.5	15.753	387.440	0.002473	6.813	4.769	0.0123
13	15.5	16.839	442.723	0.000658	7.281	5.097	0.0115
14	16.5	17.926	501.691	0.000158	7.671	5.370	0.0107
15	17.5	19.012	564.345	0.000034	8.029	5.621	0.0100
16	18.5	20.098	630.684	0.000007	8.500	5.950	0.0094

Table 9 The wave steepness of IACS Rec. No. 34 Rev. 2

No.	$T_{0\mathrm{m}1}$ [s]	T_{01} [s]	λ_i [m]	W_i	$H_{1/3,\mathrm{ref},i}$ [m]	H_i [m]	$S_{\mathrm{w},i}$
1	4.5	4.084	26.038	0.0000715	0.546	0.382	0.0147
2	5.5	4.991	38.896	0.0223373	1.411	0.988	0.0254
3	6.5	5.899	54.326	0.1591330	1.658	1.161	0.0214
4	7.5	6.806	72.328	0.2322354	2.105	1.474	0.0204
5	8.5	7.714	92.901	0.2167458	2.561	1.793	0.0193
6	9.5	8.621	116.046	0.1603112	3.016	2.111	0.0182
7	10.5	9.529	141.762	0.1030181	3.434	2.404	0.0170
8	11.5	10.436	170.051	0.0586869	3.797	2.658	0.0156
9	12.5	11.344	200.910	0.0290977	4.132	2.893	0.0144
10	13.5	12.251	234.342	0.0123031	4.478	3.135	0.0134
11	14.5	13.159	270.345	0.0043779	4.851	3.396	0.0126
12	15.5	14.066	308.920	0.0012962	5.242	3.669	0.0119
13	16.5	14.974	350.066	0.0003147	5.616	3.931	0.0112
14	17.5	15.881	393.784	0.0000611	5.867	4.107	0.0104
15	18.5	16.789	440.074	0.0000092	5.750	4.025	0.0091
16	19.5	17.696	488.936	0.0000009	5.833	4.083	0.0084

4. EXCESSIVE ACCELERATION FAILURE MODE

4.1 Vulnerability criteria for excessive acceleration

The excessive acceleration failure mode is assessed by the lateral acceleration in irregular beam waves at the height where passengers or crew members may be present.

Level 1 for the excessive acceleration failure mode assesses vulnerability based on lateral acceleration in irregular beam waves at zero forward speed at a height where passengers or crew members may be present, as follows:

$$\varphi K_L(g + 4\pi^2 h_r/T_r^2) \leq R_{EA1} \tag{17}$$

where φ is the characteristic roll amplitude obtained using the effective wave slope coefficient and wave steepness determined by the natural roll period , K_L is a factor that considers the simultaneous action of roll, yaw, and pitch motions, h_r is the height above the assumed roll axis of the location where passengers or crew members may be present, T_r is the natural roll period. The standard value R_{EA1} is 4.64 m/s^2. As this equation shows, Level 1, which serves as the environmental data, is not affected by changes in the wave scatter diagram.

Level 2 of the vulnerability criteria assesses a ship in a loading condition as not vulnerable if the long-term probability index C is less than the standard R_{EA} value of 0.00039, as follows:

$$\left.\begin{aligned} C &= \sum_{i=1}^{N} W_i C_{s,i} \leq R_{EA2} \\ C_{s,i} &= exp\left(-R_2^2/2\sigma_{LAi}^2\right) \end{aligned}\right\} \tag{18}$$

where $C_{S,i}$ is the short-term excessive acceleration failure index for short-term environmental conditions and w_i is the weighting factor for the short-term environmental condition given by the wave scatter diagram referred to in Corr. 1. R_{EA2} is 9.81m/s^2. The standard deviation of the lateral acceleration at zero speed and in a beam seaway, σ_{LAi} is determined using the spectrum of roll motion due to the action of waves. The spectral density of the sea wave elevation was obtained from the Bretschneider wave energy spectrum.

4.2 Sample ships for the vulnerability criteria of excessive acceleration

Two container ships were assessed by changing the wave scatter diagram for Corr.1 and Rev.2 used

in Level 2 of the vulnerability criteria for the excessive acceleration failure mode.

One is a C11 class Post-Panamax Containership of 262.0 m in ship length, the same as parametric rolling (Table 3). The assessment conditions for the C11 class containership are the same as those for the assessment of the excessive acceleration failure mode shown in Appendix 2, Section 3. 1 of the explanatory notes (MSC. 1/Circ. 1652). Table 10 lists the assessment conditions for C11 class containership.

The other is an 8749 TEU containership of 320 m in ship length, which was designed to reproduce an accident ship referring to the body plan shown in the investigation report (Federal Bureau of Maritime Casualty Investigation, 2011) of the container ship "CMV CHICAGO EXPRESS". The ship experienced a fatal accident due to excessive acceleration on September 2008 off the coast of Hong Kong. The principal particulars of the containership are listed in Table 11. Hereinafter, referred to as "CE".

The assessed result of Level 1 for C11 was 8.048 m/s^2, and the ship which is judged to be unacceptable. The assessed result of Level 1 for the CE was 8.703 m/s^2, and the vessel is also judged to be unacceptable.

4.3 Assessment results for excessive acceleration

Level 2 of the vulnerability criterion was calculated using two environmental data for two sample ships.

Table 12 shows the assessment results of Level 2 using wave scatter diagrams of IACS Rec. No. 34 Corr. 1 and Rev. 2 for the sample ship C11. As mentioned above, the standard value for Level 2 is 0.00039. The results using Corr. 1 were judged as unacceptable, whereas those using Rev. 2 were judged as acceptable. The ratio of these two assessment results when using Corr. 1 and Rev. 2 is 0.145. Table 13 shows the assessment results for Level 2 using the wave scatter diagrams of Corr. 1 and Rev. 1 for the sample ship CE. In the case of this vessel, the judgement remained the same, however, the assessment result using Rev.2 was lower than that using Corr. 1. The ratio of the two assessment results was 0.126.

If a ship in a loading condition fails vulnerability criteria, the operational limitations can be applied.

Table 10: Assessment condition of C11 Class Post-Panamax Containership for excessive acceleration failure mode

Item	Value
Metacentric height without free-surface correction [m]	8.00
Locational distance of bridge from the aft perpendicular [m]	177.41
Height of bridge above the keel [m]	48.72
Natural roll period T_ϕ [s]	9.6

Table 11: The principal particulars and assessment conditions of the 8749 TEU containership (CE) for excessive acceleration failure mode

Item	Value
Length between perpendiculars [m]	320.0
Breadth [m]	42.8
Draught at midship [m]	8.1
Trim [m]	2.0
Block coefficient	0.59
Metacentric height without free-surface correction [m]	8.54
Bilge keel length ratio l_{BK}/L_{pp}	0.234
Bilge keel height ratio h_{BK}/B	0.010
Bilge keel area [m^2]	32.0
Longitudinal distance of bridge from aft perpendicular [m]	77.7
Height of bridge above the keel [m]	50.0
Natural roll period T_ϕ [s]	10.5

The operational limitations related to the wave height for the two sample ships were calculated using IACS Rec. No. 34 Corr. 1 and Rev. 2. To apply the operational limitations, the ratio of the operation times under acceptable conditions to the total operation time must be greater than 0.8. The short-term excessive acceleration failure indexes $C_{S,i}$ for short-term environmental conditions using the wave scatter diagrams of IACS Rec. No. 34 Corr. 1 and Rev. 2 were calculated based on the Level 2 assessment method, and the maximum significant wave heights of the two sample ships were assessed. Since CE has passed Level 2, there is no need for operational limitation, but it was assessed to investigate the impact of the updated IACS Rec. No. 34. Table 14 presents the results of the operational limitations related to the maximum significant wave height for the two sample ships C11 and CE. The maximum significant wave

height for the sample ship CE is 1.0 m less when Rev. 2 is used than when Corr. 1 is used.

Table 12: The Level 2 vulnerability criterion for excessive acceleration in the case of C11

C11	C	Judge
Corr. 1	0.4711E-03	Fail
Rev. 2	0.6481E-04	Pass
$C_{Rev.2}/C_{corr.1}$	0.145	

Table 13: The Level 2 vulnerability criterion for excessive acceleration in the case of CE

CE	C	Judge
Corr. 1	0.3128E-03	Pass
Rev. 2	0.3932E-04	Pass
$C_{Rev.2}/C_{corr.1}$	0.126	

Table 14: Operational limitation related to maximum significant wave height for excessive acceleration in the case of C11 and CE

	C11	CE
Corr. 1	5.0 m	6.0 m
Rev. 2	5.0 m	5.0 m

4.4 Discussion on the effects of the wave scatter diagrams on the vulnerability criteria for excessive acceleration

The results presented in the previous section indicate that the judgement results of Level 2 and the maximum significant wave height for the excessive acceleration failure mode may change if the environmental data are changed. This is because the probability density of the wave periods in Rev. 2 is smaller than that of Corr. 1, as shown in Fig. 3, at approximately 10 s, which is close to the natural roll period of the two sample ships. Thus, the magnitude of harmonic roll resonance for these ships shall be reduced if we use Rev. 2 in Level 2. As a result, Level 2 criterion using Rev. 2 is less stringent.

4. CONCLUSIONS

This study examines the influences of the updated IACS Rec. No.34 on the vulnerability criteria of parametric rolling and excessive acceleration failure modes through calculations on two container ships for each mode. The results obtained are as follows.

- Changing the standard wave data from Corr. 1 to Rev. 2 can alter the vulnerability assessment value for both parametric rolling and excessive acceleration: consequently, the pass/fail judgements may change.
- When updating the environmental data in the vulnerability criteria from IACS Rec. No.34 Corr. 1 to Rev. 2, it is necessary to reconfigure the standard values and wave steepness used for the vulnerability criteria.
- Since the standard values for each failure mode were set such that the accident vessels that caused failure mode were assessed as vulnerable, the safety level does not change by revising the standard values.
- Therefore, there is no need to review the vulnerability criteria due to revision of the environmental data.

ACKNOWLEDGMENTS

This study was conducted as part of the research project of the Japan Ship Technology Association, funded by the Nippon Foundation, for the fiscal year 2023.

REFERENCES

Austefjord, H.N., Hauteclocque, G. de, Johnson, M. C., and Zhu, T. Y., 2023, “Update of wave statistics standards for classification rules”, Advances in the Analysis and Design of Marine Structures, Proceedings of the 9th International Conference on Marine Structures, PP. 43-52.

Federal Bureau of Maritime Casualty Investigation, 2011, “Fatal accident on board the CMV CCNI GUAYAS during Typhoon “KOPPU on 15 September 2009 in the sea area of Hong Kong”, Investigation report 391/09.

IACS, 2001, “Recommendation No. 34, 1992, Corr. Nov. 2001 -Standard Wave Data”.

IACS, 2022, “Recommendation No. 34, 1992, Rev. 2 Dec. 2022 -Standard Wave Data”.

IMO, 2020, “MSC.1/Circ. 1627 - Interim guidelines on the second generation intact stability criteria”.

IMO, 2023, “MSC.1/Circ. 1652 - Explanatory notes to the interim guidelines on the second generation intact stability criteria”.

Yamaguchi, M., 1984, “Approximate expressions for integral properties of the JONSWAP spectrum”, Japanese Journal of JSCE, No. 345, Vol. II-1, pp. 149-12.

Proposal of simplified operational guidance on parametric rolling and pure loss of stability and its validation using the fully probabilistic operational guidance

Masahiro Sakai, *The University of Osaka,* sakai@naoe.eng.osaka-u.ac.jp
Soichiro Okamoto, *The University of Osaka*
Mayu Takaya, *The University of Osaka*
Akihiro Oka, *The University of Osaka*
Naoya Umeda, *The University of Osaka*

ABSTRACT

This study proposes simplified operational guidance on parametric rolling and pure loss of stability within the framework of the Second Generation Intact Stability Criteria. The guidance is expected to provide both ship speed and course adjustments, thereby filling a critical gap identified at SDC 8, where concerns were raised about the absence of comprehensive measures for pure loss of stability failure modes. Although an operational guidance on parametric rolling has been issued by a classification society, it still lacks the probabilistic validation required by the interim guidelines. To overcome these situations, the simplified guidance is proposed based on methodologies derived from the vulnerability criteria and is attempted to be validated through comparative analysis with fully probabilistic operational guidance using the direct counting method. The outcomes suggest we reconsider the failure rate of 10^{-6} with a realistic duration of severe sea state.

Keywords: *Second Generation Intact Stability Criteria, Operational Guidance, Parametric Rolling, Pure Loss of Stability.*

1. INTRODUCTION

Under the 2008 Intact Stability Code (2008 IS Code), whose major parts are made mandatory by the SOLAS and Load Line Conventions, the application of physics-based criteria is permitted for hazardous phenomena such as parametric rolling, which cannot be adequately addressed by conventional empirical criteria. In relation to this, the IMO approved the Interim Guidelines for the Second Generation Intact Stability Criteria as MSC.1/Circ.1627 (IMO, 2020), followed by its Explanatory Notes as MSC.1/Circ.1652 (IMO, 2022). The member states are currently required to apply the criteria on a trial basis and report the results to the SDC Sub-Committee.

Under the Second Generation Intact Stability Criteria, ships that fail to satisfy the vulnerability criteria are permitted to operate under certain limitations, either through operational guidance or by compliance with a direct stability assessment. The operational guidance corresponds to the level 2 vulnerability criteria, including adjustments to ship speed and course. However, only a limited number of studies have been conducted in this area. For example, with regard to parametric rolling, ClassNK (2023) has published a simplified operational guidance that extends the second check of the level 2 vulnerability criterion to oblique waves (Sakai et al., 2018) with the extension of Grim's effective wave to the short-crested irregular waves (Umeda et al., 2023). Begovic et al. (2023) also demonstrated trial calculations of operational guidance for all the failure modes based on the same methods as the level 2 vulnerability criteria. Very recently, Ruponen et al. (2025) confirmed that the ClassNK-type guidance provides recommendations of safe ship speed and course in long-crested longitudinal waves for avoiding parametric rolling comparable to the deterministic direct assessment.

A major issue highlighted at SDC 8 is the absence of any operational guidance for pure loss of stability. In addition to the insufficient development of operational guidance to short-crested irregular waves for all the failure modes, no validation has yet been reported using fully probabilistic operational guidance. To address these issues, this study proposes operational guidance for parametric rolling and pure loss of stability and conducts comparative analyses with fully probabilistic operational guidance using the direct counting method,

occasionally with the extrapolation of failure rate over wave height (Shigunov, 2023).

2. PARAMETRIC ROLLING

This chapter deals with simplified operational guidance for parametric rolling. The subject ship is a C11-class post-Panamax containership, and its principal particulars are shown in Table 1. The GM and natural period are based on the values used at the model experiment conducted in 2022 (Umeda et al., 2023).

Table 1: Principal particulars of a C11-class post-Panamax containership.

Items	Values
L_{BP} [m]	262
B [m]	40
d [m]	11.5
W [kg]	67.47×10^6
C_{B}	0.56
GM [m]	2.003
T_ϕ [s]	23.7

Operational guidance

Since the use of a methodology equivalent to the second check of the level 2 vulnerability criteria is desirable for operational guidance, which evaluates parametric rolling amplitudes in waves, was used as a basis and extended to short-crested irregular waves.

First, parametric rolling in short-crested irregular waves is evaluated by calculating the Grim's effective wave height H_{eff} and encounter wave frequency $\bar{\omega}_{\mathrm{e,eff}}$ using the extended Grim's effective wave concept (Umeda and Yamakoshi, 1993; Umeda and Uchida., 2023). Here, the short-crested irregular wave is expressed by the ITTC spectrum with the cosine-squared directional distribution. The component wave direction α, ship course $\bar{\chi}$, and ship course from component wave χ is defined in Figure 1.

$$H_{\mathrm{eff}} = 4.0043\sqrt{m_{0,\mathrm{eff}}} \tag{1}$$

$$\bar{\omega}_{\mathrm{e,eff}} = \sqrt{\frac{m_{2,\mathrm{eff}}}{m_{0,\mathrm{eff}}}} \tag{2}$$

$$m_{0,\mathrm{eff}} = \int_{\alpha=-\frac{\pi}{2}}^{\alpha=\frac{\pi}{2}} \int_{\omega=0}^{\omega=\infty} S_{\mathrm{eff}}\ (\omega,\alpha)\mathrm{d}\omega\mathrm{d}\alpha \tag{3}$$

$$m_{2,\mathrm{eff}} = \int_{\alpha=-\frac{\pi}{2}}^{\alpha=\frac{\pi}{2}} \int_{\omega=0}^{\omega=\infty} \omega_e(\omega,\alpha)^2 S_{\mathrm{eff}}\ (\omega,\alpha)\mathrm{d}\omega\mathrm{d}\alpha \tag{4}$$

$$\omega_e(\omega,\alpha) = \omega - \frac{\omega^2}{g} U\cos\chi \tag{5}$$

$$S_{\mathrm{eff}}\ (\omega,\alpha) = H_\zeta(\omega,\alpha)^2\, S(\omega,\alpha) \tag{6}$$

$$S(\omega,\alpha) = D(\alpha)\ A\omega^{-5}\exp\left(-B\omega^{-4}\right) \tag{7}$$

$$A = 173H_{1/3}^2 T_{01}^{-4} \tag{8}$$

$$B = 691T_{01}^{-4} \tag{9}$$

$$D(\alpha) = \frac{2}{\pi}\cos^2\alpha \quad \left(-\frac{\pi}{2} < \alpha < \frac{\pi}{2}\right) \tag{10}$$

$$H_\zeta(\omega,\alpha) = \frac{\frac{\omega^2 L}{g}\cos\ \chi \sin\left(\frac{\omega^2 L}{2g}\cos\ \chi\right)}{\pi^2 - \left(\frac{\omega^2 L}{2g}\cos\ \chi\right)^2} \tag{11}$$

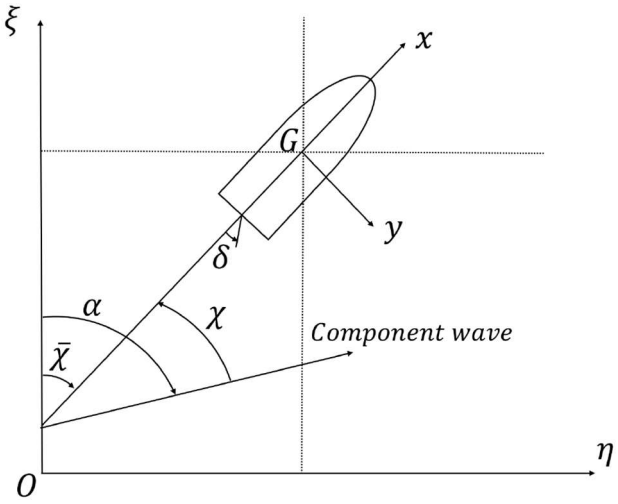

Figure 1: Space-fixed coordinate system $O-\xi\eta$ and body fixed coordinate system $G-xy$ for parametric rolling

In the second check of the level 2 vulnerability criterion for parametric rolling, the parametric rolling angle is evaluated based on the following single-degree-of-freedom roll model.

$$\ddot{\phi} + 2\alpha_\phi\dot{\phi} + \gamma_\phi\dot{\phi}^3 + \omega_\phi{}^2\frac{GZ(\phi,t)}{GM} = 0 \tag{12}$$

Here, α_ϕ and γ_ϕ are roll damping coefficients, which are allowed to be estimated using Ikeda's simplified method (Kawahara et al., 2009) with the correction of its forward speed effect (Ikeda, 2004). ω_ϕ denotes the natural roll frequency, GZ represents the righting lever in waves, and GM is the metacentric height in still water. Both GZ and GM are calculated under a static equilibrium in heave and pitch. In the second check of the level 2 vulnerability criterion for parametric rolling, the resting variation is modelled with a longitudinal irregular wave but its wave height and period are adjusted by the Grim's effective wave concept with the wave heading effect taken into account, as presented in Eq. 1. The

assessment is then conducted using the parametric rolling amplitude in the effective regular wave profiles, where the wave height corresponds to the effective wave and the wavelength is equal to the ship length. Although Grim's effective wave has a cosine wave profile in space, it is treated as if it were a regular propagating wave. The validity of this assumption has been confirmed by Sakai et al. (2019) from the perspective of encounter frequency.

The operational guidance for parametric rolling proposed in this study estimates the parametric rolling amplitude using Eq. 12, in the same manner as the second check of the level 2 vulnerability criterion for parametric rolling. In contrast, the ClassNK guidelines (ClassNK, 2023) as well as Ruponen et al. (2025) evaluate the wave encounter frequency y Eq. 2, like, so that the wave celerity of the regular waves does not satisfy the dispersion relation of water waves.

Fully probabilistic operational guidance using the direct counting method

The nonlinear three-degree-of-freedom model for heave, roll, and pitch developed by Hashimoto and Umeda (2008)—which incorporates nonlinear radiation forces, diffraction forces, buoyancy, and Froude–Krylov forces—has been validated against model experiments in regular longitudinal waves, as also included in the explanatory notes (IMO, 2023). Subsequently, Umeda et al. (2016) extended the model to a five-degree-of-freedom simulation by including sway and yaw motions, enabling its application to regular oblique waves and later to short-crested irregular waves. In this extended model. Additional hydrodynamic components, namely low-speed manoeuvring forces and rudder forces, were also introduced. This extended model was validated under wider operational conditions of the C11 class containership model in short-crested irregular head and bow quartering waves (Umeda et al., 2023).

Comparisons

In this section, the simple and fully probabilistic operational guidance for parametric rolling of a C11-class post-Panamax container ship was conducted using the above-mentioned methods, and the results were compared with the simplified operational guidance (Figures 2 and 3). In these polar charts, the radial axis represents ship speed in Froude number, while the circumferential direction corresponds to the ship heading from the main wave direction. In this study, the following waves are defined as 0 degrees and head waves as 180 degrees. The red-shaded regions indicate operational conditions judged to be dangerous according to the simplified operational guidance based on the parametric roll amplitude threshold of 25 degrees. The symbols represent the results obtained from the fully probabilistic operational guidance. Red symbols indicate operational conditions assessed as dangerous (the mean time to first occurrence of roll angles exceeding 40 degrees is SHORTER than 10^6 s or 7,200 s), and blue symbols indicate safe conditions (the mean time to first occurrence of roll angles exceeding 40 degrees is LONGER than 10^6 s or 7,200 s). Symbols with white interiors denote the use of the extrapolation of failure rate over the wave height (Shigunov, 2023) and are labelled as "Extrap." in the legend. When applying extrapolation, repeated simulations were carried out by varying the random seeds until 200 dangerous roll events occurred for each wave height sample.

The fully probabilistic operational guidance indicates that the C11-class post-Panamax containership tends to experience dangerous parametric rolling in the region from very low speeds in head seas to following seas. On the other hand, in the simplified operational guidance, when the righting lever is calculated under the quasi-static assumption of vertical motion, as in the second check of the level 2 criterion, parametric rolling exceeding 25 degrees is predicted to occur in head seas at Froude numbers up to approximately 0.08.

The comparison between the simplified operational guidance and the fully probabilistic operational guidance revealed the followings: the difference in the threshold of the mean time to first failure—whether 10^6 seconds (approximately 11 days) or 7,200 seconds (2 hours)—does not lead to a significant difference on the polar chart; and the simplified operational guidance based on the second check of the level 2 criterion does not accurately capture the range of conditions where parametric rolling is likely to occur. As suggested in ClassNK guidelines (ClassNK, 2023) and Sakai et al. (2022), this limitation of the simplified operational guidance may be overcome by incorporating the oblique wave effect and/or the variation of the righting lever due to vertical motion.

In Figure 3, even with the use of the extrapolation, no pass condition in the following seas has yet been found. The challenges associated with applying the threshold of 10^6 s for the mean time to first failure in the Direct Counting method are discussed in the Appendix.

To further investigate the limitation that the simplified operational guidance based on the second check of the level 2 criterion does not accurately capture the range of conditions where parametric rolling is likely to occur, the results calculated in

Umeda and Uchida (2023) were verified using the Direct Counting Method with the threshold of 7,200 seconds (2 hours) for the mean time to first failure. The differences between the simplified operational guidance proposed in this study and that by Umeda and Uchida (2023) are summarized as follows: the former is based on time-domain simulations, while the latter employs the averaging method; the former fully considers the GZ variation, whereas the latter considers only the GM variation; and the latter takes into account the influence of the wave excitation moment term on the right-hand side of Eq. (12). Due to these differences, the method by Umeda and Uchida (2023) may yield a more conservative assessment than the one proposed in this study. The corresponding results are presented in Figure 4. It should be noted that, compared to the comparison with the simplified guidance based on the second check of the level 2 criterion, the significant wave heights used here are smaller. Although the wave direction is defined in the same manner, the polar charts are oriented such that 0 degrees is displayed at the top. While a slight underestimation is observed around Fn = 0.05 in following waves, the simplified operational guidance by Umeda and Uchida (2023) successfully captures the range of conditions under which parametric rolling is likely to occur, and provides a conservative assessment of the vulnerability for parametric rolling.

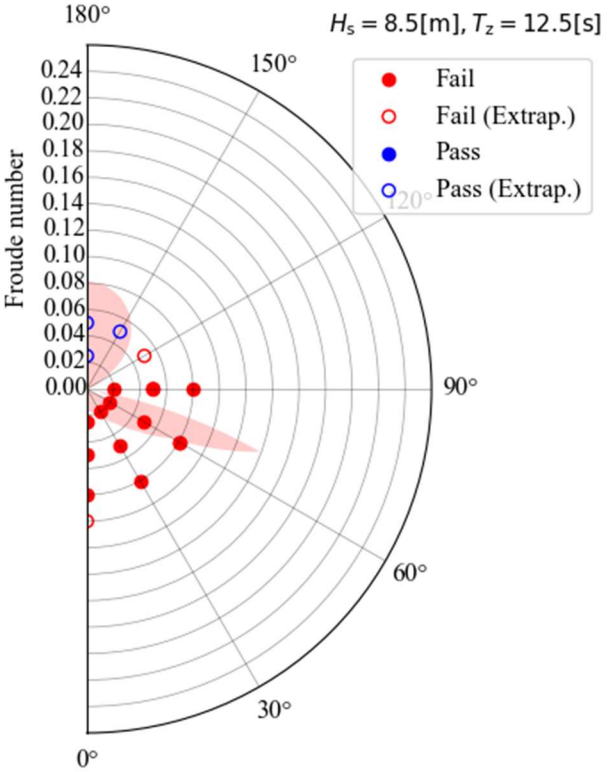

Figure 2: Simplified operational guidance and fully probabilistic operational guidance for parametric rolling, setting the threshold for the mean time to first failure to 10^6s.

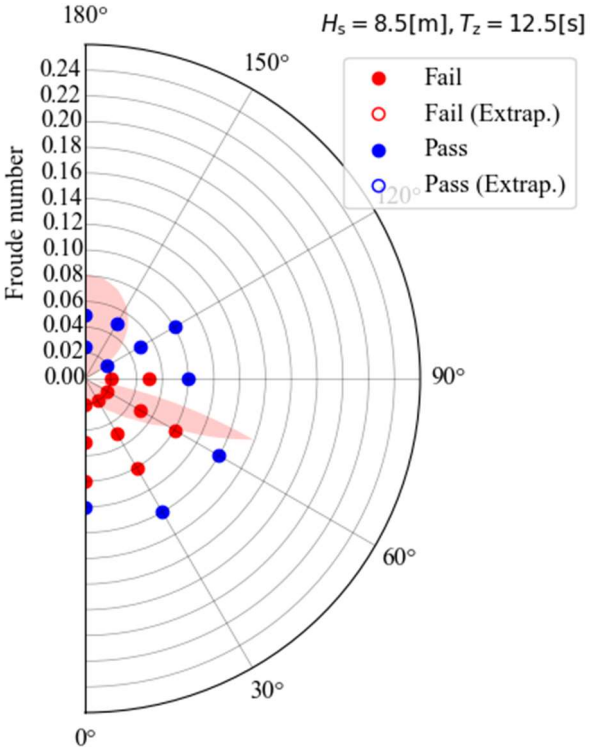

Figure 3: Simplified operational guidance and fully probabilistic operational guidance for parametric rolling, setting the threshold for the mean time to first failure to 7,200 s.

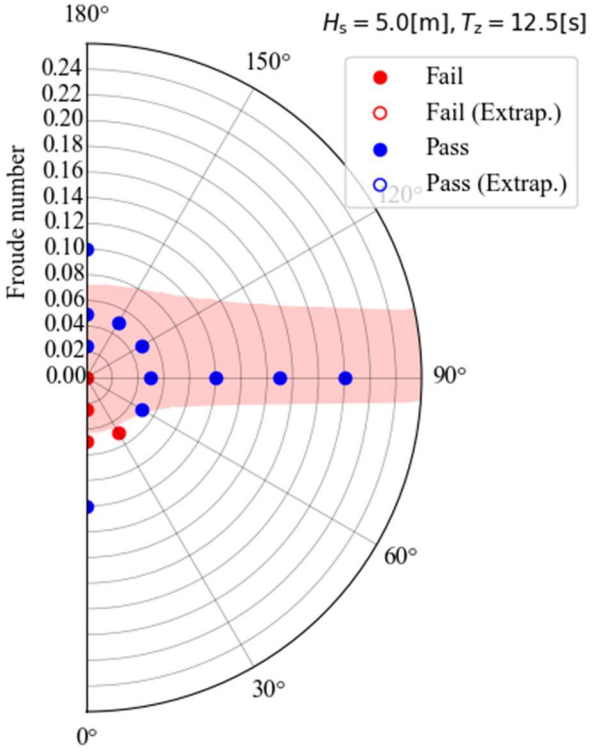

Figure 4: Simplified operational guidance proposed by Umeda and Uchida (2023) and fully probabilistic operational guidance for parametric rolling, setting the threshold for the mean time to first failure to 7,200 s.

Because of the conservative assessment under less severe sea state, the simplified guidance judges the beam sea region as dangerous as well. This is because the encounter wave period is a dominant factor for parametric rolling. In beam seas, the encounter wave period remains nearly constant regardless of ship speed. While the restoring variation due to a longitudinal effective wave disappears in long-crested irregular waves, that in short-crested irregular waves does not, as experimentally and numerically confirmed by some of the authors (Takaya et al., 2023).

3. PURE LOSS OF STABILITY

This chapter deals with simplified operational guidance for pure loss of stability. The subject ship is a RoPax ferry, and its principal particulars are shown in Table 2. The GM and natural period are based on the values used at the model experiment conducted in 2022 (Umeda et al., 2024). The critical roll angle of this ship is 25 degrees because of the lashing requirement on the vehicle deck.

Table 2: Principal particulars of a ferry.

Items	Values
L_{BP} [m]	150
B [m]	22.8
d [m]	6.26
W [kg]	1.11×10^7
GM [m]	1.81
T_ϕ [s]	13.33

Operational guidance

Since the use of a methodology equivalent to the level 2 vulnerability criteria is desirable for operational guidance, the level 2, which evaluates both the reduction of GZ and the yaw-roll coupling in waves, is extended to short-crested irregular waves.

First, in the level 2 criterion, the heeling lever due to yaw-roll coupling corresponding to a heading angle of 30 degrees in model experiments is used as a conservative estimate (Kubo et al., 2012), and it is empirically evaluated using wave height, wavelength, draft, and ship speed in Froude number, as shown in Eq. (13). The authors herewith extend this heeling lever to a function of the ship's heading angle χ (in radians) as well based on model experiments, resulting in Eq. (14). Here, these equations coincide at $\chi = \frac{\pi}{6}$ rad (i.e. 30 degrees).

$$l_{PL2} = 8\left(\frac{H_i}{\lambda}\right) d\, Fn^2 \tag{13}$$

$$l_{PL2} = \left\{-\frac{10.08}{\pi^2}\chi^2 + \frac{5.04}{\pi}\chi + 7.44\right\}\left(\frac{H_i}{\lambda}\right) d\, Fn^2 \tag{14}$$

The wave height used in this equation was estimated in the same manner as that for the simplified operational guidance for parametric rolling as described in Eqs. (1)–(11). Since the level 2 vulnerability criterion for pure loss of stability is based on the 3% significant wave height, the effective wave height is calculated as

$$H_{\mathrm{eff}} = 5.9725\sqrt{m_{0,\mathrm{eff}}} \tag{15}$$

Fully probabilistic operational guidance using the direct counting method

Kubo et al. (2012) proposed a surge-sway-yaw-roll four-degree-of-freedom simulation model, highlighting the importance of accounting the coupled effects of sway and yaw at wave crests when a ship is navigating at high speed in following seas. This model is an extension of the calm-water manoeuvring model with heel developed by Hirano et al. (1979) to oblique following waves. The mathematical model proposed by Kubo et al. (2012) was further extended to short-crested irregular astern waves and well validated with model experiments in short-crested astern waves (Umeda et al., 2023). In this study, this extended model is employed for the validation of the simplified operational guidance proposed here.

Comparisons

In this section, the simplified and fully probabilistic operational guidance for pure loss of stability of the RoPax ferry is compared (Figure 5 and 6). In these polar charts, the radial axis represents ship speed in Froude number, while the circumferential direction corresponds to the ship heading to the main wave direction. In this study, the following waves are defined as 0 degrees and head waves as 180 degrees. The red-shaded regions indicate operational conditions judged as dangerous according to the simplified operational guidance, in which the critical angle of static heel balance is 15 degrees following the level 2 criterion. The symbols represent the results obtained from the fully probabilistic operational guidance. Red symbols indicate operational conditions assessed as dangerous, in which the mean time to first occurrence of roll angles exceeding 25 degrees is SHORTER than 10^6 s or 7,200 s, blue symbols indicate safe conditions, in which the mean time to first occurrence of roll angles exceeding 25 degrees

is LONGER than 10^6 s or 7,200 s. Symbols with white interiors denote the use of the extrapolation over wave height (Shigunov, 2023) and are labelled as "Extrap." in the legend. When applying the extrapolation, repeated simulations were carried out by varying the random seeds until 200 dangerous roll events occurred for each wave height sample.

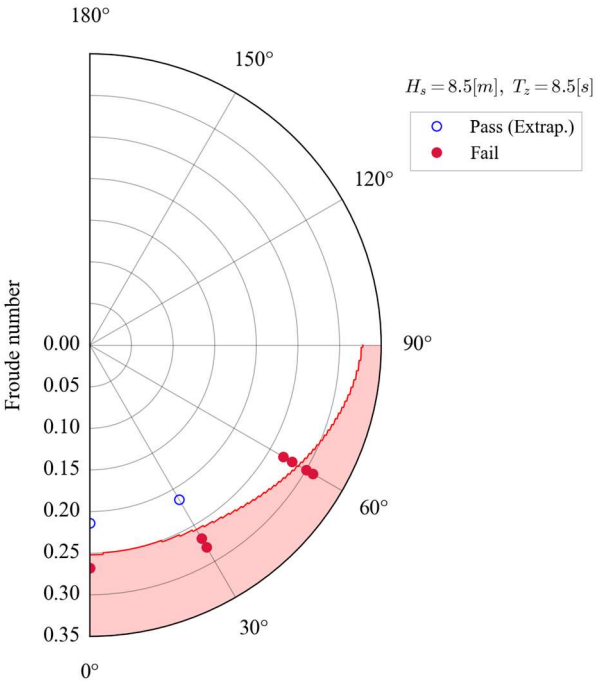

Figure 5: Simplified operational guidance and fully probabilistic operational guidance for pure loss of stability, setting the threshold for the mean time to first failure to 10^6s.

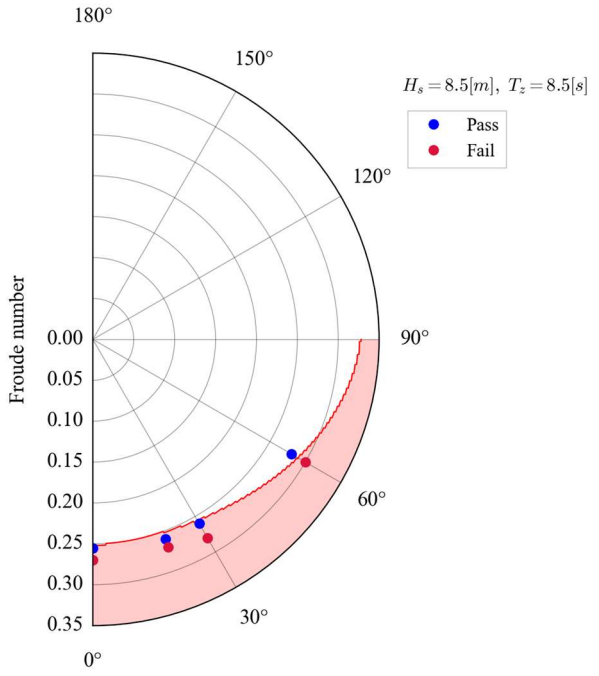

Figure 6: Simplified operational guidance and fully probabilistic operational guidance for pure loss of stability, setting the threshold for the mean time to first failure to 7,200 s.

For pure loss of stability, the fully probabilistic operational guidance generally shows good agreement with the level 2-equivalent simplified operational guidance against pure loss of stability. At the heading angle of χ = 60 degrees, when the threshold is 10^6 s (Figure 5), however, the fully probabilistic guidance is slightly more conservative. Setting the threshold for the mean time to first failure, 10^6 s, seems to be excessive for actual operation practice. It might be reasonable to use a shorter mean time based on realistic sea state duration, in other words, a higher failure rate.

CONCLUSIONS

This study proposed simplified operational guidance for parametric rolling and pure loss of stability within the framework of the Second Generation Intact Stability Criteria.

For parametric rolling, the simplified operational guidance is compared with the fully probabilistic operational guidance in which the mean time to first failure is set to be 10^6 s or 7,200 s. The difference between those threshold values has little impact on the resulting polar chart. Another unresolved issue was that the simplified operational guidance based on the second check of the level 2 criterion does not accurately capture the range of conditions where parametric rolling is likely to occur. However, it was demonstrated in this study that this limitation can be overcome by employing the simplified operational guidance proposed by Umeda and Uchida (2023), which is based on the averaging method, considers only GM variation, and includes the wave excitation moment term.

For pure loss of stability, the newly proposed simplified guidance reasonably well agrees with the fully probabilistic operational guidance, with the thresholds of 10^6 s and 7,200 s, except for the heading angle of 60 degrees.

For both failure modes, it seems to be appropriate to reduce the time to failure with a realistic sea state duration taken into account.

ACKNOWLEDGEMENT

It was carried out as a research activity of Goal-based Stability Criteria Project of Japan Ship Technology Research Association in the fiscal years of 2023, 2024, and 2025, funded by the Nippon Foundation.

REFERENCES

Begovic E., Bertorello C., Rinauro B., Rosano G., 2023, "Simplified Operational Guidance for Second Generation Intact Stability Criteria" *Ocean Engineering*, 270,113583.

ClassNK (Nippon Kaiji Kyokai), 2023, Guidelines on Preventive Measures Against Parametric Rolling.

Hashimoto H., Umeda N., 2019, "Prediction of parametric rolling in irregular head waves", *Fluid Mechanics and its Applications*, Vol. 119, pp. 275-290.

Hirano M., Takashina J., 1979, "A Calculation of Ship Turning Motion Taking Coupling Effect Due to Heel into Consideration", *Naval Architecture and Ocean Engineering*, 59, pp. 71-81.

Ikeda, Y. ,2004, "Prediction methods of roll damping of ships and their application to determine optimum stabilization devices". *Marine Technology and SNAME News*, 41(02), pp. 89–93.

IMO, 2020, "Interim Guidelines on the Second Generation Intact Stability Criteria", MSC.1-Circ. 1627.

IMO, 2022, "Explanatory Notes to the Interim Guidelines on the Second Generation Intact Stability Criteria", MSC.1-Circ. 1652.

Kawahara, Y., Maekawa, K., Ikeda, Y., 2011, "A Simple Prediction Formula of Roll Damping of Conventional Cargo Ships on the Basis of Ikeda's Method and Its Limitation". *In Contemporary Ideas on Ship Stability and Capsizing in Waves*, pp. 465–486, Springer, Dordrecht.

Kubo H., Umeda N., Yamane K., Matsuda A., 2012, "Pure Loss of Stability in Astern Seas -Is it Really Pure?-". Proceedings of *the 6th Asia-Pacific Workshop on Marine Hydrodynamics*, pp. 307-312.

Ruponen, P., Altintas, E., Matusiak, J., Mikkola, T., 2025 "A practical approach for simplified operational guidance to avoid parametric roll resonance", *Ocean Engineering*, 330, 121215.

Sakai M., Umeda N., Yano T., Maki A., Yamashita N., Matsuda A., Terada D., 2018 "Averaging methods for estimating parametric roll in longitudinal and oblique waves", *Journal of Marine Science and Technology*, 23(3), pp. 413-424.

Sakai, M., Umeda, N., Maki, A., 2019, "Encounter frequency effect on the simplified design criteria against parametric roll". *Ocean Engineering*, 182, pp. 21–27.

Sakai M., Umeda N., Maki A., 2022, "An averaging method for estimating parametric roll in regular longitudinal waves by uncoupled roll motion with restoring variation due to vertical motions". *Conference Proceedings of The Japan Society of Naval Architects and Ocean Engineers*, 35, pp. 441–445.

Shigunov, V., 2023, "Extrapolation of failure rate over wave height". *Ocean Engineering*, 272, 113801.

Takaya, M., Umeda, N., Matsuda, A., 2023, "Model experiment and simplified prediction of parametric rolling of a containership in short-crested irregular beam seas". *Proceedings of Forum of 10th Pan Asian Maritime Association of Maritime Engineering Societies and Advanced Maritime Engineering Conference*, C-7-02, pp.1-8.

Umeda, N., Yamakoshi, Y., 1993, "Probability of ship capsizing due to pure loss of stability in quartering seas". *Naval Architecture and Ocean Engineering,* The Society of Naval Architects of Japan. 30, 73–85.

Umeda N., Sakai M., Fujita N., Morimoto A., Terada D., Matsuda A., 2016, "Numerical Prediction of parametric roll in oblique waves". *Ocean Engineering*, 120, pp.212-219.

Umeda N., Uchida Y., 2023, "Simplified Operational Guidance for Preventing Parametric Rolling -Extension of Grim's Effective Wave Concept-", *ClassNK Technical Journal*, 7(1), pp. 39-48.

Umeda, N., Maruyama, Y., Okamoto, S., Oka, A., Masamoto, S., Matsuda, A., 2023, "Filling Gaps in Direct Stability Assessment Procedures". *Proceedings of the 19th International Ship Stability Workshop*, pp.193-200.

APPENDIX

One of the main issues with setting the threshold for the mean time to first failure to 10^6 s in the Direct Counting method is the excessive computational time required under conditions where large rolling is unlikely to occur. In this section, an example of this will be explained.

In the direct counting method, if the estimated mean time to first failure falls below the lower bound, the condition can immediately be judged as fail; if it exceeds the upper bound, it can be immediately judged as pass. Here, we consider the conditions under which a pass/fail judgment can be made after the first round of simulation. Under the threshold of 10^6 s, if the first failure occurs within 75.3 h, the condition can be immediately judged as failed. However, on the other hand, in order to immediately judge the condition as passed, no failure must occur within 11,000 h, which requires an extremely long computation time.

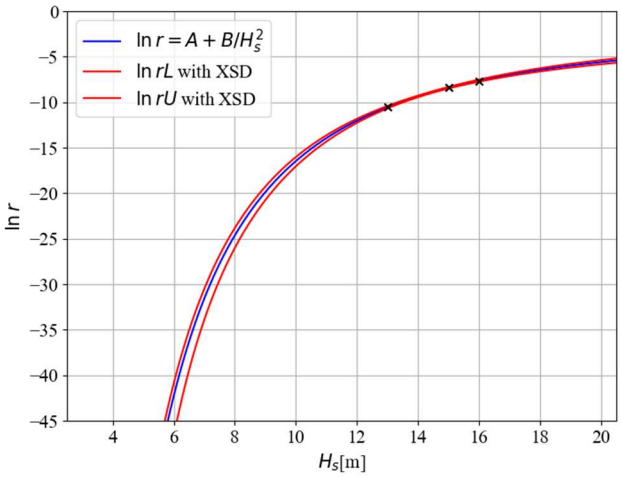

Figure 7: Extrapolation in the case of Fn = 0.025 and χ = 180 degrees.

Conducting such an extremely long-time simulation is impractical. Therefore, in this study,

the extrapolation of failure rate over the wave height (Shigunov, 2023) is employed. However, it should be noted that the use of extrapolation does not necessarily allow for an easy determination of safe (pass) conditions. For instance, in Figure 3, even with the use of the extrapolation, no condition in the following seas has yet been found that satisfies the confidence interval criteria through extrapolation within the limitations of the required extensive computational time.

In this section, the procedure for determining a pass condition using the extrapolation is demonstrated for the case of Fn = 0.025 and χ = 180 degrees. In this example, the sampled significant wave heights were set to H_S = 13, 15, and 16 m. For each wave height, the time to first failure was simulated 200 times ($N_e = 200$). As a result, the estimated mean times to first failure were $3.84 \times 10^4, 4.30 \times 10^3, 2.12 \times 10^3$ s, respectively. Based on these values, the mean time to first failure was extrapolated as a function of significant wave height as shown in Figure 7. Here, the mean time to first failure $\bar{T}$ is estimated using the following relationship (Shigunov, 2023):

$$\ln r = A + B/H_s^2 \quad (16)$$

$$\bar{T}_U = 1/r_{\mathrm{eL}} = 1/(0.5\hat{r}_{\mathrm{e}}\chi^2_{0.05/2,2N_{\mathrm{e}}}/N_{\mathrm{e}}) \quad (17)$$

$$\bar{T}_L = 1/r_{\mathrm{eU}} = 1/(0.5\hat{r}_{\mathrm{e}}\chi^2_{1-0.05/2,2N_{\mathrm{e}}}/N_{\mathrm{e}}) \quad (18)$$

Here, subscripts U and L denote the upper and lower bounds of the mean time to first failure (the 95% confidence interval) were obtained as $T_{\mathrm{L}} = 1.85 \times 10^{10}$[s] and $T_{\mathrm{U}} = 1.12 \times 10^{10}$[s]. Therefore, this condition was judged as passed.

Shigunov (2023) stated that a condition of $\ln \bar{T} > 5$ ($\bar{T} > 148$ [s]) is required, and it is suggested that $\ln \bar{T} > 6$ ($\bar{T} > 403$ [s]) is preferable. However, the fact that these values cannot be determined until all 200 simulations of the time to first failure for each wave height have been completed adds to the difficulty of the process. Furthermore, both bounds of the extrapolation curve (the red lines in Figure 7) must satisfy $\bar{T} > 10^6$, that is, $\ln \bar{r} < -13.8$ to be judged as pass. If the simulations are conducted at excessively high wave heights, the resulting confidence interval may become too wide, and there is a possibility that the results do not satisfy the required criteria for extrapolation.

Discussion to self-repeating effect in reconstruction of irregular waves for direct stability assessment

Naoya Umeda, *The University of Osaka,* umeda@naoe.eng.osaka-u.ac.jp
Yuuki Maruyama, *The University of Osaka*, yuuki_maruyama@naoe.eng.osaka-u.ac.jp
Vadim Belenky, *David Taylor Model Basin/NSWCCD,* vadim.belenky.civ@us.navy.mil
Kenneth Weems *David Taylor Model Basin/NSWCCD,* kenneth.m.weems2.civ@us.navy.mil

ABSTRACT

The paper attempts to review the principal issues related to the avoidance of self-repetition when reconstructing irregular waves for time-domain numerical simulation as a part of direct stability assessment. The issues are avoiding self-repetition by using prime numbers for ratios of frequencies, the influence of the self-repeating effect on variance and crossing rate estimates, smoothing of the spectrum as a way to estimate the autocovariance function, and the influence of wave grouping due to the Doppler Effect. As it is clear from its title, the paper aims to instigate discussion at the Workshop.

Keywords: *Direct counting method, Autocorrelation function, Encounter wave group, decorrelation time, prime number*

1. INTRODUCTION

The probabilistic characterisation of dynamic ship stability through time-domain numerical simulation or model experiment is referred to as "Direct Stability Assessment" (DSA) within the framework of the second generation intact stability criteria (IMO, 2020). The estimation of the rate of failures is performed either with direct counting or statistical extrapolation. In either case, a statistically valid model of the irregular ocean wave field is needed.

The vast majority of current simulation technology uses the Longuet-Higgins model, first introduced by St. Denis and Pierson (1953) and formalized by Longuet-Higgins (1957). It constructs the wave elevation $\zeta_{\mathrm{w}}(t)$ with an inverse Fourier transform:

$$\zeta_{\mathrm{w}}(t) = \sum_{n=1}^{N} \sqrt{2S_{\mathrm{w}}(\omega_n)\Delta\omega_n}\cos(\omega_n t + \delta_n) \quad (1)$$

using a wave spectrum $S_{\mathrm{w}}(\omega)$ to generate N sinusoidal components of frequencies ω_n with an increment $\Delta\omega_n$, while δ_n is a random phase shift that has a uniform distribution from 0 to 2 π. It is known that this modelling results in an ergodic process but not Gaussian because $\cos(\delta_n)$ follows the inverse sine distribution. However, if the N is sufficiently large, it can be regarded as Gaussian because of the central limit theorem (Yamanouchi, 1961; Shinozuka and Deodatis, 1991). Thus, the use of the Longuet-Higgins model is effective for the efficient identification of the response amplitude operators because of its inherent ergodicity, but the applicability to the direct counting method in DSA should be discussed separately.

The model (1) was originally intended for frequency domain calculation. When applied to time domain applications, patterns of almost exact repetitions were noted when using a constant frequency increment. These repetitions are reflected in the autocovariance function, computed directly from the spectrum with the well-known Wiener–Khinchin theorem (e.g. Price and Bishop, 1974), making it increase with time, which cannot be physically justified.

$$R_{\mathrm{w}}(t) = \sum_{n=1}^{N} S_{\mathrm{w}}(\omega_n)\Delta\omega_n \cos(\omega_n t) \quad (2)$$

The increase is referred as self-repeating effect or effect of self-repetition. The use of a non-uniform frequency distribution has eliminated obvious self-repeating patterns from the time histories in most cases, but does not always remove the increase from the autocovariance function (2).

There is no physical reason that the dependence of wave elevation in the future from the present moment should increase; rather, the dependence is expected to decay as the wave radiates further away from an observer. To prevent this obvious violation

of physical validity, the explanatory notes to the second generation intact stability criteria (IMO, 2023) provide ways to avoid the self-repetition, if more than one of ratios between different component frequencies are rational. The autocovariance function (2) is used as a criterion for validity; after the initial decay, the envelope should not be above 5 % of that at the lag of zero, for the duration of the simulation. The method is detailed in ITTC Recommended Procedure 7.5-02-01-09 (2024)

If the constant frequency increment is used, the simulation duration of statistical validity depends on the number of components and bandwidth of the discretised spectrum. Increasing the number of frequencies, however, increases the computational cost of the direct stability assessment. That is why the self-repeating effect, its nature and its consequences, if not avoided, still attract attention and discussions. Relevant research into this problem are works by Takaishi (1978, 1982, 1994), Takaishi et al. (1996), Belenky (2011), Maruyama et al. (2022), Pipiras et al. (2022), Tsoumpelis & Spyrou (2023), Bulian et al. (2024) and Umeda et al. (2023).

The last reference describes a method to mathematically guarantee that all ratios between the two different frequencies are irrational. A discussion at the 30th ITTC has followed (ITTC, 2024a, 2024b). This paper aims to continue this discussion, while looking further into the origin and consequences of the self-repeating effect.

2. RATIO OF FREQUENCIES

The Longuet-Higgins model (1) is essentially a sum of periodic functions and may have a period of its own. Is this a mechanism of self-repetition?

If any ratios between two different frequencies are irrational in the non-uniform frequency sampling, no self-repetition can appear. To realize such requirements, the frequencies of component waves, ω_n, can be selected as follows:

$$\omega_n = \frac{z^{\frac{n}{m}}}{y} \tag{3}$$

where z is a prime number, y and m are natural numbers, and m is larger than n. As proved in mathematics, a prime number to the power of a non-integer rational number is irrational. The ratio of an irrational number to a rational number is irrational. Therefore, the ratio of two different component wave frequencies, $\rho_{i,j}$, should be selected as follows:

$$\rho_{i,j} = \frac{\omega_i}{\omega_j} = \frac{z^{\frac{i}{m}}}{z^{\frac{j}{m}}} = z^{\frac{i-j}{m}} \tag{4}$$

Since $i - j < m$ and $\rho_{i,j}$ is a prime number to the power of a non-integer rational number, it shall be irrational. Thus, if the component wave frequencies this way, the generated wave time series shall not be are sampled repeated as well as the ship responses to the waves (Umeda et al. 2023).

Although the above discussion is exact within mathematics dealing with real numbers, the numerical simulation can be executed only within the limited precision so that an irrational number shall be approximated with a rational number with the limited number of digits. In case of the double precision of binary 64 based on the IEEE 754 standard, the number of digits is 15 in the minimum. Thus, the irrational number of $\rho_{i,j}$ can be approximated by a rational number of p/q where q is 10^{14} and p is $10^{14} \times \rho_{ij}$. On the other hand, since $\rho_{ij} = \omega_i/\omega_j = p/q$, p periods of the component wave having the frequency ω_j coincide with q periods of the component wave having the frequency ω_i. Therefore, if the greatest common divisor of p and q is s_{ij}, the self-repetition period is given by $(2\pi/\omega_i) \times 10^{14}/s_{ij}$. In case of 10 sampling frequencies from the Bretschneider spectrum with the significant wave height of 5m and the mean wave period is 9.99s, the obtained self-repetition period is about 0.4 million years. In conclusion, self-repetition exists, but its return period is extremely long. (ITTC, 2024a)

Numerical examples

Numerical examples of the above-mentioned method are provided below. Here, the Bretschneider spectrum with the significant wave height of 5m and the mean wave period of 9.99s is assumed. z=23, y=5 and m=N are used. The numbers of component waves, N, are 10, 100, 1000 and 10000. Firstly, the irregular wave signals for 9 hours were generated five times with the random phases generated by the multiplicative congruential method (Watanabe et al., 1989), in which the return period is 2^{29}=536870912 so that the use for N=1000000 is approvable. Here the time step is 0.2 seconds. Then, each 9 hours time history was divided into 5 parts, and the wave

spectra are obtained through a Fast Fourier Transformation (FFT) with and without smoothing. The smoothing was executed using with the spectral window using a triangle filter (Hino, 1977). Finally the wave spectrum to be used below are obtained by ensemble averages of the above 45 spectra.

The accuracy of realizing the wave spectra with different N is shown in Figure 1. For obtaining the converged value, N should be 1000 or over with smoothing and 10000 or over without smoothing.

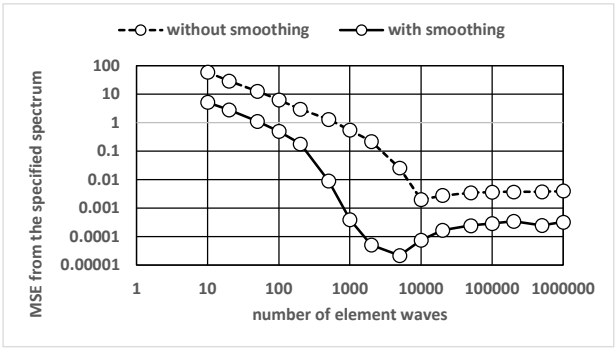

Figure 1: Mean square error of the simulated wave spectrum from the specified spectrum

The differences of realizing the wave spectra are also shown in the comparison between the specified spectrum and the simulated spectra as shown in Figure 2. The FFT results include significant oscillations if N is small. If N=10000, both simulated results show reasonable agreement with the specified one.

Secondly, by applying the Wiener-Khintchine formula (2) to the simulated spectra with and without smoothing, the autocorrelation functions are calculated as shown in Figures 3 and 4. The significant difference due to the smoothing appears when N is small, as shown in Figure 3. In contrast, if in the range where the lag is smaller than 300s, as shown in Figure 4, there is almost no difference between the two. This is because the product of the oscillation due to the FFT and slowly oscillating cosine function due to small lag can be cancelled out. However, if the lag increases further, the FFT oscillation frequency is comparable to the frequency of the cosine function. In any case, if the FFT oscillation is reduced by large N or smoothing, the autocorrelation function converges to zero.

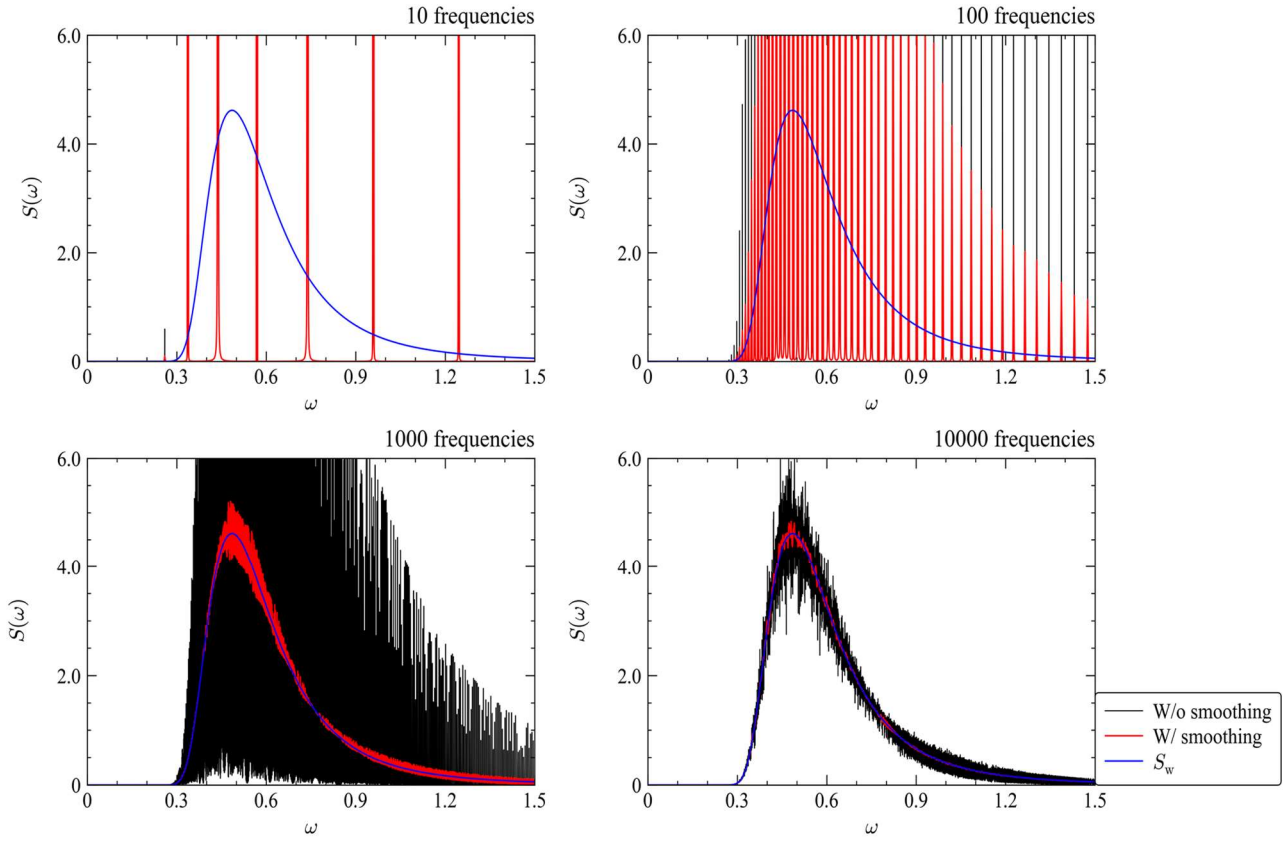

Figure 2: Wave spectra obtained from the signals generated by the present method. (Umeda et al. 2023)

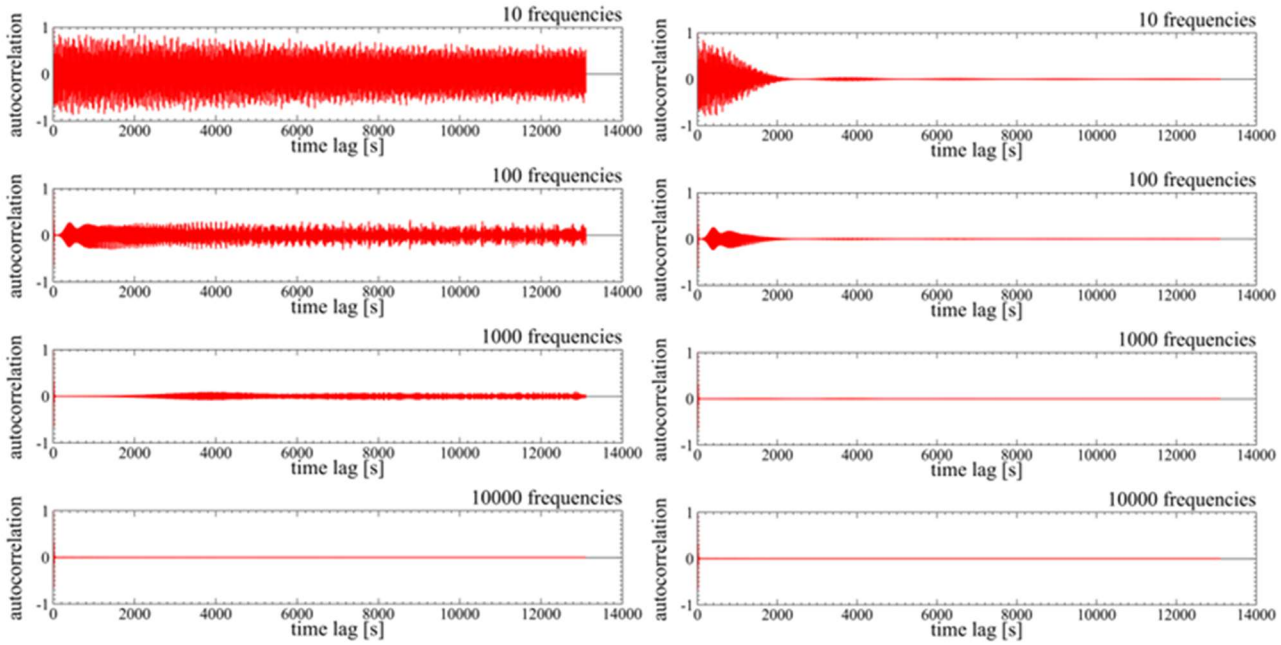

Figure 3: Autocorrelation functions obtained from the signals without smoothing (left from Umeda et al. (2023)) and with smoothing (right).

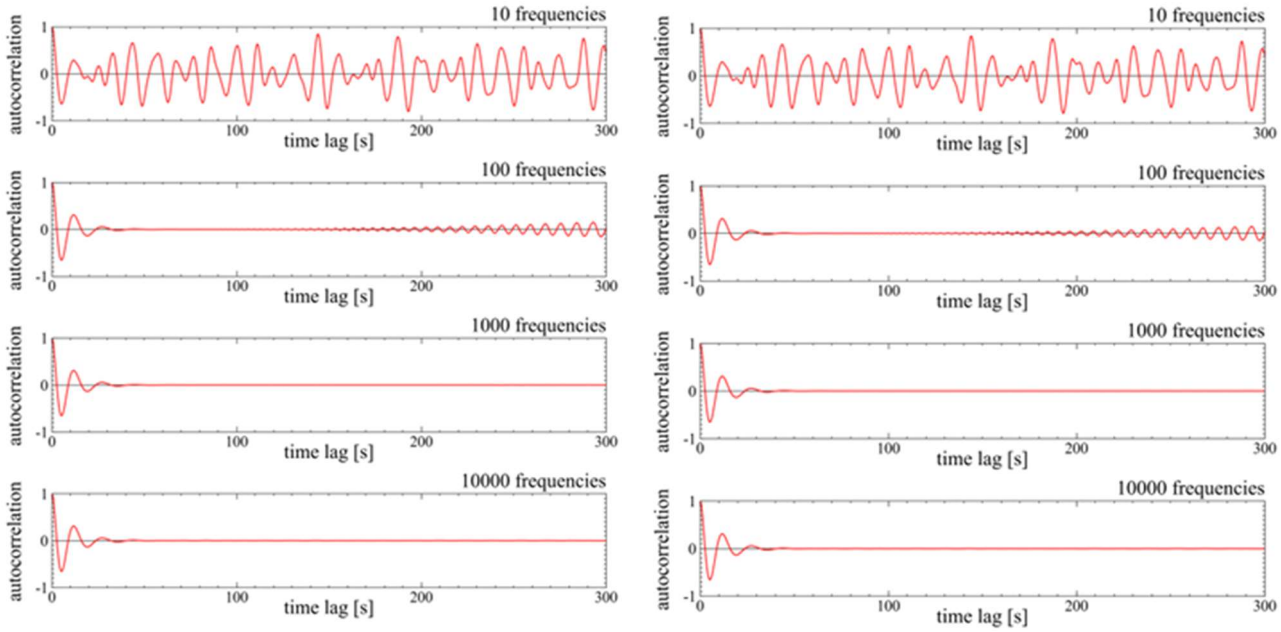

Figure 4: Enlargements of the initial part of Figure 3 without smoothing (left from Umeda et al. (2023)) and with smoothing (right).

3. INTEGRATION ERROR

Section 3 of the ITTC Recommended Procedure 7.5-02-01-09 (2024) states that the reason for self-repeating is numerical error in the spectral discretisation. A mechanism of the accumulation of this numerical error is illustrated in the procedures' Appendix A for the case of a spectrum discretisation with a constant frequency increment. The reason for the error accumulation is the rectangular integration of an oscillatory

integrand in Equation (2); this error is carried over to Equation (1).

Can this numerical error be corrected? Adaptive integration is a framework that can be applied to any numerical integration technique. First, it applies this technique for numerical integration with the entire interval. Then it divides this original interval in two halves and evaluate the integrals for each half separately. Further, it compares the original outcome with a sum of results of integration on half-intervals. If the difference is below specified tolerance, it and continues "halving" these intervals until the convergence is reached. It is, however, a very costly proposition, even if it is appropriate for an oscillatory integrand.

Spectral smoothing, described in Section 2, can be seen as a post-correction for the integration in equation (2). Thus, once the integration error is removed, the ratio of frequencies becomes a primary driver for the increase of the autocorrelation function envelope, i.e. self-repeating effect.

If the integration error is not removed, it causes the self-repetition before the frequency ratio, see an example in the formal response from the ITTC (2024b) to a written discussion from one of the authors (ITTC 2024a).

The discussion in the 30th ITTC leads to another question. Can the consequences of self-repetition be seen in quantities other than the autocovariance function? Can the absence of physical validity indicated by the autocovariance function really affect the actual output of numerical simulations, and if it does, what is this error?

4. VARIANCE ESTIMATE

Estimate of variance of roll is one of the basic values that characterise ship motion. The quantification of the statistical uncertainty of variance estimate is realised through construction of a confidence interval as described in ITTC Recommended Procedure 7.5-02-01-08 (2024).

As the confidence interval of the variance estimate of a stochastic process is affected by its self-dependence, it is expected that the confidence interval would not be correct if self-repetition is present. How can this be verified?

By definition, the confidence interval contains a true value with a given confidence probability. Therefore, if the true value is known and the confidence interval calculation is repeated with different phase sets, for example, 100 times, the true value will be captured roughly in 95 cases if the confidence probability is set to 0.95.

This idea is used to carry out statistical validation of extrapolation methods, as described in ITTC Recommended Procedure 7.5-02-01-10 (2024) and mentioned in section 5.4.4 of Appendix 4 to the Explanatory Notes for the Second Generation of Intact Stability Criteria (IMO, 2023). The average number of successes, which is referred to as a "Passing Rate," is subject to natural variability and its acceptable boundaries can be found in Table 4 of Weems et al. (2023).

The idea is to check the passing rate for the reconstructed wave elevations, for which the true value of the variance is known from the spectrum. The number of frequencies is decreased to "provoke" the self-repetition and the variance is estimated from the reconstructed time histories. For the present example, the calculations are repeated 100 times, and the passing rate (PR) is evaluated. A control sample without self-repetition is also included in the calculations. Parameters are shown in Table 1. Calculations of the confidence interval are performed following section 4.1 of ITTC 7.5-02-01-08 (2024). Results are shown in Figures 5 and 6.

The result shown in Figure 5 with self-repetitions indicates that the self-repetition did not have an obvious influence on the confidence interval of the variance estimate, which is unexpected. However, taking a closer look at these results reveals that the variability of data with self-repetition seems to be less than without it. This can be measured with the average width of confidence interval: 0.034 m^2 in Figure 5 vs. 0.06 m^2 in Figure 6.

If the self-repetition had no effect on the statistical uncertainty, one could expect that the mean width of the confidence interval would be about the same. Figure 7 shows how the average width of the confidence changes with a systematic increase in the number of frequencies.

Table 1: Parameters for Variance Estimate Test

Significant wave height, m	7.5
Modal period, s	15
Frequency range, 1/s	0.272 -1.068
Number of frequencies	21
Duration of a record, s	600
Number of records in a set	30
Variance as discretized, m^2	3.419
Control sample	
Number of frequencies	90
Variance as discretized, m^2	3.429

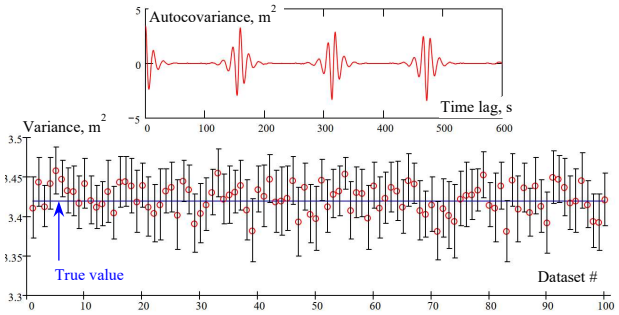

Figure 5: Confidence interval for variance estimate, self-repetition is present, PR=0.92

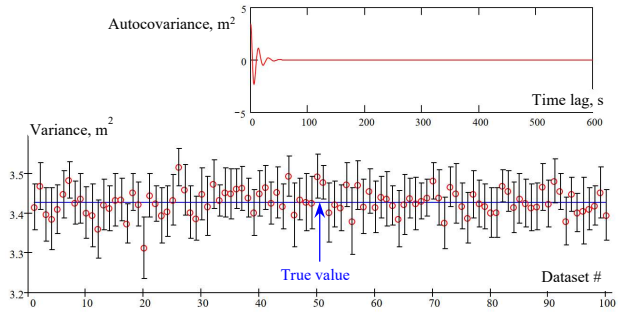

Figure 6: Confidence interval for variance estimate, self-repetition is absent (control sample), PR=0.91

The mean width of the confidence interval does not depend monotonically on the number of frequencies. There are several "dropouts", where the width of the confidence interval goes to zero (and the passing rate too). These are so-called "singularity" cases when the autocovariance function shows an integer number of repeating patterns, eventually leading to zero value for the variance of the variance. One of such cases is shown in Figure 8.

Note that the decrease of the mean width of the confidence interval occurs in the neighbourhood of the "singularity". There was one case of almost "singularity" between 26 and 27 frequencies. Some of the passing rate values were below the acceptable level of 0.9 (below the horizontal dashed red line in Figure 7a), corresponding to 6, 15, 19 and 27 frequencies. Some of these low values may be affected by the "singularities", but some could be caused by natural variability of the data.

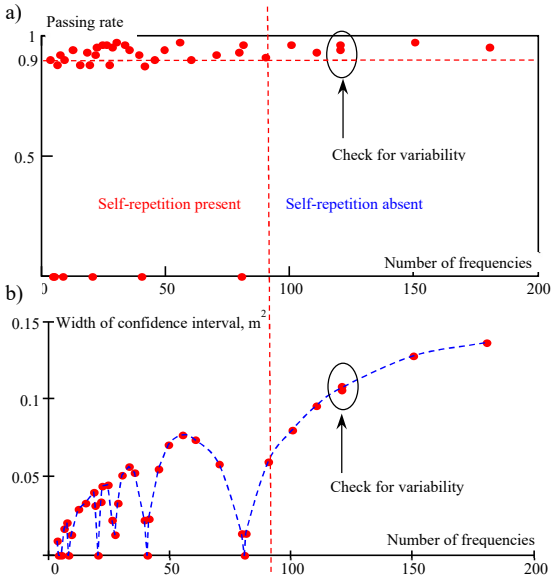

Figure 7: Passing rate (a) and mean width of the confidence interval (b) as a function of the number of frequencies

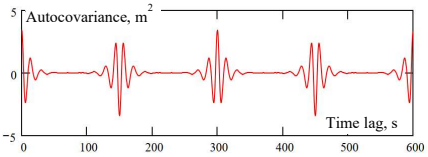

Figure 8: Autocovariance function in a "singular" case with 20 frequencies

The calculations were repeated twice for 120 frequencies with different sets of phases. As can be seen from Figure 7, two points are really close to each other, indicating that the number of frequencies is the main driver under the uniform frequency distribution.

These "singularities" are most probably an artefact of the uniform frequency distribution creating these intricate patterns of the autocovariance function. Aside from these "singularities", the growth of the mean width of the confidence interval is shown to be monotonic after self-repetition disappears. The width does not stabilise immediately after the self-repetition disappears, but shows some tendency to stabilisation for the larger number of frequencies. This tendency is probably related to the general properties of the Longuet-Higgins model (1),

which becomes "more Gaussian" with the increase in the number of frequencies, see Pipiras et al. (2025).

There is some influence of self-repetition on the confidence interval, but many questions remain unanswered, including the effect of the way in which the spectrum is discretised in the frequency domain.

5. CROSSING RATE ESTIMATE

An estimate of the exceedance rate is the ultimate result of direct stability assessment. It is therefore reasonable to check if the self-repetition will affect the estimation. Wave elevations are good for such a test, as the rate of upcrossing of a given level can be computed exactly and utilised as a true value:

$$r = \frac{1}{2\pi}\sqrt{\frac{V_{\dot{\zeta}}}{V_{\zeta}}}\cdot \exp\left(-\frac{a^2}{2\cdot V_{\zeta}}\right) \qquad (6)$$

where V_{ζ} is a variance of wave elevations (available from a spectrum), $V_{\dot{\zeta}}$ is a variance of the temporal derivative of wave elevations (also available from a spectrum), and a is a given level. Note that this equation provides a rate for all upcrossings and not for only independent upcrossings, as the independence of crossing events was not assumed in the derivation of Equation (6). A similar consideration can be found, e.g. in Belenky et al. (2019), applied to the distribution of the values of the first derivative at upcrossing. Thus, to compare an estimate of upcrossing with Equation (6), all the upcrossings should be counted. Parameters for the crossing rate test are shown in Table 2.

Table 2: Parameters for Crossing Rate Test

Significant wave height, m	7.5
Modal period, s	15
Frequency range, 1/s	0.272 -1.068
Level for crossing, m	5
Number of frequencies	21
Duration of a record, s	900
Number of records in a data set	100
Number datasets	50
Crossing rate as discretized, s^{-1}	2.291 10^{-3}
Control sample	
Number of frequencies	140
Crossing rate as discretized, s^{-1}	2.258 10^{-3}

A confidence interval for the crossing rate was constructed assuming binomial distribution for observed number of upcrossing, so lower r_L and upper r_U boundaries of confidence interval for the rate estimate $\hat{r}$ are expressed as

$$r_{L,U} = \frac{Q_B\left(0.5\left(1\pm P_\beta\right),N_t,\hat{p}\right)}{T_S N_r} \qquad (7)$$

where Q_B is a quantile of binomial distribution, $P_\beta = 0.95$ is accepted confidence probability, N_t is the total number of data points in a data set, $\hat{p}$ is a statistical frequency of observation of an upcrossing at each instant of time: $\hat{p} = \hat{r}\Delta t$, $T_s = 900\ s$ is duration of each record, $N_r = 100$ is the number of record in the dataset and Δt is the time increment.

The result of the crossing rate test with self-repetition is shown in Figure 9. The resulting passing rate was only 0.36, which is well below the 0.88 required for 50 datasets.

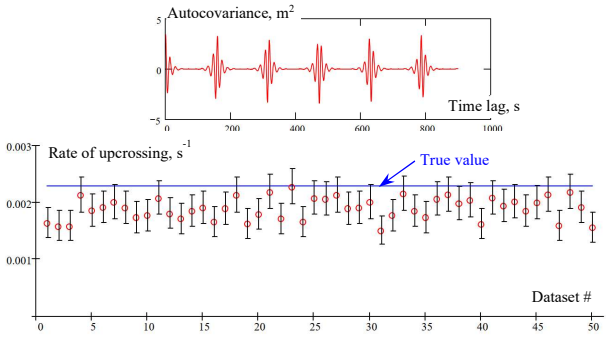

Figure 9: Upcrossing rate test with 21 frequencies: passing rate 0.36

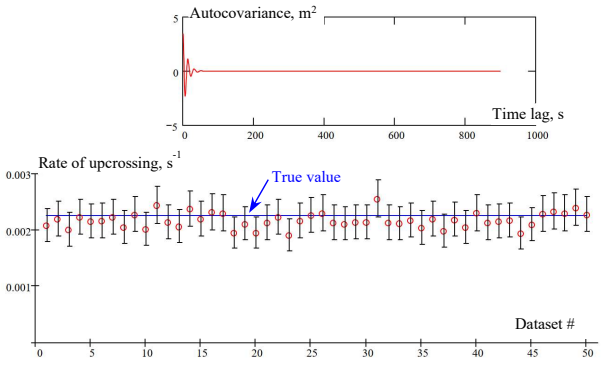

Figure 10: Upcrossing rate test with 140 frequencies: passing rate 0.92

The control sample test is shown in Figure 10. The passing rate is 0.92, confirming the setup for the test. Finally, Figure 11 shows the result for 20 frequencies, i.e. for the case of "singularity" of the variance of the variance (note integer number of pattern of autocovariance function for $T_s = 900\ s$, making three repetitions exactly). The passing rate is 0.34, consistent with the crossing test result shown in Figure 9.

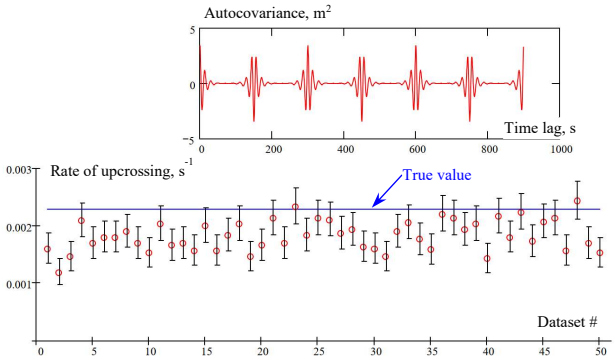

Figure 11: Upcrossing rate test with 20 frequencies: passing rate 0.34

Finally, the influence of self-repetition with the uniform frequency sampling was observed to be substantial, indicating that its avoidance is necessary for Direct Stability Assessment within the framework of the second generation intact stability criteria. The applicability of Equation (6) based on the Gaussian assumption to the case of N=21 could be another discussion item.

6. FURTHER DISCUSSION

One of the arguments in the discussion at the 30th ITTC was that smoothing of the spectrum is equivalent to cutting off the autocovariance function computed from the spectrum (ITTC, 2024b). This issue deserves additional consideration.

It is well established that a numerically calculated spectrum has significant oscillations around the specified spectrum, if N is not large enough (see Figure 2). Here, such oscillation depends on the numerical method used for calculating a spectrum from the time series, while a numerical method for calculating the time series from the spectrum is not equivalent. Thus, the smoothing is typically applied to the calculated spectrum. Indeed, regardless of the use of smoothing or not, the autocorrelation function converged to zero as shown in Figures 3 and 4, if N is large. Thus, it cannot be confirmed that smoothing artificially cuts off the autocorrelation function. However, the number of component waves, N, is more important than smoothing for the autocorrelation function. Here, it is noteworthy that a sufficiently large N is indispensable for accurately realising the spectrum shape as shown in Figure 1. Figure 4 indicates that the decorrelation time calculated from the smoothed spectrum is not significantly different from that from the non-smoothed spectrum. This fact does not support the remark of the ITTC (2024b).

Tsoumpelis & Spyrou (2023) note, "The conventional check for repetitions in data series is based on the observation of high peaks in the autocorrelation function. However, as the autocorrelation reflects averaged resemblance between sets of successive data separated by a time interval, these peaks may not imply repetition in an exact sense. " Tsoumpelis & Spyrou (2023) propose directly computing the root-mean-square of the difference of the time series data, $X(t)$, between the different lags using the following formula where $i = 1 \cdots n$, $k = m \cdots$, $m = int\left(\frac{t_n - t_1}{\tau}\right) + 1$.

$$d_k(\tau) = \sqrt{\frac{1}{n}\sum_{i=1}^{n}[X(t_i+k\tau)-X(t_i)]^2} \quad (8)$$

If the value calculated by Equation (8) is larger than the empirically determined threshold, it should be denoted as "approximated repetition". However, if the method is applied to the example of Figure 5 supplied by the ITTC (2024b) between 0 and 180 s, it is probably not judged as an "approximated repetition".

Bulian et al. (2024) examined the existence of exact or approximated self-repetition by calculating the autocorrelation function and demonstrated that a random selection of the frequencies of the component waves is more suitable than a deterministic selection for avoiding self-repetition. However, this approach does not guarantee the absence of self-repetition based on the random frequency sampling without testing. Similarly, Maruyama et al. (2022) mathematically proved that methods that divide the spectrum so that the energies of component waves are equal to each other (e.g. Shuku et al., 1979), do not always exclude self-repetitions.

7. ENCOUNTER WAVE GROUP CASE

The above discussion is based on the assumption that the autocorrelation function of a response in irregular waves would converge to zero when the lag increases. However, it is not always true in the case of an encountered wave group when a ship in astern waves runs with the group velocity of one of the incident component waves, $\frac{g}{2\omega}$. If the wave encounter frequency, ω_e, is given by

$$\omega_e = \omega - \frac{U\omega^2}{g} cos\chi \quad (9),$$

the encounter wave spectrum, $\boldsymbol{S_w^*}$, can be calculated as follows:

$$S_w^*(\omega_e) = \frac{S_w(\omega)}{\left|\frac{\partial \omega_e}{\partial \omega}\right|} = \frac{S_w(\omega)}{\left|1 - \frac{2U\omega}{g} cos\chi\right|} \quad (10)$$

where U is the ship forward velocity, ω is the wave frequency, χ is the ship course measured from the wave direction, and g is the gravitational acceleration. Thus, if $Ucos\chi = \frac{g}{2\omega}$, $S_w^*(\omega_e) = \infty$ (e.g. Price and Bishop, 1974). This means that the encounter wave at this frequency is periodic, so that the autocorrelation function involves a periodic component.

Takaishi (1978, 1982, 1994) experimentally realised this phenomenon. If the ship runs with the group velocity of a major component wave, the encounter wave becomes almost periodic, as shown in Figure 12. Takaishi found that many capsizing accidents occurred under this situation based on the casualty records and model experiments. Takaishi et al. (1996) further investigated statistical aspects of this phenomenon, such as the length of the high encounter wave group. In response to this finding, IMO (1995) approved the operational guidance for the ship master, focusing on this phenomenon as one of the major dangerous conditions at sea.

This phenomenon was revisited by Pipiras et al. (2022), which concluded that the autocorrelation function decays slowly as the time lag decreases. Pipiras et al. (2022) developed a way to estimate the confidence interval of the means under this phenomenon, but the estimation of the first passage time, which is required by the direct stability assessment, has not yet been discussed.

This encounter wave group phenomenon can be regarded as a kind of "approximated self-repetition" but it is different from the self-repetition phenomenon mentioned in Section 1. If the numerical simulation is stopped once a stability failure because of the accumulation of trapped water due to periodic wave crest encounters, the occurrence of such a stability failure itself is independent of other realizations. Thus, the event of stability failure can be regarded as a Poisson process. This means that the direct counting method can still be used for this phenomenon. If this phenomenon is filtered because the autocorrelation function is not small, one of the most dangerous situations to be avoided at sea would be overlooked.

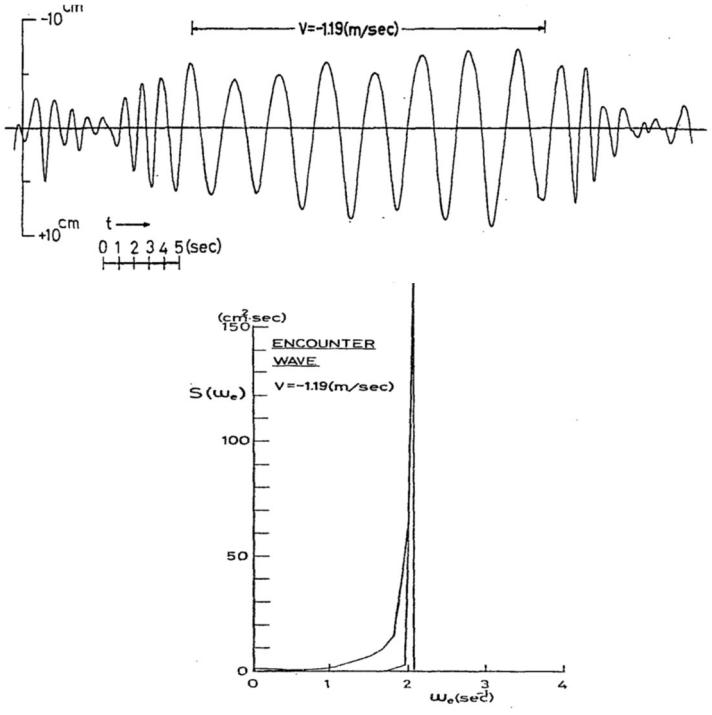

Figure 12: An example of the encounter wave spectrum and time series in the case that a wave probe runs with the group velocity of a major wave components (Takaishi, 1978).

8. CONCLUDING QUESTIONS

It is difficult to overstate the importance of a valid wave model for an accurate and efficient direct stability assessment. Avoiding self-repetition is one of the crucial factors for the successful application of DSA. While self-repeating effects have been known for some time, many of their aspects are still worth discussing. The authors were trying to provide an overview of these issues that looked to be the most important and would like to bring them up for discussion at this Workshop:

1) What is the primary driver for the self-repetition: ratio of the frequencies of components or accumulation of numerical integration errors or a combination of thereof?
2) What is the best way to check self-repetition? Should it be limited to the autocovariance function?
3) If the autocovariance function is used, how should it be computed: evaluated from the spectrum or estimated from the time series? What is the best use of each approach?
4) What is the best way to estimate the autocovariance function from a time series: directly or through computing the spectrum first? Smoothing of the wave spectrum does not seem to significantly change the decorrelation time.
5) A sufficient number of component waves are indispensable for accurately realizing the specified spectrum and avoiding increases of the autocorrelation function envelope with the increase of time lag. Is the decay of autocovariance sufficient?
6) The encounter wave grouping phenomenon in following and stern quartering waves due to the Doppler Effect is recognised as one of the major threats to ship stability. If the autocorrelation function is calculated under this phenomenon, the decorrelation time will be long. However, a direct counting method is still applicable to this phenomenon for aiming at direct stability assessment. What should be a practical approach to self-repetition in this case?

ACKNOWLEDGEMENTS

The first two authors thank Prof. Makio Ishiguro from the Institute of Statistical Mathematics, Prof. Masahiro Sakai from the University of Osaka, Prof. Daisuke Terada from Japan's Defence Academy and Dr. Sadaoki Matsui from the National Maritime Research Institute for their effective discussion with the first author.

The third and fourth authors would like to recognize support from the US Office of Naval Research under Drs. Woei-Min Lin and Bob Brizzolara, as well as fruitful discussion, help and guidance from Prof. Vladas Pipiras of the University of North Carolina at Chapel Hill.

REFERENCES

Belenky, V., 2011, "On Self-Repeating Effect in Reconstruction of Irregular Waves", in *Contemporary Ideas on Ship Stability and Capsizing in Waves*. Neves, M., Vadim L. Belenky, V. de Kat, J. Spyrou, K., Umeda, N., eds., Springer (Dordrecht, Heidelberg London, New York), ISBN 978-94-007-1481-6, pp. 549-557.

Belenky, V., Glotzer, D., Pipiras, V. and T. Sapsis, 2019 "Distribution tail structure and extreme value analysis of constrained piecewise linear oscillators", *Probabilistic Engineering Mechanics* Vol. 57, pp 1-13.

Bulian, G., Zeng, K.Z., Lu, J., Gu, M., 2024, "Comparison of Autocorrelation Function of Wave Elevation for Different Wave Generation Approaches", Proceedings of the 2nd International Conference on the Stability and Safety of Ships and Ocean Vehicles, CSSRC (Wuxi), pp. 93-104.

Hino, M. 1977, "Spectral Analysis", Asakura Shoten (Tokyo), pp. 183-236 (in Japanese).

IMO 1995, "MSC/Circ.707 - Guidance to the Master for Avoiding Dangerous Situations in Following and Quartering Seas.

IMO 2020, "MSC/Circ. 1627 - Interim Guidelines on the Second Generation Intact Stability Criteria.

IMO 2023, "MSC/Circ. 1652 - Explanatory Notes to the Interim Guidelines on the Second Generation Intact Stability Criteria".

ITTC Recommended Procedure 7.5-02-01-08 "Single Significant Amplitude and Confidence Intervals for Stochastic Processes", Rev. 01, 2024.

ITTC Recommended Procedure 7.5-02-01-09 "Avoiding self-

repeating effect in time-domain numerical simulation of ship motions", Rev. 00, 2024.

ITTC 2024a, "Written Discussion to Stability in Waves Committee Report submitted by N. Umeda", in Proceedings of the 30th International Towing Tank Conference, AMC (Hobart), Vol. 2, 2024. www.ittc.info/media/12146/26-stability-in-waves-committee-written-discussion.pdf

ITTC 2024b, "Reply to Written Discussion to Stability in Waves Committee Report submitted by N. Umeda", in Proceedings of the 30th International Towing Tank Conference, AMC (Hobart), Vol. 2, 2024. www.ittc.info/media/12146/26-stability-in-waves-committee-written-discussion.pdf

Maruyama, Y., Umeda, N., Maki, A., 2022, "Measures for Avoiding Self-Repetition Effect in the Direct Stability Assessment", Proceedings of the 18th International Ship Stability Workshop, Gdansk Univ Tech, pp. 177-183.

Longuet-Higgins, M. S., 1957,"The Statistical Analysis of a Random Moving Surface," *Phil. Trans A*., Vol. 249, pp. 321-387.

Pipiras, V, Zouboulоglou, P., Sapsis, T., 2022, "Cyclical Long Memory in Ship Motions at Non-Zero Speed", Proceedings of the 18th International Ship Stability Workshop, Gdansk Univ Tech, pp. 297-306.

Pipiras, V., Weems. K and V. Belenky, 2025 "Non-Gaussianity, discretization and their consequences for uncertainty quantification in Longuet-Higgins model of random waves" Proc. of the 20th IMAM Congress (to appear).

Price, W.G., Bishop, R.E.D., 1974, "Probabilistic Theory of Ship Dynamics", Chapman and Hall (London).

Shinozuka, M. and Deodatis, G., 1991, "Simulation of Stochastic Processes by Spectral Representation", *Applied Mechanics Reviews*, Vol. 44 (4), pp.191-204.

Shuku, M., Shimada, H., Fujii, H., Toyoda, S., Ikegami, H., Ando, H., 1979, "The motions of Moored Floating Storage Barge in Shallow Water", *Journal of the Society of Naval Architects of Japan*, Vol. 146, pp. 245-254, (in Japanese).

St. Denis, M., and Pierson, W. J. 1953, "On the Motion of Ships in Confused Seas," *Trans.*, *Soc. of Naval Architects and Marine Engineers*, Vol. 61

Takaishi, Y., 1978, "Current Status and Problems of Ship Stability Research", *Bulletin of the Society of Naval Architects of Japan*, No. 594, pp. 571-577, (in Japanese).

Takaishi, Y., 1982, "Consideration on the Dangerous Situations Leading to Capsize of Ships in Waves", Proceedings of the 2nd International Conference on Stability and Ocean Vehicles, The Society of Naval Architects of Japan (Tokyo), pp.161-169.

Takaishi, Y., 1994, "Dangerous Encounter Wave Conditions for Ships Navigating in Following and Quartering Seas", Proceedings of the 5th International Conference on Stability and Ocean Vehicles, Florida Tech (Melbourne), Vol. 1, pp.45-59.

Takaishi, Y., Watanabe, K., Masuda, K., 1996, "Statistical Properties of Encounter Wave Grouping Phenomena in Following and Quartering Seas", *Journal of the Society of Naval Architects of Japan*, Vol. 180, pp. 283-294, (in Japanese).

Tsoumpelis, D., Spyrou, K.J., 2023, "Identification of recurring patterns and repetitions in time-series, with application to pseudo-stochastic ship rolling", *Ocean Engineering*, Vol. 271, Article 113717.

Umeda, N., Maruyama, Y., Okamoto, S., Oka, A., Masamoto, S., Matsuda, A., 2023, "Filling gaps in Direct Stability Assessment Procedures", Proceedings of the 19th International Ship Stability Workshop, Istanbul Tech Univ, pp.193-200.

Watanabe, C., Natori, T., Oguni, T., 1989, "Numerical Calculation Software using Fortran 77", Maruzen (Tokyo), pp. 315-321, (in Japanese).

Weems, K., V. Belenky, B. Campbell, and V. Pipiras, 2023, "Statistical Validation of the Split-Time Method with Volume-Based Numerical Simulation", in *Contemporary Ideas on Ship Stability – From Dynamics to Criteria*, Spyrou, K., Belenky, V., Katayama, T., Bačkalov, I., Francescutto, A., eds., Springer, ISBN 978-3-031-16328-9, pp. 225-243.

Yamanouchi, Y. , 1961, "Response Theory and Ship Motions", Bulletin of the Society of Naval Architects of Japan, pp. 273-286, (in Japanese).

Session 7
Stability and safety of special vessels

Floating crane operations, where the IMO rules are dropping the load

René van den Heuvel, GustoMSC, the Netherlands, rene.vandenheuvel@nov.com
Luuk van der Linde, GustoMSC, the Netherlands, luuk.vanderLinde@nov.com

ABSTRACT

With the onset of the offshore wind industry, more and more offshore lifting operations are done with floating vessels. As the frequency of lifting operations increases, so does the expected number of incidents related to a sudden loss of hook load. While stability criteria are in place to ensure the safety of the vessel during such an incident, they do assume that the crane is a rigid part of the vessel. This is not the case, and recent incidents have shown that more emphasis should be put on the dynamic behavior of both the crane and the vessel. Disregarding or not properly addressing this behaviour in the design of the crane and vessel can lead to capital equipment losses and even loss of lives. In this paper the sudden loss of hook load phenomenon is regarded, the current rules and regulations that are in place are discussed and it is shown how the consquences of a sudden loss of hook load are quantified with a simplified approach and a more advanced time-domain analysis.

Keywords: Sudden loss of hook load, dropped load, offshore lifting

1. INTRODUCTION

Offshore floating crane operations are common practice for the installation and removal of offshore oil and gas structures. With the onset of the offshore wind industry, also components of wind turbines are installed with floating crane operations. This concerns mainly foundations, but it is also investigated to install towers, nacelles and blades while floating. With the size increase of Wind Turbine Installation (WTI) Jack-ups, it is not always possible to jack out of the water in certain ports. In that case the loading sequence needs to be performed while floating. So even jack-ups need to be able to do floating crane operations.

Compared to floating crane operations performed in the offshore oil and gas industry, floating crane lifts in the offshore wind industry are done with a higher frequency. Also, lifting is done mostly over the side instead of over the stern, as the crane is in general positioned at the side. This allows for smaller lifting radius to ensure sufficient lifting height and hoist capacity, resulting in a steep crane boom angle. An accidental sudden loss of hook load results in the vessel rolling back, pulling the crane boom along. Potentially the crane boom can come close to the vertical, with boom hoist wires temporary falling slack (reference is made to the Semi-submersible Saipem 7000 incident in 2022 (Riviera, 2022)). In a more severe scenario, the boom may even be pulled beyond the vertical tipping point, tip over against boom stoppers or even collapse (reference is made to the crane vessel Orion incident in 2020 (SWZMARITIME, 2020)).

2. OFFSHORE HEAVY LIFT CRANE

Offshore heavy lift cranes are in general of the boom hoist type. These can be tub cranes, leg encircling crane (in case of jack-ups, as seen in Figure 1) or pedestal cranes.

Figure 1: Jack-up with leg encircling heavy lift crane.

Depending on the type, a boom hoist crane can lift up to 8000 t. Figure 2 shows a typical boom hoist heavy lift crane, with corresponding nomenclature.

With a boom hoist crane, a crane boom is connected by the boom heel point to the slewing platform, and the boom is suspended with the boom hoist wire, enabling different boom angles, and thus outreaches of the crane hook. The hoist wire is normally led over an A-frame, or tower to the hoist wire winch. A boom stopper is normally in place to limit the maximum boom angle, which is typically around 85 degrees from the horizontal.

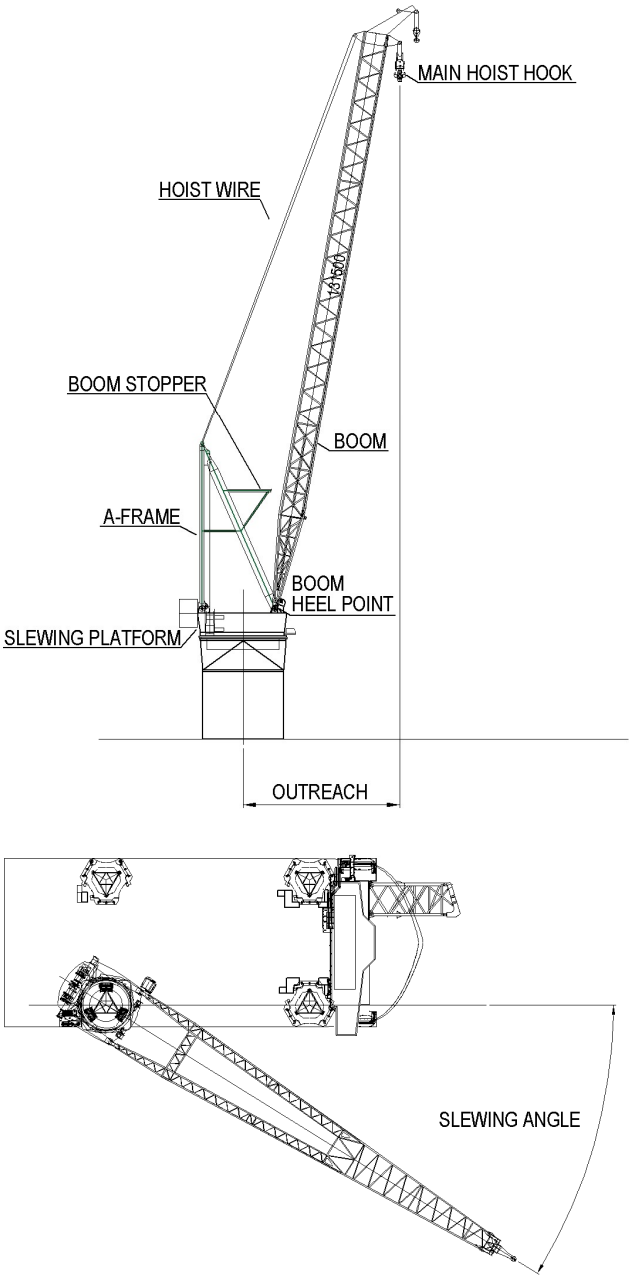

Figure 2: Boom hoist heavy lift crane nomenclature.

3. ACCIDENTAL SUDDEN LOSS OF HOOK LOAD

During floating lift operations, it is important that the vessel stays within the trim and heel limitations of the crane. In general boom hoist offshore cranes can be allowed a trim and heel angle of up to 2 degrees including wind load. Depending on deck load, vessel type and wind speed, the wind heeling angle can be easily 1 degree, so the allowable static heel angle is limited to around 1 degree. Crane operations result in an additional heeling moment due to the crane weight and the weight of the load that is lifted (hook load). If this heeling moment is not compensated the heel of the vessel will easily be more than the allowable heel angle, especially when the boom is slewed outboard to the side of the vessel. To compensate this heeling moment, counter ballast is placed on the opposite side of the vessel and is in general water ballast. During a sudden loss of hook load, which is also called a dropped load incident, the hook load is instantly removed, reducing the crane heeling moment, vessel's displacement and vertical centre of gravity significantly. As the counter ballast is still present, the vessel will roll towards the new equilibrium angle induced by the counter ballast moment. However, as it is building up rolling speed from the initial angle to the new equilibrium angle, it will overshoot this equilibrium angle to a larger heeling angle before starting to roll back to the equilibrium angle and eventually settle down at the equilibrium angle, see Figure 3. This overshoot angle or also called the dynamic roll angle needs to be taken into account when assessing the consequences of a dropped load incident.

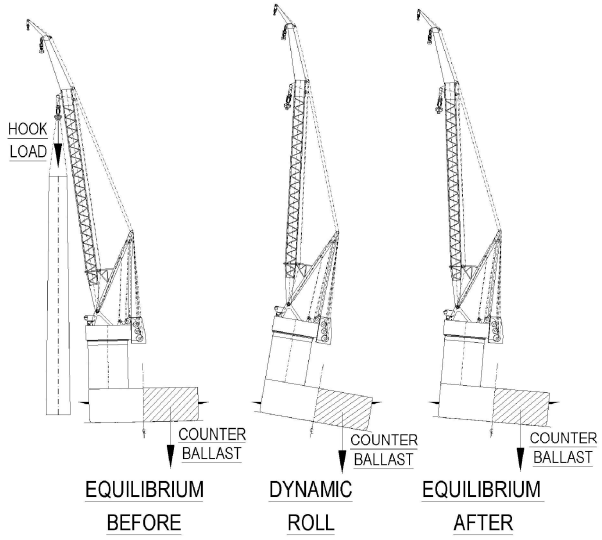

Figure 3: Dropped load incident phases.

A dropped load incident can have many causes, such as the failure of the pad eye, sling, shackles, hook, the winch brake of the lift or boom hoist wire, the breaking of the lift or boom hoist wire, or another cause. While there are safety margins and operational procedures in place to prevent the failure of any of those components (like testing, regular maintenance and inspection), a dropped load incident can still occur. In that case it must be ensured that the vessel does not capsize.

4. CURRENT RULES IN THE IS CODE

Stability criteria for floating crane operations were in place in classification society rules and in flag state rules for quite a long time. However, it was not until 2016 that with resolution MSC.415(97) (IMO, 2016), guidance for ships engaged in lifting operations were included in the Intact Stability (IS) Code (IMO, 2008), that are applicable for vessels constructed from 2020. Within the IS code in chapter 2.9 of part B, three sets of intact stability criteria for crane operations are given and two sets of criteria for sudden loss of hook load incidents are defined.

Both sets of criteria for sudden loss of hook load compare the energy build under the GZ curve from the initial heeling angle ϕ_1 to the new equilibrium angle ϕ_{e2} (area A1, Figure 4) and the area under the GZ curve between the new equilibrium angle ϕ_{e2} and the down flooding angle ϕ_f to the other side (area A2, Figure 4). If A2 is greater than A1 (with a margin which depends on the operational area), the vessel is considered safe.

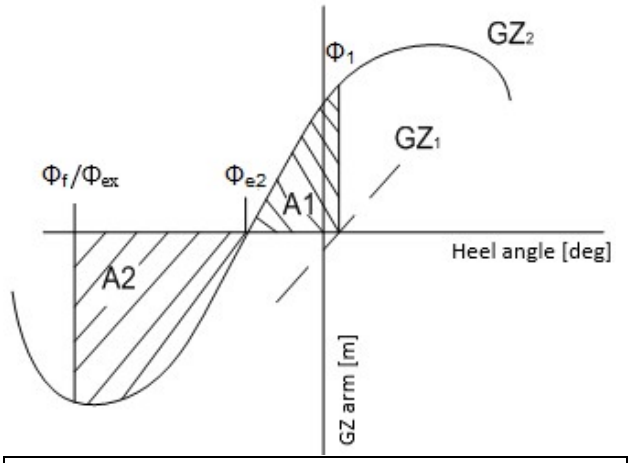

GZ_1:	Net righting lever (GZ) curve before loss of load
GZ_2:	Net righting lever (GZ) curve after loss of load
Φ_1:	Angle of static equilibrium before loss of load
Φ_{e2}:	Angle of static equilibrium after loss of load
Φ_f:	Angle of down-flooding
Φ_{ex}:	Angle of extreme roll-back, where A1=A2

Figure 4: GZ criteria plot (IMO, 2008).

The difference between the two sets is how the GZ curves are taken into account. For the standard criteria set, the GZ curves are corrected for the crane heeling moment and for the counter ballast moment. In the alternative criteria set, the GZ curves of the vessel without the moment corrections are used and the crane heeling moment and counter ballast moment are imposed separately. As the standard criteria is the most straightforward to use with stability software, only this method is evaluated in this paper.

However, letting the vessel roll dynamically to the down flooding angle may lead to large rolling angles, which may be more than the crane can handle.

5. DROPPED HOOK LOADS: THE REALITY

In the IMO stability criteria, the crane boom is considered a rigid part of the hull and stays in place. In reality with boom hoist cranes, the boom is not fixed in position, but it is supported by the hoist wires and is allowed to rotate around its heel point. After a dropped load incident, the vessel rolls to its maximum dynamic roll angle (see Figure 3) and then rolls back again towards the boom. During this phase, the rigid body assumption of vessel and crane is no longer valid. If the boom passed the vertical or its inertia is large enough, the boom will impact (or 'flip back') against the boom stopper. This can result in damage to the boom, or the boom stopper can collapse resulting in the boom impacting on the A-frame as is seen in the Orion incident (SWZMARITIME, 2020).

If no flip back happens, the vessel rolls towards the boom (slowed down by its own inertia), causing the boom hoist wires to become slack. After that, the boom will fall back into its boom hoist wires, resulting in an impact load on the boom. Additionally, axial compression and some moment induced flexure is built up (or strain energy is stored) in the boom structure while lifting. After dropping a load, this energy is released, resulting in violent vibrations in the boom that may cause high internal loads. Both the fall back of the boom and boom vibrations are visible in footage of the Saipem incident (YouTube, 2023).

While a boom collapse may induce a larger heeling moment, the vertical centre of gravity is significantly reduced, improving the stability characteristics. Therefore, a boom collapse is not

considered as an additional risk for capsizing of the vessel. It can, however, lead to severe capital loss and even personal injuries or loss of lives. As the IMO IS-code only addresses the stability of the vessel and it does not address the consequences to the combined vessel-crane system, more analysis is deemed required to determine the consequence of a dropped load incident.

6. CLASS REACTIONS

As the described boom collapse scenario is not mentioned in the IMO stability guidelines, several classification societies have reacted on the incidents by updating their rules to take this effect better into account. Based on a review of rules of four major classification societies the following was found.

American Bureau of Shipping (ABS, 2025): A risk assessment should be conducted to evaluate mitigation measures to reduce the risks associated with a sudden release of hook load in each heavy lifting operation.

Lloyd's Register (LR, 2024): Risk assessment is required for high-risk applications like heavy lift operations (with cranes or other type of lifting appliances) where there is a risk of damage to the appliance and/or vessel in case of the sudden release of the load.

Det Norske Veritas (DNV, 2024): The vessel, including the main lifting appliance(s), shall be designed and built with due consideration to the risks caused by an accidental drop of hoisted load. A high-level risk analysis shall be carried out according to recognized methods. The risk analysis shall as a minimum address the identification of potential hazard scenarios caused by accidental drop of hoisted load, including:

- dynamic motions of vessel
- cranes or part of it flipping back, e.g. boom

Bureau Veritas (BV, 2025): No additional requirements were found to address loss of load incidents except those listed in the IS code.

So, most of the considered classification societies now require a risk assessment for sudden loss of hook load incidents, which was not the case prior to 2020. For this it is important to keep in mind the dynamic roll back angle and the effects it can have on the boom. However, among the considered classification societies, only one specifically mentions this aspect.

7. RISK IMPACT ASSESSMENT WITH SIMPLIFIED APPROACH

As a first level risk impact assessment it was identified that it is undesirable that the boom passes the upright to the other side during a dropped load, so that it will not fall onto the boom stopper or A-frame. For this a simplified approach has been developed by GustoMSC, which is based on the area under the GZ curve as indicated in Figure 4. Here it is still assumed that the crane boom is a rigid part of the vessel. In this approach the angle Φ_{ex} is determined where the area A1 is equal to A2. As the energy that is build up from the new equilibrium Φ_{e2} to the dynamic roll back angle Φ_{ex}, cannot be larger than the energy that is released from the initial heeling angle Φ_1 prior to dropped load to the new equilibrium angle Φ_{e2}.

Taking into account the initial heeling angle before dropped load, the heeling angle of the boom and the dynamic roll back angle, it is important that the boom angle does not pass the upright of 90 degrees, and preferably stays below that with a few degrees of margin.

For example, as illustrated in Figure 5, the crane boom angle prior to the loss of load is 83 degrees with respect to the vessels horizontal plane. If the dynamic roll back angle is 10 degrees to SB, the boom will reach 93 degrees, hence passing the vertical position by 3 degrees. In this case either the boom angle needs to be reduced, or the hook load (and counter ballast) needs to be reduced.

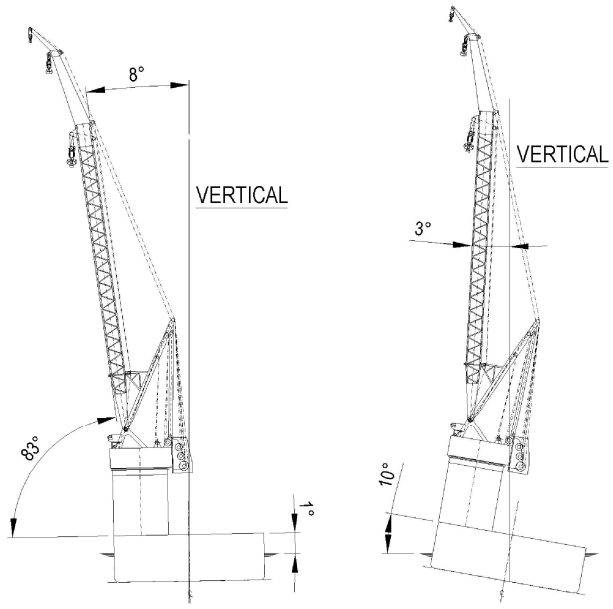

Figure 5: Crane boom positions

The simplified approach is a quick assessment to estimate whether a boom roll over will occur. It is conservative, because roll damping is not taken into account with the assumption that area's A1 and A2 are equal. The actual dynamic roll angle may be smaller as part of the energy is dissipated by the roll damping.

In addition, the dynamic behavior of the boom itself is not taken into account with the simplified approach, as it will spring up after the loss of hook load. Also, the boom hoist wires can become slack and the boom can fall back into the hoist wire introducing a large impact load. To take this into account a more advanced analysis is required taking into account the dynamic properties of both the vessel and the crane.

8. RISK IMPACT ASSESSMENT WITH TIME-DOMAIN APPROACH

A multi-body time-domain analysis method has been created by GustoMSC in Siemens NX motion (NX, 2024) to study the dynamic behaviour of the main crane boom and the floating vessel during a dropped load incident. A grid of points is analysed, covering a wide range of load – outreach combinations within the crane load chart as seen in Figure 6.

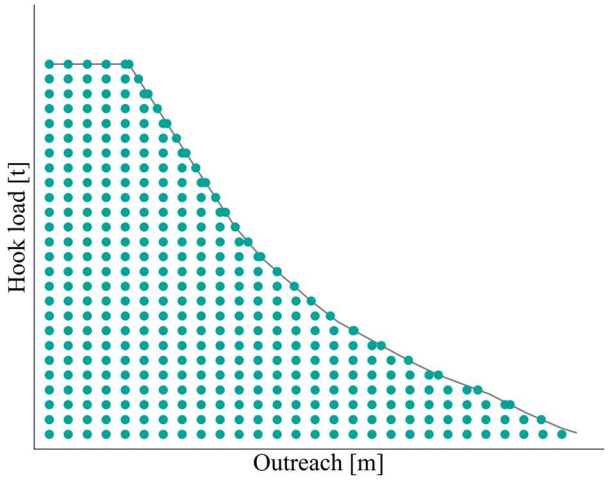

Figure 6: Grid used for time-domain analysis.

In this grid, the hook load is the total load that the main crane is lifting. The outreach is the horizontal distance from the centre of rotation of the crane to the end point of the hook, see Figure 2.

For each point, a time-domain analysis is performed in which a dropped load incident is simulated. The analysis starts from a static equilibrium position after which the lifted load is removed. During the analysis the model is checked for a set of failure criteria and any exceedance of a limit is stored. The following 6 failure criteria are implemented:

1. Stopper contact: a check if the boom stopper (if present) comes in contact with the boom.
2. Stopper force: check if the boom stopper load is above allowable.
3. Slewing torque: check if the torque around the slewing axis is above allowable.
4. HP shear force: check if the shear force at the heel point is above allowable.
5. HP normal force: check if the normal force at the heel point is above allowable.
6. Boom hoist force: check if the force in the boom hoist wires is above allowable.

If no failure criteria are exceeded, this means that no consequence is expected for that load – outreach combination. An envelope can be created for load-outreach combinations that yield limited to no consequences for safety and loss of capital in the event of a dropped load incident. This envelope is useful for crane operators as it can be judged quickly if a desired floating lift operations will create additional consequences if a load is dropped.

The multi-body time-domain model consists of two main bodies: a vessel and a boom. The vessel is modelled as a rigid body and its interaction with the waterplane is modelled with three restoring springs for heave k_{33} , roll k_{44} and pitch k_{55} acting at the Centre of Flotation (CoF), see Figure 7. These springs are linear, which is deemed acceptable for this analysis as the effect on heel angle amplitude is found to be typically below 10%. This will have a limited effect on the outcome of the analysis. The hydrodynamic added mass and damping are derived from a radiation-diffraction analysis in WAMIT® (WAMIT, 2024). An additional viscous damping contribution is also considered.

The boom body is connected to the vessel at two points: the heel point with a hinge that allows for rotation around one axis and to the top of the A-frame by a tension-only spring that represents the boom hoist wires. The boom can be rotated to analyse various slewing angles. The boom stopper is represented by a spring-damper between the A-frame and the boom. The boom body is modelled as a 'flexible body' that uses a linear combination of

mode shapes to describe the spatial deformation of the structure. This drastically reduces the degrees of freedom for the motion solver, significantly reducing the solving time compared to direct-integration methods. Reason for using a flexible body for the boom is twofold: the vibrations introduced after dropping a load can be studied and the impact load on the boom hoist wires is reduced after the boom falls back in the, previously slack, hoist wires.

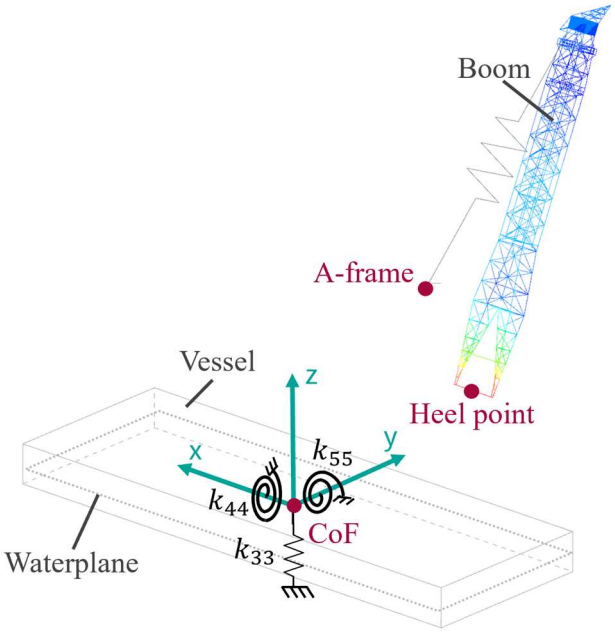

Figure 7: Schematic overview of multi-body model.

This time-domain approach is a more extensive method, but it is still found practical to use in a dropped load risk impact assessment. More detailed information on vessel stability and/or main crane component failure can also be used in optimizing the vessel and boom design.

9. COMPARISON OF APPROACHES

A comparison is made between the simplified and time-domain approach for a typical generic jack-up vessel with a leg encircling heavy lift crane. An initial loading condition with low vertical centre of gravity (VCG) and low draft is taken, representing for example a harbour lift with no variable load on deck. For a slewing angle of 90 degrees outboard, the results of both analyses are given in Figure 8.

Each grid point in Figure 8 indicates which failure criteria is/are exceeded or if no criteria is exceeded. The time-domain approach (the grid points) are compared to three curves: the simplified approach described in Section 7, the IMO Intact Stability requirements described in Section 4 and a curve based on maximum ballast capacity to stay within the maximum allowable heel angle. The IMO IS-code curves are not visible in this figure, as for this loading condition the intact criteria are not limiting and are thus outside the range of the analysed grid. This demonstrates the fact that the IMO IS-code only considers stability criteria and is not sufficient to safeguard against failure types related to the main crane boom dynamics, which are included by criteria in the more advanced time-domain analysis.

For each outreach distance, the simplified approach allows for less hook load compared to boom stopper contact as calculated in the time-domain approach. This is due to the use of damping, resulting in a smaller dynamic roll angle in the time-domain approach. The difference is, however, minor. A more significant difference can be seen when comparing the boom stopper contact with the boom stopper force. For small outreaches and medium hook loads, the boom makes contact with the boom stopper, but the impact on the boom stopper does not result in failure. Boom stopper force exceedance can be caused by the impact of the boom passing the vertical and hitting the boom stopper, but it can also be caused by boom vibrations. Especially for small outreaches, the amplitude of the vibrations can be such that the boom hits the boom stopper. This explains why an alternating pattern of contact & boom stopper force exceedance is visible.

In the top right of the grid, boom hoist wire failure can be seen. The boom is not passing the vertical, but is falling back in the boom hoist wires, causing them to fail. The simplified approach does not describe this effect. For this vessel, however, the hook loads where this happens cannot be physically achieved, because the vessel does not have sufficient ballast capacity to perform these lifts. This can be seen by the ballast capacity curve being below the grid points with boom hoist wire criteria exceedance.

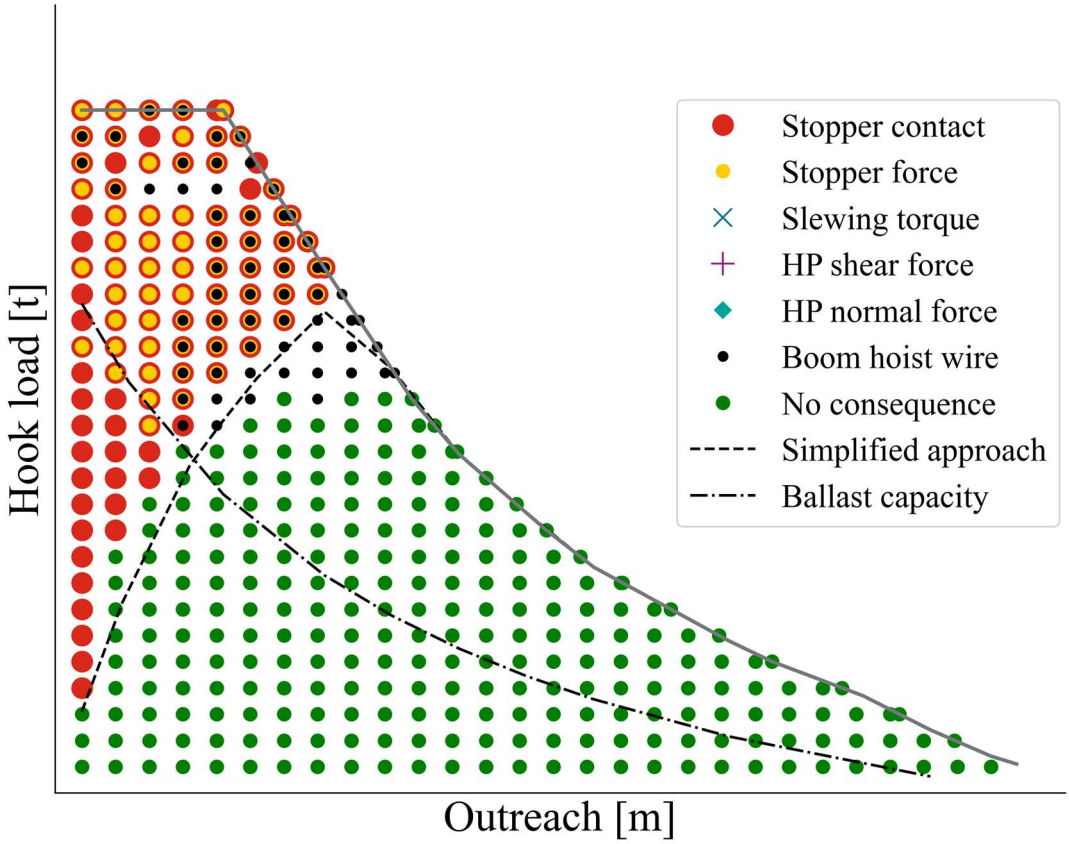

Figure 8: Dropped load simplified and time-domain analysis for slewing angle 90 degrees outboard.

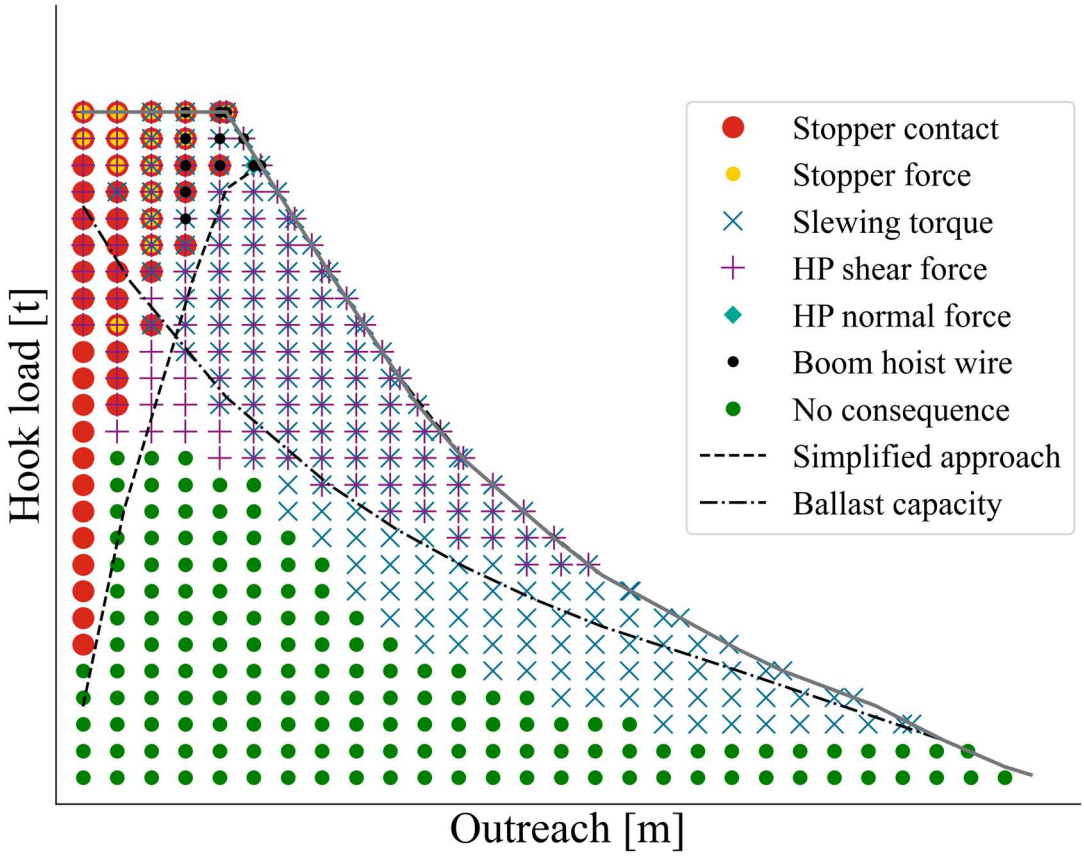

Figure 9: Dropped load simplified and time-domain analysis for slewing angle 45 degrees outboard.

In Figure 9 the results for a 45-degree slewing angle are given. The IMO IS-code stability curves are even less limiting for 45-degree slewing angle than for 90-degrees and therefore also not visible. Compared to a 90-degree slewing angle, the 45-degree slewing angle results in less cases where a boom flip back is expected with boom stopper contact and/or failure. Different crane failure mechanisms can be observed for a 45-degree slewing angle. Large loads develop around the heel point (HP) and slewing platform due to the dynamic roll of the vessel, resulting in heel point shear force limit and slewing torque exceedance.

The failure criteria of the time-domain analysis are not limited to the ones presented in this section. E.g. more criteria, like internal loads of the boom can be studied to improve the boom resistance to boom stopper impact or fall back in its hoist wires.

In conclusion, the simplified approach can be used as a fast and conservative method to analyse boom flip back. This is only applicable to the 90-degree slewing angle. For other slewing angles, such as 45 degrees, the heel point shear force or slewing torque criteria might be exceeded in case of a dropped object. The IMO IS-code stability criteria are not able to include the main crane boom failure types discussed in Section 8. Thus, if damage to equipment is desired to be prevented or loss of life due to failure of main crane components, it is required to use a more advanced method like the time-domain approach to include not only boom flip back, but also additional failure criteria such as boom hoist wire, heel point and slewing torque exceedance. Also, allowing the boom stopper to make contact, larger hook loads for small outreaches can be allowed without exceeding the max allowable boom stopper load.

10. POSSIBLE OUTCOMES OF RISK ASSESMENTS

The possible risk impacts identified with the simplified and time-domain approaches can be used as an input in a risk assessment to determine if risk control options are needed. This can be operational actions, like changing the outreach of a lift, performing the lift at different slewing angles or reducing the lifted load. Also, actions in the design of the vessel or crane can be taken to better handle loss of load incidents. For example, the boom stopper and boom structure can be designed to allow for impact loads, reducing the damage in case a load is dropped, or a system could be devised that is keeping the hoist wires more on tension during a dropped load. Important for the design of these systems is to study the dynamic behaviour of the vessel and crane as a multi-body system, where individual bodies dynamically interact during a dropped load incident.

11. CONCLUSIONS

Based on recent dropped load incidents, it has been shown that complying to the current stability criteria for dropped load incidents only is not sufficient to make sure that capital loss, injuries or even possible loss of life will not occur during a dropped load incident. Several major classification societies reacted on past incidents by adding requirements for a risk assessment in their rules. However, limited guidance is given on the contents of this risk assessment, especially regarding crane boom dynamic behaviour. It is strongly advised to also include a note in the IMO IS-code to warn about the dynamic behaviour of both the crane boom and the vessel and that this should be taken into account when assessing dropped load cases.

In this paper both a simplified approach and a time-domain approach, developed by GustoMSC, have been presented to identify and study the consequences when a dropped load incident occurs. The simplified approach can be used as a fast and conservative method to analyse boom flip back, but is not able to study other relevant failure criteria related to the main crane boom dynamics. The time-domain approach is a practical method to reduce some conservatism for boom flip back and to include main crane component failure criteria. This results in a better understanding of the boom and vessel interaction and allows for more safe, reliable and optimized floating crane operations.

REFERENCES

Riviera, 2022, https://www.rivieramm.com/news-content-hub/news-content-hub/saipem-says-wire-broke-and-caused-load-test-incident-in-norway-70713

SWZMARITIME, 2020, https://swzmaritime.nl/news/2020/09/17/installation-vessel-orion-was-whiplash-proof-but-its-crane-was-not/

IMO, 2016, Amendments to part B of the International Code on Intact Stability, 2008 (2008 IS Code), *Res. MSC.415(97)*

IMO, 2008, The International Code on Intact Stability, *Resolution MSC.267(85) – As amended*

YouTube, 2023, https://www.youtube.com/watch?v=d2XTt0eiZZ4

ABS, 2025, Rules for Building and Classing Offshore Units and Structures, *Pt 8, Chapter 4, Sec. 1.9.1*

LR, 2024, Code for Lifting Appliances in a Marine Environment, July, Incorporating Notice No. 1, *LR-CO-001, Ch. 4, Sec. 9*

DNV, 2024, Rules for Classification Ships, *DNV-RU-SHIP, Pt. 5, Ch. 10, Sec. 2.3.3*

BV, 2025, Rules for the Classification of Steel Ships, *NR 467 – January 2025, Pt. E, Ch. 8, Sec. 3*

NX, 2024, Siemens NX version 2406.3, Simcenter 3D motion solver Version 2406 (13.0)

WAMIT, 2024, WAMIT Inc. 1999-2013, *version 7.062 (x64)*

Dynamic stability of helicopters floating in waves

Simon Tödter, *Universität Duisburg-Essen,* simon.toedter@uni-due.de
Jens Neugebauer, *Universität Duisburg-Essen,* jens.neugebauer@uni-due.de
Ould el Moctar, *Universität Duisburg-Essen,* ould.el-moctar@uni-due.de
Thomas E. Schellin, *Universität Duisburg-Essen,* thomas.schellin@uni-due.de

ABSTRACT

Ditching and the subsequent dynamic flotation stability of helicopters is a major safety concern for offshore helicopter operations. Studies have shown that the majority of ditching fatalities are due to helicopter capsizing and drowning of passengers and crew. Model-scale experiments were performed to analyze the roll, pitch, and heave motions of a light multi-purpose helicopter after ditching in a seaway of 6 m significant wave height. For a helicopter equipped with different float sizes, capsize events and their occurrence probabilities were analyzed and compared for two different float volumes. It was found that increasing the float size only had a minor effect on the floatation stability.

Keywords: *Helicopter Dynamic Floating Stability, Capsize Probability, Emergency Flotation Systems, Ditching.*

1. INTRODUCTION

Offshore helicopter operations have been popularized by the oil and gas industry and, later, by offshore wind turbine operations. As wind turbines are sited further from shore, helicopter operations became more demanding in terms of passenger and crew safety. However, an emergency while flying offshore is still a significant risk. Unlike an airplane, a helicopter cannot glide to a safe harbor, but must land immediately. Consequently, a helicopter must be able to safely ditch and remain stable long enough to evacuate passengers and crew.

Although the rapid landing process is quite risky, recent studies have shown that the ditching process itself is not the most dangerous part. The majority of fatalities resulted from the helicopter capsizing and subsequent drowning. Between 1971 till 1992, 338 fatalities resulted from ditching of civil helicopters (Clifford, 1996), and 56.7% of these fatalities were due to drowning. Additionally, 82.6% of all fatalities from ditched military helicopters of the United Kingdom were due to drowning. Downie and Gosling (2020) reviewed accidents of offshore helicopters operating in the United Kingdom. The Civil Aviation Authority (CAA) reported that, between 1976 and 2012, 31 of 38 fatalities in the North Sea between the United Kingdom and Norway were due to drowning (CAA, 2014). Aziz et al. (2023) analyzed ditching accidents listed in the SKYbrary to identify risk factors for ditching. SKYbrary is an electronic repository of global safety knowledge related to aviation (SKYbrary, 2025). They summarized that 60% of ditching fatalities were due to drowning. Furthermore, the Federal Aviation Administration (FAA, 1993), reviewing ditching and effects of water impact of helicopter accidents in the United States between 1982 and 1989, concluded that ten out of twenty post-impact injuries were due to drowning.

Brooks et al. (2008) compared in detail the ditching of helicopters registered in Canada. Of the 46 cases they considered, in at least 21 cases the helicopter capsized and, in 33 cases, the helicopter sank. However, the final floating position of the helicopter was not reported in all cases. All accidents occurred during daylight hours, resulting in a high survival rate of 78%. Taber and McCabe (2007) analyzed 511 helicopter ditching reports. Of the 382 cases that reported the final position of the helicopter, in 85% of the cases the helicopter capsized. They also emphasized that simply attaching external floats does not increase the survival probability if the floats are not appropriate or not properly attached. However, capsizing, inverting, and sinking of the helicopter minimize the survival rate of passengers and crew.

The number of drowning fatalities combined with the large number of capsized helicopters re-

quires an evolution of flotation systems to increase the safety for passengers and crew during offshore helicopter operations (Reader, 1990). Therefore, an analysis of the performance of existing flotation systems is necessary. Taber and McCabe (2007) recommend that traditional floats may not be sufficient to provide an adequate level of safety. However, to date, the design of flotation systems is still based on classic cylindrical designs.

To increase the safety of ditching helicopters, the European Union Aviation Safety Agency (EASA) introduced the certification specifications CS-27 for offshore helicopters (EASA, 2020), which requires the experimental investigation of the dynamic floating stability in a sea state modeled by irregular waves. Until now, only a few studies considered a helicopter's dynamic floating stability. Kidwell and Crago (1970) studied a helicopter floating in regular and irregular waves. The study considered harmonic waves having a height of 4.72 m and varying steepness, and irregular waves having a significant wave height of 3.44 m representing the North Sea at a Beaufort Force 6 wind. They concluded that it is impossible for a twin-float helicopter to capsize in regular, non-breaking waves. Only breaking waves hitting the helicopter in beam seas could cause the helicopter to capsize. Wilson and Tucker (1987), conducting model-scale experiments for sea states 4, 5 and 6, concluded that, although the helicopter is only likely to survive in sea states 5 and 6, it always survives in sea state 4. Delorme et al. (2009) considered irregular waves of sea states 3 and 5 to analyze the functionality of floats attached at the top of a helicopter's fuselage to prevent total inversion after capsizing. Preventing inversions keeps air inside the fuselage, which protects passengers and crew from drowning. Kraskowski (2019) experimentally and numerically studied heave, roll, and pitch motions of a floating helicopter. Additionally, Katsuno et al. (2025) numerically investigated the dynamic floating behavior of a helicopter after ditching. Tödter et al. (2024) experimentally studied the dynamic floating stability of a modern light multi-purpose helicopter with and without opened cabin doors and with and without scoops attached to the floats. They showed that the resulting capsize probabilities were significantly higher than those allowed for by EASA (2020).

In the present study, we first analyzed the flotation behavior of a light multi-purpose helicopter equipped with a state-of-the-art flotation system. Then, we compared the effect of an increased float volume on the helicopter's dynamic floating behavior and its resistance against capsizing.

2. EXPERIMENAL SETUP

The experiments were performed at a scale of $\lambda = 12$. In the following, the helicopter's properties as well as our results refer to full-scale.

Helicopter design and properties

The helicopter under study belongs to a 3-ton class of light multi-purpose helicopters. We considered its heaviest mass configuration of about 3000 kg. The helicopter model comprised a fuselage (1) with removable doors (2), a simplified tail boom (3) showing the position of the fenestron (4), and a landing gear system (5) having cylindrical front (6) and rear floats (7) that can be exchanged in a modular fashion. The positions of all components are presented in Figure 1. The helicopter was not moored during the experiments, allowing unrestricted six degrees-of-freedom motions.

Figure 1 shows a schematic side, top, and front view of the helicopter, indicating the main particulars and the origin and orientation of the body-fixed coordinate system. Here, the X-axis points backwards, the Y-axis points to starboard, and the Z-axis points upwards. Consequently, pitch angles are positive if the helicopter nose moves upwards, roll angles are positive if the helicopter portside moves upwards, and yaw angles are positive if the helicopter nose turns to starboard. The helicopter was equipped with a state-of-the-art cylindrical float system, herewith referred to as float design 1. Table 1 lists the helicopter's main particulars as well as the positions of the helicopter's center of gravity (CoG) X_{CoG}, Y_{CoG}, and Z_{CoG}, its moments of inertia I_{XX}, I_{YY}, and I_{ZZ} about the X, Y and Z axes, respectively, and the maximum draft of the helicopter D_{max} normalized against length L, width B, height H_H, and mass m.

We considered one additional float design. Design 2 consisted of larger cylindrical floats having the total volume increased to 188.1% of the volume of float design 1. Due to the increased size and weight of the floats, the helicopter's moment of

inertia I_{XX} increased by about 22.8% for the design 2. The variation of I_{YY} and I_{ZZ} was not monitored.

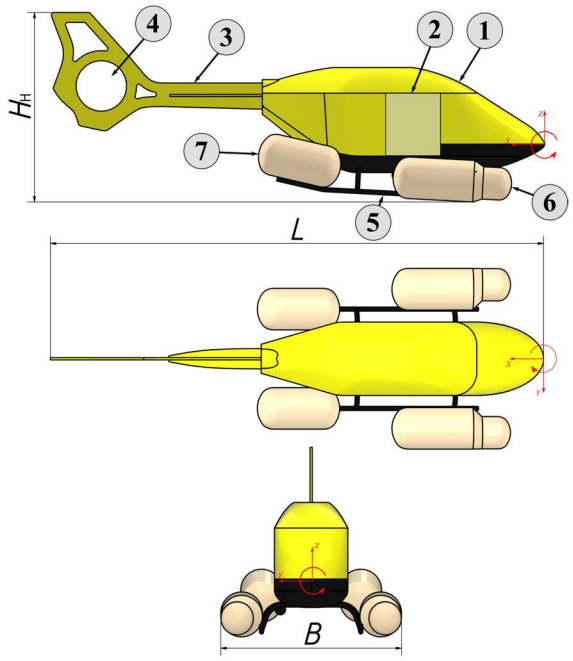

Figure 1: Schematic presentation of the helicopter equipped with state-of-the-art floats (design 1) showing the model-fixed coordinate system with its origin.

Table 1: Normalized particulars of the helicopter equipped with state-of-the-art floats (design 1).

L/B	2.794
L/H_H	2.480
D_{max}/H_H	0.163
X_{CoG}/L	0.326
Y_{CoG}/B	0.020
Z_{CoG}/H_H	0.130
$I_{XX}/(mBH_H)$	0.048
$I_{YY}/(mLH_H)$	0.063
$I_{ZZ}/(mLB)$	0.086

Figure 2 presents comparable top, side, and front views of the helicopter equipped with float designs 1 and 2. Table 2 lists the associated percentage differences of helicopter mass, position of CoG, longitudinal moment of inertia, and float volume between those for the helicopter equipped with the state-of-the-art float design 1 and the lager floats of design 2. A relatively greater difference turned out to be the Y-position of the CoG for the helicopter equipped with float design 2. However, the magnitude of this Y-position was small, so that the absolute deviation was less than 0.02 m.

Figure 3 shows the floating position of the helicopter equipped with the two float designs. For design 1 the trim angle was 8.5 deg, while it was reduced to 7.6 deg for design 2. The heel was 1.8 and 2.4 deg for designs 1 and 2, respectively. The normalised maximum draught D_{max}/H_H was reduced to 0.136 for design 2.

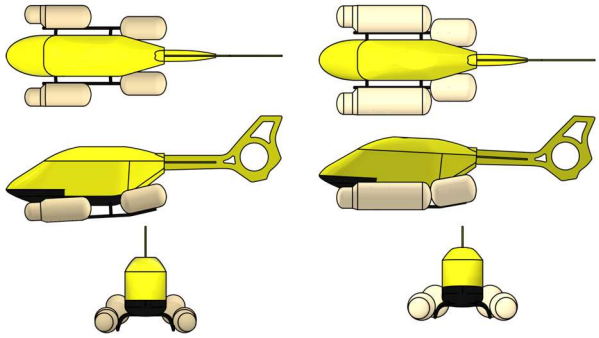

Figure 2: Top, side, and front views of the helicopter equipped with float designs 1 (left) and 2 (right).

Table 2: Percentage variation of helicopter mass, position of CoG, longitudinal moment of inertia, and float volume between float designs 1 and 2.

	Design 2
Mass m	2.8%
CoG X	1.4%
CoG Y	-19.6%
CoG Z	-2.2%
Inertia I_{XX}	22.8%
Float volume V	88.1%

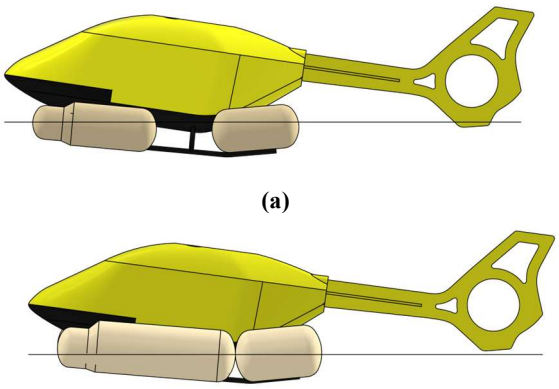

(a)

(b)

Figure 3: Floating position of the helicopter equipped with floats of design 1 (a) and design 2 (b).

The helicopter was equipped with a small inertia measurement unit (IMU), type Lord 3DM-GX5-25, to monitor translational accelerations in X-, Y-, and Z-direction and roll, pitch, and yaw angles at a sampling rate of 100 Hz. The recorded data was transmitted wirelessly to prevent model motions from being influenced by cables. For float design 1, the distances between the helicopter's CoG and the IMU's measurement point were $0.062L$, $-0.020B$, and $0.100H_H$, respectively.

Wave Basin

The tests were conducted in the deep-water towing tank of the Technical University of Berlin.

The basin had a length of 250 m, a width of 8.1 m, and a water depth of 4.3 m. Consequently, all tests were performed under deep-water condition. One end of the basin was equipped with a flap-type wave generator actively damping reflected waves. At the far end of the basin, beaches were placed to reduce wave reflections.

Wave modeling

The seaway was modeled as a long-crested JONSWAP spectrum with a significant wave height $H_S = 6$ m, a zero-crossing wave period $T_Z = 7.9$ s corresponding to a peak period $T_P = 10.2$ s, and an overshoot factor $\gamma = 3.3$ as expressed by Equations 1 to 4, where ω is the circular frequency between 0.31 and 2.09 rad/s corresponding to a period of 20 and 3 s, respectively, and ω_P is the circular frequency at the spectrum's peak. This condition, representing the North-Atlantic climate, has been identified as the most severe condition for helicopter operations (EASA, 2020). Using a JONSWAP spectrum having the mentioned parameters is prescribed by EASA's certification specification CS-27 (EASA, 2020):

$$S(\omega) = \frac{5}{16}\omega_P^4 H_S^2 \omega^{-5} \cdot \exp\left(-\frac{5}{4}\left(\frac{\omega_P}{\omega}\right)^4\right)\gamma^r \cdot \alpha_\gamma \quad (1)$$

$$r = \exp\left(-0.5\left(\frac{\omega - \omega_P}{\sigma\omega_P}\right)^2\right) \quad (2)$$

$$\sigma = \begin{cases} 0.07 \text{ for } \omega \leq \omega_P \\ 0.09 \text{ for } \omega > \omega_P \end{cases} \quad (3)$$

$$\alpha_\gamma = (1 - 0.287 \cdot \ln(\gamma)) \quad (4)$$

Analog wave gauges were placed in front of the test section to record free-surface elevations. Figure 4 compares the experimentally measured and computed sea spectra obtained over a 541 min long test duration combining multiple experiments.

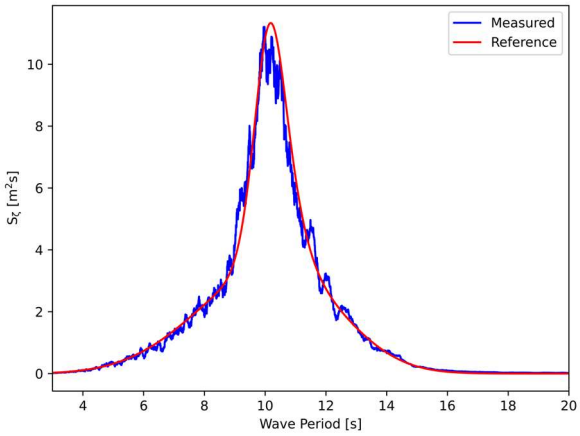

Figure 4: Comparison of measured and computed sea spectra.

Test procedure

Assessing the capsize probability was required to quantify the helicopter's dynamic floating stability. This was done according to EASA's specification CS-27 (EASA, 2020), defining the method to assess a small helicopter's dynamic flotation stability. The capsize probability P_{capsize} was calculated from the number of capsizing events N_{capsize}, the test duration T_{test}, and the test criterion $T_{\text{criterion}} = 5$ min, which considers the assumed time to evacuate a helicopter after ditching. The required test duration $T_{\text{test,req}}$ resulted from the maximum allowed capsize probability $P_{\text{capsize,max}} = 3\%$ and the associated confidence interval $C = 95\%$:

$$P_{\text{capsize}} = \frac{N_{\text{capsize}} \cdot T_{\text{criterion}}}{T_{\text{test}}} \quad (5)$$

$$T_{\text{Test,req}} = -\frac{T_{\text{criterion}} \cdot \ln(1 - C)}{P_{\text{capsize,max}}} \quad (6)$$

The resulting test duration was 499 min. It is noted here that the Interim Guidelines on the Second Generation Intact Stability Criteria (IMO, 2020) contain provisions for the assessment of failure rates in case of ships. The corresponding methodologies could be conceptually relevant also for the case under study. However, they have not been considered at the current stage.

For the present study, the test duration run time was subdivided into multiple shorter test runs of varying randomly selected phase angles for wave generation. At the beginning of each test run, the helicopter was manually aligned at a yaw angle of 0 deg, which corresponded to head wave conditions.

3. RESULTS

Floating behavior

Figure 5 presents comparative time histories of the dynamic flotation behavior of the helicopter in irregular waves. The helicopter, here equipped with float design 1, started to float at a yaw angle of around 0 deg, which corresponded to head wave conditions. As a result, the helicopter started to pitch in approaching waves. As time progressed, the helicopter began yawing about a 90 deg angle. From then on, the helicopter floated in beam waves, which reduced its pitch motions, but increased its roll motions. These time histories characterized the typical dynamic motion behavior of the helicopter after ditching, demonstrating that the roll motions were most important when evaluating the helicopter's floating stability.

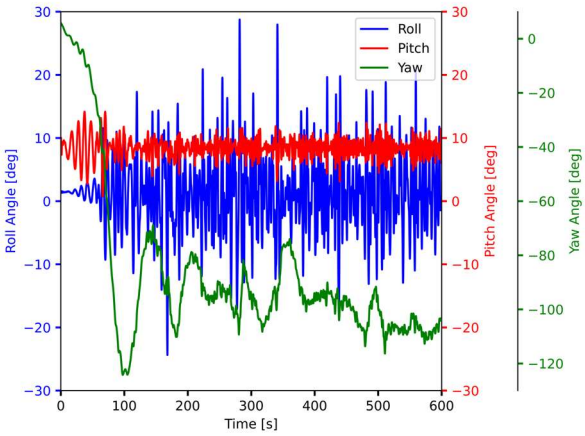

Figure 5: Time histories of roll, pitch and yaw motions for the helicopter equipped with float design 1.

To compare the motions of the helicopter equipped with the two different float designs, short-term statistics were generated considering the exceedance rate r_{ex}. The exceedance rate of amplitude a was determined using the number of larger amplitudes $n_{>a}$ and the test duration T_{test} as shown in Equation 7:

$$r_{ex}(a) = n_{>a} \cdot T_{\text{test}}^{-1} \tag{7}$$

Figure 6 plots the associated comparative exceedance rates of roll, pitch, and heave versus their amplitudes for the helicopter equipped with float design 1, obtained over a 499 min long test duration. The maximum roll angle turned out to be 33.5 deg; the maximum pitch angle, 23.5 deg; and the maximum heave amplitude, 5.54 m. As seen, for heave and roll amplitudes, the corresponding exceedance rates decreased steadily with increasing motion amplitudes.

For pitch motions, however, amplitudes declined faster in the range of exceedance rates between 7.8 and 11.6 deg. This was due to the helicopter changing its heading, starting from a 0 deg and turning to a 90 deg yaw angle. Consequently, the encountered number of high pitch amplitudes was fewer compared to the higher number of encountered low pitch amplitudes. This behavior was strongly influenced by the initial yaw angle of the helicopter at the beginning of an experimental run. Starting the experiments at the initial yaw angle of 90 deg would have avoided large pitch amplitudes, thereby allowing focusing on roll motions.

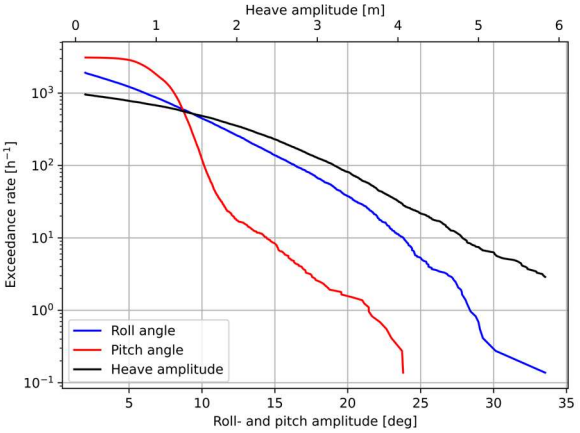

Figure 6: Roll, pitch and heave amplitude exceedance rates for the helicopter equipped with float design 1.

Figure 7 plots the comparative exceedance rate of roll motions versus the roll amplitude for the helicopter equipped with float designs 1 and 2. Here, only test runs were considered having the same waves, which reduced the full-scale average test duration to 380.2 minutes. To assess the most likely maximum roll amplitude within the assumed evacuation period of five minutes ($T_{\text{criterion}}$), the roll amplitude at an exceedance rate of 12 h^{-1} = 5 min^{-1} was evaluated. Here, the roll amplitudes, listed in Table 3, were 23.04 and 22.31 deg for the helicopter equipped with float designs 1 and 2, respectively. The exceedance probability of roll amplitudes obtained at an exceedance rate of 12 h^{-1} was between 0.62 and 0.75% (Table 4).

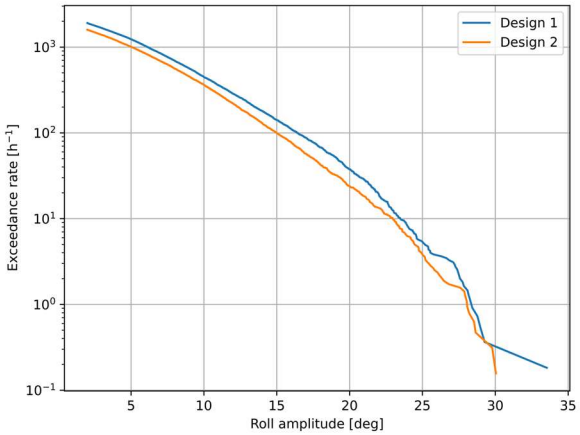

Figure 7: Comparative roll amplitude exceedance rates for the helicopter equipped with float designs 1 and 2.

Therefore, higher roll angles were unlikely to occur, and the roll angles at 12 h^{-1} exceedance rate were suitable to properly design the helicopter's flotation system for dynamic floating stability. However, the maximum measured roll amplitudes of 33.54 and 30.04 deg for designs 1 and 2, respectively, were significantly higher than roll amplitudes at an exceedance rate of 12 h^{-1}. In comparison to the median roll amplitudes of 6.37 and 6.28 deg, this indicated that large roll amplitudes and, consequently, capsizing were rare events, which had to be considered separately.

Table 3: Median and maximum roll amplitudes, and roll amplitudes at an exceedance rate of 12 h^{-1} for the helicopter equipped with float designs 1 and 2.

	Design 1	Design 2
Median	6.37 deg	6.28 deg
At 12 h^{-1}	23.04 deg	22.31 deg
Maximum	33.54 deg	30.04 deg

Table 4: Roll angle exceedance probabilities at an exceedance rate of 12 h^{-1}.

Design 1	Design 2
0.62%	0.75%

Capsize events

From observation of the experimental results, two conditions had to be met for capsizing to occur. The first condition required that the helicopter must remain floating in beam waves (Kidwell and Crago, 1970; Tödter et al., 2024). Figure 8 shows the evolution of pre-capsize yaw angles for thirteen capsize events. The helicopter always floated in approaching beam seas with an encounter angle between 70 and 120 deg. Note that the helicopter needed some time before reaching a yaw angle of about 90 deg. This time decreased at larger initial yaw angles or when the helicopter initially yawed. For the analyzed thirteen capsize cases, the time for the helicopter to reach a yaw angle magnitude of more than 70 deg ranged from 0.7 to 3.6 min. In one case the helicopter took 8.0 min to turn about 70 deg.

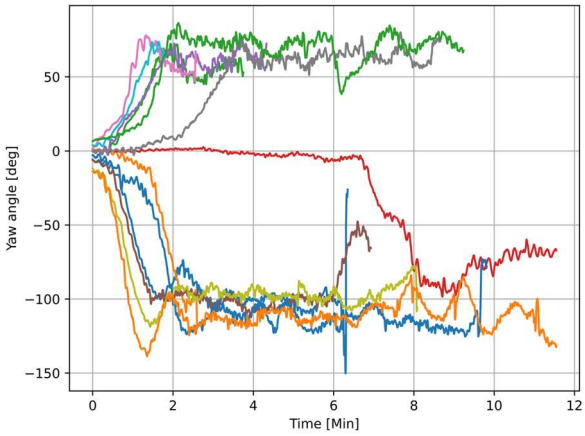

Figure 8: Time histories of yaw angle for thirteen capsize events for the helicopter equipped float design 1.

Assuming that five minutes are required to evacuate the helicopter after ditching, this showed the importance of the helicopter's heading during ditching. If the helicopter's initial wave encounter angle was close to 0 deg and the yaw rate was small enough, it retained its heading for a longer evacuating time, thereby decreasing the risk of capsizing. However, this situation was only valid for ditching in long-crested seas. Short-crested seas might have reduced the turning time due to larger initial encounter angles, even for the helicopter ditching in head waves.

Due to the different yaw direction and time variation to reach beam sea conditions, experimental results may have scattered and the repeatability was reduced. There are different approaches to tackle this problem. One method would have been to fix the model until the first waves approached the helicopter. However, releasing the model too early or too late might have falsified the test results.

The second possibility was to apply a light and soft mooring. The mooring system must have been capable to allow roll, pitch, yaw, and heave motions. Additionally, it must have been strong enough to ensure a constant yaw angle before waves approached, but it had to be light enough to not influence the model's behavior. For a model weight of less than 2 kg this could have been

critical. However, mooring would have always changed the outcome of the tests. Due to the suppression of drift, other waves would have hit the helicopter, yielding another capsize probability. The outcome considering a moored and non-moored model was the same only if the helicopter did not capsize at all.

The third approach was to start each test with a yaw angle of 90 deg. Such tests would have had to be highly repeatable, and yaw motions during a test would have been minimized. However, this method would have neglected the turning duration, which may have yielded an over predicted capsize probability.

The second mandatory condition to be met was that of a breaking wave hitting the helicopter. Therefore, the total stability failure was then triggered by the external force on the helicopter due to the wave impact. Figure 9 shows the evolution of water surface's vertical velocity $v_{\zeta H}$, indicating the wave steepness for different capsize events at $t = 0$ s. As seen, the free surface elevation changed quickly, indicating that waves became steep and generated breaking waves that hit the helicopter and initiated the capsize event. These breaking waves occurred when the water surface's vertical velocity exceeded 1 m/s. In the figure there is a time shift between the onset of high wave steepness and the moment of capsizing. This was caused by the changing distance between helicopter model's motion and the wave probes.

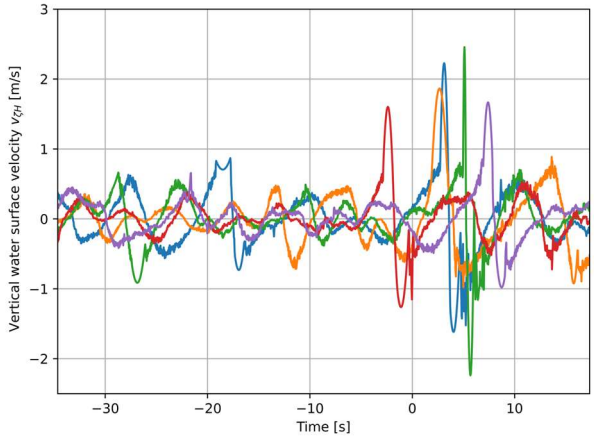

Figure 9: Time histories of the water surface's vertical velocity $v_{\zeta H}$.

As a result of a breaking wave hitting the helicopter floating in beam seas, capsizing occurred about its *X*-axis. Figure 10 shows the evolution of the roll angle for the helicopter equipped with float design 1. We defined capsizing when the helicopter exceeded a roll angle of 70 deg. However, the helicopter did not return to the upright position when exceeding roll angles of 35 deg. Most of the time, the roll angle amplitude was less than 28.4 deg. When a breaking wave hit the helicopter, the roll angle increased rapidly, and the helicopter capsized.

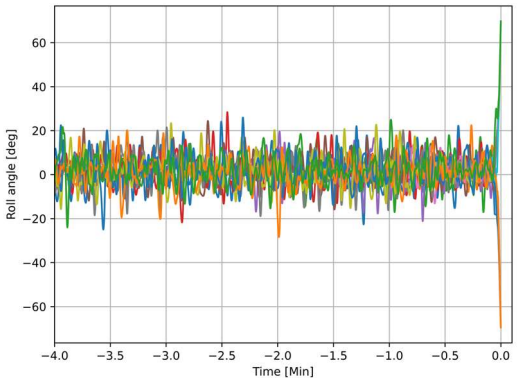

Figure 10: Time histories of roll angle obtained from thirteen capsize events of the helicopter equipped with float design 1, where $t = 0$ s designates the moment of capsizing.

Depending on the float volume, the helicopter showed a minor change of resistance to capsizing. When equipped with state-of-the-art floats (design 1), the capsize probability evaluated according to equation 5 turned out to be 11.6%. When equipped with float design 2, which was a scaled-up version of float design 1 with an increased volume of 188.1% compared to the original volume, the capsize probability was slightly reduced to 9.7%. Thus, simply increasing the size of floats did not increase the level of safety significantly. Table 5 summarizes the evaluated capsize probabilities.

Table 5: Capsize probability of the helicopter equipped with the float designs 1 and 2.

	Design 1	Design 2
Capsize probability	11.6%	9.7%

4. SUMMARY

The present study analyzed the dynamic floating behavior and the associated capsize probability of a helicopter after ditching in a seaway having a significant wave height of 6 m. The floating helicopter always tended to yaw about the 90 deg wave encounter angle, i.e., when floating in beam waves, and this demonstrated that roll motions were dominant from a safety point of

view. Here, roll amplitudes up to 33.5 deg were evaluated.

Capsizing of the helicopter occurred only when a breaking wave hit the helicopter while floating in beam waves. Therefore, the total stability failure was triggered by the external force on the helicopter due to the wave impacts. The different float volumes demonstrated that cylindrical floats did not provide a high level of safety against wave impact induced capsizing. Also, increasing the float volume did not significantly modify the resistance against capsizing.

5. ACKNOWLEDGEMENTS

This study was part of the research project EvoS-BraWa, funded by the Bavarian Ministry of Economic Affairs and the Regional Development and Energy (StMWi) of the Bavarian Aviation Research Program (BayLu25), under grant ROB-2-3410.20-04-10-36 / BLU-2109-0036.

REFERENCES

Aziz, A., Amir, M.A.U., Roshamida, A.J., Samsudheen, I., Sariff, E.S.M., Rahman, A., Rosly, A., 2023, “Helicopter ditching incident analysis: Classification of risk factors”, Journal of Engineering Science and Technology 18(1), pp.113-122.

Brooks, C.J., MacDonald, C.V., Donati, L., Taber, M.J., 2008, “Civilian Helicopter Accidents into Water: Analysis of 46 Cases, 1979-2006”, Aviation, Space, and Environmental Medicine 79(10), pp. 935-940.

Civil Aviation Authority, 2014, “Safety Review of Public Sector Transport Helicopter in Support of the exploitation of oil and gas”, CAP 1145, https://www.caa.co.uk/publication/download/14777.

Clifford, W.S., 1996, “Helicopter crashworthiness. Study I. A review of UK military and world civil helicopter water impacts over the period 1971-1992”, CAA Paper 96005, https://www.caa.co.uk/Documents/Download/10717/45efcfb9-b756-432e-b542-337c52ef0f2d/87.

Delorme, L., Denante, M., Santucci, P., De Gelas, A., 2009, “New floatation devices to avoid helicopters’ total inversion after capsize”, Proceedings of the 10th International Conference on Stability of Ships and Ocean Vehicles, St. Petersburg, Russia.

Downie, M., Gosling, D., 2020, “Offshore helicopter travel: is the UK oil and gas industry failing offshore workers?”, New solutions: a journal of environmental and occupational health policy 29(4), pp. 504-518.

European Union Aviation Safety Agency, 2020, “Certification Specifications and Acceptable Means of Compliance for Small Rotorcraft”, Certification specification CS-27, Amendment 9, Technical Report.

Federal Aviation Administration, 1993, “Rotorcraft ditchings and water-related impacts that occurred from 1982 to 1989 – Phase II”, DOT/FAA//CT-92/14.

International Maritime Organization, 2020, “Interim Guidelines on the Second Generation Intact Stability Criteria, MSC.1/Circ.1627 Annex.

Katsuno, E.T., Peters, A., el Moctar, O., 2025, "Numerical Seakeeping Analysis for a Floating Helicopter after Ditching in Waters", Journal of Offshore Mechanics and Arctic Engineering 147(1), pp. 011401

Kidwell, J.C., Crago, W.A., 1970, “Model testing to establish ditching and flotation stability characteristics of a helicopter”, Proceedings of the 26th Annual National Forum of the American Helicopter Society, Washington D.C., United States of America.

Kraskowski, M., 2019, “Numerical and experimental analysis of the helicopters’ flotation system”, Proceedings of the 45th European Rotorcraft Forum, Warsaw, Poland.

Reader, D.C., 1990, “Helicopter Ditchings - British Military Experience 1972-1988”, RAF IAM Report No 677.

SKYbrary Aviation Safety. 3 Apr. 2025, www.skybrary.aero.

Taber, M.J., McCabe, J., 2007, “An examination of survival rates based on external flotation devices: A helicopter ditching review from 1971 to 2005”, SAFE Journal 35(1), pp. 1-6.

Tödter, S., Neugebauer, J., el Moctar, O., Harms, S., Schellin, T.E., 2024, “Experimental Investigation of the Flotation Stability of a Helicopter After Ditching”, Proceedings of the 50th European Rotorcraft Forum, Marseille, France.

Wilson, F.T., Tucker, R.C.S., 1987, “Ditching and Flotation Characteristics of the EH101 helicopter”, Proceedings of the 13th European Rotorcraft Forum, Arles, France.

Damage stability assessment of large inland passenger ships using time-domain flooding simulations

Milica Vidić,
Grupo Integrado de Ingeniería, CITENI, Campus Industrial, Universidade da Coruña,
milica.vidic@udc.es
Nathalie Reinach,
Development Centre for Ship Technology and Transport Systems (DST e. V.),
reinach@dst-org.de
Igor Bačkalov,
Development Centre for Ship Technology and Transport Systems (DST e. V.),
backalov@dst-org.de
Marcos Míguez González,
Grupo Integrado de Ingeniería, CITENI, Campus Industrial, Universidade da Coruña,
marcos.miguez@udc.es

ABSTRACT

The paper presents the outcomes of a series of time-domain flooding simulations performed on a state-of-the-art Western European large inland passenger ship (LIPS). The simulations were carried out for several damage cases corresponding to the requirements of the existing damage stability regulations applicable to this vessel type. The results show that the spaces occupied by passengers and crew, following the damage, may be flooded within a rather short time which would be insufficient to conduct the evacuation. This cannot be inferred from the damage stability calculations required by the rules which indicate that the ship may be regarded as safe in the same damage cases. Therefore, it appears that the current regulatory framework for LIPS, based on traditional concepts of passenger ship damage stability, may not provide for sufficient safety in case of flooding.

Keywords: *Large inland passenger ships, River cruiser, Damage stability, Time-domain flooding simulations.*

1. INTRODUCTION

Safety and survivability of seagoing passenger ships have been central concerns for ship designers, ship owners, researchers, and regulators throughout modern times. In contrast to seagoing vessels, inland vessels have been receiving limited attention from the global ship safety community, partly due to the fact that these vessels are within the scope of different regional and national bodies. As such, unlike the SOLAS regulations, rules and regulations for different types of inland vessels are not harmonized and often feature outdated concepts. Previous research on damage stability regulations for large inland passenger ships (LIPS) (Vidić and Bačkalov, 2022) also indicates a lack of clarity regarding the safety level provided by these rules, which most often follow a deterministic approach and analyze the floating position and *GZ*-curve characteristics of a ship in a set of prescribed damage cases. Despite its deficiencies, this approach does provide some insight into ship survivability in terms of maintaining buoyancy and sufficient reserve stability, but a crucial aspect of passenger ship survivability – human safety – remains unclear, as it can only be inferred indirectly from the vessel's condition.

In ensuring sufficient overall safety of the ship, there is a growing emphasis on adopting a holistic approach that integrates passive measures implemented during the design phase, with operational measures, ensuring their complementarity (Bačkalov et al., 2016). Moreover, current research highlights the need to align survivability assessment more closely with physical reality by transitioning towards direct numerical analyses (Mauro et al.,

2023). Time-domain flooding simulations, in particular, are a powerful tool for capturing the dynamics and progression of flooding, which can inform potential improvements to regulations and, consequently, enhance the safety-by-design of vessels. Additionally, such simulations can indicate the time available for orderly evacuation and abandonment (Ruponen et al., 2019), thereby facilitating the assessment of onboard survivability and aiding the selection and implementation of appropriate operational measures (see also Jasionowski and Vassalos, 2006; Bulian, 2008; Spanos and Papanikolaou 2014; Mauro and Vassalos, 2024).

In this preliminary study, the flooding process of a contemporary LIPS was analyzed in various side and bottom damage scenarios using the time-domain flooding simulation tool of NAPA that was initially developed by Ruponen (2007). The damage scenarios were selected to align with several representative damage cases required to be analyzed by the current regulations applicable to the sample ship. In doing so, the outcomes of the regulatory procedure are put in perspective by calculating the available time for evacuation and assessing the consequences of flooding in terms of the potential loss of life.

2. SAMPLE SHIP

The sample ship, shown in Fig. 1, is a large inland passenger ship and a typical representative of the Western European river cruise ship design. It is intended for cruises on the Rhine and Danube rivers and can accommodate up to 180 passengers and 40 crew members.

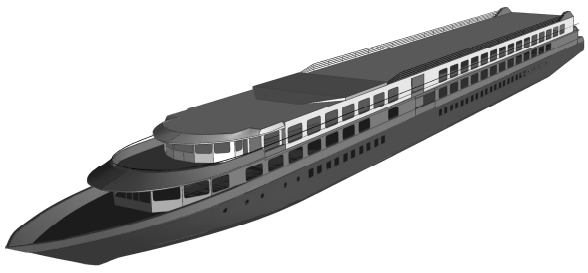

Figure 1: Sample ship

The ship complies with the European Standard laying down Technical Requirements for Inland Navigation vessels (ES-TRIN; see CESNI, 2025), which is the currently applicable standard for ships operating on the inland waterways of the European Union (EU). An additional assessment of the ship's intact and damage stability according to other rules and regulations for LIPS can be found in Bačkalov and Vidić (2020) and Vidić and Bačkalov (2022). The main particulars of the sample ship are given in Table 1.

Table 1: Main particulars of the sample ship

Length overall	109.9 m
Length at waterline	105 m
Beam at the bulkhead deck	10.8 m
Depth to bulkhead deck	3.3 m
Design draught	1.65 m
Displacement	1607 t
GM in design condition	4.01 m
Trim in design condition (positive by bow)	0.289 m

The watertight subdivision of the sample ship is shown in Fig. 2. The subdivision of the ship includes 12 main watertight bulkheads which extend up to the bulkhead deck and divide the ship into compartments whose length varies between 5 and 15 m. The ship has a double bottom which is 1 m high except in the 2-meter-wide section along the centerline where its height is reduced to 0.5 m. The double bottom extends from 3 to 97.5 m from the aftmost section of the ship and is stepped in the way of the engine room which is positioned aft. The collision bulkhead is located 105 m from the aftmost section.

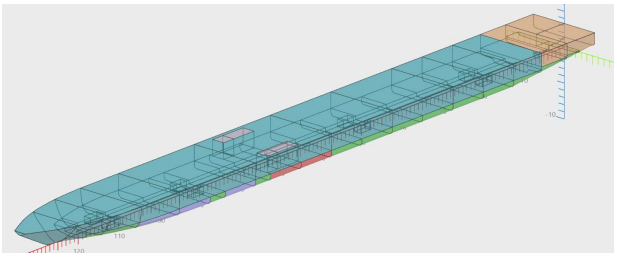

Figure 2: Main subdivision of the sample ship

The compartments below the bulkhead deck house the passenger and crew cabins, kitchen, storage areas, and entertainment rooms, all aligned on both sides of a central, 1.2-meter-wide corridor. Within the double bottom, there are large ballast, fuel oil, and freshwater tanks, along with several smaller sludge tanks. The ship also includes two upper decks featuring more passenger cabins, restaurants and lounges, and a sun deck. The average area of the cabins below the bulkhead deck is 14 m^2.

3. METHODOLOGY

The goal of this study was to make a preliminary assessment of the time-to-flood in some of the most critical cases that stood out from the results of the application of the ES-TRIN standard. Therefore, a limited number of most relevant damage scenarios

was selected for analysis, and several simplifications were introduced in the calculations.

Damage scenarios

As a first step, a complete set of all damage cases for the sample ship was generated according to the procedure described in ES-TRIN. This standard requires the verification of compliance with one- and two-compartment status, in several loading conditions, in final and intermediate stages of flooding, which occurred due to bottom and side damages (see Chapter 19, Article 19.03.9. in CESNI, 2025). Based on the damage extents provided in ES-TRIN, which are shown in Table 2, 63 damage cases were created including 26 damage cases associated with damages of lesser extent. The main set of damage cases was created simply by applying the damage extents according to the definitions for the one- and two-compartment status, where:

- for the one-compartment status the bulkheads can be assumed to be intact if the distance between two adjacent bulkheads is greater than the damage length, and
- for the two-compartment status each bulkhead within the extent of damage is to be assumed to be damaged.

Since the standard requires for any smaller damages to be taken into account if they produce more detrimental effects with respect to heeling or metacentric height, an additional set of damage cases associated with side damages of lesser extent was created, where only the compartments above the double bottom were damaged while the double bottom stayed intact.

In order to select the damage cases for time-domain simulations, damage stability calculations were performed for each damage case in the design loading condition that assumes the ship at the start of the voyage, with full supplies and 100% of passengers and crew, taking into account the moment due to one-sided accumulation of persons.

The damage cases were then ranked based on the following parameters in the final stage of flooding:

- Static equilibrium angle[1]
- Down-flooding angle
- Value of the remaining righting lever
- Area between the righting arm curve and the passenger heeling arm
- Remaining freeboard and distance of non-watertight openings from the waterline
- Combined heel and trim angle

After the ranking, five of the most critical damage cases (four side damage cases, and one bottom damage case) were chosen for the flooding simulations in such a way that they cover different locations along the ship's length.

When it comes to the breach shape and size selection, the side damages with the extents foreseen by ES-TRIN would lead to a trivial result of almost instantaneous flooding. On the other hand, in the absence of methodical records of accidents of inland vessels (see Bačkalov et al., 2023), the selection of any other opening shape and size proves to be a challenging task and the only guidelines available when choosing these parameters are the ones present in the current rules and regulations. Therefore, although the damage extents given in Table 2 were used as a starting point, some modifications were introduced.

Box-shaped penetration was assumed, and breaches of various sizes were defined to create examples of different damage scenarios, but in such a way that they lead to the flooding of the same watertight compartments as in the previously selected damage cases. The transverse dimension of the damage openings was retained as specified in the ES-TRIN regulations for all damage cases considered. The choice of the damage length and vertical extent of side damages was informed in part by an analysis of the dimensions of the bows of several inland vessels, representatives of different classes of European inland ships, that may be expected to be involved in a potential collision with a European LIPS. Based on the bow cross-sections of these vessels at the x-coordinate that corresponds to the value of the adopted damage penetration (the transverse dimension), the damage opening lengths were chosen to be between 1 and 6 m. Regarding the vertical dimension of the side damage cases, it was determined, again based on the bow cross-sections, that the damage would start vertically from a level that is approximately at the middle of the height of the double bottom of the sample ship.

[1] Refers to the heeling angle in the final stage of flooding taking into account the moment due to one-sided accumulation of persons M_p, according to the definition in Chapter 19 of the ES-TRIN standard (see CESNI, 2025).

Table 2: Damage extents which define damage cases according to ES-TRIN

Damage	Longitudinal	Transverse	Vertical
Side, one-compartment	$\max\{0.1L_{WL}; 4\}$ = 10.5 m	B/5 = 2.16 m	from vessel bottom to top without delimitations
Side, two-compartment	$\max\{0.05L_{WL}; 2.25\}$ = 5.25 m	0.59 m	from vessel bottom to top without delimitations
Bottom, one-compartment	$\max\{0.1L_{WL}; 4\}$ = 10.5 m	B/5 = 2.16 m	0.59 m
Bottom, two-compartment	$\max\{0.05L_{WL}; 2.25\}$ = 5.25 m	B/5 = 2.16 m	0.59 m

The tops of the damage openings were selected in such a way that they represent both scenarios where the damage is fully below the initial draught, and above it, but in no case higher than 2 m (the level of maximum draught achieved in the final stage of flooding in any of the cases).

In the case of bottom damages, in the absence of any other data that can be used to assess this value, the damage penetration (the vertical dimension) was kept at 0.59 m, as it is defined in the ES-TRIN rules (see Table 2), and the damage length was arbitrarily chosen to be 1 m.

The final damage locations and dimensions for each of the damage cases are given in Table 3, with the breaches and the subdivision in the area of the breach shown in Figure A1 in the Appendix I.

Table 3: Breach location, surface and dimensions

Damage case	X_{start} [m]	X_{end} [m]	Z_{min} [m]	Z_{max} [m]	Breach area [m^2]
Side-1	21.5	22.5	0.5	2.0	1.5
Side-2	27.5	28.5	0.5	2.0	1.5
Side-3	61.5	67.5	0.5	1.5	6.0
Side-4	81.5	82.5	0.5	2.0	1.5
Damage case	**X_{start} [m]**	**X_{end} [m]**	**Y_{min} [m]**	**Y_{max} [m]**	**Breach area [m^2]**
Bottom-1	89	90	-1.13	1.13	2.2

Calculation parameters

The time-domain flooding simulation tool of NAPA that was used in the study is a fast tool that employs a simple quasi-static approach for the evaluation of ship motions, with an additional option to include the dynamic roll motion calculations. The quasi-static approach alone is mainly suitable for the analysis of the progressive phase of the flooding process, as it does not account for the dynamic effects that are dominant in the transient flooding phase. For the same reason, the use of this model is only justified in calm water or in sufficiently small waves such that the wave-induced motions do not significantly affect the progressive phase of flooding (see Ruponen, 2007).

NAPA's flooding simulation tool utilizes a hydraulic model for the calculation of the flow rates, and a pressure-correction algorithm to solve the governing equations (continuity and Bernoulli). It was previously used and described in a number of studies addressing, among other things, the survivability of damaged passenger ships and decision support systems in flooding emergencies (see e.g. Ruponen et al., 2015; Ruponen et al., 2019; Ruponen and Lindroth, 2016). Recently, the tool was also tested in an international benchmark study of numerical flooding simulation codes (Ruponen et al., 2022).

For the present study, considering its main goal and the limited wave heights on inland waterways it was concluded that the use of a quasi-static approach may be acceptable in this stage for the flooding calculations of LIPS. In the presented simulations, a fully quasi-static approach is used, without the inclusion of the dynamic roll motions calculations.

Accurate modelling of internal subdivision of the ship is another factor that plays a significant role in time-domain flooding simulations, especially in the case of cruise ships, whose internal subdivision is complex and dense. Apart from the main watertight compartments, proper representation of non-watertight bulkheads and doors is an important issue, as these structures may significantly affect the flooding progression (Ruponen et al., 2017). Jalonen et al. (2017) also showed that there is a significant difference between different types of non-watertight structures in terms of leakage and pressure heads. In the present study, all non-watertight bulkheads and doors were modelled. However, since the exact type for each door and non-watertight bulkhead was not known, a major simplification was introduced where the room walls were modelled as watertight, while the room doors were all considered to be open.

The watertight doors were considered to be closed. Other smaller internal openings between adjacent rooms were neglected. All watertight compartments were considered to be fully vented, and the openings in the deck that include a number of pipes and hatches were modelled according to their type and surface area. The hull breaches were modelled as openings with a commonly used value of 0.6 for the discharge coefficient (the so-called industry standard value (Ruponen et al., 2022)). Regarding the permeabilities of different spaces, in the absence of more accurate information, the values provided in ES-TRIN were used.

All flooding simulations were performed for the ship at the design draught (in line with Paterson et al., 2018) and with the tanks filled according to the corresponding loading condition at the start of the voyage. Each damage case was simulated with and without the passenger crowding moment, which is included in the damage stability assessment within the ES-TRIN regulations and calculated as:

$$M_p = g \cdot P \cdot y \text{ [kNm]}, \quad (1)$$

where P is the total mass of persons on board, assuming an average mass per person of 0.075 t, y is the lateral distance of the center of gravity of P from the center line, and g is the gravitational acceleration.

Due to the relatively short flooding time, a constant time step of 0.1 s was used in all simulations.

4. RESULTS

The results of the flooding simulations are shown in Table A1 in the Appendix II. Each damage case was simulated twice – once without any external moments, and once with the heeling moment caused by the accumulation of persons on one side. The simulations that included the heeling moment started from the equilibrium angle resulting from the action of the moment, and the simulations without the heeling moment started from the upright equilibrium condition. Alongside the total time-to-flood, the approximate time that is needed to flood accommodation spaces in the damaged watertight compartments is shown. The difference between these two times is the time required for the final equalization of liquids in tanks and the floodwater that does not affect the flooding of the accommodation spaces (e.g. the flow through smaller tank ventilation pipes). Therefore, the "approximate time to flood accommodation spaces" can practically be seen as the time within which the evacuation of passengers should take place. The number of passengers expected in the flooded spaces is also provided for each damage scenario, based on the maximum capacity of passenger cabins and the expected number of crew and passengers in other rooms. Finally, the maximum heel and trim angles that occur during the flooding process are shown, as well as the final heel and trim angles and draft. Here it is worth noting once more that the quasi-static approach that was used in this study does not account for dynamic effects, which can influence the maximum heel and trim angles; therefore, the provided results should be viewed with this limitation in mind.

If no crowding of persons is present, the heel angles in the final state of equilibrium vary between -0.4 and 1.2° and the trim angles do not surpass 1.2°. The maximum angles of heel during flooding are up to 0.5° larger than the ones in the final stage and are reached within the first minute after the start of the flooding process in each of the simulated scenarios. The trim angle increases steadily from the start to the end of the flooding process, when it also reaches its maximum value in all of the analyzed scenarios. The final draft of the ship is between 0.19 and 0.41 m higher than the design draught, depending on the damage case. In all cases considered, the ship complies with the damage stability standards put forward by the applicable regulations for inland vessels in Europe.

The resulting times until equilibrium and times to flood the accommodation spaces, however, provide a considerably different view of ship safety than its floating position. In the majority of simulated cases, the total time-to-flood is less than 10 minutes, and varies between 2.1 and 9.5 minutes. Only in one of the scenarios, the final time-to-flood is up to 20.3 minutes. The approximate time to flood the accommodation spaces is, in most cases, 30-50% shorter than the total time-to-flood. Finally, if the breach area, the number of passengers in flooded spaces and the time to flood accommodation spaces are shown side by side, the results are put in perspective. In damage scenarios Side-2 and Side-4 where 22 and 25 persons can be found at the moment of damage, a breach with an area of only 1.5 m^2 can lead to a flooding process in which the accommodation spaces are flooded in only 7 minutes.

Finally, the results also show that the heeling moment due to one-sided accumulation of passengers has a limited effect on both the floating position and the flooding times. The heel angle values in the final stage of flooding are increased, as expected, but are only up to 1.1° higher when compared to the cases without the heeling moment. The maximum heel angles during flooding are also increased, but in no case more than 0.9°, and they are again reached within the first minute after the flooding starts. The effect of the heeling moment on the total time-to-flood is very limited, and these values are, in all cases, higher or lower for only a fraction of a minute compared to the cases without the heeling moment effect. When it comes to the approximate time needed to flood the accommodation spaces, this process seems to last longer compared to cases when there is no heeling moment present. In most cases, the flooding time is increased up to 30%, apart from one case where it is almost doubled. However, considering the limited number of damage scenarios analyzed in this study, it is challenging to draw a definitive conclusion regarding the impact of one-sided passenger accumulation on the estimated time to flood the accommodation spaces.

5. CONCLUSIONS

The paper presented an initial study into the damage stability assessment of large inland passenger ships (LIPS) – the so-called river cruisers – based on time-domain flooding simulations. The study was performed on an existing, state-of-the-art Western European LIPS. The analysis was carried out for a limited number of carefully selected damage cases considered by the existing regulations applicable to this ship type (CESNI, 2025). The study has shown that in most of the analyzed damage scenarios, even though the damage stability regulations were complied with, the time to flood the spaces occupied by passengers and crew seems to be insufficient to conduct evacuation. Even though the presented analysis was performed on one vessel only, in a limited number of damage scenarios and by employing a simplified quasi-static approach, it did demonstrate that the passenger ship safety may not be adequately accounted for by the present regulations. It is therefore evident that the investigated topic requires more attention and wider consideration. Future work by the authors is to include a more extensive analysis of flooding considering a wider set of breaches and damage cases for the sample ship, as well as for other LIPS designs. More realistic modeling of non-watertight bulkheads and doors is planned, and the use of different models that can properly account for the dynamic effects affecting the flooding process will be considered. Finally, an investigation into the evacuation process and required time for orderly evacuation and abandonment would be necessary to complement the analysis.

REFERENCES

Bačkalov, I., Vidić, M., 2020, “Damage stability of river cruisers: A case for harmonization of international regulations”, Proceedings of the Sustainable and Safe Passenger Ships Conference, Athens, Greece, pp. 119-132.

Bačkalov, I., Vidić, M., Rudaković, S., 2023, “Lessons learned from accidents on some major European inland waterways”, *Ocean Engineering*, 273, 113918.

Bačkalov, I., Bulian, G., Rosén, A., Shigunov, V., Themelis, N., 2016, “Improvement of ship stability and safety in intact condition through operational measures: challenges and opportunities”, *Ocean Engineering*, Vol. 120, pp 353-361.

Bulian, G., 2008. “Time-based damaged ship survivability: A quasi-static equivalent method”. *International Shipbuilding Progress* 55, pp. 183–226.

CESNI – European Committee for Drawing up Standards in the Field of Inland Navigation, 2025, “European Standard Laying Down Technical Requirements for Inland Navigation Vessels (ES-TRIN)”, Strasbourg, France.

Jalonen, R., Ruponen, P., Weryk, M., Naar, H., Vaher, S., 2017, “A study on leakage and collapse of non-watertight ship doors under floodwater pressure”, *Marine Structures*, Vol. 51, pp. 188-201.

Jasionowski, A., Vassalos, D., 2006, “Conceptualising risk”, Proceedings of the 9th International Conference on Stability of Ships and Ocean Vehicles, STAB2006, Rio de Janeiro, Brasil.

Mauro, F., Vassalos, D., 2024, “Time to capsize for damaged passenger ships in adverse weather conditions. A Multimodal analysis”. *Ocean Engineering* 299, 117409.

Mauro, F., Vassalos, D., Paterson, D., Boulougouris, E., 2023, “Evolution of ship damage stability assessment—Transitioning designers to direct numerical simulations”, *Ocean Engineering* 268, 113387.

Paterson, D., Vassalos, D., Atzampos, G., Boulougouris, E., Cichowicz, J., Luhmann, H., 2018, “Rebooting SOLAS – impact of drafts on damage survivability of cruise ships”,

Proceedings of the 13th International Conference on the Stability of Ships and Ocean Vehicles, Kobe, Japan, pp. 663-674.

Ruponen, P., 2007, "Progressive flooding of a damaged passenger ship", Doctoral dissertation, Helsinski, Finland.

Ruponen, P., Lindroth, D., 2016, "Time-domain simulation for regulatory flooding analysis", Proceedings of the 13th International Symposium on Practical Design of Ships and Other Floating Structures PRADS2016, Copenhagen, Denmark.

Ruponen, P., Lindroth, D., Pennanen, P., 2015, "Prediction of survivability for decision support system in ship flooding emergency", Proceedings of the 12th International Conference on Stability of Ships and Ocean Vehicles, Glasgow, UK, pp. 987-997.

Ruponen, P., Lindroth, D., Routi, A., Aartovaara, M., 2019, "Simulation-based analysis method for damage survivability of passenger ships", *Ship Technology Research*, 66:3, pp 180-192.

Ruponen, P., Pulkkinen, A., Laaksonen, J., 2017, "A method for breach assessment onboard a damaged passenger ship", *Applied Ocean Research*, Vol. 64, pp. 236-248.

Ruponen, P., van Basten Batenburg, R., van't Veer, R., Braidotti, L., Bu, S., Dankowski, H., Lee, G. J., Mauro, F., Ruth, E., Tompuri, M., 2022, "International benchmark study on numerical simulation of flooding and motions of a damaged cruise ship", *Applied Ocean Research*, 129, 103403.

Spanos, D., Papanikolaou, A., 2014, "On the time for the abandonment of flooded passenger ships due to collision damages", *Journal of Marine Science and Technology* 19, pp. 327–337.

Vidić, M. and Bačkalov, I., 2022, "An Analysis of Stability Requirements for Large Inland Passenger Ships", *Ocean Engineering* 261, 112148.

APPENDIX I: DAMAGE SCENARIOS

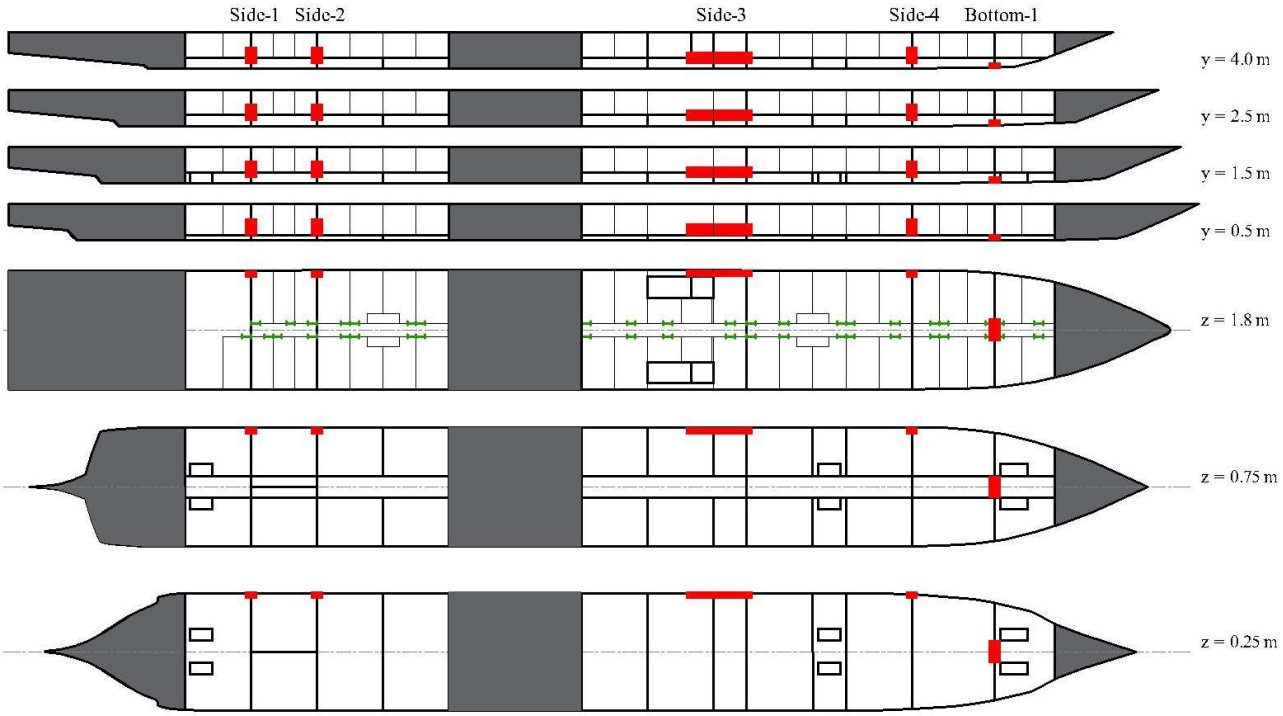

Figure A1: Damage scenarios

APPENDIX II: TIME-DOMAIN FLOODING SIMULATION RESULTS WITH AND WITHOUT THE EFFECT OF THE MOMENT DUE TO ONE-SIDED ACCUMULATION OF PERSONS

Table A1: Simulation results, based on quasi-static approach, with and without the effect of the moment due to one-sided accumulation of persons (M_p)

Damage scenario	Breach area [m^2]	Time until equilibrium [min]	Approximate time to flood accommodation spaces [min]	Passengers in the flooded spaces	Maximum heel angle during flooding [°]	Final flooding heel angle [°]	Maximum trim angle during flooding [°]	Final flooding trim angle [°]	Final draught [m]
Side-1	1.5	3.4	1.8	10	1.3	1.1	-0.2	-0.2	1.84
Side-1 with *Mp*		3.3	3.3	10	2.2	1.8	-0.2	-0.2	1.84
Side-2	1.5	7.5	7.5	22	1.5	1.2	-0.2	-0.2	1.91
Side-2 with *Mp*		8.6	8.6	22	2.3	2.1	-0.2	-0.2	1.91
Side-3	6.0	20.3	15.8	27	0.6	-0.4	0.6	0.61	2.06
Side-3 with *Mp*		19.9	19.9	27	1.3	1	0.6	0.61	2.06
Side-4	1.5	9.5	6.2	25	0.5	0	0.7	0.7	1.99
Side-4 with *Mp*		9.2	7.0	25	1.3	1.1	0.7	0.7	1.99
Bottom-1	2.2	2.1	1.3	10	0	0	1.2	1.2	1.88
Bottom-1 with *Mp*		2.1	1.4	10	0.9	0.9	0.7	0.7	1.88

Session 8
Emerging technologies and impact on stability and safety

Development of an infinite element for deep-water waves for ultra-fast modeling of water wave problems

Justin M. Harler, *Naval Surface Warfare Center, Carderock Division,* justin.m.harler.civ@us.navy.mil
Arthur M. Reed, *Naval Surface Warfare Center, Carderock Division,* arthur.m.reed.civ@us.navy.mil

ABSTRACT

The infinite element method that has been developed and implemented in the fields of acoustic and electromagnetic waves offers the potential for much greater computational efficiency than comparable boundary element or computational fluid dynamics (CFD) methods. The infinite element method has not yet been implemented in the field of hydrodynamics for deep water waves. The principal challenge is that deep water gravity waves are dispersive (wave velocity is a function of the wave frequency), while acoustic and electromagnetic waves, where the technique has been successfully implemented, are non-dispersive (wave velocity is independent of wave frequency). There has been work using infinite elements for *shallow* water waves, which are also non-dispersive. The approach for this development is to start with a two-dimensional, vertically oscillating body and if successful, this will be expanded to three dimensions and then developed for a body that is both oscillating and translating, where waves are radiating away in multiple directions relative to the vessel. The current focus is on finding an expansion of the velocity potential valid both near the body and at infinity to be used in constructing the infinite element.

Keywords: *Infinite Element, Water Waves, Computation.*

1. INTRODUCTION

All problems involving ships on the surface of the ocean (the free surface) involve waves (a.k.a. surface gravity waves), including ambient ocean waves or the waves resulting from the vessel's motions (Beck, et al., 1996). The most familiar and simple of these problems is the seakeeping of a vessel at zero speed, where the vessel responds to ambient waves while diffracting the incident waves and radiating away waves resulting from the motions of the vessel, acting as a "wave maker." Another basic problem is that of a vessel moving at steady forward speed in calm water, where it produces the familiar V-shaped Kelvin wave wake composed of transverse and diverging waves. A variation on the Kelvin wave problem is that of a ship maneuvering in calm water, which results in a distortion of the V-shaped wave pattern. The combination of all of these problems is the seakeeping problem when the ship is able to maintain a straight course and constant speed in the mean; and the maneuvering-in-waves problem when the waves are large enough that the vessel is no longer able to avoid significant variations in speed and heading (Beck & Reed, 2001).

The common thread in all of these problems is the fact that the generation of waves by the vessel results in significant forces exerted on the vessel. In the zero-speed seakeeping problem, there are the radiation and diffraction forces (added-mass and damping, and exciting force terms, respectively, in the linearized equations of motion), which strongly influence the responses of the vessel to the ambient seas. The waves in the case of the Kelvin-wave problem result in the wave resistance of the vessel, a force that can be of minimal significance at low speeds where viscous forces dominate, but which becomes the dominant force at higher speeds. The same comments that apply to the wave-resistance problem, apply to the calm-water maneuvering problem. For the seakeeping and maneuvering-in-waves problems, all of the above wave forces apply, plus there is a family of second-order wave forces and moments (i.e., zero-speed drift forces and moments, added resistance in waves, etc.).

Classically, the above problems have been solved by means of analysis that resulted in much-simplified problems that could be solved analytically and results produced with pencil, paper and mechanical calculators. However, with the advent of

digital computers in the 1960's researchers started to solve these problems using numerical techniques. First were the boundary element methods (BEM) where sources and sinks, vortex lattices, or velocity potentials were distributed on the vessel's wetted surface—in most cases these BEM solutions necessitated the assumptions of potential flow, which were appropriate for many of the problems, even today. The essence of the BEM methods is that the solution only involves a problem on an interface, the wetted surface of the vessel, or the wetted surface of the vessel and the free surface (Beck, et al., 1996).

More recently, in the last 25 years or so, computational fluid dynamics (CFD) methods that discretize the entire fluid volume have come to be viable. Solutions of the Reynolds averaged Navier-Stokes equations (RANS), the unsteady RANS (URANS) (Stern, et al., 2013), Euler's equation solvers (Dommermuth, et al., 2010, 2014), large eddy simulations (LES), Direct Numerical Solution (DNS), etc.—referred to in this paper as full-domain finite (fluid) element (FEM) techniques. Contemporary FEM are using 100s of millions if not billions of cells. On the discrete cells of the FEM, techniques such as finite differences are used to compute the gradients necessary to set up the equations needed to solve the fluid dynamic equations of motion. Due to their fine discretization of the fluid domain, the FEM methods are capable of capturing much of the physics of the fluid flow problem quite accurately.

The BEM methods discussed above are relatively slow for larger problems but the full-domain FEM methods are even slower, by several orders of magnitude. To put the computing efforts into perspective, it is useful to speak of the computing effort required to solve a seakeeping or maneuvering-in-waves problem, where there is a meaningful time scale. A 3-D BEM can take 100's to 1000's of cpu seconds for each second of full-scale time simulated. On the other hand, the full-domain FEM methods take 10,000 to 10^6 cpu seconds per real-time second simulated. As a consequence of this discrepancy in execution time versus real time, none of these methods are useful for producing the millions of hours of motion time histories that are necessary for the thorough characterization of a ship during a design. This has resulted in continued reliance on reduced order methods such as blended methods to compute ship motions in waves (Beck & Reed, 2001).

However, to the authors' knowledge, no one has yet used infinite element technology to model these large ocean problems. Burnett (1994), Burnett & Holford (1997a,b, 1998a,b,c, 1999) and Burnett & Labianca (1999) are widely recognized as having "revolutionized" the modeling of scattering of acoustic and electromagnetic waves in essentially unbounded spaces, having shown that the infinite element method (IEM) performs several orders of magnitude faster than the BEM. That technology was patented in the 1990s (and licensed by Bell Labs to software firms), making it unavailable to the research community for the next 20 years. These patents have now expired so this is an unusual and propitious moment in time to take advantage of this "re-emerging" powerful technology. The remainder of this paper explains efforts to expand and apply the IEM technology to achieve ultra-fast modeling of surface gravity-wave problems in the fields of naval architecture and ocean engineering.

2. CURRENT STATE-OF-THE-ART

Beginning in the late 1970's and early 1980's, FE methods were applied to shallow water surface gravity-wave problems (cf., Bettess & Zienkiewicz, 1977). Subsequently, a number of other authors have solved the shallow water progressive wave problem using finite element techniques (Keramedis, et al., 1984; Hanert, et al., 2002; Bunya, et al., 2009; Kubatko, et al., 2009; Staroszczyk, 2009). These shallow water wave solutions are characterized by solutions that are non-dispersive; they are the equivalent of an acoustic or electromagnetics problem, where the energy is traveling at the wave phase speed.

In the 1990's Wu & Eatock Taylor (1994, 2003; Wu, et al., 1998) extended the use of finite-element techniques to finite-depth surface gravity-wave problems, where dispersion applies (group velocity at which energy is propagated is less than the wave phase velocity) and their solutions allowed waves that were fully nonlinear. More recently, van der Vegt & Tomar (2005) and Tomar & van der Vegt (2007) have reformulated the finite-depth surface gravity-wave problem using the formality of Zienkiewicz (1971). To do this, van der Vegt and Tomar have relied heavily on the works of Brezzi, et al. (1999) and Arnold, et al. (2002).

With the exception of Bettess & Zienkiewicz (1977), all of the works cited above have either performed their FE analysis in a finite domain, or a domain with periodic end conditions. Thus their works are not truly applicable to the problems of ship hydrodynamics for a vessel operating in unrestricted waters of infinite extent. Bettess & Zienkiewicz (1977) employed infinite elements to extend their shallow water wave solution to infinite extent; however, they took advantage of the shallow water, non-dispersive, aspect of the gravity-wave behavior to accomplish this.

As described above, 3-D finite (fluid) element method techniques require 100s of millions of elements to discretize the fluid domain for a ship hydrodynamics problem. Employing infinite element technology will allow the required number of elements to be reduced by orders of magnitude while maintaining the extremely low sparsity characteristic of FE matrices, thereby reducing the execution time by even more orders of magnitude. This has the potential for producing accurate solution methods/techniques that can execute at or faster than real time.

3. TECHNICAL APPROACH

History

What follows is a capsule summary of the history and key features of the IEM technology that are germane to this project, the role of patents in its evolution in the R&D world, and why it is fundamentally orders of magnitude faster than the BEM for all types of waves (acoustics, EM, surface gravity waves, etc.).

In the early 1990s Burnett and his coworker (Burnett, 1994; Burnett & Holford, 1997a,b, 1998a,b, 1999) developed a radically new theoretical framework for modeling the scattering and radiation of sound from structures (submarines then mines later on). It was a so-called "infinite element", which captured all the physics in a sector of space from close to the the structure to infinity and preserved the sparsity (hence computational speed) of FEM technology that yielded much faster speeds than BEM technology. Figure 1 defines the general concept and Fig. 2 shows an actual mesh of elements surrounding a submarine hull (which would be a surface ship in this proposed work). Typically, a few layers of standard finite elements closely surround the structure and then a single layer of infinite elements models the rest of the exterior region out to infinity.

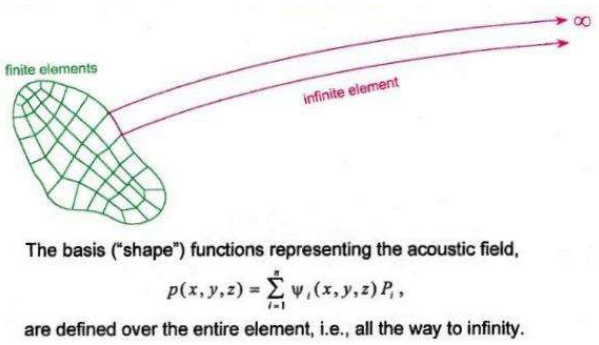

Figure 1: Infinite element concept diagram.

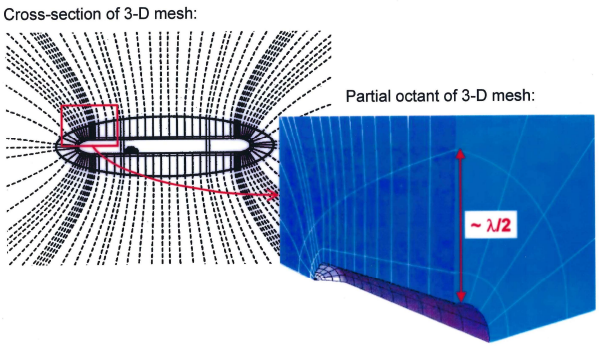

Figure 2: Diagram of Burnette's ellipsoidal infinite element surrounding a submarine hull.

This IEM technology speeded up scattering computations for small-to-medium size ship-like problems (long, narrow structures) relative to the BEM by over 400 times, for exactly the same 3-D physics and to the same accuracy (Burnett, 1994). As problems grow computationally larger (e.g., higher frequencies) the speedup increases indefinitely: the cpu time of BEM modeling for ship-like structures was shown to be proportional to N^3 (where N is the number of degrees of freedom—unknowns—in the model) whereas the cpu time of IEM modeling was shown to be proportional to $N^{3/2}$. Thus, the ratio of cpu times, or speedup, of the IEM relative to the BEM grows as $N^{(3-3/2)} = N^{3/2}$. For ship-like problems this yielded the above 400 times speedup for models with N = 26,000; it yields 6,800 times speedup for N = 100,000, and it yields speedups of millions for much larger and more realistic problems.

Dramatic speedups like this are intrinsic to the underlying mathematics of the BEM as compared to the IEM, for the following reasons (Burnett, 1994):

- Almost the entire cost of such modeling is solving the linear algebraic system of equations resulting from the problem discretization, $[K]\{a\} = \{f\}$. In the BEM, the $[K]$ matrix is small but *fully populated*; in the IEM it is larger but *extremely sparse*. The cost is much more sensitive to the sparsity of [K] than it is to its size.

- The reason for the fully populated BEM matrix is the use of Green functions, which are *globally* supported. Green functions are intrinsic to BEM formulations. The IEM uses only *locally* supported functions, so products of functions are identically zero in almost all matrix terms; i.e., matrices are very sparse.

The conclusion is that the IEM is intrinsically faster than the BEM for essentially any type of physics. Ergo, the dramatic speedups of the IEM relative to the BEM for acoustics and electromagnetic problems should also be realized for surface gravity-wave problems.

The IEM was a very transformative technology, hailed by leaders in industry and academia as "revolutionary" and many said it would change the direction of acoustics and other fields involving wave propagation.

Then, in the mid-1990s Bell Labs patented the technology (and licensed it to software firms in Europe). That effectively ended the revolution, relegating it to a historical curiosity that no one could use in the research community, although over the years the elements gradually became known in the field as "Burnett infinite elements." Now, twenty years later, the patents have started expiring (twenty years after the filing dates) and colleagues in Europe, upon learning of the expirations, have said that it looks like the revolution will now finally happen.

In anticipation of the patent expirations, Burnett has recently been resurrecting the IEM technology and bringing it up to today's IT standards (Burnett, 2015). This work has already yielded a speedup of 1400 times for the same physics to the same accuracy—reducing modeling times from days to minutes, or hours to seconds. In parallel with that effort, Burnett is currently working on a novel way to expand the IEM technology to achieve a speedup of a different part of these analyses (post-processing the scattered field) that is expected to be in the factor of a thousand to a million range (Burnett, 2015).

In summary, the technical approach is to use similar mathematical techniques, as were used for acoustic and EM infinite elements, to derive surface gravity-wave infinite elements.

Current Work

For water waves, the infinite elements in the current work will essentially be 2-D in 3-D space, since the vertical dependence is known. 2-D infinite elements are oriented transverse to the body with waves traveling along the element. 3-D infinite elements will be wedge-shaped with waves traveling out across the element. This means that theproblem of interest will have significantly fewer infinite elements than the acoustics and electromagnetics problems, but will have temporal convolution integrals to account for the wave "memory" effects resulting from dispersion. A CFD code might only need to extend to infinity in the viscous wake region behind the vessel.

For the current phase, work is focused on developing an infinite element for a vertically oscillating body on the free surface in two dimensions (vertical and horizontal) with the fluid extending to infinity. This gives an infinite element for waves propagating in only one (the horizontal) dimension.

The approach taken has been to break down the steps presented by Burnette (Burnette, 1998b) in his development of an acoustic infinite element and imitate the steps from a hydrodynamic perspective. Those pieces can be summarized as follows:

1. Define or develop the coordinate system on which to build the infinite element.

2. Develop a series expansion representation of the field variable.

3. Define mapping functions that map the internal coordinate system within each element to the global coordinate system.

4. Define shape functions that interpolate the field variable between nodes of the element.

5. Combine the expansion of item 2 with the governing physics equations, boundary conditions, and shape functions to build the element matrices.

Item 1 was nontrivial for Burnette's work, as the elements were built in a 3-D ellipsoidal coordinate system. This will likely be revisited in the future, but for the current phase of this work, 2-D Cartesian coordinates will serve. The majority of research so

far has been focused on item 2. Burnette provides a multipole expansion for acoustic pressure; the main challenge in the current work is to find an appropriate expansion for fluid velocity potential.

The water waves approach employs the wave function expansion theorem presented by Ursell (1968). The theorem states that sufficiently far from a submerged infinitely long cylinder of arbitrary cross-section, the wave function is the sum of a wave source, a wave dipole, regular standing waves and wave-free potentials. In two dimensions, a solution to the source portion of Ursell's expansion theorem can be taken from (Thorne, 1953), where Thorne provides a velocity potential solution for a logarithmic singularity:

$$\Phi(x,y,t) = [\ln\frac{r}{r'} + 2PV\int_0^\infty \frac{e^{-s(y+f)}}{K-s}\cos(sx)\,ds]\cos(\sigma t) - 2\pi e^{-Ky}\cos(Kx)\sin(\sigma t) \quad (1)$$

where x is the horizontal dimension, y the vertical, increasing with depth, f is the depth of the source, σ is the radial frequency, $K = \frac{\sigma^2}{g}$, r and r' are the radial distances of the point (x, y) from the points $(0, f)$ and $(0, -f)$, respectively.

4. CONCLUSION AND FUTURE WORK

The development of an infinite element for surface gravity waves in water of infinite depth is in the first stages, and progress continues by working to apply Ursell's wave function expansion theorem. The wave-free potentials used in this theorem need to be developed for two dimensions. Following success of these fundamental steps of the theory development, future work will include:

1. Extending the 2-D element for an oscillating body to 3-D as pie-shaped elements covering the entire annular region exterior to the body.

2. Development of a radiation condition that does not require waves to be traveling radially away from the body, as does the Sommerfeld radiation condition which could be applied for an oscillating body with zero forward speed.

3. Solve the problem of a steadily translating body (Kelvin wake problem), where waves are moving in multiple directions relative to the track of the body.

4. Solve the problem of a vessel translating and oscillating, combining the solutions of tasks 1 and 3.

The infinite element solutions developed for the above problems will be implemented in code to verify the concept.

REFERENCES

Arnold, D. N., F. Brezzi, B. Cockburn & L. D. Marini (2002) Unified analysis of discontinuous Galerkin methods for elliptic problems. SIAM J. Numer. Anal., 39(5):1749–79.

Beck, R. F. & A. M. Reed (2001) Modern computational methods for ships in a seaway. Trans. SNAME, 109:1–51.

Beck, R. F., A. M. Reed & E. P. Rood (1996) Application of modern numerical methods in marine hydrodynamics. Trans. SNAME, 104:519–37.

Becker, E. (1958) Das Wellenbild einer unter der Oberfläche eines Stromes schwerer Flüssigkeit pulsierenden Quelle. (Wave formation from a source pulsating under the surface of a stream of dense fluid.) Z. angew. Math. Mech., 38(9/10):391–99.

Bettess, P. & O. C. Zienkiewicz (1977) Diffraction and refraction of surface waves using finite and infinite elements. Int'l. J. Numer. Methods Engrg., 11:1271–90.

Brezzi, F., G. Manzini, D. Marini, P. Pietra & A. Russo (1999) Discontinuous finite elements for diffusion problems. In: Atti Convegno in Onore di F. Brioschi, Instituto Lombardo, Accademia di Scienze e Lettere, Milan, Italy, pp. 197–217.

Bunya, S., E. J. Kubatko, J. J. Westerink & C. Dawson (2009) A wetting and drying treatment for the Runge–Kutta discontinuous Galerkin solution to the shallow water equations. Comput. Methods Appl. Mech. Engrg., 198:1548–62.

Burnett, D. S. (1987) Finite Element Analysis: From Concepts to Applications. Reading, Mass: Addison-Wesley, xix+844 pp.

—— (1994) A three-dimensional acoustic infinite element based on a prolate spheroidal multipole expansion. J. Acoust. Soc. Am., 96(5):2798-2816.

—— (2015) Speeding up PC-ACOLOR three orders of magnitude; same 3-D physics. FY15 annual report for ONR Dept. 322, Program Officer Kyle Becker.

Burnett, D. S. & R. L. Holford (1997a) 3-D acoustic infinite element based on a prolate spheroidal multipole expansion. United States patent number 5,604,891. Filing date: Oct 27, 1994; Issue date: Feb. 18, 1997; Expiration date: Oct 27, 2014.

—— (1997b) 3-D acoustic infinite element based on an oblate spheroidal multipole expansion. United States patent

number 5,604,893. Filing date: May 18, 1995; Issue date: Feb. 18, 1997; Expiration date: May 18, 2015.

—— (1998a) Prolate and oblate spheroidal acoustic infinite elements. Comput. Methods Appl. Mech. Engrg., 158:117–42.

—— (1998b) An ellipsoidal acoustic infinite element. Comput. Methods Appl. Mech. Engrg. 164:49–76.

—— (1998c) Multipole-based 3-D infinite elements: an ellipsoidal acoustic element and a spherical electromagnetic element. Computational Methods for Unbounded Domains, T. L. Geers (ed.), Kluwer, Proceedings IUTAM symposium, Boulder, Colorado.

—— (1999) 3-D acoustic infinite element based on an ellipsoidal multipole expansion. United States patent number 5,963,459. Filing date: Mar 6, 1997; Issue date: Oct. 5, 1999; Expiration date: Mar 6, 2017.

Burnett, D. S. & F. M. Labianca (1999) 3-D electromagnetic infinite element. United States patent number 5,966,524. Filing date: Sept. 29, 1997; Issue date: Oct. 12, 1999; Expiration date: Sept. 29, 2017.

Dommermuth, D. G., T. C. Fu, K. A. Brucker, T. T. O'Shea & D. C. Wyatt (2010) Numerical prediction of a seaway. Proc. 28th Symp. Naval Hydrodynamics, Pasadena, CA, 14 pp.

Dommermuth, D. G., C. D. Lewis, V. H. Tran & M. A. Valenciano (2014) Direct simulations of wind-driven breaking ocean waves with data assimilation. Proc. 30th Symp. Naval Hydrodynamics, Hobart, Tasmania, Australia, 36 pp.

Hanert, E., V. Legat & E. Deleersnijder (2002) A comparison of three finite elements to solve the linear shallow water equations. Ocean Modelling, 5:17–35.

Keramidas, G. A., S. E. Ramberg & O. M. Griffin (1984) Finite element modelling of surface waves in a channel. Appl. Math. Modelling, 8:298–304.

Kubatko, E. J., S. Bunya, C. Dawson & J. J. Westerink (2009) Dynamic p-adaptive Runge–Kutta discontinuous Galerkin methods for the shallow water equations. Comput. Methods Appl. Mech. Engrg., 198:1766–74.

Staroszczyk, R. (2009) A Lagrangian finite element analysis of gravity waves in water of variable depth. Archives of Hydro-Engineering and Environmental Mechanics. 56(1–2):43–61.

Stern, F., J. Yang, Z. Wang, H. Sadat-Hosseini, M. Mousaviraad, S. Bhushan & T. Xing (2013) Computational ship hydrodynamics: Nowadays and way forward. Int'l. Shipbuilding Progress, 60:3–105.

Stoker, J. J. (1957) Water Waves. New York: Wiley-InterScience, xxviii+567 pp.

Thorne R. C. (1953) Multipole Expansions in the Theory of Surface Waves.

Tomar S. K. & J. J. W. van der Vegt (2007) A Runge–Kutta discontinuous Galerkin method for linear free-surface gravity waves using high order velocity recovery. Comput. Methods Appl. Mech. Engrg., 196:1984–96.

Ursell F. (1968) The Expansion of Water-wave Potentials at Great Distances. Department of Mathematics, University of Manchester.

van der Vegt, J. J. W. & S. K. Tomar (2005) Discontinuous Galerkin Method for Linear Free-Surface Gravity Waves. J. Scientific Computing, 22/23:531–67.

Wehausen, J. V. & E. V. Laitone (1960). Surface waves. Encyclopedia of Physics, Ed. by S. Flügge & C. Truesdell, Vol. IX/Fluid Dynamics III, Berlin, Germany: Springer-Verlag, pp. 446–778.

Wu, G. X. & R. Eatock Taylor (1994) Finite element analysis of two-dimensional non-linear transient water waves. Applied Ocean Research, 16:363–72.

—— (2003) The coupled finite element and boundary element analysis of nonlinear interactions between waves and bodies. Ocean Engineering 30:387–400.

Wu, G. X., Q. W. Ma & R. Eatock Taylor (1998) Numerical simulation of sloshing waves in a 3D tank based on a finite element method. Applied Ocean Research, 20:337–55.

Zienkiewicz, O. C. (1971) The Finite Element Method in Engineering Science. New York: McGraw-Hill, xiv+521 pp.

Development of an onboard machine learning based early warning system for dynamic ship stability loss after damage

Bart Mak, *MARIN,* b.mak@marin.nl
Thomas P. Scholcz, *MARIN,* t.p.scholcz@marin.nl
Riaan van 't Veer, *MARIN,* r.vantveer@marin.nl

ABSTRACT

When water runs into a damaged ship, different scenarios may develop such as loss of transverse stability and buoyancy loss. An Early Warning System (EWS) could warn the crew in advance such that risk mitigating actions can be taken. We describe the development of such a system relying on the prediction of a machine learning model trained on a dataset of dynamic flooding simulations. An interval of 6DOF ship motions recorded just after damage are used as input features whereas the quantities of interest are damage location, ship attitude after 30 minutes and time to capsize. We show that the machine learning model is very well capable to predict the damage locations from the ship motions and also the prediction of ship attitude after 30 minutes is promising. The prediction of time to capsize is more difficult and not reliable. We identify room for improvement by including related features such as stability metrics in order to improve the results.

Keywords: *Damage stability, Dynamic flooding, Simulations, Early warning system, Machine learning,*

1. INTRODUCTION

When water runs into a damaged ship, different scenarios may develop. Large heel angles could develop during transient and progressive flooding with eventually loss of transverse stability; buoyancy loss may lead to significant trim, list or sinking; structural damages might occur beyond structural capacity, and so on. The possible developing scenarios, time-to-sink or time-to-capsize, are complex to predict since they depend on the ship operational condition (loading condition) in combination with the environmental conditions (sea states) and the time dependent flooding rates of transient water through the damage and progressive flooding through the ship labyrinth. In calm water conditions, the developing ship stability after damage can be very different from the situation in high sea states.

Early Warning Systems (EWS) facilitate important risk-mitigation actions before critical events such as capsizing due to ship damage occurs. Such a life-saving EWS (see Figure 1) should account for complex physical mechanisms that cause the instability of the ship.

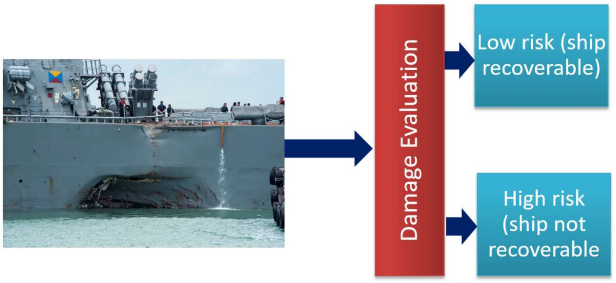

Figure 1: Schematic of an EWS

The flooding of ship compartments can be numerically simulated in the time domain using dynamic flooding simulation software. These numerical simulations are, however, too slow to be of use in an EWS. Besides this, to run the simulations, the damage location and its dimension and the current operational conditions should be known at the time of the event, which is often not or only partly the case.

In this paper we present a machine learning model trained on flooding simulation data of a damaged frigate allowing to quickly forecast the end state of the ship as well as the time-to-sink and time-to-capsize. This machine learning model is to be subsequently exploited by the EWS which uses the predictions from the machine learning model for the decision to warn the crew of the frigate.

2. EARLY WARNING SYSTEMS

Classic onboard EWSs rely on tools that need input from sensors, see (Jasionowski, 2011). Multiple sensors need to be installed on the ship to estimate the damage size and location. A hydrostatic model is then used to predict the flooding extent and the outcome is used to inform the crew.

Machine learning based early warning systems in the maritime domain are developed for various maritime applications, see for example (Pinheiro et al, 2023) and (Zhizheng et al., 2024). Only a few studies are dedicated to the real-time onboard prediction of survivability of ships. A case-based reasoning system using machine learning was developed by (Louvros et al., 2023). A database is created with a representative number of damage cases. A time-domain code is subsequently used to simulate progressive flooding for each damage case and the data is used to train a machine learning model. When an actual damage occurs on the ship, the most similar case is identified by the case-based reasoning system using a similarity metric, see (Ölçer et al., 2006). After this identification step, the pre-trained machine learning model quickly predicts the flooding scenario which is then exploited by the EWS.

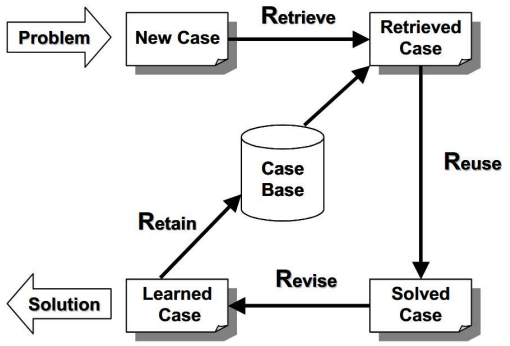

Figure 2: Case Based Reasoning for flooding crisis management, see (Ölçer et al., 2023).

Case based reasoning relies on using information from previous situations to decide the outcomes for new cases. It solves a problem by retrieving, reusing, revising and retaining past cases based on their degree of match (or similarity) to the current situation. Here, we deviate from this approach in the sense that we would like to estimate the damage size and location from *ship motions* using a machine learning model rather than relying on manual input of the damage size and location. The similarity of the prediction with the true damage could be verified by the crew a posteriori to check the reliability of the machine learning model. The following steps are identified:

1. Predict the damage size and location from a small duration of ship motions recorded after damage.
2. (Optional) Check the similarity of the predicted versus the actual damage size and location.
3. Predict the flooding scenario using the machine learning model.

The EWS cannot only raise an alarm but also reports the damage size and location directly from the ship motions. From experience, we know that information carried by ship motions is rich. For example, wave statistics can be obtained by training machine learning models on ship motions, see (Mak, B. and Duz, B, 2019) and (Scholcz, T.P. and Mak, B., 2020). By simulating various damage scenarios in combination with different sea states a dataset is generated with a high coverage. The machine learning model is trained using this dataset and subsequently used by the EWS to predict the flooding scenario.

3. DYNAMIC FLOODING SIMULATIONS

The dynamic flooding simulations are performed with MARIN's FREDYN time-domain simulation. The ship motions are solved in 6-DoF. For this demonstration case, the ship is at zero speed. The selected wave heading is kept by a soft-mooring arrangement that does not affect the first order ship motions. By doing so, the effect of various wave headings can be investigated consistently and the database for the EWS can be prepared.

The flooding model of FREDYN has recently been renewed and denoted as a so-called Unified Internal Flow model (UIF). The UIF solver aims to provide a generic simulation model for all kinds of fluid behaviour in the ship. For example, it can deal with slow and rapid ship ballasting, complex progressive flooding through any labyrinth of compartments. The UIF model does model the U-tank inertia and moonpool pumping modes. In some ship internal flooding situations, the fluid inertia effects are relevant, while in others they are less important or not significant at all. The basic idea behind the UIF solver is that the fluid inertia aspects are implicitly included in the equations. If the

internal geometry and fluid conditions are such that the inertia aspects play a roll, it will be picked up by the solver. The details of the solver can be found in (Van 't Veer, et al, 2023).

The sample ship in the calculations is a Generic Destroyer (Frigate). The ship's length is about 132 m with a beam of about 19 m. The outline of the ship is depicted in Figure 3. A realistic loading condition has been set which is used throughout all simulations. For practical use on board, the database should be extended with various other loading conditions.

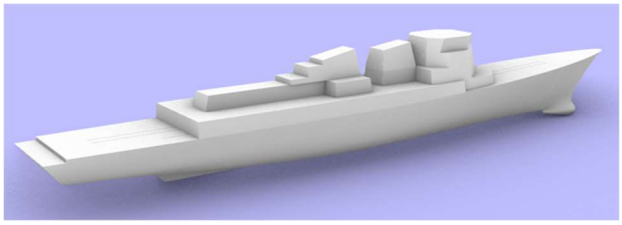

Figure 3: Ship outline.

The internal geometry of the ship consists of 12 zones denoted A to L. Each zone (B to K) has a length of 11.40 m. The layout is depicted in Figure 4. The ship has a number of decks. It is assumed that all door openings in a zone are open. Up- and down-flooding is thus modelled in a zone. Within each zone, the doors on deck 1 and 2 allow progressive flooding of the subdivision. As soon as the water reaches deck 3, multiple zones could be flooded by progressive flooding since the doors on deck 3 are assumed open. This is just a configuration and model choice.

The external damage is assumed to extend from bottom up to the main deck. A rectangular shaped damage is assumed with a length of 8 m. The single zone damage is smaller than the rule-based design damage, but it could represent a weapon attack damage. Due to the open doors in the corridors on deck 3, multiple zones could be flooded over time.

The intention of the paper is to demonstrate the EWS capabilities and to explore the associated techniques using an assumed ship condition and assumed damage extent.

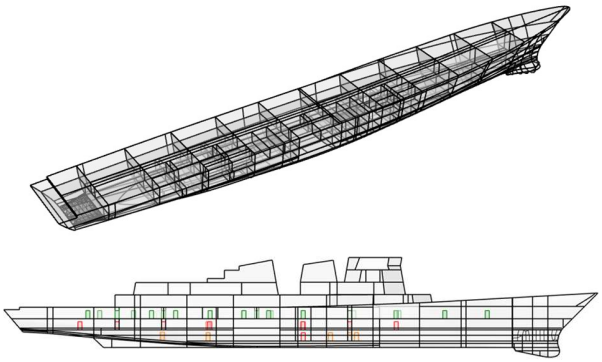

Figure 4: Ship internal sub-division.

The applied UIF model assumes fully ventilated compartments; air entrapment is not modelled. The time step in the simulations is 0.125 seconds. The simulation time is 3 hours, but if stability is lost and heel angles are beyond 70 degrees, the simulation is stopped. The calculation time of a single simulation is just below real time using a single CPU node. Using MARIN's calculation cluster, the preparation of the database for the machine learning model took just over 4 days. But this could have been much quicker utilizing a larger number of computing nodes.

The simulation data set consisted of 1920 simulations covering all damage locations. The sea state height, wave spectrum peak period and wave heading was different in each simulation. The JONSWAP wave spectrum definition was used. Wind was not modelled since it normally has a minor impact on progressive flooding under the assumption of a constant wave heading.

4. MACHINE LEARNING

The dataset that was generated is to be used in a supervised learning setup. We use data that can be available shortly after a damage occurs as input to derive quantities that are available in the dataset, but otherwise not directly observable or derivable.

Supervised machine learning relies on good data coverage, meaning that the dynamics (so called features) and associated resultants (labels) of entirely new scenarios fall within the features and relations between features and labels of the data that was available beforehand.

We model the relations between features and labels with neural networks. Without going into too much detail, neural networks allow for error reduction by gradient descent methods, even for complex feature transformations, such as

convolutions. This in turn opens up a wide range of modelling components, allowing problem specific neural network architectures, fully capturing the relevant dynamics.

Quantities of interest

As easily accessible features, we use full 6DOF ship motions measured at 1 Hz, with a sample length of 1.0 or 2.5 minutes.

With supervised learning we need to specify the Quantities of Interest (QoIs), the labels we want to know from the input data. For the EWS we consider three main quantities: the damage location, what the ship will do in the 30 minutes after damage has occurred and the time to capsize. For the estimate of what the status of the ship will be after 30 minutes, we are only interested in heave, roll and pitch, as these are the quantities directly related to survivability of the ship.

Encoding

One-hot-encoding is used to encode the damage location and size. It is a simplified way to encode damage as the size is fixed and only the location varies discretely from section A to L. In later experiments the encoding could be made more complex and realistic. For now, it is used to demonstrate the potential of the current approach.

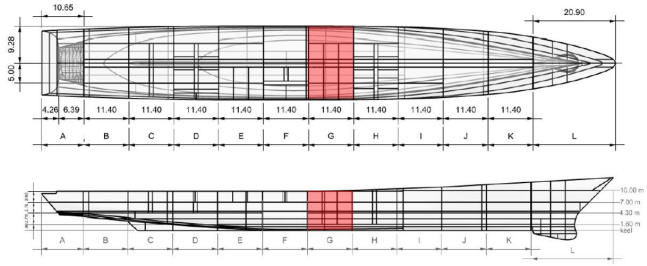

Figure 5: one-hot encoding of the ship damage

Design of Experiments

The damage location and size is not the only feature that determines the safety of the vessel. The sea-state is important as well. Nested Latin Hypercube Sampling is used to generate a space-filling design in the sea state parameter Hs, Tp and dp for each encoded damage of the ship. Starting with a minimum number of 10 steps per sea state parameter we obtain 30 samples/encoded damage resulting in 8*30 = 240 samples for the smallest training set. By changing the seed of the LHS generator, these designs do not overlap. Subsequently, LHS nesting is used to increase the total number of samples to 480, 960 and 1920 respectively. The result is a sequency of space-filling LHS designs with increasing sample density. This sequence can be used to check when a plateau is reached in the machine learning performance with respect to the number of samples used for training.

Network architecture

We distinguish three main types of neural network architectures for the different types of regression. For value-based outputs, like the final state, we use an encoder-regressor model with convolutions as encoder and a couple of fully-connected layers as regressor. The choice for convolutions is based on earlier results for ship motion time series data and makes use of the encoding strength of convolutions on 2D data (channels x time) with a good balance in sample frequency and filter size.

For binary classification outputs, such as for the capsize indicator, we use a similar neural network, but we use the traditional classification output, only changing the final activation function (sigmoid) and the loss function (cross-entropy).

For multiclass classification, such as for the damage location, we use convolutional encoder-decoder networks with Intersection-over-Union losses.

To improve network expressiveness, the convolution layers and hidden fully-connected layers have a mix of activation functions: tanh, elu and linear.

Training

To ensure fair evaluation, a test set is first split off of the data. Training and validation is done on the 3rd nested LHS, which is half of the data. The other half (not an LHS) is used as test set.

For model training, the Adam optimizer was used. Typical learning rates were between 0.0001 and 0.001. Batch sizes range from 4 to 256 and epoch numbers are between 500 and 2000.

Results

As expected from the dynamics involved, the ship motions in the first minute after water intake strongly depend on the damage location. Of course, conditions can play an important role as well, but condition coverage in the training data should allow the model to generalize over conditions. As seen in Figure 6, with only 1 minute of motion data after the

damage event, a perfect relation to the damage location is found.

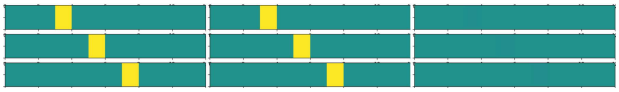

Figure 6: Damage locations in test set based on 1 minute of motion data. Left shows the expected location, middle shows the retrieved location and right shows the error. This is the raw neural network output, without any threshold.

For the ship attitude prediction after 30 minutes, a slightly longer input signal of 2.5 minutes was used. As output signal, a 100 second average was used. Figure 7 shows that roll, pitch and heave are predicted with reasonable accuracy. However, there are serious outliers. The reason for the outliers may have to do with the unpredictability of exact capsize moments, as we will see next.

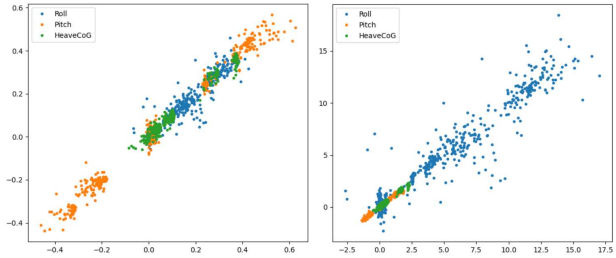

Figure 7: Ship attitude prediction (vertical labels) compared to true attitude, 30 minutes after damage event. Left shows raw neural network output, scaled to be between -1 and 1, right shows results scaled back to operational units.

Exact capsize moments are expected to be hard to predict. A ship may show little change in attitude for a while, which is still the case for the majority of scenarios after 30 minutes, but actual stability may be changing in the meantime. Also, progressive flooding may suddenly change the situation. As a consequence, even with longer samples to start with, no reliable result was obtained.

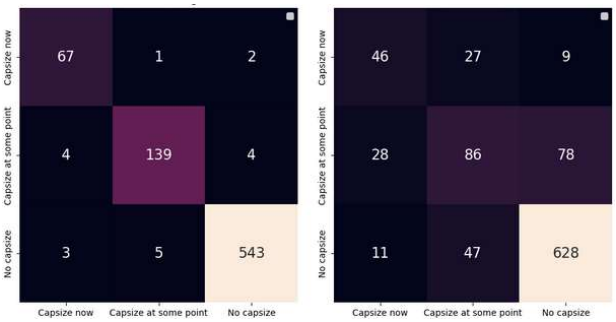

Figure 8: Confusion matrices for capsize now (within 10 minutes), a capsize sometime later or no capsize. Left shows the result on the training set. Right shows the result on the test set. The vertical labels denote the truth; the horizontal labels denote the predictions. Grouping the two capsize labels, in 32% of the cases where a capsize happened, no capsize was predicted.

The best result seems to be the prediction if a capsize will happen or not, see Figure 8. This shows very good results on the training set, but on the test set 32% of capsizes are missed, with added inaccuracies about when the capsize will happen.

5. CONCLUSIONS

Early Warning Systems facilitate risk mitigating actions before critical events, such as capsizing, occur. We show that such an EWS can be developed based on machine learning models trained on a dataset of dynamic flooding simulations. The input of this machine learning model consist of an interval of 6DOF ship motions recorded just after the damage whereas the quantities of interest are the damage location, the attitude of the ship after 30 minutes and the time to capsize.

The demonstrated approach works perfectly for quickly indicating the damage location. Also for an early estimate of what the ship will do in the next 30 minutes, the approach looks promising. Time-to-capsize estimates are so far not reliable. Further research could focus on related quantities, such as stability metrics, total water ingress and wave conditions, that can be used with first principles approaches to better estimate time to capsize.

ACKNOWLEDGEMENT

This work was partially funded by the EU European Defence Fund Project KOIOS (EDF-2021-DIGIT-R-FL-KOIOS). KOIOS is a project Funded by the European Union. Views and opinions expressed are however those of the author(s) only and do not necessarily reflect those of the European Union or European Defence Fund. Neither the European Union nor the granting authority can be held responsible for them.

REFERENCES

Jasionowski, A., "Decision support for ship flooding crisis management", 2011, *Ocean Engineering* 28(14), pp. 1568-1581.

Pinheiro L., Gomes A. H., Lopes N., Lopes S., Prior A., Santos J. A., Fortes, C.J.E.M., 2023, "Neural networks for optimization of an early warning system for moored ships in harbours", *Coastal Engineering Proceedings*.

Zhizheng W., Shengzheng W., He X., Faqin S., Qian L., Leyao L., Feng Q, 2024, "Research on ship safety risk early warning model integrating transfer learning and multi-

modal learning", *Applied Ocean Research* 150 pp. 104-139.

Louvros, P., Stefanidis, F., Boulougouris, E., Komianos, A., Vassalos, D., 2023, "Machine Learning and Case-Based Reasoning for Real-Time Onboard Prediction of the Survivability of Ships", 2023, *Journal of Marine Science and Engineering* 11(5):890.

Ölçer, A., Majumder, J., 2006, "A Case-based Decision Support System for Flooding Crises Onboard Ships", *Quality and Reliability Engineering International* 22(1), pp. 0748-8017.

Scholcz, T.P. and Mak, B., 2020, "Ship As a Wave Buoy: Estimating Full Directional Wave Spectra From In-Service Ship Motion Measurements Using Deep Learning", *International Conference on Offshore Mechanics and Arctic Engineering* Volume 1: Offshore Technology.

Mak, B. and Duz, B., 2019, "Ship As a Wave Buoy: Estimating Relative Wave Direction From In-Service Ship Motion Measurements Using Machine Learning", *International Conference on Offshore Mechanics and Arctic Engineering,* Volume 9.

Van 't Veer, R., and Van den Berg, J. and Boonstra, S., 2023, "A Unified Internal Flow Model with Fluid Momentum for General Application in Shipflooding and Beyond", *Journal of Marine Science and Engineering,* 11, 1175.

Uncertainty-aware decision support for real-time damage stability assessment in maritime emergencies

Panagiotis Louvros, *University of Strathclyde,* panagiotis.louvros@strath.ac.uk
Evangelos Stefanou, *University of Strathclyde,* evangelos.stefanou@strath.ac.uk
Nay Min Htein, *University of Strathclyde,* nay.min@strath.ac.uk
Evangelos Boulougouris, *University of Strathclyde,* evangelos.boulougouris@strath.ac.uk
Dracos Vassalos, *University of Strathclyde, d.vassalos@strath.ac.uk*

ABSTRACT

Effective decision-making in maritime emergencies relies on the accurate assessment of flooding progression and damage stability, yet significant uncertainties often impede timely and reliable predictions. This research presents a novel probabilistic decision support framework for real-time damage stability assessment, integrating advanced uncertainty quantification methods to enhance situational awareness and risk-informed decision-making.

Building upon existing machine learning (ML) and case-based reasoning (CBR) methodologies, this study introduces a Bayesian inference and Dempster-Shafer theory-based approach to quantify and propagate uncertainty in flooding scenarios. By incorporating probabilistic reasoning, the proposed framework provides confidence intervals for key stability indicators, such as time-to-capsize (TTC) and progressive flooding rates, ensuring that decision-makers are informed of the reliability of each prediction. A Monte Carlo-based sensitivity analysis further assesses the impact of input variability, improving the robustness of predictions under diverse damage conditions.

The decision support system is validated through extensive numerical simulations, demonstrating its ability to provide actionable insights with quantified uncertainty. Results indicate that integrating probabilistic methods into damage stability assessment significantly enhances prediction reliability compared to deterministic approaches, reducing the likelihood of unnecessary evacuations or delayed emergency responses.

By advancing uncertainty-aware decision support in maritime safety, this research contributes to improving emergency preparedness, aligning with evolving International Maritime Organization (IMO) safety frameworks.

Keywords: *damage stability, uncertainty, decision support, flooding, real time.*

INTRODUCTION

Maritime emergencies, particularly those involving flooding and damage stability, pose significant challenges to decision-makers due to the inherent uncertainties and the need for rapid, accurate assessments. Traditional approaches often rely on deterministic models that may not fully capture the variability and complexity of real-world scenarios. This paper addresses these challenges by presenting a comprehensive probabilistic decision support framework for real-time damage stability assessment, leveraging advanced uncertainty quantification and simulation validation techniques.

Motivation

In maritime emergencies, the ability to predict flooding progression and assess damage stability is crucial for ensuring the safety of the vessel and its crew. However, the presence of uncertainties—stemming from incomplete data, model approximations, and varying environmental conditions—can significantly affect the reliability of these predictions. Therefore, there is a pressing need for a decision support system that can quantify and manage these uncertainties to provide more robust and reliable assessments.

Contributions

The primary contributions of this work are the development of a probabilistic decision support framework that integrates Bayesian inference and Dempster-Shafer theory for data fusion and uncertainty quantification, incorporating Monte Carlo-based sensitivity analysis to assess the impact of input variability on flooding predictions. Lastly, confidence intervals for key stability indicators are provided, enhancing situational awareness and risk-informed decision-making.

BACKGROUND

Flooding risk assessment

Flooding risk assessment methods have evolved significantly to address the complex challenges of ship safety and stability in dynamic and emergency scenarios. These approaches increasingly rely on forensic investigations, probabilistic modelling, and quantitative analyses to identify vulnerabilities and guide design or operational improvements.

Forensic investigations, such as those highlighted in FLARE (FLARE, D5.9) play a pivotal role in understanding critical scenarios. By analyzing past incidents, reconstructing events, and extracting actionable lessons, these studies provide valuable insights into the mechanisms of flooding progression. Vassalos & Paterson (2021) emphasize the importance of incorporating these insights into the design of inherently safer vessels. This integration allows for the mitigation of flooding risks through advanced structural solutions and refined operational risk assessments. As forensic methods and tools have become more accessible and precise, they enable a deeper understanding of flooding phenomena. This, in turn, fosters innovation and improved measures for risk mitigation.

Probabilistic assessments and advanced numerical simulations are also reshaping flooding risk evaluation. Taimuri et al., (2023) demonstrate the application of these techniques in predicting flooding dynamics and assessing ship stability following hard groundings. Their methodology incorporates hydrodynamic topologies, ship dynamics, operational conditions, and structural properties. This holistic approach creates a more robust framework for evaluating damage extent and survivability under challenging conditions. By considering the progression of flooding and its interactions with design features, such assessments provide critical insights into safety margins and operational strategies.

Overall, the integration of forensic and probabilistic approaches into flooding risk assessments enhances the maritime industry's ability to prevent incidents, improve survivability, and achieve the twin goals of safety and operational efficiency.

Decision support systems

Decision support systems have found use in many sectors, and especially with the advent of sophisticated analysis tools, have greatly increased their presence.

DSS have found use in business settings(Arnott & Pervan, 2016), healthcare (Khalfallah et al., 2023), supply chain management (Gunasekaran & Ngai, 2012), agriculture (Manos et al., 2006), environmental issues (Matthies et al., 2007) and many more.

Below are some examples of decision support systems used in the naval architecture sector and especially surrounding vessel damage stability.

In Jasionowski, (2011) the author presents a decision support system that aims to help the crew on board in a flooding emergency. The author focuses on the concept of life-cycle risk formulated as a "vulnerability log" that captures the vulnerability of the vessel to flooding, from the opening of watertight doors, for example. Following that metric, the crew can appreciate the capacity of the vessel to withstand damage or to improve the watertight integrity during an accident.

In Pennanen et al., (2015), the authors introduce the concept behind a decision support tool for flooding emergencies. Further in Pennanen et al., (2015), the author demonstrates a complete methodology that also incorporates a vulnerability metric but also uses sensors to determine breach location and do time domain predictions of the survivability of the vessel. The decision support aspect of it is presented to the decision maker through the NAPA emergency computer and its functions are certainly helpful in understanding the gravity of each damage scenario. Further exploration of this approach is found in Ruponen et al., (2019). Similar work was carried out earlier by (Varela et al., (2014), which incorporated a hydraulic model,

progressive flooding algorithm and a 3D representation of the vessel and floodwater. Another approach by Ölçer & Majumder, (2006) uses Case-based reasoning to access a database of pre-run damage stability calculations and extract the relevant information to be given to the crew as a decision support function. Decision support methodologies have been developed for other naval architecture applications such as design (Ölçer et al., 2006).

Traditional deterministic models, such as those based on hydrostatic and hydrodynamic principles, provide valuable insights into flooding progression and damage stability. However, these models often assume perfect knowledge of input parameters and do not account for the uncertainties that arise in real-world scenarios. As a result, their predictions may be overly optimistic or pessimistic, leading to suboptimal decisions.

Machine Learning and Case-Based Reasoning

Case-based reasoning, or CBR, is a problem-solving approach that relies on relevant past cases to find solutions to emerging situations. (Kolodner, 1992) In this process, similar situations, which happened in the past, are searched for, and the experience gained in those situations is used. The problems and their solutions are represented by cases, and these cases are generally stored in a dynamic database (or case base).

Machine learning (ML) is a field of computer science that uses specialized algorithms, techniques, and processes for generating solutions to complicated problems that are hard to tackle with conventional programming approaches. Arthur Samuel's definition of machine learning in 1959 defined a subset in computing & programming. Samuel, (1959) demonstrated that machines can "learn" given only general directions and rules, in this instance, the game of checkers. Most importantly, in machine learning, the programmer does not design the program to solve a problem explicitly in predefined steps but instead sets up a framework of rules and functions that can achieve that by “learning”. This “learning” is possible given a labelled dataset that essentially contains examples of input-output pairs that the algorithm then “learns” to reproduce for new input data and provide correct results. This is called supervised machine learning. ML algorithms can solve many complex problems using this generic approach.

METHODOLOGY

The proposed decision support framework combines advanced uncertainty quantification methods with machine learning and case-based reasoning to provide reliable and actionable insights into the damaged stability status of the vessel during maritime emergencies. The following sections detail the key components of the framework. Figure 6 also gives an overview of the overall methodology.

The core of the framework is a set of predictions (ML & CBR) that are computed in real-time and are then fed into a probabilistic decision support system that integrates Bayesian inference and Dempster-Shafer theory to quantify and propagate uncertainty in flooding scenarios. This system provides confidence intervals for key stability indicators, such as time-to-capsize[1] (TTC) and Survival factor, ensuring decision-makers are informed of the reliability of each prediction. Time to capsize is a continuous variable usually in minutes, while survival factor is defined within SOLAS and captures the “state” of the vessel, 1 for certain survival and 0 for non-survival cases, with numbers in between also defined. (International Maritime Organization., 2009).

Data-driven damage stability predictions

The raw damage stability predictions are provided from 2 data-driven methods, machine learning and case-based reasoning. Both methods rely on a database of damage stability cases that is provided. Another similarity is that they are capable of providing predictions very fast and with low computational cost.

More information about these models is presented in Louvros et al. (2023).

Uncertainty Quantification

In the most general sense, the uncertainty in an estimated or scientifically calculated value which is the root-sum-square of the uncertainty in each input variable multiplied by the sensitivity of the result to a change in that variable.(ITTC, 2017).

[1] Generally defined as the time until the vessel sinks, capsizes

Accurate damage stability assessment depends on input data, yet such data is inherently uncertain. This research identifies key sources of uncertainty—ranging from human and sensor errors to discretization of continuous variables—and embeds them explicitly within the decision-support methodology. Human observations (e.g., crew-reported damage) and technical sensors are prone to errors such as false positives/negatives or drift, while practical input constraints, like compartmental discretization, result only in approximate representations of ship conditions.

To address these limitations, the methodology integrates probabilistic modelling at multiple stages. Rather than relying on deterministic inputs, observational data and human assessments are treated as probabilistic distributions centred on estimated values, acknowledging inherent subjectivity and cognitive biases (see Figure 1). For example, a damage opening size may be over- or under-estimated, as was the case in MV Concordia or HNoMS Helge Ingstad lately. Additionally, a priori statistical distributions of damage parameters (e.g., breach length, location) are incorporated to refine predictions through weighted averaging.

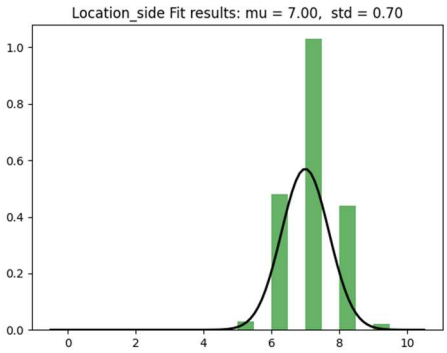

Figure 1. Location density of damage distribution used in MC analysis. X-axis corresponds to vessel length split in ten parts. Y-axis is part of total sample.

By applying a distribution of input data and then sampling all the possible permutations, an extended "input space" is created. After evaluating each of the generated inputs, using the two methods, a distribution of predictions is generated, as seen in Figure 2.

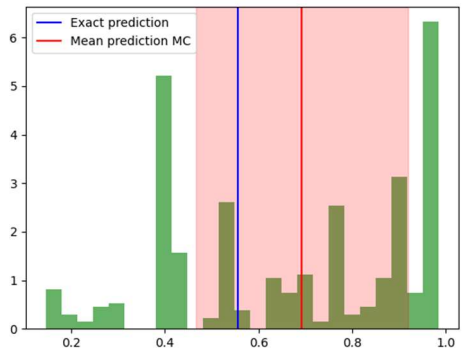

Figure 2. Survival factor histogram from 400 samples of a case showing the variability in the results when noise is added. The exact prediction is a derived from the given input while the distribution of the other predictions is the result of each of the 400 randomly sampled cases derived from the damage values distribution (as seen in Figure 1).

Since the variability in the input data is normally distributed, any prediction from the distribution can be evaluated as equally possible. The variability of the predictions, or lack thereof, provides important information regarding the uncertainty.

Despite these refinements, cumulative uncertainties remain due to model calibration, training data limitations, and the somewhat arbitrary nature of the similarity function. Recognizing this, the methodology emphasizes probabilistic outputs and avoids binary decisions, aiming instead to support situational awareness and informed judgment under uncertainty.

Bayesian Inference

Bayesian inference (Bayes & Price, 1763) is a statistical method that updates the probability of a hypothesis as more evidence or information becomes available. In the context of damage stability assessment, Bayesian inference can be used to quantify the uncertainty in flooding predictions by updating the probability distributions of key parameters based on new data.

To integrate predictions from two methods—Machine Learning (ML) and Case-Based Reasoning (CBR)—the combined prediction is computed as a weighted average, where the weights are inversely proportional to the variances (i.e., squared standard deviations) of each prediction methods are equally accurate except for their estimated uncertainty (Bishop, 2006).

The combined prediction is calculated as:

$$CB = \frac{\left(\frac{\text{ML Prediction}}{\text{ML Std}^2} + \frac{\text{CBR Prediction}}{\text{CBR Std}^2}\right)}{\left(\frac{1}{\text{ML Std}^2} + \frac{1}{\text{CBR Std}^2}\right)} \quad 1.$$

where:

ML Prediction and *CBR Prediction* are the individual outputs from each method.

ML Std and *CBR Std* are the associated standard deviations (uncertainties).

This formulation gives greater weight to predictions with lower variance, reflecting higher confidence in those estimates.

Dempster-Shafer Theory

Dempster-Shafer theory (Koks & Challa, 2005; Shafer, 2016) is a mathematical framework for combining evidence from different sources and reasoning with uncertainty. It extends the traditional probability theory by allowing for the representation of ignorance and the combination of evidence from multiple sources. This method is used to aggregate all predictions into a single data point expressed through the setting of threshold values that correspond to a "dangerous situation". Instead of providing exact Sfac or TTC values, those predictions are used to express the "belief" or "disbelief" that a dangerous flooding incident is expected. This danger is understood here to mean that there is a significant risk to human life, and an evacuation should be ordered. The belief then means that this dangerous scenario is happening/will happen, and the disbelief is the inverse. By adjusting the thresholds for SFAC and TTC, the belief-disbelief can be moved accordingly, corresponding to more "aggressive" or "conservative" outcomes.

For each prediction generated by the Decision Support Tool (DST), the framework quantifies confidence using three distinct components based on the Dempster-Shafer Theory of evidence:

Belief (b): Represents the degree of confidence that the prediction satisfies a specified condition (e.g., remaining below a critical threshold).

Disbelief (d): Reflects the degree of confidence that the prediction contradicts the specified condition.

Uncertainty (u): Captures the residual uncertainty due to lack of evidence, such that the total sum of belief, disbelief, and uncertainty is equal to one (i.e., $b + d + u = 1$).

Given a predicted value, its associated standard deviation (σ), and a predefined threshold (T), the belief masses are calculated as follows:

Given:

Prediction = predicted value

σ = standard deviation of the prediction

T = threshold value

The components are calculated as follows:

$$b = \max\left(0, \min\left(1, \frac{T - \text{prediction}}{2 \cdot \sigma}\right)\right) \quad 2.$$

$$d = \max\left(0, \min\left(1, \frac{\text{prediction} - T}{2 \cdot \sigma}\right)\right) \quad 3.$$

$$u = 1 - b - d. \quad 4.$$

This formulation enables the DST to express not only whether a condition is likely to be satisfied or not, but also how uncertain the system is due to prediction variance. By incorporating standard deviation directly into the belief structure, the method supports more nuanced and risk-aware decision-making.

To aggregate evidence from two sources, the DST framework uses Dempster's Rule of Combination, (Koks & Challa, 2005; Shafer, 2016) which accounts for both agreement and conflict between them. Each source provides belief masses in terms of belief (b), disbelief (d), and uncertainty (u). The rule first calculates a **conflict factor** (k), representing the degree of disagreement:

$$k = b_1 \cdot d_2 + d_1 \cdot b_2 \quad 5.$$

If $k = 1$, the sources are in total conflict and cannot be combined.

When $k < 1$, the combined belief masses are computed using the following normalized formulas:

Combined Belief:

$$b_{\text{combined}} = \frac{b_1 \cdot b_2 + b_1 \cdot u_2 + u_1 \cdot b_2}{1 - k} \quad 6.$$

Combined Disbelief:

$$d_{\text{combined}} = \frac{d_1 \cdot d_2 + d_1 \cdot u_2 + u_1 \cdot d_2}{1 - k} \quad 7.$$

Combined Uncertainty:

$$u_{\text{combined}} = \frac{u_1 \cdot u_2}{1 - k} \quad 8.$$

The normalization term *(1 − k)* ensures that conflicting evidence reduces overall confidence, preventing overestimation of certainty when sources disagree.

The combination of all the above is presented to the user as seen below (Figure 3 and Figure 4).

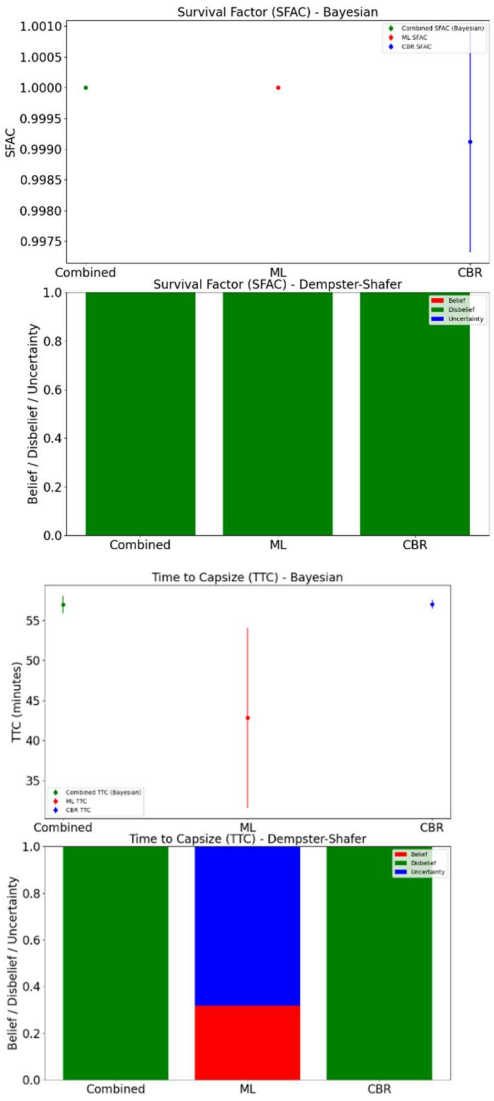

Figure 3. Example of both fusion and uncertainty quantification methods. Notice the DST outputs for belief in a dangerous situation=Red, Disbelief=Green, Uncertainty=Blue.

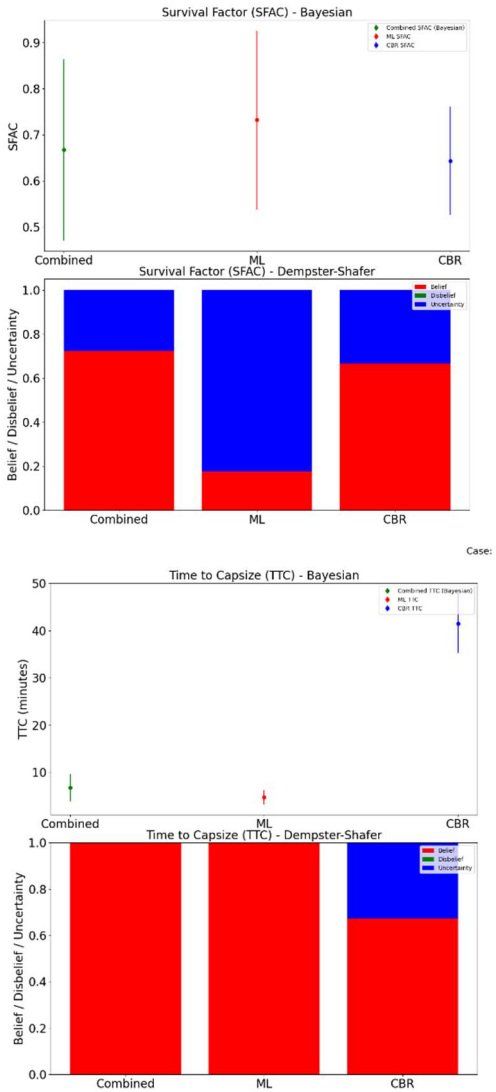

Figure 4. Example of methodology where belief is returned as high with also considerable uncertainty in SFAC.

Decision support

The objective of the methodology presented has always been to furnish a decision support system with the necessary data to aid the crew during the emergency.

The main item of information that is missing during an emergency flooding incident is the projected time to capsize, and in other cases, whether the vessel will sink or not. Usually, such an answer is hard to provide since the physical phenomena linked with damaged stability are either hard to calculate, and several key input data are missing, such as the vessel's loading condition, breach size, extent of flooding, flooding rates, etc.

For a decision support system to function as intended, the inputs must be simple to come by and adequately describe largely the phenomenon of flooding and loss of stability.

In the present methodology, the inputs (from the crew or sensors) have to do with the damage extent and location. Based on these features, CBR is able to find similar cases, and machine learning has trained models using them as input features to "explain" the target features that are common for both methodologies and are mostly the time to capsize (continuous) and survival factor (continuous but also binary or class).

In Figure 5 predictions after 10 simulated damage data updates showing values for TTC & SFAC including confidence intervals and belief in a hazardous situation. It is a demonstration of sequential damage updates given and used to derive predictions that is processed according to the methodology presented before.

The data returned can be explained simply by the "belief" metric and more elaborately by the actual values returned and associated confidence intervals. The belief is characterized as "High", "Medium" or "Low" and should be understood as "The belief that the vessel is in imminent peril."

A high belief, therefore signifies a high certainty that the vessel may sink while a low belief that the vessel is expected to remain afloat and upright. This can also be easily codified with colours. Uncertainty in the belief can be handled conservatively by being assigned as potentially dangerous.

For the actual values of TTC and SFAC, the safe or unsafe consequence of the value requires understanding and calibration. The limits used in this methodology are:

1. SFAC: Anything above 0.9 is safe, below unsafe.
2. TTC: 50 min and above is indicating of a survival case.

Note that the values used are not necessarily indicative of reality.

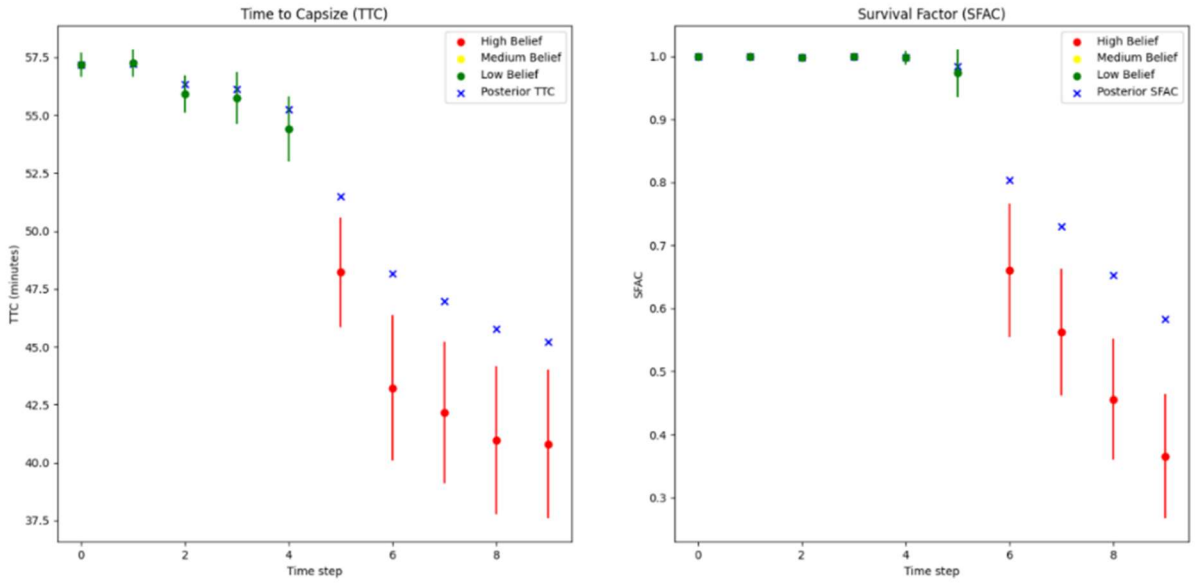

Figure 5. Predictions after 10 simulated damage data updates showing values for TTC & SFAC including confidence intervals and belief in a hazardous situation.

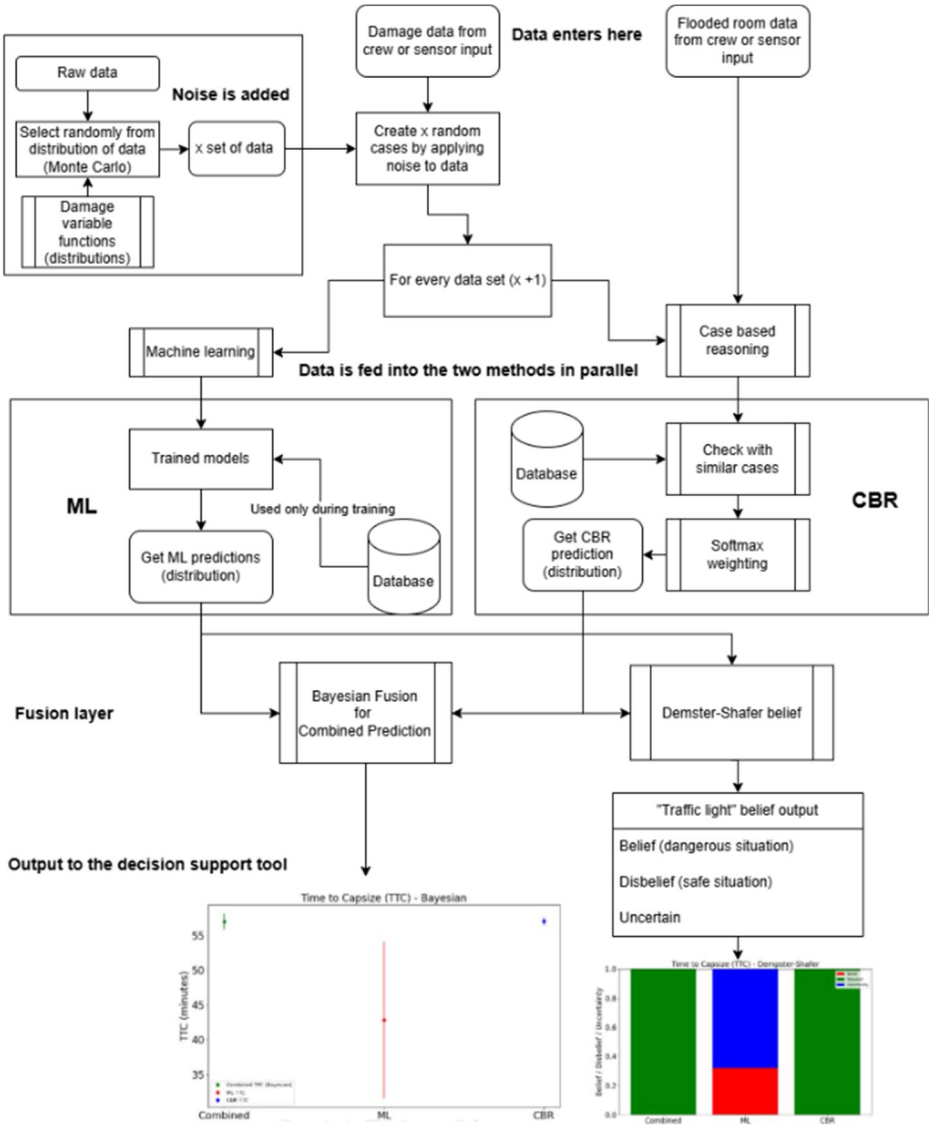

Figure 6. Complete methodology presented as a flowchart

CONCLUSION

This paper presents a novel probabilistic decision support framework for real-time damage stability assessment in maritime emergencies. By integrating advanced uncertainty quantification methods, the framework provides reliable and actionable insights, enhancing situational awareness and risk-informed decision-making. The computational cost of the methodology is kept very low as the "heavy" computations are not needed in real-time. The results of several realistic case studies demonstrate the effectiveness and robustness of the proposed approach, paving the way for its practical application in maritime safety and emergency management.

REFERENCES

Louvros, P., Stefanidis, F., Boulougouris, E., Komianos, A., & Vassalos, D. (2023). Machine Learning and Case-Based Reasoning for Real-Time Onboard Prediction of the Survivability of Ships. *Journal of Marine Science and Engineering*, *11*(5), 890.

https://doi.org/10.3390/jmse11050890

Flooding Accident Response (FLARE) deliverable D5.9 (Forensic Investigation of critical scenarios)

Bayes, T., Price, R. (1763). An Essay towards solving a Problem in the Doctrine of Chance. By the late Rev. Mr. Bayes, communicated by Mr. Price, in a letter to John Canton, A.M.F.R.S. *Philosophical Transactions of the Royal Society of London*. **53**: 370–418. doi:10.1098/rstl.1763.0053.

Arnott, D., & Pervan, G. (2016). A Critical Analysis of Decision Support Systems Research Revisited: The rise of Design. In L. P. Willcocks, C. Sauer, & C. M. Lacity (Eds.), *Enacting Research Methods In Information Systems* (1st ed., Vol. 3, pp. 43–103). Springer International Publishing AG Switzerland. https://doi.org/10.1007/978-3-319-29272-4

Bishop, C. M. (2006). *Pattern Recognition and Machine Learning. Springer.*

Gunasekaran, A., & Ngai, E. W. T. (2012). Decision support systems for logistics and supply chain management. *Decision Support Systems*, *52*(4), 777–778. https://doi.org/10.1016/J.DSS.2011.11.012

International Maritime Organization. (2009). *SOLAS, consolidated edition, 2009 : consolidated text of the International Convention for the Safety of Life at Sea, 1974, and its Protocol of 1988 : articles, annexes and certificates.* International Maritime Organization.

ITTC. (2017). *ITTC Quality System Manual Recommended Procedures and Guidelines, Guideline to Practical Implementation of Uncertainty Analysis*.

Jasionowski, A. (2011). Decision support for ship flooding crisis management. *Ocean Engineering*, *38*(14–15), 1568–1581. https://doi.org/10.1016/j.oceaneng.2011.06.002

Khalfallah, H. Ben, Jelassi, M., Demongeot, J., & Saoud, N. B. Ben. (2023). Decision support systems in healthcare: systematic review, meta-analysis and prediction, with example of COVID-19. *AIMS Bioengineering*, *10*(1), 27–52. https://doi.org/10.3934/bioeng.2023004

Koks, D., & Challa, S. (2005). *An Introduction to Bayesian and Dempster-Shafer Data Fusion*.

Kolodner, J. L. (1992). An Introduction to Case-Based Reasoning*. In *Artificial Intelligence Review* (Vol. 6).

Manos, B., Bournaris, T., Kamruzzaman, M., Begum, M., Anjuman, A., & Papathanasiou, J. (2006). Regional Impact of Irrigation Water Pricing in Greece under Alternative Scenarios of European Policy: A Multicriteria Analysis. *Regional Studies*, *40*(9), 1055–1068. https://doi.org/10.1080/00343400600928335

Matthies, M., Giupponi, C., & Ostendorf, B. (2007). Environmental decision support systems: Current issues, methods and tools. *Environmental Modelling & Software*, *22*(2), 123–127. https://doi.org/10.1016/J.ENVSOFT.2005.09.005

Ölçer, A. I., & Majumder, J. (2006). A Case-based decision support system for flooding crises onboard ships. *Quality and Reliability Engineering International*, *22*(1), 59–78. https://doi.org/10.1002/qre.748

Ölçer, A. I., Tuzcu, C., & Turan, O. (2006). An integrated multi-objective optimisation and fuzzy multi-attributive group decision-making technique for subdivision arrangement of Ro-Ro vessels. *Applied Soft Computing Journal*, *6*(3), 221–243. https://doi.org/10.1016/j.asoc.2005.01.004

Pennanen, P., Ruponen, P., & Ramm-Schmidt, H. (2015). Integrated decision support system for increased passenger ship safety. *Damaged Ship III*. https://www.researchgate.net/publication/283878182

Ruponen, P., Pennanen, P., & Manderbacka, T. (2019). On the alternative approaches to stability analysis in decision support for damaged passenger ships. *WMU Journal of Maritime Affairs*, *18*(3), 477–494. https://doi.org/10.1007/s13437-019-00186-8

Samuel, A. L. (1959). *Some Studies in Machine Learning Using the Game of Checkers*.

Shafer, G. (2016). Dempster's rule of combination. *International Journal of Approximate Reasoning*, *79*, 26–40. https://doi.org/10.1016/J.IJAR.2015.12.009

Taimuri, G., Ruponen, P., & Hirdaris, S. (2023). A novel method for the probabilistic assessment of ship grounding damages and their impact on damage stability. *Structural Safety*, *100*, 102281. https://doi.org/10.1016/J.STRUSAFE.2022.102281

Varela, J. M., Rodrigues, J. M., & Guedes Soares, C. (2014). On-board decision support system for ship flooding emergency response. *Procedia Computer Science*, *29*, 1688–1700. https://doi.org/10.1016/j.procs.2014.05.154

Vassalos, D., & Paterson, D. (2021). Towards unsinkable ships. *Ocean Engineering*, *232*, 109096. https://doi.org/10.1016/J.OCEANENG.2021.109096

SCHOOL OF NAVAL ARCHITECTURE
AND MARINE ENGINEERING
NATIONAL TECHNICAL UNIVERSITY OF ATHENS

H.I.M.T.
HELLENIC INSTITUTE
OF MARINE TECHNOLOGY